Synthesis of DNA and RNA containing rigid spin- and fluorescent labels for studies by EPR and fluorescence spectroscopies

Anna-Lena Johanna Segler

Faculty of Physical Sciences
University of Iceland
2021

Synthesis of DNA and RNA containing rigid spin- and fluorescent labels for studies by EPR and fluorescence spectroscopies

Anna-Lena Johanna Segler

Dissertation submitted in partial fulfillment of a
Philosophiae Doctor degree in Chemistry

Advisor
Prof. Snorri Th. Sigurdsson

PhD Committee
Prof. Guðmundur G. Haraldsson
Prof. Óttar Rolfsson
Asst. Prof. Benjamín Ragnar Sveinbjörnsson

Opponents
Prof. Claudia Höbartner
Dr. Stefán Jónsson

Faculty of Physical Sciences
School of Engineering and Natural Sciences
University of Iceland
Reykjavik, September 2021

Synthesis of DNA and RNA containing rigid spin- and fluorescent labels for studies by EPR and fluorescence spectroscopies
Rigid spin- and fluorescent labels for DNA and RNA
Dissertation submitted in partial fulfillment of a *Philosophiae Doctor* degree in Chemistry

Faculty of Physical Sciences
School of Engineering and Natural Sciences
University of Iceland
Dunhagi 3
107, Reykjavik
Iceland
Telephone: 525 4000

Bibliographic information:
Anna-Lena Johanna Segler, 2021, *Synthesis of DNA and RNA containing rigid spin- and fluorescent labels for studies by EPR and fluorescence spectroscopies*, PhD dissertation, Faculty of Physical Sciences, University of Iceland, 248 pp.

ISBN 978-9935-9564-8-4

Printing: Háskólaprent ehf.
Reykjavik, Iceland, September 2021

Abstract

To gain information about the function of nucleic acids, their structure and dynamics need to be investigated. Electron paramagnetic resonance (EPR)- and fluorescence spectroscopies are highly sensitive and valuable techniques to study nucleic acids. These methods require incorporation of spin- and fluorescent labels prior to measurements. This doctoral dissertation focuses on the synthesis of rigid spin- and fluorescent labels and their incorporation into DNA and RNA for the study of structure and dynamics of nucleic acids by EPR- and fluorescence spectroscopies.

The first part of the thesis describes a protecting group strategy to address a long-standing problem associated with spin-labeling by chemical synthesis of nucleic acids, namely reduction of nitroxides during solid-phase synthesis. A benzoyl group was used to protect the nitroxide by reducing the nitroxide to the corresponding hydroxylamine, followed by benzoylation. The method was used to incorporate the rigid spin label **Çm** into RNA with quantitative spin-labeling efficiency. This protecting-group strategy can be used as a general method to incorporate nitroxide spin-labels into nucleic acids by the phosphoramidite approach.

The second part of this thesis focuses on labeling of specific nucleic acids with rigid spin- and fluorescent labels, namely **Ç**, **Çm** and **Çmf**. The rigid spin labels **Ç** and **Çm** were incorporated into DNA and RNA, respectively, for measurements in the research group of Prof. Thomas F. Prisner at the Goethe University in Frankfurt, by pulsed electron-electron double resonance (PELDOR) spectroscopy. Furthermore, **Çmf**, the fluorescent derivative of **Çm**, was incorporated into various RNAs to investigate them by fluorescence spectroscopy, by the research group of Prof. Josef Wachtveitl at the Goethe University in Frankfurt.

The third part of the thesis describes the design and synthesis of the new rigid spin labels **Ċ** and **Ċm** for DNA and RNA, respectively, that are carbazole-derived nitroxides and analogues of cytidine. Crystal structure analysis indicated that **Ċ** and **Ċm** are more rigid than the rigid spin labels **Ç** and **Çm**. **Ċ** and **Ċm** were incorporated into several oligonucleotides and showed to be non-perturbing of duplex structure. These new rigid spin labels are promising candidates for future studies of DNA and RNA structures and dynamics by pulsed EPR methods.

Útdráttur

Til að fá vitneskju um virkni kjarnsýra er nauðsynlegt að rannsaka byggingu og hreyfingu þeirra. Litrófsgreiningar sem byggja á rafeindasegulómun (e. electron paramagnetic resonance, EPR) og fljúrljómun eru mjög næmar og gagnlegar aðferðir til að rannsaka kjarnsýrur. Til að unnt sé að beita slíkum mæliaðferðum er nauðsynlegt að innleiða meðseglandi- og flúrljómandi merki inn í kjarnsýrurnar. Þessi doktorsritgerð lýsir efnasmíði á stífum spuna- og flúrljómandi merkjum og innleiðingu þeirra inn í DNA og RNA til rannsókna á byggingu og hreyfingu kjarnsýra með EPR- og flúrljómunarlitrófsgreiningum.

Fyrsti hluti ritgerðarinnar lýsir hvernig tekið var á þrálátu vandamáli sem tengist spunamerkingu kjarnsýra, nánar tiltekið afoxun nítroxíða þegar kjarnsýrur eru smíðaðar á föstu efni (e. solid-phase synthesis). Bensóýl hópur var notaður til að vernda nítroxíðið með því að afoxa það í hýdroxýlamín, sem í kjölfarið var bensóýlað. Þessi aðferð var notuð til að innleiða stífa spunamerkið **Çm** ólaskað inn í RNA. Þessa verndunaraðferð ætti að nýtast almennt til að innleiða nítroxíð spunamerki inn í kjarnsýrur með fosfóramidíð efnasmíðum (e. phosphoramidite approach).

Í öðrum hluta ritgerðarinnar er fjallað um merkingu ákveðinna kjarnsýra með stífum spuna- og flúrljómandi merkjum, nánar tiltekið **Ç**, **Çm** og **Çmf**. Stífu spunamerkin **Ç** og **Çm** voru innleidd í DNA og RNA sameindir til rannsókna í rannsóknarhópi prófessor Thomas F. Prisner við Goethe Háskólann í Frankfurt, með PELDOR (e. pulsed electron-electron double resonance) litrófsgreiningu. Þar að auki var **Çmf**, flúrljómandi afleiðan af **Çm**, innleidd í ýmsar RNA sameindir til rannsókna með flúrljómun í rannsóknarhópi prófessor Josef Wachtveitl við Goethe Háskólann í Frankfurt.

Loks lýsir þriðji hluti ritgerðinnar hönnun og smíði á nýjum stífum spunamerkjum, **Ċ** og **Ċm**, fyrir DNA og RNA, sem hafa karbasól byggingu og eru afleiður af sýtidíni. Kristalgreining bendir til að **Ċ** og **Ċm** séu enn stífari en spunamerkin **Ç** og **Çm**. **Ċ** og **Ċm** voru innleidd í ýmis fákirni (e. oligonucleotides) og var sýnt fram á að **Ċ** og **Ċm** raska ekki byggingu tvístrendinga (e. duplex). Þessi nýju stífu spunamerki eru vænleg fyrir rannsóknir á byggingu og hreyfingu DNA og RNA með púlsuðum EPR mælingum.

Table of Contents

List of Figures

List of Schemes

List of Tables

List of Publications

I. Gustmann H., Segler A. J., Gophane D. B., Reuss A. J., Grünewald C., Braun M., Weigand J. E., Sigurdsson S. T. and Wachtveitl J., Structure guided fluorescence labeling reveals a two-step binding mechanism of neomycin to its RNA aptamer. *Nucleic Acids Res.*, **2019**, *47*, 15-28.

II. Juliusson H. Y.,† Segler A. J.† and Sigurdsson S. T., Benzoyl-protected hydroxylamines for improved chemical synthesis of oligonucleotides containing nitroxide spin labels. *Eur. J. Org. Chem.*, **2019**, *2019*, 3799-3805. †These authors contributed equally.

III. Segler A. J. and Sigurdsson S. T., A carbazole-derived nitroxide that is an analogue of cytidine – a rigid spin label for DNA and RNA. **2021**, https://doi.org/10.1021/acs.joc.1c01176.

Abbreviations

A	adenine
Ac	acetyl
Boc	*tert*-butyloxycarbonyl
Bz	benzoyl
C	cytidine
Calcd	calculated
CD	circular dichroism
CW	continuous wave
CRC	collaborative research centre
Cryo-EM	cryogenic electron microscopy
Ç	rigid spin-labeled nucleoside “C-spin” for DNA
Çm	rigid spin-labeled nucleoside “C-m-spin for RNA
Ċ	rigid spin-labeled nucleoside “C-dot for DNA
Ċm	rigid spin-labeled nucleoside “C-m-dot for RNA
DEER	double electron-electron resonance
DMA	dimethylacetamide
DMF	dimethylformamide
DMAP	dimethylamino pyridine
DMTCl	4,4′ Dimethoxytrityl chloride
DNA	deoxyribonucleic acid
DPAGE	denaturing polyacrylamide gel electrophoresis
DQC	double quantum coherence
E	FRET efficiency
ENDOR	electron nuclear double resonance
EPR	electron paramagnetic resonance
FRET	Förster resonance energy transfer
G	guanine
HPLC	high-performance liquid chromatography
iBu	isobutyryl
K_d	dissociation constant
*m*CPBA	*meta*-chloroperbenzoic acid
mRNA	messenger RNA
miRNA	micro RNA
NaOAC	sodium acetate
NMR	nuclear magnetic resonance
NOE	nuclear Overhauser effect
nt	nucleotides
PAc	phenoxyacetyl

PELDOR	pulsed electron-electron double resonance
PPG	photolabile protecting group
RIDME	relaxation induced dipolar modulation enhancement
RNA	ribonucleic acid
rRNA	ribosomal RNA
SDSL	site-directed spin labeling
SELEX	systematic evolution of ligands by exponential enrichment
SIFTER	single frequency technique for refocusing dipolar couplings
siRNA	small interfering RNA
snRNA	small nuclear RNA
T	thymine
TBAF	tetrabutylammonium fluoride
TBDMS	*tert*-butyldimethylsilyl
TBDPS	*tert*-butyldiphenylsilyl
TEMPO	2,2,6,6-tetramethylpiperidine-1-oxyl
TFA	trifluoroacetic acid
THF	tetrahydrofuran
TLC	thin layer chromatography
tRNA	transfer RNA
T_M	melting temperature
UV-vis	ultraviolet-visible
ε	molar extinction coefficient
Φ	fluorescence quantum yield

Acknowledgements

I wish to express my deepest gratitude to my advisor Prof. Snorri Þór Sigurðsson for his continuous guidance, encouragements, and patience throughout my PhD studies. I thank him sincerely for his unwavering support, for believing in me and helping me grow, professionally and personally. His endless source of knowledge, scientific mindset, problem-solving abilities and writing skills have been inspiring.

I sincerely thank my doctoral committee members, Prof. Guðmundur G. Haraldsson, Prof. Óttar Rolfsson and Asst. Prof. Benjamín Ragnar Sveinbjörnsson for their insightful comments and encouragements. I would also like to thank my distinguished opponents, Prof. Claudia Höbartner and Dr. Stefán Jónsson for taking their time to review my work.

I am grateful for the fruitful collaboration I have had during my studies and would like to thank my collaborators in Frankfurt Prof. Josef Wachtveitl and Prof. Thomas F. Prisner and their present and past group members, especially Dr. Henrik Gustmann, Christoph Kaiser, Florian Hurter, Konstantinos Stamatakis, Dr. Nicole Erlenbach, Dr. Thilo Hetzke, Dr. Jörn Plackmeyer, Dr. Alberto Collauto and Maximilian Gauger. I would also like to thank Dr. Haraldur Yngvi Júlíusson for a gainful in-house collaboration, Prof. Krishna K. Damodaran for solving the crystal structures of **Ċ** and **Ċm** and Dr. Sigríður Jónsdottir for assistance with collecting analytical data for structural characterization of new compounds.

I would like to thank past and present members of the Sigurdsson Research Group for helpful discussions in the laboratory and at group meetings. I am extremely grateful to Dr. Thomas Halbritter, Dr. Sucharita Mandal and Dr. Haraldur Yngvi Júlíusson for their close friendship, support, and their immense help during my doctoral studies.

I gratefully acknowledge The Icelandic Centre of Research (Rannís) and the University of Iceland Teaching Assistantship Grant for funding. I also thank the Collaborative Research Centre 902 (CRC 902, funded by the German research foundation, DFG) for funding my travels to Germany, and for giving me the opportunity to participate in the summer- and winter schools of the CRC 902.

My deepest thanks go to my family for all their love and support, especially my parents, my siblings, and my partner, you mean the world to me.

1 Objective and scope of the PhD thesis

To yield a deeper understanding of the function of nucleic acids it is of utmost importance to investigate their structure and dynamics. This doctoral dissertation is based on the synthesis of rigid spin- and fluorescent labels and their incorporation into DNA and RNA for the study of structure and dynamics of nucleic acids by both electron paramagnetic resonance (EPR)- and fluorescence spectroscopy.

The thesis is divided into three objectives. The first objective, described in **Chapter 3**, focuses on a protecting group strategy for improved spin-labeling efficiency of nucleic acids through the phosphoramidite approach. The second objective, presented in **Chapter 4**, describes the labeling of various DNA and RNA constructs with rigid labels, through the phosphoramidite approach, for analysis by both EPR- and fluorescence spectroscopies. The third objective, discussed in **Chapter 5**, is the design and synthesis of new rigid carbazole-derived nitroxide spin-labels and their incorporation into both DNA and RNA.

In **Chapter 2**, an introduction is given to this doctoral dissertation. The importance and the function of nucleic acids is described, with emphasis on various RNAs. The most common techniques used for the study of nucleic acids are discussed, with the focus on EPR spectroscopy. Furthermore, various semi-rigid and rigid nitroxide spin-labels for EPR studies are introduced. Finally, different spin-labeling methods for nucleic acids are described where the phosphoramidite approach, including the solid-phase synthesis of oligonucleotides, is explained in detail.

In **Chapter 3**, the advantages and limitations of spin-labeling by the phosphoramidite approach are introduced. Different approaches are described to address these limitations. A protecting group strategy for nitroxides is discussed where the rigid spin label **Çm**[1] (**Figure 1.1**) is used for evaluating the method. The synthesis of **Çm-Bz** (**Figure 1.1**), the benzoyl protected form of **Çm**, is presented as well as the incorporation of **Çm** into RNA by usage of the protected form. It was shown that the benzoyl group was stable through the RNA synthesis and that it was easily removed using standard oligonucleotide deprotection conditions, returning **Çm** in quantitative yields. This strategy, to protect the nitroxide during oligonucleotide synthesis, has eliminated the biggest problem of nitroxide spin-labeling by

the phosphoramidite approach, namely, the reduction of the nitroxide to the EPR-silent amine. This method opened new possibilities to spin-label longer RNAs and DNAs, which is exploited in **Chapter 4**.

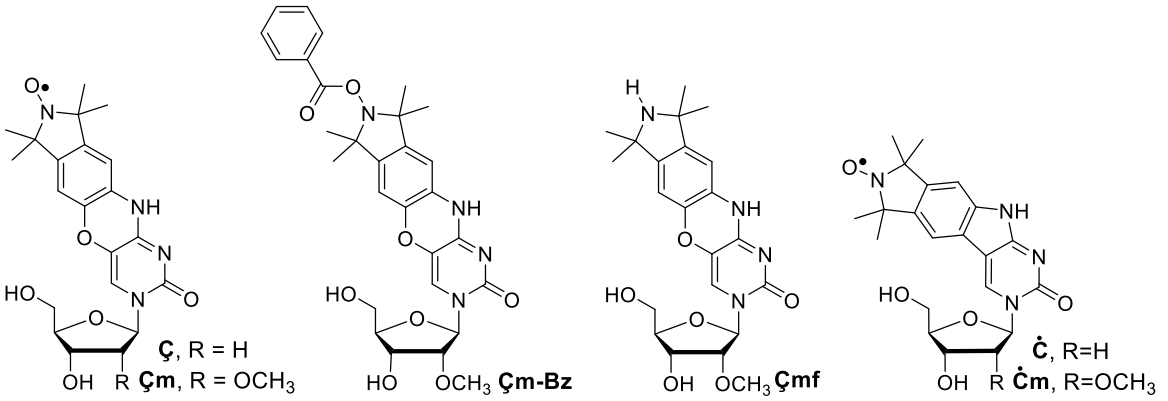

Figure 1.1. Structures of rigid spin labels **Ç**, **Çm**, **Ċ** and **Ċm**, the benzoyl protected **Çm-Bz** and the fluorescent label **Çmf**.

Chapter 4 describes labeling of nucleic acids with rigid spin- and fluorescent labels. The projects involving spin labeled nucleic acids are carried out in a collaboration with Prof. Thomas F. Prisner at the Goethe University in Frankfurt, Germany, where pulsed EPR methods are used to study the structure and dynamics of the spin-labeled nucleic acids. The spin labels **Ç**[2] and **Çm** were incorporated into various DNA and RNA constructs, respectively, by the use of the benzoyl protection of nitroxides, described in **Chapter 3**. A background is given to every project and preliminary data from the collaborators described.

The latter part of **Chapter 4** describes the incorporation of **Çmf**,[1] the fluorescent derivative of **Çm**, into various RNAs. These projects were run in a collaboration with Prof. Josef Wachtveitl at the Goethe University in Frankfurt, Germany, where fluorescent studies were performed on the RNA samples to investigate their structure and dynamics. Each project is explained in detail and preliminary results from the collaborators are shown.

In **Chapter 5**, the design and synthesis of the new rigid spin labels **Ċ** and **Ċm** (**Figure 1.1**) is described. At the beginning of the chapter, the rigidity of **Ç** and **Çm** is discussed and questioned and the design of **Ċ** and **Ċm** is explained. This is followed by an introduction to different C-C cross-coupling reactions, which is the key step in the synthesis of **Ċ** and **Ċm**. Furthermore, different synthesis routes and reaction conditions that were tested for the synthesis of **Ċ** and **Ċm** are described in detail. The incorporation of **Ċ** and **Ċm** into DNA and RNA, respectively, is subsequently outlined. The rigid spin labels were

incorporated into the nucleic acids with high spin-labeling efficiency and were shown to be non-perturbing of duplex structure. These new rigid spin labels **Ċ** and **Ċm** are promising candidates for future studies of DNA and RNA structures and dynamics by pulsed EPR methods.

2 Introduction

Nucleic acids are biopolymers that are essential to all known forms of life. They were first discovered by the Swiss scientist Friedrich Mischer in 1869 as he isolated a few unknown phosphate rich molecules from white blood cells and since he discovered them inside the cells' nuclei he named them nuclein.[3-5] In 1889 Richard Altmann, a former student of Friedrich Mischer, discovered that nuclein behaved as acids and therefore renamed them to nucleic acids.[3] Albrecht Kossel performed groundbreaking work in the years 1885-1901 when he isolated the five bases of nucleic acids, adenine, thymine, cytosine, guanine, and uracil.[6] In 1938, William Astbury and his PhD student Florence Bell published the first X-ray photographs of DNA but the quality was low and, therefore, they were not able to propose a structure of the DNA.[7] In 1953, Rosalind Franklin came very near to solving the structure of DNA when she published the first high-resolution crystallographic photograph of DNA fibers.[8] By varying the water content of the DNA samples, she discovered that there were two forms of DNA, a dry "A" form and a wet "B" form. Further, she concluded that the nucleobases, that are forming hydrogen bonds, are turned inwards and the phosphate groups are turned outwards of what she suggested being a helical structure. In the same year, James Watson and Francis Crick solved the double helical structure of DNA.[9] Their discovery has been said to be one of the biggest breakthrough in scientific history.

Nucleic acids consist of two main types, deoxyribonucleic acid (DNA) and ribonucleic acid (RNA).[10] DNA has the important role to store and preserve genetic information and is well-suited for this purpose as the double helical structure always keeps a back-up of the genetic information and the DNA backbone is resistant to cleavage because it has no hydroxyl group at the 2'-position of the ribose.[5, 11] Even though DNA stores the genetic code in current times, there is a theory that RNA could have existed before DNA. It has been postulated that RNA emerged at the beginning of life on Earth and was at that time the genetic polymer of the first protocells.[12] The functions of RNA will be discussed in the following section.

2.1 Functions of RNA

RNA is transcribed from DNA into messenger RNA (mRNA), which is involved in the process of translation of the genetic code to proteins.[13-14] mRNA carries the genetic code to the ribosome, which is a ribonucleoprotein machinery made of proteins and ribosomal RNA (rRNA). In the ribosome, transfer RNA (tRNA) binds to the mRNA and transfers the right amino acid, decided by a three-letter genetic code, to a growing polypeptide chain.[15-16] In earlier times, this process was thought to be the main function of RNA but in the last decades it has been realized that RNA performs a variety of other functions in the cell.[17]

Various non-coding RNAs take part in gene regulation. For example, small nuclear RNAs (snRNAs) participate in gene regulation in the spliceosome, a large ribonucleoprotein complex made of snRNAs and various proteins.[18-19] In the spliceosome, the snRNAs take part in splicing of introns on pre-mRNA, a step in the process of production of mature-mRNA.[20] Both micro RNA (miRNA) and small interfering RNA (siRNA) are gene silencing RNAs.[21-22] miRNA consists of about 22 nucleotides (nt) and is a single-stranded RNA that binds to mRNA which leads to termination of gene expression or to degradation of the mRNA.[23-25] siRNA is a 20-27 nt long double-stranded RNA. It degrades mRNA after its transcription, preventing translation by binding to the mRNA.[22, 26] Another group of RNAs named ribozymes have catalytic behavior similar to enzymes and can catalyze a variety of biochemical reactions, for example cleavage and ligation of phosphodiester bonds.[27] Ribozymes have roles in replication, mRNA processing, splicing and are catalysts in the peptide formation in the aforementioned ribosome.[27-31]

Another group of non-coding regulatory RNAs are riboswitches that are typically found in the 5′-untranslated regions of bacterial mRNAs but have also been found in archaic and eukaryotic cells.[32-34] Riboswitches consist of two interacting domains, the aptamer region and the expression platform and together they can switch the gene expression “on” or “off”.[33-34] The aptamer binds with high affinity and specificity to a metabolite, which results in a structural change of the aptamer that regulates the gene expression.[35] About fifty natural riboswitches have been discovered, which has opened many possibilities in structural and synthetic biology through control of gene expression using simple-structured RNA without the involvement of proteins.[36] However, it is hard to reprogram gene expression with natural riboswitches because they and their ligands are inside the cells. Therefore, it is necessary to design and develop synthetic riboswitches that can bind to ligands *in vitro*.[37]

As for natural riboswitches, aptamers are the key part of synthetic riboswitches to recognize and bind ligands. By doing so they fold into a well-defined three-dimensional structure.[36] Aptamers are single stranded RNA or DNA oligonucleotides that contain between 25-100[38] nt and are known to bind amino acids,[39] proteins,[40-41] drugs,[42-43] and other small molecules.[44] Because of their high affinity and specificity, they have yielded a spectrum of applications as diagnostic agents,[45-46] biosensors,[47-48] and therapeutics.[49-51] A few synthetic aptamers will be introduced in **Chapter 4** of this dissertation.

Synthetic aptamers have been discovered by *in vitro* selection from a random library or "pool" of nucleic acids through a process called systematic evolution of ligands by exponential enrichment (SELEX) (**Figure 2.1**).[52] The typical SELEX method mainly consists of three steps: selection, partitioning and amplification.[53-54] The SELEX cycle begins with a large random library of RNA or DNA that are incubated with a target molecule that is normally immobilized on a surface. The second step is partitioning or in other words, elution. Here the unbound or the weakly bound oligonucleotides are removed. The bound oligonucleotides are eluted and amplified which yields in an enriched pool of binding aptamers. This enriched pool is subjected to a new SELEX cycle. Normally this cycle is repeated 10-20 times, until the resulting library is enriched enough with sequences that bind to the target with high affinity and specificity.

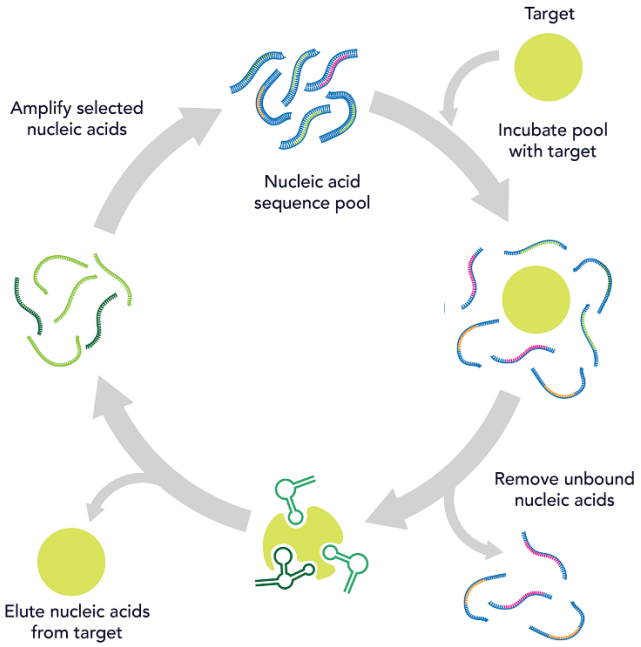

Figure 2.1. A scheme of the process of systematic evolution of ligands by exponential enrichment (SELEX). Figure courtesy of Integrated DNA Technology Inc.

To get an even better and deeper understanding of the properties and processes of nucleic acids, it is essential to study their structure and dynamics. The most commonly used techniques for such studies are described below.

2.2 Structure determination of nucleic acids

X-ray crystallography is one of the most powerful and sophisticated techniques used to study biomolecules.[55] It can resolve the three-dimensional structure of biomolecules at atomic resolution,[56-57] by passing X-rays through a crystalline sample, which gives a diffraction pattern.[58] The density of the electrons are laid out by measuring the angles and intensities of the rays, which provides the precise positions of the atoms. Though X-ray crystallography is a very useful technique, it does not come without limitations. To get structural information by X-ray crystallography, a highly diffractive single crystal is needed.[59] Growing crystals can be a tedious and time-consuming task and requires a large amount (milligrams) of the nucleic acid with high-purity.[60] Another drawback is that nucleic acids cannot be studied in their preferred solution state and, therefore, the crystal structure may not represent a biologically active conformation.[61] Also, X-ray crystallography provides a static view and, therefore, it is near impossible to study conformational changes with this technique.

Cryo-electron microscopy (cryo-EM) has in the last decades become a more frequently used technique to determine the structure and dynamics of nucleic acids[62-65] and proteins.[66] For this microscopic technique no crystals are needed as the measured sample is cryogenically preserved in aqueous solution during the measurement and, therefore, biomolecules can be investigated in their native state.[67] In cryo-EM, a transmission electron microscope is used to yield a magnified image of a sample by passing electron-beams through it, under cryogenic conditions to protect the sample from radiation damage.[68] In recent years, cryo-EM has emerged as a powerful tool but still the resolution has been low compared to X-ray crystallography, with a resolution of 2-4 Å.[69] However, two independent groups have recently been able to obtain images of proteins on an atomic scale with resolutions of 1.22 Å[70] and 1.25 Å.[71]

Nuclear magnetic resonance (NMR) spectroscopy is a high-resolution technique that is widely used to study nucleic acids[72] in solution under biologically relevant conditions.[73-76] Furthermore, NMR yields information about nucleic acid dynamics,[77] which is often related to their function.[78-80] However, NMR has some disadvantages. Due to inherently low

sensitivity of NMR, investigation of nucleic acids requires large amounts of isotopically labeled samples. Also, the measurements are normally limited to biomolecules that are smaller than 50 kDa because the increased anisotropy, associated with slower tumbling of large molecules in solution, leads to broadening of NMR peaks and the lack of spectral resolution due to the large number of signals.[81-82] Furthermore, three-dimensional structures of biomolecules by NMR are usually determined from nuclear Overhauser effect (NOE) experiments that give through-space information by dipolar coupling of nuclear spins.[83] Distances between the nuclear spins up to 5-6 Å can be determined[76, 83] and thus, it is not a well suited method to study three-dimensional structures of biomolecules. Finally, recording NMR and analyzing the data can be a very time-consuming process.

Fluorescence spectroscopy, a single-chromophore technique, is also used for the study of nucleic acids.[84-85] Even though it is a low-resolution technique, it is highly sensitive and therefore only small amounts of samples are needed. Furthermore, the measurements can be performed under biologically relevant conditions. Information can be gained by the ability of fluorophores to reflect changes in their microenvironment and can be seen by, for example, fluorescence emission quenching, spectral shifting, depolarization (anisotropy) and fluorescence lifetime measurements.[84]

Förster resonance energy transfer (FRET) is a low-resolution fluorescence-technique used to study both structure and dynamics of nucleic acids.[86-87] It is a photophysical process where electronic energy of a fluorophore (donor), in its excited state (S_1 state), is transferred to another molecule (acceptor) in its ground state (S_0) which consequently gets excited (S_1 state) (**Figure 2.2A**).[88] The FRET efficiency (E), which is the probability that the excited donor returns to the ground state through FRET, is related inversely proportional to the sixth power of the distance (r) between the donor- and acceptor molecules and the Förster distance (R_0), which is the distance between donor and acceptor when E is 50% (equation 1).

$$E = \frac{R_0^6}{R_0^6 + r^6} \qquad \text{(equation 1)}$$

Therefore, small changes in distance between the donor and acceptor can have a large impact on E.[89] The FRET efficiency increases as the distance decreases between the donor- and acceptor molecules. E is also dependent on the relative orientation of the donor- and acceptor molecule, yielding lower E when the molecules are perpendicular to each other and higher E when the molecules are parallel to each other.[89-90]

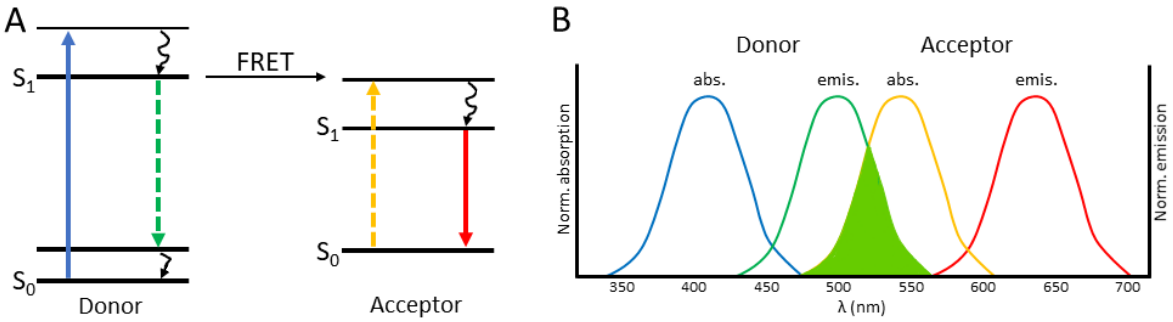

Figure 2.2. FRET spectroscopy. A Jablonski diagram showing the FRET process (A). Absorption and emission spectra of donor- and acceptor molecules (B).

The acceptor can either be a different chromophore than the donor resulting in heterotransfer (hetero-FRET) or it can be an identical molecule which results in homotransfer (homo-FRET).[91] Most FRET measurements rely on hetero-FRET. For hetero-FRET to occur, the emission of the donor and the absorption of the acceptor need to overlap (**Figure 2.2B**).[89] With hetero-FRET, the distance between the donor and acceptor can be measured in the range of 10-100 Å.[92] Hetero-FRET has been used to a large extent to study tertiary structures of nucleic acids and can be used for single-molecule studies.[84, 88, 90, 93]

As mentioned above, homo-FRET can occur between two identical fluorophores when there is an overlap between the excitation and emission spectra of the fluorophore. Therefore, a fluorophore with a small stokes-shift should be used.[88] Homo-FRET can be monitored by fluorescence anisotropy which is reduced by increased homo-FRET efficiency.[94]

Several other biophysical techniques are useful to yield low-resolution structural information on nucleic acids, such as non-denaturing gel electrophoresis,[95] Raman spectroscopy[96-97] and circular dichroism (CD) spectroscopy, which can be used to monitor formation or disruption of duplexes or to analyze helical structures (A, B and Z form) of nucleic acids.[98]

Another useful technique to study the structure and dynamics of nucleic acids is electron paramagnetic resonance (EPR) spectroscopy and will be discussed in detail in the following section.

2.3 EPR spectroscopy

Electron paramagnetic resonance (EPR) spectroscopy was first reported by the physicist Evgenii Konstantinovich Zavoisky in 1945.[99] EPR spectroscopy is a magnetic resonance spectroscopy like NMR, but instead of measuring nuclear spins, it detects transitions of

unpaired electron spins from a lower to a higher energy level. This transition is induced by absorption of electromagnetic radiation in the presence of an applied external magnetic field.[100-102] EPR spectroscopy is a useful technique for the investigation of structure and dynamics of nucleic acids.[103-105] It is a highly sensitive technique and can be used to study the local environment of paramagnetic centers.[106]

EPR spectroscopy can be divided into two main categories, namely continuous wave (CW) and pulsed EPR. In CW-EPR spectroscopy, the sample is continuously irradiated with monochromatic microwaves and the magnetic field is swept over a defined range.[107] CW-EPR spectroscopy can be used to study dynamics of paramagnetic centers by line-broadening of EPR spectra.[108] Moreover, distances up to 25 Å can be measured between two spin centers.[109]

In pulsed EPR, the magnetic field is kept constant and the sample is irradiated with high-power microwave pulses.[106] Pulsed dipolar spectroscopies, such as pulsed electron-electron double resonance (PELDOR), also called double electron-electron resonance (DEER), relaxation induced dipolar modulation enhancement (RIDME), single frequency technique for refocusing dipolar couplings (SIFTER) and double quantum coherence (DQC) can be used to measure the distances in the range of 15-160 Å between two paramagnetic centers using their dipolar coupling.[110-113]

The four-pulse PELDOR sequence (**Figure 2.3B**) is a well-established technique to measure the distance (r_{AB}) between two spin centers (A and B) (**Figure 2.3A**).[114] PELDOR is performed with two different frequencies; a detection frequency (ν_A) that is in resonance with spin A and an inversion frequency (ν_B) that is in resonance with spin B (**Figure 2.3A**, **B**).[115] An EPR signal (refocused Hahn echo) is created with the three pulses of frequency ν_A (detection sequence). A π-pulse of frequency ν_B (inversion pulse) is used to invert spin B at different times (T), between the second and third pulse of the detection sequence. This inversion of spin B modulates the signal of spin A, depending on the strength of the dipolar coupling. The modulated EPR signal from spin A is monitored by integrating the intensity of the refocused Hahn echo as a function of time (T) (**Figure 2.3C**, left). The time dependent signal (**Figure 2.3C**, left) oscillates with the dipolar frequency ν_d between spins A and B which is inversely proportional to the distance (r_{AB}) between the spins (equation 2).

$$\nu_d = \frac{\mu_0 \beta^2 g_A g_B}{4\pi h r_{AB}^3}(3\cos^2(\theta) - 1) \qquad \text{(equation 2)}$$

Here μ_0 is the permeability of vacuum, β is the Bohr magneton, h is the Planck constant, g is the g-factor of the electron spins and θ is the angle between r and the external magnetic field B_0.[116] Fourier transforming the time dependent signal yields a spectrum of the dipolar frequency ν_d. The PELDOR time trace can be converted to a distance distribution using simulations or Tikhonov regularization (**Figure 2.3C**, right). In addition to distance measurements, PELDOR spectroscopy can also give information on the relative orientation between spin centers which is especially useful for studies on the structure and dynamics of nucleic acids.[117-119]

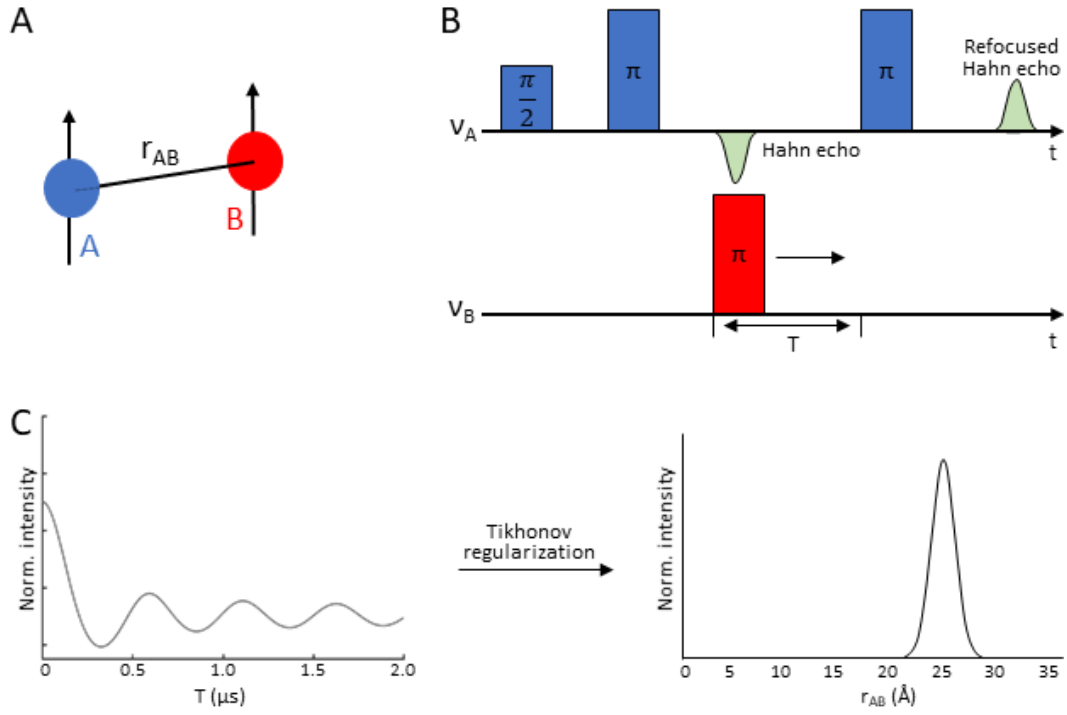

Figure 2.3. PELDOR distance measurements. A. The distance r_{AB} between two electron-spins. B. A four-pulse PELDOR sequence where ν_A and ν_B are the detection and inversion frequencies, respectively. C. A PELDOR time-trace (left) and the distance distribution (right) between electron spins A and B obtained by Tikhonov regularization.

EPR spectroscopy has some advantages over other techniques in the study of nucleic acids. It is a very sensitive technique, being about three orders of magnitude more sensitive than NMR spectroscopy.[120] Because of its sensitivity, only very small amount of sample is needed for measurements, compared to NMR spectroscopy and X-ray crystallography. Furthermore, there is no size limitation for the system under study as only the paramagnetic center and its interactions with the biomolecular system are monitored by EPR. However, because nucleic acids and most other biomolecules are diamagnetic, paramagnetic molecules, called spin labels, need to be incorporated into biomolecules at specific sites.[120-121] There is a wide range

of spin labels used for studies of biomolecules, from paramagnetic metal ions,[122] such as Gd(III) (**Figure 2.4A**)[123] and Mn(II),[124] to organic molecules such as carbon-based trityl radicals (**Figure 2.4B**)[125-126] but the most common spin labels used are organic aminoxyl radicals, called nitroxides (**Figure 2.4C**).[127-129]

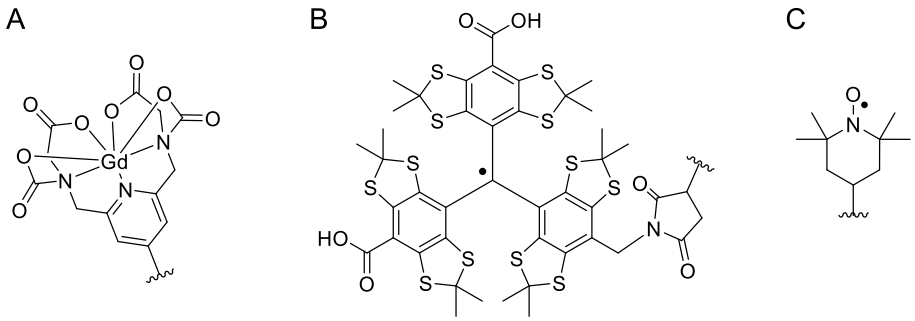

Figure 2.4. Examples of paramagnetic compounds used for EPR applications. A. PyMTA-Gd(III). B. A carbon-based trityl radical. C. The piperidine-based nitroxide radical TEMPO.

2.4 Nitroxide spin labels

Nitroxides are highly persistent due to the delocalization of the radical between the nitrogen and the oxygen atoms and the shielding effect of the alkyl groups flanking the radical center.[130-133] Nitroxide spin labels are found in various shapes and sizes and a few of them will be discussed below where the main focus is laid on their mobility inside nucleic acids.

2.4.1 Flexible and semi-rigid spin labels

Flexible spin labels are covalently attached through single-bond tethers and can therefore move independently of the labeled nucleic acid. Such flexibility complicates EPR analysis of nucleic acids as the motion of the spin label has to be taken into account when movements of the labeled nt are studied (**Figure 2.5**) and therefore such flexibility leads to a large distance distribution.[134]

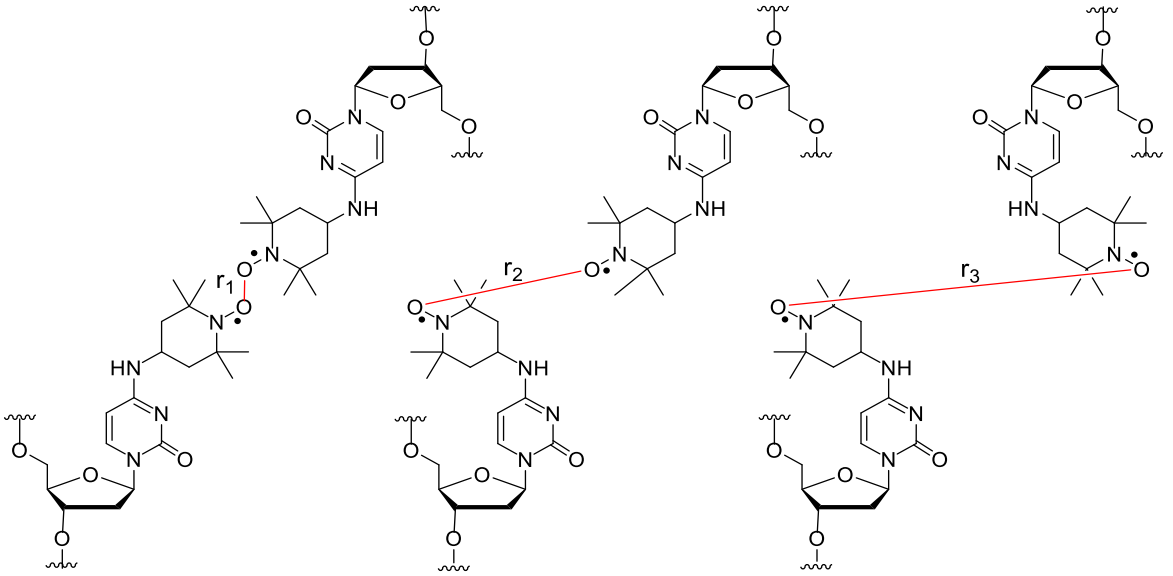

Figure 2.5. Flexible spin labels incorporated into nucleic acids. The labels have many different conformers that have therefore multiple distances between the paramagnetic centers, resulting in a large distance distribution.

Conformationally unambiguous spin labels such as compound **1**[135] and $^{\mathbf{ExIm}}$**U**[136] (**Figure 2.6**) are semi-rigid spin labels that give more accurate distance measurements than flexible spin labels. The spin label rotates around a single bond, but the bond lies on the same axis as the nitroxide which results in minimal displacement of the nitroxide upon rotation of this single bond. The rotation does not change the spatial positioning of the nitroxide compared to the nucleoside it is connected to and thus, the nitroxide does not move independently to the nucleic acid. CW-EPR spectra of conformationally unambiguous benzimidazole-derived spin labels $^{\mathbf{Im}}$**U**[137] and $^{\mathbf{Ox}}$**U**[137] (**Figure 2.6**), incorporated into duplex DNA, and $^{\mathbf{Im}}$**Um**[138] (**Figure 2.6**), incorporated into RNA, showed restricted mobility. $^{\mathbf{Im}}$**U** and $^{\mathbf{Im}}$**Um** showed even less mobility than $^{\mathbf{Ox}}$**U** presumable due to the internal hydrogen bonding between the N-H of the imidazole and the O4 on the uridine. Furthermore, PELDOR distance measurements of these labels incorporated into nucleic acids showed a strong angular dependence.[136, 138-139] The benzimidazole-derived spin label **E**$^{\mathbf{Im}}$**Um**[140] (**Figure 2.6**) was designed as a reductive-resistant label as the nitroxide is shielded by tetra ethyl groups. *In-cell* PELDOR experiments of duplex RNA, doubly-labeled with **E**$^{\mathbf{Im}}$**Um**, identified small distance changes that indicated compaction of RNA duplexes inside the cell.[140] In the next section even less mobile spin labels will be discussed, namely rigid spin labels.

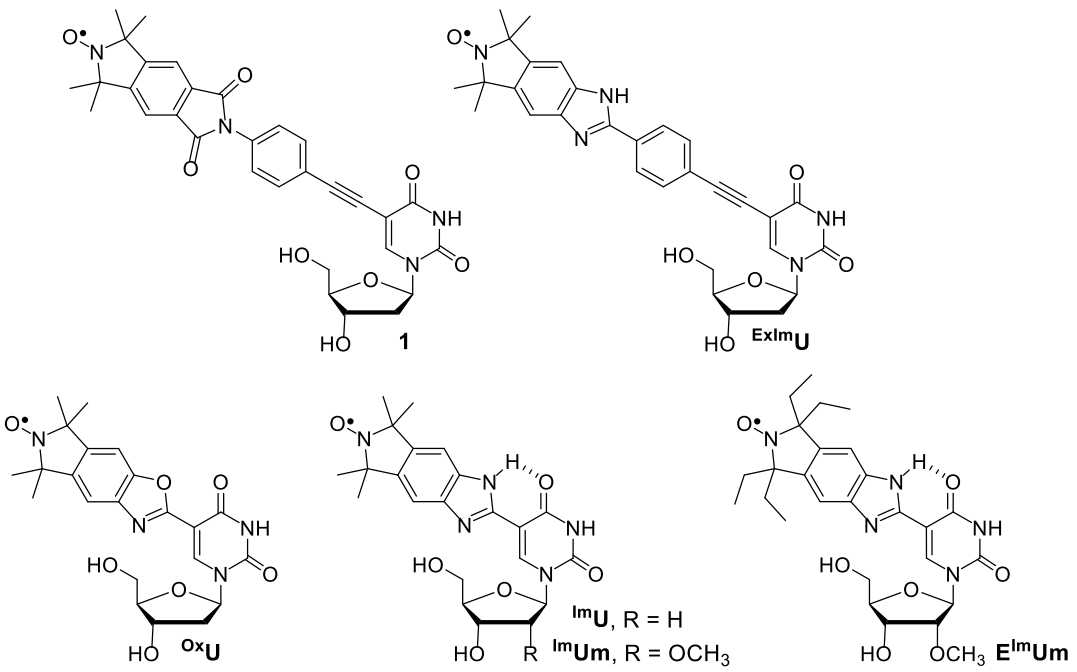

Figure 2.6. Conformationally unambiguous nitroxide spin labels for DNA and RNA labeling.

2.4.2 Rigid spin labels

Rigid spin labels are labels where the nitroxide is fused to the nucleobase through two bonds. When such spin labels are incorporated into nucleic acids, they have no independent motion due to movement of a linker and only follow the motion of the nucleic acid, which results in more accurate distance measurements. Another advantage using rigid spin labels is that the relative orientation of two labels inside a nucleic acid can be determined by dipolar EPR spectroscopy which is not possible for flexible spin labels.[119] With rigid spin labels it is even possible to perform PELDOR measurements at room temperature,[141] which is a rare advantage of rigid spin labels over more flexible labels, as PELDOR studies are usually performed at cryogenic temperatures. **Q** (**Figure 2.7**), designed by Hopkins *et al.*, is the first reported rigid spin label where the nitroxide is fused to a non-natural nucleoside.[142-143] **Q** has been used to study sequence-dependent dynamics of duplex DNA.[144]

The Sigurdsson research group has designed the rigid spin labels **Ç**[2] and **Çm**[1] (**Figure 2.7**) for DNA and RNA, respectively, that are cytidine derivatives. These rigid spin labels have been used to gain valuable information on structure and dynamics of nucleic acids. **Ç** has been used to obtain information on internal motions of DNA,[145] to investigate conformational changes of the cocaine aptamer,[146] and to determine the helix orientation of a highly flexible DNA.[13] **Çm** has been used to investigate the influence of Mg^{2+} on the conformational flexibility of the tetracycline aptamer.[147]

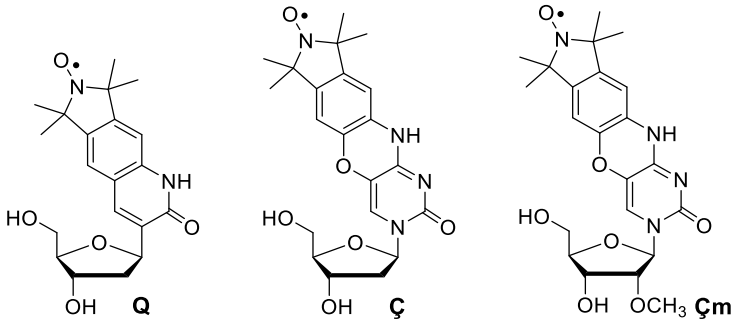

Figure 2.7. Structures of the rigid nitroxides **Q**, **Ç** and **Çm**.

2.5 Site-directed spin labeling of nucleic acids

For incorporation of spin-labels into nucleic acids at specific sites of interest a method known as site-directed spin labeling (SDSL) is used,[108, 121, 128, 133, 148-149] which is essential for EPR studies of biomolecules. Spin labels can be incorporated into nucleic acids noncovalently or covalently (**Figure 2.8**). Noncovalent spin labeling can be performed through noncovalent interactions, such as hydrogen bonding and π-π stacking between the spin label and the nucleic acid (**Figure 2.8A**).[150-151] Covalent modified spin labels can be incorporated post-synthetically where the spin labels are incorporated into the nucleic acids after oligonucleotide synthesis **(Figure 2.8B**) or through the phosphoramidite approach (**Figure 2.8C**).[128] All three spin-labeling methods will be discussed in more detail in the following sections.

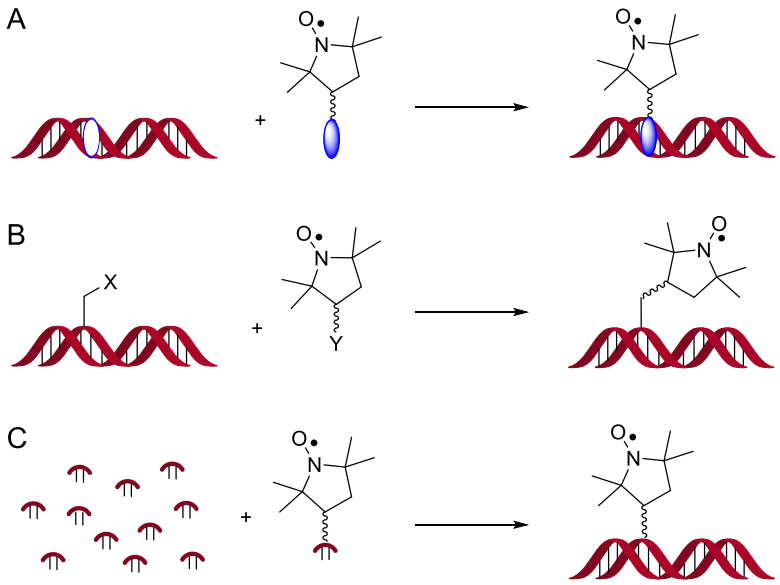

Figure 2.8. Site-directed spin labeling (SDSL) of nucleic acids. A. Noncovalent spin labeling by usage of an abasic site. B. Post-synthetic spin-labeling where X and Y represent functional groups that undergo a reaction to form a covalent bond between the spin label and the oligonucleotide. C. The phosphoramidite approach.

2.5.1 Noncovalent spin labeling

For noncovalent spin labeling, a specific site is needed with high affinity towards the spin label, similar to a ligand-receptor interaction. In this case, the ligand is a spin label (**Figure 2.8A**).[108, 128, 148] The spin labels bind noncovalently through hydrogen bonding, π-π stacking, ionic interactions, and Van der Waals interactions. Abasic sites have been used inside nucleic acids to bind nucleobase analogues such as **ç**[152] and **Ǵ**[153] noncovalently (**Figure 2.9**).

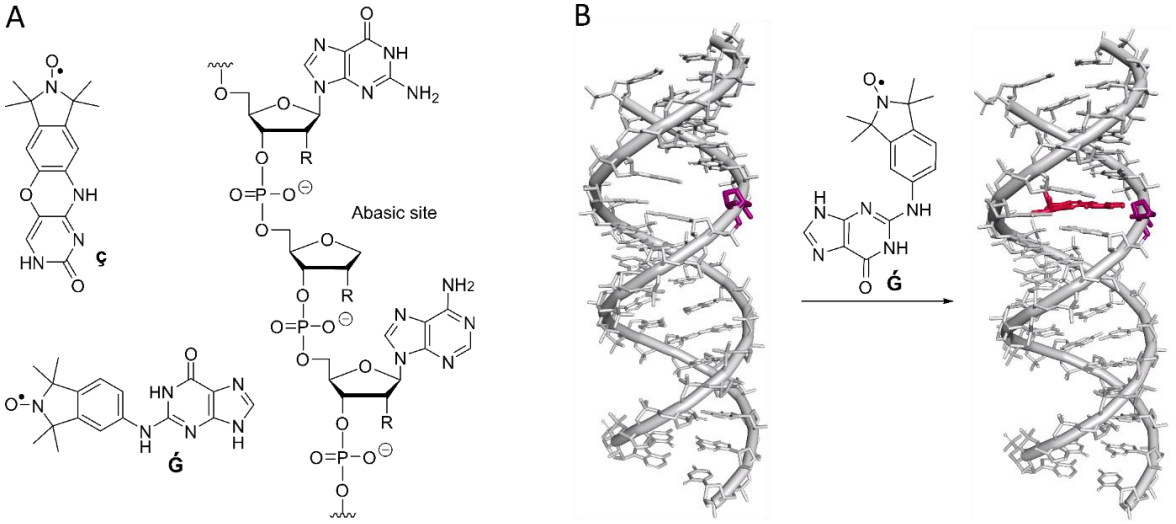

Figure 2.9. Noncovalent spin labeling approach. A. Nucleobase analogues **ç**[154] and **Ǵ**[153] that have been used for noncovalent spin labeling of abasic sites inside nucleic acids. B. Tertiary structure of an RNA containing an abasic site (colored in purple) where **Ǵ** (colored in red) binds noncovalently.

Furthermore, an unmodified RNA has been spin labeled by use of noncovalent labeling.[151] A nitroxide derivative of tetramethyl rhodamine (TMR) was reported to bind to the malachite green aptamer with high affinity, even at ambient temperatures (**Figure 2.10**). Noncovalent spin labeling usually has only few-step synthesis to produce the spin labeled ligand and with this method, the chemistry-related challenges associated with the phosphoramidite approach and the post-synthetic spin labeling are circumvented.[128] For noncovalent labeling to be useful, it requires spin labeled ligands that bind with high affinity and specificity to the binding site to yield enough spin labeled sample to use for EPR measurements.[148]

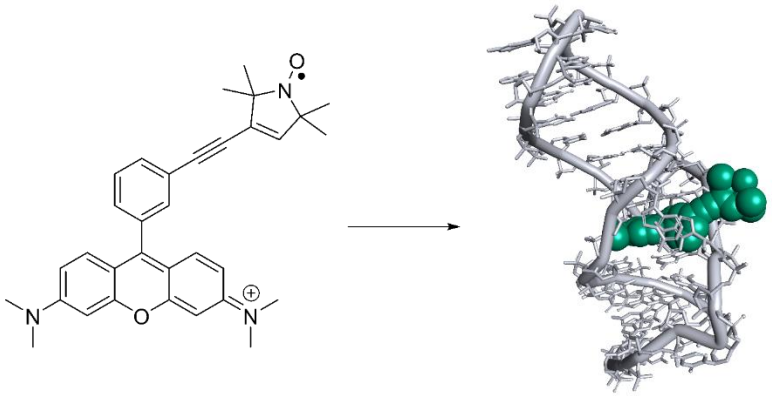

Figure 2.10. Noncovalent spin labeling. Binding of a nitroxide derived tetramethyl rhodamine (TMR) to the malachite green aptamer.[151]

2.5.2 Post-synthetic spin labeling

Post-synthetic spin labeling requires oligonucleotides that have uniquely reactive groups at specific sites where the spin label can be incorporated through a chemical reaction (**Figure 2.8B**).[108, 128, 148, 155] The reactive functional groups can be incorporated using either chemical or enzymatic synthesis. The spin labels that are to be incorporated into the oligonucleotide contain a functional group that is reactive towards the reactive group on the oligonucleotide. One advantage of post-synthetic spin labeling is that often the modified oligonucleotides and the reagents used are commercially available which excludes extensive synthetic effort producing a spin-labeled phosphoramidite for the phosphoramidite approach. Another advantage is that the spin label does not get exposed to the reagents used for solid-phase synthesis, which could partially reduce the spin label.[156] Disadvantages of this method is that the spin labeling can be incomplete and side reactions may occur between the spin labeling reagent and the nucleophilic groups present in the nucleic acids, such as the exocyclic amino groups of the nucleobases, the N7 of purines, and nonbridging oxygen atoms of the phosphodiesters.[148]

2.5.3 The phosphoramidite approach

The first attempt of making synthetic DNA was published in 1955 by Michelson and Todd where they were able to synthesize a dinucleotide.[157] For the next two and a half decades, much effort was put into the improvement of the synthesis of oligonucleotides,[158] which led to the groundbreaking development of the phosphoramidite approach which was published by Caruthers in 1981.[159] The phosphoramidite approach for spin labeling involves spin-labeled phosphoramidite building blocks (**Figure 2.8C**) that are incorporated during

automated solid-phase oligonucleotide synthesis.[108, 128, 148] The phosphoramidites are made of 2'-deoxyribonucleosides (**Figure 2.11A**) for DNA and ribonucleosides (**Figure 2.11B**) for RNA where the 5'-hydroxyl is protected as a dimethoxytrityl ether (DMT) (**Figure 2.11**, red) and the 3'-hydroxyl is phosphitylated (**Figure 2.11**, blue). Furthermore, the exocyclic amino groups of C, A and G are protected as amides (**Figure 2.11**, yellow) and the 2'-hydroxyl group of the ribonucleoside phosphoramidite is silyl-protected (**Figure 2.11**, green).

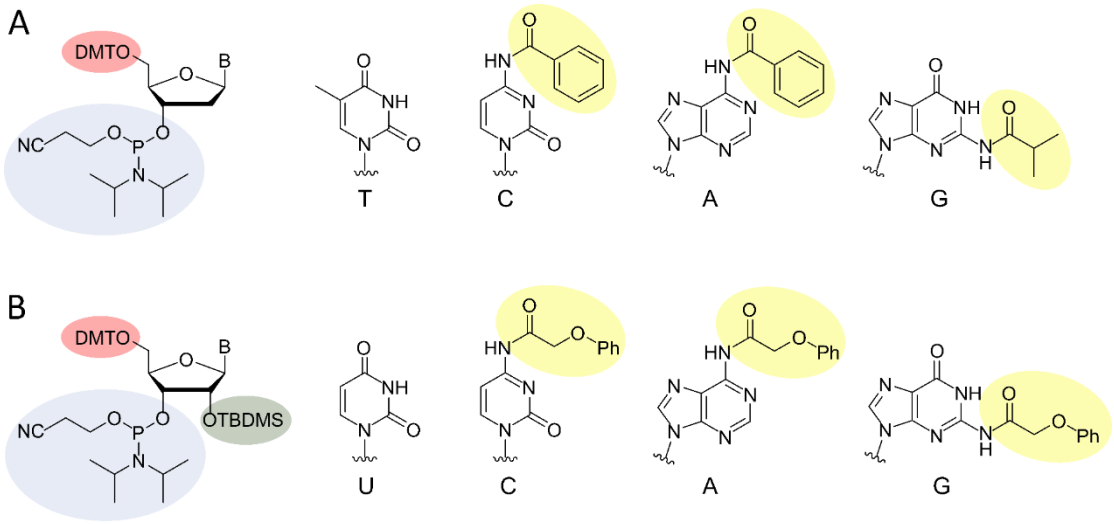

Figure 2.11. Structure of 2'-deoxyribonucleoside (A) and ribonucleoside (B) phosphoramidites used for automated solid-phase oligonucleotide synthesis. The 5'-hydroxyl is protected as a dimethoxytrityl ether (DMT) (red), the 3'-hydroxyl is phosphitylated (blue), the 2'-hydroxyl group of ribonucleoside phosphoramidites is silyl protected (green) and the exocyclic amino groups of C, A and G are protected as amides (yellow).

Opposite to the direction of DNA synthesis in Nature, the solid phase synthesis is performed from the 3'- to the 5'-terminus. The first oligonucleotide is connected to the solid phase through its 3'-hydroxyl group. The seven-step cycle of DNA solid-phase oligonucleotide synthesis is shown in **Figure 2.12**. Step 1 is the detritylation of the 5'-hydroxyl group of the first oligonucleotide under acidic conditions. Step 2 is the addition of the next nucleotide in the oligonucleotide sequence which is performed by activation of the phosphoramidite and coupling to the deprotected 5'-hydroxyl group of the growing chain of the oligonucleotide. In step 3, the 5'-hydroxyl groups that did not couple to the added phosphoramidite are acetylated. This step, called capping, is important to prevent further coupling, which would yield in N-1 sequences. Oxidation of the phosphorus is performed in step 4 and finally detritylation of the 5'-hydroxyl group in step 5 starts a new cycle of the oligonucleotide

synthesis. After the last nt has been added to the oligonucleotide, the final step of the synthesis (6) is either detritylation of the 5'-hydroxyl group or the DMT group is kept on ("trityl-on" synthesis) for HPLC purification of the oligonucleotide. The oligonucleotide is then removed from the solid phase and the protecting groups removed under basic conditions.

An advantage of the phosphoramidite method is that intricate labels such as rigid spin labels can be incorporated into nucleic acids, which would not be possible post-synthetically or by noncovalent labeling. This dissertation describes labeling of nucleic acids by rigid labels and therefore the phosphoramidite approach was the only labeling method used.

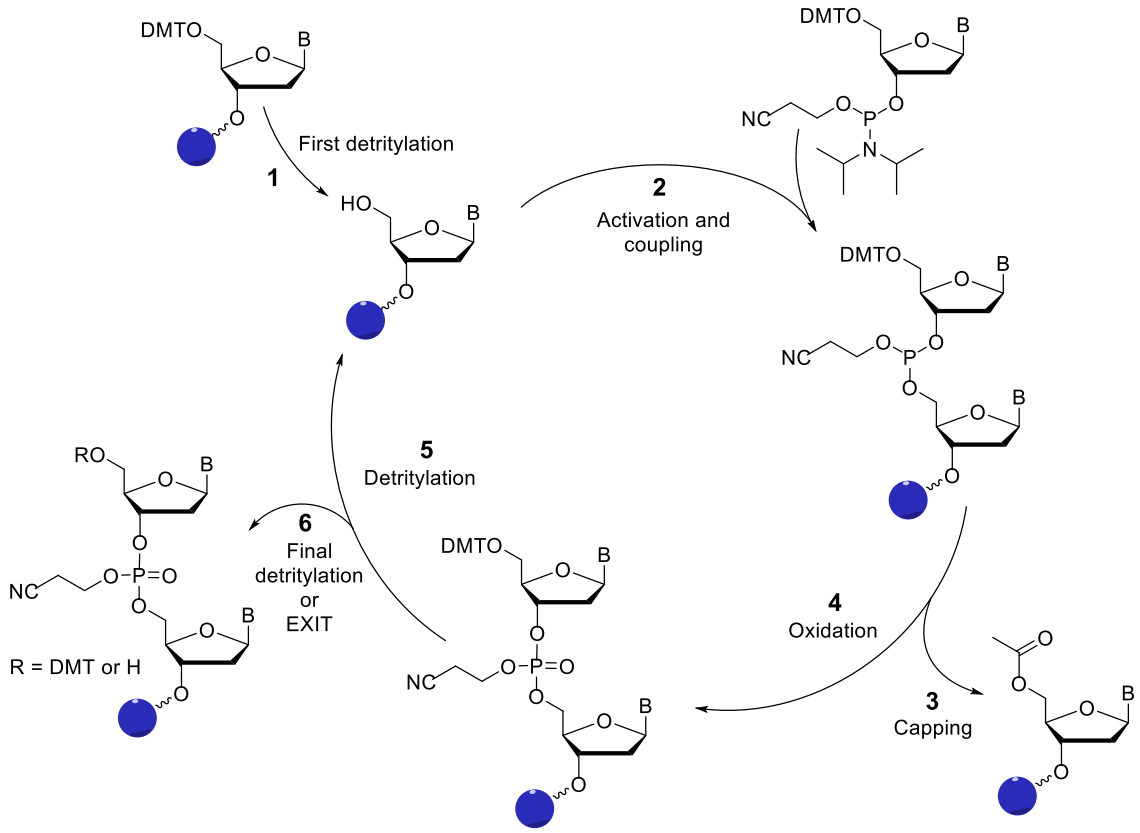

Figure 2.12. The synthetic cycle of automated solid-phase synthesis of DNA oligonucleotides.

2.6 Contribution of this PhD thesis to biophysical studies of nucleic acids

The work presented within this doctoral thesis focuses on the synthesis of rigid spin- and fluorescent labels and their incorporation into DNA and RNA for the study of structure and dynamics of nucleic acids by both EPR- and fluorescence spectroscopy.

In **Chapter 3**, a protecting group strategy is presented for nitroxide radicals that is suitable for oligonucleotide synthesis by the phosphoramidite approach. A known problem is that during solid-phase oligonucleotide synthesis, nitroxides can get partially reduced by the reagents used for the synthesis yielding a mixture of spin labeled oligonucleotides and of oligonucleotides with a reduced label. For longer oligonucleotides (15<nt), the separation is tedious and often the mixture inseparable. The reduction was circumvented by the protection of the nitroxides, by first reducing the nitroxide to its corresponding hydroxylamine and then protecting it with a benzoyl group. The benzoyl protecting group was shown to be stable through the oligonucleotide solid-phase synthesis. It can be readily removed after the synthesis, using standard deprotection conditions for oligonucleotides. This protecting group strategy made it possible to produce DNA and RNA oligonucleotides by the phosphoramidite approach that had near to quantitative spin labeling efficiency.

Chapter 4 describes labeling of DNA and RNA with rigid labels. The first part of the chapter describes the rigid spin labels **Ç** and **Çm** and their incorporation into DNA and RNA to investigate their structure and dynamics by PELDOR spectroscopy. The rigid spin-label **Ç** for DNA was incorporated into an RNA-cleaving DNAzyme to investigate the cleaving activity. The rigid spin label **Çm** for RNA was firstly incorporated into a series of RNA duplexes to investigate their internal dynamics. Secondly, **Çm** was incorporated into the tetramethyl rhodamine (TMR) aptamer to study the binding of the ligand to its aptamer. Thirdly, **Çm** was incorporated into an RNA hairpin loop to study the conformational change by addition of Mg^{2+}.

In the second part of this chapter, the rigid fluorescent label **Çmf** was incorporated into RNA to study by fluorescence spectroscopy. **Çmf** was incorporated into the neomycin aptamer to investigate the binding mechanism of the ligand to the aptamer. To investigate **Çmf** as a donor molecule for FRET experiments, it was incorporated together with a quencher first into a series of duplex RNAs and subsequently into the neomycin aptamer. Initial results have shown that the fluorescence of **Çmf** is being quenched and therefore indicating that these labels are a good FRET pair. Finally, **Çmf** was incorporated into the i-Mango III aptamer to test the ability of **Çmf** and the binding ligand of the aptamer as a FRET pair, where **Çmf** is the donor and the ligand is the acceptor. Initial results have shown that an energy transfer is occurring between **Çmf** and the ligand.

Chapter 5 discusses the design, synthesis, and incorporation of new carbazole-derived rigid nitroxide spin-labels **Ċ** and **Ċm** into DNA and RNA, respectively. **Ċ** and **Ċm** have an

aromatic ring system which makes their structure very rigid. **Ċ** and **Ċm** were incorporated into nucleic acids by the phosphoramidite approach, giving spin labeled DNAs and RNAs that had a high spin count. **Ċ** and **Ċm** had a minimal effect on the conformation and duplex stability of B-DNA and A-RNA, respectively. These new rigid spin labels are promising candidates for future studies of DNA and RNA structures and dynamics by pulsed EPR methods.

3 A protecting group strategy for nitroxide radicals and application for chemical synthesis of oligonucleotides

Although nitroxides are persistent radicals that are the most frequently used spin labels for nucleic acids, it is well known that they can get partially reduced when spin-labeled oligonucleotides are synthesized using solid-phase synthesis. In this chapter, a protecting group strategy is introduced for nitroxide radicals to circumvent the reduction. This project was a collaboration with Dr. Haraldur Yngvi Júlíusson, a former group member of the Sigurdsson research group. The goal of the project was to enable the synthesis of longer DNA and RNA oligonucleotides (>15 nt). Dr. Júlíusson worked on spin labels for DNA and the author of this dissertation on labels for RNA.

3.1 Nitroxide reduction during solid-phase synthesis

To be able to incorporate rigid[1-2] or semi-rigid[135, 137] spin labels into nucleic acids, they need to be incorporated through the phosphoramidite approach by solid-phase oligonucleotide synthesis. The phosphoramidite approach has the drawback that during solid-phase synthesis of oligonucleotides, the nitroxide gets exposed to reagents that can reduce it to the corresponding hydroxylamine and further to the corresponding amine (**Figure 3.1**), both of which are EPR silent.[156, 160]

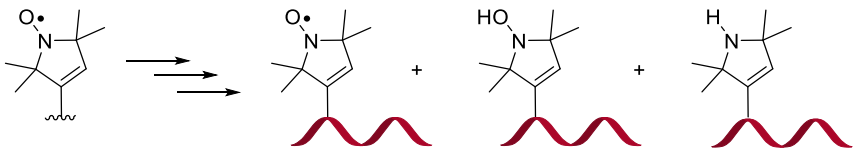

Figure 3.1. Reduction of nitroxides. During solid-phase synthesis, nitroxides get partially reduced to their hydroxylamines and further to the amines.

The reagents that cause reduction of the nitroxide are trichloroacetic acid used for detritylation, the tetrazole activator and the iodine oxidizer.[156] It has been reported that acids,

including trichloroacetic acid, can reduce nitroxides through a disproportionation reaction, where one nitroxide is oxidized to an oxoammonium salt and another nitroxide is reduced to the hydroxylamine.[160-162] The oxoammonium salt is reduced to the hydroxylamine which is further reduced to the corresponding amine.[131] In earlier times of solid-phase synthesis, 1*H*-tetrazole was used as an activator for the coupling step (described in **Chapter 2**) but it was soon replaced by 5-ethylthio 1*H*-tetrazole for DNA synthesis[163-164] and 5-benzylthiol 1*H*-tetrazole for RNA synthesis,[165-166] as they are more acidic and have greater solubility in acetonitrile (solvent used to dissolve the activator).[163] 5-Ethylthio 1*H*-tetrazole and 5-benzylthio 1*H*-tetrazole are weak acids with pKa values of 4.3 and 4.1 and being acids they reduce the nitroxide through the same mechanism as trichloroacetic acid does. The iodine oxidizing solution reduces the nitroxide in a similar manner, also through a disproportionation reaction.[131, 160, 167]

The reduction of nitroxides is not a severe problem for short oligonucleotides, that is shorter than 15 nt, because the oligonucleotides with the spin label and the reduced label can be separated by denaturing polyacrylamide gel electrophoresis (DPAGE) or by HPLC. When the oligonucleotides are longer, the separation is tedious and time-consuming or even impossible. One of the goals of this PhD project was to synthesize longer spin-labeled RNAs; between 20-50 nt long. What made this task even harder was that the coupling time of RNA phosphoramidites during the solid-phase synthesis of oligonucleotides is more than two-times longer than for DNA phosphoramidites, and this increased exposure of the tetrazole activator during the coupling of the nucleotides yielded samples that had very low spin-labeling efficiency (< 20%).

To try to circumvent or minimize the reduction of nitroxides during solid-phase synthesis, the trichloroacetic acid used for detritylation has been replaced with the weaker acid dichloroacetic acid and the iodine oxidation solution with *tert*-butyl hydroperoxide.[156, 160, 168] Even though this has improved the synthesis of spin-labeled oligonucleotides to some extent, it has not solved the problem.

One solution would be to protect the nitroxide with a protecting group. When choosing a protecting group for a nitroxide a few things should be kept in mind. First, the protecting group should be easily accessible and preferably it should be commercially available. Secondly, it is required that the protecting group is stable under the conditions used for the synthesis of oligonucleotides. Thirdly, the protecting group should be readily removeable after the synthesis under standard oligonucleotide deprotection conditions.

3.2 Reported protecting groups for nitroxides

Various protecting groups have been used to protect nitroxides; all known examples are shown in **Figure 3.2**. Nitroxides have been protected against reduction as *O*-methyl hydroxylamines (**Figure 3.2A**, compound **2**).[169] The protecting group is removed by the oxidizing agent *meta*-chloroperbenzoic acid (*m*CPBA). The methoxy protecting group is not suitable for protection of nitroxides through solid-phase synthesis, because removal with *m*CPBA would not only remove the protecting group but also oxidize nitrogen atoms in the heterocyclic nucleobases present in nucleic acids.[170-171] *Tert*-butyldimethylsilyl (TBDMS) has been used to protect the nitroxide of 2,2,6,6-tetramethylpiperidyl-1-oxyl (TEMPO) (**Figure 3.2A**, compound **3**) for the synthesis of a nitroxide-nitroxide biradical.[172] The TBDMS group was removed by hydrofluoric acid but less than 50% of the nitroxide was recovered after removal of the protecting group.

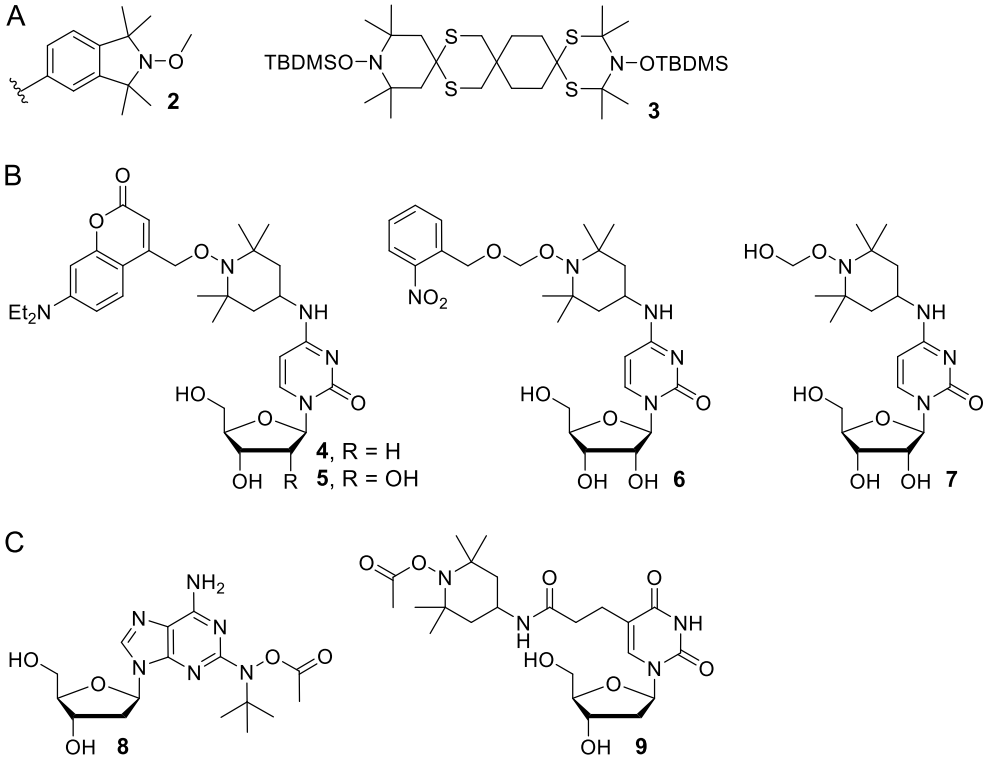

Figure 3.2. Protected nitroxides **2**, **3** (A); **4**, **5**, **6**, **7** (B); **8**, **9** (C).

Nitroxide protecting groups have also been specially developed for solid-phase oligonucleotide synthesis. For example, photolabile protecting groups (PPG) have been used to protect the nitroxide of TEMPO for both DNA and RNA synthesis (**Figure 3.2B**).[173-176]

A few different protecting groups were evaluated and coumarin-derived compounds **4** and **5** (**Figure 3.2B**) and 2-nitrobenzyloxymethyl (NBOM) derivative **6** (**Figure 3.2B**) gave the best results. Coumarin was used for both DNA and RNA but NBOM only for RNA. The PPGs were removed by irradiation with UV light. By removing coumarin they got an 85:15 ratio of the nitroxide and the amine for both DNA and RNA strands. In contrast, when NBOM was removed with UV light, only traces of the amine were present. Nonetheless, they got a byproduct, which turned out to be hemiacetal **7** (**Figure 3.2B**). By heating the oligonucleotide to 90 °C for 1 h, most of the hemiacetal-byproduct could be removed. There are however, drawbacks using PPGs for protection of nitroxides. Additional synthetic steps are needed to prepare the protecting groups and to incorporate them. Furthermore, in order to remove the groups, special equipment is needed to irradiate the oligonucleotides with the right wavelength.

Two examples have been reported where acetyl was used to protect nitroxides during solid-phase synthesis. Acetyl is routinely used as a protecting group for solid-phase oligonucleotide synthesis of DNA to protect the exocyclic amines of C, G and A, and would therefore be a good candidate as a general protecting group for nitroxides. Compound **8** was incorporated into DNA by using an acetylated hydroxylamine (**Figure 3.2C**).[177] The acetyl group was removed under standard deprotection conditions for oligonucleotides (aq. ammonium hydroxide), however, the structure of this nitroxide is very different from the nitroxides that are normally used for spin labeling. Acetyl has also been used to protect the nitroxide of a TEMPO moiety, a common spin label, during DNA synthesis (**Figure 3.2C**, compound **9**).[178] However, the protecting group was not removed using standard oligonucleotide deprotecting conditions. Instead, it required incubation in aq. NaOH (0.5 M) for complete removal of the protecting group. Unfortunately, these conditions are too harsh for RNA oligonucleotides and could lead to hydrolysis and breakdown of the oligonucleotide.

3.3 Selection of a protecting group

There are various other protecting groups used to protect exocyclic amines as amides on unmodified phosphoramidites C, G and A. The most common groups used are acetyl (Ac), isobutyryl (iBu), benzoyl (Bz) and phenoxyacetyl (PAc) (**Figure 3.3**).[179] Because Ac did not seem suitable for RNA, it was decided to evaluate Bz as a protecting group.

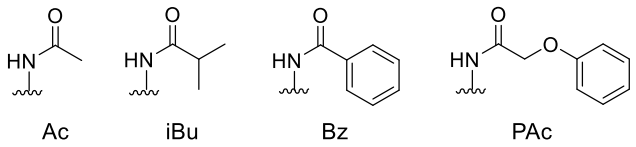

Figure 3.3. Protecting groups used to protect exocyclic amines as amides on the nucleobases of C, G and A during oligonucleotide synthesis.

Compound **10** (**Scheme 3.1**) was used as a model compound to optimize the reaction conditions for the incorporation of Bz and to evaluate Bz as a protecting group. The nitroxide of compound **10** was reduced with *L*-ascorbic acid to the corresponding hydroxylamine **11**, which was subsequently benzoylated with benzoyl chloride to yield **12** in quantitative yield. Oxygen can oxidize the hydroxylamine back to the nitroxide and therefore both the reduction and benzoylation were performed under an inert atmosphere of argon. Unfortunately, model compound **12** was not soluble in all the solutions used for solid-phase synthesis and therefore, another molecule had to be used for the evaluation of Bz as a protecting group, which will be described in the next section.

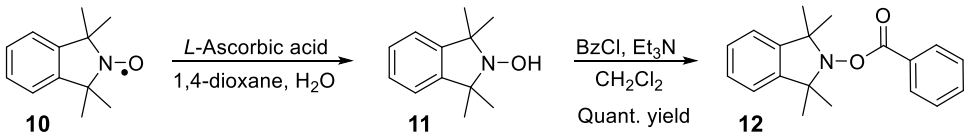

Scheme 3.1. Benzoyl protection of **10**.

3.4 Synthesis and stability of Çm-Bz

We decided to use the rigid spin label **Çm**, introduced in **Chapter 2**, as a test-system to evaluate Bz as a protecting group for nitroxides. **Çm** is soluble in all the solutions used for solid-phase synthesis. Furthermore, an advantage of using **Çm** for the development of a general nitroxide protecting group strategy is that when **Çm** is reduced to its hydroxylamine or to its amine it becomes fluorescent, which makes it easy to detect and to monitor.

The synthesis of **Çm-Bz** (**Scheme 3.2**) began by protection of the 5′- and 3′-hydroxyl groups of **Çm** with TBDMS to avoid benzoylation of the hydroxyl groups. The resulting nitroxide radical **13** was reduced with *L*-ascorbic acid to yield the corresponding hydroxylamine that was subsequently benzoylated to yield benzoyl protected nucleoside **14**. The TBDMS groups were finally removed with TBAF to give **Çm-Bz**.

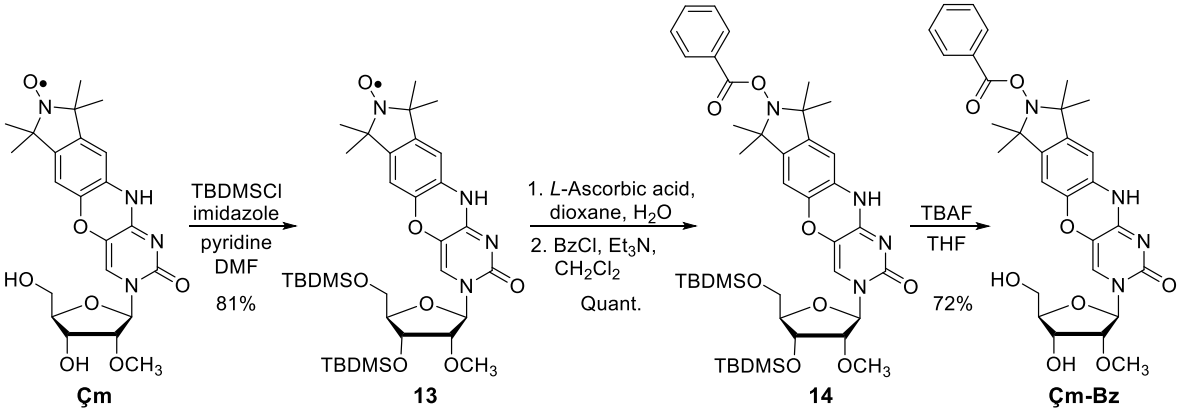

Scheme 3.2. Synthesis of benzoyl protected **Çm-Bz**.

After synthesizing the benzoyl protected nucleoside **Çm-Bz**, the stability of the protecting group was investigated under the reaction conditions that are used for both DNA and RNA solid-phase oligonucleotide synthesis (**Table 3.1**). The stability was monitored over a course of 5 d (data not shown). Bz was found to be stable in the detritylation solution (**Table 3.1**, reaction 1) and in both capping solutions (**Table 3.1**, reactions 2 and 3) for at least 5 d. In the activation solutions that include 5-ethylthio 1*H*-tetrazole or 5-benzylthio 1*H*-tetrazole (**Table 3.1**, reactions 4 and 5), a slight removal of the Bz protecting group was observed after 24 h. The protecting group was unstable in the iodine oxidation solution (**Table 3.1**, reaction 6) as it had been removed after only 30 min of incubation. In contrast, the Bz group was stable for at least 5 d in the oxidation solution containing *tert*-butyl hydroperoxide (**Table 3.1**, reaction 7).

Table 3.1. Reaction conditions used for solid-phase oligonucleotide synthesis.

Reaction	Role	Reaction conditions	Stability of Bz
1	Detritylation	3% Dichloroacetic acid, CH_2Cl_2	5 d
2	Capping (Cap A)	Acetic anhydride, THF	5 d
3	Capping (Cap B)	*N*-methyl imidazole, pyridine, THF	5 d
4	Activation (DNA)	5-Ethylthio 1*H*-tetrazole, CH_3CN	24 h
5	Activation (RNA)	5-Benzylthio 1*H*-tetrazole, CH_3CN	24 h
6	Oxidation	I_2, pyridine, H_2O, THF	30 min
7	Oxidation	*tert*-butyl hydroperoxide, toluene	5 d

The removal of the Bz group was tested in standard deprotection conditions for RNA oligonucleotides ($MeNH_2/NH_3$ in H_2O/EtOH, 65 °C) and was removed within 1 h (data not shown) which is a slightly longer time than used for standard deprotection of RNA oligonucleotides.[180]

Having established that the benzoyl protecting group was stable under the conditions used for oligonucleotide synthesis and that it could be readily removed under standard deprotection conditions for RNAs, it was proceeded to convert **Çm-Bz** into its phosphoramidite. The 5‘-hydroxyl was protected as a 4,4′-dimethoxytrityl (DMT) ether to yield **15** and the 3’-hydroxyl was subsequently phosphitylated to give phosphoramidite **16**.

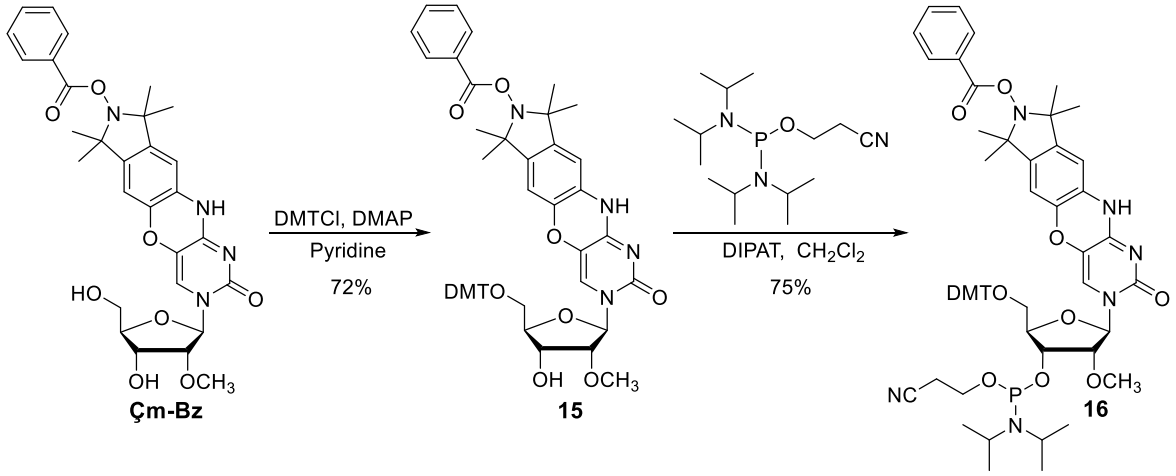

Scheme 3.3. Synthesis of phosphoramidite **16**.

3.5 Synthesis and characterization of Çm-labeled RNA

Phosphoramidite **16** was used to synthesize a short, spin-labeled RNA oligonucleotide **I** (**Table 3.2**), which allows separation by DPAGE of oligonucleotides containing the reduced label from spin-labeled oligonucleotides. For comparison, an RNA of the same sequence (**II**, **Table 3.2**) was synthesized with phosphoramidite **18** of the unprotected **Çm** (**Scheme 3.4**). Both phosphoramidites **16** and **18** coupled well, as judged by the strong dark orange color of the trityl cation that appeared during removal of the DMT protecting groups.

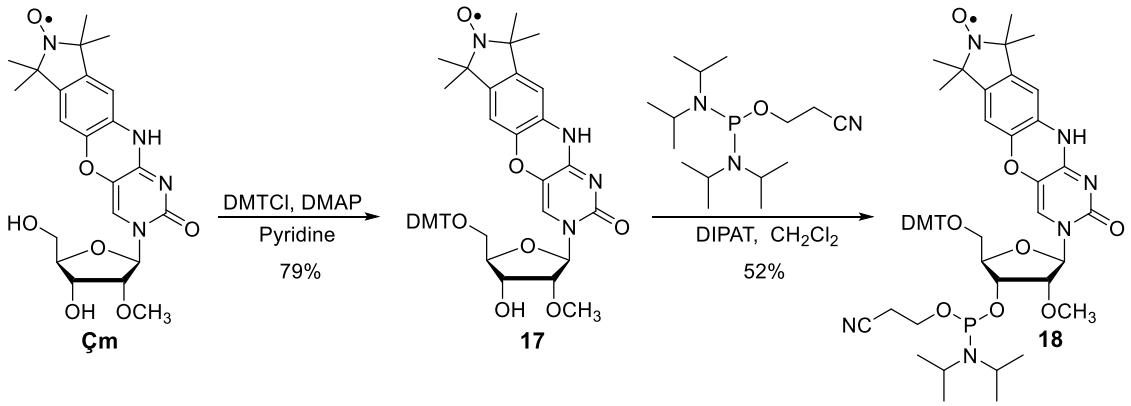

Scheme 3.4. Synthesis of phosphoramidite **18**.

Table 3.2. Spin labeled oligonucleotides. Monoisotopic masses and spin labeling efficiency.

	Sequence	Calcd mass	Found mass	Radical (%)
I	5‘-UGCAU**Çm**UU-3‘	2662.4	2662.3	96
II	5‘-UGCAU**Çm**UU-3‘	2662.4	2662.7	49
III	5‘-AGA-UGC-GCG-**Çm**GC-GCG-ACU-GAC-3‘	6953.0	6952.5	93

For further analysis of the spin labeling, the crude oligonucleotides **I** and **II** were analyzed by DPAGE (**Figure 3.4**). Because the reduced label of **Çm** is fluorescent, it is easy to distinguish between the reduced label and **Çm** by visualization. For oligonucleotide **I** (**Figure 3.4A**, lane 1) no fluorescent band was observed. On the other hand, oligonucleotide **II** (**Figure 3.4A**, lane 2), synthesized with the unprotected **Çm**, contained a strong fluorescent band which stems from the amine of the reduced **Çm**. The **Çm**-labeled oligonucleotide runs faster in the gel than the fluorescent band because of the amine of the reduced label. DPAGE separation of oligonucleotides is based on size and charge. The amine of the reduced **Çm** has a positive charge when it is loaded on to the gel (pH 8) which results in one less net charge, slowing the oligonucleotide down.

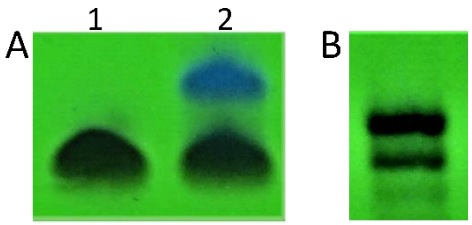

Figure 3.4. Analysis of spin-labeled oligonucleotides by DPAGE. A. Crude 8-nt long RNA oligonucleotides **I** (lane 1) and **II** (lane 2). B. Crude 21-nt long RNA oligonucleotide **III**.

To analyze and quantify the amount of **Çm** in the spin labeled RNAs, the crude oligonucleotides **I** and **II** were enzymatically digested with snake venom phosphodiesterase, nuclease P_1 and calf spleen alkaline phosphatase, and the digests were analyzed by HPLC (**Figure 3.5**). The HPLC chromatogram for oligonucleotide **I** (**Figure 3.5A**) contained five peaks, one for each natural nucleoside and a strongly retained nucleoside that was shown by co-injection to be **Çm**. Oligonucleotide **II** (**Figure 3.5B**) also contained the four peaks for the natural nucleosides and one peak for **Çm** but it also contained a peak for the reduced form of **Çm**. Both oligonucleotides, **I** and **II**, were purified and their spin labeling efficiency was determined by spin-counting using CW-EPR spectroscopy. A stock solution of 4-hydroxy-TEMPO was prepared and diluted into samples of different concentrations (0-0.5 mM), and each sample was measured by EPR spectroscopy. The area under the peaks of each spectrum, obtained by double integration, was plotted against its concentration to yield a standard curve, which was used to determine the amount of spin label. Oligonucleotide **I** had nearly quantitative spin labeling efficiency, whereas **II** only contained around 50% of nitroxide in the sample (**Table 3.2**).

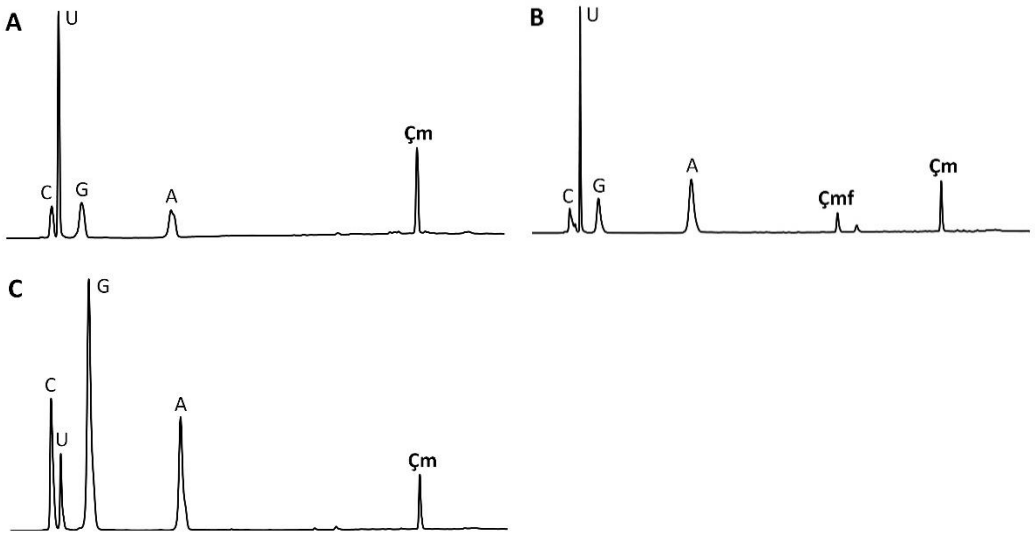

Figure 3.5. HPLC chromatograms of RNA oligonucleotides after enzymatic digestion with snake venom phosphodiesterase, nuclease P1, and alkaline phosphatase. A. Crude oligonucleotide **I**. B. Crude oligonucleotide **II**. C. Purified oligonucleotide **III**.

Now that it had been shown that the benzoyl protecting group for nitroxides had worked well for short oligonucleotides, it was of interest to see if this protecting group strategy would also work for longer RNA sequences. A 21-nt long RNA (**III**, **Table 3.2**) was synthesized

by using phosphoramidite **16**. Analysis by DPAGE showed no fluorescent band in the gel, indicating that no reduction of **Çm** had occurred (**Figure 3.4B**). Oligonucleotide **III** was purified and the spin labeling efficiency was determined. Spin count showed almost quantitative amount of nitroxide in the sample (**III**, **Table 3.2**) whereas spin count of the same oligonucleotide synthesized using phosphoramidite **18**, with the unprotected **Çm**, gave only 13% spin count (data not shown). Oligonucleotide **III** was enzymatically digested and the digest analyzed by HPLC (**Figure 3.5C**). As for oligonucleotide **I**, four peaks were seen for the natural nucleosides and one for **Çm**. These results show that this protecting group strategy can be used for at least 21-nt long RNA synthesis which yields in quantitative spin labeling of the RNA.

3.6 Conclusion

The nitroxide of **Çm** was protected by benzoylation of the hydroxylamine to yield **Çm-Bz**. The Bz protecting group was shown to be stable in all reagents used for the solid-phase oligonucleotide synthesis. **Çm** was incorporated into two RNA strands, an 8-mer and a 21-mer, using the benzoyl protected phosphoramidite. The benzoyl protecting group was stable through the chemical synthesis of the oligonucleotides and furthermore it was readily removed by standard oligonucleotide deprotection conditions to give nitroxide-labeled oligonucleotides. DPAGE was used to visually evaluate the oligonucleotides. Spin-counting by EPR spectroscopy and enzymatic digestion, analyzed by HPLC, demonstrated nearly quantitative spin-labeling efficiency. These results show that this protecting group strategy for nitroxides can be used as a general method to prepare spin labeled RNA oligonucleotides by synthesis through the phosphoramidite approach. This protecting group strategy was also used for DNA by Dr. Haraldur Yngvi Júlíusson where he incorporated **Ç**, the DNA derivative of **Çm**, into DNAs in various lengths, up to a 36-mer, with quantitative spin labeling efficiency.

4 Preparation of DNA and RNA oligonucleotides containing the spin labels Ç and Çm and the fluorescent probe Çmf for biophysical studies

4.1 Introduction

This PhD project has been closely involved in the Collaborative Research Centre (CRC) 902, which is an extensive collaboration between 19 research groups at the Goethe University Frankfurt, the Max Planck Institute for Biophysics (Frankfurt), the Max Planck Institute for Brain Research (Frankfurt), and the Technical University of Darmstadt. The goal of the CRC 902 is to study the structural diversity and conformational dynamics of RNA in order to better understand its biological functions. The Sigurdsson research group has over the years synthesized RNA and DNA samples both with spin labels and with fluorescent labels that have been investigated by research groups that are part of this consortium. The spin labeled samples are investigated in the group of Prof. Thomas F. Prisner at the Goethe University Frankfurt, using pulsed EPR spectroscopy. The fluorescently labeled RNA samples are investigated in the group of Prof. Josef Wachtveitl at the same institution, by steady-state and ultra-fast fluorescence spectroscopies.

4.2 Spin labeling of nucleic acids with Ç and Çm

As explained in detail in **Chapter 2**, **Ç**[2] and **Çm**[1] (**Figure 4.1**) are rigid spin labels for DNA and RNA, respectively. Due to their rigidity, they have been used for various nucleic acid systems to investigate their structure and dynamics by EPR.[141, 145-147, 181] Part of this PhD work was to synthesize **Çm** and incorporate into RNA. During this work, all reaction conditions for the synthesis up to the phosphoramidite of **Çm** were optimized. For example, the oxidation to produce **Ç** and **Çm** had been performed with tungsten and hydrogen peroxide which usually took 2 days and the conversion to the nitroxide was only between 25-50%. The oxidation was optimized by first protecting the 3'- and 5'-hydroxyl groups

with TBDMS and subsequently oxidizing with *m*CPBA in the presence of NaN_3. The reaction only took 2-4 h and yielded in 70-85% of the nitroxide.

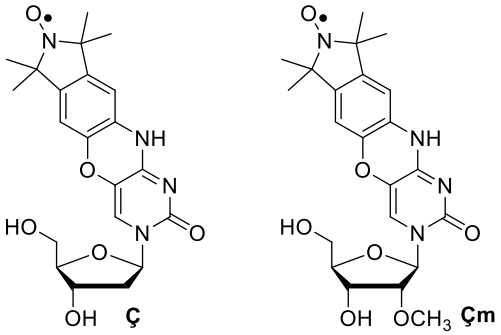

Figure 4.1. Structure of rigid spin labels **Ç** for DNA and **Çm** for RNA.

The development of a protecting group for nitroxides (**Chapter 3**) made it possible to synthesize longer oligonucleotides (20-50 nt long), in high yields, with near to quantitative spin labeling efficiency. Both **Ç** and **Çm** were incorporated into various nucleic acid constructs and each project will be briefly described in the following sections.

4.2.1 Ç-labeled 8-17 DNAzyme that cleaves RNA

It is common knowledge that DNA stores the genetic information of all living organisms but in the last decades it has been discovered that DNA can also catalyze various reactions similar to enzymes and ribozymes.[182] These catalytic DNAs are called DNAzymes. They are single-stranded DNAs that have been discovered through *in-vitro* selection.[183] The first DNAzyme that was discovered was able to cleave RNA,[184] but in the following years more DNAzymes were found that could catalyze cleavage[185-186] and ligation[187-188] of RNA, as well as cleavage[189] and ligation of DNA.[190]

The 8-17 DNAzyme is a 36-nt long RNA cleaving DNAzyme that contains a small 15-nt long cleaving site (**Figure 4.2A**, numbered nucleotides).[191] The same catalytic motif as found in 8-17 DNAzyme has been selected under different conditions,[185-186, 192] which indicates that it is an efficient DNAzyme. The catalytic core of the 8-17 DNAzyme is flanked by two substrate-recognizing arms that bind to the RNA, that is to be cleaved, through Watson-Crick base pairing. The activity of the DNAzyme has been tested in presence of different ions and was found to be most effective in presence of Pb^{2+}. The crystal structure of the 8-17 DNAzyme (**Figure 4.2B**, colored in pink) has been published, bound to a DNA

oligonucleotide substrate (**Figure 4.2B**, colored in green) that had one ribonucleotide at the cleavage site.[191]

Because it is not possible to gain information about the conformational dynamics of the DNAzyme by crystallography, PELDOR spectroscopy will be used to investigate the structure and dynamics of the 8-17 DNAzyme, both with a cleavable and a non-cleavable substrate to investigate if the DNAzyme undergoes changes upon cleavage. Furthermore, the effect of monovalent and divalent ions on the structure and dynamics will be studied. For these PELDOR experiments, the 8-17 DNAzyme was spin-labeled with **Ç** at positions 6 and 30 (**Figure 4.2**, **Ç** colored in red).

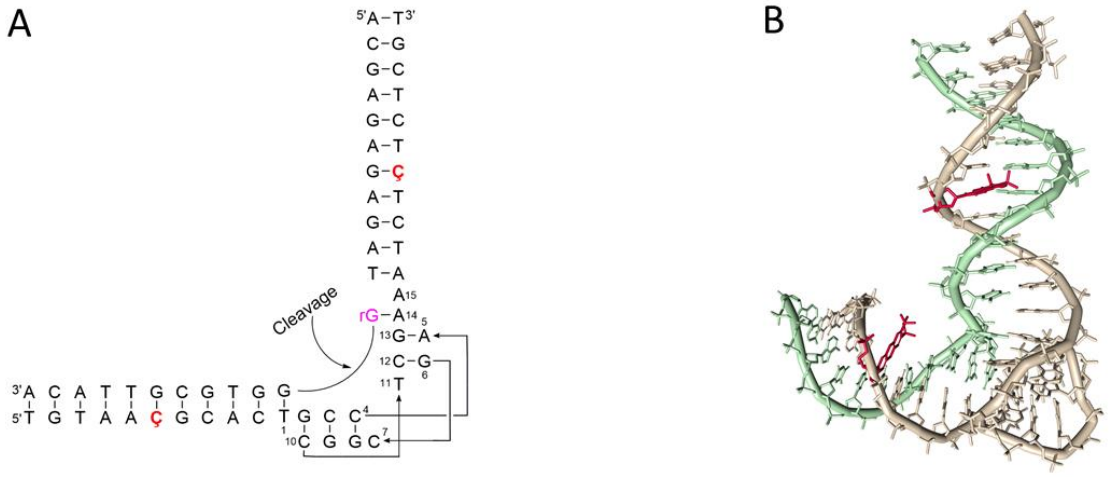

Figure 4.2. The RNA cleaving 8-17 DNAzyme and the cleaving strand. (A) Secondary structure (cleavage site at rG, colored in pink) and (B) its X-ray structure.[191] The DNAzyme is labeled with **Ç** (colored in red) at positions 6,30.

To determine if the spin-labeling affected the catalytic activity of the 8-17 DNAzyme, it was incubated with a cleavable substrate and the reaction analyzed as a function of time by DPAGE and UV-shadowing (**Figure 4.3**). The **Ç**-labeled DNAzyme is clearly active (**Figure 4.3C**). However, this is only a quantitative assay and thus, it cannot be determined if the spin labeled DNAzyme is as active as the unlabeled one (**Figure 4.3B**). Slightly stronger substrate bands for the spin labeled DNAzyme could be due to different loading of the samples; the cleavage band also seems stronger. The unlabeled DNAzyme does also show cleavage activity without Pb^{2+} (**Figure 4.3A**). The **Ç**-labeled 8-17 DNAzyme will be investigated in the laboratory of Prof. Prisner where PELDOR will be used to study the cleavage of the DNAzyme in the presence and absence of different divalent metal ions, such as Mg^{2+}, Pb^{2+}, and Zn^{2+} at different concentrations.

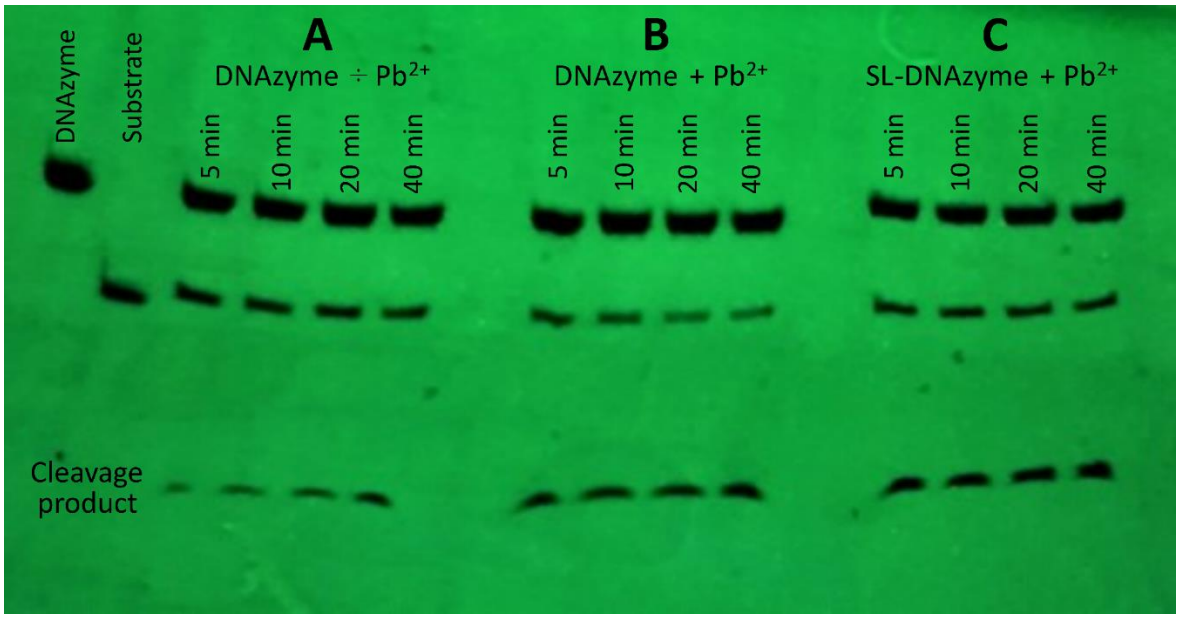

Figure 4.3. Analytical denaturing polyacrylamide gel analysis of the cleavage activity of the 8-17 DNAzyme. The DNAzyme and the cleavable substrate were mixed in a buffer (800 mM KCl, 200 mM NaCl, 100 mM Hepes-NaOH, pH 7.5) and aliquots were removed after 5, 10, 20 and 40 min. A. DNAzyme ÷ Pb^{2+}: Unmodified 8-17 DNAzyme without Pb^{2+}. B. DNAzyme + Pb^{2+}: Unmodified 8-17 DNAzyme with Pb^{2+}. C. SL-DNAzyme + Pb^{2+}: **Ç**-labeled 8-17 DNAzyme with Pb^{2+}.

4.2.2 Spin-labeled RNA duplexes for the study of duplex dynamics

As mentioned before, orientation-selective PELDOR spectroscopy has been used to investigate internal motions of DNA duplexes, doubly-labeled with **Ç**.[145] The distances and orientations were obtained between two **Ç** labels inside each duplex. Analysis of the EPR data made it possible to distinguish between different movements of the DNA duplexes, namely, bending, twisting, and stretching motions. The internal motions of RNA duplexes have yet to be investigated for comparison. Therefore, a series of 20-nt long RNA duplexes were synthesized, doubly labeled with **Çm** (**Figure 4.4**), using the same sequence as for the DNA duplexes (U instead of T) but including U-overhangs to prevent end-to-end stacking of the RNA duplexes.[193] The duplexes contained **Çm** at the same position (labeling position 1) in one strand but the position varied in the complementary strand (positions 8 to 15) (**Figure 4.4**).

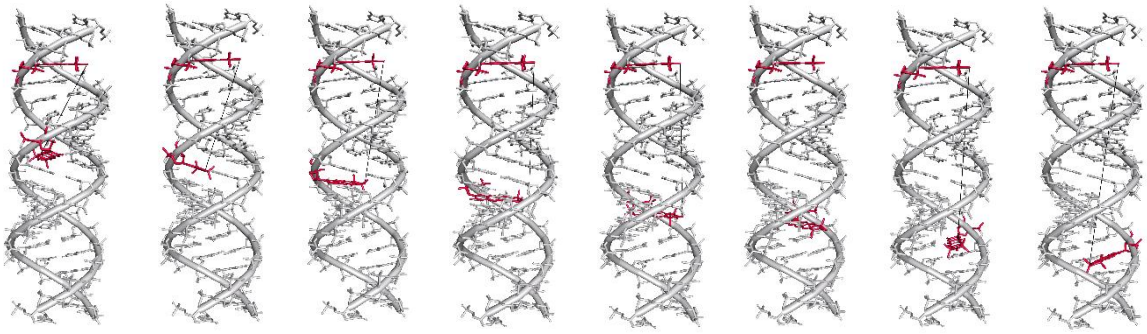

Figure 4.4. A series of doubly labeled RNA duplexes each containing two **Çm** labels (label in pink).

Çm-labeled oligoribonucleotides **IV-XIII** were synthesized through automated solid-phase synthesis (**Table 4.1**) by usage of the phosphoramidite of **Çm-Bz** (**Chapter 3**). The incorporation of the label was confirmed by mass spectrometry (**Table 4.1**) and CW-EPR spectroscopy (**Figure 4.5**). The **Çm**-labeled oligonucleotides were purified and their spin labeling efficiency was determined by spin-counting (**Table 4.1**) using CW-EPR spectroscopy. Both the incorporation of the spin label and the amount of spin label in each sample were further analyzed by HPLC chromatography of the digested oligonucleotides. Examples of HPLC chromatograms of the digested oligonucleotides are shown in **Figure 4.6**.

Table 4.1. Sequences of **Çm** labeled RNA oligonucleotides, their monoisotopic masses and their spin labeling efficiency, determined by spin counting.

	Sequence	Calcd mass	Found mass	Radical (%)
IV	5‘-UGU-**Çm**AG-UCG-CGC-GCG-CGC-AUC-3‘	6891.00	6889.5	88
V	5‘-UGU-**Çm**AG-UGC-GCG-CGC-GCG-AUC-3‘	6931.01	6929.4	92
VI	5‘-UGA-UGC-GCG-CG**Çm**-GCG-ACU-GAC-3‘	6954.04	6952.5	89
VII	5‘-UGA-UCG-CGC-G**Çm**G-CGC-ACU-GAC-3‘	6914.03	6911.5	94
VIII	5‘-UGA-UGC-GCG-**Çm**GC-GCG-ACU-GAC-3‘	6954.04	6955.5	99
IX	5‘-UGA-UCG-CG**Çm**-GCG-CGC-ACU-GAC-3‘	6914.03	6915.5	88
X	5‘-UGA-UGC-G**Çm**G-CGC-GCG-ACU-GAC-3‘	6954.04	6953.5	97
XI	5‘-UGA-UCG-**Çm**GC-GCG-CGC-ACU-GAC-3‘	6914.03	6912.5	99
XII	5‘-UGA-UG**Çm**-GCG-CGC-GCG-ACU-GAC-3‘	6954.04	6952.5	87
XIII	5‘-UGA-U**Çm**G-CGC-GCG-CGC-ACU-GAC-3‘	6914.03	6915.5	96

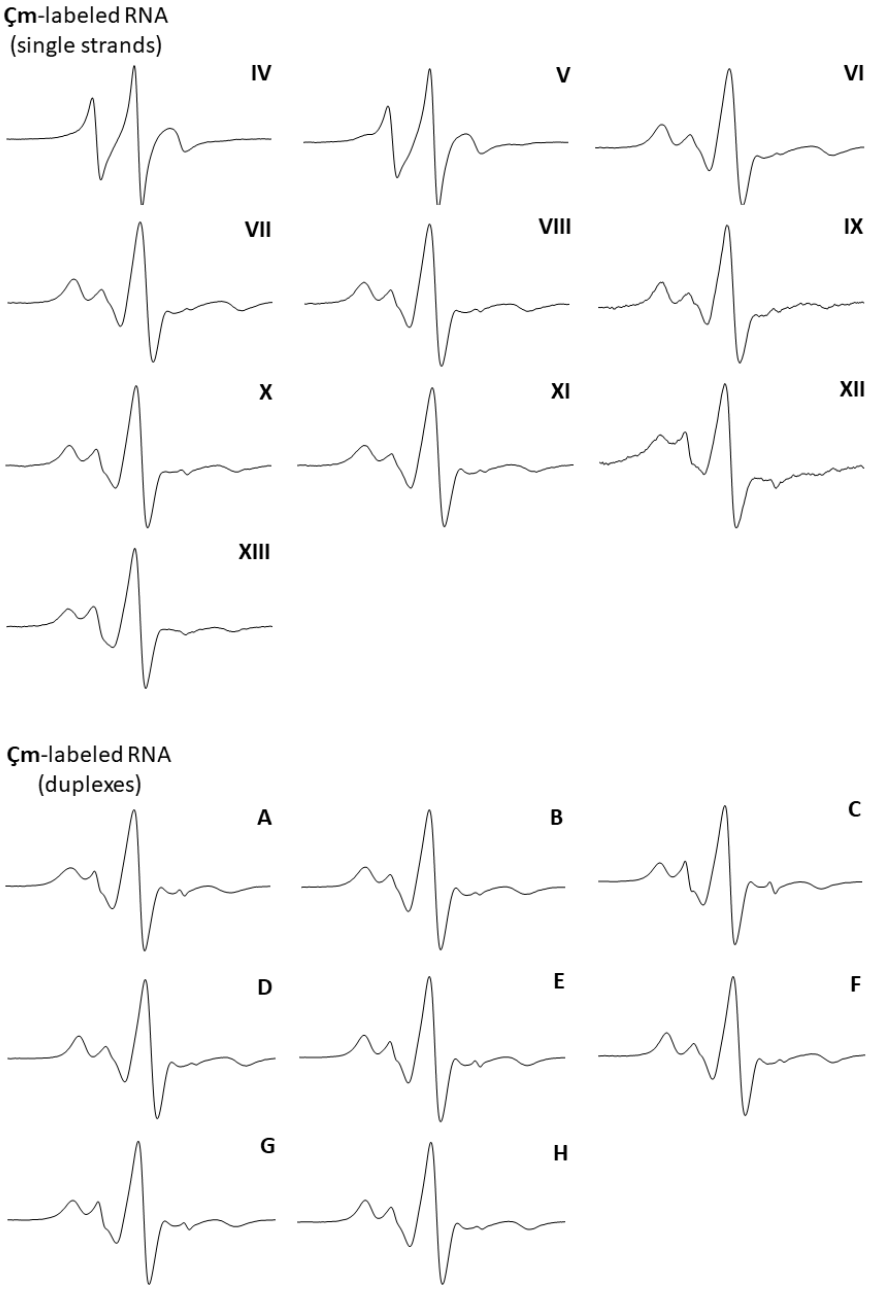

Figure 4.5. CW-EPR spectra of **Çm**-labeled oligonucleotides. EPR spectra were recorded at 22 °C in a phosphate buffer (2 nmol of RNA; 10 mM phosphate, 100 mM NaCl, 0.1 mM Na_2EDTA, pH 7.0).

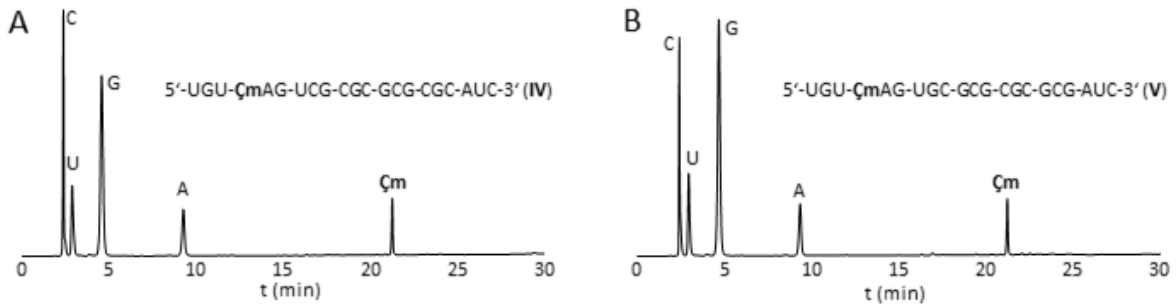

Figure 4.6. HPLC chromatograms of oligonucleotides after enzymatic digestion with snake venom phosphodiesterase, nuclease P_1, and alkaline phosphatase.[156, 194]

RNA duplexes **A-H** (**Table 4.2**) were formed by annealing spin-labeled oligonucleotides **IV**-**XIII** (**Table 4.1**) to their complementary strands. The duplex formation was confirmed by CW-EPR spectroscopy (**Figure 4.4**). The samples were sent to the laboratory of Prof. Prisner where Mr. Maximilian Gauger and Dr. Nicole Erlenbach carried out PELDOR experiments at different frequency bands (X-, Q- and G-band).

Table 4.2. Modeled and measured distances between two spin labels inside **Çm** labeled duplexes.

	Labeling position	Duplex	Modeled distance (Å)	Measured distance (Å)*
A	1,8	5'-UGU**Çm**AGUCGCG CGCGCGCAUC -3' 3'- CAG UCAGCG**Çm**GCGCGCGUAGU-5'	22.1	21.7
B	1,9	5'-UGU**Çm**AGUGCGCG CGCGCGAUC -3' 3'- CAG UCACGCG**Çm**GCGCGCUAGU-5'	24.2	24.1
C	1,10	5'-UGU**Çm**AGUCGCGCG CGCGCAUC -3' 3'- CAG UCAGCGCG**Çm**GCGCGUAGU-5'	26.0	28.4
D	1,11	5'-UGU**Çm**AGUGCGCGCG CGCGAUC -3' 3'- CAG UCACGCGCG**Çm**GCGCUAGU-5'	28.1	29.9
E	1,12	5'-UGU**Çm**AGUCGCGCGCG CGCAUC -3' 3'- CAG UCAGCGCGCG**Çm**GCGUAGU-5'	30.2	30.6
F	1,13	5'-UGU**Çm**AGUGCGCGCGCG CGAUC -3' 3'- CAG UCACGCGCGCG**Çm**GCUAGU-5'	32.6	34.7
G	1,14	5'-UGU**Çm**AGUCGCGCGCGCG CAUC -3' 3'- CAG UCAGCGCGCGCG**Çm**GUAGU-5'	35.6	37.2
H	1,15	5'-UGU**Çm**AGUGCGCGCGCGCG AUC -3' 3'- CAG UCACGCGCGCGCG**Çm**UAGU-5'	38.8	37.7

*Measurements performed by Mr. Maximilian Gauger and Dr. Nicole Erlenbach.

The measured distances between the spin labels in each duplex were in good agreement with the modeled distances (**Table 4.2**). Furthermore, due to the rigidity of **Çm**, orientation-selective PELDOR data were acquired for comparison to molecular dynamics (MD) simulations of different movements of the duplexes. The simulation was performed by Dr. Lukas Stelzl using the DESRES[195] force field. The measured and simulated data are still being analyzed and, therefore, there has not yet been drawn a conclusion on the internal dynamics of the duplex RNAs.

It has been seen by the crystal structure of **Ç** inside duplex DNA,[154] that it is non perturbing of the DNA duplex. However, it is not known if **Çm** alters the structure of an A-form RNA helix. Pulsed electron nuclear double resonance (ENDOR) is a pulsed EPR technique that can be used to measure hyperfine coupling constants of nuclear spins that are coupled to

unpaired electron spins.[196] PELDOR can normally be used to measure distances between 15-80 Å[110-113] but with ENDOR it is possible to measure distances under 15 Å with atomic resolution.[197] It was decided to use ^{19}F as it has a high gyromagnetic ratio and would be the only F atom present in the RNA duplex, making it easier to measure nitroxide-fluorine distances. Therefore, three duplexes were synthesized, each labeled with **Çm** (**Figure 4.7**, colored in pink) on one strand and a 2'-deoxy-2'-F modified nucleotide on the opposing strand (**Figure 4.7**, colored in orange). Mr. Gauger measured the three samples by ^{19}F-ENDOR and yielded distances that were in good agreement with distances obtained by DESRES MD simulation (data not shown) indicating that **Çm** is nonperturbing of A-form RNA duplexes.

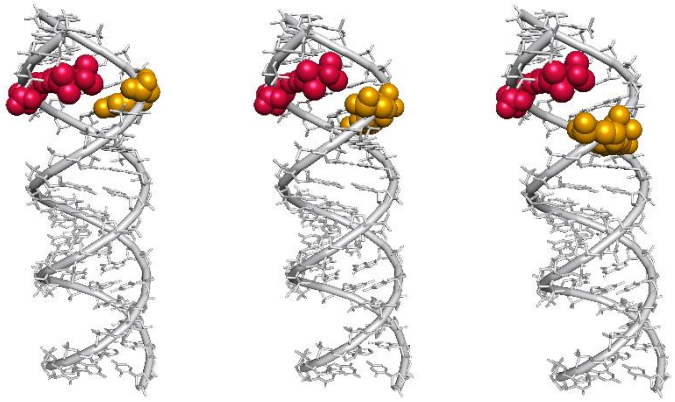

Figure 4.7. A series of RNA duplexes each containing **Çm** (label in pink) and a 2'deoxy-2'-F labeled nucleotide (orange).

4.2.3 The TMR3 aptamer

NMR can give information on secondary and tertiary structures as well as the dynamical behavior of nucleic acids in solution at atomic resolution.[76-77] NMR is an excellent technique to investigate local structures but it is not suited for determining distances longer than about 5 Å.[76] Moreover, for large, flexible nucleic acids and their complexes it can be hard to obtain high quality NMR data due to resonance overlap, line broadening, and low proton density.[181] PELDOR can be used to measure longer distances in biomolecules, between 15-80 Å.[112-113] Therefore, combining these two techniques, NMR and PELDOR, will give detailed information on the structure and dynamics of biomolecules. Indeed, the global structure and dynamics of a highly flexible DNA duplex, labeled with the rigid label **Ç**, has been investigated using a combination of NMR and PELDOR.[181] In the current project, NMR and

PELDOR spectroscopies will also be used to investigate a three-way junction RNA that binds to a ligand.

The tetramethylrhodamine (TMR) binding aptamer TMR3 is one of four aptamers that was selected through SELEX against a carboxylic acid derivative of TMR called 5-TAMRA (**Figure 4.8**).[198] The TMR3 aptamer is a 54-nt long RNA that binds to its ligand with a K_d in the high nM range. The group of Prof. Wöhnert made a minimized version of the TMR3 aptamer that is 48-nt long and investigated and solved the structure of the apo and the bound form by multidimensional NMR (**Figure 4.8**).[199] To gain information on the global structure of the TMR3 aptamer, long-distance EPR constraints between the rigid spin label **Çm** will be combined with the NMR data to determine the helix orientations and flexibilities in the presence and absence of the ligand.

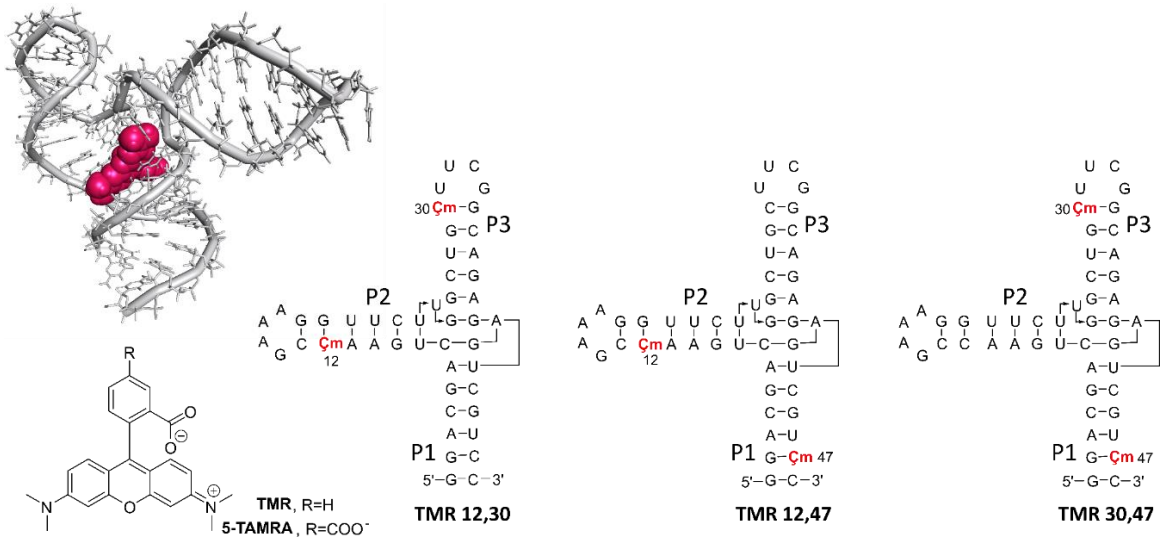

Figure 4.8. The TMR3 aptamer and its ligand (left).[199] Secondary structures of **Çm**-labeled TMR aptamers (right). The TMR aptamer is labeled with **Çm** (label in red) at positions 12,30 (left), 12,47 (middle) and 30,47 (right).

Çm was incorporated into the NMR model of the TMR3 aptamer at different positions, choosing positions in helices P1, P2 and P3 where **Çm** does not seem to be perturbing. The distances between the labels were 30.0-34.4 Å, which is suitable for PELDOR measurements. Three doubly **Çm**-labeled TMR3 aptamer constructs were chosen; **TMR 12,30** (**Figure 4.8**, left), **TMR 12,47** (**Figure 4.8**, middle), and **TMR 30,47** (**Figure 4.8**, right). The three TMR3 aptamers were synthesized through automated solid-phase synthesis by usage of the phosphoramidite of **Çm-Bz**. The spin-labeling efficiency of the samples were between 70-90%, determined by spin counting and by HPLC analysis of the enzymatic

digested samples (data not shown). Dr. Thilo Hetzke, in Prof. Prisner's laboratory, measured samples **TMR 12,30** and **TMR 12,47**, with and without ligand (**Table 4.3**).

Table 4.3. Comparison of distances between two **Çm** labels inside the TMR3 aptamer. Modeled (d_{model}) and measured distances ($d_{meas.}$) by PELDOR with TMR (+TMR) and without TMR (-TMR).

	d_{model} (Å)	$d_{meas.}$ (Å)*	
Sample	+ TMR	+ TMR	-TMR
TMR 12,30	30.7	32.6	-
TMR 12,47	30.0	30.5	34.3
TMR 30,47	34.4		

*Measured by Dr. Thilo Hetzke

TMR 12,47 has a similar distance distribution with and without the ligand (**Table 4.3**), which could indicate that helices P1 and P2 have a preformed structure before the ligand binds to the aptamer. For **TMR 12,30** without the ligand, not one clear distance distribution was observed but rather many smaller distance distributions, which is an indication of some degree of flexibility inside the apo form of the aptamer, likely in the P3 helix. The distances between the labels in **TMR 12,30** and **TMR 12,47** when bound to the ligand were in good agreement with the modeled distances (**Table 4.3**). **TMR 30,47** is still under investigation in the group of Prof. Prisner.

4.2.4 RNA hairpin loop

An RNA hairpin loop (**Figure 4.9**) was designed by the group of Assoc. Prof. Katja Petzold to study the dynamics of RNA by NMR. The RNA hairpin loop was designed as a minimalistic system to study how local dynamics, such as the unpaired U-bulge, influence the global helical motion. The group used a 2D NMR method called selective optimized proton experiments (SELOPE) to obtain ^{1}H 1D and 2D spectra of the RNA that was not isotopically labeled.[200] SELOPE is performed by selective excitation of specific groups of protons and the spectra are edited and de-crowded using coherence transfer through homonuclear *J*-couplings. It was observed by NMR that this RNA hairpin loop undergoes a conformational change by addition of Mg^{2+} and Petzold's group proposed a tertiary structure for both conformers (**Figure 4.9**), which will be tested by PELDOR.

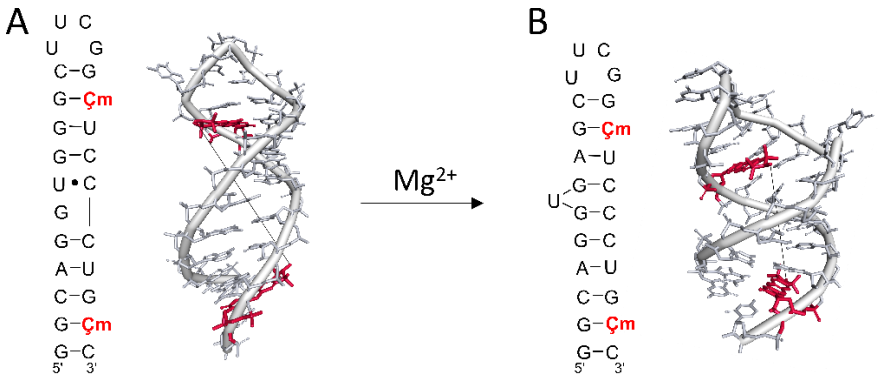

Figure 4.9. An RNA hairpin loop labeled with **Çm**. The hairpin is labeled at positions 17 and 24 (**Çm** is labeled in red). The RNA undergoes a conformational change by addition of Mg^{2+} from an elongated structure (A) to a more compressed structure (B).[200]

The models of the proposed tertiary structures were used to choose two labeling positions for **Çm** inside the RNA (**Figure 4.9**). Positions 17 and 24 were chosen where **Çm** did not perturb the RNA structure. The distances between the spin labels in both conformers were acceptable for PELDOR experiments (25.7 Å for A, 19.7 Å for B). The **Çm**-labeled RNA was synthesized by solid-phase synthesis with quantitative spin labeling efficiency, determined by HPLC analysis of the enzymatically digested oligonucleotide. The RNA is currently being measured by Mr. Gauger in the group of Prof. Prisner in Frankfurt.

4.3 Fluorescent labeling of nucleic acids

Fluorescence spectroscopy is a very sensitive technique to study nucleic acids, giving information about global structures and dynamics.[84, 90] Ideal fluorescent probes for investigation of nucleic acids are fluorescent analogues of natural DNA and RNA bases that do not cause perturbation of the native structure and can be incorporated into nucleic acids the same way as natural nucleosides.[201]

4.3.1 Site-directed labeling of nucleic acids with fluorophores

Fluorescent nucleosides can be incorporated during solid-phase synthesis through the phosphoramidite approach, post-synthetically, post-transcriptionally or enzymatically.[91, 202] When using the phosphoramidite approach the nucleoside containing the fluorescent nucleobase is converted into a phosphoramidite and is incorporated through solid-phase synthesis the same way as natural nucleosides. When incorporated post-synthetically or post-transcriptionally, the labeling position of interest on the nucleic acid has a reactive group

that can be used to incorporate the fluorophore with chemical reactions often by the use of C-C cross-coupling reactions or by click chemistry.[201-202] Nucleic acids can also be fluorescently labeled by enzymes, using fluorescently-labeled primers or by use of fluorescent nucleotides in a pool that the enzymes employ to synthesize the nucleic acid strand.[201]

4.3.2 Fluorescent nucleobase analogues

The list of fluorescent nucleobase analogues is extensive and is beyond the scope of this dissertation and, therefore, only a few examples will be discussed in this section. One of the first reported fluorescent nucleobase analogues and probably the most prominent one is 2,6-diaminopurine (**2AP**, **Figure 4.10**) that is a derivative of adenosine and forms a base-pair with thymidine.[203] The fluorescence of **2AP** is quenched drastically when inside nucleic acids but it is sensitive to its micro-environment as the fluorescence of the label changes upon bending, kinking and base flipping and folding of the DNA or RNA to which it is attached.[204]

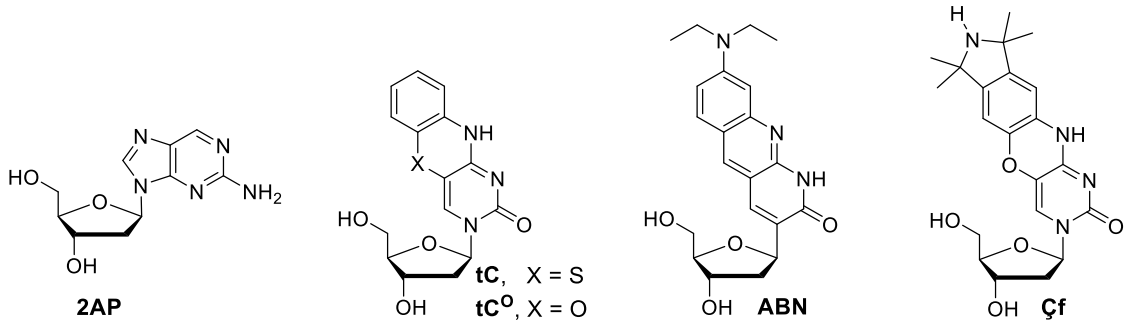

Figure 4.10. Fluorescent nucleobase analogues for DNA.

The fluorescent phenothiazine-based tricyclic cytidine analogue **tC** (**Figure 4.10**) was first reported by Matteucci and coworkers as a helix stabilizer for antisense applications[205] but later the phenothiazine-derived nucleoside was used as a fluorescent probe by Wilhelmsson and coworkers.[206] The fluorescence of **tC** slightly enhanced when the label was incorporated into DNA (fluorescence quantum yield, Φ = 0.16-0.21) but it was insensitive to its micro-environment; there was almost no change in fluorescence observed with respect to the flanking bases.[207-208] The phenoxazine-derivative **tC^O** (**Figure 4.10**) is another related cytidine analogue, where the sulfur of **tC** has been exchanged by an oxygen. It was also synthesized by Matteucci and coworkers[205] for the same purpose as **tC** but was investigated

and later used by Wilhelmsson and coworkers.[209] **tC^{O}** has much greater brightness than **tC** inside duplex DNA[207] but similar to **tC**, it is not sensitive to its micro-environment.[209]

The recently reported fluorescent nucleobase analogue **ABN** (**Figure 4.10**) is the brightest and most red-shifted nucleobase analogue known.[210] **ABN** has a push-pull system that yields in a $\varepsilon_{442} = 20\,000\ M^{-1}\ cm^{-1}$ and $\Phi_{em,540} = 0.39$ in water. When ABN is base paired with adenine in duplex DNA the fluorescence quantum yield increases ($\Phi_{em} = 0.50–0.53$). Furthermore, the brightness of **ABN** allows detection of single-molecules.

Çf is a fluorescent cytidine analogue (**Figure 4.10**) that is the direct synthetic precursor of the rigid spin label **Ç**.[2] It base pairs with guanine in DNA. **Çf** is exceptionally sensitive to its micro-environment.[211] When incorporated into DNA duplex, **Çf** can distinguish between pairing with the four bases dG, dC, dA and T[45] and an extensive flanking sequence effect was observed.[212] Furthermore, conformational dynamics of bulges and internal loops in duplex DNA were studied by a combination of EPR and fluorescence spectroscopies by using both the spin label **Ç** and the fluorescent label **Çf**.[168]

4.4 Çmf labeling of RNA

It was of interest to evaluate the rigid fluorescent label **Çmf**, the RNA derivative of **Çf**, as a fluorescent probe for RNA. **Çmf** was synthesized as previously described.[1] The phosphoramidite of **Çmf** (**20**, **Scheme 4.1**) had previously been synthesized by Dr. Dnyaneshwar Gophane, a former group member of the Sigurdsson Group, but had not yet been published. The 3'-hydroxyl of **Çmf** was protected as a 4,4-dimethoxytrityl ether and the 5'-hydroxyl was phosphitylated to yield phosphoramidite **20** (**Scheme 4.1**). Phosphoramidites are usually purified by precipitation to remove the excess phosphitylating reagent. However, phosphoramidite **20** required rapid purification on a filter column that had been basified prior to use. This method gave a pure product in good yields.

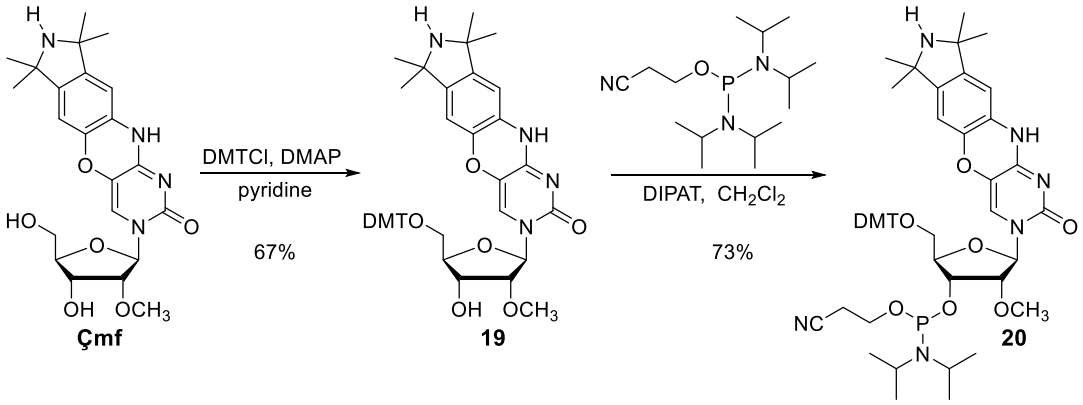

Scheme 4.1. Synthesis of the phosphoramidite (**20**) of **Çmf**.

Dr. Gophane synthesized **Çmf**-labeled RNA single-strands and duplexes and Dr. Henrik Gustmann, a former group member of the group of Prof. Wachtveitl, studied the photophysical properties of **Çmf** inside the RNA.[213] The results showed that **Çmf** is non perturbing of duplex structure. Furthermore, it was demonstrated that **Çmf** is sensitive to its micro-environment as the fluorescence of the label was affected by base pairing, stacking and solvent accessibility. Therefore, **Çmf** was incorporated into various RNA constructs and each project will be discussed briefly in the following sections.

4.4.1 The neomycin aptamer

The neomycin aptamer (**Figure 4.11A**) is a riboswitch that was discovered through *in-vitro* selection.[214] It is a 27-nt long RNA that binds with high affinity and specificity to the aminoglycoside antibiotic neomycin (**Figure 4.11B**). Aptamers can normally bind to ligands through two different mechanisms, namely conformational selection and induced fit.[215-216] When the ligand binds through conformational selection, it binds to a preformed structure of the aptamer.[217] When a ligand binds via the induced fit mechanism, it first binds loosely to the aptamer and then drives the aptamer to change its conformation to bind tightly to the ligand. The structure of the neomycin aptamer has been solved by NMR both with and without ligand.[218] The binding pocket seemed to only go through minor structural changes when neomycin bound to the aptamer which indicated the binding mechanism to be conformational selection.

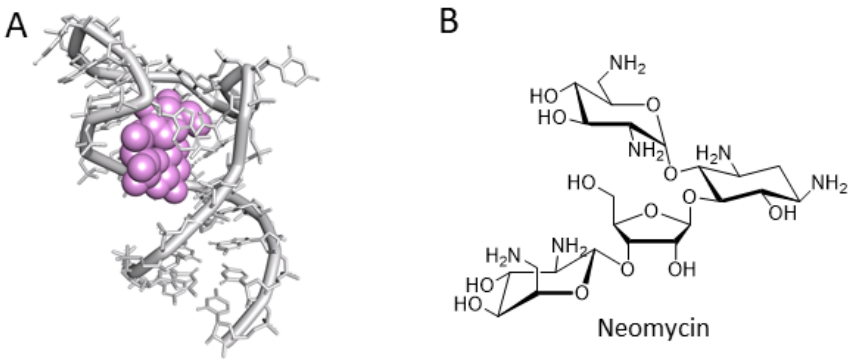

Figure 4.11. The neomycin aptamer. Tertiary structure of the neomycin aptamer bound to its ligand (A) aminoglycoside antibiotic neomycin (B).

The neomycin aptamer was labeled with **Çmf** to study the dynamics of the binding by fluorescence spectroscopy. Four samples of the **Çmf**-labeled aptamer were prepared by solid phase synthesis by using phosphoramidite **20**: **Çmf6**, **Çmf8**, **Çmf15** and **Çmf22** (**Figure 4.12**). The incorporation of **Çmf** into the aptamer was confirmed by mass analysis of the four oligonucleotides and by HPLC analysis of the digested samples (data not shown).

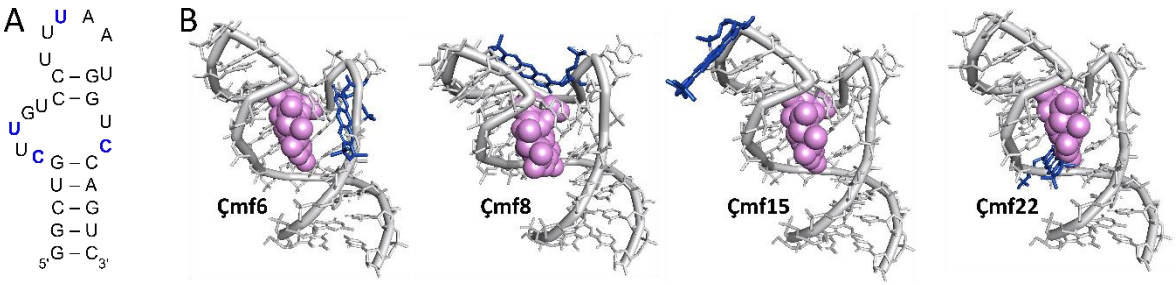

Figure 4.12. The **Çmf**-labeled neomycin aptamer. A. Secondary structure of the neomycin aptamer labeled with **Çmf** (blue) at position 6, 8, 15 or 22. B. Tertiary structures of the **Çmf**-labeled (blue) neomycin aptamer bound to its ligand.[219]

Dr. Gustmann investigated the **Çmf** labeled neomycin-aptamer samples and confirmed the previously proposed conformational selection mechanism for the binding of neomycin to the aptamer.[213] Furthermore, fluorescence-monitored stopped-flow measurements, indicated that ligand binding went through a two-step binding process. The first step is unspecific ligand binding near or in the binding pocket and in the second step the ligand is bound specifically through hydrogen bonding and electrostatic interactions.

4.4.2 Evaluation of tCnitro and Çmf for FRET experiments

Similar to PELDOR measurements (discussed in **Chapter 2**), using rigid labels for FRET, results in more detailed information about distances and orientation between two chromophores inside nucleic acids.[220] As explained in **Chapter 2**, to measure hetero-FRET, the emission of the donor and the absorption of the acceptor need to overlap.[89] **tCnitro** (**Figure 4.13**) is a cytidine analogue that has been used for DNA as a FRET acceptor, paired with the fluorescent cytidine derivative **tC^{O}**, a FRET donor.[221] **tCnitro** is a quencher which quenches the fluorescence of **tC^{O}** when FRET occurs. This FRET pair gave detailed structural information on duplex DNA. Because **Çmf** is a rigid fluorescent probe that has proven valuable to study dynamics of RNA and its emission overlaps with the absorption of **tCnitro** it was of interest to investigate their ability as a FRET pair inside RNA (**Figure 4.13**).

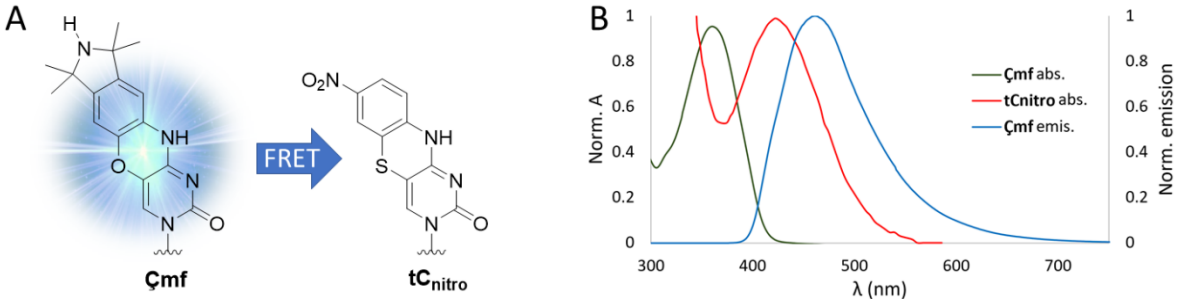

Figure 4.13. A. Structures of **Çmf** (FRET donor) and **tC$_{nitro}$**[222] (FRET acceptor). B. Absorption (black) and emission (blue) spectra of **Çmf** and the absorption (red) spectrum of **tC$_{nitro}$**.

To evaluate **Çmf** and **tCnitro** as a FRET pair, they were incorporated into 12 RNA duplexes at various positions, with **Çmf** on one strand and **tCnitro** on the opposing strand (**Table 4.4**). The oligonucleotides were synthesized by solid-phase synthesis using phosphoramidite **20** and the phosphoramidite of **tCnitro** (the 2'-deoxycytidine derivative is commercially available from Glen Research) and duplexes were formed. Dr. Gustmann performed steady-state fluorescence measurements and calculated the FRET efficiencies (E) between **Çmf** and **tCnitro** inside the duplexes (**Table 4.4**) and compared to the efficiency simulated by Mr. Florian Hurter (PhD student in the group of Prof. Wachtveitl), showing that they were in good agreement (**Table 4.4**).

Table 4.4. RNA duplexes labeled with **Çmf** (blue) and **tCnitro** (orange) at different labeling positions. FRET efficiency (E), both simulated and calculated. Distances (d) between the labels, both calculated and modeled.

Duplex	E_{calcd}*	E_{sim}**	d_{calcd} (Å)*	d_{model} (Å)
5'-UAÇmfGCAGCGACGCAU-3' 3'-AUG CGUCGCUGCGUA-5'	0.88	1.00	7.5	2.7
5'-UAÇmfGCAGCGACGCAU-3' 3'-AUG CGUCGCUGCGUA-5'	0.84	1.00	10.2	8.6
5'-UAÇmfGCAGCGACGCAU-3' 3'-AUG CGUCGCUGCGUA-5'	0.80	0.96	15.8	16.8
5'-UAÇmfGCAGCGACGCAU-3' 3'-AUG CGUCGCUGCGUA-5'	0.47	0.47	23.8	24.6
5'-UACGÇmfAGCGACGCAU-3' 3'-AUGCG UCGCUGCGUA-5'	0.94	1.00	7.5	8.8
5'-UACGÇmfAGCGACGCAU-3' 3'-AUGCG UCGCUGCGUA-5'	0.97	0.99	8.9	4.2
5'-UACGÇmfAGCGACGCAU-3' 3'-AUGCG UCGCUGCGUA-5'	0.93	1.00	10.8	9.9
5'-UACGÇmfAGCGACGCAU-3' 3'-AUGCG UCGCUGCGUA-5'	0.74	0.91	17.6	19.6
5'-UACGCAGÇmfGACGCAU-3' 3'-AUGCGUCG CUGCGUA-5'	0.90	1.00	8.1	8.8
5'-UACGCAGÇmfGACGCAU-3' 3'-AUGCGUCG CUGCGUA-5'	0.91	1.00	8.0	4.1
5'-UACGCAGÇmfGACGCAU-3' 3'-AUGCGUCG CUGCGUA-5'	0.68	0.99	12.8	14.9
5'-UACGCAGÇmfGACGCAU-3' 3'-AUGCGUCG CUGCGUA-5'	0.88	0.99	12.3	3.3

* Data collected by Dr. Henrik Gustmann. **Simulated by Mr. Florian Hurter.

The FRET efficiency was the highest when **tCnitro** and **Çmf** were near to each other and became lower as the labels were further apart from each other, as expected. The distances between the FRET pairs were mostly in good agreement with the modeled distances except for the samples where the FRET efficiency was near to quantitative. The error is likely caused by the low fluorescence resulting from the quenching of the fluorescence (**Table 4.4**). The overall data from the labeled duplexes confirms that **tCnitro** and **Çmf** function well as a FRET pair.

4.4.3 The neomycin aptamer studied by FRET

After validating **Çmf** and **tCnitro** as a FRET pair, they were incorporated into the neomycin aptamer to investigate the global structure of the aptamer by FRET both with and without the ligand. The labels were modeled at different positions inside the aptamer and it was decided to incorporate **tCnitro** at the third position and **Çmf** at positions 6, 8 and 15, as

those positions had been used before for the fluorescence binding studies of the neomycin aptamer (**Figure 4.14**). The sample **tCnitro3** was synthesized as a negative control. All four samples were synthesized through solid-phase synthesis and the labeling was confirmed by mass spectrometry.

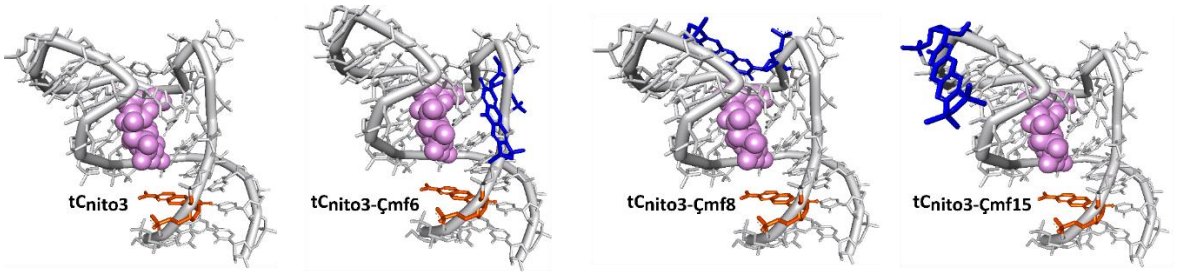

Figure 4.14. The neomycin aptamer[219] labeled with both **Çmf** (blue) and **tC$_{nitro}$**[222] (orange) for hetero-FRET measurements.

These samples are currently being investigated by Mr. Hurter. Preliminary data indicates that the simulated and calculated FRET efficiencies are in good agreement (**Table 4.4**). For samples **tCnitro3-Çmf6** and **tCnitro3-Çmf8**, where **Çmf** and **tCnitro** are near to each other, the FRET efficiency is over 90%. This shows that **tCnitro** is clearly quenching the fluorescence of **Çmf**. The FRET efficiency did not change for **tCnitro3-Çmf6** when the ligand was added to the aptamer but for **tCnitro3-Çmf8** the FRET efficiency dropped when the ligand was added, being an indication of a change in the environment of the FRET pair.

Table 4.5. FRET measurements of the neomycin aptamer with **tCnitro** and **Çmf**. Modeled distance (d_{model}) between **tCnitro** and **Çmf** inside the neomycin aptamer. FRET efficiency (E) both simulated and calculated for the aptamer bound to neomycin (+ Neo) and calculated FRET efficiency of the aptamer without neomycin (- Neo). Fluorescence lifetimes of the aptamer with (+ Neo) and without (- Neo).

	d_{model} (Å)	E_{sim}*	E_{calcd}*		Lifetime (ns)*	
Sample	+Neo	+ Neo	- Neo	+ Neo	- Neo	+ Neo
tCnitro3-Çmf6	12.2	0.95	0.98	0.97	0.033	0.069
tCnitro3-Çmf8	20.5	0.94	0.93	0.79	0.121	0.751
tCnitro3-Çmf15	23.5	0.31	0.41	0.48	3.248	3.619

*Data collected and simulated by Mr. Florian Hurter.

Mr. Hurter performed fluorescence lifetime measurements on all three samples with and without the ligand (**Table 4.5**). The fluorescence lifetime of sample **tCnitro3-Çmf8** was

short, as expected, as the FRET efficiency is near to quantitative. In contrast, the lifetime for sample **tCnitro3-Çmf15** is longer. The lifetime for sample **tCnitro3-Çmf8** changed when the aptamer bound to neomycin, indicating a change in the environment of the FRET pair. Mr. Hurter is still investigating the samples and will for example perform fluorescence-monitored stopped-flow measurements.

As discussed in **Chapter 2**, FRET can also occur between two of the same fluorophores. The neomycin aptamer was doubly labeled with **Çmf** to evaluate as a label for homo-FRET (**Figure 4.15**) but one sample was mono labeled with **Çmf** at position 3 as a negative control (**Figure 4.15**). These samples are awaiting measurements in the laboratory of Prof. Wachtveitl.

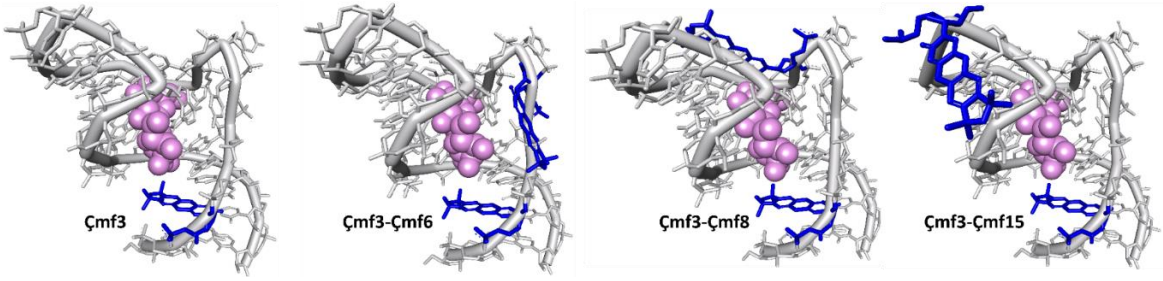

Figure 4.15. The neomycin aptamer doubly labeled with **Çmf** (blue) for homo-FRET measurements.

4.4.4 The i-Mango III aptamer studied by FRET

The i-Mango III aptamer was selected *in-vitro* against the thiazole orange dye TO1-biotin (**Figure 4.16A**), which binds with high affinity (K_d = 3-6 nM).[223] When the i-Mango III aptamer binds to the TO1-biotin ligand it lights up and is highly fluorescent (ε = 77500 $M^{-1}cm^{-1}$, Φ = 0.66) which makes it a good candidate for live cell RNA visualization. The structure of the i-Mango III aptamer, bound to its ligand, was solved by X-ray crystallography (**Figure 4.16A**). The i-Mango III aptamer is a 37-nt long aptamer that has a unique tertiary fold with a helical region and a G-quadruplex on which the TO1-biotin ligand stacks (**Figure 4.16A**). Because the crystal structure only gives a static view of the aptamer-ligand complex, it was of interest to use FRET to obtain information about the structure and dynamics of the aptamer with and without ligand. The global structure of the aptamer as well as the flexibility in absence and presence of the ligand will be investigated. It was of interest to use **Çmf** and the i-Mango III aptamer-ligand complex as a FRET pair as the absorption of the complex (acceptor) overlaps with the emission of **Çmf** (donor) (**Figure 4.16B**).

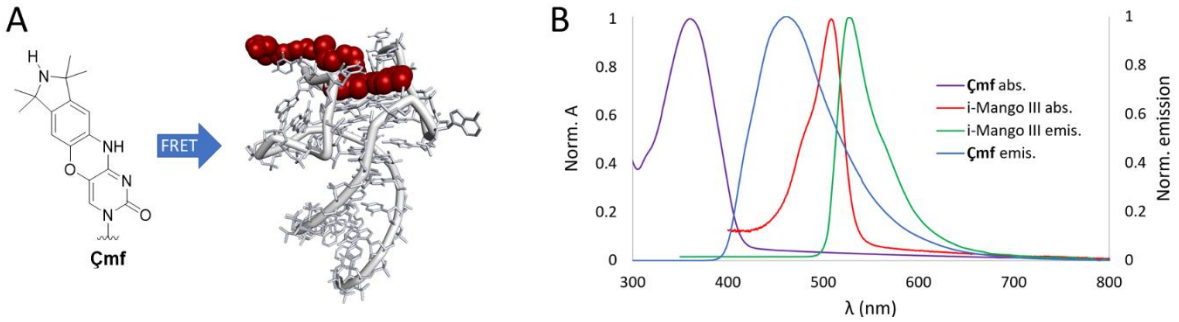

Figure 4.16. A. Structures of **Çmf** (FRET donor) and the i-Mango III aptamer[223] bound to TO1-biotin (red) (FRET acceptor). B. Absorption and emission spectra of **Çmf** and of the i-Mango III aptamer bound to TO1-biotin.

Different positions were modeled for **Çmf** inside the i-Mango III aptamer as **Çmf** and TO1-biotin need to be at least 10 Å apart to yield reliable FRET data, **Çmf** should not have any steric clashes with the aptamer and it should not be in a very flexible region or in the binding pocket of the aptamer. It was decided to label the i-Mango III aptamer with **Çmf** at positions C_{1A} and at C_{28} (**Table 4.6**). The tertiary structure of **Çmf$_{C1A}$** and **Çmf$_{C28}$** are shown in **Figure 4.17**.

Table 4.6. Sequences of the **Çmf**-labeled i-Mango III aptamers and the modeled distance between **Çmf** and TO1-biotin. The sequences are numbered as in the paper from Trachman RJ *et al.*[223]

	Sequence	d_{model} (Å)
Çmf$_{C1A}$	5‘-GUA **Çmf**$_{1A}$GA AGG AAG GU$_{10}$U UGG C$_{15}$AU GGG GUA GUU GUC$_{28}$ GUA C-3‘	23.2
Çmf$_{C1A}$	5‘-GUA C$_{1A}$GA AGG AAG GU$_{10}$U UGG C$_{15}$AU GGG GUA GUU GU**Çmf**$_{28}$ GUA C-3‘	19.3

The samples are being investigated by Mr. Hurter and preliminary data have shown that the binding affinity of the ligand to the aptamer is similar to the unlabeled aptamer. Furthermore, steady-state fluorescence measurements indicate an energy transfer occurring between **Çmf** and the TO1-biotin ligand inside the aptamer. Mr. Hurter continues to investigate the aptamers to obtain for example the FRET efficiency and the distance between the donor and acceptor.

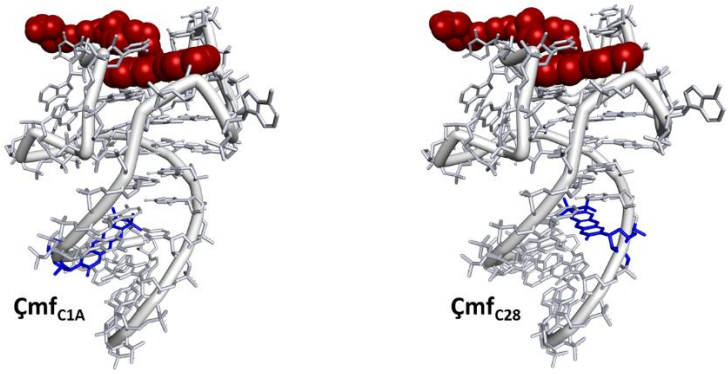

Figure 4.17. Tertiary structures of **Çmf**-labeled (blue) i-Mango III aptamers[223] **Çmf$_{C1A}$** and **Çmf$_{C28}$** bound to the TO1-biotin ligand (red).

4.5 Conclusion

In the first part of this chapter, incorporation of rigid spin labels **Ç** and **Çm** into DNA and RNA were described, for investigation of their structure and dynamics by PELDOR spectroscopy. The rigid spin-label **Ç** was incorporated into an RNA-cleaving DNAzyme, while **Çm** was incorporated into a series of RNA duplexes to investigate internal dynamics of RNA, the tetramethyl rhodamine (TMR) aptamer and an RNA hairpin loop to study a Mg^{2+}-dependent conformational change. In the second part of this chapter, the rigid fluorescent label **Çmf** was described and how it was incorporated into RNA to study by fluorescence spectroscopy. **Çmf** was incorporated into the neomycin aptamer to investigate the binding mechanism of the ligand to the aptamer, and to evaluate **Çmf** as a donor molecule for FRET. **Çmf** was also incorporated into the i-Mango III aptamer, using **Çmf** and TO1-biotin, the binding ligand of the aptamer, as a FRET pair to study the structure and dynamics of this aptamer.

5 A carbazole-derived nitroxide that is an analogue of cytidine – a rigid spin label for DNA and RNA

5.1 Introduction

Rigid spin labels are valuable probes to study the structure and dynamics of nucleic acids. As detailed in **Chapter 2**, the rigidity results in more accurate distance measurements between spin labels and the relative orientation of two rigid spin labels can be determined by dipolar EPR spectroscopy.[119] For example, **Ç**[2] and **Çm**[1] have been used to gain valuable information on structure and dynamics[145-147, 181] of nucleic acids and can be used to measure PELDOR at room temperature.[141] Although **Ç** and **Çm** are excellent spin labels due to their rigidity, they seem to have some degree of flexibility in the middle of the conjugated ring system (**Figure 5.1**), where the cytidine and the benzene are connected by an oxygen and a nitrogen atom. Although the X-ray crystal structure of **Ç**-labeled DNA showed that **Ç** has a planar geometry inside DNA, the crystal structure of **ç** (**Figure 5.1**), the nucleobase of **Ç**, has a 20° bend over the oxazine linkage.[154] The non-planar geometry of **ç** indicates some flexibility at the oxazine linkage that could affect the use of **Ç** and **Çm** as rigid spin labels. The flexibility could arise from the fact that **Ç** and **Çm** contain 16 π-electrons, thus they are formally anti-aromatic according to Hückel's rule.

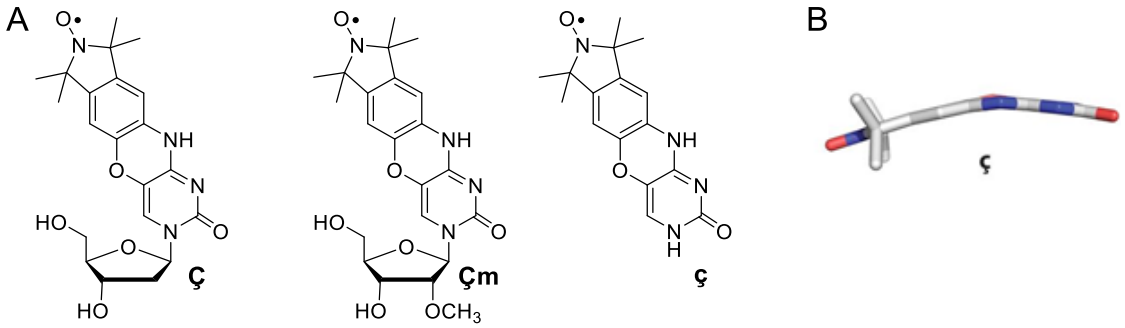

Figure 5.1. A. Structures of rigid spin labels **Ç** and **Çm** and their nucleobase **ç**.[154] B. Crystal structure of **ç**.

5.2 Rigid spin labels Ċ and Ċm

5.2.1 Design of Ċ and Ċm

The motivation of this project was to make a fully aromatic system that would presumably result in an even more rigid spin label than **Ç** and **Çm**. The design of the new labels was based on removing the oxygen in the oxazine linkage of **Ç** and **Çm** to yield **Ċ** (c-dot) and **Ċm** (cm-dot) for DNA and RNA, respectively (**Figure 5.2**). Here the π-system contains 14 π-electrons, which is aromatic according to Hückel's rule. **Ċ** and **Ċm** are carbazole analogues and derivatives of cytidine and should form base pairs with guanine (**Figure 5.2**).

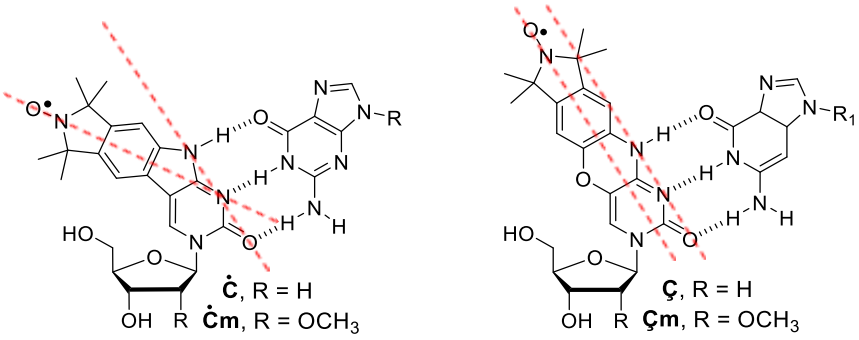

Figure 5.2. Structures of the rigid nitroxide spin labels **Ċ**, **Ċm**, **Ç** and **Çm** base paired with G.

In the case of **Ç**/**Çm**, a line going through the N-O bond would be parallel to a line through the heteroatoms of the nucleobase that are involved in hydrogen bonding (**Figure 5.2**). In contrast, such lines would not be parallel for **Ċ**/**Ċm** (**Figure 5.2**). In other words, the isoindoline moiety is tilted towards the center of the nucleic acid helix. When designing new labels for nucleic acids it is essential that they fit into the DNA and RNA structure of choice. Here, the question was if the isoindoline moiety of **Ċ**/**Ċm** would clash with the backbone of the duplex. Therefore, a molecular model of both spin labels inside DNA and RNA duplexes was examined. A molecular model of **Ċ** inside a B-form DNA duplex showed that the spin label was well accommodated inside the major groove of the helix (**Figure 5.3A**). Similar results were seen for **Ċm** inside an A-form RNA duplex (**Figure 5.3B**).

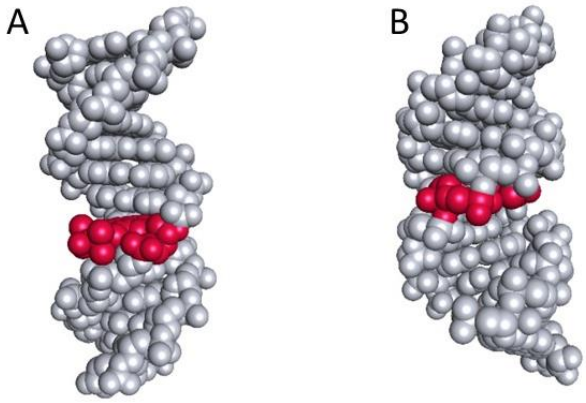

Figure 5.3. Space-filling models of **Ċ**- and **Ċm**-labeled oligonucleotide duplexes. A. B-form DNA duplex with **Ċ** projected into the major groove. B. A-form RNA duplex containing **Ċm**. The spin-labeled nucleotides are shown in pink.

5.2.2 Intramolecular C-C cross-coupling reactions

The key synthetic step in the synthesis of **Ċ** and **Ċm** is a C-C cross-coupling reaction to prepare the ring-closed carbazole derivative (**Scheme 5.1**). C-C bond formation between two aryls usually involves one or two halides as leaving groups.[224]

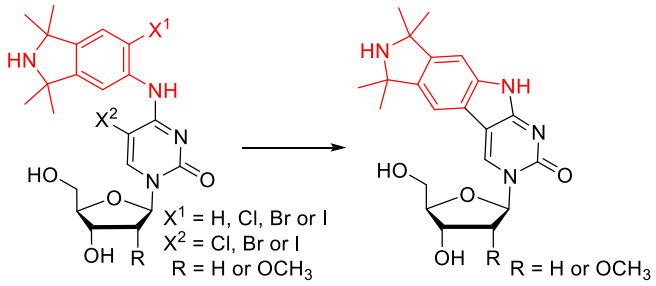

Scheme 5.1. C-C cross-coupling reaction to yield the ring-closed precursor of **Ċ** and **Ċm**.

Various examples have been reported of palladium catalyzed intramolecular C-C cross-coupling reactions between two aryls (**Scheme 5.2**). Most of the reactions have utilized $Pd(OAc)_2$ as a catalyst with different bases and solvents, performed at various temperatures (**Scheme 5.2A**).[43, 225-230] $Pd(OAc)_2(PPh_3)_2$ has also been used as a source of palladium catalysis for intramolecular C-C cross-coupling reactions under basic conditions (**Scheme 5.2B**).[231-232] Moreover, C-C cross-coupling has been performed by microwave (μW) irradiation under basic conditions with $PdCl_2(PPh_3)_2$[233] (**Scheme 5.2C**) or $Pd_2(dba)_3$ (**Scheme 5.2D**).[234] All these palladium-catalyzed reactions only required one leaving group (X); iodo, bromo or chloro. A palladium catalyzed cross-coupling reaction was deemed to be a good choice for the synthesis of **Ċ** and **Ċm**.

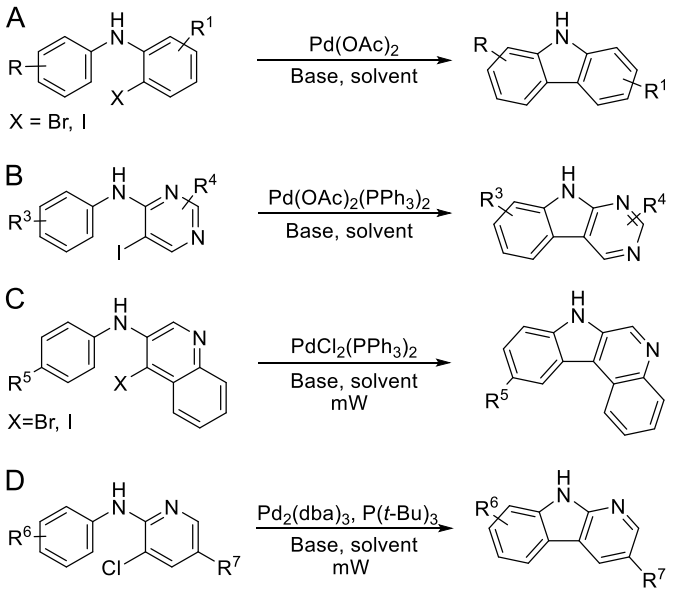

Scheme 5.2. Palladium catalyzed intramolecular C-C cross-coupling reactions.[43, 225-234]

An intramolecular cross-coupling reaction can also be performed by photo catalysis under basic conditions (**Scheme 5.3**)[235-236] but these reactions require special photoreactors.

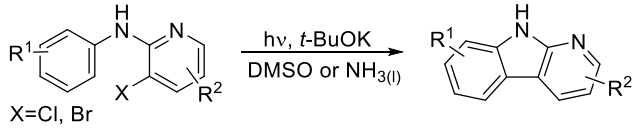

Scheme 5.3. Photo catalyzed intramolecular C-C cross-coupling reactions.[235-236]

A carbazole-like 2‘-deoxycytidine analogue (**24**) has been synthesized through a Stille-biaryl coupling of a 5-iodo-2’-deoxyuridine (**21**), followed by cyclization (**Scheme 5.4**).[237] This analogue has the same substructure as **Ċ**, only missing the five-membered ring with the nitroxide and the four methyl groups. Even though this synthetic route could yield the desired compounds (**Ċ** and **Ċm**), it would include a few additional steps to prepare a triorganotin tetramethyl isoindoline derivative (**Scheme 5.1**, red).[238]

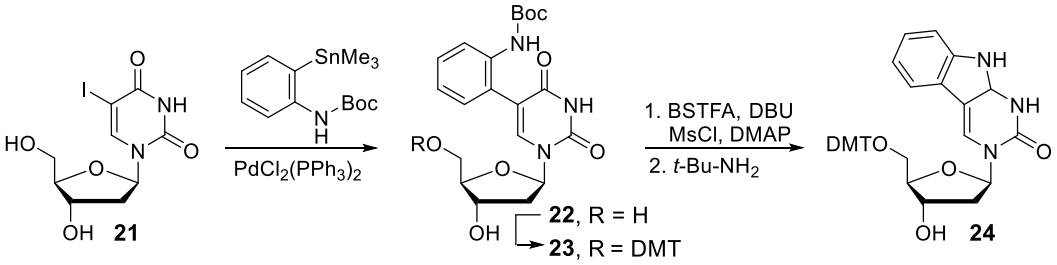

Scheme 5.4. Synthesis of **24**, a carbazole-like 2’-deoxycytidine analogue.[237]

Another carbazole analogue (**27**) has been described that has the same core-ring system as **Ċ** and **Ċm** and was incorporated into peptide nucleic acids (**Scheme 5.5**).[239] The cytosine analogue was synthesized by reductive nickel-mediated cyclization of a cytosine intermediate. For this intramolecular C-C cross-coupling reaction, both aryls needed a bromide substituent. Because the structure of **27** had the same carbazole core-ring system as **Ċ** and **Ċm** we decided to test the reaction conditions shown in **Scheme 5.5** for **Ċ** and **Ċm**, before trying the aforementioned palladium catalyzed reactions.

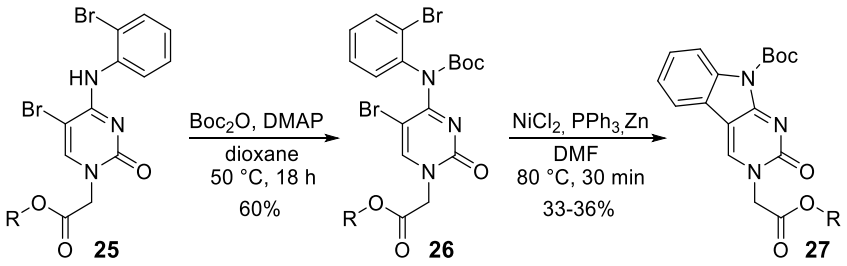

Scheme 5.5. Boc protection followed by a reductive nickel-mediated cyclization of a cytosine analogue.[239]

5.2.2 Early attempts at synthesis of Ċ and Ċm

For the reductive nickel-mediated cyclization (**Scheme 5.5**), both the tetramethyl isoindoline (**Scheme 5.1**, marked in red) and the cytidine (**Scheme 5.1**, marked in black) needed a bromide substituent. The synthesis of bromo-tetramethyl isoindoline-amine **29** (**Scheme 5.6**) was first attempted with the bromo-tetramethyl nitro-isoindoline **28**[240] by hydrogenation using palladium catalysis but these conditions resulted in removal of the bromide. Therefore, milder reaction conditions were used with iron-dust under acidic conditions,[241] which gave quantitative yields of **29**.

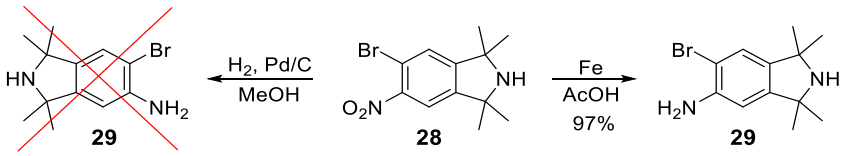

Scheme 5.6. Synthesis of bromo-tetramethyl isoindoline-amine **29**.

Compound **30**[1], with acyl- (Ac) protected 3'- and 5'-hydroxyl groups, was chlorinated[2] and coupled to compound **29** (**Scheme 5.7**). The secondary amines were protected by *tert*-butoxycarbonyl (boc) groups to eliminate poisoning of the catalysts[242-243] used in the

following C-C cross-coupling reaction. The cyclization step of **31** to form **32** was attempted with the reaction conditions used to form **27** (**Scheme 5.5**), with nickel and zinc catalysis using triphenylphosphine. However, these reaction conditions only yielded in a complex mixture without forming the desired product.

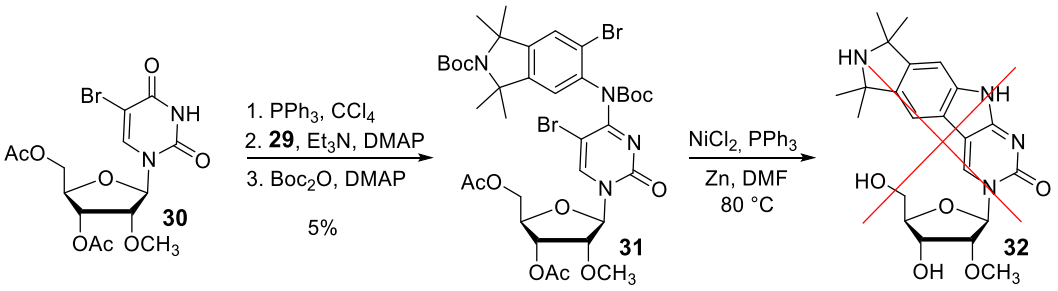

Scheme 5.7. Synthesis of boc protected nucleoside **31** and the proposed synthesis of cyclized nucleoside **32**.

At this point different protecting groups were considered for the 3'- and 5'-hydroxy groups as acetyl is not stable enough under the C-C cross-coupling conditions used to synthesize **32** (**Scheme 5.7**). The 3'- and 5'-hydroxyl groups on 2'-*O*-methyluridine were protected with Ac, pivaloyl, TBDMS or TBDPS and their stability was tested under the conditions used to form **27** (**Scheme 5.8**). None of the groups were stable enough under these conditions and were all removed in less than 30 min (data not shown).

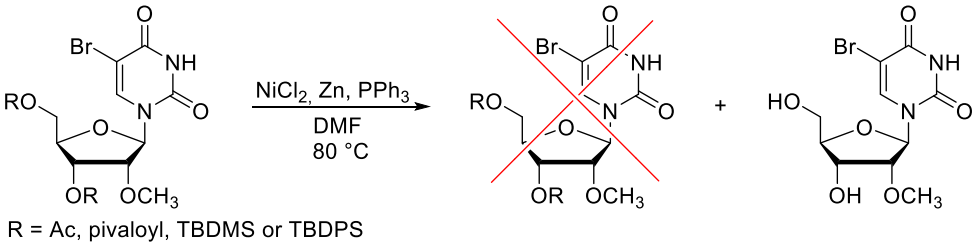

Scheme 5.8. Nucleoside protected with acetyl, pivaloyl, TBDMS or TBDPS, stirred under nickel and zinc catalysis, conditions used to synthesize **27**.

Therefore, we turned to palladium catalyzed intramolecular C-C cross-coupling reactions for the synthesis of **Ċ** and **Ċm**. For the palladium catalyzed reactions shown in **Scheme 5.2**, only one of the aryl groups needed a halogen substituent and most often iodide was used for that purpose. 2'-*O*-methyluridine was iodinated to form **33** (**Scheme 5.9**). Of all the protecting groups tested previously (**Scheme 5.8**), TBDPS was determined to be the most stable, and thus, selected as a protecting group for the 3'- and 5'-hydroxyl groups to form

34, followed by chlorination of the fourth position of the nucleobase[2] to yield **35** (**Scheme 5.9**).

Instead of using a tetramethyl amino-isoindoline derivative, which would require a few steps to synthesize (**Scheme 5.1**, colored in red), aniline was used as a model compound. Reaction with nucleoside **35** gave compound **36** (**Scheme 5.9**), followed by boc protection of the amine at the fourth position on the nucleobase resulted in nucleoside **37**.

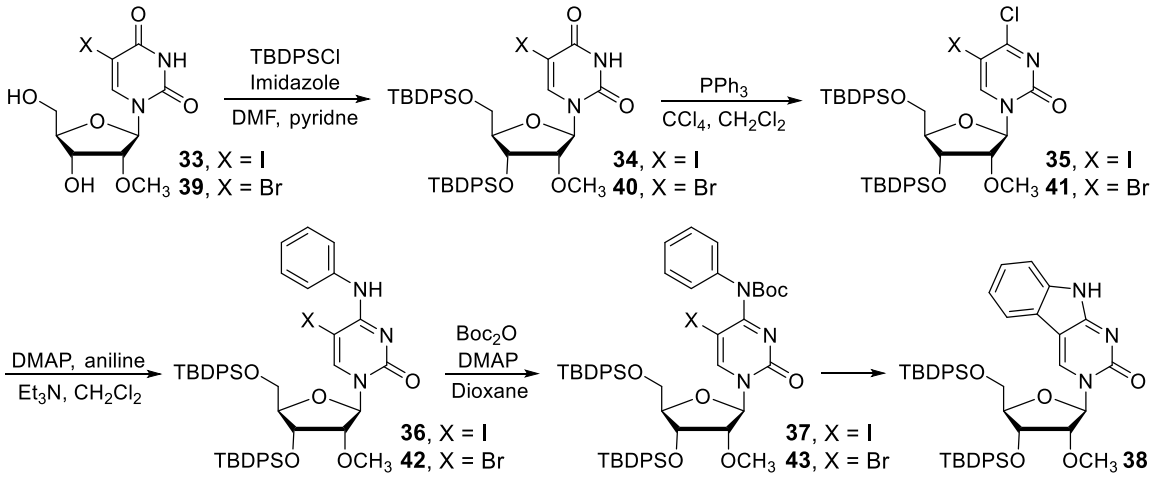

Scheme 5.9. Synthesis of the cyclized nucleoside **38**. The yields were as follows: **34** (55%), **40** (88%), **35** (72%), **41** (80%), **36** (53%), **42** (80%), **37** (78%), **43** (73%) and **38** (22% from **37**, 45% from **43**).

A few different C-C cross-coupling reaction conditions were tested on **37** to form **38** (**Scheme 5.9**) and are listed in **Table 5.1**. The first reaction was performed with $Pd(OAc)_2$, under basic conditions with Cs_2CO_3 in DMA at 80 °C, over a time course of 24 h (**Table 5.1**, reaction 1).[43] The second reaction was also performed with $Pd(OAc)_2$ but the base used here was K_2CO_3 and the reaction was done in toluene at 130 °C, over 24 h (**Table 5.1**, reaction 2).[230] Neither of these reactions yielded the desired product. The third reaction included $PdCl_2(PPh_3)_2$ with NaOAc as a base in DMA at 130 °C and the reaction was monitored over 24 h (**Table 5.1**, reaction 3). Delightfully, these reaction conditions gave the desired product **38** in 22% yield.

Table 5.1. Different conditions for an intramolecular C-C cross-coupling reaction to yield **38**.

	Catalyst	Cat. amount (%)	Base	Solvent	X	T (°C)	Yield (%)
1[43]	$Pd(OAc)_2$	30	Cs_2CO_3	DMA	I	80	0
2[230]	$Pd(OAc)_2$	120	K_2CO_3	toluene	I	130	0

3[233]	$PdCl_2(PPh_3)_2$	10	NaOAc	DMA	I	130	22
4[233]	$PdCl_2(PPh_3)_2$	20	NaOAc	DMA	Br	150	45

In order to optimize the reaction conditions to form **38**, bromide was incorporated instead of iodide at the fifth position of the nucleobase (**39**, **Scheme 5.9**). Exchanging the iodide by bromide did not give higher yields for the C-C cross-coupling reaction to form **38**; **37** to **38** gave 22% and **43** to **38** gave 20% yield (data not shown). This exchange did though give higher yields for most of the synthetic steps towards **38**, especially the TBDPS protection of **39** to form **40** and the coupling of aniline to nucleoside **41** to give **42** (**Scheme 5.9**). The higher yields are presumably due to the steric hindrance of iodide compared to bromide. Due to higher overall yields of the synthesis towards **43**, it was used further to optimize the reaction conditions to generate **38**. The C-C cross-coupling reaction of nucleoside **43** was performed at different temperatures; 80, 130 and 150 °C (data not shown). The yields of **38** were higher at 150 °C than at 130 °C but the desired product did not form at 80 °C (data not shown). Finally, the amount of catalyst needed was varied, using 10, 20 and 30 mol% catalyst (data not shown). The yields were nearly the same for 20 and 30 mol% catalyst but almost double as high than when 10 mol% was used (data not shown). The highest yields for **38** were obtained by reacting nucleoside **43** at 150 °C with 20 mol% catalyst for 14 h, giving the desired product in 45% yield (**Table 5.1**, reaction 4). These yields were satisfactory and, therefore, the same conditions were used to synthesize **Ċ** and **Ċm**, as described below.

5.2.2 Synthesis of Ċ and Ċm

The synthesis of **Ċ** and **Ċm** began by TBDPS protection of the 3'- and 5'-hydroxyl groups of nucleosides **44** and **45**, respectively, followed by chlorination of the fourth position[2] of the nucleobase to give **48** and **49** (**Scheme 5.10**). Nucleosides **48** and **49** were subsequentially coupled with tetramethyl isoindoline derivative **50**[142] to yield nucleosides **51** and **52**, respectively. The secondary amines of **51** and **52** were protected by boc, followed by the intramolecular palladium catalyzed C-C cross-coupling reaction.[233] Boc-deprotection was subsequently performed to yield carbazole derivatives **53** and **54**. These three steps, the Boc protection, the C-C cross-coupling reaction, and boc deprotection were performed without isolating the intermediate products. The overall yield for the three steps was 47%

for **53** and 59% for **54**, (**Scheme 5.10**), markedly higher than for model compound **38** (33%) (**Scheme 5.9**). In the case of **38**, the boc protecting group had been removed during the C-C cross-coupling reaction. For **53** and **54**, the boc protecting groups had only partially been removed and thus, the mixture was subjected to treatment with trifluoroacetic acid (TFA). Oxidation with *m*CPBA in the presence of NaN_3[137] yielded nitroxides **55** and **56** and removal of the TBDPS groups gave the rigid nitroxides **Ċ** and **Ċm**.

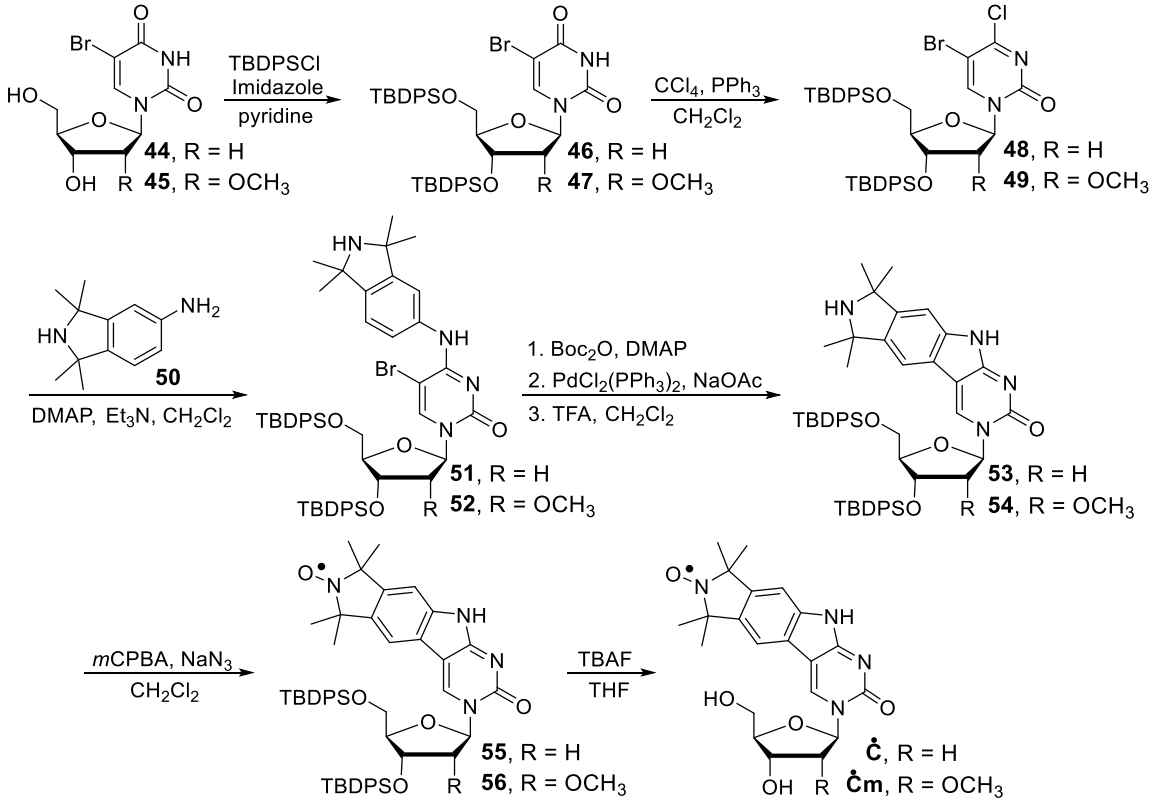

Scheme 5.10. Synthesis of nitroxides **Ċ** and **Ċm**. Yields were as follows: **46** (95%), **47** (80%), **48** (88%), **49** (77%), **51** (66%), **52** (63%), **53** (47%, 3 steps), **54** (59%, 3 steps), **55** (65%), **56** (76%), **Ċ** (84%) and **Ċm** (67%).

5.2.3 Crystal structures of Ċ and Ċm

To investigate the three-dimensional structure of **Ċ** and **Ċm**, specially with regards to the planarity of the aromatic system, single crystals were grown and their crystal structures were determined. As had been expected, the crystal structure of **Ċ** adopted a planar geometry (**Figure 5.4A**). **Ċm**, on the other hand, had a slight twist from the plane which yielded in a 9° overall bend (**Figure 5.4B**). The non-planar geometry is most likely due to the crystal packing. Nonplanar crystal structures of aromatic polycycles, resulting from intermolecular interactions are quite common as the energy required for bending is small.[244-245] The bend of **Ċm** is different to what was found in the aforementioned **ç** (**Figure 5.4C**), where the bend

is only at the position of the oxazine linkage, similar to a hinge. The crystal structure of **Ċm** on the other hand, slightly winds up on itself which results in a bend that is spread over the whole nucleobase. Taking these facts together, that the crystal structure of **Ċ** is planar, that the bend of **Ċm** is smaller than for **ç** and that the bend of **Ċm** spreads over the nucleobase and is not just at one location as for **ç**, indicates that **Ċ** and **Ċm** are more rigid than **Ç** and **Çm**.

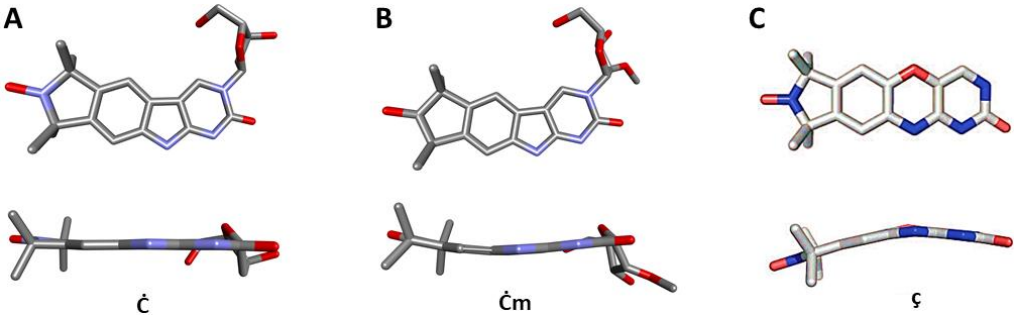

Figure 5.4. Side- and top-views of the crystal structures of **Ċ** (A), **Ċm** (B) and **ç** (C).

5.2.3 Phosphoramidite synthesis of Ċ and Ċm

To circumvent the reduction of the nitroxides of **Ċ** and **Ċm** during solid-phase synthesis, the protecting group strategy discussed in **Chapter 3** was used to protect the nitroxides.[194] The nitroxides of **55** and **56** were reduced with *L*-ascorbic acid to their hydroxylamines, followed by benzoylation to give **57** and **58** (**Scheme 5.11**). The TBDPS groups were removed by TBAF to yield nucleosides **59** and **60**. The 5'-hydroxyl groups were protected as 4,4'-dimethoxytrityl ethers to yield **61** and **62**. Phosphitylation of the 3'-hydroxyl groups yielded phosphoramidites **63** and **64** that were used for incorporation of **Ċ** and **Ċm** into DNA and RNA oligonucleotides, respectively, by solid-phase synthesis.

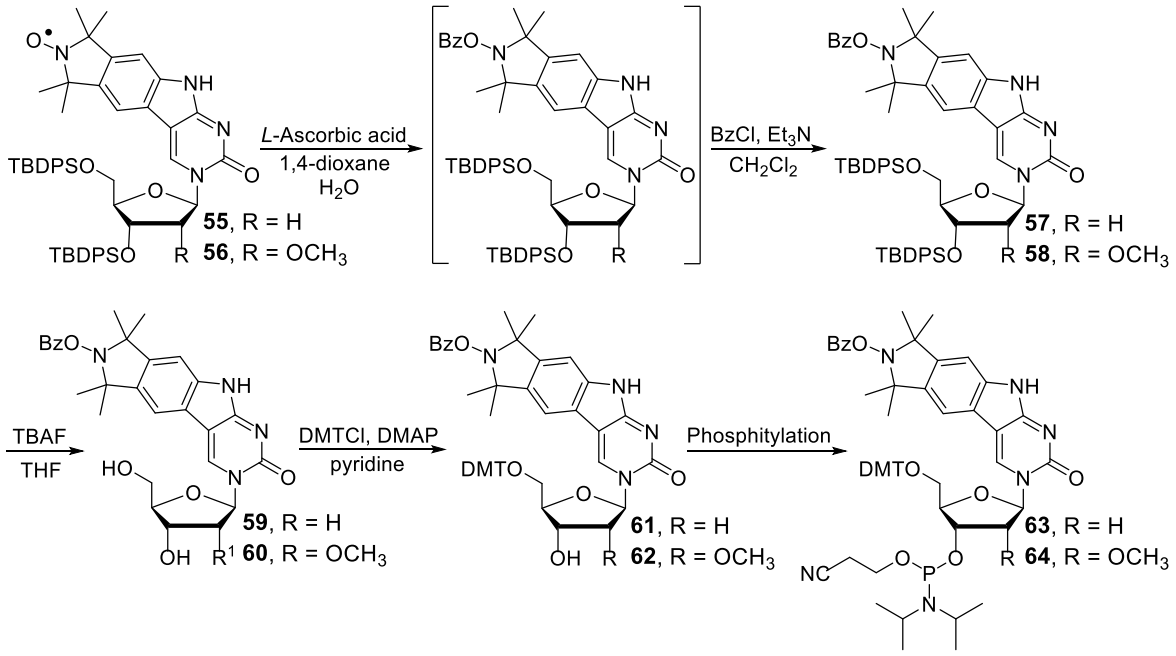

Scheme 5.11. Synthesis of benzoyl-protected **Ċ** and **Ċm** and their corresponding phosphoramidites. Yields were as follows: **57** (51%, 2 steps), **58** (43%, 2 steps), **59** (77%), **60** (74%), **61** (81%), **62** (75%), **63** (91%) and **64** (65%).

5.3 Ċ-labeled oligonucleotides

Phosphoramidite **63** was used to incorporate **Ċ** into six oligodeoxynucleotides through automated solid-phase synthesis (**Table 5.2**). The oligonucleotides varied in length and position of the spin label. The spin-labeled phosphoramidite coupled well during the solid-phase synthesis as suggested by a strong orange color of the trityl cation that appeared during removal of the DMT group. Furthermore, analysis by denaturing polyacrylamide gel electrophoresis (DPAGE) showed no failure bands for the synthesized oligonucleotides (data not shown), which would have been an indication of only partial coupling of phosphoramidite **63**. The labeling of the oligodeoxynucleotides with **Ċ** was further confirmed by mass spectrometry (**Table 5.2**). The oligodeoxynucleotides were purified by DPAGE and their spin-labeling efficiency was determined by spin-counting using CW-EPR spectroscopy. As can be seen in **Table 5.2**, all oligonucleotides (**XIV**-**XIX**) were quantitatively spin labeled.

Table 5.2. Spin-labeled DNA oligonucleotides, monoisotopic masses, and spin-labeling efficiency.

	Sequence	(calcd)	(found)	Radical (%)

XIV	5’-d(GACCTCG**Ċ**ATCGTG)-3’	4424.83	4425.84	100
XV	5’-d(GA**Ċ**CTCGCATCGTG)-3’	4424.83	4426.63	97
XVI	5’-d(**Ċ**ACGATGCGAGGTC)-3’	4473.85	4474.58	95
XVII	5’-d(GACCTCG**Ċ**ATCGTGGACCTCG CATCGTG GACCTCGCATCGTG)-3’	13024.22	13024.10	96
XVIII	5’-d(GT**Ċ**AGTGCGCGCGCGCGATC)-3’	6319.14	6321.08	100
XIX	5’-d(GATCGCGCG**Ċ**GCGCACTGAC)-3’	6288.14	6292.53	96

To further analyze the spin labeling efficiency, **XIV**-**XIX** were enzymatically digested and the digests were analyzed by HPLC (**Figure 5.5**). All chromatograms had five peaks, one for each natural nucleoside and one for **Ċ**, the identity of which was confirmed by co-injection of the free nucleoside **Ċ**. Quantification of the nucleosides in the digest showed that **Ċ** had the expected ratio compared to the other four nucleosides in all the samples, further confirming quantitative spin labeling of all DNA oligonucleotides.

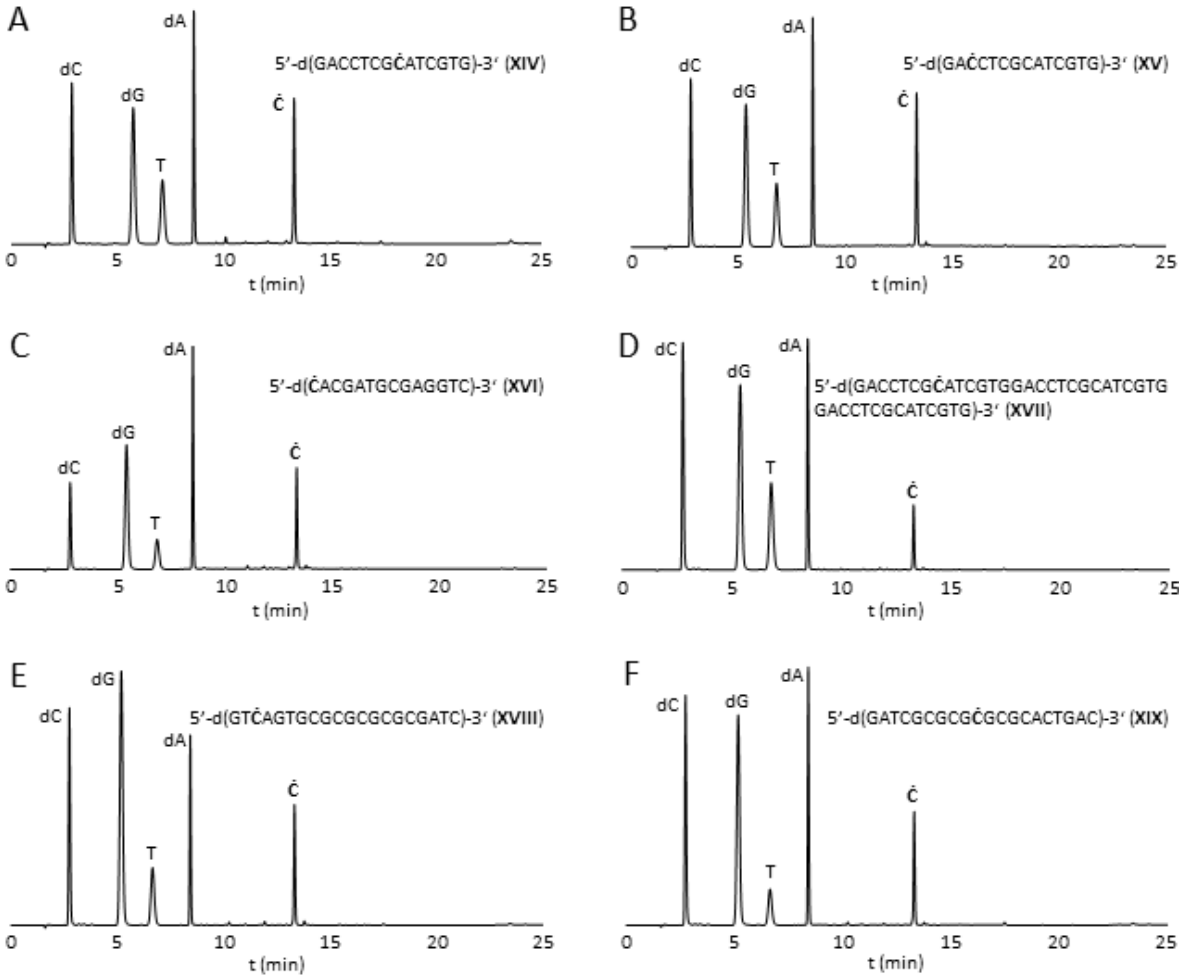

Figure 5.5. HPLC chromatograms of oligodeoxynucleotides after enzymatic digestion with snake venom phosphodiesterase, nuclease P_1, and alkaline phosphatase.[156, 194]

DNA duplexes **J**-**L**, **N** and **P** were formed by annealing spin-labeled oligonucleotides **XIV**-**XIX** (**Table 5.2**) to their complementary strands (**Table 5.3**). The duplex formation was confirmed by CW-EPR spectroscopy (**Figure 5.6**). The CW-EPR spectra of **Ċ**, the **Ċ**-labeled DNA single-strand **XIV**, and the corresponding DNA duplex **J**, are shown in **Figure 5.6**. **Ċ** shows three fairly sharp lines (**Figure 5.6A**) due to the fast tumbling of the nucleoside in solution. The lines broadened after incorporation of **Ċ** into the oligonucleotide (**Figure 5.6B**), consistent with incorporation into an oligonucleotide that has a longer rotational correlative time. Upon annealing to its complementary strand, the CW-EPR spectrum broadened further, showing a splitting of the high- and low-field components (**Figure 5.6C**), which is characteristic for duplexes containing rigid spin labels.[1-2] All the oligodeoxynucleotides were characterized by CW-EPR spectroscopy and are shown in **Figure 5.7**.

Figure 5.6. CW-EPR spectra of free nitroxide **Ċ** (A), spin labeled DNA oligonucleotide **XIV** (B) and spin labeled DNA duplex **J** (C). EPR spectra were recorded at 22 °C in a phosphate buffer (2 nmol of sample; 10 mM phosphate, 100 mM NaCl, 0.1 mM Na_2EDTA, pH 7.0).

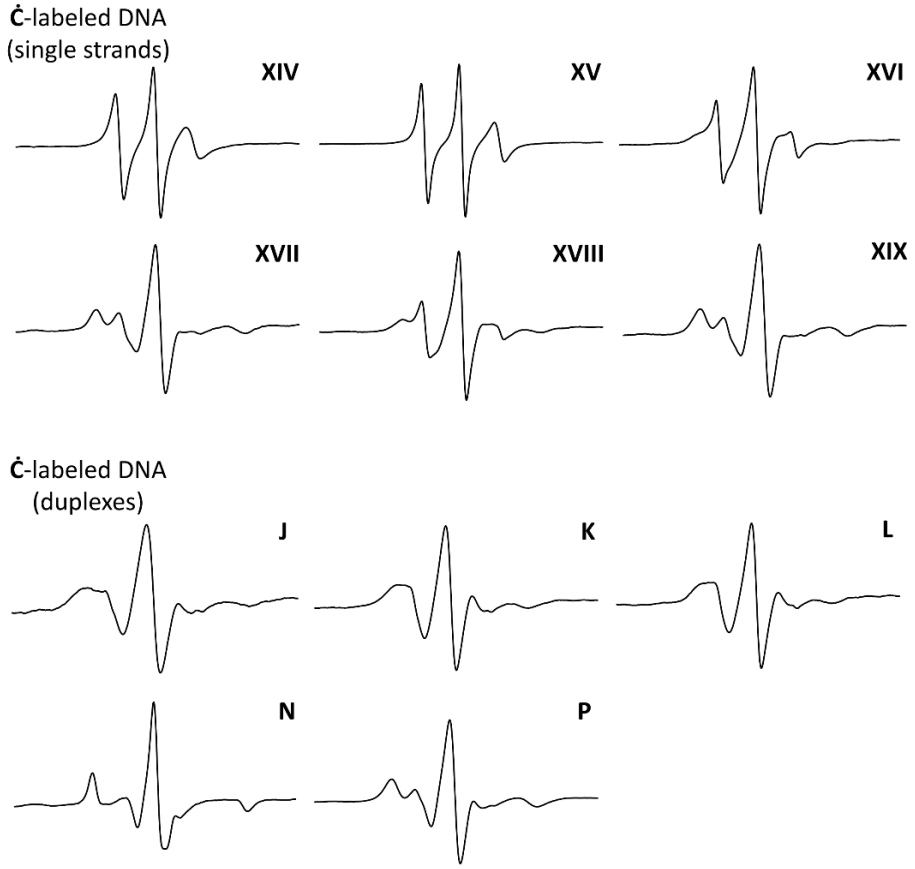

Figure 5.7. CW-EPR spectra of **Ċ**-labeled oligodeoxynucleotides. EPR spectra were recorded at 22 °C in a phosphate buffer (2 nmol of RNA; 10 mM phosphate, 100 mM NaCl, 0.1 mM Na_2EDTA, pH 7.0).

Thermal denaturation studies of duplexes **I-P** were performed to see if **Ċ** causes any destabilization of the duplexes. The thermal denaturation curves showed a cooperative melting-transition and confirmed duplex formation of the **Ċ**-labeled oligonucleotides (**Figure 5.8**). The melting temperatures (T_Ms) of the **Ċ**-labeled duplexes were slightly lower than the unmodified duplexes (0.5-3.0 °C, **Table 5.3**). Comparison of the T_Ms of duplex **J** and of the same duplex labeled with **Ç** at the same position showed that the T_M of duplex **J** is 1.9 °C lower than for the **Ç**-labeled duplex.[156] However, in general the decrease of the T_Ms

compared to the unmodified duplexes is minor and shows that **Ċ** is well accommodated within DNA duplexes.

Table 5.3. Sequences of spin-labeled DNA duplexes and their thermal denaturation analysis.

	Sequence	T_M (°C)	ΔT_M
I	5'-d(GACCTCGCATCGTG)-3' 3'-d(CTGGAGCGTAGCAC)-5'	63.0	
J	5'-d(GACCTCG**Ċ**ATCGTG)-3' 3'-d(CTGGAGCGTAGCAC)-5'	60.0	-3.0
K	5'-d(GA**Ċ**CTCGCATCGTG)-3' 3'-d(CTGGAGCGTAGCAC)-5'	60.9	-2.1
L	5'-d(GACCTCGCATCGTG)-3' 3'-d(CTGGAGCGTAGCA**Ċ**)-5'	62.5	-0.5
M	5'-d(GACCTCGCATCGTGGACCTCGCATCGTGGACCTCGCATCGTG)-3' 3'-d(CTGGAGCGTAGCACCTGGAGCGTAGCACCTGGAGCGTAGCAC)-5'	83.7	
N	5'-d(GACCTCG**Ċ**ATCGTGGACCTCGCATCGTGGACCTCGCATCGTG)-3' 3'-d(CTGGAGCGTAGCACCTGGAGCGTAGCACCTGGAGCGTAGCAC)-5'	83.1	-0.6
O	5'-d(GTCAGTGCGCGCGCGCGATC)-3' 3'-d(CAGTCACGCGCGCGCGCTAG)-5'	79.2	
P	5'-d(GT**Ċ**AGTGCGCGCGCGCGATC)-3' 3'-d(CAGTCACGCG**Ċ**GCGCGCTAG)-5'	77.0	-2.2

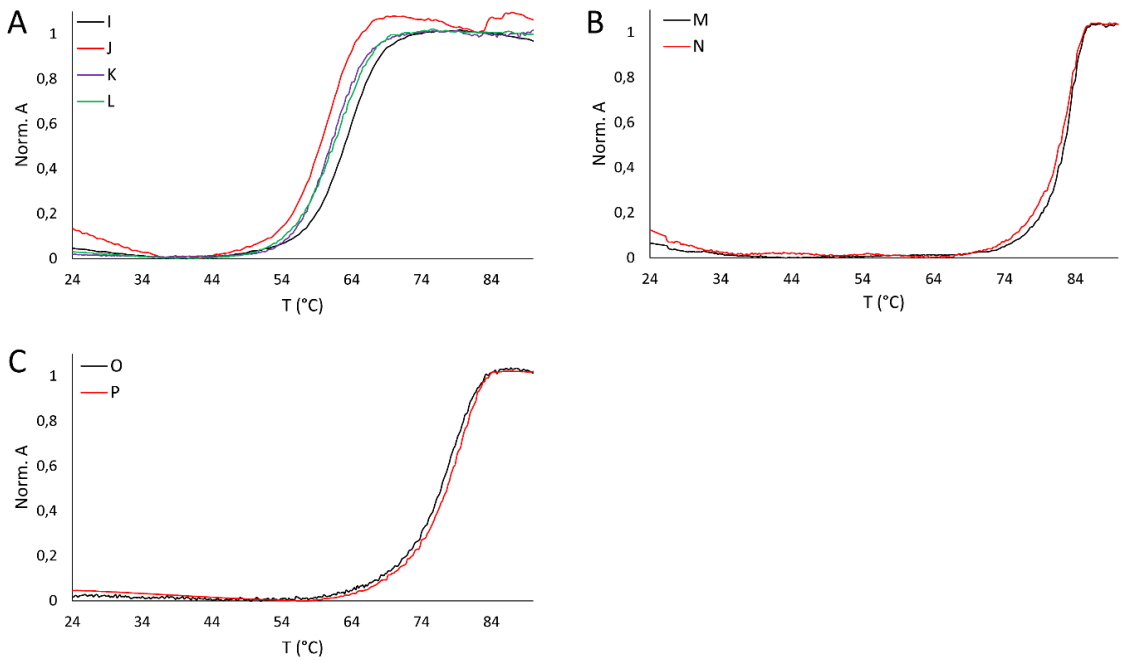

Figure 5.8. Thermal denaturing analysis of duplexes **I**, **J**, **K**, **L** (A); **M**, **N** (B); **O**, **P** (C). The duplexes were prepared by dissolving complementary single-stranded oligonucleotides (4.0 nmol) in a phosphate buffer (100 µL; 10 mM phosphate, 100 mM NaCl, 0.1 mM Na_2EDTA, pH 7.0), followed by annealing. The samples were diluted to 1.0 mL with the phosphate buffer, degassed with Ar and heated from 24 to 90 °C (1.0 °C/min). The absorbance at 260 nm was subsequently recorded at 0.2 °C intervals.

To determine whether **Ċ** causes any structural perturbation of B-form DNA helices, circular dichroism (CD) spectra were recorded of the **Ċ**-labeled and the unmodified duplexes. The CD spectra (**I-P**, **Figure 5.9**) all possessed negative and positive molar ellipticities at ca. 250 and 280 nm, respectively, characteristic of right-handed B-DNA.

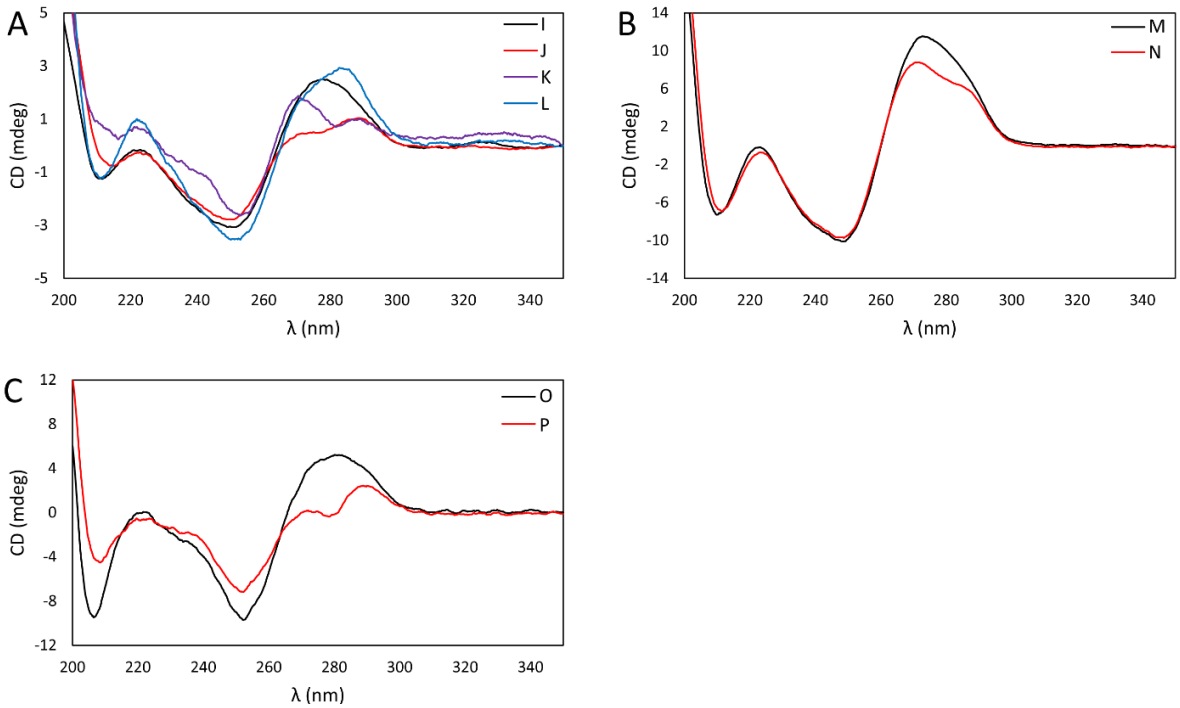

Figure 5.9. CD spectra of duplexes **I**, **J**, **K**, **L** (A); **M**, **N** (B); **O**, **P** (C). The duplexes were prepared by dissolving complementary single-stranded oligonucleotides (2.5 nmol of each) in a phosphate buffer (100 µL; 10 mM phosphate, 100 mM NaCl, 0.1 mM Na_2EDTA, pH 7.0) and annealing. The annealed samples were diluted to 200 µL with the same buffer before CD measurements.

However, the CD spectra were different for the **Ċ**-labeled and unmodified duplexes, more precisely, there is a decrease in the CD signal between 270 and 280 nm for the modified duplex (**Figure 5.9C**). This suggests that **Ċ** is perturbing the DNA duplex, resulting in a different CD spectra. On the other hand, the decrease in T_M was only minor compared to the unmodified duplexes, which indicated that **Ċ** was not having a major effect on the duplex stability. Therefore, we looked for another reason that could explain the differences in the CD spectra. Delightfully, we found an article where similar changes in the CD-spectra were described by Wypijewska del Nogal *et al*. for 2CNqA, an analogue of adenosine, in DNA duplexes.[246] The authors ascribe this discrepancy to "differences in molar absorptivity of the adenine that is exchanged with a 2CNqA in the modified duplex",[246] but 2CNqA absorbs strongly between 275 and 290 nm.[247] Nucleoside **Ċ** has an absorption maximum at 279 nm and a very high molar extinction coefficient (ε = 42800 M^{-1} cm^{-1}). This is the same area

where the CD spectra differ between **Ċ**-modified and unmodified duplexes (**Figure 5.10**). Thus, the difference in the CD spectra could originate due to strong absorption of **Ċ** at 279 nm. To investigate this issue further, a carbazole-analogue (**68**, **Scheme 5.12**) was synthesized, where the five-membered ring of **Ċ**, containing the nitroxide and the four methyl groups, had been removed. This nucleoside should be less perturbing of DNA duplex structure than **Ċ** and thus show less changes in the CD spectra if the origin of the effect in the CD spectra resulted from perturbation by the unnatural nucleoside.

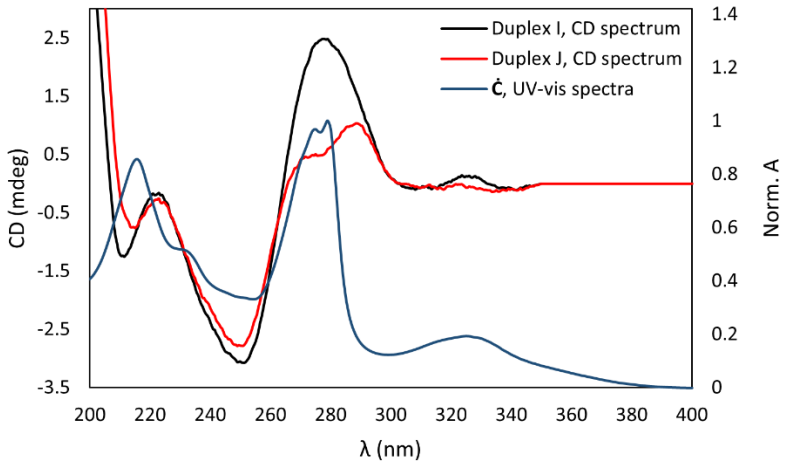

Figure 5.10. Comparison of the CD spectra of DNA duplexes with the absorption spectrum of **Ċ**. CD spectra of duplex **I** (black) and **J** (red) and the absorption spectrum of **Ċ** (blue).

5.3.1 Synthesis of a carbazole derivative and incorporation into DNA

Synthesis of **68** followed closely that of **Ċ**, beginning by coupling of nucleoside **48** with aniline followed by boc-protection of the secondary amine on the nucleobase of **65** to give **66** (**Scheme 5.12**). An intramolecular palladium catalyzed C-C cross-coupling reaction,[233] followed by boc-deprotection and removal of the TBDPS groups yielded the carbazole derivative **68**. The 5'-hydroxyl group was protected as a 4,4'-dimethoxytrityl ether and phosphitylation of the 3'-hydroxyl group yielded phosphoramidite **69** that was used to incorporate **68** into DNA oligonucleotide **XX** (**Table 5.4**) through solid-phase synthesis.

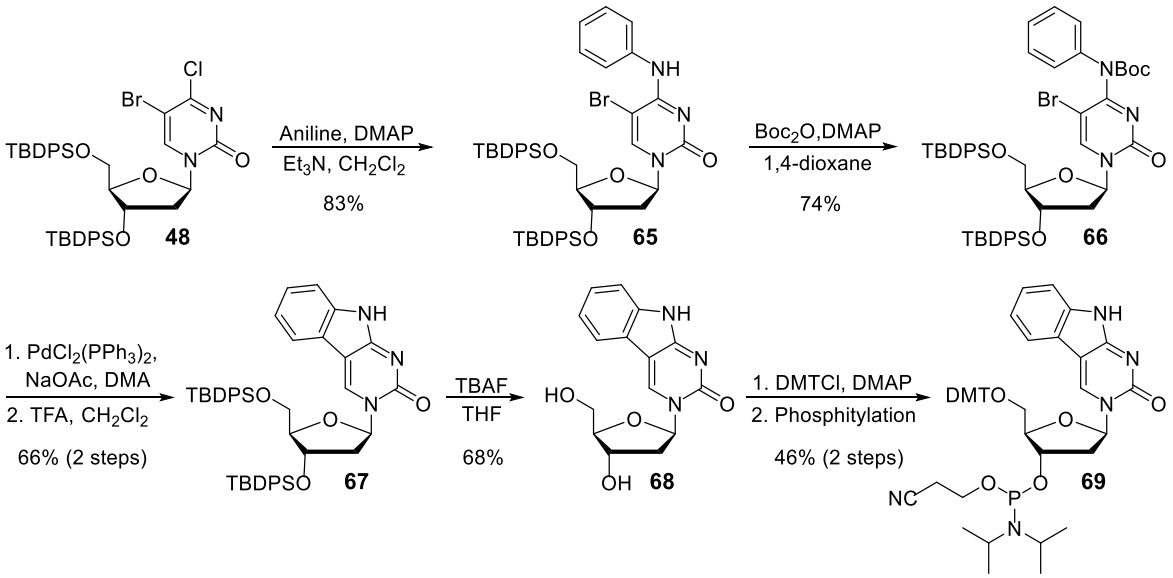

Scheme 5.12. Synthesis of nucleoside **68** and its corresponding phosphoramidite **69**.

Incorporation of nucleoside **68** into oligonucleotide **XX** was confirmed by mass spectrometry (**Table 5.4**) and further by HPLC of the digested oligodeoxynucleotide (**Figure 5.11**) where the chromatogram of the digest had five peaks, one for each natural nucleoside and one for nucleoside **68**.

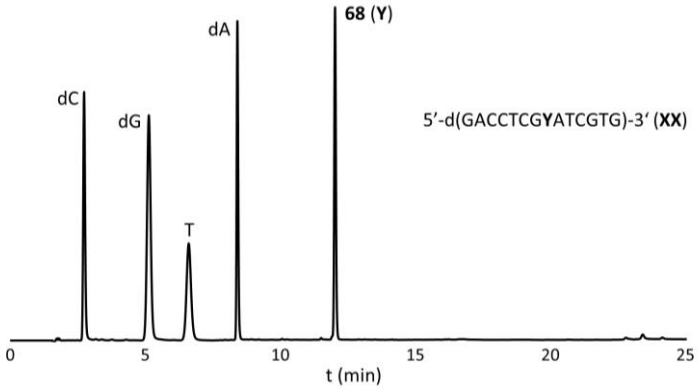

Figure 5.11. HPLC chromatogram of oligodeoxynucleotide **XX** after enzymatic digestion with snake venom phosphodiesterase, nuclease P_1, and alkaline phosphatase.[156, 194] Y stands for nucleoside **68**.

Thermal denaturation experiments of duplex **Q** (**Table 5.4**), containing **68**, showed a 1.2 °C decrease of the T_M compared to the unmodified duplex (**I**, **Table 5.4**), indicating that nucleoside **68** is non perturbing of the duplex structure.

Table 5.4. Sequences of oligonucleotide **XX** and DNA duplexes **I** and **Q**. Monoisotopic mass of oligonucleotide **XX**. Thermal denaturation analysis of duplexes. Y stands for nucleoside **68**.

	Sequence	(calcd)	(found)	T_M (°C)	ΔT_M
XX	5'-d(GACCTCG**Y**ATCGTG)-3'	4311.75	4314.30		
I	5'-d(GACCTCGCATCGTG)-3' 3'-d(CTGGAGCGTAGCAC)-5'			63.0	
Q	5'-d(GACCTCG**Y**ATCGTG)-3' 3'-d(CTGGAGCGTAGCAC)-5'			61.8	-1.2

The CD spectrum of DNA duplex **Q** (**Figure 5.12**, red line) had a strong resemblance to the CD spectra of the **Ċ**-labeled duplexes, with a decrease in the spectral intensity at ca. 274 nm compared to the unmodified duplex **I** (**Figure 5.12**, black line). The decrease in the intensity was blue-shifted compared to the **Ċ**-labeled duplexes, moving from 279 nm to 274 nm, as does the maximum in the absorption spectrum of **68** (**Figure 5.12**, blue line). It is noteworthy that there are actually two maxima in this region of the absorption spectrum of **68** (278 and 274 nm) with a small local minimum between the two peaks. This minimum in the UV spectrum is mirrored as a small bump in the CD spectrum of duplex **Q** labeled with **68**. This data is a further indication that the difference in the CD spectra of the **Ċ**-modified and unmodified DNA duplexes is not due to conformational rearrangement of the duplex itself. Instead, the strong absorption of **Ċ** at 279 nm, which is unusual for nucleosides, affects the CD spectra of the **Ċ**-labeled duplexes. It seems that both **Ċ** and **68** absorb different polarized light than the natural nucleosides inside the duplex, resulting in a decrease in the CD spectra of the modified duplexes.

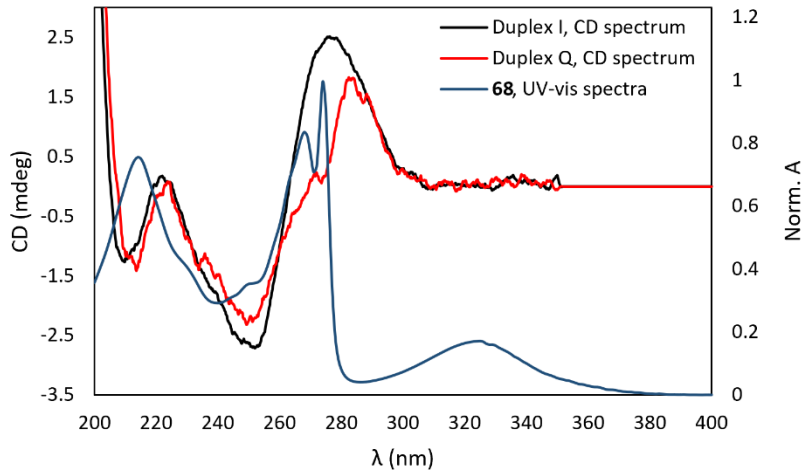

Figure 5.12. Comparison of CD spectra of DNA duplexes and of the absorption spectrum of **68**. CD spectra of duplex **I** (black) and **Q** (red) and the absorption spectrum of nucleoside **68** (blue).

5.4 Ċm labeled oligonucleotides

Phosphoramidite **64** was used to incorporate **Ċm** into one 14- and two 21-nt long RNAs through automated solid-phase synthesis (**Table 5.5**). As for the DNA synthesis, the phosphoramidite coupled well during the RNA solid-phase synthesis and spin-counting by CW-EPR spectroscopy confirmed high spin labeling efficiency (**Table 5.5**).

Table 5.5. Spin-labeled RNA oligonucleotides, monoisotopic masses, and spin-labeling efficiency.

	Sequence	(calcd)	(found)	Radical (%)
XXI	5'-GACCUCG**Ċm**AUCGUG-3'	4620.73	4622.90	99
XXII	5'-UGU**Ċm**AGUCGCGCGCGCGCAUC-3'	6877.02	6881.32	95
XXIII	5'-UGAUGCG**Ċm**GCGCGCGACUGAC-3'	6940.06	6944.60	90

Oligoribonucleotides **XXI**-**XXIII** were enzymatically digested and the digests were analyzed by HPLC (**Figure 5.13**), showing the natural nucleosides and **Ċm**. Quantification of the five peaks gave the expected ratios.

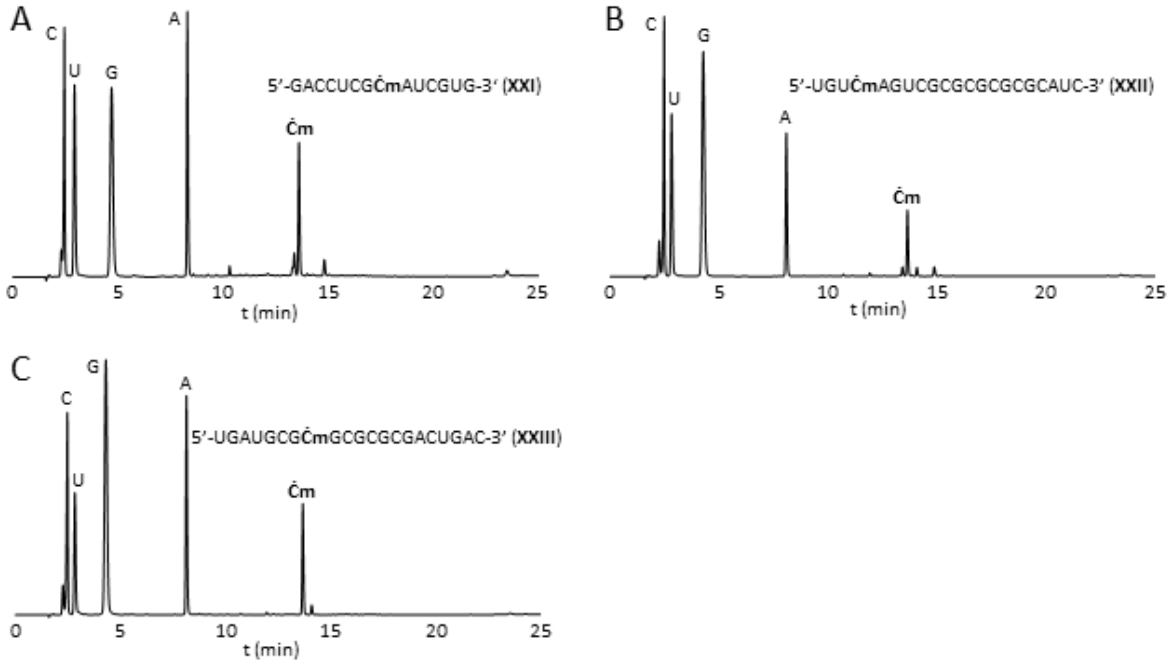

Figure 5.13. HPLC chromatograms of RNA oligonucleotides after enzymatic digestion with snake venom phosphodiesterase, nuclease P_1, and alkaline phosphatase.[156, 194]

CW-EPR spectra of RNA duplexes **S** and **U** (**Table 5.6**) showed the expected line-shape for a rigid spin label in a duplex RNA (**Figure 5.14**). CW-EPR spectra for all spin-labeled RNA oligonucleotides are shown in **Figure 5.14**. Thermal denaturation experiments resulted in sigmoidal melting curves that also confirmed duplex formation of the **Ċm**-labeled oligonucleotides (**Figure 5.15**). The melting temperatures of the **Ċm**-labeled duplexes were slightly lower (2.5 and 3.2 °C) than for the corresponding unmodified duplexes, indicating only minor destabilization (**Table 5.6**).

Table 5.6. Sequences of RNA duplexes and their thermal denaturation analysis.

	Sequence	T_M (°C)	ΔT_M
R	5'-GACCUCGCAUCGUG-3' 3'-CUGGAGCGUAGCAC-5'	73.5	
S	5'-GACCUCG**Ċm**AUCGUG-3' 3'-CUGGAGCG UAGCAC-5'	70.3	-3.2
T	5'-UGUCAGUCGCGCGCGCGCAUC -3' 3'- CAGUCAGCGCGCGCGCGUAGU-5'	85.9	
U	5'-UGU**Ċm**AGUCGCGCGCG CGCAUC -3' 3'- CAG UCAGCGCGCG**Ċm**GCGUAGU-5'	83.4	-2.5

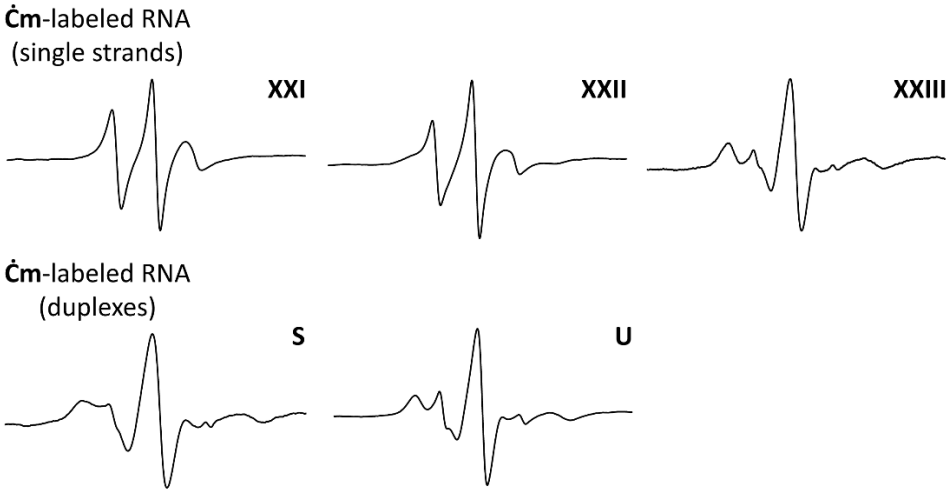

Figure 5.14. EPR spectra of **Ċm**-labeled oligoribonucleotides. EPR spectra were recorded at 22 °C in a phosphate buffer (2 nmol of RNA; 10 mM phosphate, 100 mM NaCl, 0.1 mM Na_2EDTA, pH 7.0).

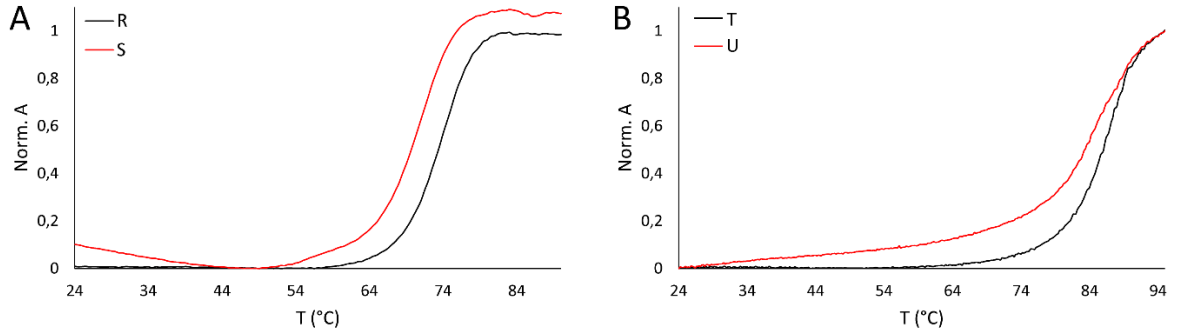

Figure 5.15. Thermal denaturing analysis of duplexes **R**, **S** (A); **T**, **U** (B). The duplexes were prepared by dissolving complementary single-stranded oligonucleotides (4.0 nmol) in a phosphate buffer (100 µL; 10 mM phosphate, 100 mM NaCl, 0.1 mM Na_2EDTA, pH 7.0), followed by annealing. The samples were diluted to 1.0 mL with the phosphate buffer, degassed with Ar and heated from 24 to 90 °C (1.0 °C/min). The absorbance at 260 nm was subsequently recorded at 0.2 °C intervals.

The CD spectra for the unmodified and **Ċm**-labeled RNA duplexes showed negative and positive molar ellipticities at ca. 210 and 263 nm, respectively, typical for A-form RNA (**Figure 5.16**). Thus, both the thermal denaturation studies and the CD spectra indicate that **Ċm** fits well in A-form RNA duplexes.

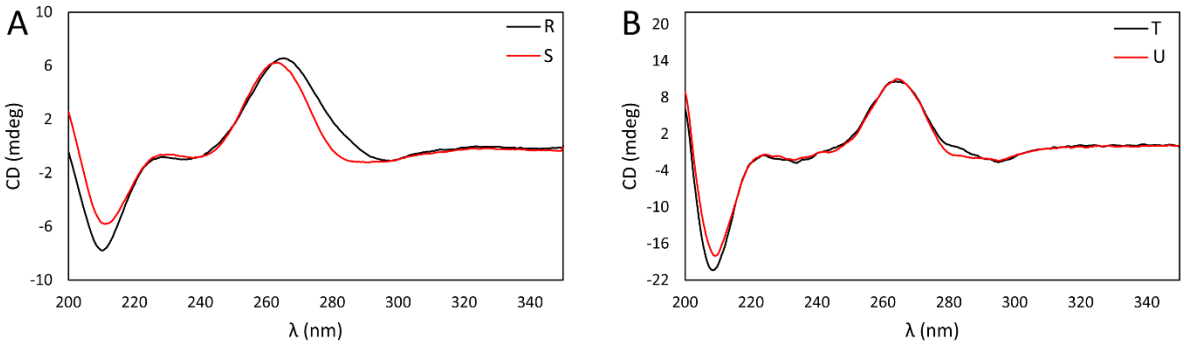

Figure 5.16. CD spectra of duplexes **R**, **S** (A); **T**, **U** (B). The duplexes were prepared by dissolving complementary single-stranded oligonucleotides (2.5 nmol of each) in a phosphate buffer (100 µL; 10 mM phosphate, 100 mM NaCl, 0.1 mM Na_2EDTA, pH 7.0) and annealing. The annealed samples were diluted to 200 µL with the same buffer before CD measurements.

5.5 Conclusion

The rigid spin labels **Ċ** and **Ċm** were synthesized and characterized, the key-step being an intramolecular C-C cross-coupling reaction. Comparison of the single-crystal X-ray structures of **Ċ** and **Ċm** with the known structure of **ç**,[154] the nucleobase of **Ç** and **Çm**, indicated that **Ċ** and **Ċm** are more rigid than the known rigid spin labels **Ç** and **Çm**. However, it remains to be seen if this will result in better performance of **Ċ** and **Ċm** as spin

labels compared to **Ç** and **Çm**. Another advantage of **Ċ** and **Ċm**, compared to **Ç** and **Çm**, is that their synthesis is two steps shorter. **Ċ** and **Ċm** were incorporated into DNA and RNA, respectively, analyzed and the data substantiates the incorporation of the spin labels with high spin-labeling efficiency. Thermal denaturation experiments and CD spectra confirmed that the spin labels are nonperturbing of duplex structures. The CD spectra of **Ċ**-labeled duplexes differed from the unmodified DNA duplexes, which was explained by the strong absorption of **Ċ** at the area the CD spectra differed. These new rigid spin labels **Ċ** and **Ċm** are promising candidates for future studies of DNA and RNA structures and dynamics by pulsed EPR methods.

6 Conclusions

This doctoral dissertation describes the synthesis of rigid spin- and fluorescent labels and their incorporation into DNA and RNA for the study of structure and dynamics of nucleic acids by electron paramagnetic resonance (EPR) and fluorescence spectroscopies. In the first part, the reduction of nitroxides during solid-phase oligonucleotide synthesis, a well-known problem, is addressed. A general method is described to protect nitroxides during oligonucleotide synthesis and by that circumventing the reduction. The nitroxide of **Çm** was protected, by first reducing it to the corresponding hydroxylamine and subsequently benzoylating it to form **Çm-Bz**. To incorporate **Çm** into RNA, **Çm-Bz** was converted into a phosphoramidite which was used for solid-phase oligonucleotide synthesis. The benzoyl group was stable through the RNA synthesis and was readily removed using standard oligonucleotide deprotection conditions, returning **Çm** in quantitative yields. This protecting-group strategy has made it possible to synthesize longer spin-labeled DNAs and RNAs and can be used as a general method to incorporate spin labels into nucleic acids by the phosphoramidite approach.

The second part of this thesis focuses on labeling of nucleic acids with rigid spin- and fluorescent labels. The projects including spin labeled nucleic acids were run in a collaboration with Prof. Thomas F. Prisner at the Goethe University in Frankfurt, Germany, where pulsed EPR methods are used to study the structure and dynamics of the spin-labeled nucleic acids. The rigid spin label **Ç** was incorporated into a DNAzyme by the use of the phosphoramidite of the benzoyl protected nitroxide **Ç-Bz**. **Çm** was similarly incorporated into RNA duplexes, the tetramethyl rhodamine aptamer and an RNA hairpin. The spin labels were incorporated into the nucleic acids with high spin-labeling efficiency. Furthermore, **Çmf**, the fluorescent derivative of **Çm**, was incorporated into various RNAs. The projects including **Çmf** labeling were run in a collaboration with Prof. Josef Wachtveitl at the Goethe University in Frankfurt, Germany, where fluorescent studies were performed on the RNA samples to investigate their structure and dynamics. Each project is explained in detail and preliminary results from the collaborators are presented.

In the third part of the thesis, the new rigid spin labels **Ċ** and **Ċm** are introduced. Their design and synthesis are described, and they are compared to **Ç** and **Çm**, with regards to

their rigidity. **Ċ** and **Ċm** were incorporated into DNA and RNA, respectively, with high spin-labeling efficiency and it was demonstrated that the labels were non-perturbing of duplex structure. These new rigid spin labels **Ċ** and **Ċm** are promising candidates for future studies of DNA and RNA structures and dynamics by pulsed EPR methods.

References

1. Höbartner, C.; Sicoli, G.; Wachowius, F.; Gophane, D. B.; Sigurdsson, S. T., Synthesis and characterization of RNA containing a rigid and nonperturbing cytidine-derived spin label. *J. Org. Chem.* **2012,** *77* (17), 7749-7754.
2. Barhate, N.; Cekan, P.; Massey, A. P.; Sigurdsson, S. T., A nucleoside that contains a rigid nitroxide spin label: A fluorophore in disguise. *Angew. Chem. Int. Ed.* **2007,** *46* (15), 2655-2658.
3. Dahm, R., Discovering DNA: Friedrich Miescher and the early years of nucleic acid research. *Hum. Genet.* **2008,** *122* (6), 565-581.
4. Lamm, E.; Harman, O.; Veigl, S. J., Before Watson and Crick in 1953 came Friedrich Miescher in 1869. *Genetics* **2020,** *215* (2), 291-296.
5. Minchin, S.; Lodge, J., Understanding biochemistry: Structure and function of nucleic acids. *Essays Biochem.* **2019,** *63* (4), 433-456.
6. Wall, W. J., *The search for human chromosomes : A history of discovery*. Springer, Cham: 2016.
7. Ferry, G., Molecular biology: Of DNA and broken dreams. *Nature* **2014,** *510* (7503), 32-33.
8. Franklin, R. E.; Gosling, R. G., The structure of sodium thymonucleate fibres. I. The influence of water content. *Acta Crystallogr.* **1953,** *6* (8-9), 673-677.
9. Watson, J. D.; Crick, F. H. C., Molecular structure of nucleic acids: A structure for deoxyribose nucleic acid. *Nature* **1953,** *171* (4356), 737-738.
10. Blanco, A.; Blanco, G., Chapter 6 - Nucleic Acids. In *Medical biochemistry*, Blanco, A.; Blanco, G., Eds. Academic Press: 2017; pp 121-140.
11. Voet, D.; Voet, J. G., *Biochemistry*. John Wiley and Sons: Hoboken, NJ, 2011.
12. Sutherland, J. D., The origin of life—Out of the blue. *Angew. Chem. Int. Ed.* **2016,** *55* (1), 104-121.
13. Clark, D. P.; Pazdernik, N. J.; McGehee, M. R., Chapter 13 - Protein synthesis. In *Molecular biology*, Third Edition ed.; Clark, D. P.; Pazdernik, N. J.; McGehee, M. R., Eds. Academic Cell: 2019; pp 397-444.
14. Sharp, P. A., The centrality of RNA. *Cell* **2009,** *136* (4), 577-580.
15. Neelagandan, N.; Lamberti, I.; Carvalho, H. J. F.; Gobet, C.; Naef, F., What determines eukaryotic translation elongation: recent molecular and quantitative analyses of protein synthesis. *Open Biol.* **2020,** *10* (12), 200292.
16. Kapp, L. D.; Lorsch, J. R., The molecular mechanics of eukaryotic translation. *Annu. Rev. Biochem.* **2004,** *73* (1), 657-704.
17. Breaker, Ronald R.; Joyce, Gerald F., The expanding view of RNA and DNA function. *Chem. Biol.* **2014,** *21* (9), 1059-1065.
18. Matera, A. G.; Wang, Z., A day in the life of the spliceosome. *Nat. Rev. Mol. Cell Biol.* **2014,** *15* (2), 108-121.
19. Wilkinson, M. E.; Charenton, C.; Nagai, K., RNA splicing by the spliceosome. *Annu. Rev. Biochem.* **2020,** *89* (1), 359-388.
20. Bohnsack, M. T.; Sloan, K. E., Modifications in small nuclear RNAs and their roles in spliceosome assembly and function. *Biol. Chem.* **2018,** *399* (11), 1265-1276.

21. Wilson, R. C.; Doudna, J. A., Molecular mechanisms of RNA interference. *Annu. Rev. Biophys.* **2013,** *42* (1), 217-239.
22. Carthew, R. W.; Sontheimer, E. J., Origins and mechanisms of miRNAs and siRNAs. *Cell* **2009,** *136* (4), 642-655.
23. Chen, L.; Heikkinen, L.; Wang, C.; Yang, Y.; Sun, H.; Wong, G., Trends in the development of miRNA bioinformatics tools. *Briefings Bioinf.* **2019,** *20* (5), 1836-1852.
24. O'Brien, J.; Hayder, H.; Zayed, Y.; Peng, C., Overview of microRNA biogenesis, mechanisms of actions, and circulation. *Front. Endocrinol.* **2018,** *9* (402), 1-12.
25. Ali Syeda, Z.; Langden, S. S. S.; Munkhzul, C.; Lee, M.; Song, S. J., Regulatory mechanism of microRNA expression in cancer. *Int. J. Mol. Sci.* **2020,** *21* (5), 1723.
26. Dana, H.; Chalbatani, G. M.; Mahmoodzadeh, H.; Karimloo, R.; Rezaiean, O.; Moradzadeh, A.; Mehmandoost, N.; Moazzen, F.; Mazraeh, A.; Marmari, V.; Ebrahimi, M.; Rashno, M. M.; Abadi, S. J.; Gharagouzlo, E., Molecular mechanisms and biological functions of siRNA. *Int. J. Biomed. Sci* . **2017,** *13* (2), 48-57.
27. Park, S. V.; Yang, J.-S.; Jo, H.; Kang, B.; Oh, S. S.; Jung, G. Y., Catalytic RNA, ribozyme, and its applications in synthetic biology. *Biotechnol. Adv.* **2019,** *37* (8), 107452.
28. Fedor, M. J.; Williamson, J. R., The catalytic diversity of RNAs. *Nat. Rev. Mol. Cell Biol.* **2005,** *6* (5), 399-412.
29. Westhof, E.; Lescoute, A., Ribozymes. In *Encyclopedia of virology (third edition)*, Mahy, B. W. J.; Van Regenmortel, M. H. V., Eds. Academic Press: Oxford, 2008; pp 475-481.
30. Ferré-D'Amaré, A. R.; Scott, W. G., Small self-cleaving ribozymes. *Cold Spring Harbor Perspect. Biol.* **2010,** *2* (10), a003574.
31. Scheitl, C. P. M.; Ghaem Maghami, M.; Lenz, A.-K.; Höbartner, C., Site-specific RNA methylation by a methyltransferase ribozyme. *Nature* **2020,** *587* (7835), 663-667.
32. Bédard, A.-S. V.; Hien, E. D. M.; Lafontaine, D. A., Riboswitch regulation mechanisms: RNA, metabolites and regulatory proteins. *Biochim. Biophys. Acta, Gene Regul. Mech.* **2020,** *1863* (3), 194501.
33. Pavlova, N.; Kaloudas, D.; Penchovsky, R., Riboswitch distribution, structure, and function in bacteria. *Gene* **2019,** *708*, 38-48.
34. Etzel, M.; Mörl, M., Synthetic riboswitches: From plug and pray toward plug and play. *Biochemistry* **2017,** *56* (9), 1181-1198.
35. Sherwood, A. V.; Henkin, T. M., Riboswitch-mediated gene regulation: Novel RNA architectures dictate gene expression responses. *Annu. Rev. Microbiol.* **2016,** *70* (1), 361-374.
36. Husser, C.; Dentz, N.; Ryckelynck, M., Structure-switching RNAs: From gene expression regulation to small molecule detection. *Small Struct.* **2021,** *2* (4), 2000132.
37. Berens, C.; Groher, F.; Suess, B., RNA aptamers as genetic control devices: The potential of riboswitches as synthetic elements for regulating gene expression. *Biotechnol. J.* **2015,** *10* (2), 246-257.
38. Menger, M.; Glökler, J.; Rimmele, M., Application of aptamers in therapeutics and for small-molecule detection. In *RNA towards medicine. Handbook of experimental pharmacology*, Erdmann, V.; Barciszewski, J.; Brosius, J., Eds. Springer, Berlin, Heidelberg: 2006; Vol. 173, pp 359-373.
39. Yarus, M., The genetic code and RNA-amino acid affinities. *Life* **2017,** *7* (2), 13.
40. Keefe, A. D.; Pai, S.; Ellington, A., Aptamers as therapeutics. *Nat. Rev. Drug Discovery* **2010,** *9* (7), 537-550.

41. Bjerregaard, N.; Andreasen, P. A.; Dupont, D. M., Expected and unexpected features of protein-binding RNA aptamers. *WIREs RNA* **2016,** *7* (6), 744-757.
42. Zhou, J.; Rossi, J., Aptamers as targeted therapeutics: Current potential and challenges. *Nat. Rev. Drug Discovery* **2017,** *16* (3), 181-202.
43. Nimjee, S. M.; White, R. R.; Becker, R. C.; Sullenger, B. A., Aptamers as therapeutics. *Annu. Rev. Pharmacol. Toxicol.* **2017,** *57* (1), 61-79.
44. Ruscito, A.; DeRosa, M. C., Small-molecule binding aptamers: Selection strategies, characterization, and applications. *Front. Chem.* **2016,** *4* (14).
45. Zhang, Y.; Lai, B. S.; Juhas, M., Recent advances in aptamer discovery and applications. *Molecules* **2019,** *24* (5), 941.
46. Kumar Kulabhusan, P.; Hussain, B.; Yüce, M., Current perspectives on aptamers as diagnostic tools and therapeutic agents. *Pharmaceutics* **2020,** *12* (7), 646.
47. Deisingh, A. K., Aptamer-based biosensors: Biomedical applications. In *RNA towards medicine*, Erdmann, V.; Barciszewski, J.; Brosius, J., Eds. Springer, Berlin, Heidelberg: 2006.
48. Zhou, W.; Jimmy Huang, P.-J.; Ding, J.; Liu, J., Aptamer-based biosensors for biomedical diagnostics. *Analyst* **2014,** *139* (11), 2627-2640.
49. Ni, S.; Zhuo, Z.; Pan, Y.; Yu, Y.; Li, F.; Liu, J.; Wang, L.; Wu, X.; Li, D.; Wan, Y.; Zhang, L.; Yang, Z.; Zhang, B.-T.; Lu, A.; Zhang, G., Recent progress in aptamer discoveries and modifications for therapeutic applications. *ACS Appl. Mater. Interfaces* **2021,** *13* (8), 9500-9519.
50. Kaur, H.; Bruno, J. G.; Kumar, A.; Sharma, T. K., Aptamers in the therapeutics and diagnostics pipelines. *Theranostics* **2018,** *8* (15), 4016-4032.
51. Kang, K. N.; Lee, Y. S., RNA aptamers: A review of recent trends and applications. In *Future trends in biotechnology. Advances in biochemical engineering/biotechnology*, Zhong, J. J., Ed. Springer, Berlin, Heidelberg: 2012; Vol. 131, pp 153-169.
52. Stoltenburg, R.; Reinemann, C.; Strehlitz, B., SELEX—A (r)evolutionary method to generate high-affinity nucleic acid ligands. *Biomol. Eng.* **2007,** *24* (4), 381-403.
53. Komarova, N.; Kuznetsov, A., Inside the black box: What makes SELEX better? *Molecules* **2019,** *24* (19), 3598.
54. Dong, Y.; Wang, Z.; Wang, S.; Wu, Y.; Ma, Y.; Liu, J., Introduction of SELEX and important SELEX variants. In *Aptamers for analytical applications*, 2018; pp 1-25.
55. Llamas-Saiz, A. L.; van Raaij, M. J., X-Ray crystallography of biological macromolecules: Fundamentals and applications. In *Proteins in solution and at interfaces*, 2013; pp 1-22.
56. Egli, M., Nucleic acid crystallography: current progress. *Curr. Opin. Chem. Biol.* **2004,** *8* (6), 580-591.
57. Egli, M.; Pallan, P. S., Crystallographic studies of chemically modified nucleic acids: A backward glance. *Chem. Biodiversity* **2010,** *7* (1), 60-89.
58. Ryu, W.-S., Chapter 2 - Virus structure. In *Molecular virology of human pathogenic viruses*, Ryu, W.-S., Ed. Academic Press: Boston, 2017; pp 21-29.
59. Holbrook, E. L.; Holbrook, S. R., Crystallisation of nucleic acids. In *eLS*, 2010.
60. Mooers, B. H. M., Crystallographic studies of DNA and RNA. *Methods* **2009,** *47* (3), 168-176.
61. Nelson, J. A.; Uhlenbeck, O. C., When to believe what you see. *Mol. Cell* **2006,** *23* (4), 447-450.
62. Stojković, V.; Myasnikov, A. G.; Young, I. D.; Frost, A.; Fraser, J. S.; Fujimori, D. G., Assessment of the nucleotide modifications in the high-resolution cryo-electron

microscopy structure of the Escherichia coli 50S subunit. *Nucleic Acids Res.* **2020,** *48* (5), 2723-2732.
63. Dai, X.; Li, Z.; Lai, M.; Shu, S.; Du, Y.; Zhou, Z. H.; Sun, R., In situ structures of the genome and genome-delivery apparatus in a single-stranded RNA virus. *Nature* **2017,** *541* (7635), 112-116.
64. Taoka, M.; Nobe, Y.; Yamaki, Y.; Sato, K.; Ishikawa, H.; Izumikawa, K.; Yamauchi, Y.; Hirota, K.; Nakayama, H.; Takahashi, N.; Isobe, T., Landscape of the complete RNA chemical modifications in the human 80S ribosome. *Nucleic Acids Res.* **2018,** *46* (18), 9289-9298.
65. Gopal, A.; Zhou, Z. H.; Knobler, C. M.; Gelbart, W. M., Visualizing large RNA molecules in solution. *RNA* **2012,** *18* (2), 284-299.
66. Murata, K.; Wolf, M., Cryo-electron microscopy for structural analysis of dynamic biological macromolecules. *Biochim. Biophys. Acta, Gen. Subj.* **2018,** *1862* (2), 324-334.
67. Renaud, J.-P.; Chari, A.; Ciferri, C.; Liu, W.-t.; Rémigy, H.-W.; Stark, H.; Wiesmann, C., Cryo-EM in drug discovery: achievements, limitations and prospects. *Nat. Rev. Drug Discov.* **2018,** *17* (7), 471-492.
68. Milne, J. L. S.; Borgnia, M. J.; Bartesaghi, A.; Tran, E. E. H.; Earl, L. A.; Schauder, D. M.; Lengyel, J.; Pierson, J.; Patwardhan, A.; Subramaniam, S., Cryo-electron microscopy – a primer for the non-microscopist. *FEBS J.* **2013,** *280* (1), 28-45.
69. Bai, X.-C., Seeing atoms by single-particle cryo-EM. *Trends Biochem. Sci.* **2021,** *46* (4), 253-254.
70. Nakane, T.; Kotecha, A.; Sente, A.; McMullan, G.; Masiulis, S.; Brown, P. M. G. E.; Grigoras, I. T.; Malinauskaite, L.; Malinauskas, T.; Miehling, J.; Uchański, T.; Yu, L.; Karia, D.; Pechnikova, E. V.; de Jong, E.; Keizer, J.; Bischoff, M.; McCormack, J.; Tiemeijer, P.; Hardwick, S. W.; Chirgadze, D. Y.; Murshudov, G.; Aricescu, A. R.; Scheres, S. H. W., Single-particle cryo-EM at atomic resolution. *Nature* **2020,** *587* (7832), 152-156.
71. Yip, K. M.; Fischer, N.; Paknia, E.; Chari, A.; Stark, H., Atomic-resolution protein structure determination by cryo-EM. *Nature* **2020,** *587* (7832), 157-161.
72. Barnwal, R. P.; Yang, F.; Varani, G., Applications of NMR to structure determination of RNAs large and small. *Arch. Biochem. Biophys.* **2017,** *628*, 42-56.
73. Melissa, G.; Xiaoyan, S.; Anette, C.-N.; Qi, Z.; M., A.-H. H., Review NMR studies of RNA dynamics and structural plasticity using NMR residual dipolar couplings. *Biopolymers* **2007,** *86* (5-6), 384-402.
74. Al-Hashimi, H. M., Dynamics-based amplification of RNA function and its characterization by using NMR spectroscopy. *ChemBioChem* **2005,** *6* (9), 1506-1519.
75. Emwas, A.-H.; Szczepski, K.; Poulson, B. G.; Chandra, K.; McKay, R. T.; Dhahri, M.; Alahmari, F.; Jaremko, L.; Lachowicz, J. I.; Jaremko, M., NMR as a "gold standard" method in drug design and discovery. *Molecules* **2020,** *25* (20), 4597.
76. Cheung, T.; Ramesh, V., Biomolecular NMR spectroscopy and structure determination of DNA. In *Biomolecular and bioanalytical techniques*, 2019; pp 421-469.
77. Bothe, J. R.; Nikolova, E. N.; Eichhorn, C. D.; Chugh, J.; Hansen, A. L.; Al-Hashimi, H. M., Characterizing RNA dynamics at atomic resolution using solution-state NMR spectroscopy. *Nat. Methods* **2011,** *8* (11), 919-931.
78. Bonvin, A. M. J. J.; Boelens, R.; Kaptein, R., NMR analysis of protein interactions. *Curr. Opin. Chem. Biol.* **2005,** *9* (5), 501-508.

79. Al-Hashimi, H. M., NMR studies of nucleic acid dynamics. *J. Magn. Reson.* **2013,** *237*, 191-204.
80. Shajani, Z.; Varani, G., NMR studies of dynamics in RNA and DNA by 13C relaxation. *Biopolymers* **2007,** *86* (5-6), 348-359.
81. Xu, Y.; Matthews, S., TROSY NMR spectroscopy of large soluble proteins. In *Modern NMR methodology*, Heise, H.; Matthews, S., Eds. Springer Berlin Heidelberg: Berlin, Heidelberg, 2013; pp 97-119.
82. Markley, J. L., View from nuclear magnetic resonance spectroscopy. In *Integrative structural biology with hybrid methods. Advances in experimental medicine and biology*, Nakamura, H.; Kleywegt, G.; Burley, S.; Markley, J., Eds. Springer: Singapore, 2018; Vol. 1105.
83. Purslow, J. A.; Khatiwada, B.; Bayro, M. J.; Venditti, V., NMR methods for structural characterization of protein-protein complexes. *Front. Mol. Biosci.* **2020,** *7* (9).
84. Millar, D. P., Fluorescence studies of DNA and RNA structure and dynamics. *Curr. Opin. Struct. Biol.* **1996,** *6* (3), 322-326.
85. Zhao, L.; Xia, T., Probing RNA conformational dynamics and heterogeneity using femtosecond time-resolved fluorescence spectroscopy. *Methods* **2009,** *49* (2), 128-135.
86. Robinson, P. J.; Woolhead, C. A., Implementation of FRET technologies for studying the folding and conformational changes in biological structures. In *FRET – Förster resonance energy transfer*, 2013; pp 357-396.
87. Wilhelmsson, L. M., Förster resonance energy transfer (FRET) between nucleobase analogs – a tool for detailed structure and dynamics investigations. In *Fluorescent analogues of biomolecular building blocks: Design and applications*, 2016; pp 224-241.
88. Energy transfer. In *Principles of fluorescence spectroscopy*, 3 ed.; Lakowicz, J. R., Ed. Springer, Boston, MA: Boston, 2006.
89. Sahoo, H., Förster resonance energy transfer – A spectroscopic nanoruler: Principle and applications. *J. Photochem. Photobiol., C* **2011,** *12* (1), 20-30.
90. Klostermeier, D.; Millar, D. P., Time-resolved fluorescence resonance energy transfer: A versatile tool for the analysis of nucleic acids. *Biopolymers* **2002,** *61* (3), 159-179.
91. Wood, S.; Rueda, D., Fluorescence labeling of nucleic acids. In *Encyclopedia of biophysics*, Roberts, G. C. K., Ed. Springer Berlin Heidelberg: Berlin, Heidelberg, 2013; pp 809-812.
92. Didenko, V. V., DNA Probes using fluorescence resonance energy transfer (FRET): Designs and applications. *BioTechniques* **2001,** *31* (5), 1106-1121.
93. Sanders, Joshua C.; Holmstrom, Erik D., Integrating single-molecule FRET and biomolecular simulations to study diverse interactions between nucleic acids and proteins. *Essays in Biochem.* **2021,** *65* (1), 37–49.
94. Kashida, H.; Kawai, H.; Azuma, H.; Araki, Y.; Wada, T.; Asanuma, H., Quantitative analyses of Förster resonance energy transfer between identical pyrene chromophores (homo-FRET) in DNA scaffolds. *ChemPhotoChem* **2021,** *5* (2), 167-172.
95. Woodson, S. A.; Koculi, E., Chapter 9 - Analysis of RNA folding by native polyacrylamide gel electrophoresis. In *Methods Enzymol.*, Academic Press: 2009; Vol. 469, pp 189-208.
96. Thomas, G. J., Raman spectroscopy of proteins and nucleic acid assemblies. *Annu. Rev. Biophys. Biomol. Struct.* **1999,** *28* (1), 1-27.

97. Benevides, J. M.; Overman, S. A.; Thomas Jr, G. J., Raman, polarized Raman and ultraviolet resonance Raman spectroscopy of nucleic acids and their complexes. *J. Raman Spectrosc.* **2005,** *36* (4), 279-299.
98. Kypr, J.; Kejnovská, I.; Bednářová, K.; Vorlíčková, M., Circular dichroism spectroscopy of nucleic acids. In *Comprehensive chiroptical spectroscopy*, Berova, N.; Polavarapu, P. L.; Nakanishi, K.; Woody, R. W., Eds. 2012; pp 575-586.
99. Salikhov, K. M.; Zavoiskaya, N. E., Zavoisky and the discovery of EPR. *Resonance* **2015,** *20* (11), 963-968.
100. Eaton, G. R.; Eaton, S. S., 2.2 - Electron paramagnetic resonance spectroscopy. In *Comprehensive coordination chemistry II*, McCleverty, J. A.; Meyer, T. J., Eds. Pergamon: Oxford, 2003; pp 37-48.
101. Weil, J. A.; Bolton, J. R., Basic principles of paramagnetic resonance. In *Electron paramagnetic resonance*, Weil, J. A.; Bolton, J. R., Eds. John Wiley & Sons, Inc.: 2006; pp 1-35.
102. Gerson, F.; Huber, W., Physical fundamentals of electron spin resonances. In *Electron spin resonance spectroscopy of organic radicals*, Gerson, F.; Huber, W., Eds. Wiley-VCH Verlag GmbH & Co. KGaA: 2003; pp 3-9.
103. Nguyen, P.; Qin, P. Z., RNA dynamics: perspectives from spin labels. *Wiley Interdiscip. Rev.: RNA* **2012,** *3* (1), 62-72.
104. Bennati, M.; Prisner, T. F., New developments in high field electron paramagnetic resonance with applications in structural biology. *Rep. Prog. Phys.* **2005,** *68* (2), 411.
105. Krstić, I.; Endeward, B.; Margraf, D.; Marko, A.; Prisner, T. F., Structure and dynamics of nucleic acids. *Top. Curr. Chem.* **2012,** *321*, 159-198.
106. Roessler, M. M.; Salvadori, E., Principles and applications of EPR spectroscopy in the chemical sciences. *Chem. Soc. Rev.* **2018,** *47* (8), 2534-2553.
107. Misra, S. K., Introduction. In *Multifrequency electron paramagnetic resonance*, Misra, S. K., Ed. Wiley-VCH Verlag GmbH & Co. KGaA: 2011; pp 1-22.
108. Zhang, X.; Cekan, P.; Sigurdsson, S. T.; Qin, P. Z., Chapter 15 - Studying RNA using site-directed spin-labeling and continuous-wave electron paramagnetic resonance spectroscopy. In *Methods in Enzymol.*, Academic Press: 2009; Vol. 469, pp 303-328.
109. Kim, N. K.; Murali, A.; DeRose, V. J., A distance ruler for RNA using EPR and site-directed spin labeling. *Chem. Biol.* **2004,** *11* (7), 939-48.
110. Duss, O.; Yulikov, M.; Jeschke, G.; Allain, F. H. T., EPR-aided approach for solution structure determination of large RNAs or protein–RNA complexes. *Nat. Commun.* **2014,** *5*, 3669.
111. Jeschke, G., The contribution of modern EPR to structural biology. *Emerging Top. Life Sci.* **2018,** *2* (1), 9-18.
112. Reginsson, Gunnar W.; Schiemann, O., Studying biomolecular complexes with pulsed electron–electron double resonance spectroscopy. *Biochem. Soc. Trans.* **2011,** *39* (1), 128-139.
113. Schiemann, O.; Prisner, T. F., Long-range distance determinations in biomacromolecules by EPR spectroscopy. *Q. Rev. Biophys.* **2007,** *40* (1), 1-53.
114. Martin, R. E.; Pannier, M.; Diederich, F.; Gramlich, V.; Hubrich, M.; Spiess, H. W., Determination of end-to-end distances in a series of TEMPO diradicals of up to 2.8 nm length with a new four-pulse double electron electron resonance experiment. *Angew. Chem. Int. Ed.* **1998,** *37* (20), 2833-2837.
115. Fajer, P. G.; Brown, L.; Song, L., Practical pulsed dipolar ESR (DEER). In *ESR spectroscopy in membrane biophysics*, Springer US: Boston, MA, 2007; pp 95-128.

116. Abdullin, D.; Schiemann, O., Pulsed dipolar EPR spectroscopy and metal Ions: methodology and biological applications. *ChemPlusChem* **2020,** *85* (2), 353-372.
117. Endeward, B.; Marko, A.; Denysenkov, V. P.; Sigurdsson, S. T.; Prisner, T. F., Chapter fourteen - Advanced EPR methods for studying conformational dynamics of nucleic acids. In *Methods in Enzymol.*, Qin, P. Z.; Warncke, K., Eds. Academic Press: 2015; Vol. 564, pp 403-425.
118. Prisner, T. F.; Marko, A.; Sigurdsson, S. T., Conformational dynamics of nucleic acid molecules studied by PELDOR spectroscopy with rigid spin labels. *J. Magn. Reson.* **2015,** *252*, 187-198.
119. Schiemann, O.; Cekan, P.; Margraf, D.; Prisner, T. F.; Sigurdsson, S. T., Relative orientation of rigid nitroxides by PELDOR: Beyond distance measurements in nucleic acids. *Angew. Chem. Int. Ed.* **2009,** *48* (18), 3292-3295.
120. Sahu, I. D.; Lorigan, G. A., Electron spin resonance spectroscopy | spin labeling and spin trapping. In *Encyclopedia of Analytical Science (Third Edition)*, Worsfold, P.; Poole, C.; Townshend, A.; Miró, M., Eds. Academic Press: Oxford, 2019; pp 315-327.
121. Sowa, G. Z.; Qin, P. Z., Site-directed spin labeling studies on nucleic acid structure and dynamics. In *Progress in nucleic acid research and molecular biology*, Conn, P. M., Ed. Academic Press: 2008; Vol. 82, pp 147-197.
122. Mabbs, F. E.; Collison, D., *Electron paramagnetic resonance of d transition metal compounds*. Elsevier Science: 2013.
123. Potapov, A.; Yagi, H.; Huber, T.; Jergic, S.; Dixon, N. E.; Otting, G.; Goldfarb, D., Nanometer-scale distance measurements in proteins using Gd3+ spin labeling. *J. Am. Chem. Soc.* **2010,** *132* (26), 9040-9048.
124. Martorana, A.; Yang, Y.; Zhao, Y.; Li, Q.-F.; Su, X.-C.; Goldfarb, D., Mn(ii) tags for DEER distance measurements in proteins via C-S attachment. *Dalton Trans.* **2015,** *44* (48), 20812-20816.
125. Fleck, N.; Heubach, C. A.; Hett, T.; Haege, F. R.; Bawol, P. P.; Baltruschat, H.; Schiemann, O., SLIM: A short-linked, highly redox-stable trityl label for high-sensitivity in-cell EPR distance measurements. *Angew. Chem. Int. Ed.* **2020,** *59* (24), 9767-9772.
126. Krumkacheva, O.; Bagryanskaya, E., Trityl radicals as spin labels. In *Electron Paramagnetic Resonance: Volume 25*, The Royal Society of Chemistry: 2017; Vol. 25, pp 35-60.
127. Berliner, L. J., *Spin labeling : Theory and applications*. Springer Sience & Business Media: 2012; Vol. 8.
128. Shelke, S. A.; Sigurdsson, S. T., Site-directed spin labelling of nucleic acids. *Eur. J. Org. Chem.* **2012,** *2012* (12), 2291.
129. Haugland, M. M.; Anderson, E. A.; Lovett, J. E., Tuning the properties of nitroxide spin labels for use in electron paramagnetic resonance spectroscopy through chemical modification of the nitroxide framework. In *Electron paramagnetic resonance: Volume 25*, The Royal Society of Chemistry: 2017; Vol. 25, pp 1-34.
130. Elajaili, H.; Sedhom, J.; Eaton, S. S.; Eaton, G. R., Persistence of nitroxide radicals in solution. *Appl. Magn. Reson.* **2019,** *50* (10), 1177-1181.
131. Volodarsky, L. B.; Reznikov, V. A.; Ovcharenko, V. I., *Synthetic chemistry of stable nitroxides*. Taylor & Francis: 1993.
132. Karoui, H.; Moigne, F. L.; Ouari, O.; Tordo, P., Nitroxide radicals: Properties, synthesis and applications. In *Stable radicals*, 2010; pp 173-229.
133. Haugland, M. M.; Lovett, J. E.; Anderson, E. A., Advances in the synthesis of nitroxide radicals for use in biomolecule spin labelling. *Chem. Soc. Rev.* **2018,** *47* (3), 668-680.

134. Jeschke, G.; Chechik, V.; Ionita, P.; Godt, A.; Zimmermann, H.; Banham, J.; Timmel, C. R.; Hilger, D.; Jung, H., DeerAnalysis2006—a comprehensive software package for analyzing pulsed ELDOR data. *Appl. Magn. Reson.* **2006,** *30* (3), 473-498.
135. Sajid, M.; Jeschke, G.; Wiebcke, M.; Godt, A., Conformationally unambiguous spin labeling for distance measurements. *Chem. Eur. J.* **2009,** *15* (47), 12960-12962.
136. Gophane, D. B.; Endeward, B.; Prisner, T. F.; Sigurdsson, S. T., Conformationally restricted isoindoline-derived spin labels in duplex DNA: Distances and rotational flexibility by pulsed electron–electron double resonance spectroscopy. *Chem. Eur. J.* **2014,** *20* (48), 15913-15919.
137. Gophane, D. B.; Sigurdsson, S. T., Hydrogen-bonding controlled rigidity of an isoindoline-derived nitroxide spin label for nucleic acids. *Chem. Commun.* **2013,** *49* (10), 999-1001.
138. Gophane, D. B.; Endeward, B.; Prisner, T. F.; Sigurdsson, S. T., A semi-rigid isoindoline-derived nitroxide spin label for RNA. *Org. Biomol. Chem.* **2018,** *16* (5), 816-824.
139. Erlenbach, N.; Endeward, B.; Schöps, P.; Gophane, D. B.; Sigurdsson, S. T.; Prisner, T. F., Flexibilities of isoindoline-derived spin labels for nucleic acids by orientation selective PELDOR. *Phys. Chem. Chem. Phys.* **2016,** *18* (24), 16196-16201.
140. Collauto, A.; von Bülow, S.; Gophane, D. B.; Saha, S.; Stelzl, L. S.; Hummer, G.; Sigurdsson, S. T.; Prisner, T. F., Compaction of RNA duplexes in the cell. *Angew. Chem. Int. Ed.* **2020,** *59* (51), 23025-23029.
141. Gränz, M.; Erlenbach, N.; Spindler, P.; Gophane, D. B.; Stelzl, L. S.; Sigurdsson, S. T.; Prisner, T. F., Dynamics of nucleic acids at room temperature revealed by pulsed EPR spectroscopy. *Angew. Chem. Int. Ed.* **2018,** *57* (33), 10540-10543.
142. Miller, T. R.; Hopkins, P. B., Toward the synthesis of a second-generation nitroxide spin probe for DNA dynamics studies. *Bioorg. Med. Chem. Lett.* **1994,** *4* (8), 981-986.
143. Miller, T. R.; Alley, S. C.; Reese, A. W.; Solomon, M. S.; McCallister, W. V.; Mailer, C.; Robinson, B. H.; Hopkins, P. B., A probe for sequence-dependent nucleic acid dynamics. *J. Am. Chem. Soc.* **1995,** *117* (36), 9377-9378.
144. Okonogi, T. M.; Alley, S. C.; Reese, A. W.; Hopkins, P. B.; Robinson, B. H., Sequence-dependent dynamics of duplex DNA: The applicability of a dinucleotide model. *Biophys. J.* **2002,** *83* (6), 3446-3459.
145. Marko, A.; Denysenkov, V.; Margraf, D.; Cekan, P.; Schiemann, O.; Sigurdsson, S. T.; Prisner, T. F., Conformational flexibility of DNA. *J. Am. Chem. Soc.* **2011,** *133* (34), 13375-13379.
146. Grytz, C. M.; Marko, A.; Cekan, P.; Sigurdsson, S. T.; Prisner, T. F., Flexibility and conformation of the cocaine aptamer studied by PELDOR. *Phys. Chem. Chem. Phys.* **2016,** *18* (4), 2993-3002.
147. Hetzke, T.; Vogel, M.; Gophane, D. B.; Weigand, J. E.; Suess, B.; Sigurdsson, S. T.; Prisner, T. F., Influence of Mg2+ on the conformational flexibility of a tetracycline aptamer. *RNA* **2019,** *25* (1), 158-167.
148. Shelke, S. A.; Sigurdsson, S. T., Site-directed spin labeling for EPR studies of nucleic acids. In *Nucleic Acids Mol. Biol.*, Springer, Cham: 2016; Vol. 31.
149. Babaylova, E. S.; Malygin, A. A.; Lomzov, A. A.; Pyshnyi, D. V.; Yulikov, M.; Jeschke, G.; Krumkacheva, O. A.; Fedin, M. V.; Karpova, G. G.; Bagryanskaya, E. G., Complementary-addressed site-directed spin labeling of long natural RNAs. *Nucleic Acids Res.* **2016,** *44* (16), 7935-7943.

150. Kamble, N. R.; Sigurdsson, S. T., Purine-derived nitroxides for noncovalent spin-labeling of abasic sites in duplex nucleic acids. *Chem. Eur. J.* **2018,** *24* (16), 4157-4164.
151. Saha, S.; Hetzke, T.; Prisner, T. F.; Sigurdsson, S. T., Noncovalent spin-labeling of RNA: The aptamer approach. *Chem. Commun.* **2018,** *54*, 11749-11752.
152. Shelke, S. A.; Sigurdsson, S. T., Noncovalent and site-directed spin labeling of nucleic acids. *Angew. Chem. Int. Ed.* **2010,** *49* (43), 7984-7986.
153. Kamble, N. R.; Granz, M.; Prisner, T. F.; Sigurdsson, S. T., Noncovalent and site-directed spin labeling of duplex RNA. *Chem. Commun.* **2016,** *52* (100), 14442-14445.
154. Edwards, T. E.; Cekan, P.; Reginsson, G. W.; Shelke, S. A.; Ferré-D'Amaré, A. R.; Schiemann, O.; Sigurdsson, S. T., Crystal structure of a DNA containing the planar, phenoxazine-derived bi-functional spectroscopic probe Ç. *Nucleic Acids Res.* **2011,** *39* (10), 4419-4426.
155. Verma, S.; Eckstein, F., Modified oligonucleotides: Synthesis and strategy for users. *Annu. Rev. Biochem.* **1998,** *67* (1), 99-134.
156. Cekan, P.; Smith, A. L.; Barhate, N.; Robinson, B. H.; Sigurdsson, S. T., Rigid spin-labeled nucleoside Ç: a nonperturbing EPR probe of nucleic acid conformation. *Nucleic Acids Res.* **2008,** *36* (18), 5946-5954.
157. Michelson, A. M.; Todd, A. R., Nucleotides part XXXII. Synthesis of a dithymidine dinucleotide containing a 3′: 5′-internucleotidic linkage. *J. Chem. Soc.* **1955,** (0), 2632-2638.
158. Beaucage, S. L.; Iyer, R. P., Advances in the synthesis of oligonucleotides by the phosphoramidite approach. *Tetrahedron* **1992,** *48* (12), 2223-2311.
159. Beaucage, S. L.; Caruthers, M. H., Deoxynucleoside phosphoramidites—A new class of key intermediates for deoxypolynucleotide synthesis. *Tetrahedron Lett.* **1981,** *22* (20), 1859-1862.
160. Piton, N.; Mu, Y.; Stock, G.; Prisner, T. F.; Schiemann, O.; Engels, J. W., Base-specific spin-labeling of RNA for structure determination. *Nucleic Acids Res.* **2007,** *35* (9), 3128-3143.
161. Rozantsev, E. G.; Sholle, V. D., Synthesis and reactions of stable nitroxyl radicals. II. Reactions. *Synthesis* **1971,** *1971* (8), 401-414.
162. Abakumov, G. A.; Tikhonov, V. D., Interaction of the stable radical 2,2,6,6-tetramethylpiperidone-4-oxy-1 with acids. *Bull. Acad. Sci. USSR, Div. Chem. Sci.* **1969,** *18* (4), 724-727.
163. Sproat, B.; Colonna, F.; Mullah, B.; Tsou, D.; Andrus, A.; Hampel, A.; Vinayak, R., An efficient method for the isolation and purification of oligoribonucleotides. *Nucleosides Nucleotides* **1995,** *14* (1-2), 255-273.
164. Tsou, D.; Hampel, A.; Andrus, A.; Vinayak, R., Large scale synthesis of oligoribonucleotides on high-loaded polystyrene (HLP) support. *Nucleosides Nucleotides* **1995,** *14* (7), 1481-1492.
165. Pitsch, S.; Weiss, P. A.; Wu, X.; Ackermann, D.; Honegger, T., Fast and reliable automated synthesis of RNA and partially 2′-O-protected precursors ('caged RNA') based on two novel, orthogonal 2′-O-protecting groups, preliminary communication. *Helv. Chim. Acta* **1999,** *82* (10), 1753-1761.
166. Welz, R.; Müller, S., 5-(Benzylmercapto)-1H-tetrazole as activator for 2′-O-TBDMS phosphoramidite building blocks in RNA synthesis. *Tetrahedron Lett.* **2002,** *43* (5), 795-797.
167. Gannett, P. M.; Darian, E.; Powell, J.; Johnson Il, E. M.; Mundoma, C.; Greenbaum, N. L.; Ramsey, C. M.; Dalal, N. S.; Budil, D. E., Probing triplex formation by EPR

spectroscopy using a newly synthesized spin label for oligonucleotides. *Nucleic Acids Res.* **2002,** *30* (23), 5328-5337.
168. Cekan, P.; Sigurdsson, S. T., Conformation and dynamics of nucleotides in bulges and symmetric internal loops in duplex DNA studied by EPR and fluorescence spectroscopies. *Biochem. Biophys. Res. Commun.* **2012,** *420* (3), 656-661.
169. Chalmers, B. A.; Morris, J. C.; Fairfull-Smith, K. E.; Grainger, R. S.; Bottle, S. E., A novel protecting group methodology for syntheses using nitroxides. *Chem. Commun.* **2013,** *49* (88), 10382-10384.
170. Tsunoda, H.; Ohkubo, A.; Taguchi, H.; Seio, K.; Sekine, M., Synthesis and properties of DNA oligomers containing 2'-deoxynucleoside N-oxide derivatives. *J. Org. Chem.* **2008,** *73* (4), 1217-1224.
171. Mfuh, A. M.; Larionov, O. V., Heterocyclic N-oxides - An emerging class of therapeutic agents. *Curr. Med. Chem.* **2015,** *22* (24), 2819-2857.
172. Dane, E. L.; Corzilius, B.; Rizzato, E.; Stocker, P.; Maly, T.; Smith, A. A.; Griffin, R. G.; Ouari, O.; Tordo, P.; Swager, T. M., Rigid orthogonal bis-TEMPO biradicals with improved solubility for dynamic nuclear polarization. *J. Org. Chem.* **2012,** *77* (4), 1789-1797.
173. Seven, I.; Weinrich, T.; Gränz, M.; Grünewald, C.; Brüß, S.; Krstić, I.; Prisner, T. F.; Heckel, A.; Göbel, M. W., Photolabile protecting groups for nitroxide spin labels. *Eur. J. Org. Chem.* **2014,** *2014* (19), 4037-4043.
174. Weinrich, T.; Gränz, M.; Grünewald, C.; Prisner, T. F.; Göbel, M. W., Synthesis of a cytidine phosphoramidite with protected nitroxide spin label for EPR experiments with RNA. *Eur. J. Org. Chem.* **2017,** *2017* (3), 491-496.
175. Weinrich, T.; Jaumann, E. A.; Scheffer, U. M.; Prisner, T. F.; Göbel, M. W., A cytidine phosphoramidite with protected nitroxide spin label: Synthesis of a full-length TAR RNA and investigation by in-line probing and EPR spectroscopy. *Chem. Eur. J.* **2018,** *24* (23), 6202-6207.
176. Weinrich, T.; Jaumann, E. A.; Scheffer, U. M.; Prisner, T. F.; Göbel, M. W., Phosphoramidite building blocks with protected nitroxides for the synthesis of spin-labeled DNA and RNA. *Beilstein J Org Chem* **2018,** *14*, 1563-1569.
177. Kurita, M.; Higuchi, Y.; Mirc, J. W.; Matsumoto, S.; Usui, K.; Suemune, H.; Aso, M., Synthesis and electron paramagnetic resonance studies of oligodeoxynucleotides containing 2-N-tert-butylaminoxyl-2′-deoxyadenosines. *Chem. Bio. Chem.* **2016,** *17* (24), 2346-2352.
178. Sato, Y.; Hayashi, H.; Okazaki, M.; Aso, M.; Karasawa, S.; Ueki, S.; Suemune, H.; Koga, N., Water-proton relaxivities of DNA oligomers carrying TEMPO radicals. *Magn. Reson. Chem.* **2008,** *46* (11), 1055-1058.
179. Johnsson, R. A.; Bogojeski, J. J.; Damha, M. J., An evaluation of selective deprotection conditions for the synthesis of RNA on a light labile solid support. *Bioorg. Med. Chem. Lett.* **2014,** *24* (9), 2146-2149.
180. Vargeese, C.; Shaffer, C.; Bowman, K. Deprotection and purification of oligonucleotides and their derivatives. *WO 2004/007748 A2*, **2004**.
181. Grytz, C. M.; Kazemi, S.; Marko, A.; Cekan, P.; Guntert, P.; Sigurdsson, S. T.; Prisner, T. F., Determination of helix orientations in a flexible DNA by multi-frequency EPR spectroscopy. *Phys. Chem. Chem. Phys.* **2017,** *19* (44), 29801-29811.
182. Silverman, S. K., Nucleic acid enzymes (ribozymes and deoxyribozymes): In vitro selection and application. In *Wiley encyclopedia of chemical biology*, Begley, T. P., Ed. John Wiley & Sons, Inc.: 2008; pp 1-17.

183. Joyce, G. F., Directed evolution of nucleic acid enzymes. *Annu. Rev. Biochem.* **2004,** *73* (1), 791-836.
184. Breaker, R. R.; Joyce, G. F., A DNA enzyme that cleaves RNA. *Chem. Biol.* **1994,** *1* (4), 223-229.
185. Li, J.; Zheng, W.; Kwon, A. H.; Lu, Y., In vitro selection and characterization of a highly efficient Zn(II)-dependent RNA-cleaving deoxyribozyme. *Nucleic Acids Res.* **2000,** *28* (2), 481-8.
186. Santoro, S. W.; Joyce, G. F., A general purpose RNA-cleaving DNA enzyme. *Proc. Natl. Acad. Sci. U. S. A.* **1997,** *94* (9), 4262-4266.
187. Purtha, W. E.; Coppins, R. L.; Smalley, M. K.; Silverman, S. K., General deoxyribozyme-catalyzed synthesis of native 3‘−5‘ RNA linkages. *J. Am. Chem. Soc.* **2005,** *127* (38), 13124-13125.
188. Ponce-Salvatierra, A.; Wawrzyniak-Turek, K.; Steuerwald, U.; Höbartner, C.; Pena, V., Crystal structure of a DNA catalyst. *Nature* **2016,** *529* (7585), 231-234.
189. Chandra, M.; Sachdeva, A.; Silverman, S. K., DNA-catalyzed sequence-specific hydrolysis of DNA. *Nat. Chem. Biol.* **2009,** *5* (10), 718-720.
190. Cuenoud, B.; Szostak, J. W., A DNA metalloenzyme with DNA ligase activity. *Nature* **1995,** *375* (6532), 611-614.
191. Liu, H.; Yu, X.; Chen, Y.; Zhang, J.; Wu, B.; Zheng, L.; Haruehanroengra, P.; Wang, R.; Li, S.; Lin, J.; Li, J.; Sheng, J.; Huang, Z.; Ma, J.; Gan, J., Crystal structure of an RNA-cleaving DNAzyme. *Nat. Commun.* **2017,** *8* (1), 2006.
192. Peracchi, A., Preferential activation of the 8–17 deoxyribozyme by Ca 2+ Ions: Evidence for the identity of 8–17 with the catalytic domain of the MG5 deoxyribozyme. *J. Biol. Chem.* **2000,** *275* (16), 11693-11697.
193. Erlenbach, N.; Grünewald, C.; Krstic, B.; Heckel, A.; Prisner, T. F., "End-to-end" stacking of small dsRNA. *RNA* **2019,** *25* (2), 239-246.
194. Juliusson, H. Y.; Segler, A.-L. J.; Sigurdsson, S. T., Benzoyl-protected hydroxylamines for improved chemical synthesis of oligonucleotides containing nitroxide spin labels. *Eur. J. Org. Chem.* **2019,** *2019* (23), 3799-3805.
195. Tan, D.; Piana, S.; Dirks, R. M.; Shaw, D. E., RNA force field with accuracy comparable to state-of-the-art protein force fields. *Proc. Natl. Acad. Sci. U. S. A.* **2018,** *115* (7), E1346-E1355.
196. Gemperle, C.; Schweiger, A., Pulsed electron-nuclear double resonance methodology. *Chem. Rev.* **1991,** *91* (7), 1481-1505.
197. Meyer, A.; Dechert, S.; Dey, S.; Höbartner, C.; Bennati, M., Measurement of angstrom to nanometer molecular distances with 19F nuclear spins by EPR/ENDOR spectroscopy. *Angew. Chem. Int. Ed.* **2020,** *59* (1), 373-379.
198. Carothers, J. M.; Goler, J. A.; Kapoor, Y.; Lara, L.; Keasling, J. D., Selecting RNA aptamers for synthetic biology: investigating magnesium dependence and predicting binding affinity. *Nucleic Acids Res.* **2010,** *38* (8), 2736-2747.
199. Duchardt-Ferner, E.; Juen, M.; Bourgeois, B.; Madl, T.; Kreutz, C.; Ohlenschläger, O.; Wöhnert, J., Structure of an RNA aptamer in complex with the fluorophore tetramethylrhodamine. *Nucleic Acids Res.* **2019,** *48* (2), 949-961.
200. Schlagnitweit, J.; Steiner, E.; Karlsson, H.; Petzold, K., Efficient detection of structure and dynamics in unlabeled RNAs: The SELOPE approach. *Chem. Eur. J.* **2018,** *24* (23), 6067-6070.
201. Xu, W.; Chan, K. M.; Kool, E. T., Fluorescent nucleobases as tools for studying DNA and RNA. *Nat. Chem.* **2017,** *9* (11), 1043-1055.

202. Klöcker, N.; Weissenboeck, F. P.; Rentmeister, A., Covalent labeling of nucleic acids. *Chem. Soc. Rev.* **2020,** *49* (23), 8749-8773.
203. Ward, D. C.; Reich, E.; Stryer, L., Fluorescence studies of nucleotides and polynucleotides: I. Formycin, 2-aminopurine riboside, 2,6-diaminopurine riboside, and their derivatives. *J. Biol. Chem.* **1969,** *244* (5), 1228-1237.
204. Lobsiger, S.; Blaser, S.; Sinha, R. K.; Frey, H.-M.; Leutwyler, S., Switching on the fluorescence of 2-aminopurine by site-selective microhydration. *Nat. Chem.* **2014,** *6* (11), 989-993.
205. Lin, K.-Y.; Jones, R. J.; Matteucci, M., Tricyclic 2'-deoxycytidine analogs: Syntheses and incorporation into oligodeoxynucleotides which have enhanced binding to complementary RNA. *J. Am. Chem. Soc.* **1995,** *117* (13), 3873-3874.
206. Wilhelmsson, L. M.; Holmén, A.; Lincoln, P.; Nielsen, P. E.; Nordén, B., A highly fluorescent DNA base analogue that forms Watson−Crick base pairs with guanine. *J. Am. Chem. Soc.* **2001,** *123* (10), 2434-2435.
207. Chicas, K.; Hudson, R. H. E., Expanding the nucleic acid chemist's toolbox: Fluorescent cytidine analogs. In *Fluorescent analogues of biomolecular building blocks: Design and applications*, Wilhelmsson, M.; Tor, Y., Eds. 2016; pp 174-207.
208. Sandin, P.; Wilhelmsson, L. M.; Lincoln, P.; Powers, V. E. C.; Brown, T.; Albinsson, B., Fluorescent properties of DNA base analogue tC upon incorporation into DNA — negligible influence of neighbouring bases on fluorescence quantum yield. *Nucleic Acids Res.* **2005,** *33* (16), 5019-5025.
209. Sandin, P.; Börjesson, K.; Li, H.; Mårtensson, J.; Brown, T.; Wilhelmsson, L. M.; Albinsson, B., Characterization and use of an unprecedentedly bright and structurally non-perturbing fluorescent DNA base analogue. *Nucleic Acids Res.* **2007,** *36* (1), 157-167.
210. Samaan, G. N.; Wyllie, M. K.; Cizmic, J. M.; Needham, L.-M.; Nobis, D.; Ngo, K.; Andersen, S.; Magennis, S. W.; Lee, S. F.; Purse, B. W., Single-molecule fluorescence detection of a tricyclic nucleoside analogue. *Chem. Sci.* **2021,** *12* (7), 2623-2628.
211. Cekan, P.; Sigurdsson, S. T., Single base interrogation by a fluorescent nucleotide: each of the four DNA bases identified by fluorescence spectroscopy. *Chem. Commun.* **2008,** (29), 3393-3395.
212. Gardarsson, H.; Sigurdsson, S. T., Large flanking sequence effects in single nucleotide mismatch detection using fluorescent nucleoside Çf. *Bioorg. Med. Chem.* **2010,** *18* (16), 6121-6126.
213. Gustmann, H.; Segler, A.-L. J.; Gophane, D. B.; Reuss, A. J.; Grünewald, C.; Braun, M.; Weigand, J. E.; Sigurdsson, S. T.; Wachtveitl, J., Structure guided fluorescence labeling reveals a two-step binding mechanism of neomycin to its RNA aptamer. *Nucleic Acids Res.* **2018,** *47* (1), 15-28.
214. Weigand, J. E.; Sanchez, M.; Gunnesch, E.-B.; Zeiher, S.; Schroeder, R.; Suess, B., Screening for engineered neomycin riboswitches that control translation initiation. *RNA* **2008,** *14* (1), 89-97.
215. Munzar, J. D.; Ng, A.; Corrado, M.; Juncker, D., Complementary oligonucleotides regulate induced fit ligand binding in duplexed aptamers. *Chem. Sci.* **2017,** *8* (3), 2251-2256.
216. Munzar, J. D.; Ng, A.; Juncker, D., Comprehensive profiling of the ligand binding landscapes of duplexed aptamer families reveals widespread induced fit. *Nat.Commun.* **2018,** *9* (1), 343.

217. Zhou, H.-X., From induced fit to conformational selection: A continuum of binding mechanism controlled by the timescale of conformational transitions. *Biophys. J.* **2010,** *98* (6), L15-L17.
218. Duchardt-Ferner, E.; Weigand, J. E.; Ohlenschläger, O.; Schmidtke, S. R.; Suess, B.; Wöhnert, J., Highly modular structure and ligand binding by conformational capture in a minimalistic riboswitch. *Angew. Chem. Int. Ed.* **2010,** *49* (35), 6216-6219.
219. Duchardt-Ferner, E.; Weigand, J. E.; Ohlenschläger, O.; Schmidtke, S. R.; Suess, B.; Wöhnert, J., Highly Modular Structure and Ligand Binding by Conformational Capture in a Minimalistic Riboswitch. *Angew. Chem. Int. Ed.* **2010,** *49*, 6216-6219.
220. Bood, M.; Sarangamath, S.; Wranne, M. S.; Grøtli, M.; Wilhelmsson, L. M., Fluorescent nucleobase analogues for base-base FRET in nucleic acids: synthesis, photophysics and applications. *Beilstein J Org Chem* **2018,** *14*, 114-129.
221. Börjesson, K.; Preus, S.; El-Sagheer, A. H.; Brown, T.; Albinsson, B.; Wilhelmsson, L. M., Nucleic acid base analog FRET-pair facilitating detailed structural measurements in nucleic acid containing systems. *J. Am. Chem. Soc.* **2009,** *131* (12), 4288-4293.
222. Preus, S.; Börjesson, K.; Kilså, K.; Albinsson, B.; Wilhelmsson, L. M., Characterization of nucleobase analogue FRET acceptor tCnitro. *J. Phys. Chem. B* **2010,** *114* (2), 1050-1056.
223. Trachman, R. J.; Autour, A.; Jeng, S. C. Y.; Abdolahzadeh, A.; Andreoni, A.; Cojocaru, R.; Garipov, R.; Dolgosheina, E. V.; Knutson, J. R.; Ryckelynck, M.; Unrau, P. J.; Ferré-D'Amaré, A. R., Structure and functional reselection of the Mango-III fluorogenic RNA aptamer. *Nat. Chem. Biol.* **2019,** *15* (5), 472-479.
224. Yin, L.; Liebscher, J., Carbon−carbon coupling reactions catalyzed by heterogeneous palladium catalysts. *Chem. Rev.* **2007,** *107* (1), 133-173.
225. Gotham, V. J. B.; Hobbs, M. C.; Burgin, R.; Turton, D.; Smythe, C.; Coldham, I., Synthesis and activity of a novel inhibitor of nonsense-mediated mRNA decay. *Org. Biomol. Chem.* **2016,** *14* (5), 1559-1563.
226. Campeau, L.-C.; Parisien, M.; Jean, A.; Fagnou, K., Catalytic direct arylation with aryl chlorides, bromides, and iodides: Intramolecular studies leading to new intermolecular reactions. *J. Am. Chem. Soc.* **2006,** *128* (2), 581-590.
227. Iwaki, T.; Yasuhara, A.; Sakamoto, T., Novel synthetic strategy of carbolines via palladium-catalyzed amination and arylation reaction. *J. Chem. Soc. Perkin Trans.1* **1999,** (11), 1505-1510.
228. Mineno, M.; Sera, M.; Ueda, T.; Mizuno, M.; Yamano, M.; Mizufune, H.; Zanka, A., Rapid access to diverse α-carbolines through sequential transition metal catalyzed amination and direct C–H arylation. *Tetrahedron* **2014,** *70* (35), 5550-5557.
229. Kong, X.; Zhang, H.; Cao, C.; Zhou, S.; Pang, G.; Shi, Y., Synthesis of fluorinated carbazoles via C–H arylation catalyzed by Pd/Cu bimetal system and their antibacterial activities. *Bioorg. Med. Chem.* **2016,** *24* (6), 1376-1383.
230. Mahalingam, M.; Mohan, P. S.; Gayathri, K.; Gomathi, R.; Subhapriya, P., Photo-induced antimicrobial and DNA cleavage studies of indoloquinolines and 1,8-naphtharidine. *J. Chem. Sci.* **2013,** *125* (5), 1015-1027.
231. Zhang, Y.-M.; Razler, T.; Jackson, P. F., Synthesis of pyrimido[4,5-b]indoles and benzo[4,5]furo[2,3-d]pyrimidines via palladium-catalyzed intramolecular arylation. *Tetrahedron Lett.* **2002,** *43* (46), 8235-8239.
232. Gatti, R. G. P.; Bäckvall, J.-E.; Chiong, H. A., Bis(triphenylphosphine)palladium(II) acetate. In *Encyclopedia of reagents for organic synthesis*, John Wiley & Sons, Ltd: 2001.

233. Bogányi, B.; Kámán, J., A concise synthesis of indoloquinoline skeletons applying two consecutive Pd-catalyzed reactions. *Tetrahedron* **2013,** *69* (45), 9512-9519.
234. Hostyn, S.; Van Baelen, G.; Lemière, G. L. F.; Maes, B. U. W., Synthesis of α-carbolines starting from 2,3-dichloropyridines and substituted anilines. *Adv. Synth. Catal.* **2008,** *350* (16), 2653-2660.
235. Budén, M. E.; Vaillard, V. A.; Martin, S. E.; Rossi, R. A., Synthesis of carbazoles by intramolecular arylation of diarylamide anions. *J. Org. Chem.* **2009,** *74* (12), 4490-4498.
236. Laha, J. K.; Barolo, S. M.; Rossi, R. A.; Cuny, G. D., Synthesis of carbolines by photostimulated cyclization of anilinohalopyridines. *J. Org. Chem.* **2011,** *76* (15), 6421-6425.
237. Matteucci, M. D.; von Krosigk, U., Hybridization properties of oligonucleotides bearing a tricyclic 2′-deoxycytidine analog based on a carbazole ring system. *Tetrahedron Lett.* **1996,** *37* (29), 5057-5060.
238. Stille, J. K., The palladium-catalyzed cross-coupling reactions of organotin reagents with organic electrophiles. *Angew. Chem. Int. Ed.* **1986,** *25* (6), 508-524.
239. Suchý, M.; Hudson, R. H. E., Pyrimidine-fused heterocyclic frameworks based on an N4-arylcytosine scaffold: Synthesis, characterization, and PNA oligomerization of the fluorescent cytosine analogue 5,6-benzopC. *J. Org. Chem.* **2014,** *79* (8), 3336-3347.
240. Fairfull-Smith, K. E.; Brackmann, F.; Bottle, S. E., The synthesis of novel isoindoline nitroxides bearing water-solubilising functionality. *Eur. J. Org. Chem.* **2009,** *2009* (12), 1902-1915.
241. Ci, Z.; Yu, X.; Bao, M.; Wang, C.; Ma, T., Influence of the benzo[d]thiazole-derived π-bridges on the optical and photovoltaic performance of D–π–A dyes. *Dyes and Pigm.* **2013,** *96* (3), 619-625.
242. Albers, P.; Pietsch, J.; Parker, S. F., Poisoning and deactivation of palladium catalysts. *J. Mol. Catal. A: Chem.* **2001,** *173* (1), 275-286.
243. Keddie, D. J.; Johnson, T. E.; Arnold, D. P.; Bottle, S. E., Synthesis of profluorescent isoindoline nitroxides via palladium-catalysed Heck alkenylation. *Org. Biomol. Chem.* **2005,** *3* (14), 2593-2598.
244. Marczyk, J.; Waluk, J.; Fetzer, J. C., Determination of structure of nonplanar polycyclic aromatic hydrocarbons by polarized spectroscopy. *Polycyclic Aromat. Compd.* **1996,** *9* (1-4), 283-290.
245. Pascal, R. A., Twisted acenes. *Chem. Rev.* **2006,** *106* (12), 4809-4819.
246. Wypijewska del Nogal, A.; Füchtbauer, A. F.; Bood, M.; Nilsson, J. R.; Wranne, M. S.; Sarangamath, S.; Pfeiffer, P.; Rajan, V. S.; El-Sagheer, A. H.; Dahlén, A.; Brown, T.; Grøtli, M.; Wilhelmsson, L. M., Getting DNA and RNA out of the dark with 2CNqA: a bright adenine analogue and interbase FRET donor. *Nucleic Acids Res.* **2020,** *48* (14), 7640–7652.
247. Foller Larsen, A.; Dumat, B.; Wranne, M. S.; Lawson, C. P.; Preus, S.; Bood, M.; Gradén, H.; Marcus Wilhelmsson, L.; Grøtli, M., Development of bright fluorescent quadracyclic adenine analogues: TDDFT-calculation supported rational design. *Sci. Rep.* **2015,** *5* (1), 12653.

Publications

I. Gustmann H., Segler A. J., Gophane D. B., Reuss A. J., Grünewald C., Braun M., Weigand J. E., Sigurdsson S. T. and Wachtveitl J., Structure guided fluorescence labeling reveals a two-step binding mechanism of neomycin to its RNA aptamer. *Nucleic Acids Res*., **2019**, *47*, 15-28.

II. Juliusson H. Y.,† Segler A. J.† and Sigurdsson S. T., Benzoyl-protected hydroxylamines for improved chemical synthesis of oligonucleotides containing nitroxide spin labels. *Eur. J. Org. Chem.*, **2019**, *2019*, 3799-3805. †These authors contributed equally.

III. Segler A. J. and Sigurdsson S. T., A carbazole-derived nitroxide that is an analogue of cytidine – a rigid spin label for DNA and RNA. **2021**, https://doi.org/10.1021/acs.joc.1c01176.

Article I

Published online 20 November 2018

Nucleic Acids Research, 2019, Vol. 47, No. 1 **15–28**
doi: 10.1093/nar/gky1110

Structure guided fluorescence labeling reveals a two-step binding mechanism of neomycin to its RNA aptamer

Henrik Gustmann [1], Anna-Lena J. Segler[2], Dnyaneshwar B. Gophane[2], Andreas J. Reuss[1], Christian Grünewald[3], Markus Braun[1], Julia E. Weigand [4], Snorri Th. Sigurdsson [2,*] and Josef Wachtveitl [1,*]

[1]Institute of Physical and Theoretical Chemistry, Goethe-University Frankfurt am Main, Max-von-Laue-Strasse 7, 60438 Frankfurt, Germany, [2]Science Institute, University of Iceland, Dunhaga 3, 107 Reykjavik, Iceland, [3]Institute for Organic Chemistry and Chemical Biology, Goethe-University Frankfurt am Main, Max-von-Laue-Strasse 7, 60438 Frankfurt, Germany and [4]Department of Biology, Technical University Darmstadt, Schnittspahnstraße 10, 64287 Darmstadt, Germany

Received July 26, 2018; Revised October 1, 2018; Editorial Decision October 20, 2018; Accepted October 22, 2018

ABSTRACT

The ability of the cytidine analog $Ç_m^f$ to act as a position specific reporter of RNA-dynamics was spectroscopically evaluated. $Ç_m^f$-labeled single- and double-stranded RNAs differ in their fluorescence lifetimes, quantum yields and anisotropies. These observables were also influenced by the nucleobases flanking $Ç_m^f$. This conformation and position specificity allowed to investigate the binding dynamics and mechanism of neomycin to its aptamer N1 by independently incorporating $Ç_m^f$ at four different positions within the aptamer. Remarkably fast binding kinetics of neomycin binding was observed with stopped-flow measurements, which could be satisfactorily explained with a two-step binding. Conformational selection was identified as the dominant mechanism.

INTRODUCTION

RNA is a ubiquitous biopolymer and essential to life. After the discovery of ribozymes in the laboratories of Altman (1) and Cech (2), the 'RNA world' hypothesis was put forth (3,4), in which RNA is the central biopolymer during the evolution of life, that both carries genetic information and catalyzes reactions. Since this hypothesis was proposed, many more roles of RNA, such as regulation of gene expression have been discovered (5,6). In particular, for gene regulation mediated by riboswitches (7–10), RNA motifs found in the 5′-untranslated regions of bacterial mRNAs (11) rely on binding to small molecules that induce conformational transitions in the RNA. The ligands bind to the aptamer region of the riboswitch and induce secondary structural changes (12,13) that determine the output of the expression platform (12,14). Central for the overall function is thus the aptamer, which binds the ligand with an extraordinary high affinity and specificity (15). It is therefore of great interest to study such binding motifs and to obtain a molecular picture of the mechanisms with which RNA binds its cognate ligand.

Prior to the discovery of riboswitches, RNA aptamers for a wide range of ligands have been found with the help of *in vitro* selection, using the technique of systematic evolution of ligands by exponential enrichment (SELEX) (16–18). One example is the 27 nucleotide **N1** neomycin-sensing aptamer, one of the smallest known aptamers (Figure 1A and C) (13) that binds with high affinity ($K_d = 10 \pm 2.0$ nM) to the aminoglycoside antibiotic neomycin (Figure 1B) (19). The aptamer consists of a closing stem as well as an internal loop and a terminal loop that are connected by a short helical stem region. Nuclear magnetic resonance (NMR) studies have revealed that the binding pocket of the aptamer is formed by the internal and the terminal loop, in which the two helical stems form a continuous A-form helix with stacking between G5:C23 and G9:C22 (Figure 1A and C) (19,20). The A-form helix is intersected by a bulging internal loop (C6, U7, U8) that together form the binding pocket with A17 of the terminal loop (19). NMR and electron paramagnetic resonance (EPR) spectroscopic studies have shown that the binding pocket is preformed and that neomycin is bound to the aptamer via a conformational selection mechanism (19–21). When bound, ring I and ring II of neomycin are clamped between G5:C23 and U13:U18 of the aptamer (Figure 1) while forming hydrogen bonds to G9

*To whom correspondence should be addressed. Tel: +49 069 798 29351; Fax: +49 069 798 29709; Email: wveitl@theochem.uni-frankfurt.de
Correspondence may also be addressed to Snorri Th. Sigurdsson. Tel: +354 525 4801; Email: snorrisi@hi.is

and U10, in addition to electrostatic interactions to G9 and A17 (19).

Structural information is indispensable for understanding RNA–ligand recognition. However, the mechanistic picture is not complete without information on the dynamics of the aptamer. Optical spectroscopy is a valuable technique to obtain information about motion on all time scales relevant for molecular dynamics, from fs to minutes. Although UV/vis spectroscopy can be useful for this purpose, the absorption changes upon ligand binding to RNA are typically rather unspecific. In contrast, fluorescence spectroscopic values like quantum yield, lifetime or anisotropy allow deeper insights of micro-environment changes upon ligand binding at a defined position within the RNA. However, fluorescence studies require reporter labels since neither RNA nor most ligands are fluorescent (22). Fluorescent labels have to meet several requirements, depending on the application. In particular, it should be possible to incorporate them site-specifically. In addition, they should be non-perturbing, highly fluorescent and should not absorb in the same spectral region as the RNA or the ligands. For RNA and DNA, 2-aminopurine is perhaps the most widely used fluorescent label (23–26). Furthermore, several other fluorescent base analogs have been developed and characterized in the last years (26–40). For example there are many pyrene- (28–32), phenothiazine- (34), isothiazole- (33) and phenylpyrrole-derivatives (36) of nucleic acid bases.

A very valuable feature of spectroscopic labels is multifunctionality, where the same label can be used for different spectroscopic methods that give complementary information. One paragon is **Ç** (41), a cytidine analog that is successfully used as rigid spin label for DNA. Pulsed electron-electron double resonance (PELDOR, sometimes called DEER) experiments can determine precise distances between two spin labels, as well as information about their relative orientation (41–50). Reduction of the nitroxide in **Ç** with a mild reducing agent yields a strongly fluorescent nucleoside (41). Thus, the nitroxide acts as an efficient fluorescence quencher (51–53). The fluorescent and isosteric $\mathbf{Ç^f}$ is the direct synthetic precursor of **Ç**. Therefore, it can be used as a rigid, non-perturbing fluorescent probe for steady-state and time-resolved fluorescence studies of nucleic acids (41,43,46,54–56). The structural similarity of both labels makes the results of EPR and fluorescence studies highly comparable (42,43,46,47,50,54–56). More recently, we have prepared the analogous nucleoside label $\mathbf{Ç_m}$ (45), containing a 2′-methoxy group (Figure 2) and established as a label for EPR studies of RNA (45,57). However, $\mathbf{Ç_m^f}$ has not yet been used as a fluorescent label in RNA. Here, we present a detailed characterization of $\mathbf{Ç_m^f}$ as a fluorescent label for both steady-state and time-resolved fluorescence measurements in RNA single-strands and duplexes. In the discussion, we compare our results on $\mathbf{Ç_m^f}$ with the photophysical properties of tC°. tC° is a recently well characterized fluorescent cytosine analog by the Wilhelmsson group which shows high structural as well as photophysical similarity to $\mathbf{Ç_m^f}$ (58). Furthermore, we have incorporated $\mathbf{Ç_m^f}$ into the neomycin aptamer and investigated the change in fluorescence upon ligand binding, including fast-binding kinetics using stopped-flow measurements. Our results can be explained by a two-step binding mechanism of neomycin to its aptamer.

MATERIALS AND METHODS

Preparation of oligonucleotides

The benchmark non-selfcomplementary oligoribonucleotide (29) that was used for characterization of $\mathbf{Ç_m^f}$ contained the $\mathbf{Ç_m^f}$ label in the center of a 15-mer (5′-UAC-GCA-N$\mathbf{Ç_m^f}$N-ACG-CAU-3′). An unlabeled 15-mer complementary to this sequence (3′-AUG-CGU-N′GN′-UGC-GUA-5′) was annealed to form the corresponding duplex. To study flanking sequence effects on the $\mathbf{Ç_m^f}$ signal, the bases immediately flanking the label (N in the strand and N′ in the counter-strand) were permuted such that for each oligomer the $\mathbf{Ç_m^f}$ was flanked on both sides with either A, C, G or U, to yield four duplexes (Supplementary Table S1). The corresponding unlabeled RNA duplexes were also prepared for comparison in the thermal denaturation experiments (see below).

The neomycin aptamer (5′-GGC-UGC-UUG-UCC-UUU-AAU-GGU-CCA-GUC-3′) was singly labeled with $\mathbf{Ç_m^f}$ at the positions 6, 8, 15 and 22 (Table 1).

The synthesis of the $\mathbf{Ç_m^f}$-labeled benchmark oligoribonucleotides as well as the synthesis of the $\mathbf{Ç_m^f}$-labeled neomycin aptamers are described in the Supplementary Data.

Sample preparation

The RNA model sequences were dissolved in 20 mM sodium cacodylate buffer with pH 7.4. This buffer was chosen, because the pH-value of sodium cacodylate buffer is not temperature dependent, which is essential for the melting studies (59). All experiments were carried out with a 7 μM RNA model strand solution. The neomycin aptamer samples were dissolved in 20 mM sodium cacodylate and 100 mM NaCl buffer at pH 7.4. All steady-state experiments of the aptamer samples were carried out with a 1 μM aptamer (without neomycin; **−Neo**) solution. Neomycin was added in excess (4 μM neomycin; **+ Neo**). Before each series of measurements, the samples (model strands and aptamers) were annealed. The samples were heated up to 90°C for 2 min and left to cool down to room temperature.

Steady-state spectroscopy

Steady-state absorption spectra were recorded in 10 × 4 mm UV-grade quartz cuvettes (29-F/Q/10, Starna GmbH, Pfungstadt, Germany) on a JASCO V-650 spectrometer (JASCO Germany GmbH, Groß-Umstadt, Germany). The spectra were offset corrected and normalized. Emission spectra were recorded in 10 × 4 mm UV-grade quartz cuvettes (29-F/Q/10, Starna GmbH) with a JASCO FP 8500 fluorescence spectrometer. Prior to normalization, the spectra were corrected for offset, absorption and reabsorption artifacts as well as the spectral characteristics of the experimental equipment. The JASCO FP 8500 spectrometer was equipped with a 100 mm integrating sphere (ILF-835, JASCO) and used for absolute fluorescence quantum yield

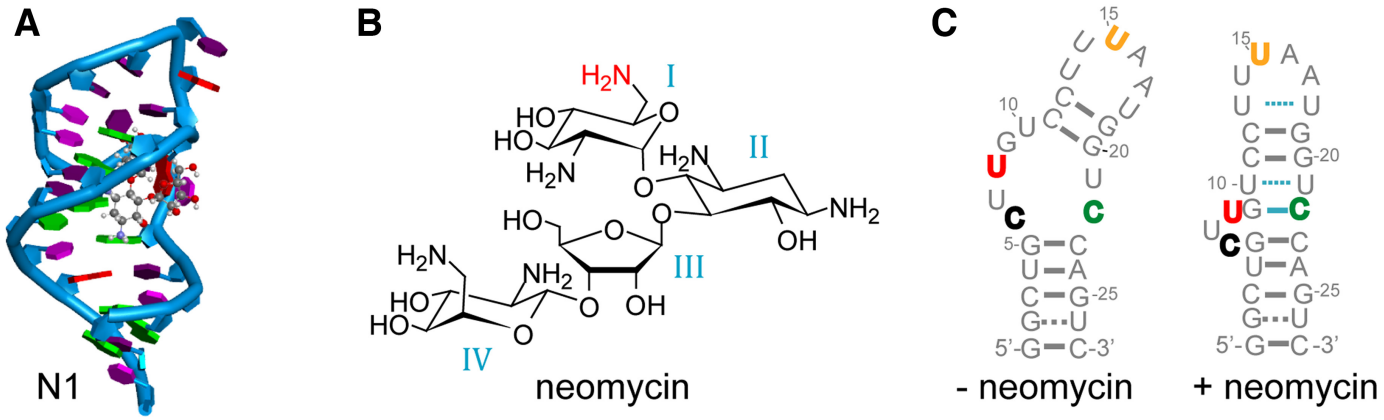

Figure 1. (**A**) NMR structure (NDB/PDB-ID: 2KXM) of the **N1** neomycin aptamer with bound ligand (here ribostamycin) (20). (**B**) Structure of neomycin B. The NH_2-group marked in red, protonated at physiological pH, contributes to the H-bonding pattern of the neomycin aptamer (19). (**C**) Predicted structures of the ligand unbound (left) and bound (right) state of the neomycin aptamer (19,20). Bold-colored letters mark the different **Ç$_m$^{f}** labeling positions.

Table 1. Sequences of the **Ç$_m$^{f}**-labeled neomycin aptamer samples

Sample	Sequences
Ç$_m$^{f}6	5′-GGC-UG**Ç$_m$^{f}**-UUG-UCC-UUU-AAU-GGU-CCA-GUC-3′
Ç$_m$^{f}8	5′-GGC-UGC-U**Ç$_m$^{f}**G-UCC-UUU-AAU-GGU-CCA-GUC-3′
Ç$_m$^{f}15	5′-GGC-UGC-UUG-UCC-UU**Ç$_m$^{f}**-AAU-GGU-CCA-GUC-3′
Ç$_m$^{f}22	5′-GGC-UGC-UUG-UCC-UUU-AAU-GGU-**Ç$_m$^{f}**CA-GUC-3′

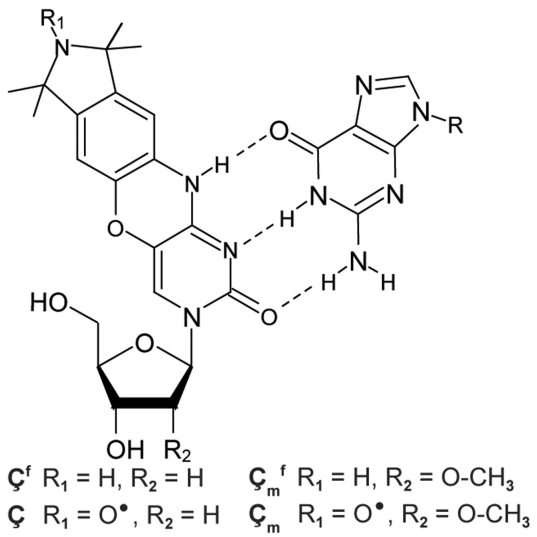

Figure 2. **Ç**, **Ç^f**, **Ç$_m$** and **Ç$_m$^{f}** base paired with guanine.

(QY) determinations. For anisotropy studies, the spectrometer was equipped additionally with two automatized polarization filters as polarizer and analyzer (FDP-837, JASCO).

Thermal denaturation experiments

For the melting analyses, the absorption changes of the RNA band at 260 nm was recorded from 20°C to 90°C. The change of the **Ç$_m$^{f}** emission around 460 nm upon excitation of the label at 360 nm, was also recorded in the same temperature range. The full absorption as well as the emission spectra were recorded at 5°C intervals (Supplementary Figures S6 and 8). Thus, it was possible to detect changes of the spectral position and shape of the observed signal bands. To determine the melting temperatures and the thermodynamic parameters, the signal changes at single wavelengths were recorded every 0.5°C. The temperature was changed between the single measuring points with a rate of 1°C/min. The heating and cooling curves were averaged to compensate for possible hysteresis effects. For the determination of the melting temperatures and the thermodynamic parameters, the method described by Mergny and Lacroix was used (Supplementary Figure S7) (59). A slope correction that accounts for the increase of collisional quenching with temperature was performed for the emission data recorded around 460 nm (cf. Supplementary Figure S9 and Table S4), but this procedure did not affect the determined melting point significantly.

Isothermal titration calorimetry

For isothermal titration calorimetry (ITC) experiments, an iTC200 microcalorimeter (MicroCal, GE Healthcare, Buckinghamshire, UK) was used. The sample cell of the iTC200 was filled with the RNA sample (10 μM RNA, 20 mM sodium cacodylate, 200 mM NaCl, pH 7.4). The injector syringe was filled with a neomycin solution (75 μM neomycin, 20 mM sodium cacodylate, 200 mM NaCl, pH 7.4). After equilibrating the system at 20°C for 10 min, the measurements were started with an initial 120 s delay and a 0.2 μl injection. Subsequently 20 injections of 2.0 μl at a 180 s interval were made. The sample cell was stirred with a speed of 750 rpm (60). The software NITPIC was used to integrate the injection peaks to yield the associated heat for

each injection (61,62), the experimental binding isotherm was subsequently plotted and the curve fit with a one-site binding model using the software SEDPHAT (63). This fit made it possible to determine the dissociation constant (K_D).

Time-resolved fluorescence

The fluorescence lifetimes were measured with a partially home-built time-correlated single photon counting (TCSPC) setup as previously described (40). For excitation, a mode-locked titanium-doped sapphire (Ti:Sa) laser (Tsunami 3941-X3BB, Spectra-Physics, Darmstadt, Germany) was pumped by a 10 W continuous wave diode pumped solid state laser (Millennia eV, Spectra-Physics, 532 nm). The Ti:Sa laser provided pulses of 775 nm central wavelength with a repetition rate of 80 MHz. With the help of an acousto-optic modulator, the repetition rate was reduced to 8 MHz and the excitation wavelength of 388 nm was obtained by SHG in a BBO crystal (frequency doubler and pulse selector, Model 3980, Spectra-Physics). Excitation pulses of about 0.1 nJ at 388 nm were applied to the sample. The sample was prepared in a 10 × 4 mm quartz cuvette (29-F/Q/10, Starna) with a fixed temperature of 20°C. Emission filters (GG395, GG400, Schott AG, Mainz, Germany) suppressed excitation stray light. The instrument response function (IRF, FWHM 200 ps) was obtained without emission filters using a TiO_2 suspension as scattering sample. For single-photon detection, a photomultiplier tube (PMT, PMA-C 182-M, PicoQuant, Berlin, Germany) and a TimeHarp 260 PICO Single PCIe card (PicoQuant) were used. Multi-exponential fitting was carried out with FluoFit Pro 4.6 (PicoQuant) (64).

Fluorescence stopped-flow

Mixing experiments were performed with a SFM-20 stopped-flow setup (65) (Bio-Logic Science Instruments, Seyssinet-Pariset, France) using a Berger ball mixer (66) and cuvette (FC08) with an approximate volume of 20 μl and a light path of 0.8 mm. The mixing was controlled and triggered by a Microprocessor unit (MPS-60, Bio-Logic), which was driven by the Bio-Kine 32 software (Version 4.42, Bio-Logic Science Instruments). For each mixing experiment, two sample solutions (volume: each 33 μl) were injected in the Berger ball mixer via two syringes (Hamilton 1010C, Hamilton Company, Reno, USA) for 9.5 ms, resulting in a flow rate of 6.95 ml/s. The injection was stopped by a hard-stop valve. For excitation and detection, the stopped-flow setup was fiber-coupled (OBF-832, JASCO) with a JASCO FP 8500 fluorescence spectrometer. The sample was excited with 360 nm light and the resulting fluorescence at 460 nm was measured under an angle of 90° with the PMT-detector of the FP 8500. With the help of an A/D-adapter (BNC-2110, National Instruments, Austin, USA) the PMT-signal was transferred to a transient recorder board (PCI-6052E, National Instruments). Data acquisition was controlled by the Bio-Kine 32 software. The transients were digitized with 6000 equidistant points of 10 μs.

For ligand-concentration dependence studies, a fluorescent-labeled aptamer solution (**$Ç_m^f$6**: 2.7 μM, **$Ç_m^f$8**: 4 μM) was mixed with ligand solutions of 8 different concentrations (0, 2, 4, 8, 16, 24, 32, 40 μM). For each concentration, at least 20 single mixing transients were averaged. Prior to fitting of all transients, the offset was corrected (subtraction of the fluorescence signal of unbound labeled aptamer) and the start point of the dynamic analysis was set to the end of the mixing, which is given by the hard stop. The corrected set of transients was processed using the Dynafit software (Biokin Ltd., Watertown, USA) to test different reaction models and to derive the reaction constants for the best model (67).

RESULTS

Photophysical properties of $Ç_m^f$ in single- and double-stranded RNA

Steady-state spectra and quantum yields. Steady-state fluorescence measurements of the singly **$Ç_m^f$**-labeled double-strands (ds) and single-strands (ss) are shown in Figure 3 (Supplementary Figure S8). Both the four spectra of the single- and the double strands are similar to each other, but the two sets of double- and single-strand spectra show pronounced spectral differences with respect to each other. Specifically, the emission spectra of the duplexes show a vibrational fine structure with maxima at 420, 448, 480 and 520 nm, which has already been described for **$Ç^f$** in DNA and was used for mismatch detection (54). The fluorescence spectrum of ds-C**$Ç_m^f$**C is slightly blue-shifted in comparison to the other spectra of the double-strands. Thus, double- and single-strands can be spectrally distinguished based on the fine structure of the spectra of the double-strands.

As might be expected, the double- and single-stranded RNAs differ significantly in their fluorescence quantum yields (QY, Table 2). While the ds RNAs show an average quantum yield (QY_{av}) of 24%, the single-strands show a QY_{av} of 44%. In comparison to the fluorophore itself (QY = 38%) (68), QY decreases upon incorporation into double-stranded RNA but increases upon incorporation into single-stranded RNA. The QYs of the double-stranded RNAs are affected by the flanking nucleobases: the QYs are slightly higher for the purines.

Fluorescence anisotropy. The steady-state fluorescence anisotropy (r_f) of the **$Ç_m^f$**-labeled double- and single-stranded RNA is significantly higher than the anisotropy of the fluorophore itself in solution. This confirms that the motion of the label is restricted after incorporation into the RNA. Additionally, the anisotropy of the double-stranded RNA is systematically higher (by a factor 1.4) than the anisotropy of the single-strands (Table 2), which is consistent with a greater order of the more rigid duplex. The anisotropy values for the samples with purine bases adjacent to the fluorophore site are slightly lower than for the samples with adjacent pyrimidine bases.

Thermal denaturation. To determine the effect of **$Ç_m^f$** on duplex stability, which would indicate possible structural perturbations, thermal denaturation experiments were performed on both labeled and unlabeled RNA duplexes, by

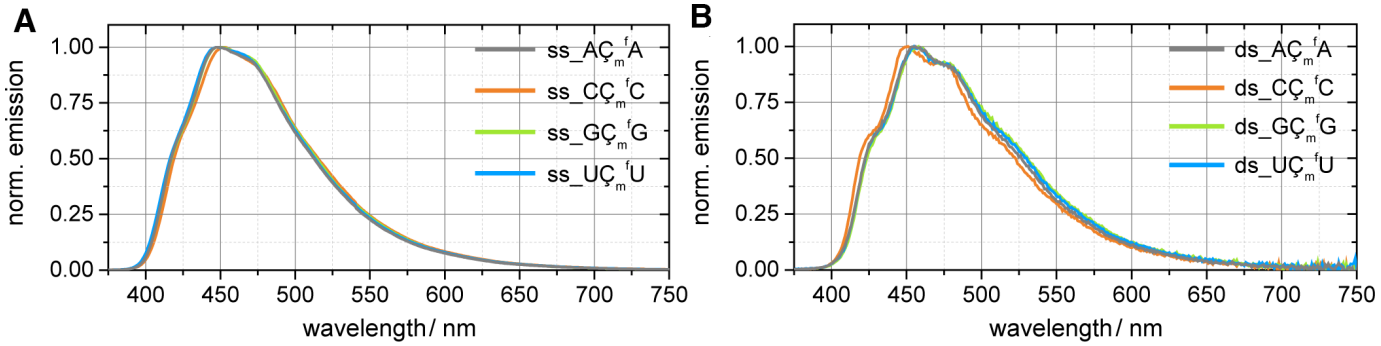

Figure 3. Normalized emission spectra of **Çm^f**-labeled (**A**) single-stranded and (**B**) double-stranded RNA at 20°C.

Table 2. Fluorescence lifetime (τ), quantum yield (QY) and steady-state anisotropy (r_f) of Çm^f labeled single- (ss) and double-stranded (ds) RNA at 20°C

	Sample	τ_{pop}/ns	τ_1/ns	τ_2/ns	χ^2	τ_{av}/ns	QY/%	r_f
	Çm^f	0.3	4.1 (96%)	1.4 (4%)	1.1	4.1	38	0.04
ds	**AÇm^{f}A**	1.5	4.6 (89%)	7.6 (11%)	1.2	5.3	25	0.12
	CÇm^{f}C	1.7	4.1 (96%)	6.8 (4%)	1.1	4.5	22	0.14
	GÇm^{f}G	2.3	4.7 (97%)	7.5 (3%)	1.3	5.2	26	0.14
	UÇm^{f}U	1.6	4.2 (97%)	7.4 (3%)	1.1	4.6	22	0.17
ss	**AÇm^{f}A**	1.5	6.4 (71%)	8.5 (29%)	1.1	7.5	54	0.08
	CÇm^{f}C	1.5	5.1 (77%)	8.2 (23%)	1.1	6.4	39	0.11
	GÇm^{f}G	1.6	5.6 (69%)	8.2 (31%)	1.1	7	42	0.09
	UÇm^{f}U	1.9	3.9 (36%)	6.8 (64%)	1.2	6.5	41	0.09

τ_{pop} = lifetime with a negative amplitude, representing the population of a fluorescent state. τ_n = lifetime with a positive amplitude, representing the depopulation of a fluorescent state. τ_{av} = average fluorescence lifetime. X^2 = reduced chi-square value, as measure of the quality of the fit (cf. Supplementary Data).

monitoring both steady-state RNA absorption (at 260 nm) and **Çm^f** fluorescence (Table 3). The melting temperatures recorded by the two methods (T_{m_abs} and T_{m_em}) are very similar, which indicates a homogeneous melting behavior of the labeled RNA duplex. The difference of only −1 to 3°C in T_m between unlabeled and labeled RNA duplexes provides evidence for a negligible effect of the label on duplex stability. The melting temperatures of C**Çm^f**C and G**Çm^f**G were higher than the melting temperatures of A**Çm^f**A and U**Çm^f**U, presumably because of the higher CG-content of the former. Table 3 also shows the free enthalpies (ΔG) that were determined from the melting data obtained from the 260 nm absorption.

The fluorescence signal of the single-stranded RNA decreased with increasing temperature (Figure 4A). This may be due to enhanced quenching through an increased flexibility of the strands, which in turn could lead to higher collision rates due to less steric shielding. For ss_A**Çm^f**A, ss_C**Çm^f**C and ss_U**Çm^f**U this led to a strong quenching, while ss_G**Çm^f**G was only slightly affected. The latter effect may be due to stacking effects around the label. Interestingly, in case of pyrimidines flanking the label (ss_U**Çm^f**U and ss_C**Çm^f**C), a slight emission increase between 20°C and 50°C is notable. This might be due to conformational changes, which increase the solvent shielding of **Çm^f** and as a consequence the QY in this temperature region.

The fluorescence-monitored melting curves of the RNA duplexes show a very different behavior (Figure 4B). Initially, the emission decreased with increasing temperature. Subsequently, a steep and strong increase of the emission was observed due to the melting of the RNA duplexes and thereby an increase of unpaired RNA strands. After melting of the RNA duplexes, the fluorescence intensity decreased, most likely due to collisional quenching.

The fine structure of the emission spectra of the duplexes disappeared upon heating (Supplementary Figure S8). This effect can be used for further analysis of the melting process: The emission spectrum of a sample at 20°C should represent a nearly 100% double-stranded RNA, while in a first approximation the emission spectrum with the highest QY should stem from a nearly 100% single-stranded RNA. Furthermore, we assume the decay of the fine structure to be linear with temperature. Under these assumptions, it is possible to reconstruct all normalized emission spectra based on a certain ratio of these two spectral extremes (Figure 5). A MATLAB script (Supplementary Data) was used to perform a nonlinear least-squares fitting of the spectra. This method, which we refer to as a spectrally resolved melting analysis, yielded a decrease of the double stranded RNA content as a function of increasing temperature (Figure 5B). Thus, the temperature which shows apparently 50% double stranded RNA can be interpreted as the melting temperature (T_{m_sr}), which is 14–22°C lower than the melting temperatures determined by the conventional melting analyses. One plausible explanation for this deviation is that T_{m_sr} reflects the breaking of the Watson–Crick hydrogen-bonds of **Çm^f** and thus the very first step of the (local) melting process. This is followed by the separation of the two complemen-

Table 3. Melting temperatures and thermodynamic parameters of the unlabeled and labeled RNAs

	Unlabeled		Ç$_m$^{f} -labeled					
Sample	T_{m_abs}/°C	-ΔG_{abs} (37°C)/ kcal/mol	T_{m_abs}/°C	T_{m_em}/°C	T_{m_sr}/°C	-ΔG_{abs} (37°C)/ kcal/mol	ΔT_{m_abs}/°C	$\Delta\Delta G_{abs}$ (37°C)/kcal/mol
AÇ$_m$^{f}A	70	18	67	67	45	13	3	−5
CÇ$_m$^{f}C	81	20	82	81	63	15	−1	−5
GÇ$_m$^{f}G	78	18	76	76	56	14	2	−4
UÇ$_m$^{f}U	70	17	72	70	56	15	−2	−2

T_{m_abs} = absorption monitored melting temperature; T_{m_em} = emission monitored melting temperature; T_{m_sr} = spectrally resolved melting analysis; $\Delta T_{m\_abs} = T_{m\_abs}$ (unlabeled) – T_{m_abs} (labeled); ΔG_{abs} = determined via melting analysis; $\Delta\Delta G_{abs} = \Delta G_{abs}$ (unlabeled) – ΔG_{abs} (labeled).

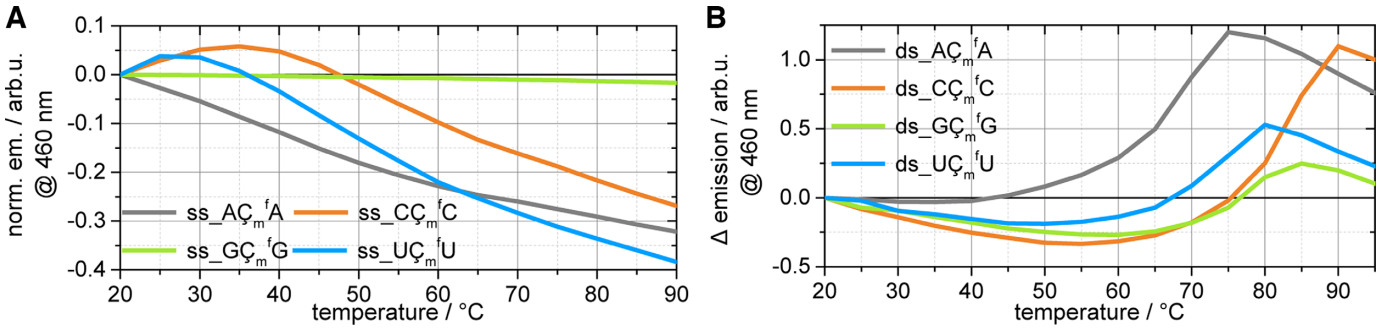

Figure 4. Fluorescence monitored melting curves of **Ç$_m$^{f}**-labeled (**A**) single-strands and (**B**) double-strands at 460 nm. All curves were set to zero at 20°C.

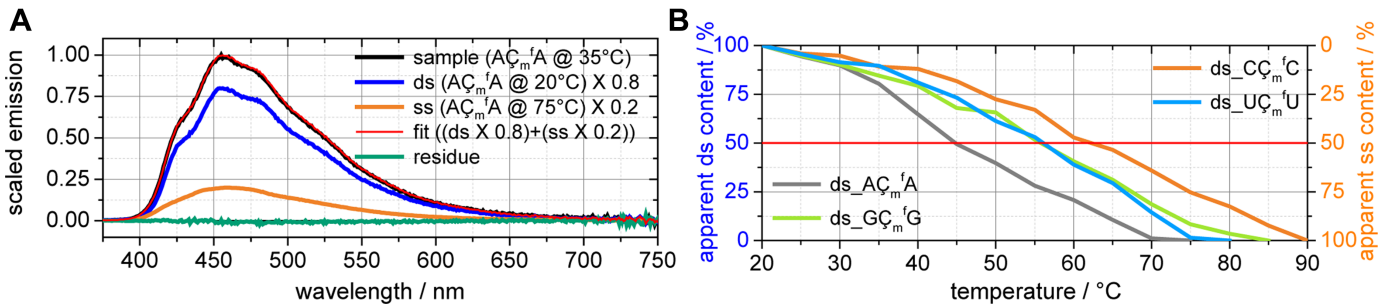

Figure 5. (**A**) Spectrally resolved melting analysis of the emission spectra of ds_AÇ$_m$^{f}A at 35°C. (**B**) Temperature dependence of the double-to-single-stranded-content of the four labeled double-stranded samples, determined by spectrally resolved melting analysis.

tary strands at a higher temperature (T_{m_abs}, T_{m_em}). Thus, the spectrally resolved melting analysis can be used for local probing of the melting process.

Fluorescence lifetime. The fluorescence lifetime (Figure 6) of **Ç$_m$^{f}** increased upon incorporation into either RNA single-strands or duplexes. Furthermore, the fluorescence lifetime of the single-strands was noticeably longer than that of the duplexes. It is also worth noting that the fluorescence lifetimes of the RNA where the label was flanked by pyrimidines (C**Ç$_m$^{f}**C and U**Ç$_m$^{f}**U) were shorter than for flanking purines (A**Ç$_m$^{f}**A and G**Ç$_m$^{f}**G) (Table 2). Specifically, the order observed was C**Ç$_m$^{f}**C < U**Ç$_m$^{f}**U < G**Ç$_m$^{f}**G < A**Ç$_m$^{f}**A. Hence, it is possible to use fluorescence lifetimes to distinguish between **Ç$_m$^{f}**-labeled single and double-stranded RNA and between neighboring purine and pyrimidine bases within this set of samples.

To describe the fluorescence decays satisfactorily, at least three exponential decay components were needed (Table 2). As we have previously shown, the fluorescence decay of **Ç$_m$^{f}** in an aqueous solution can be described by a short component of 0.3 ns (τ_{pop}, negative amplitude), which represents the population of the emitting state; the actual decay was fitted by two longer lifetimes (τ_1 = 4.1 ns and τ_2 = 1.4 ns) (68). As alluded to above, all the decay components of **Ç$_m$^{f}** in RNA are significantly prolonged, whereby the single-stranded RNA decay components are longer than those for double-stranded RNA by a factor of ca. 1.4. Notably, the amplitude of τ_2 is stronger for the single-strands than for the double-strands. With the help of temperature-dependent TCSPC measurements (Supplementary Figures S11–13 and Tables S8–15), it was possible to assign τ_2 to the amount of single-strands in the sample (Table 2).

Ç$_m$^{f}-labeled neomycin aptamers

Selection of labeling positions. For the fluorescently-labeled neomycin aptamer, four labeling positions were selected based on the NMR structure and the proposed binding model (19, 20): the cytidines or uridines at positions C6,

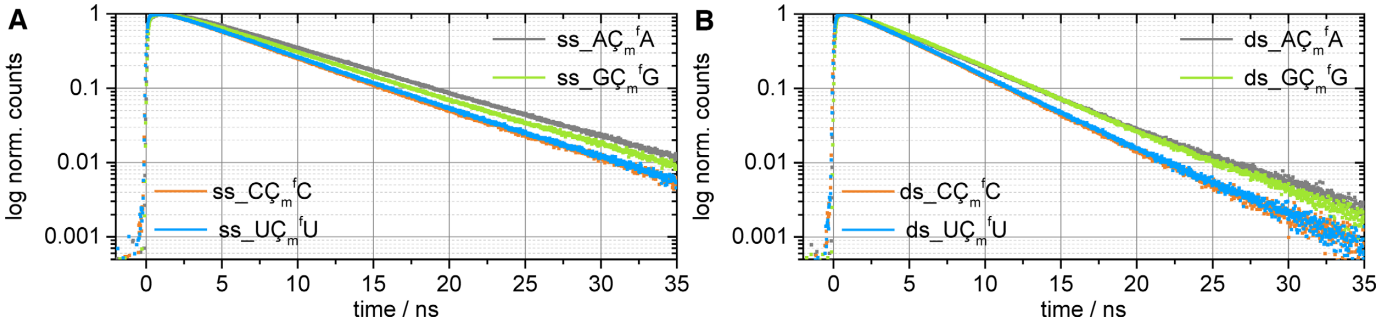

Figure 6. Normalized fluorescence decays of **Çm^f** labeled (**A**) single- and (**B**) double stranded RNAs.

U8, U15 and C22 were exchanged with **Çm^f** (Figures 1C and 7). Positions C6, U8 and U15 are located on both sides of the binding pocket and were chosen to avoid interference of the label with the binding event. Previous mutational analyses have shown that nucleotides at positions 6, 8 and 15 can be replaced by any nucleotide without loss of regulatory activity *in vivo* (60,69).

U15 and C22 should serve as reference or negative control samples: For **Çm^f** at position C22 we expected major interference (steric hindrance) between the label and the ligand. For **Çm^f** at the remote position U15, on the other hand, we did not expect any pronounced sensitivity for ligand binding or RNA conformational changes. All the RNAs were synthesized via solid phase chemical synthesis (See Supplementary Data).

ITC was performed to test the binding affinity of the **Çm^f**-labeled aptamers. As can be seen in Table 4, the K_D values of aptamers **Çm^{f}6**, **Çm^{f}8** and **Çm^{f}15** are 50- to 80-fold higher than the unlabeled aptamer. The K_D thus corresponds to the binding of the ligand ribostamycin to the wild-type (K_D 330 nM) (19). Ribostamycin binding to the neomycin aptamer is analogous to that of neomycin and accordingly shows regulatory activity *in vivo* (20). Thus, although significantly increased, the measured K_D values of **Çm^{f}6**, **Çm^{f}8** and **Çm^{f}15** are within a physiologically relevant range. In contrast, the ca. 2000-fold lower binding affinity of **Çm^{f}22** shows that there is effectively no ligand binding, as expected.

Çm^{f}15 should not sterically interfere with ligand binding. However, it is not unlikely that electrostatic repulsion increases the K_D for any of the labeling positions. It therefore can be assumed that the binding affinity at position 15 is reduced mainly by electrostatic effects. In addition, it has been shown that mutations at position 15 modulate the preformation of the terminal loop (60). Thus, although they do not alter ligand interactions within the binding pocket, mutations at this position can reduce binding affinity by affecting conformational selection.

Steady-state fluorescence. The emission spectra of the **Çm^f** labeled aptamers (Figure 8) are quite similar to each other and to the free chromophore in solution (68). The unstructured spectra span from ca. 400 to 650 nm with a maximum at 460 nm. The only exception is the spectrum of **Çm^{f}22**, both in the presence and absence of neomycin. This spectrum shows the typical vibrational fine structure for a base-paired **Çm^f**, as described above. Upon addition of neomycin, the following effects were observed (Figure 8 and Table 4): The QYs of **Çm^{f}6** (+25%) and **Çm^{f}8** (+43%) increase significantly, while there is no significant (+4%) change for **Çm^{f}15** and even a slight decrease for **Çm^{f}22** (−10%).

Steady-state fluorescence anisotropy studies showed only slight differences for the four labeling positions (Table 4). Furthermore, the presence of the ligand does not have any significant effect on the anisotropy. However, the fluorescence anisotropy of **Çm^{f}22** is slightly higher than the fluorescence anisotropy of the other samples, presumably due to the expected misfolding of **Çm^{f}22**. This is independent of the presence of the neomycin ligand.

Thermal denaturation. Thermal denaturation was monitored by either absorption at 260 nm or by fluorescence at 460 nm. The thermal denaturation curves of the labeled and unlabeled aptamer samples as a function of absorbance show that **Çm^f** only has a minor effect on the melting temperature (Table 4). Upon addition of neomycin, T_m increases for most of the samples. For the unlabeled aptamer, the increase was 10°C, while for **Çm^{f}6**, **Çm^{f}8** and **Çm^{f}15** the increase was 5–7°C. A decrease of the melting temperature of 2°C was observed for **Çm^{f}22**, further showing that a label in position 22 interferes with folding of the aptamer.

The results of fluorescence-monitored thermal denaturation experiments (Figure 9 and Table 4) differ from the absorption-monitored experiments. This was expected, since the **Çm^f** is a site-specific probe for the local RNA melting. In the case of **Çm^{f}6**, **Çm^{f}8** and **Çm^{f}15**, the emission intensity generally decreases with rising temperature, due to collisional quenching. Without the ligand, the melting of the aptamer can be observed as a small increase in emission, which reduces the effect of the collisional quenching on the signal. Thus, this leads to a plateau-like range within the melting curve. In the presence of the ligand, the melting of the **Çm^{f}6** and **Çm^{f}8** aptamers can be observed as a region of a more pronounced signal decrease, while for **Çm^{f}15** the effect of neomycin is only very weak. The melting curve of **Çm^{f}22**, with and without neomycin, shows the typical sigmoidal shape for an RNA duplex.

As described above, the fluorescence signal is influenced by several parallel processes during the thermal denaturation experiments. Thus, the information density of these experiments is principally quite high. On the other hand, this complicates the analysis of these processes, especially in direct comparison with absorption monitored thermal denaturation experiments. Therefore, because of possible com-

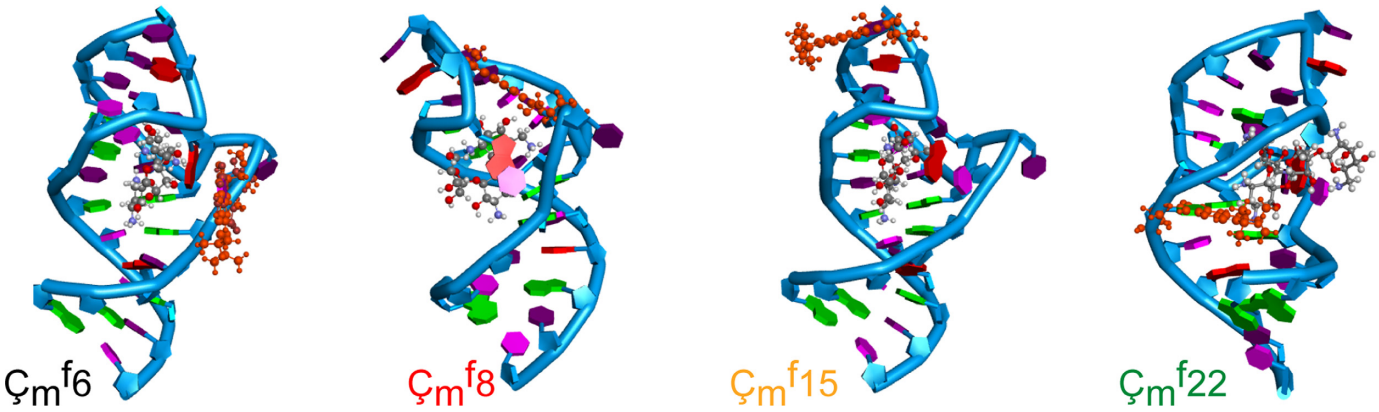

Figure 7. Positions of **Çm^f**-labeling within the neomycin aptamer (20), outlined in PDB ID: 2KXM (NDB/PDB). **Çm^f** (orange) is highlighted in ball-and-stick representation.

Table 4. Spectral shape (np/p), change of fluorescence quantum yield (ΔQY), average fluorescence lifetime (τ_{av}), steady-state fluorescence anisotropy (r_f), melting temperature (determined via absorption at 260 nm or emission at 460 nm) and K_D for different **Çm^f** labeled and unlabeled neomycin aptamers (**N1**) without (−**Neo**) and with neomycin (+**Neo**)

Sample	Neo	np/p	ΔQY/%	τ_{av}/ns	r_f	T_{m-em}/°C	T_{m-ab}/°C	K_D/nM
N1	–						56	6
	+						66	
Çm^{f}6	–	np		5.4	0.15	46 [+]	50	375
	+	np	+25	5.9	0.14	50 [–]	55	
Çm^{f}8	–	np		5.0	0.16	50 [+]	56	318
	+	np	+43	4.5	0.15	51 [–]	61	
Çm^{f}15	–	np		5.5	0.14	59 [+]	54	480
	+	np	+4	5.8	0.15	57 [–]	61	
Çm^{f}22	–	p		4.6	0.17	59 [+]	57	11 700
	+	p	−10	4.4	0.17	59 [+]	55	

np = not paired, p = paired; [–]/[+] indicating the trend of the ΔQY upon melting.

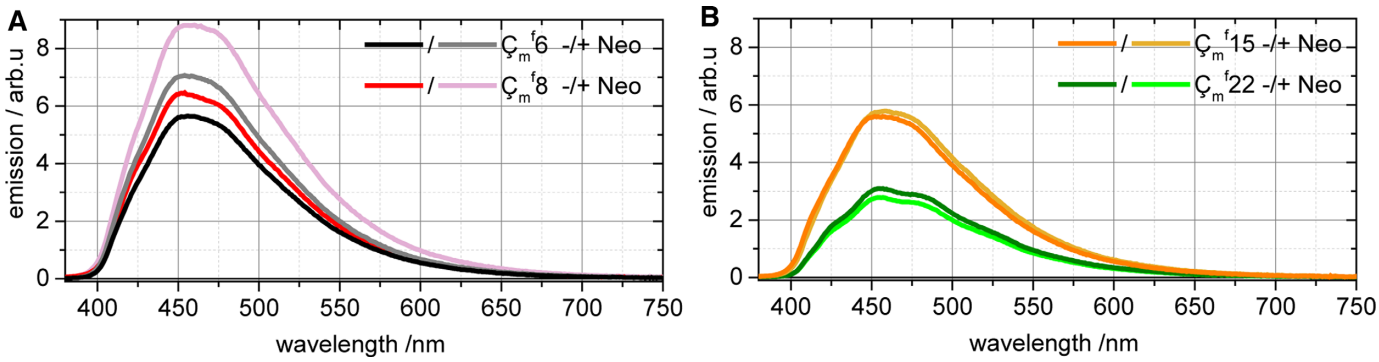

Figure 8. Concentration corrected steady-state emission spectra of (**A**) **Çm^{f}6**, **Çm^{f}8**, (**B**) **Çm^{f}15** and **Çm^{f}22** without (– **Neo**) and with neomycin (+ **Neo**).

pensation or superposition of effects the determination of T_{m-em} is more uncertain than the determination of T_{m-ab}.

The fluorescence-determined melting temperatures for the labeled aptamers range from 46°C to 59°C. The highest values were found for **Çm^{f}15** and **Çm^{f}22**, reflecting the high local stability of the stem and the terminal loop regions. On the other hand, the melting temperatures for **Çm^{f}6** and **Çm^{f}8**, placed in the internal loop, are significantly lower. This indicates that melting of the internal loop is the first stage in the unfolding of the aptamer. Furthermore, the higher melting temperatures of the ligand-bound state of **Çm^{f}6** and **Çm^{f}8** are consistent with stabilization of the folded internal loop by the ligand. On the other hand, the melting temperatures of **Çm^{f}15** and **Çm^{f}22** are slightly lower or not affected by the ligand. Thus, the binding of neomycin does not affect the stability of the terminal loop and the stem region.

Time resolved emission. The fluorescence lifetimes of the four fluorescently labeled aptamers differ slightly but sig-

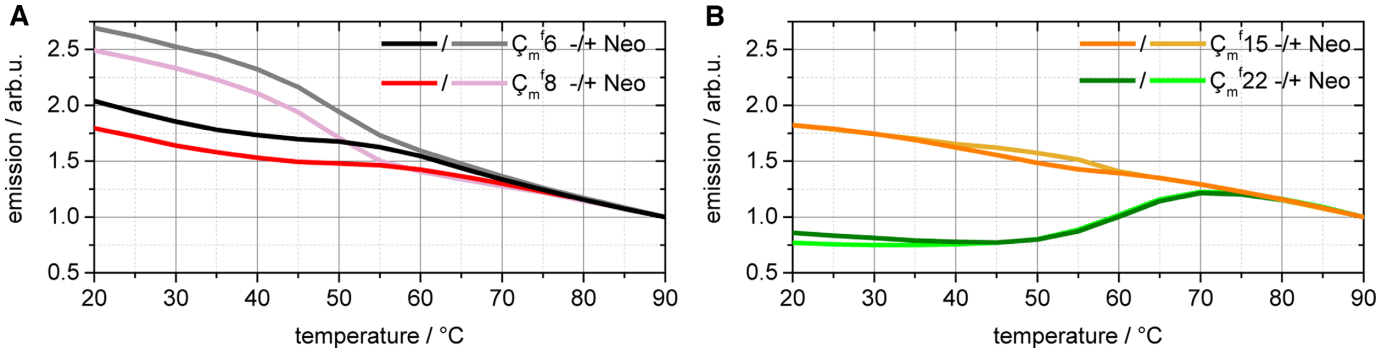

Figure 9. Melting curves of the **Çm^f** labeled neomycin aptamer without (−**Neo**) and with neomycin (+**Neo**) at 460 nm. The curves were normalized to the emission intensity at 90°C. (**A**) **Çm^{f}6**, **Çm^{f}8** (**B**) **Çm^{f}15**, **Çm^{f}22**.

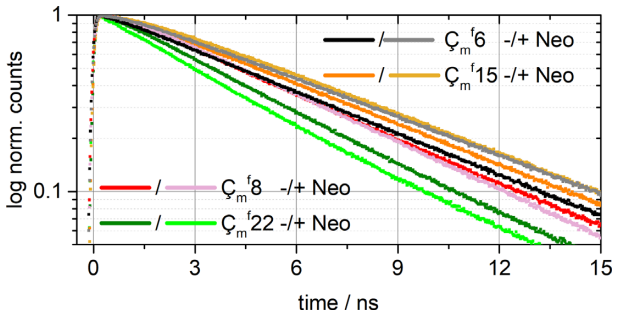

Figure 10. Normalized fluorescence decay of the different **Çm^f** labeled neomycin aptamer without (−**Neo**) and with neomycin (+**Neo**).

nificantly from each other (Figure 10 and Table 4). The average lifetimes in the absence of the neomycin ligand range from 4.6 to 5.4 ns, which is similar to what was observed for duplex RNA. Upon ligand binding, either a slight (5–10%) increase or decrease of the average fluorescence lifetime was observed, depending of the labeling position. This is a smaller difference in lifetimes than was observed between RNA single- and double-strands (ca. 40%). It is noteworthy that the fluorescence lifetimes of **Çm^{f}22** with and without neomycin are significantly shorter than the fluorescence lifetimes of the other samples, which indicates baseparing. This is in accord with the observed fine structure of the respective emission spectra for this sample and its fluorescence-monitored melting curves (Figure 9B).

Fluorescence stopped-flow. **Çm^{f}6** and **Çm^{f}8** were chosen for fluorescence stopped-flow measurements due to their large QY changes upon ligand binding (Figure 8A and Supplementary Figures S16–18). These experiments showed fast, ligand concentration-dependent binding kinetics; as the concentration of neomycin was raised, the binding rate increased (Figure 11). The increase in amplitude of the signal change leveled off after the addition of 4–6 equivalents neomycin.

The transients where analyzed with the DynaFit4 software. A one- and a two-step (with and without back reaction) as well as a Michaelis–Menten (70) model were tested (Table 5 and Supplementary Figures S16–18). The appropriate model was identified by the quality of the fit (RMSD) and the Akaike information criterion (ΔAIC) (71,72). It is evident from this analysis that the two-step model, in comparison to all other tested models, fits all the measured data by far the best (Tables 5–7 and Figure 11).

In the case of **Çm^{f}6**, the kinetics of the ligand-binding reaction can be described by a first reaction step with a bimolecular reaction rate constant of $k_1 = 425\ (\mu Ms)^{-1}$ and a second reaction step with a rate constant of $k_2 = 80\ s^{-1}$ (Figure 11A). The back-rates are significantly smaller than the corresponding rates of the forward reactions ($k_{-1} = 48\ s^{-1}$, $k_{-2} = 31\ s^{-1}$). Both reaction steps result in a fluorescence signal change of similar size (r(AL*) = 52%, r(AL) = 48%).

For **Çm^{f}8**, the first reaction rate constant was $k_1 = 207\ (\mu Ms)^{-1}$ and the second was $k_2 = 417\ s^{-1}$ (Figure 11A). As in the case of **Çm^{f}6**, the satisfactory fitting of both reaction steps requires the inclusion of back reactions. In this case the back-rates are significantly smaller ($k_{-1} = 113\ s^{-1}$, $k_{-2} = 125\ s^{-1}$) than the corresponding rates of the forward reactions. In contrast to **Çm^{f}6**, the first and the second reaction step of **Çm^{f}8** do not cause strong changes of the fluorescence signal. The signal response of the first reaction step is significantly weaker (r(AL*) = 22%) than the response of the second step (r(AL) = 78%).

In both labeled aptamer samples, **Çm^f** is a local probe for the micro-environment of the label. Because of the rigid incorporation of the label into the RNA, the nucleic acid itself dominates this micro-environment. Thus, local structural changes and local dynamics of the RNA can be monitored with the help of **Çm^f**. Therefore, the different dynamics of the two different **Çm^f**-labeled aptamers was expected.

Since sample heterogeneity is a common feature in complex biological systems, we tested our datasets for heterogeneity according to the described models. The datasets were fitted assuming two different aptamer species (A and B), which represent different aptamer structures. The increased number of fitting parameters would in fact improve the fits (data shown in the Supplementary Tables S17 and 18). Nevertheless, the fits yield unrealistic values and amplitudes which are subject to high errors. Furthermore, the converged fits always prefer one of the given species by more than 90%. Thus, we refrain to discuss a possible sample heterogeneity with quite complicated dynamics and concentrate on the analysis of the fit for a homogeneous sample, which should dominate the binding process of the aptamer.

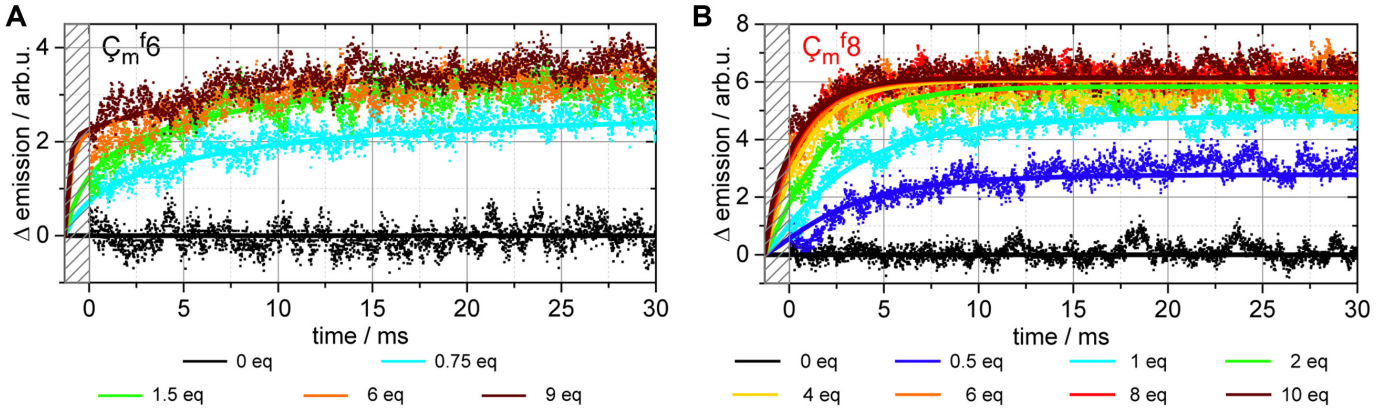

Figure 11. (**A**) Transient fluorescence signals after stopped-flow mixing of (**A**) 2.7 μM **Çm^{f}6** and (**B**) 4 μM **Çm^{f}8** with different concentrations of neomycin (indicated as equivalents of the aptamer concentration). The data are shown as points while the fits for a two-step model are displayed as solid lines.

Table 5. Reaction schemes of tested binding models

Model	Reaction scheme
One-step	$A + L \underset{k_{-1}}{\overset{k_1}{\rightleftharpoons}} AL$
Two-step (no back reaction)	$A + L \xrightarrow{k_1} AL^* \xrightarrow{k_2} AL$
Michaelis–Menten	$A + L \underset{k_{-1}}{\overset{k_1}{\rightleftharpoons}} AL^* \xrightarrow{k_2} AL$
Two-step	$A + L \underset{k_{-1}}{\overset{k_1}{\rightleftharpoons}} AL^* \underset{k_{-2}}{\overset{k_2}{\rightleftharpoons}} AL$

A = aptamer, L = ligand, AL* = ligand bound intermediate state, AL = final, ligand bound state, k_n = rate of reaction step n, k_{-n} = back-rate of reaction step n.

Table 6. Fit results of the tested binding models for the transient **Çm^{f}6** stopped-flow data

Model	$k_1/(\mu Ms)^{-1}$	k_{-1}/s^{-1}	k_2/s^{-1}	k_{-2}/s^{-1}	r(AL*)/%	r(AL)/%	RMSD	ΔAIC
One-step	131	3				100	0.0036	10 662
Two-step (no back reaction)	311		113		61	39	0.0029	1210
Michaelis-Menten	662	178	141		55	45	0.0028	387
Two-step	425	48	80	31	52	48	0.0028	0

k_n = rate of reaction step n, k_{-n} = back-rate of reaction step n, r(AL*) = signal response of component AL*, r(AL) = signal response of component AL, AIC = Akaike information criterion, RMSD = root-mean-square deviation.

Table 7. Fit results of the tested binding models for the transient Çm^{f}8 stopped-flow data

Model	$k_1/(\mu Ms)^{-1}$	k_{-1}/s^{-1}	k_2/s^{-1}	k_{-2}/s^{-1}	r(AL*)/%	r(AL)/%	RMSD	ΔAIC
One-step	92	6				100	0.0046	9194
Two-step (no back reaction)	120		637		44	56	0.0043	5228
Michaelis-Menten	141	100	609		44	56	0.0043	4956
Two-step	207	113	417	125	22	78	0.0040	0

k_n = rate of reaction step n, k_{-n} = back-rate of reaction step n, r(AL*) = signal response of component AL*, r(AL) = signal response of component AL, AIC = Akaike information criterion, RMSD = root-mean-square deviation.

DISCUSSION

Çm^f in single- and double-stranded RNA

Fluorescent labels provide unique insights into structural dynamics of RNA. Prior to a reliable analysis of aptamer conformation, a detailed characterization of the photophysical properties of the **Çm^f** fluorophore in model RNA was required. Altogether, the structural and photophysical properties (absorption and emission spectra; QY; fluorescence lifetime; structure; rigid incorporation into RNA; etc.) of **Çm^f** in RNA is very similar to the recently introduced fluorescent cytosine analog tC° (58) Nevertheless, **Çm^f** can be distinguished by several properties and details: the main difference between tC° and **Çm^f** is the quasi bifunctionality of **Çm^f**. As already described in the introduction, the fluorophore **Çm^f** is the isosteric precursor of the nitroxide spin-label **Çm**, which can be used for EPR studies on RNA. This

offers the possibility for highly comparable fluorescence and EPR studies on the same or very similar samples.

The emission spectra of **Ç$_m^f$** did not change significantly upon incorporation into RNA single-strands, although and in contrast to tC° the QY as well as the fluorescence lifetime of the fluorophore increased notably. As we have previously shown, both values of **Ç$_m^f$** are strongly affected by solvent interactions (68). Therefore, the shielding of the chromophore against quenching solvent interactions, the stabilization of its S_1 state and consequently the decrease of the non-radiative decay rate is a likely explanation for the higher QY and the longer fluorescence lifetime of **C$_m^f$** in RNA single-strands. The enhanced shielding might be due to steric effects of the neighboring nucleobases as well as base-stacking interactions. This would also provide a consistent explanation for the higher QY in the case of neighboring purine bases, which are expected to stack better.

Incorporation of **Ç$_m^f$** into RNA duplexes, on the other hand, leads to a lower QY and to a fine structured emission spectrum. Both effects are much more pronounced for **Ç$_m^f$** than for tC° (58). Gardarsson *et al*. have shown that deprotonation at the N5 position of **Ç^f** or weakening of the N-H-bond decreases the QY of the chromophore and leads to a similarly structured emission spectrum (54). Therefore, it is possible that formation of a hydrogen bond between **Ç$_m^f$** and guanine in a base pair destabilizes the S_1 state, which would counteract and overcompensate the stabilizing effects of steric shielding and base stacking. The significant changes in the spectral shape of the emission spectra and the large changes of the QY upon duplex formation of **Ç$_m^f$**-labeled RNA oligonucleotides make **Ç$_m^f$** a sensitive probe of its micro-environment.

Thermal denaturation experiments of the **Ç$_m^f$**-labeled duplexes were performed to evaluate whether **Ç$_m^f$** caused any structural perturbations. These experiments were monitored by two different methods: the absorption change at 260 nm yields the global melting temperature and detection of the **Ç$_m^f$** emission at 460 nm provides information on the melting transition in the vicinity of the label (Table 3 and Figure 4). The similar T_m-values obtained in global and local melting assays support the assumption that the double-strands melt uniformly. The small T_m-differences between the labeled and unlabeled duplexes (3°C or less, ΔG 0–5 kcal/mol) indicate that **Ç$_m^f$**, like tC°, has no appreciable effect on RNA duplex stability. The increased T_m of ds_C**Ç$_m^f$**C and ds_G**Ç$_m^f$**G compared to ds_U**Ç$_m^f$**U and ds_A**Ç$_m^f$**A are simply due to higher CG content.

Interestingly, we observed fine-structure in the emission spectra of **Ç$_m^f$** in RNA, but, in contrast to tC°, only when base-paired. This provided an opportunity to extract more information from the thermal denaturation data, using what we refer to as spectrally resolved melting analysis, which allows probing of the local melting process. This evaluation yields the temperature where half of the sample appears to be base paired at the position of the label. This temperature was found to be significantly lower than the melting temperatures of the RNA duplexes and might identify an early step in the overall melting process.

The significant anisotropy differences between the free label in solution, labeled single-strands and labeled double-strands further substantiate the rigid incorporation of **Ç$_m^f$** in RNA. The slight variation of the anisotropy values with the neighboring bases of the label might be due to the different fluorescence lifetimes of the fluorophore in the different RNA strands. This can be explained with the (anti-)correlation of these properties (cf. Perrin equation (73)).

Ç$_m^f$-labeled neomycin aptamers

The experiments for the model strands demonstrate that the steady-state emission signal of **Ç$_m^f$** is an excellent probe for the micro-environment of the label. The QY of **Ç$_m^f$** depends on the labeling position and responds in a characteristic way to ligand interaction or binding. ITC measurements indicate, that neomycin is specifically bound by **Ç$_m^f$6**, **Ç$_m^f$8** and **Ç$_m^f$15**, while there is no efficient neomycin binding by **Ç$_m^f$22**. The considerably increased K_Ds of **Ç$_m^f$6**, **Ç$_m^f$8** and **Ç$_m^f$15** in comparison to the unlabeled aptamer might be due to the positively charged **Ç$_m^f$** at pH 7.4, which could reduce the affinity of the protonated neomycin electrostatically.

Despite the finding that **Ç$_m^f$22** does not bind the ligand specifically, the QY of **Ç$_m^f$22** is reduced in the presence of the ligand. This might be due to unspecific interactions between the label and the ligand, which also lead to a noticeable destabilization of the labeled aptamer within the absorption monitored thermal denaturation experiments. The fine structure of the **Ç$_m^f$22** emission as well as the strong fluorescence quenching found in the emission monitored thermal denaturation experiments are both due to hydrogen bonds between **Ç$_m^f$** and the complementary guanosine. This effect is independent of the presence of the ligand. Thus, at least a significant amount of **Ç$_m^f$22** has to be base paired at the labeling position.

The fluorescence signals of **Ç$_m^f$15** are not affected by the addition of neomycin at all and only very weak signal changes are observable within the thermal denaturation experiments. It can thus be concluded, that the micro-environment of **Ç$_m^f$** at position 15 does not change upon ligand binding, which meets our expectations for this reference aptamer, since position 15 is not directly involved in the formation of the binding pocket (Figure 7). The strongest changes in the emission can be seen for **Ç$_m^f$6** and **Ç$_m^f$8**, which is indicative for direct interactions between ligand and label as well as larger structural changes of the aptamer in the label region. This is in agreement with a direct involvement of these residues in ligand binding (Figure 7).

In comparison with the unlabeled neomycin aptamer, absorption monitored melting experiments show that the fluorescence labeling does not critically destabilize the aptamers **Ç$_m^f$6** and **Ç$_m^f$8** in the ligand-free state. In the ligand-bound state a destabilization, in comparison with the unlabeled neomycin aptamer, is noticeable. Fluorescence monitored melting curves provide further site-specific information on the interactions between label, ligand and aptamer: the fold without ligand of **Ç$_m^f$6** and **Ç$_m^f$8** results in a slight quenching of the fluorophore. In the presence of the ligand the QY of **Ç$_m^f$6** and **Ç$_m^f$8** increases, the fluorescence quenching is thus overcompensated, indicating a different fold of the aptamer at the labeled positions or direct interactions between label and ligand.

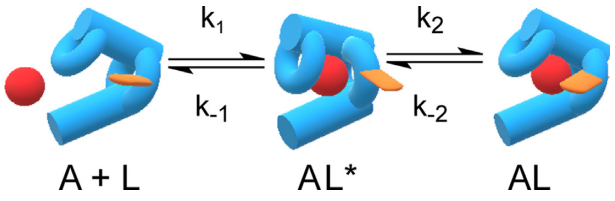

Figure 12. Cartoon of the proposed two-step binding model. The ligand is depicted as red sphere, the label as orange plate and the aptamer as blue clamp. A = aptamer, L = ligand, AL* = ligand bound intermediate state, AL = final, ligand bound state, k_n = rate of reaction step n, k_{-n} = back-rate of reaction step n.

Generally, with the help of the fluorescence monitored melting experiments stabilization and destabilization effects due to ligand binding can be observed and discussed on a local level. A detailed explanation of these effects in different regions of the tertiary structure of the aptamer is not straightforward with the current dataset. Nevertheless, these relatively weak stability changes provide evidence for at least small conformational changes upon ligand binding.

To test this conclusion, the steady-state fluorescence anisotropy was measured: based on the assumption, that at all labeling positions the chromophore is rigidly incorporated into the neomycin aptamer, it is possible to conceptually connect the fluorescence anisotropy to the volume of the aptamer. Consequently, it seems as if the volume and the shape of the neomycin aptamer does not change significantly upon ligand binding. In the case of extended tertiary structural changes, one would expect a stronger change of the anisotropy. Thus, the more or less constant fluorescence anisotropy value confirms the preformation of the aptamer and the conformational selection binding mechanism. Nevertheless, small conformational changes, which do not significantly change the shape of the aptamer, cannot be ruled out via fluorescence anisotropy methods.

In accordance to the low sub-μM K_Ds of the $\mathbf{Ç_m^f 6}$ and $\mathbf{Ç_m^f 8}$ labeled aptamers, the stopped-flow measurements show very rapid binding dynamics. It becomes apparent, that a two-step binding model—with a back and forward reaction for each step—describes the data best. Based on these findings it is possible to propose the following binding mechanism of the neomycin aptamer (Figure 12): the aptamer is mostly preformed in solution (pH 7.4, 20°C). In a first step, neomycin enters the preformed binding pocket of the aptamer. Unspecific interactions between ligand and fluorescent label cause an increase of the emission signal. In a second step, specific interactions, like hydrogen bonds and electrostatic interactions, between the ligand and the binding pocket are formed. This induces small conformational changes in the area of the binding pocket. Thus, the overall shape of the aptamer is not distorted but the microenvironment (orientation, solvent accessibility) of the fluorescent label is modified. This affects the non-radiative de-excitation rate of the label and also results in an increased QY.

CONCLUSION

This study presents the features and the potential of $\mathbf{Ç_m^f}$ as a fluorescent RNA label. A 5′-dimethoxytritylated phosphoramidite was synthesized from the fluorescent nucleoside $\mathbf{Ç_m^f}$ (45), which was then incorporated into RNA via solid-phase oligonucleotide synthesis.

The stability of the duplexes was not affected by insertion of the fluorescent label. As with DNA the emission spectra become structured upon duplex formation. As the QY is affected by the flanking bases of the fluorophore, it was possible to distinguish between pyrimidine and purine neighboring bases. Fluorescence lifetime measurements allowed distinguishing between labeled double- and single-strands and also between flanking bases of the fluorophore. The $\mathbf{Ç_m^f}$-fluorophore is sensitive to its micro-environment such as base pairing, stacking and solvent accessibility. Thus, specific $\mathbf{Ç_m^f}$-labeled RNA samples are perfectly suitable for duplexation and ligand binding studies. Time resolved fluorescence measurements of $\mathbf{Ç_m^f}$-labeled samples allow structural dynamics studies. Our results can thus serve as benchmarks for analogous experiments on functional RNAs for example aptamers.

Subsequently, a ligand binding study of the neomycin aptamer was performed. The aptamer was singly labeled at four different positions. With steady-state fluorescence methods, it was possible to confirm the previously proposed conformational selection mechanism, with a widely preformed aptamer, as binding model for the neomycin aptamer. Moreover, it was possible to observe the dynamics of the ligand binding process with the help of fluorescence-monitored stopped-flow measurements. It comes clear that the ligand binding is in fact a two-step process. We propose an unspecific ligand binding near or in the binding pocket as a first step. In the second step, the ligand is bound specifically with the help of H-bonds and electrostatic interactions. It is proposed, that this second step causes only minor conformational changes.

In general, our results open the door for further RNA binding studies with $\mathbf{Ç_m^f}$. In the case of the neomycin aptamer further pH- or salt-concentration-dependent studies as well as studies with other label positions are conceivable. $\mathbf{C_m^f}$ in combination with other RNA-labels should enable FRET measurements. These would allow a direct comparison between UV/vis and PELDOR data. Furthermore, the presented results provide evidence for a kinetic contribution to the regulatory mechanism of the neomycin aptamer. In comparison and in combination with other studies on dynamics and structure this might help to understand the regulatory mechanisms of riboswitches in greater detail.

DATA AVAILABILITY

OPTIMUS is free for academic use and available under http://optimusfit.org.

DynaFit 4 is free for academic use and available under http://www.biokin.com/dynafit.

SEDPHAT is free for academic use and available under http://www.analyticalultracentrifugation.com/sedphat/.

NITPIC is free for academic use and available under http://biophysics.swmed.edu/MBR/software.html.

SUPPLEMENTARY DATA

Supplementary Data are available at NAR Online.

ACKNOWLEDGEMENTS

We thank L. Tapmeyer, A. Völklein, J. Martin and M. Kuth for their support regarding several steady-state and time resolved absorption and fluorescence measurements. We thank Prof. A. Heckel for access to his absorption spectrometer with sample changer. We thank Prof. J. Wöhnert for access to his ITC. Furthermore, we thank Dr M. Vogel and Prof. B. Süß for fruitful discussions concerning the neomycin aptamer.

FUNDING

Deutsche Forschungsgemeinschaft (DFG) through the Collaborative Research Center (CRC) 902; 'Molecular Principles of RNA-based Regulation' sub-projects A7, B14 and Mercator Fellowship. Funding for open access charge: DFG (CRC902); sub-projects A7, B14 and Mercator Fellowship.

Conflict of interest statement. None declared.

REFERENCES

1. Altman,S. (1990) Enzymatic cleavage of RNA by RNA (Nobel lecture). *Angew. Chem. Int. Ed. Engl.*, **29**, 749–758.
2. Cech,T.R. (1990) Self-splicing and enzymatic activity of an intervening sequence RNA from Tetrahymena (Nobel Lecture). *Biosci. Rep.*, **10**, 239–261.
3. Gilbert,W. (1986) Origin of life: the RNA world. *Nature*, **319**, 618.
4. Robertson,M.P. and Joyce,G.F. (2012) The origins of the RNA world. *Cold Spring Harb. Perspect. Biol.*, **4**, a003608.
5. Morris,K. V. and Mattick,J.S. (2014) The rise of regulatory RNA. *Nat. Rev. Genet.*, **15**, 423–437.
6. Cech,T.R. and Steitz,J.A. (2014) The noncoding RNA revolution—trashing old rules to forge new ones. *Cell*, **157**, 77–94.
7. Serganov,A. and Nudler,E. (2013) A decade of riboswitches. *Cell*, **152**, 17–24.
8. Chen,X., Li,N. and Ellington,A.D. (2007) Ribozyme catalysis of metabolism in the RNA world. *Chem. Biodivers.*, **4**, 633–655.
9. Breaker,R.R. (2012) Riboswitches and the RNA world. *Cold Spring Harb. Perspect. Biol.*, **4**, a003566.
10. Breaker,R.R. (2009) Riboswitches: from ancient gene-control systems to modern drug targets. *Future Microbiol.*, **4**, 771–773.
11. Garst,A.D., Edwards,A.L. and Batey,R.T. (2011) Riboswitches: structures and mechanisms. *Cold Spring Harb. Perspect. Biol.*, **3**, a003533.
12. Batey,R.T. (2015) Riboswitches: still a lot of undiscovered country. *RNA*, **21**, 560–563.
13. Weigand,J.E., Sanchez,M., Gunnesch,E.-B.E.-B., Zeiher,S., Schroeder,R. and Suess,B. (2008) Screening for engineered neomycin riboswitches that control translation initiation. *RNA*, **14**, 89–97.
14. Berens,C., Groher,F. and Suess,B. (2015) RNA aptamers as genetic control devices: The potential of riboswitches as synthetic elements for regulating gene expression. *Biotechnol. J.*, **10**, 246–257.
15. Weigand,J.E. and Suess,B. (2009) Aptamers and riboswitches: perspectives in biotechnology. *Appl. Microbiol. Biotechnol.*, **85**, 229–236.
16. Ellington,A.D. and Szostak,J.W. (1990) In vitro selection of RNA molecules that bind specific ligands. *Nature*, **346**, 818–822.
17. Tuerk,C. and Gold,L. (1990) Systematic evolution of ligands by exponential enrichment: RNA ligands to bacteriophage T4 DNA polymerase. *Science*, **249**, 505–510.
18. Robertson,D.L. and Joyce,G.F. (1990) Selection in vitro of an RNA enzyme that specifically cleaves single-stranded DNA. *Nature*, **344**, 467–468.
19. Duchardt-Ferner,E., Gottstein-Schmidtke,S.R., Weigand,J.E., Ohlenschläger,O., Wurm,J.-P., Hammann,C., Suess,B. and Wöhnert,J. (2016) What a difference an OH makes: Conformational dynamics as the basis for the ligand specificity of the neomycin-sensing riboswitch. *Angew. Chem. Int. Ed.*, **55**, 1527–1530.
20. Duchardt-Ferner,E., Weigand,J.E., Ohlenschläger,O., Schmidtke,S.R., Suess,B. and Wöhnert,J. (2010) Highly modular structure and ligand binding by conformational capture in a minimalistic riboswitch. *Angew. Chem. Int. Ed.*, **49**, 6216–6219.
21. Krstić,I., Frolow,O., Sezer,D., Endeward,B., Weigand,J.E., Suess,B., Engels,J.W. and Prisner,T.F. (2010) PELDOR spectroscopy reveals preorganization of the neomycin-responsive riboswitch tertiary structure. *J. Am. Chem. Soc.*, **132**, 1454–1455.
22. Perez-Gonzalez,C., Lafontaine,D.A. and Penedo,J.C. (2016) Fluorescence-based strategies to investigate the structure and dynamics of aptamer-ligand complexes. *Front. Chem.*, **4**, 1–22.
23. Ward,D.C. and Reich,E. (1969) Studies of nucleotides and polynucleotide. *J. Biochem. Chem.*, **244**, 1228–1237.
24. Jean,J.M. and Hall,K.B. (2001) 2-Aminopurine fluorescence quenching and lifetimes: Role of base stacking. *Proc. Natl. Acad. Sci. U.S.A.*, **98**, 37–41.
25. Jones,A.C. and Neely,R.K. (2015) 2-aminopurine as a fluorescent probe of DNA conformation and the DNA-enzyme interface. *Q. Rev. Biophys.*, **48**, 244–279.
26. Rist,M.J. and Marino,J.P. (2002) Fluorescent nucleotide base analogs as probes of nucleic acid structure, dynamics and interactions. *Curr. Org. Chem.*, **6**, 775–793.
27. Matarazzo,A. and Hudson,R.H.E. (2015) Fluorescent adenosine analogs: a comprehensive survey. *Tetrahedron*, **71**, 1627–1657.
28. Reuss,A.J., Grünewald,C., Gustmann,H., Engels,J.W. and Wachtveitl,J. (2017) Three-state fluorescence of a 2-functionalized pyrene-based RNA label. *J. Phys. Chem. B*, **121**, 3032–3041.
29. Förster,U., Lommel,K., Sauter,D., Grünewald,C., Engels,J.W. and Wachtveitl,J. (2010) 2-(1-ethynylpyrene)-adenosine as a folding probe for RNA—pyrene in or out. *Chembiochem*, **11**, 664–672.
30. Förster,U., Grünewald,C., Engels,J.W. and Wachtveitl,J. (2010) Ultrafast dynamics of 1-ethynylpyrene-modified RNA: A photophysical probe of intercalation. *J. Phys. Chem. B*, **114**, 11638–11645.
31. Förster,U., Gildenhoff,N., Grünewald,C., Engels,J.W. and Wachtveitl,J. (2009) Photophysics of 1-ethynylpyrene-modified RNA base adenine. *J. Lumin.*, **129**, 1454–1458.
32. Grünewald,C., Kwon,T., Piton,N., Förster,U., Wachtveitl,J. and Engels,J.W. (2008) RNA as scaffold for pyrene excited complexes. *Bioorg. Med. Chem.*, **16**, 19–26.
33. Rovira,A.R., Fin,A. and Tor,Y. (2015) Chemical mutagenesis of an emissive RNA alphabet. *J. Am. Chem. Soc.*, **137**, 14602–14605.
34. Sandin,P., Wilhelmsson,L.M., Lincoln,P., Powers,V.E.C., Brown,T. and Albinsson,B. (2005) Fluorescent properties of DNA base analogue tC upon incorporation into DNA - Negligible influence of neighbouring bases on fluorescence quantum yield. *Nucleic Acids Res.*, **33**, 5019–5025.
35. Shin,D., Sinkeldam,R.W. and Tor,Y. (2011) Emissive RNA alphabet. *J. Am. Chem. Soc.*, **133**, 14912–14915.
36. Wojciechowski,F. and Hudson,R.H.E. (2008) Fluorescence and hybridization properties of peptide nucleic acid containing a substituted phenylpyrrolocytosine designed to engage guanine with an additional H-Bond. *J. Am. Chem. Soc.*, **130**, 12574–12575.
37. Wilhelmsson,L.M. and Tor,Y. (2010) Fluorescent analogs of biomolecular building blocks: Design and applications. *Chem. Rev.*, **110**, 2579–2619.
38. Wilhelmsson,L.M. (2010) Fluorescent nucleic acid base analogues. *Q. Rev. Biophys.*, **43**, 159–183.
39. Trojanowski,P., Plötner,J., Grünewald,C., Graupner,F.F., Slavov,C., Reuss,A.J., Braun,M., Engels,J.W. and Wachtveitl,J. (2014) Photo-physical properties of 2-(1-ethynylpyrene)-adenosine: influence of hydrogen bonding on excited state properties. *Phys. Chem. Chem. Phys.*, **16**, 13875–13888.
40. Reuss,A.J., Grünewald,C., Braun,M., Engels,J.W. and Wachtveitl,J. (2016) The three possible 2- (pyrenylethynyl) adenosines: Rotameric energy barriers govern the photodynamics of these structural isomers. *Chemphyschem*, **17**, 1369–1376.
41. Barhate,N., Cekan,P., Massey,A.P.P. and Sigurdsson,S.T.T. (2007) A nucleoside that contains a rigid nitroxide spin label: A fluorophore in disguise. *Angew. Chem. Int. Ed. Engl.*, **46**, 2655–2658.
42. Marko,A., Denysenkov,V., Margraf,D., Cekan,P., Schiemann,O., Sigurdsson,S.T. and Prisner,T.F. (2011) Conformational flexibility of DNA. *J. Am. Chem. Soc.*, **133**, 13375–13379.

43. Cekan,P., Jonsson,E.O. and Sigurdsson,S.T. (2009) Folding of the cocaine aptamer studied by EPR and fluorescence spectroscopies using the bifunctional spectroscopic probe Ç. *Nucleic Acids Res.*, **37**, 3990–3995.
44. Shelke,S.A., Sandholt,G.B. and Sigurdsson,S.T. (2014) Nitroxide-labeled pyrimidines for non-covalent spin-labeling of abasic sites in DNA and RNA duplexes. *Org. Biomol. Chem.*, **12**, 7366–7374.
45. Höbartner,C., Sicoli,G., Wachowius,F., Gophane,D.B. and Sigurdsson,S.T. (2012) Synthesis and characterization of RNA containing a rigid and nonperturbing cytidine-derived spin label. *J. Org. Chem.*, **77**, 7749–7754.
46. Cekan,P. and Sigurdsson,S.T. (2008) Single base interrogation by a fluorescent nucleotide: each of the four DNA bases identified by fluorescence spectroscopy. *Chem. Commun.*, **0**, 3393–3395.
47. Schiemann,O., Cekan,P., Margraf,D., Prisner,T.F. and Sigurdsson,S.T. (2009) Relative orientation of rigid nitroxides by PELDOR: Beyond distance measurements in nucleic acids. *Angew. Chem. Int. Ed. Engl.*, **48**, 3292–3295.
48. Edwards,T.E., Cekan,P., Reginsson,G.W., Shelke,S. a, Ferré-D'Amaré,A.R., Schiemann,O. and Sigurdsson,S.T. (2011) Crystal structure of a DNA containing the planar, phenoxazine-derived bi-functional spectroscopic probe Ç. *Nucleic Acids Res.*, **39**, 4419–4426.
49. Prisner,T.F., Marko,A. and Sigurdsson,S.T. (2015) Conformational dynamics of nucleic acid molecules studied by PELDOR spectroscopy with rigid spin labels. *J. Magn. Reson.*, **252**, 187–198.
50. Grytz,C.M., Marko,A., Cekan,P., Sigurdsson,S.T. and Prisner,T.F. (2016) Flexibility and conformation of the cocaine aptamer studied by PELDOR. *Phys. Chem. Chem. Phys.*, **18**, 2993–3002.
51. Likhtenshtein,G.I., Yamauchi,J., Nakatsuji,S., Smirnov,A.I. and Tamura,R. (2008) *Nitroxides: Applications in Chemistry, Biomedicine, and Materials Science*, WILEY-VCH Verlag GmbH & Co. KGaA, Weinheim.
52. Likhtenstein,G.I., Ishii,K. and Nakatsuji,S. (2007) Dual chromophore-nitroxides: Novel molecular probes photochemical and photophysical models and magnetic materials. *Photochem. Photobiol.*, **83**, 871–881.
53. Stryer,L. and Griffith,O.H. (1965) A spin-labeled hapten. *Proc. Natl. Acad. Sci. U.S.A.*, **54**, 1785–1791.
54. Gardarsson,H., Kale,A.S. and Sigurdsson,S.T. (2011) Structure-function relationships of phenoxazine nucleosides for identification of mismatches in duplex DNA by fluorescence spectroscopy. *Chembiochem*, **12**, 567–575.
55. Cekan,P. and Sigurdsson,S.T. (2012) Conformation and dynamics of nucleotides in bulges and symmetric internal loops in duplex DNA studied by EPR and fluorescence spectroscopies. *Biochem. Biophys. Res. Commun.*, **420**, 656–661.
56. Gardarsson,H. and Sigurdsson,S.T. (2010) Large flanking sequence effects in single nucleotide mismatch detection using fluorescent nucleoside Çf. *Bioorg. Med. Chem.*, **18**, 6121–6126.
57. Tkach,I., Pornsuwan,S., Höbartner,C., Wachowius,F., Sigurdsson,S.T., Baranova,T.Y., Diederichsen,U., Sicoli,G. and Bennati,M. (2013) Orientation selection in distance measurements between nitroxide spin labels at 94 GHz EPR with variable dual frequency irradiation. *Phys. Chem. Chem. Phys.*, **15**, 3433–3437.
58. Füchtbauer,A.F., Preus,S., Börjesson,K., McPhee,S.A., Lilley,D.M.J. and Wilhelmsson,L.M. (2017) Fluorescent RNA cytosine analogue—an internal probe for detailed structure and dynamics investigations. *Sci. Rep.*, **7**, 2393.
59. Mergny,J.-L. and Lacroix,L. (2003) Analysis of thermal melting curves. *Oligonucleotides*, **13**, 515–537.
60. Weigand,J.E., Gottstein-Schmidtke,S.R., Demolli,S., Groher,F., Duchardt-Ferner,E., Wöhnert,J. and Suess,B. (2014) Sequence elements distal to the ligand binding pocket modulate the efficiency of a synthetic riboswitch. *Chembiochem*, **15**, 1627–1637.
61. Keller,S., Vargas,C., Zhao,H., Piszczek,G., Brautigam,C.A. and Schuck,P. (2012) High-precision isothermal titration calorimetry with automated peak-shape analysis. *Anal. Chem.*, **84**, 5066–5073.
62. Scheuermann,T.H. and Brautigam,C.A. (2015) High-precision, automated integration of multiple isothermal titration calorimetric thermograms: New features of NITPIC. *Methods*, **76**, 87–98.
63. Zhao,H., Piszczek,G. and Schuck,P. (2015) SEDPHAT—a platform for global ITC analysis and global multi-method analysis of molecular interactions. *Methods*, **76**, 137–148.
64. Enderlein,J. and Erdmann,R. (1997) Fast fitting of multi-exponential decay curves. *Opt. Commun.*, **134**, 371–378.
65. Berger,R.L. and Friauf,B.B.B. (1968) High speed optical stopped-flow apparatus high speed optical stopped-flow apparatus. *Rev. Sci. Instrum.*, **39**, 486–493.
66. Berger,R.L., Balko,B. and Chapman,H.F. (1968) High resolution mixer for the study of the kinetics of rapid reactions in solution. *Rev. Sci. Instrum.*, **39**, 493–498.
67. Kuzmic,P. (1996) Program DYNAFIT for the analysis of enzyme kinetic data: application to HIV proteinase. *Anal. Biochem.*, **273**, 260–273.
68. Gustmann,H., Lefrancois,D., Reuss,A.J., Gophane,D.B., Braun,M., Dreuw,A., Sigurdsson,S.T. and Wachtveitl,J. (2017) Spin the light off: rapid internal conversion into a dark doublet state quenches the fluorescence of an RNA spin label. *Phys. Chem. Chem. Phys.*, **19**, 26255–26264.
69. Weigand,J.E., Schmidtke,S.R., Will,T.J., Duchardt-Ferner,E., Hammann,C., Wöhnert,J., Suess,B., Wohnert,J. and Suess,B. (2011) Mechanistic insights into an engineered riboswitch: a switching element which confers riboswitch activity. *Nucleic Acids Res.*, **39**, 3363–3372.
70. Johnson,K.A. and Goody,R.S. (2011) The original Michaelis constant: translation of the 1913 Michaelis – Menten paper. *Biochemistry*, **50**, 8264–8269.
71. Akaike,H. (1974) A new look at the statistical model identification. *IEEE Trans. Autom. Control*, **19**, 716–723.
72. Myung,J., Tang,Y. and Pitt,M.A. (2009) Evaluation and comparison of computational models. *Methods Enzymol.*, **454**, 287–304.
73. Lakowicz,J.R. (2006) *Principles of Fluorescence Spectroscopy*. 3rd edn. Springer Science+Business Media, LCC, NY.

Supporting Information

Structure guided fluorescence labeling reveals a two-step binding mechanism of neomycin to its RNA aptamer

Henrik Gustmann[1], Anna-Lena Johanna Segler[2], Dnyaneshwar B. Gophane[2], Andreas J. Reuss[1], Christian Grünewald[3], Markus Braun[1], Julia E. Weigand[4], Snorri Th. Sigurdsson[2,*], and Josef Wachtveitl[1,*]

[1] Institute of Physical and Theoretical Chemistry, Goethe-University Frankfurt am Main, Max-von-Laue-Str. 7, 60438 Frankfurt, Germany
[2] Science Institute, University of Iceland, Dunhaga 3, 107 Reykjavik, Iceland
[3] Institute for Organic Chemistry, Goethe-University Frankfurt am Main, Max-von-Laue-Str. 7, 60438 Frankfurt, Germany
[4] Department of Biology, Technical University Darmstadt, Schnittspahnstraße 10, 64287 Darmstadt, Germany

* To whom correspondence should be addressed:
Josef Wachtveitl; Tel: +49 (0)69 798 29351; Fax: +49 (0)69 798 29709; Email: wveitl@theochem.uni-frankfurt.de.
Snorri Th. Sigurdsson, Tel: +354 525 4801; Email: snorrisi@hi.is.

Experimental procedures

General. All reagents were purchased from Sigma-Aldrich Co. and were used without further purification. Dichloromethane, pyridine and acetonitrile were dried over calcium hydride and freshly distilled before use. All moisture- and air-sensitive reactions were carried out in oven-dried glassware under inert atmosphere. Thin-layer chromatography (TLC) was performed using glass plates pre-coated with silica gel (0.25 mm, F-25, Silicycle) and compounds were visualized under UV light and by *p*-anisaldehyde staining. Column chromatography was performed using 230–400 mesh silica gel (Silicycle). ^{1}H-, ^{13}C- and ^{31}P-NMR spectra were recorded with a Bruker Avance 400 MHz spectrometer. Commercial grade $CDCl_3$ was passed over basic alumina shortly before use with tritylated compounds. Chemical shifts are reported in parts per million (ppm) relative to the partially deuterated NMR solvent $CDCl_3$ (7.26 ppm for ^{1}H NMR and 77.16 ppm for ^{13}C). ^{31}P-NMR chemical shifts are reported relative to 85% H_3PO_4 as an external standard. Mass spectrometric analyses were performed with an HRMS-ESI (Bruker, MicroTOF-Q) in positive ion mode.

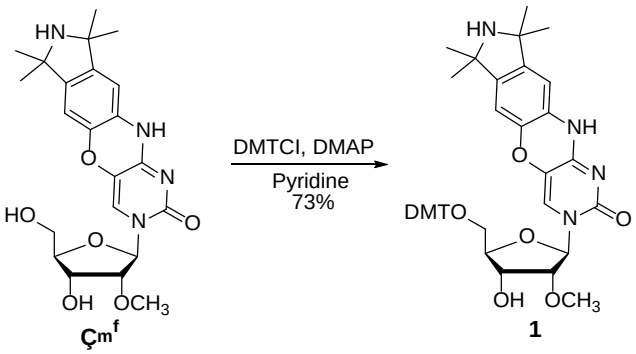

Çm[f] **1**

5′-Dimethoxytritylated Çm[f] (1)

Residual methanol was co-evaporated with toluene (3x10 mL) from **Çm[f]** (200 mg, 0.45 mmol). Anhydrous pyridine (10 mL) was added. DMTCl (305 mg, 0.90 mmol) and DMAP (6 mg, 0.05 mmol) were added and the solution was stirred for 18 h, after which MeOH (1 mL) was added and the solvent was removed *in vacuo*. The residue was purified by column chromatography using neutral silica gel (Et_3N:MeOH:CH_2Cl_2; 1:3:96 to 1:10:89) to yield **1** as a yellow solid (246 mg, 73%).

TLC (MeOH:CH_2Cl_2; 20:80), R_f (**Çm[f]**) = 0.20, R_f (**1**) = 0.60

HRMS-ESI *m/z* calcd. for $C_{43}H_{47}N_4O_8$ $(M+H)^+$ 747.3388, found 747.3385.

^{1}H NMR (400 MHz, $CDCl_3$): δ = 7.72 (s, 1H), 7.65 (s,1H), 7.50 (s, 1H), 7.49 (s, 1H), 7.42-7.38 (m, 4H), 7.31 (t, *J* = 7.6 Hz, 2H), 7.22-7.18 (m, 1H), 6.88-6.84 (m, 4H), 6.06 (s, 1H), 5.87 (s, 1H), 5.51-4.48 (m, 1H), 4.01-3.98 (m, 1H), 3.91 (d, *J* = 5.4 Hz, 1H), 3.74 (s, 1H), 3.72 (s, 1H), 3.57-3.48 (m, 2H), 1.41 (s, 1H), 1.40 (s, 1H), 1.38 (s, 1H), 1.35 (s, 1H) ppm.

^{13}C NMR (101 MHz, $CDCl_3$): δ 158.54, 155.22, 153.93, 144.40, 144.36, 143.66, 141.96, 135.85, 135.60, 130.09, 130.06, 128.25, 128.01, 127.92, 126.89, 125.37, 121.62, 113.34, 113.30, 111.24, 108.29, 87.86, 86.77, 83.81, 82.84, 68.24, 62.86, 62.80, 60.90, 58.51, 55.19, 55.17, 46.13, 31.70, 31.67, 31.49, 10.59 ppm.

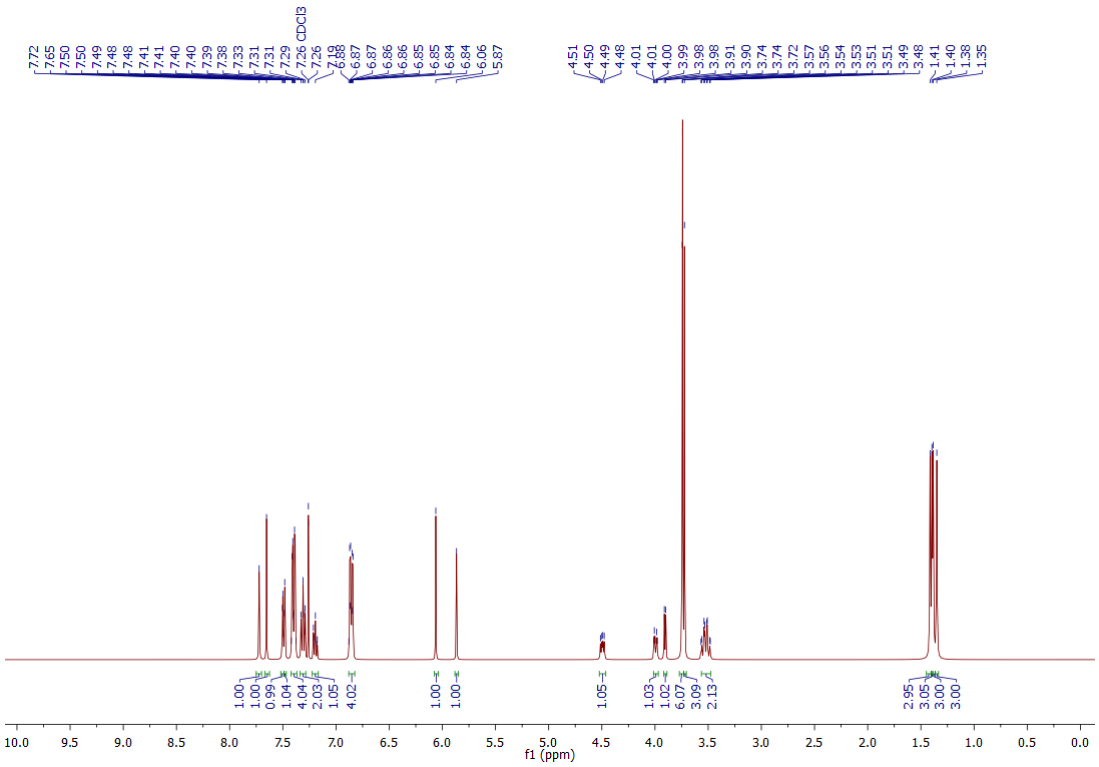

***Figure S1**. [1]H-NMR (400 MHz, $CDCl_3$) spectrum of **1**.*

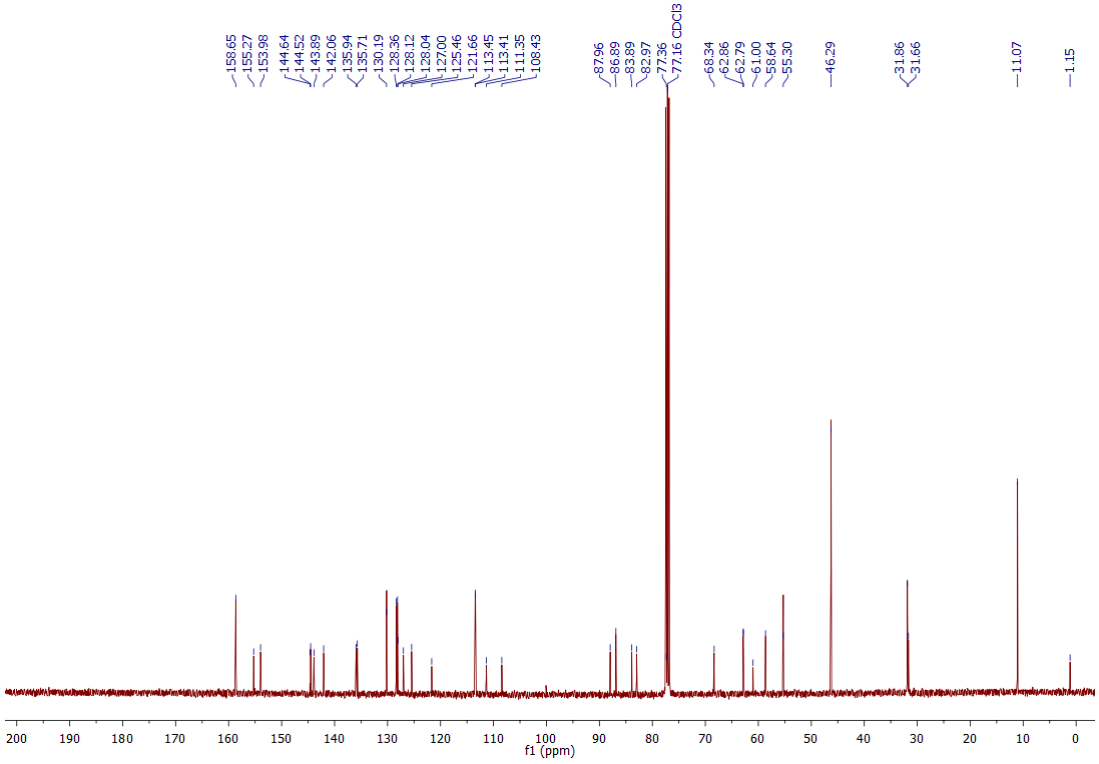

***Figure S2**. [13]C-NMR (101 MHz, $CDCl_3$) spectrum of **1**.*

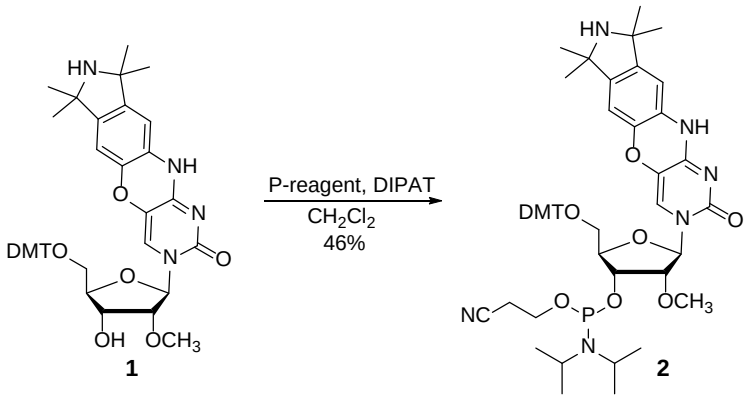

Ç$_m^f$ phosphoramidite (2)

Diisopropylammonium tetrazolide (34 mg, 0.20 mmol) and compound 1 (100 mg, 0.13 mmol) were dissolved in CH_2Cl_2 (6 mL). 2-Cyanoethyl *N*,*N*,*N*′,*N*′-tetraisopropylphosphorodiamidite (128 µL, 0.08 mmol) was added and the reaction mixture was stirred for 4 h. CH_2Cl_2 (15 mL) was added and the organic phase was washed with saturated aqueous $NaHCO_3$ (15 mL), dried over Na_2SO_4 and the solvent was removed under vacuum. The residue was precipitated by dissolving it in CH_2Cl_2 (1 mL) followed by a slow addition of *n*-hexane (10 mL). The precipitate was further purified by column chromatography using neutral silica gel (Et_3N:CH_3CN; 0:100 to 10:90) to yield **2** as a yellow solid (58 mg, 46%).

TLC (Et_3N/CH_3CN; 20:80), R_f (**1**) = 0.20, R_f (**2**) = 0.60

HRMS-ESI *m/z* calcd for $C_{52}H_{64}N_6O_9P$ $(M+H)^+$ 947.4467, found 947.4467.

^{1}H NMR (400 MHz, $CDCl_3$): δ = 7.74 (s, 1H), 7.7 (s, 1H), 7.70 (s, 1H), 7.61 (s, 1H), 7.53-7.51 (d, *J* = 7.5 Hz, 2H), 7.48-7.46 (d, *J* = 7.3 Hz, 2H), 7.45-7.41 (m, 8H), 7.33-7.29 (t, *J* = 7.7 Hz, 2H), 7.32-7.28 (t, *J* = 7.8 Hz, 2H), 7.22-7.19 (t, *J* = 7.5 Hz, 2H), 6.87-6.83 (m, 8H), 6.04 (s, 1H), 5.94 (s, 1H), 5.93 (s, 1H), 5.88 (s, 1H), 4.67-4.62 (m, 1H), 4.44-4.39 (m, 1H), 4.26-4.22 (m, 2H), 4.01-3.96 (dd, *J* = 11.4 Hz, 2.7 Hz, 2H), 3.74 (s, 3H), 3.73 (s, 3H), 3.72 (s, 3H), 3.66 (s, 3H), 3.65 (s, 3H), 3.58-3.55 (m, 3H), 3.55-3.51 (m, 1H), 3.49-3.43 (m, 3H), 3.30-3.23 (m, 1H), 2.64-2.60 (td, *J* = 6.3, 6.3, 1.8 Hz, 2H), 2.44-2.41 (t, *J* = 6.4 Hz, 2H), 1.45-1.42 (m, 12H), 1.37 (s, 3H), 1.36 (s, 3H), 1.21-1.18 (m, 12H), 1.16 (s, 1H), 1.15 (s, 1H), 1.06 (s, 1H), 1.04 (s, 1H) ppm.

^{13}C NMR (101 MHz, $CDCl_3$): δ = 158.60, 155.13, 155.02, 153.95, 153.91, 144.30, 144.26, 142.07, 142.02, 135.68, 135.62, 135.47, 135.41, 130.24, 130.26, 128.44, 128.07, 127.94, 127.90, 126.98, 125.64, 125.56, 121.63, 121.22, 117.61, 117.49, 113.27, 113.24, 113.21, 111.36, 111.23, 108.26, 108.20, 88.61, 88.52, 86.83, 88.71, 83.67, 82.86, 81.73, 81.56, 69.78, 69.63, 69.24, 69.08, 63.09, 61.24, 60.40, 60.10, 58.70, 58.52, 58.39, 58.22, 58.05, 55.22, 55.20, 43.39, 43.26, 31.55, 31.40, 24.83, 24.77, 24.71, 24.65, 24.60, 24.58, 24.53, 20.41, 20.35 ppm.

^{31}P NMR (400 MHz, $CDCl_3$): δ = 150.45, 149.00 ppm.

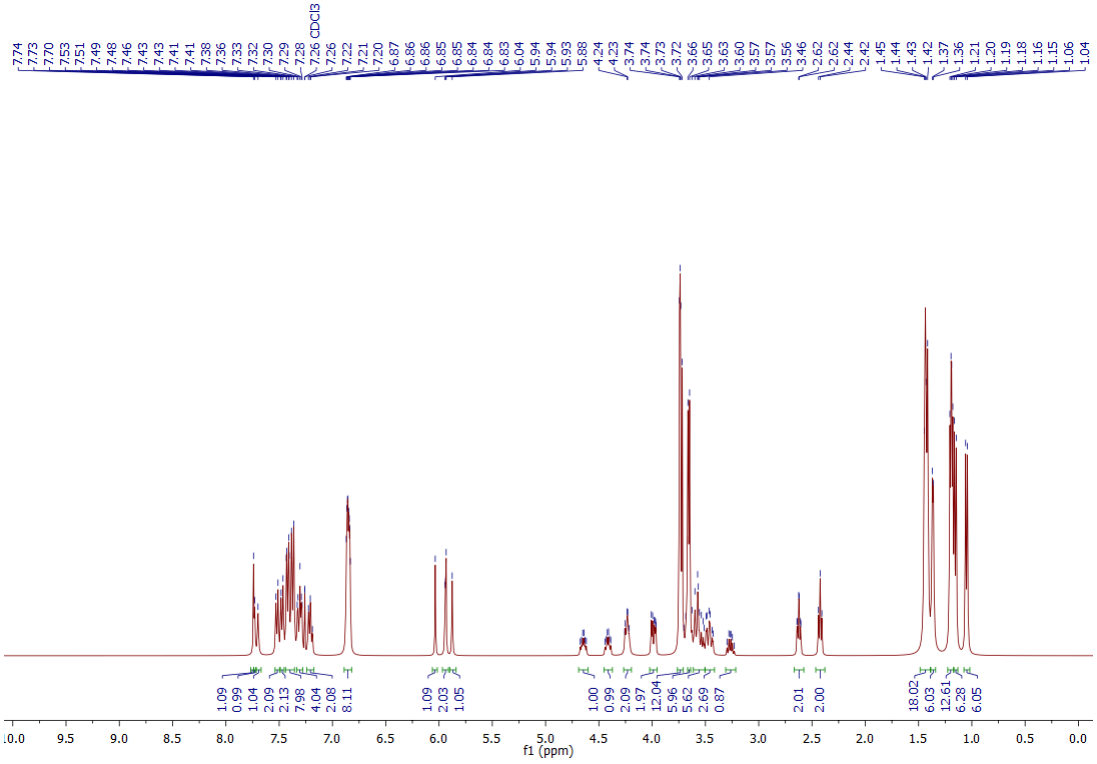

***Figure S3**. ^{1}H-NMR (400 MHz, $CDCl_3$) spectrum of **2**.*

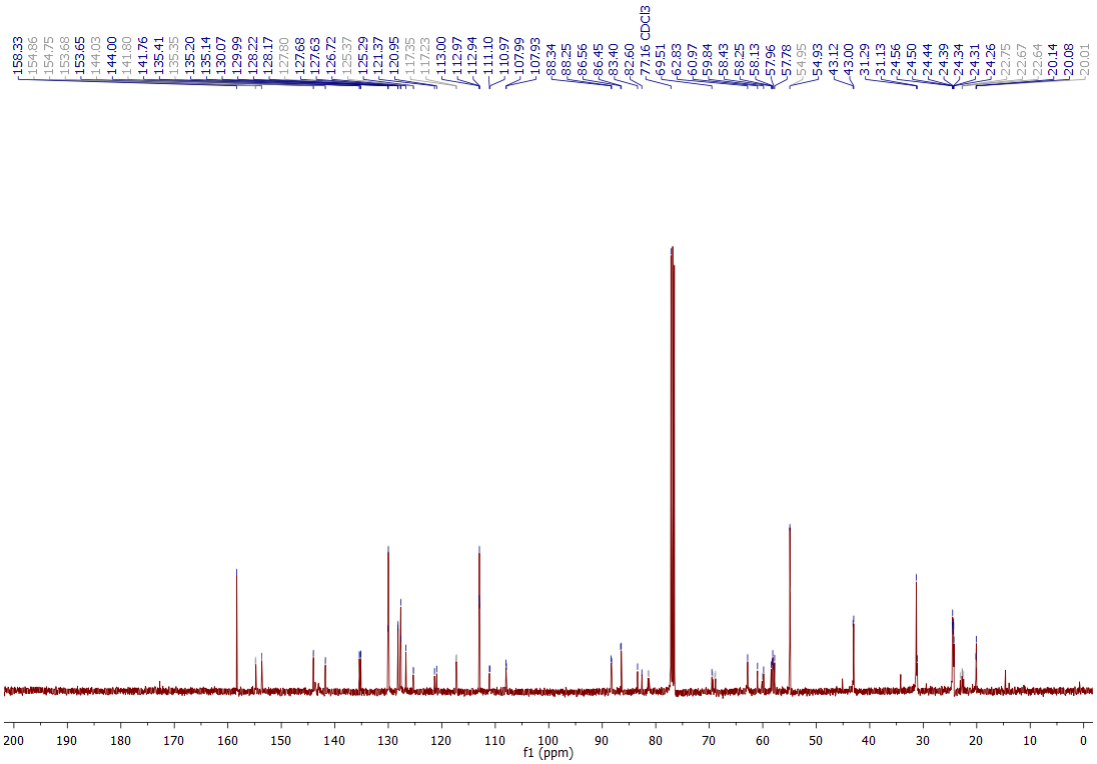

***Figure S4**. ^{13}C-NMR (101 MHz, $CDCl_3$) spectrum of **2**.*

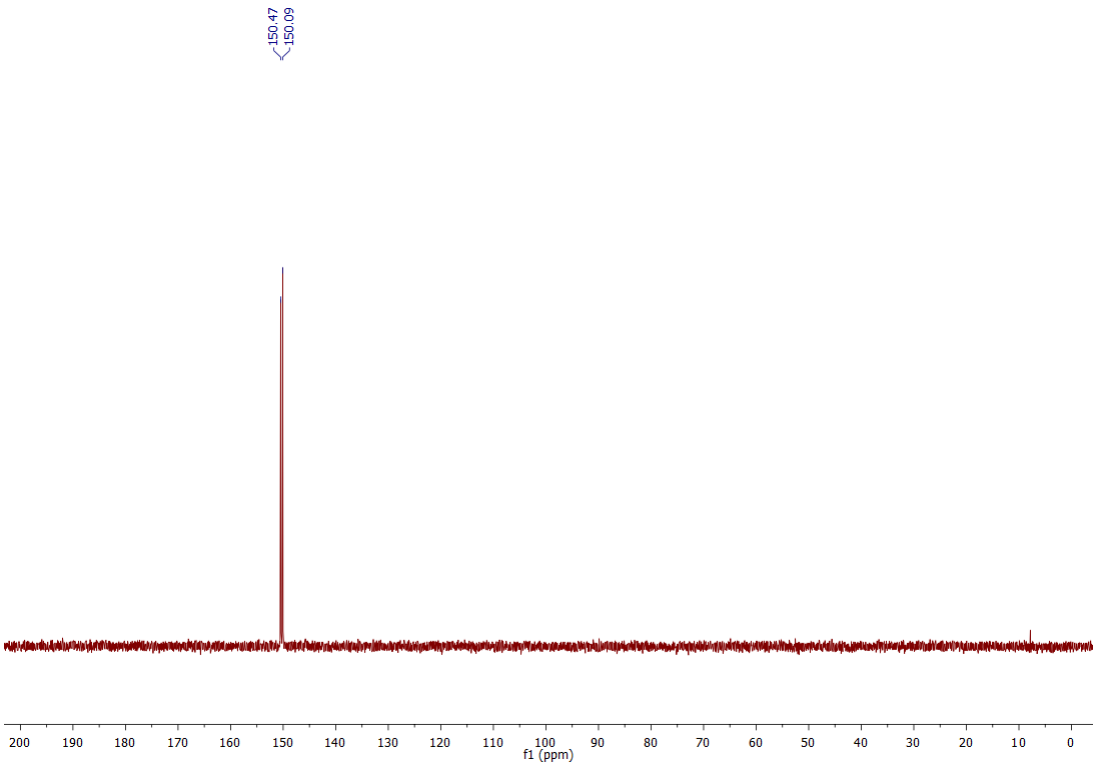

***Figure 5**. ^{31}P-NMR (400 MHz, $CDCl_3$) spectrum of **2**.*

RNA synthesis of $Ç_m^f$-labeled neomycin aptamer N1, purification and characterisation

RNA syntheses were performed on an automated ASM800 DNA synthesizer (BIOSSET Ltd., Russia) using phosphoramidite chemistry. 2'-O-TBDMS protected ribonucleoside phosphoramidites were used for all unmodified RNA oligonucleotide positions, purchased from ChemGenes Corp., USA. The activators 5-benzylthiotetrazole and 5-ethylthiotetrazole, acetonitrile for oligomer synthesis and controlled pore glass (CPG) columns (1000 Å) were purchased from ChemGenes Corp., USA. All other reagents and solvents were purchased from Sigma-Aldrich Co. **$Ç_m^f$**-modified RNA's were synthesised using phosphoramidites. Since these phosphoramidites have limited solubility in acetonitrile, they were dissolved in 1,2-dichloroethane, at a concentration of 100 mM. 5-ethylthiotetrazole was used as a coupling agent for the phosphoramidites. Coupling time was 20-30 min. For other phosphoramidites, the coupling time was set to 3 min using 5-benzylthiotetrazole (250 mM) as a coupling agent. Oxidation was performed with *tert*-butylhydroperoxide (1 M) in toluene. Capping and detritylation were performed under standard conditions for RNA synthesis with 2'-O-TBDMS phosphoramidites. After completion of RNA synthesis, the oligonucleotides were deprotected and cleaved from the resin by adding a 1:1 solution (2 mL) of CH_3NH_2 (8 M in EtOH) and NH_3 (33% w/w in H_2O) and heating for 40 min at 65 °C. The solvent was removed under reduced pressure and the 2'-O-TBDMS-protection groups were removed by incubation in $Et_3N{\cdot}3HF$ (300 µL) for 1.5 h at 55 °C in DMF (100 µL), followed by addition of sterilized and deionized water (100 µL). The resulting solution was transferred into a Falcon tube (50 mL) and the RNA was precipitated with 1-butanol (20 mL) at -20 °C over night. All oligonucleotides were subsequently purified by 20% DPAGE and extracted from the gel slices using the "crush and soak method" with Tris buffer containing 250 mM NaCl, 10 mM Tris, 1 mM Na_2EDTA, pH 7.5. The solutions were filtered through 0.45 µm, 25 mm diameter GD/X syringe filters (Whatman, USA) and were subsequently desalted using Sep-Pak cartridges (Waters, USA), following the instructions provided by the manufacturer. Dried oligonucleotides were dissolved in sterilized and deionized water (200 µL for each oligonucleotide). Concentrations of the oligonucleotides were determined by recording the UV absorbance at 260 nm using a Perkin Elmer Inc. Lambda 25 UV/Vis spectrometer and calculated by Beer′s law. The mass of the **$Ç_m^f$**-labeled oligonucleotides was determined with MALDI-TOF analyses (in linear mode, external calibration): 5'-(GGC-UG**$Ç_m^f$**-UUG-UCC-UUU-AAU-GGU-CCA-GUC): 8735.85 (Calcd. 8737.18); 5'-(GGC-UGC-U**$Ç_m^f$**G-UCC-UUU-AAU-GGU-CCA-GUC): 8736.38 (Calcd. 8736.20); 5'-(GGC-UGC-UUG-UCC-UU**$Ç_m^f$**-AAU-GGU-CCA-GUC): 8731.13 (Calcd. 8736.20); 5'-(GGC-UGC-UUG-UCC-UUU-AAU-GGU-**$Ç_m^f$**CA-GUC) 8734.03 (Calcd. 8737.18). The unlabeled strands were prepared via solid phase synthesis and purified via ion exchange HPLC by BioSpring GmbH (Frankfurt, Germany).

$Ç_m^f$-labeled model sequences

***Table S1**. Double-stranded and single-stranded model sequences.*

Sample	Sequence
ds_A$Ç_m^f$A	5'-UAC-GCA-A$Ç_m^f$A-ACG-CAU-3' 3'-AUG-CGU-UGU-UGC-GUA-5'
ds_C$Ç_m^f$C	5'-UAC-GCA-C$Ç_m^f$C-ACG-CAU-3' 3'-AUG-CGU-GGG-UGC-GUA-5'
ds_G$Ç_m^f$G	5'-UAC-GCA-G$Ç_m^f$G-ACG-CAU-3' 3'-AUG-CGU-CGC-UGC-GUA-5'
ds_U$Ç_m^f$U	5'-UAC-GCA-U$Ç_m^f$U-ACG-CAU-3' 3'-AUG-CGU-AGA-UGC-GUA-5'
ss_A$Ç_m^f$A	5'-UAC-GCA-A$Ç_m^f$A-ACG-CAU-3'
ss_C$Ç_m^f$C	5'-UAC-GCA-C$Ç_m^f$C-ACG-CAU-3'
ss_G$Ç_m^f$G	5'-UAC-GCA-G$Ç_m^f$G-ACG-CAU-3'
ss_U$Ç_m^f$U	5'-UAC-GCA-U$Ç_m^f$U-ACG-CAU-3'

Absorption melting experiments

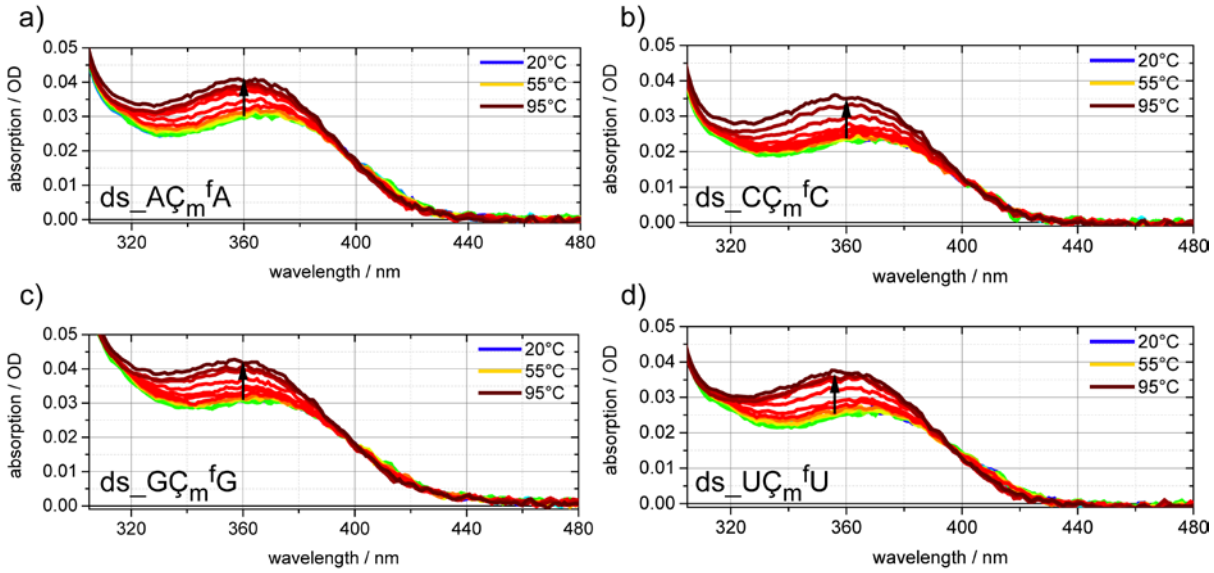

***Figure S6**. Absorption of **Çm**f upon melting of the double-strands. a) ds_A**Çm**fA, b) ds_C**Çm**fC, c) ds_G**Çm**fG and d) ds_U**Çm**fU.*

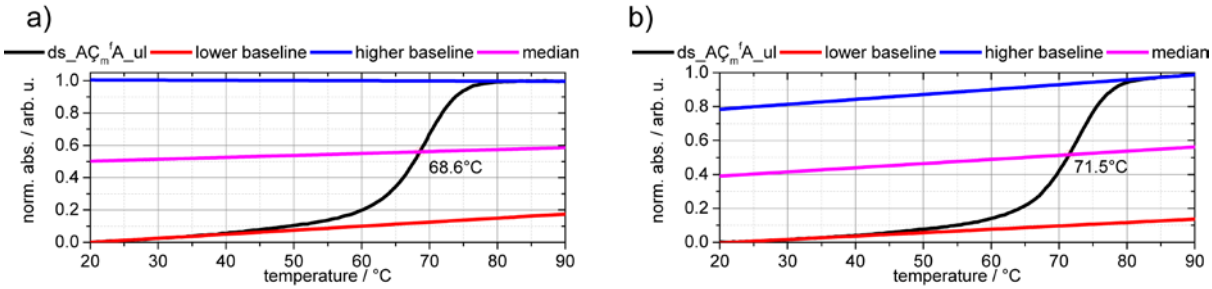

***Figure S7**. Exemplary absorption melting curve analysis of ds_A**Çm**fA_ul. a) cooling curve observed at 260 nm, b) heating curve observed at 260 nm.*

Emission melting experiments

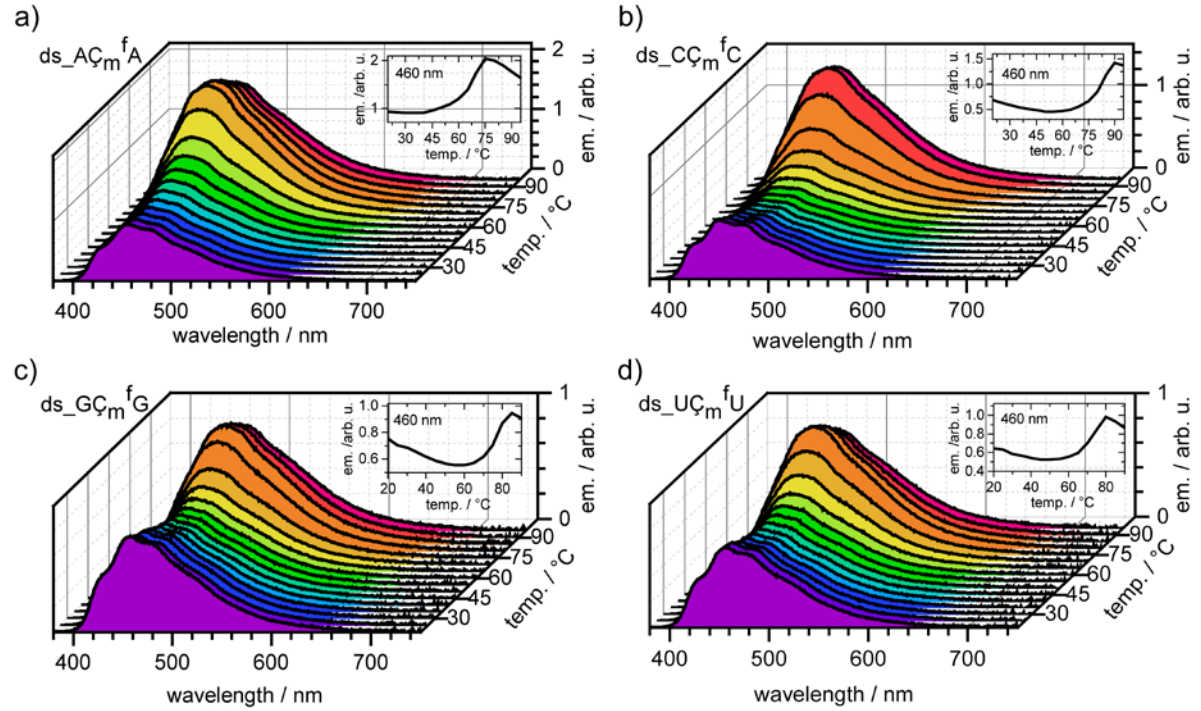

***Figure S8**. Emission of **Çm**f upon melting of the double-strands. a) ds_A**Çm**fA, b) ds_C**Çm**fC, c) ds_G**Çm**fG, d) ds_U**Çm**fU.*

***Table S2**. Melting temperatures of the **Çm**f-labeled benchmark sequences determined by the emission change at different excitation wavelengths.*

Sample	T_{melt} at 448 nm / °C	T_{melt} at 461 nm / °C	T_{melt}@475 nm / °C	mean T_{melt} / °C
ds_A**Çm**fA	67.4	67.3	67.3	67.3
ds_C**Çm**fC	81.2	81.3	80.6	81.0
ds_G**Çm**fG	75.9	75.7	75.7	75.8
ds_U**Çm**fU	70.1	69.9	70.4	70.1

***Table S3**. Melting temperatures and thermodynamic parameters of the unlabeled and labeled model sequences.*

Sample	**Unlabeled**				**Labeled**					ΔT_m / °C	ΔΔG/ kcal/ mol
	T_{m_ab}/ °C	-ΔH/ kcal/ mol	-ΔS/ cal/ mol	$-\Delta G_{abs}$/ kcal/ mol	T_{m_ab}/ °C	T_{m_em}/ °C	$-\Delta H_{abs}$/ kcal/ mol	$-\Delta S_{abs}$/ cal/ mol	$-\Delta G_{abs}$/ kcal/ mol		
A**Çm**fA	70	102	272	18	67	67	56	140	13	3	-5
C**Çm**fC	81	95	245	20	82	81	59	141	15	1	-5
G**Çm**fG	78	90	231	18	76	76	54	129	14	2	-4
U**Çm**fU	70	94	248	17	72	70	70	177	15	2	-2

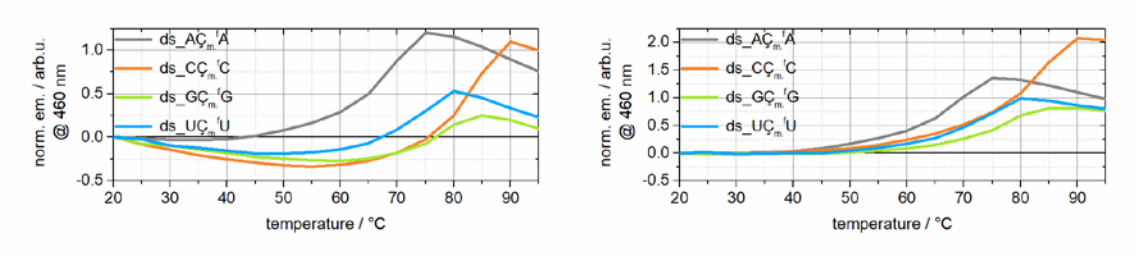

***Figure S9**. Fluorescence monitored melting curves of **Çm**^{f}-labeled double-strands at 460 nm. All curves were set to zero at 20 °C. Without (a) and with (b) baseline correction for collisional quenching effects.*

***Table S4**. Melting temperatures of the **Çm**^{f}-labeled benchmark sequences determined by the emission change at 460 nm. Compression of determined values with and without baseline correction for collisional quenching effects.*

Sample	T_{melt} at 461 nm / °C (without baseline correction)	T_{melt} at 461 nm / °C (with baseline correction)
ds_A**Çm**^{f}A	67	67
ds_C**Çm**^{f}C	81	80
ds_G**Çm**^{f}G	76	76
ds_U**Çm**^{f}U	70	72

MATLAB script for spectrally resolved melting analysis

```
%Spectrally resolved melting analysis
%_____________________________________________________________________________
%Script determines the amount of double stranded RNA in a Cmf-labeled RNA sample

%-------------------------------------------------------------------------
%The fitfunction is defined seperatly as meltfit.m:
%function Fitting = meltfit(x,lb_x,ub_x)
%global ds ss sample
%Fitting = sample - ((1-x)*ss + x*ds);
%end
%-------------------------------------------------------------------------

option = optimset('Display','iter','TolFun',1e-30,...    %options of fit
    'TolX',1e-60,'MaxIter',500,'MaxFunEvals',1000);

global ds ss sample %global variables

ds = ds_inp(123:475); % spectrum of 100% double strand. Cropped to exclude excitation peak.
ss = ss_inp(123:475); % spectrum of 100% single strand. Cropped to exclude excitation peak.
sample = sample_inp(123:475); % spectrum unknown amount of double and single strand. Croped to
exclude excitation peak.

x=0.5; %start value
x_lb=0; %lower boundary
x_ub=1; %upper boundary

[fit,resnorm,residual] = lsqnonlin(@meltfit,x,x_lb,x_ub,option); %Fit of function meltfit

%-------------------------------------------------------------------------
%Plotting of results

figure
plot(fit*ds, 'r')
hold on
plot((1-fit)*ss, 'g')
plot(sample, 'k')
plot(fit*ds+(1-fit)*ss,'m')
plot(residual,'b')
legend ('ds', 'ss', 'sample', 'fit', 'res')
grid on

%-------------------------------------------------------------------------
```

Steady-State emission measurements

***Table S5**. Absolute quantum yields of the single **Ç$_m^f$**-labeled single- (ss) and double-stranded (ds) RNA model sequences.*

Sample	Quantum yield / %		
	ds	ss	ss/ds
A**Ç$_m^f$**A	25	54	2.2
C**Ç$_m^f$**C	22	39	1.8
G**Ç$_m^f$**G	26	42	1.6
U**Ç$_m^f$**U	22	41	1.9
mean	24	44	1.8

***Table S6**. Steady-state anisotropy of the single **Ç$_m^f$**-labeled single- (ss) and double-stranded (ds) RNA model sequences.*

Sample	Steady-state anisotropy at 20 °C		
	ds	ss	ds/ss
A**Ç$_m^f$**A	0.12	0.08	1.5
C**Ç$_m^f$**C	0.14	0.11	1.3
G**Ç$_m^f$**G	0.14	0.09	1.6
U**Ç$_m^f$**U	0.17	0.09	1.9
mean	0.14	0.09	1.6

Reduced chi-square (χ^2)

In case of the time-resolved emission measurements, the reduced chi-square-value (χ^2) is used as measure of the quality of the fit:

$$\chi^2 = \frac{1}{N-p}\sum_{i=1}^{N}\frac{(Decay(i) - Fit(i))^2}{Decay(i)}$$

I = channel

N = number of channels/ data points

P = number of fitted parameters

N-p = degree of freedom

Decay(i) = array of N measured intensity (count) values

Fit(i) = array of N calculated intensity values

Time-resolved emission measurements at 20°C

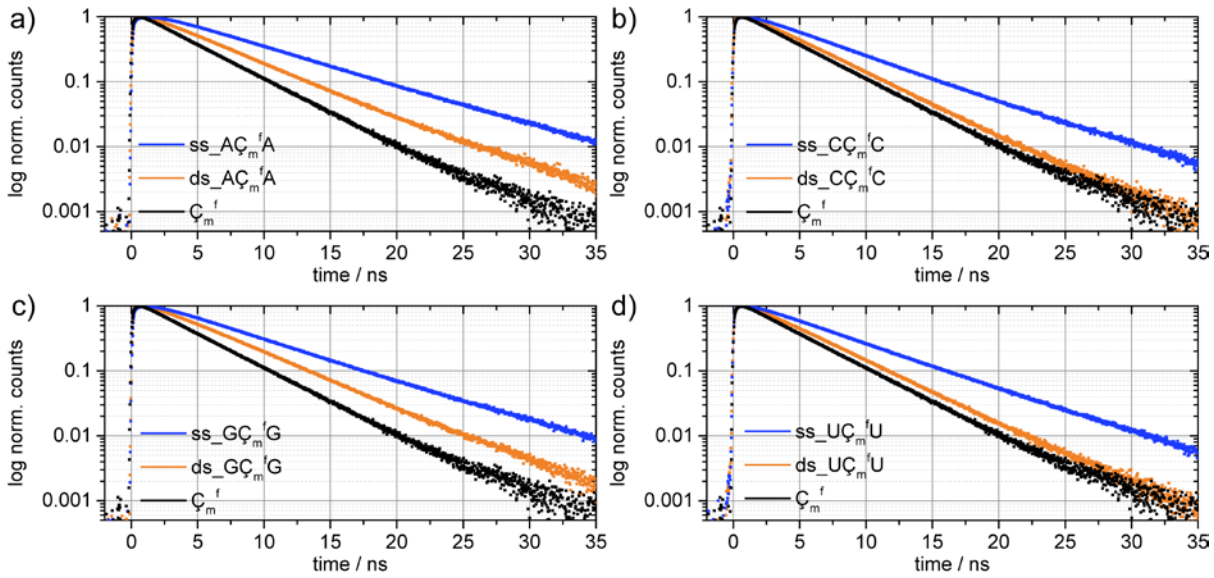

***Figure S10**. Comparison of normalized fluorescence decays of **Çm**^{f}-labeled single and double strands with the free label in solution. a) A**Çm**^{f}A, b) C**Çm**^{f}C, c) G**Çm**^{f}G, d) U**Çm**^{f}U.*

***Table S7**. Comparison of the average fluorescence lifetimes (τ_{av}) of **Çm**^{f}-labeled single and double strands and the free label in solution at 20 °C.*

Sample	τ_{av}	$\Delta\ \tau_{av}$	$1/\ \tau_{av}$
Çm^f	4.2	0.1	0.24
ds_A**Çm**^{f}A	5.3	0.1	0.19
ss_A**Çm**^{f}A	7.5	0.1	0.13
ds_C**Çm**^{f}C	4.5	0.1	0.22
ss_C**Çm**^{f}C	6.4	0.1	0.16
ds_G**Çm**^{f}G	5.2	0.1	0.19
ss_G**Çm**^{f}G	7	0.1	0.14
ds_U**Çm**^{f}U	4.6	0.1	0.22
ss_U**Çm**^{f}U	6.5	0.1	0.15

Temperature dependent fluorescence lifetime measurements

The assignment of decay components of the fluorescence lifetime for the labeled RNA double- and single-strands enables a more detailed analysis of the melting process via the temperature dependence of the fluorescence lifetime. Therefore, the samples were heated up in 10°C steps and the fluorescence lifetime was measured for every step.

The compression and discussion of three trajectories of the three lifetime components can be quite complicated for the different samples (see **Table S8–Table S15**). Especially because partial

compensation can never be ruled out completely. Hence, the average lifetimes (τ_{av}) were calculated for each temperature to quantify the observed effects. For an additional graphical evaluation, the normalized fluorescence decay at 20°C was subtracted from the normalized decay at all other temperatures. The differences were plotted as temperature dependent transient maps. Additionally, a cut through each of these maps at 20 ns was plotted.

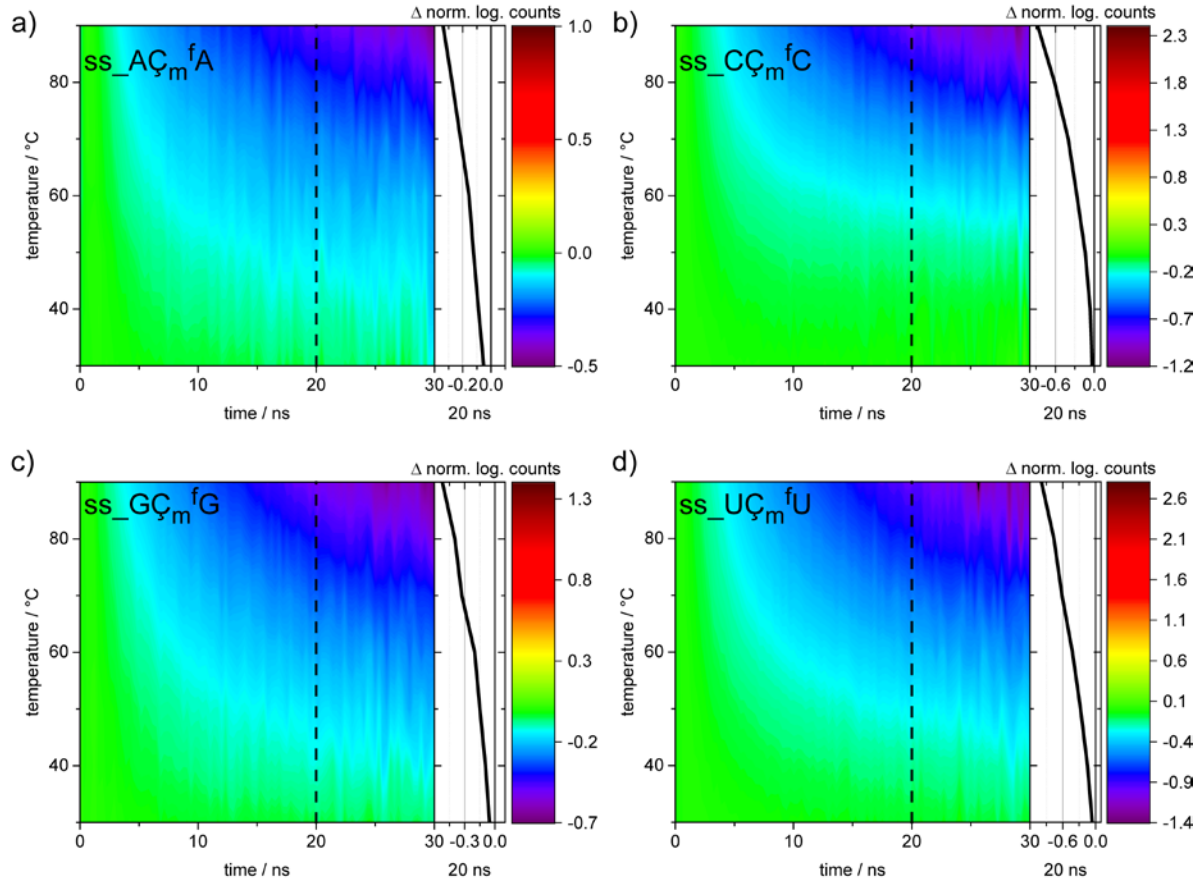

***Figure S11**. Temperature dependent transient maps of fluorescence lifetime measurements on the **Çm^f**-labeled single strands. a) ss_A**Çm^f**A, b) ss_C**Çm^f**C, c) ss_G**Çm^f**G, d) ss_U**Çm^f**U.*

Initially, a decrease of the fluorescence lifetime can be observed for all double- and single-strands. This is true for all decay components and can be explained with increased collisional quenching due to increased movement at higher temperatures. However, the increase varies for the four single-stranded samples (collisional quenching effect: ss_C**Çm^f**C > ss_U**Çm^f**U > ss_G**Çm^f**G> ss_A**Çm^f**A) and is not perfectly linear. Hence, τ_{av} is not only affected by collisional quenching. One reason for this order might be intramolecular base stacking interactions and other shielding effects against unspecific solvent interactions. These effects might be bigger in case of neighbouring purine bases, which explains the observed order. The kink in decrease might be due to the break of these effects. Albeit, in this case the pronounced kink for ss_C**Çm^f**C is remarkable, because here one would expect only weak stacking interactions.

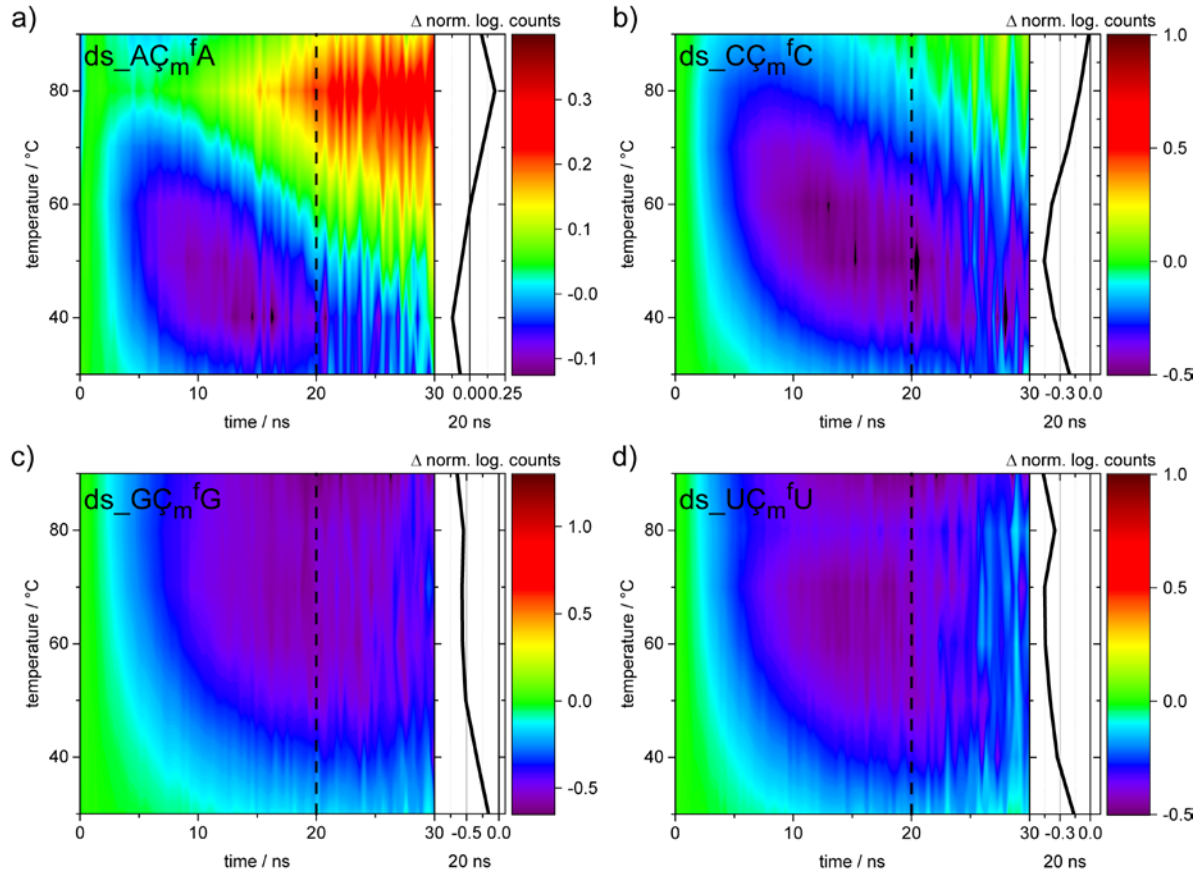

***Figure S12**. Temperature dependent transient maps of fluorescence lifetime measurements on the **Çm**f-labeled double-strands. a) ds_A**Çm**fA, b) ds_C**Çm**fC, c) ds_G**Çm**fG, d) ds_U**Çm**fU.*

For the double-stranded samples the trajectories are more complicated. The τ_{av} of the double-strands is decreasing with rising temperature, too. However, near the respective melting temperatures, τ_{av} becomes constant or increases again. This effect must be due to the melting of the double-strands and can be observed especially via the overall contribution of the longest decay component τ_2, which increases starting from around the melting point of the duplexes. The increasing amount of single-strands with longer fluorescence lifetimes increases the average lifetime of the melting double-strands sample. For ds_A**Çm**fA and ds_C**Çm**fC the increase of τ_{av} upon melting is so strong that the effect of the collisional quenching is compensated. For ds_G**Çm**fG and ds_U**Çm**fU the increase upon melting and the decrease due to collisional quenching are equally pronounced which leads to roughly steady fluorescence lifetimes starting from the melting point of the samples.

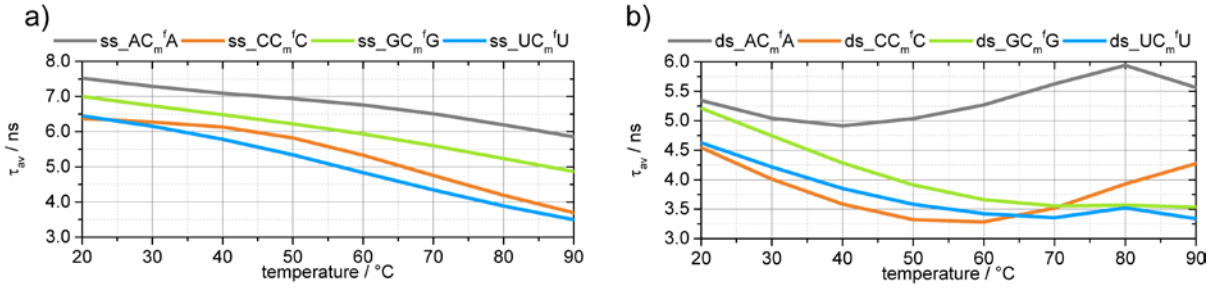

***Figure S13**. Temperature dependency of the τ_{av} for the **Çm**f-labeled a) single- (ss) and b) double-strands (ds).*

In some cases, and after complete separation of the strands the collisional quenching effect dominates again. This leads once more to a decrease of the fluorescence lifetimes. This only can be seen for the samples with low melting points (ds_A**Ç$_m^f$**A and ds_U**Ç$_m^f$**U). Especially, it is very pronounced for ds_A**Ç$_m^f$**A. For the samples with higher melting points, there has still to be compensation between lifetime increase due to higher amounts of labeled single-strands and lifetime decrease due to more collusions at higher temperatures.

***Table S8**. Temperature dependent fluorescence lifetime of ds_AÇ$_m^f$A.*

Temperature / °C	τ_{pop} / ns	τ_1 / ns	τ_2 / ns	χ^2	τ_{av} / ns
20	1.5	4.6 (89%)	7.6 (11%)	1.2	5.3
30	1.4	4 (86%)	7.4 (14%)	1.1	5.0
40	1.0	3.6 (83%)	7.4 (17%)	1.1	4.9
50	0.8	3.2 (76%)	7.2 (24%)	1.1	5.0
60	0.7	2.8 (67%)	7 (33%)	1.1	5.3
70	0.5	2.6 (52%)	6.7 (48%)	1.1	5.6
80	0.4	3.3 (39%)	6.6 (61%)	1.0	5.9
90	0.4	3 (41%)	6.3 (59%)	1.1	5.6

τ_{pop} = lifetime with a negative amplitude, representing the population of a fluorescent state. τ_n = lifetime with a positive amplitude, representing the depopulation of a fluorescent state. τ_{av} = average fluorescence lifetime. X^2 = reduced chi-square, as measure of the goodness of the fit.

***Table S9**. Temperature dependent fluorescence lifetime of ss_AÇ$_m^f$A.*

Temperature / °C	τ_{pop} / ns	τ_1 / ns	τ_2 / ns	χ^2	τ_{av} / ns
20	1.5	6.4 (71%)	8.5 (71%)	1.1	7.5
30	1.3	6.1 (69%)	8.3 (69%)	1.1	7.3
40	1	5.6 (52%)	7.7 (52%)	1.2	7.1
50	0.9	5.1 (40%)	7.4 (40%)	1.1	6.9
60	0.7	4.7 (37%)	7.3 (37%)	1.1	6.8
70	0.6	4.2 (34%)	7 (34%)	1.0	6.5
80	0.5	3.9 (35%)	6.7 (35%)	1.1	6.2
90	0.4	3.5 (35%)	6.4(35%)	1.1	5.9

τ_{pop} = lifetime with a negative amplitude, representing the population of a fluorescent state. τ_n = lifetime with a positive amplitude, representing the depopulation of a fluorescent state. τ_{av} = average fluorescence lifetime. X^2 = reduced chi-square, as measure of the goodness of the fit.

***Table S10**. Temperature dependent fluorescence lifetime of ds_C**Ç**$_m^f$C.*

Temperature / °C	τ_{pop} / ns	τ_1 / ns	τ_2 / ns	χ^2	τ_{av} / ns
20	1.7	4.1 (96%)	6.8 (4%)	1.1	4.5
30	1.7	3.4 (93%)	6 (7%)	1.3	4.0
40	1.6	2.9 (92%)	5.7 (8%)	1.3	3.6
50	1.2	2.5 (92%)	5.9 (8%)	1.3	3.3
60	1.0	2.2 (89%)	5.9 (11%)	1.3	3.3
70	0.8	1.9 (82%)	5.6 (18%)	1.3	3.5
80	0.5	1.8 (71%)	5.5 (29%)	1.3	3.9
90	0.4	1.8 (50%)	5.1 (50%)	1.2	4.3

τ_{pop} = lifetime with a negative amplitude, representing the population of a fluorescent state. τ_n = lifetime with a positive amplitude, representing the depopulation of a fluorescent state. τ_{av} = average fluorescence lifetime. X^2 = reduced chi-square, as measure of the goodness of the fit.

***Table S11**. Temperature dependent fluorescence lifetime of ss_C**Ç**$_m^f$C.*

temperature / °C	τ_{pop} / ns	τ_1 / ns	τ_2 / ns	χ^2	τ_{av} / ns
20	1.5	5.1 (77%)	8.2 (23%)	1.1	6.4
30	1.3	4.4 (60%)	7.5 (40%)	1.1	6.3
40	1	4.1 (55%)	7.2 (45%)	1.1	6.1
50	0.7	3.7 (53%)	6.9 (47%)	1.1	5.8
60	0.5	3.4 (54%)	6.4 (46%)	1.1	5.3
70	0.5	3 (57%)	5.8 (43%)	1.1	4.8
80	0.4	2.7 (60%)	5.2 (40%)	1.1	4.2
90	0.3	2.4 (60%)	4.6 (40%)	1.2	3.7

τ_{pop} = lifetime with a negative amplitude, representing the population of a fluorescent state. τ_n = lifetime with a positive amplitude, representing the depopulation of a fluorescent state. τ_{av} = average fluorescence lifetime. X^2 = reduced chi-square, as measure of the goodness of the fit.

***Table S12**. Temperature dependent fluorescence lifetime of ds_G**Ç**$_m^f$G.*

Temperature / °C	τ_{pop} / ns	τ_1 / ns	τ_2 / ns	χ^2	τ_{av} / ns
20	2.3	4.7 (97%)	7.5 (3%)	1.3	5.2
30	2.1	4.2 (96%)	7.2 (4%)	1.4	4.7
40	1.7	3.7 (92%)	6.2 (8%)	1.3	4.3
50	1.4	3.3 (92%)	6.3 (8%)	1.3	3.9
60	1	2.9 (89%)	6 (11%)	1.2	3.7
70	0.8	2.5 (83%)	5.5 (17%)	1.2	3.6
80	0.5	2.3 (73%)	5 (27%)	1.2	3.6
90	0.3	2.2 (61%)	4.5 (39%)	1.2	3.5

τ_{pop} = lifetime with a negative amplitude, representing the population of a fluorescent state. τ_n = lifetime with a positive amplitude, representing the depopulation of a fluorescent state. τ_{av} = average fluorescence lifetime. X^2 = reduced chi-square, as measure of the goodness of the fit.

***Table S13**. Temperature dependent fluorescence lifetime of ss_G**Ç**$_m^f$G.*

Temperature / °C	τ_{pop} / ns	τ_1 / ns	τ_2 / ns	χ^2	τ_{av} / ns
20	1.6	5.6 (69%)	8.2 (31%)	1.1	7.0
30	1.3	5.4 (69%)	8 (31%)	1.1	6.7
40	1.1	5 (62%)	7.6 (38%)	1.1	6.5
50	0.8	4.7 (56%)	7.2 (44%)	1.2	6.2
60	0.6	4.2 (47%)	6.7 (53%)	1.1	5.9
70	0.5	3.7 (43%)	6.3 (57%)	1.2	5.6
80	0.5	3.2 (37%)	5.7 (63%)	1.1	5.2
90	0.4	3 (38%)	5.4 (62%)	1.2	4.9

τ_{pop} = lifetime with a negative amplitude, representing the population of a fluorescent state. τ_n = lifetime with a positive amplitude, representing the depopulation of a fluorescent state. τ_{av} = average fluorescence lifetime. X^2 = reduced chi-square, as measure of the goodness of the fit.

***Table S14**. Temperature dependent fluorescence lifetime of ds_U**Ç**$_m^f$U.*

Temperature / °C	τ_{pop} / ns	τ_1 / ns	τ_2 / ns	χ^2	τ_{av} / ns
20	1.6	4.2 (97%)	7.4 (3%)	1.1	4.6
30	1.4	3.8 (96%)	6.8 (4%)	1.2	4.2
40	1.3	3.3 (94%)	6.2 (6%)	1.2	3.8
50	1	3 (93%)	6.3 (7%)	1.2	3.6
60	0.7	2.6 (89%)	5.8 (11%)	1.2	3.4
70	0.6	2.3 (83%)	5.2 (17%)	1.1	3.4
80	0.4	2.1 (66%)	4.6 (34%)	1.2	3.5
90	0.3	1.9 (55%)	4.1 (45%)	1.2	3.3

τ_{pop} = lifetime with a negative amplitude, representing the population of a fluorescent state. τ_n = lifetime with a positive amplitude, representing the depopulation of a fluorescent state. τ_{av} = average fluorescence lifetime. X^2 = reduced chi-square, as measure of the goodness of the fit.

***Table S15**. Temperature dependent fluorescence lifetime of ss_U**Ç**$_m^f$U.*

Temperature / °C	τ_{pop} / ns	τ_1 / ns	τ_2 / ns	χ^2	τ_{av} / ns
20	1.9	3.9 (36%)	6.8 (64%)	1.2	6.5
30	1.2	4.3 (40%)	6.7 (60%)	1.3	6.2
40	0.9	3.9 (46%)	6.5 (54%)	1.1	5.8
50	0.7	3.4 (49%)	6.1 (51%)	1.2	5.3
60	0.6	3 (51%)	5.7 (49%)	1.2	4.8
70	0.5	2.7 (55%)	5.2 (45%)	1.2	4.3
80	0.4	2.4 (54%)	4.7 (46%)	1.2	3.9
90	0.3	2.1 (52%)	4.1 (48%)	1.2	3.5

τ_{pop} = lifetime with a negative amplitude, representing the population of a fluorescent state. τ_n = lifetime with a positive amplitude, representing the depopulation of a fluorescent state. τ_{av} = average fluorescence lifetime. X^2 = reduced chi-square, as measure of the goodness of the fit.

Femtosecond transient absorption spectroscopy

Transient absorption spectroscopy (TAS) of the **Çm^f**-labeled double-strands was performed with a home-built pump-probe setup.(1) As source for the femtosecond laser pulses, an oscillator-amplifier system (CPA-2001, Clark-MXR, Michigan, USA) operating at a repletion rate of 1 kHz (775 nm, pulse width of 150 fs) was used. Excitation at 388 nm was obtained by second harmonic generation (SHG) of the 775 nm beam in a beta-barium borate (β-BaB2O4, BBO) crystal. Probe pulses with a spectral range from 380 nm to 680 nm were generated in a CaF_2 crystal. These pulses were split into a signal and a reference beam. For detection, each probe pulse was guided to a spectrograph (HR320, HORIBA, Kyoto, Japan). The signals were detected with the help of a photodiode array combined with a signal processing chip (S8865-128, Hamamatsu Photonics, Hamamatsu, Japan)) and a driver circuit (C9118, Hamamatsu Photonics). For digitalization, a data acquisition card (NI-PCI-6120, National Instruments, Austin, USA) was used. The samples were prepared in UV-grade quartz cuvettes with 1 mm optical path length (21/Q/1, Starna GmbH). To prevent possible reexcitation of already excited molecules, the cuvette was moved in the two directions perpendicular to the excitationpulses. The sample was excited with pulse energies of ≤ 30 nJ in the magic angle (54.7°) to eliminate anisotropy.(2) Data processing was performed with the OPTIMUS 2.08 software.(3)

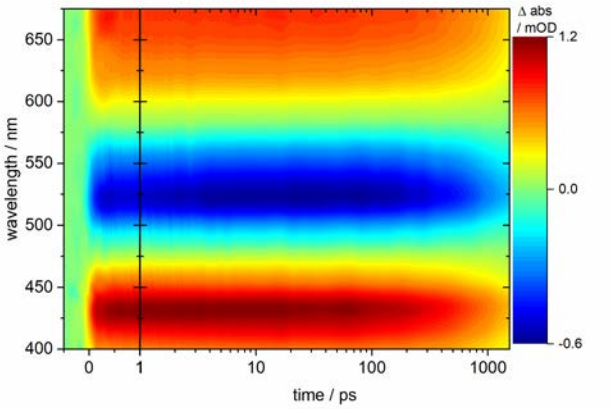

***Figure S13**. Transient card of ds_AÇm^{f}A, as an example for the transient absorption measurements.*

For all **Çm^f**-labeled double-strands, three different transient absorption signals between 400 nm and 675 nm can be identified, which were very similar to the transient absorption signals of the free label in solution: A positive band is observed between 400 nm and 475 nm and another one between 580 nm and 675 nm. The two bands are attributed to excited-state absorption (ESA). Between the ESA signals, from 475 nm to 580 nm, a negative signal was detected. All three signals appear instantaneously after photoexcitation. As the negative signal coincides spectrally with the steady-state fluorescence even though it is partially compensated by the neighbouring ESA, it is identified as stimulated emission (SE). Due to the high-energy ESA, it is also not possible to see the ground state bleach (GSB) as a negative signal in the transient card. All signals gain intensity within the first 10 ps of the measurement. Thereafter, there is a decay of the signals which is not completed within the measurement window.

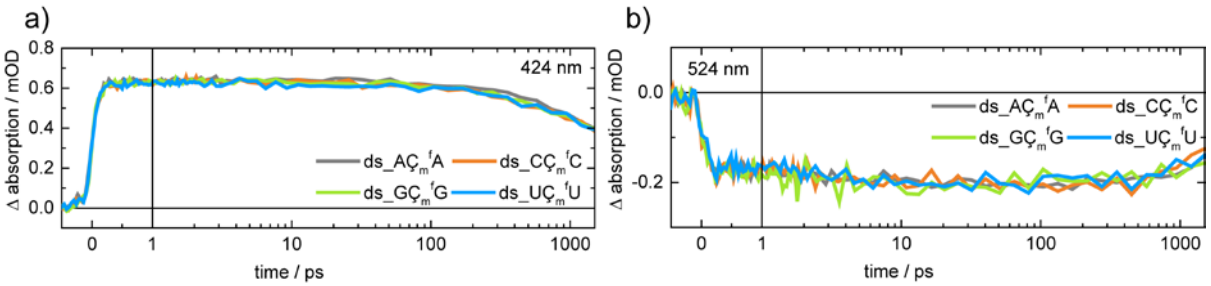

***Figure S14**. Selected normalized transients of the femtosecond transient absorption measurement of the **Çm**^{f}-labeled double strands at a) 424 nm and b) 524 nm.*

In **Figure S14** selected normalized transients for the ESA (424 nm) and the SE (524 nm) for the four different **Çm**^{f}-labeled double-strands are presented. It can be noticed, that these fast dynamics (ps range) of the fluorescence label are not affected by the direct neighbouring nucleotides. Also, with help of the fluorescence lifetime measurements, the ns components of the four samples differ significantly. Nevertheless, this time a range cannot be observed with the help of the above described transient absorption setup.

The $Ç_m^f$-labeled neomycin aptamer N1

__Table S16__. Sequences of the __$Ç_m^f$__-labeled neomycin aptamer.

Sample	Sequence
$Ç_m^f$6	5‘-GGC-UG**$Ç_m^f$**-UUG-UCC-UUU-AAU-GGU-CCA-GUC-3‘
$Ç_m^f$8	5‘-GGC-UGC-U**$Ç_m^f$**G-UCC-UUU-AAU-GGU-CCA-GUC-3‘
$Ç_m^f$15	5‘-GGC-UGC-UUG-UCC-UU**$Ç_m^f$**-AAU-GGU-CCA-GUC-3‘
$Ç_m^f$22	5‘-GGC-UGC-UUG-UCC-UUU-AAU-GGU-**$Ç_m^f$**CA-GUC-3‘

Steady-state emission experiments

The addition of 10 mM $MgCl_2$ and 1 mM spermidine to **$Ç_m^f$8** (1 µM; with and without neomycin) increases the fluorescence quantum yield of the sample (**Figure S15a**). Nevertheless, the relative fluorescence quantum yield increase upon ligand is not affected by the presence of Mg^{2+} and spermidine in this concentration.

The spectral shapes for ss_C**$Ç_m^f$**C, ds_C**$Ç_m^f$**C and **$Ç_m^f$22** are all similar to each other with and without neomycin (**Figure S15b**).

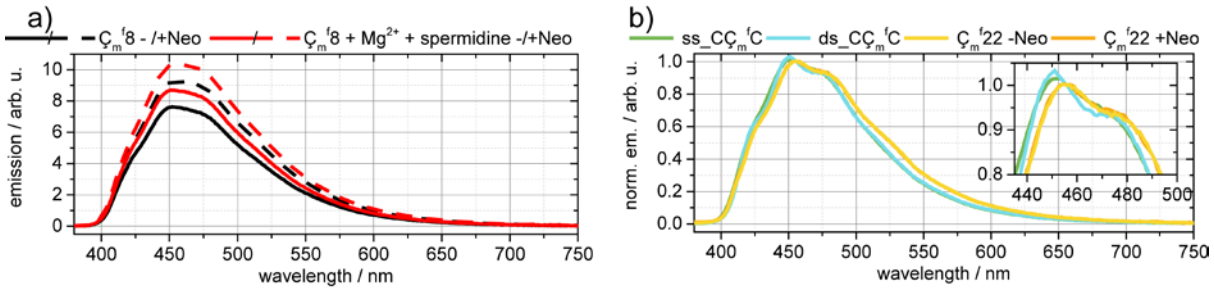

__Figure S15__. a) Influence of spermidine and Mg^{2+} on the steady-state signal of __$Ç_m^f$8__ with and without neomycin. The fluorescence quantum yield increases upon spermidine and Mg^{2+} addition, but the quantum yield is not affected upon addition of neomycin. b) Normalized emission spectra of ss_C__$Ç_m^f$__C and ds_C__$Ç_m^f$__C in comparison to __$Ç_m^f$22__ with (+ __Neo__) and without neomycin (- __Neo__).

Stopped-flow measurements

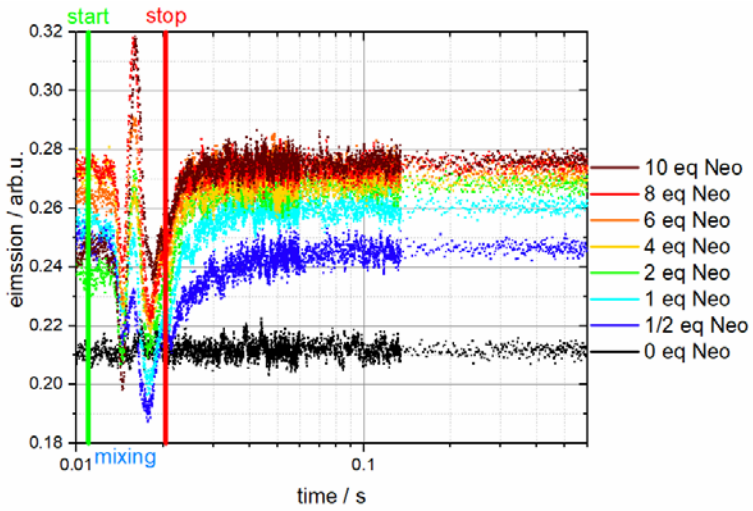

***Figure S16**. Raw data: Transient fluorescence signals after stopped-flow mixing of 4 µM **Çₘᶠ8** with different concentrations of neomycin solutions. Show is the complete measurement with prior period and mixing phase. The binding dynamic is finished within 30 ms after stop of mixing.*

DynaFit4 analysis

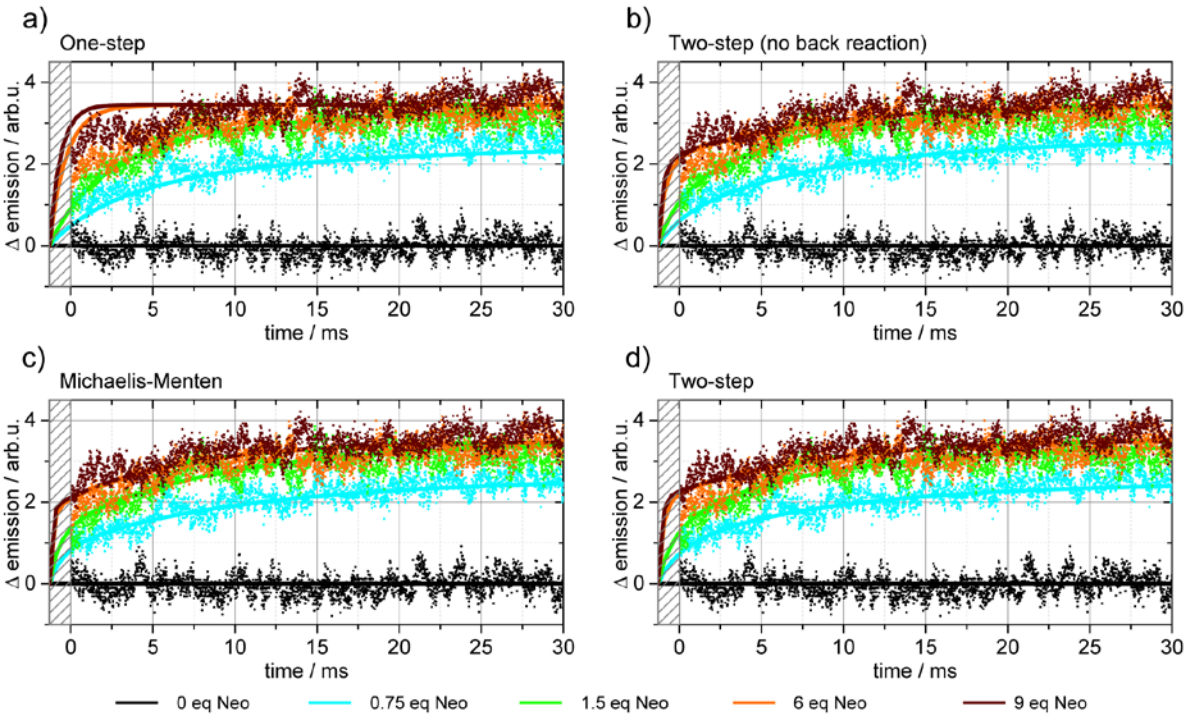

***Figure S17**. Transient fluorescence signals after stopped-flow mixing of 2.7 µM **Çₘᶠ6** with different concentrations of neomycin solutions in comparison to fits of four different kinetic binding models. a) One-step binding model, b) two-step binding model (without back reactions), c) Michaelis-Menten binding model, d) Two-step binding model.*

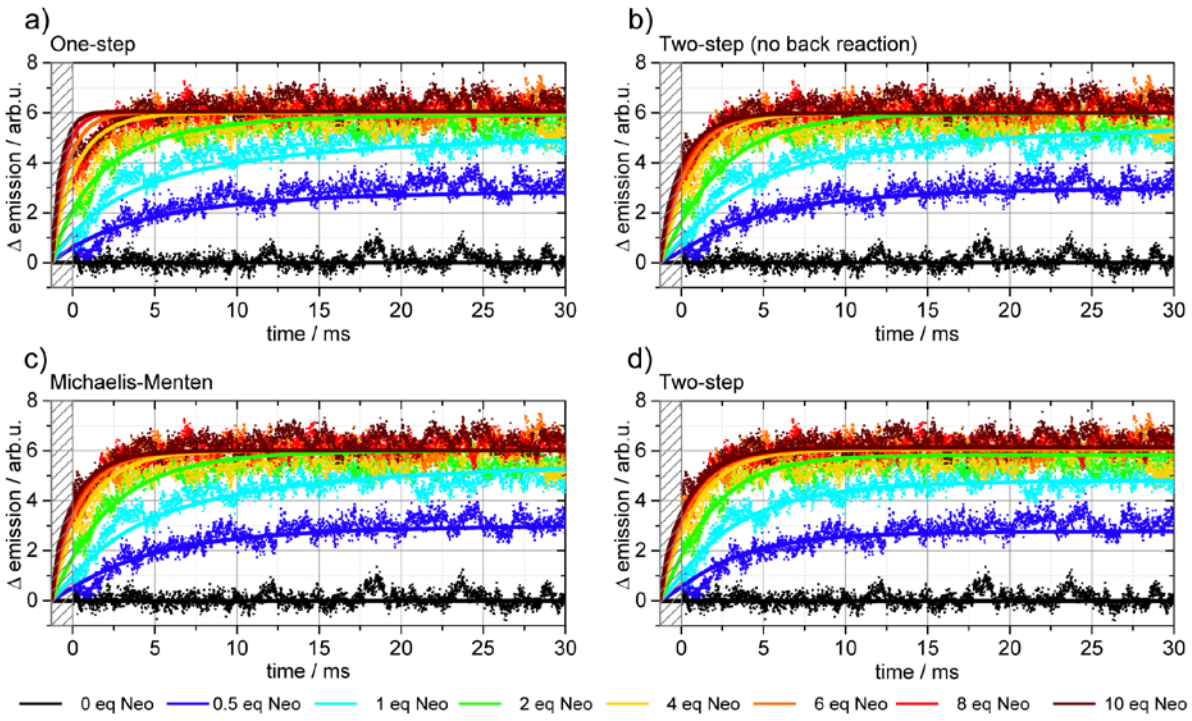

***Figure S18**. Transient fluorescence signals after stopped-flow mixing of 4 µM **Çm^{f}8** with different concentrations of neomycin solutions in comparison to fits of four different kinetic binding models. a) One-step binding model, b) two-step binding model (without back reactions), c) Michaelis-Menten binding model, d) Two-step binding model.*

In **Figure S17** and **Figure S18** the transient fluorescence signals after stopped-flow mixing of **Çm^{f}6** and **Çm^{f}8** with different concentrations of a neomycin solutions in comparison to fits of the four different kinetic binding models are shown. The fits for the one-step model do not rise fast enough to describe the transients of the lower neomycin concentration. In case of the higher neomycin concentrations the signal rise is to strong and fast. The situation is quite similar in the case of the two-step model without backreaction and in case of the Michaelis-Menten model. Although, in these cases the transients with lower neomycin concentrations are better described as with the one step model. The two-step model with backreactions describes the data quite well. Nevertheless, the fit of the 0.5 eq (**Çm^{f}8**) neomycin transient is not perfect. This might be due to additional diffusion effects, which only become important in under equimolar situations.

DynaFit4 analysis considering a heterogeneous sample

***Table S17**. Fit results of the tested binding models for the transient **$Ç_m^f$6** stopped-flow data considering a heterogeneous sample.*

Model	x	k_{1x} / $(\mu Ms)^{-1}$	k_{-1x} / s^{-1}	k_{2x} / s^{-1}	k_{-2x} / s^{-1}	$r(A_x)$ / arb.u.	$r(A_xL^*)$ / arb.u.	$r(A_xL)$ / arb.u.	RMSD	ΔAIC
One-step	-	131	3	-	-	0.094	-	0.12	0.0036	13654
Two-step (no back reaction)	-	311	-	113	-	0.094	0.11	0.12	0.0029	4201
Michaelis-Menten	-	662	178	141	-	0.094	0.11	0.12	0.0028	3379
Two-step	-	425	48	80	31	0.094	0.11	0.125	0.0028	2992
2 x one-step	**A**	0.002	$6{\cdot}10^{-7}$	-	-	$5{\cdot}10^{-8}$	-	8.8	0.0029	4532
	B	297	$6{\cdot}10^{-7}$	-	-	0.094	-	0.12		
2 x two-step (no back reaction)	**A**	0.03	-	$6{\cdot}10^{4}$	-	0.094	930	10^{-7}	0.0026	0
	B	10^{3}	-	92	-	$5{\cdot}10^{-8}$	0.014	0.025		
2 x Michaelis-Menten	**A**	0.05	$3{\cdot}10^{3}$	$2{\cdot}10^{3}$	-	0.094	34	10^{-7}	0.0026	27
	B	10^{3}	10^{-6}	92	-	$5{\cdot}10^{-8}$	0.014	0.025		
2 x two-step	**A**	0.02	501	321	1	0.084	15	0.0099	0.0029	291
	B	795	10^{-7}	26	60	0.0099	0.026	0.057		

x = different aptamer structures (A vs. B), k_{nx} = rate of reaction step n, k_{-nx} = back-rate of reaction step n, $r(A_xL^*)$ = signal response of component A_xL^*, $r(A_xL)$ = signal response of component A_xL, AIC = Akaike information criterion, RMSD = root-mean-square deviation

***Table S18**. Fit results of the tested binding models for the transient **$Ç_m^f$8** stopped-flow data considering a heterogeneous sample.*

Model	x	k_{1x} / $(\mu Ms)^{-1}$	k_{-1x} / s^{-1}	k_{2x} / s^{-1}	k_{-2x} / s^{-1}	$r(A_x)$ / arb.u.	$r(A_xL^*)$ / arb.u.	$r(A_xL)$ / arb.u.	RMSD	ΔAIC
One-step	-	92	6	-	-	0.1055	-	0.14	0.0046	16553
Two-step (no back reaction)	-	120	-	637	-	0.1055	0.12	0.14	0.0043	12604
Michaelis-Menten	-	141	100	609	-	0.1055	0.11	0.14	0.0043	12324
Two-step	-	207	113	417	125	0.1055	0.11	0.14	0.0040	7359
2 x one-step	**A**	170	0.68	-	-	0.11	-	0.13	0.0036	373
	B	0.02	172	-	-	$5{\cdot}10^{-8}$	-	3.2		
2 x two-step (no back reaction)	**A**	0.004	-	188	-	0.0072	20	10^{-7}	0.0036	174
	B	286	-	277	-	0.099	0.12	0.13		
2 x Michaelis-Menten	**A**	0.09	108	39	-	0.11	0.64	10^{-7}	0.0036	306
	B	176	1.3	1.5	-	$5{\cdot}10^{-8}$	0.026	0.037		
2 x two-step	**A**	0.04	296	136	0.2	0.034	2.7	10^{-7}	0.0036	0
	B	207	5	72	133	0.072	0.096	0.11		

x = different aptamer structures (A vs. B), k_{nx} = rate of reaction step n, k_{-nx} = back-rate of reaction step n, $r(A_xL^*)$ = signal response of component A_xL^*, $r(A_xL)$ = signal response of component A_xL, AIC = Akaike information criterion, RMSD = root-mean-square deviation

Dynafit4 script $Ç_m^f6$

```
[task]
        data = progress
        task = fit
        model = onestep ?
[mechanism]
        E + S <==> ES : k1 k-1
[constants]
        k1 = 130 ?
        k-1 = 3 ?
[responses]
        E=0.094                         ; fluorescence signal of labeled aptamer
        S=0.000                         ; fluorescence signal of ligand
        ES=0.12                         ; fluorescence signal of labeled aptamer + ligand
[concentrations]
[data]
        directory ./Fit
        extension txt
        delay      0.0013               ; start of fit before time zero
        offset = 0                      ; signal offset
        file eq0 |  conc S = 0, E=1.33    ; S=concentration ligand, E=concentration labeled aptamer
        file eq05 | conc S = 1, E=1.33    ; S=concentration ligand, E=concentration labeled aptamer
        file eq1 |  conc S = 2, E=1.33    ; S=concentration ligand, E=concentration labeled aptamer
        file eq4 |  conc S = 8 , E=1.33   ; S=concentration ligand, E=concentration labeled aptamer
        file eq6 |  conc S = 12, E=1.33   ; S=concentration ligand, E=concentration labeled aptamer
[output]
  directory ./Fit/Res
;--------------------------------------------------------------------
```

```
[task]
        data = progress
        task = fit
        model = twostep_no_back ?
[mechanism]
        E + S ---> ES : k1
        ES ---> ES* : kr
[constants]
        k1 = 520.0 ?
        kr = 178.0 ?
[responses]
        E=0.094                 ; fluorescence signal of labeled aptamer
        S=0.000                 ; fluorescence signal of ligand
        ES=0.11 ?               ; fluorescence signal of labeled aptamer + ligand
        ES*=0.12 ?              ; fluorescence signal of labeled aptamer + ligand
[concentrations]
;--------------------------------------------------------------------
[task]
        data = progress
        task = fit
        model = twostep ?
[mechanism]
        E + S <==> ES : k1 k-1
        ES <==> ES* : kr kr-1
[constants]
        k1 = 675 ?
        k-1 = 109 ?
        kr = 102 ?
        kr-1 = 35 ?
```

```
[responses]
        E=0.094                 ; fluorescence signal of labeled aptamer
        S=0.000                 ; fluorescence signal of ligand
        ES=0.11                 ; fluorescence signal of labeled aptamer + ligand
        ES*=0.125               ; fluorescence signal of labeled aptamer + ligand
[concentrations]
;--------------------------------------------------------------------
[task]
  data  = progress
  task  = fit
  model = michaelis ?
[mechanism]
  E + S <==> ES    : k1 k-1
  ES ---> ES*    : kr
[constants]
  k1 = 682  ?
  k-1 = 180.0 ?
  kr = 142.0 ?
[responses]
        E=0.094                 ; fluorescence signal of labeled aptamer
        S=0.000                 ; fluorescence signal of ligand
        ES=0.11 ?               ; fluorescence signal of labeled aptamer + ligand
        ES*=0.12 ?              ; fluorescence signal of labeled aptamer + ligand
[concentrations]
[end]
```

Dynafit4 script $Ç_m^f8$

```
[task]
        data = progress
        task = fit
        model = onestep ?
[mechanism]
        E + S <==> ES : k1 k-1
[constants]
        k1 = 93.0 ?
        k-1 = 5 ?
[responses]
        E=0.1055                ; fluorescence signal of labeled aptamer
        S=0.000                 ; fluorescence signal of ligand
        ES=0.1432               ; fluorescence signal of labeled aptamer + ligand
[concentrations]
[data]
        directory ./Fit
        extension txt
        delay     0.0013        ; start of fit before time zero
        offset = 0              ; signal offset
        file eq0 |  conc S = 0, E=2     ; S=concentration ligand, E=concentration labeled aptamer
        file eq05 |  conc S = 1 , E=2   ; S=concentration ligand, E=concentration labeled aptamer
        file eq1 |  conc S = 2, E=2     ; S=concentration ligand, E=concentration labeled aptamer
        file eq2 |  conc S = 4, E=2     ; S=concentration ligand, E=concentration labeled aptamer
        file eq4 |  conc S = 8 , E=2    ; S=concentration ligand, E=concentration labeled aptamer
        file eq6 |  conc S = 12, E=2    ; S=concentration ligand, E=concentration labeled aptamer
        file eq8 | conc S = 16, E=2     ; S=concentration ligand, E=concentration labeled aptamer
        file eq10 | conc S = 20, E=2    ; S=concentration ligand, E=concentration labeled aptamer
[output]
```

```
directory ./Fit/Res

;--------------------------------------------------------------------

[task]

        data = progress

        task = fit

        model = twostep_no_back ?

[mechanism]

        E + S ---> ES : k1

        ES ---> ES* : kr

[constants]

        k1 = 235.0 ?

        kr = 505.0 ?

[responses]

        E=0.1055                ; fluorescence signal of labeled aptamer

        S=0.000                 ; fluorescence signal of ligand

        ES=0.10998 ?            ; fluorescence signal of labeled aptamer + ligand

        ES*=0.1432              ; fluorescence signal of labeled aptamer + ligand

[concentrations]

;--------------------------------------------------------------------

[task]

        data = progress

        task = fit

        model = twostep ?

[mechanism]

        E + S <==> ES : k1 k-1

        ES <==> ES* : kr kr-1

[constants]

        k1 = 208 ?

        k-1 = 120 ?
```

```
        kr = 430 ?
        kr-1 = 120 ?
[responses]
        E=0.1055                ; fluorescence signal of labeled aptamer
        S=0.000                 ; fluorescence signal of ligand
        ES=0.11216 ?            ; fluorescence signal of labeled aptamer + ligand
        ES*=0.1432              ; fluorescence signal of labeled aptamer + ligand
[concentrations]
;--------------------------------------------------------------------
[task]
data  = progress
task  = fit
model = michaelis-menten ?
[mechanism]
E + S <==> ES    : k1 k-1
ES ---> ES*    : kr
[constants]
k1 = 170 ?
k-1 = 0.0001 ?
kr = 440 ?
[responses]
        E=0.1055                ; fluorescence signal of labeled aptamer
        S=0.0                   ; fluorescence signal of ligand
        ES=0.11 ?               ; fluorescence signal of labeled aptamer + ligand
        ES*=0.1432              ; fluorescence signal of labeled aptamer + ligand
[concentrations]
[end]
```

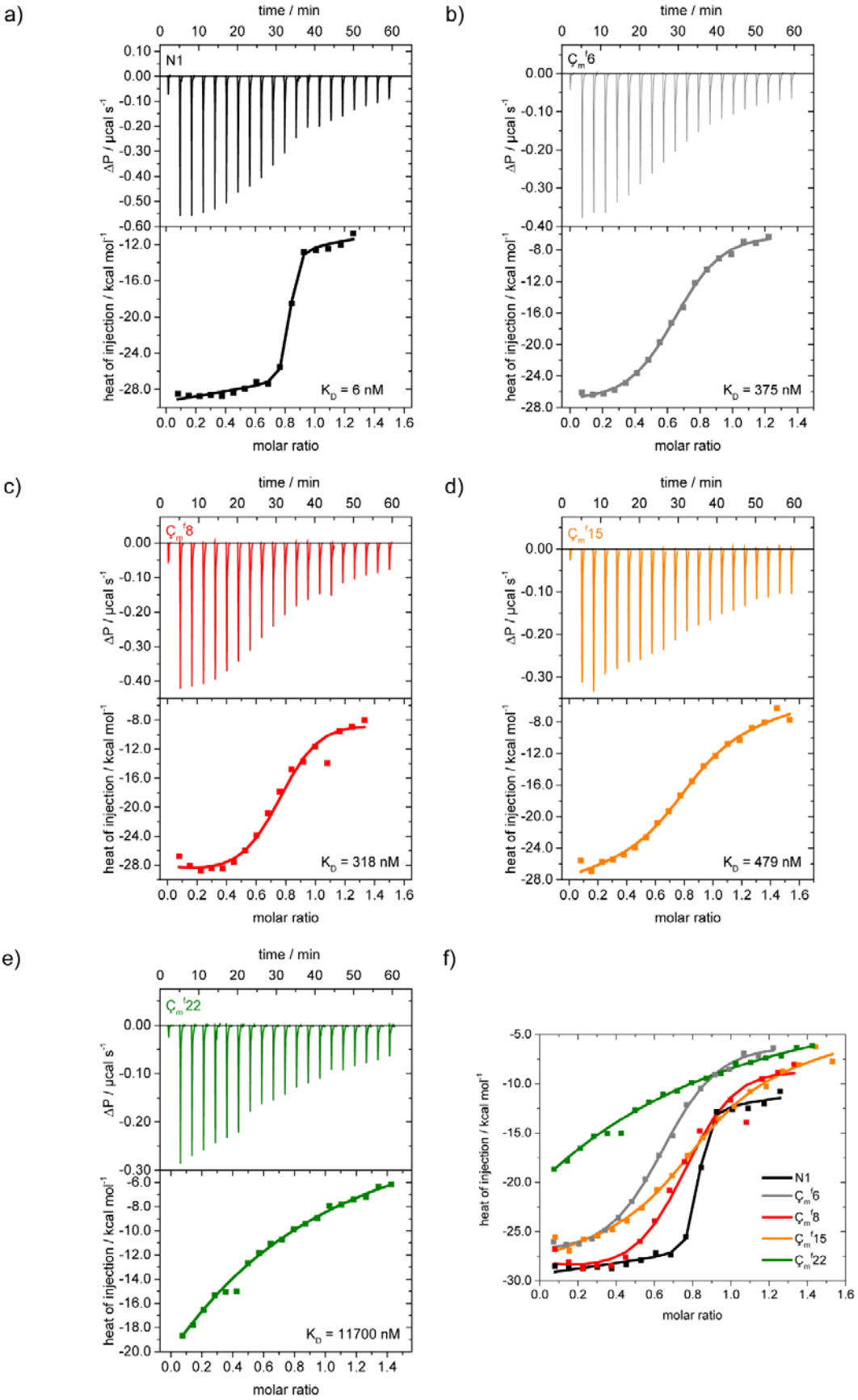

***Figure S19**. ITC-data of a) neomycin aptamer **N1**, b) **Çm^f6**, c) **Çm^f8**, d) **Çm^f15**, e) **Çm^f22** and the f) direct comparison of all five measurements.*

1. Trojanowski,P., Plötner,J., Grünewald,C., Graupner,F.F., Slavov,C., Reuss, a J., Braun,M., Engels,J.W. and Wachtveitl,J. (2014) Photo-physical properties of 2-(1-ethynylpyrene)-adenosine: influence of hydrogen bonding on excited state properties. *Phys. Chem. Chem. Phys.*, **16**, 13875–13888.

2. Lessing,H.E. and von Jena,A. (1976) Separation of rotational diffusion and level kinetics in transient absorption spectroscopy. *Chem. Phys. Lett.*, **42**, 213–217.

3. Slavov,C., Hartmann,H. and Wachtveitl,J. (2015) Implementation and Evaluation of Data Analysis Strategies for Time-Resolved Optical Spectroscopy. *Anal. Chem.*, **87**, 2328–2336.

Article II

ChemPubSoc Europe

DOI: 10.1002/ejoc.201900553

EurJOC European Journal of Organic Chemistry

Full Paper

Nitroxide-Labeled Oligonucleotides | *Very Important Paper* |

VIP

Benzoyl-Protected Hydroxylamines for Improved Chemical Synthesis of Oligonucleotides Containing Nitroxide Spin Labels

Haraldur Y. Juliusson,[a][‡] Anna-Lena J. Segler,[a][‡] and Snorri Th. Sigurdsson*[a]

Abstract: Oligonucleotides containing nitroxide spin labels, used in biophysical studies of nucleic acids, are frequently prepared by chemical synthesis. However, during the synthesis of spin-labeled oligonucleotides, the nitroxides are partially reduced to the corresponding amines. Here we report that a benzoylated hydroxylamine can be used as a protected form of the nitroxide to avoid this reduction. The benzoyl group is stable through the oligonucleotide synthesis and is readily removed under standard oligonucleotide deprotection conditions, yielding a hydroxylamine that is oxidized in situ to the nitroxide. This method was used to incorporate the rigid spin labels **Ç** and **Çm** into DNA and RNA oligonucleotides, respectively, including a doubly labeled 36-nucleotide long DNAzyme. Enzymatic digestion of the spin-labeled oligonucleotides and subsequent HPLC analysis showed that the nitroxides were intact. This protecting group strategy facilitates the high-yielding synthesis of spin-labeled DNA and RNA oligonucleotides using the phosphoramidite method.

Introduction

Nucleic acids are essential for life as they contain the cellular blueprint in living organisms and are active participants in the cellular machinery, for example in regulation of gene expression.[1] Therefore, it is of great interest to determine their structure and dynamics in order to gain insights into their function. Several different techniques are used for such studies. X-ray crystallography can provide three-dimensional structures and precise arrangements of atoms in space, but growing a highly-diffractive single crystal can be a laborious and time-consuming task.[2] Moreover, the crystals of the biomolecules might not represent their biologically active conformation.[3] Nuclear magnetic resonance (NMR) spectroscopy provides high-resolution structural information under biologically relevant conditions as well as information on dynamics.[4] However, NMR has inherently low sensitivity and, therefore, a relatively large amount of sample is required and the measurements can be time-consuming.[5] Förster resonance energy transfer (FRET) is a technique that measures the distances between two or more chromophores.[6] FRET has been used extensively to study tertiary structures of nucleic acids and has enabled studies of single molecules.[7]

Electron paramagnetic resonance (EPR) spectroscopy is another method to study the structure and dynamics of nucleic acids. For structural studies, continuous wave (CW) EPR can be used to measure distances up to 25 Å.[8] Pulsed dipolar spectroscopy, such as pulsed electron-electron double resonance (PELDOR), also called double electron-electron resonance (DEER), relaxation induced dipolar modulation enhancement (RIDME), single frequency technique for refocusing dipolar couplings (SIFTER) and double quantum coherence (DQC) can be used to measure distances between 15–160 Å.[9] Information about dynamics of nucleic acids can be obtained directly from line-broadening of CW-EPR spectra[10] and from orientation studies using pulsed EPR.[11] In EPR spectroscopy, transitions between spin states of unpaired electrons in a magnetic field are measured. Since nucleic acids and most other biomolecules are diamagnetic, a paramagnetic center needs to be introduced. Paramagnetic metal ions have been used as spin labels for EPR[12] but more often organic radicals, such as nitroxides, are employed for spin labeling.[13]

Incorporation of spin labels at specific sites in nucleic acids is called site-directed spin-labeling (SDSL) and is performed either through covalent or noncovalent binding.[14] Covalent spin-labeling is either carried out post-synthetically or by using spin-labeled phosphoramidites as building blocks in chemical synthesis of nucleic acids.[14a,14b,14d] Post-synthetic labeling requires oligonucleotides that have reactive groups at specific sites for modification with the spin label after the oligonucleotide synthesis.[14a,14b,14d] An advantage of post-synthetic labeling is that the label is not exposed to the reagents used for oligonucleotide synthesis, but drawbacks include non-specific reactions with other functional groups present in nucleic acids and incomplete spin labeling. Also, the spin labels that are incorporated post-synthetically contain flexible tethers, that render distance measurements less accurate and relative orientation of labels cannot be determined.[15]

With the phosphoramidite method, it is possible to incorporate intricate labels with unique structural features, such as rigid labels, into nucleic acids.[16] Drawbacks of the phosphoramidite approach include the synthetic effort required to prepare spin-

[a] *Department of Chemistry, Science Institute, University of Iceland*
Dunhaga 3, 107 Reykjavik, Iceland
E-mail: snorrisi@hi.is
https://notendur.hi.is/snorrisi/
[‡] These authors contributed equally to this work
Supporting information and ORCID(s) from the author(s) for this article are available on the WWW under https://doi.org/10.1002/ejoc.201900553.

labeled phosphoramidites and exposure of the nitroxides to reagents used in the solid-phase synthesis, resulting in a partial[17] or even complete[18] reduction of the nitroxide to its corresponding amine. For oligonucleotides shorter than ca. 15-nucleotide (nt) long, the desired spin-labeled product can be readily separated from the reduced material by denaturing polyacrylamide gel electrophoresis (DPAGE). For longer oligonucleotides, on the other hand, the separation is usually a tedious and nontrivial task that often results in a mixture of spin-labeled and reduced material. Protecting the nitroxide with a group that is stable through the oligonucleotide synthesis would eliminate this drawback of spin-labeling nucleic acids by the phosphoramidite method.

Nitroxides have been protected as *O*-methyl hydroxylamines under reaction conditions that would otherwise reduce the nitroxide.[19] The methyl group can be removed by treatment with *meta*-chloroperbenzoic acid (*m*-CPBA), but this reagent can also oxidize nitrogen atoms in the heterocyclic nucleobases present in nucleic acids. The *tert*-butyldimethylsilyl (TBDMS) group has been used to protect the hydroxylamine of 2,2,6,6-tetramethylpiperidyl-1-oxyl (TEMPO) for the synthesis of a nitroxide-nitroxide biradical,[20] however, less than 50 % of the nitroxide was recovered after removal of the TBDMS groups. Photolabile protecting groups have been used to protect TEMPO during oligonucleotide synthesis, of both DNA and RNA; irradiation with light gave high yields of spin-labeled oligonucleotides.[21] Photoprotection of nitroxides is a useful method for photocaging, allowing a controlled release of the protecting group in functional nucleic acids.[22] However, additional synthetic effort is required to prepare and incorporate the photolabile protecting group and specialized equipment is needed to irradiate the oligomers with the right wavelength for deprotection. An ideal protecting group for routine preparation of spin-labeled oligonucleotides would be removed by using standard oligonucleotide deprotecting conditions, returning the radical without having to include an additional deprotection step. An acetyl group has been used to protect a TEMPO moiety attached to a deoxyuridine phosphoramidite during incorporation into DNA. After oligomer deprotection using standard conditions,[23] complete removal of the acetyl group required additional incubation with aqueous NaOH (0.5 M), conditions that are not compatible with RNA. During the course of this work, we also became aware of a report describing the incorporation of 2-*N*-*tert*-butylaminoxyl-2′-deoxyadenosine into DNA, utilizing acetylated hydroxylamine,[24] however, the structure of this nitroxide is very different from the nitroxides that are normally used for spin labeling.

Here we describe a protecting group strategy for chemical synthesis of nitroxide-labeled DNA and RNA that is based on protection of the corresponding hydroxylamine with a benzoyl group, which is compatible with the conditions of solid-phase synthesis of oligonucleotides. The benzoyl group is quantitatively removed under standard conditions used for oligonucleotide deprotection, yielding a hydroxylamine that oxidizes in situ to the corresponding nitroxide radical.[21a,25] This method was used to synthesize fully spin-labeled DNA and RNA oligonucleotides in high yields.

Results and Discussion

The main incentive for carrying out this work was to enable incorporation of rigid spin labels into long sequences (> 15 nt) by solid-phase synthesis, but such spin labels cannot be incorporated by post-synthetic labeling. Specifically, we were interested in incorporating the spin labels **Ç**[16] and **Çm**[26] (Figure 1) into DNA and RNA oligonucleotides, respectively. These spin labels are valuable probes of both structure and dynamics of nucleic acids.[16,26] An advantage of using these labels for developing a general nitroxide protecting group strategy is that reduction of the nitroxides yields the fluorescent amines **Çf**[16] and **Çmf**[27] (Figure 1), allowing for easy detection.

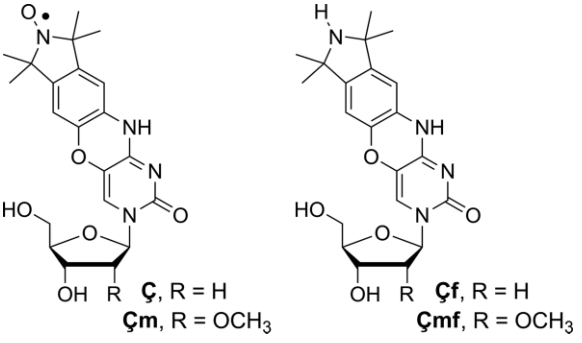

Figure 1. The rigid spin labels **Ç**[16] and **Çm**[26] and their corresponding amines **Çf**[16] and **Çmf**.[27]

The synthesis of **Ç-Bz** and **Çm-Bz** (Scheme 1) began by protecting the 5′- and 3′-hydroxyl groups of **Ç** and **Çm** with TBDMS. The resulting nitroxide radicals **1** and **2** were reduced with ascorbic acid to yield the corresponding hydroxylamines that were subsequently benzoylated, followed by removal of the TBDMS groups to give **Ç-Bz** and **Çm-Bz**. The benzoyl protecting group was shown to be stable under all reaction conditions used for oligonucleotide synthesis for more than five days, except when exposed to either 5-ethylthio tetrazole or 5-benzylthio tetrazole, present in the activation solutions, where slight removal of the benzoyl group was observed after 24 h (data not shown).

The benzoyl protecting group was readily removed within one and two hours under deprotecting conditions for RNA ($MeNH_2/NH_3$ in H_2O/EtOH) and DNA (satd. aq. NH_3), respectively. The 5′-hydroxyl groups of **Ç-Bz** and **Çm-Bz** (Scheme 1) were protected as 4,4′-dimethoxytrityl (DMT) ethers and subsequently phosphitylated to give phosphoramidites **3** and **4**, respectively, in good yields.

Phosphoramidite **4** was used to synthesize an 8-nt long, spin-labeled RNA oligomer (**I**, Table 1). This oligomer was chosen because short oligonucleotides that contain a reduced spin label can be separated by DPAGE from oligomers containing the nitroxide, thus allowing direct visualization of both products. An RNA of the same sequence was also synthesized with a phosphoramidite of the unprotected **Çm**[26] (**II**, Table 1) for comparison.

The phosphoramidite containing the protected spin label coupled well during the solid-phase synthesis as indicated by a strong orange color of the trityl cation that appears during re-

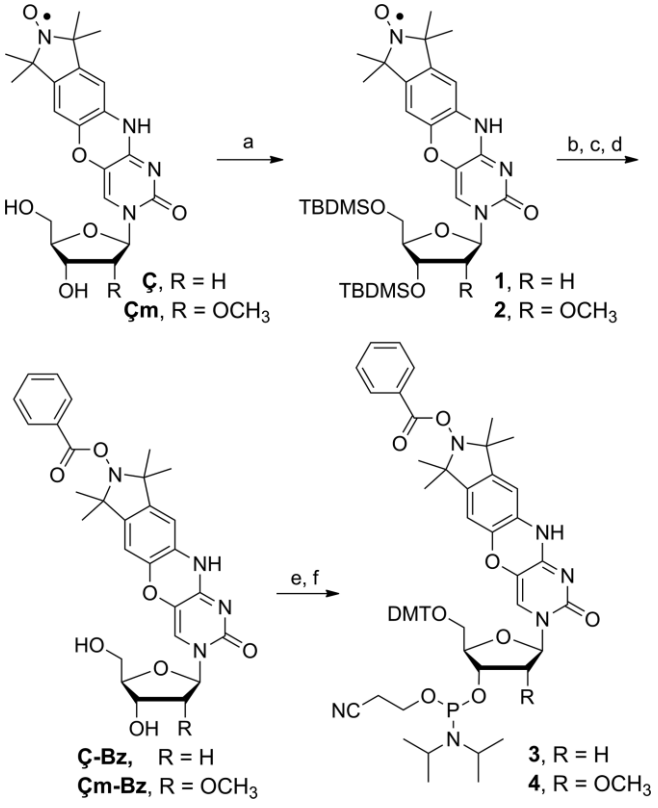

Scheme 1. Synthesis of **Ç-Bz** and **Çm-Bz** and their corresponding phosphoramidites. **a**. Imidazole, *tert*-butyldimethylsilyl chloride (TBDMSCl), DMF, pyridine. **b**. *L*-Ascorbic acid, 1,4-dioxane, H_2O. **c**. Benzoyl chloride (BzCl), Et_3N. **d**. *tert*-Butyl ammonium fluoride (TBAF), THF. **e**. 4,4′-Dimethoxytrityl chloride (DMTCl), 4-dimethylaminopyridine (DMAP), pyridine. **f**. 2-Cyanoethyl-*N*,*N*,*N*′,*N*′-tetraisopropylphosphorodiamidite, diisopropylammonium tetrazolide (DIPAT), CH_2Cl_2.

Table 1. Spin-labeled DNA and RNA oligonucleotides synthesized by solid-phase synthesis. Oligonucleotides **II*** and **VI*** were synthesized with the phosphoramidite of unprotected nitroxide spin-labels **Çm**[26] and **Ç**,[16] respectively. PHO is a phosphate.

No.	Sequence
I	5′-UGCAU**Çm**UU-3′
II*	5′-UGCAU**Çm**UU-3′
III	5′-AGA-UGC-GCG-**Çm**GC-GCG-ACU-GAC-3′
IV	5′-PHO-d(TGAGGTAGTAGGTTGTATA**Ç**T)-3′
V*	5′-PHO-d(TGAGGTAGTAGGTTGTATA**Ç**T)-3′
VI	5′-d(TGTAA**Ç**GCACTACCAGCGGCTGGAAATCT**Ç**TCTCGT)-3′

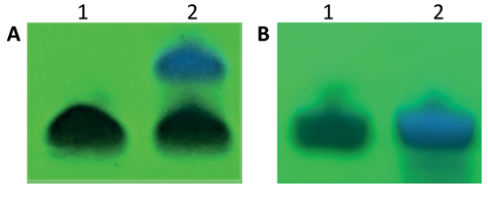

Figure 2. Analysis of spin-labeled oligonucleotides by DPAGE. **A**. Crude 8-mer RNA oligonucleotides **I** (lane 1) and **II** (lane 2) (5′-UGCAU**Çm**UU-3′), synthesized using **4** and the phosphoramidite of unprotected **Çm**,[26] respectively. **B**. Crude 21-mer DNA oligonucleotides **IV** (lane 1) and **V** (lane 2) [5′-d(PHO-TGAGGTAGTAGGTTGTATA**Ç**T)-3′], synthesized using **3** and the phosphoramidite of unprotected **Ç**,[16] respectively. PHO is a phosphate.

moval of the DMT group. Figure 2**A** shows a denaturing polyacrylamide gel of crude RNA **I** (lane 1) and RNA **II** (lane 2). No fluorescent band was detected for RNA **I** (Figure 2**A**, lane 1), synthesized with **Çm-Bz**. In contrast, RNA **II** (Figure 2**A**, lane 2), synthesized with the unprotected **Çm**, contained a strong fluorescent by-product, which indicated a partial reduction of the nitroxide to the corresponding **Çmf**.

For further analysis, crude RNAs **I** and **II** were digested with snake venom phosphodiesterase, nuclease P1 and calf spleen alkaline phosphatase, and the digest was analyzed by HPLC (Figure 3).[16] The HPLC chromatogram for RNA **I** (Figure 3**A**) contained five peaks, one for each natural nucleoside and a strongly retained nucleoside that was shown by co-injection to be **Çm**, while RNA **II** (Figure 3**B**) showed a peak for both **Çm** and **Çmf** along with the natural unmodified nucleosides.

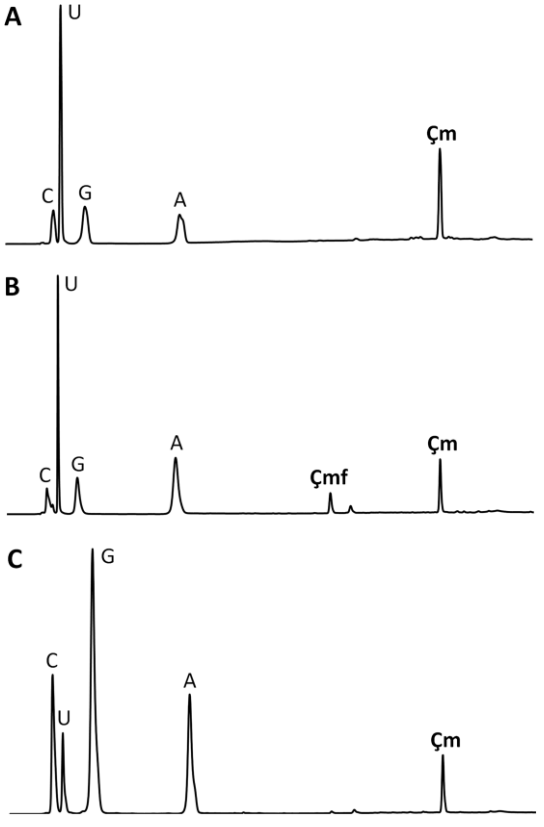

Figure 3. HPLC chromatograms of RNA oligonucleotides after enzymatic digestion with snake venom phosphodiesterase, nuclease P1, and alkaline phosphatase. **A**. Crude RNA **I** (5′-UGCAU**Çm**UU-3′) synthesized using **4**. **B**. Crude RNA **II** (5′-UGCAU**Çm**UU-3′) synthesized using the phosphoramidite of unprotected **Çm**.[26] **C**. RNA **III** (5′-AGAUGCGCG**Çm**GCGCGACUGAC-3′) synthesized using **4**.

Phosphoramidite **4** was also used to synthesize a 21-nt long RNA (**III**, Table 1), which was enzymatically digested and analyzed by HPLC (Figure 3**C**). In this case, a small peak (< 5 %) can be seen for **Çmf**, along with **Çm** and the natural nucleosides. These results show that the benzoyl protecting group on **Çm** was stable during the oligonucleotide synthesis and was completely removed during the deprotection, giving high yields of spin-labeled RNA.

In an analogous manner to the RNA synthesis, phosphoramidite **3** and a phosphoramidite of **Ç** that does not contain

the benzoyl protecting group were used to synthesize two 21-mer DNA oligonucleotides of the same sequence, (**IV** and **V**, Table 1). Here the spin-label was placed close to the 3′-end, which increases the exposure of the label to the chemicals used in each cycle of the oligonucleotide synthesis. Figure 2**B** shows DPAGE analysis of crude DNA **IV** (Figure 2**B**, lane 1) and crude DNA **V** (Figure 2**B**, lane 2). No fluorescent band was detected for DNA **IV** while DNA **V** showed a strong fluorescent band that overlapped with the band of the spin-labeled oligonucleotide.

These crude DNA samples were digested and analyzed by HPLC (Figure 4). While the digest of oligomer **IV** (Figure 4**A**) showed the natural nucleosides and **Ç**, the digest of oligomer **V** contained a very small peak for **Ç** along with some strongly retained impurities (Figure 4**B**). The quality of the synthesis of spin-labeled DNA was also reflected in the yields of purified material obtained from a 1 µmol synthesis, that gave 180 and 11 nmols of oligomers **VI** and **V**, respectively. Moreover, the small amount of oligo **V** obtained after repeated purifications gave a ca. 50:50 mixture of oligonucleotides containing **Ç** and **Çf**. To demonstrate the use of this method for the synthesis of a longer oligonucleotide, a 36-nt DNAzyme (**VI**, Table 1) containing **Ç** at two positions (6 and 31) was prepared. No fluorescent bands were detected upon purification of the oligonucleotide by DPAGE. Enzymatic digestion followed by HPLC analysis showed four peaks for the natural nucleosides and a peak for **Ç** (Figure 4**C**) in the ratios expected for a fully spin-labeled oligonucleotide.

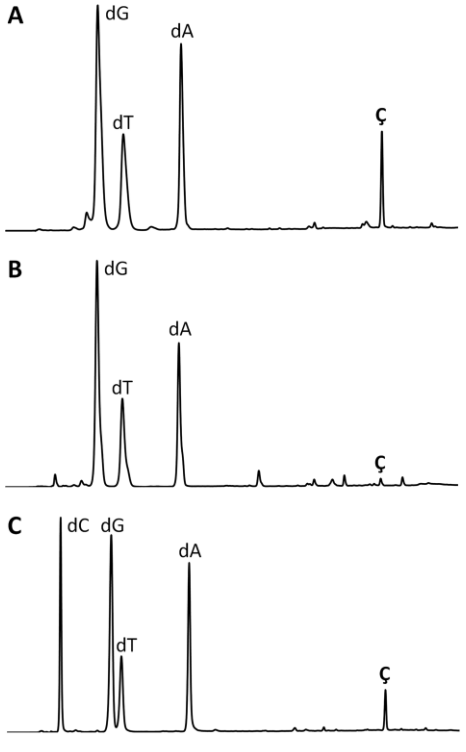

Figure 4. HPLC chromatograms of DNA oligonucleotides after enzymatic digestion with snake venom phosphodiesterase, nuclease P1, and alkaline phosphatase. **A**. Crude DNA **IV** [5′-d(PHO-TGAGGTAGTAGGTTGTATA**Ç**T)-3′] synthesized using **3**. **B**. Crude DNA **V** [5′-d(PHO-TGAGGTAGTAGGTTGTATA**Ç**T)-3′] synthesized using the phosphoramidite of unprotected **Ç**.[16] **C**. DNAzyme **VI** [5′-d(TGTAA**Ç**GCACTACCAGCGGCTGGAAATCT**Ç**TCTCGT)-3′] synthesized using **3**. PHO is a phosphate.

Conclusions

The nitroxide functional groups of **Ç** and **Çm** were protected by benzoylation of the corresponding hydroxylamines. The resulting **Ç-Bz** and **Çm-Bz** were converted into phosphoramidites and used for oligonucleotide synthesis of DNA and RNA of various lengths. The benzoyl protecting group was stable through the chemical synthesis of the oligonucleotides and was readily removed by standard oligonucleotide deprotection conditions to give nitroxide-labeled oligonucleotides; enzymatic digestion and HPLC analysis were used to quantify the spin label in the samples. These results show that this protecting group strategy for nitroxides can be used as a general method to prepare spin-labeled nucleic acids using the phosphoramidite approach.

Experimental Section

General Materials and Methods. All commercially available reagents were purchased from Sigma-Aldrich, Inc. or Acros Organics and used without further purification. 2′-Deoxyuridine and 2′-*O*-methyluridine were purchased from Rasayan Inc. USA. CH_2Cl_2, pyridine, and CH_3CN were dried with calcium hydride and freshly distilled before use. All moisture- and air-sensitive reactions were carried out in oven-dried glassware under an inert atmosphere of Ar. Thin-layer chromatography (TLC) was performed using glass plates pre-coated with silica gel (0.25 mm, F-25, Silicycle) and compounds were visualized under UV light and by *p*-anisaldehyde staining. Column chromatography was performed using 230–400 mesh silica gel (Silicycle). For acid-sensitive compounds the silica gel was basified by passing 3 % Et_3N in CH_2Cl_2 through the column before use. ^{1}H-, ^{13}C- and ^{31}P-NMR spectra were recorded with a Bruker Avance 400 MHz spectrometer. Commercial grade $CDCl_3$ was passed over basic alumina shortly before dissolving tritylated nucleosides for NMR analysis. Chemical shifts (δ) are reported in parts per million (ppm) relative to the partially deuterated NMR solvent $CDCl_3$ (7.26 ppm for ^{1}H NMR and 77.16 ppm for ^{13}C). ^{31}P-NMR chemical shifts are reported relative to 85 % H_3PO_4 as an external standard. All coupling constants were measured in Hertz (Hz). Nitroxide radicals show broadening and loss of NMR signals due to their paramagnetic nature and therefore, those NMR spectra are not shown. Mass spectrometric analyses of all organic compounds were performed on an ESI-HRMS (Bruker, MicrOTOF-Q) in a positive ion mode.

TBDMS-Ç (1). To a solution of **Ç**[16] (130 mg, 0.30 mmol) in DMF (3 mL) and pyridine (3 mL) were added imidazole (62 mg, 0.91 mmol) and TBDMSCl (137 mg, 0.91 mmol) and the resulting solution was stirred at 22 °C for 24 h. H_2O (50 mL) was added and the organic phase was extracted with EtOAc (3 × 10 mL). The combined organic phases were dried with Na_2SO_4 and concentrated in vacuo. The residue was purified by flash column chromatography using gradient elution ($MeOH/CH_2Cl_2$, 0:100 to 10:90), to yield **1** (160 mg, 95 %) as a yellow solid. HRMS (ESI): *m/z* calcd. for $C_{33}H_{53}N_4O_6Si_2 + Na^+$: 680.3401 $[M + Na]^+$, found 680.3396.

TBDMS-Ç-Bz (5). To a solution of **1** (53 mg, 0.08 mmol) in 1,4-dioxane (3.5 mL) was added *L*-ascorbic acid (72 mg, 0.41 mmol) in H_2O (1 mL) and the reaction mixture stirred at 40 °C for 30 min. H_2O (3.5 mL) and CH_2Cl_2 (5 mL) were added and the mixture was stirred for 5 min. The organic phase was separated and used directly in the next step by passing it through a plug of Na_2SO_4 under an inert atmosphere of Ar, into a solution of BzCl (46 µL, 0.41 mmol) and Et_3N (23 µL, 0.16 mmol) in CH_2Cl_2 (2 mL). The reaction was

stirred at 22 °C for 30 min, the solvent removed in vacuo and the residue purified by flash column chromatography using gradient elution ($MeOH/CH_2Cl_2$, 0:100 to 10:90), to yield **5** (55 mg, 95 %) as a yellow solid. ^1H NMR (400 MHz, $CDCl_3$): δ = 8.10–8.03 (m, 2H), 7.53 (d, *J* = 7.4 Hz, 1H), 7.40–7.44 (m, 3H), 7.19 (s, 1H), 6.34 (s, 1H), 6.22 (t, *J* = 6.1 Hz, 1H), 4.40–4.24 (m, 1H), 3.84 (dt, *J* = 8.6, 2.9 Hz, 2H), 3.76–3.66 (m, 1H), 2.36–2.22 (m, 1H), 2.26–2.32 (m, 1H), 2.06–1.90 (m, 1H), 1.42 (d, *J* = 10.1 Hz, 12H), 0.90 (s, 9H), 0.81 (s, 9H), 0.09 (d, *J* = 8.8 Hz, 6H), 0.00 ppm (s, 6H); ^{13}C NMR (101 MHz, $CDCl_3$): δ = 166.13, 160.85, 142.58, 140.14, 139.53, 133.08, 129.62, 128.54, 127.76, 121.42, 112.27, 108.11, 100.88, 87.59, 85.80, 71.24, 68.60, 67.27, 66.52, 62.49, 41.78, 26.06, 25.71, 18.49, 17.95, –4.55 –4.85, –5.46 ppm; HRMS (ESI): *m/z* calcd. for $C_{40}H_{58}N_4O_7Si_2 + Na^+$: 785.3742 $[M + Na]^+$, found 785.3736.

Ç-Bz. To a solution of **5** (118 mg, 0.16 mmol) in THF (3 mL) was added TBAF (0.5 mL, 0.50 mmol, 1.0 M in THF) at 0 °C and the reaction mixture was stirred at 0 °C for 8 h. The solvent was removed in vacuo and the residue purified by flash column chromatography using gradient elution ($MeOH/CH_2Cl_2$, 0:100 to 25:75), to yield **Ç-Bz** (67 mg, 81 %) as a yellow solid. ^1H NMR (400 MHz, $CDCl_3$): δ = 8.09 (d, *J* = 7.3 Hz, 2H), 7.70–7.62 (m, 2H), 7.55 (t, *J* = 7.7 Hz, 2H), 6.66 (s, 2H), 6.23 (t, *J* = 6.4 Hz, 1H), 4.39 (dt, *J* = 6.6, 3.5 Hz, 1H), 3.94 (m, *J* = 3.1 Hz, 1H), 3.81–3.73 (m, 2H), 2.34 (ddd, *J* = 13.5, 6.0, 3.7 Hz, 1H), 2.17 (dt, *J* = 13.4, 6.5 Hz, 1H), 1.47 ppm (s, 12H); ^{13}C NMR (101 MHz, $CDCl_3$): δ = 170.9, 146.8, 143.8, 143.0, 137.4, 133.1, 132.5, 112.7, 91.5, 90.1, 74.6, 72.4, 65.2, 62.1, 62.1, 44.3, 31.7, 27.4, 23.3, 16.5 ppm; HRMS (ESI): *m/z* calcd. for $C_{28}H_{30}N_4O_7 + Na^+$: 557.2012 $[M + Na]^+$, found 557.2007.

Ç-Bz-DMT (6). Ç-Bz (16 mg, 0.03 mmol), DMTCl (21 mg, 0.06 mmol) and DMAP (0.8 mg, 0.01 mmol) were added to a round-bottomed flask and dried in vacuo for 16 h. Pyridine (2 mL) was added and the solution stirred for 16 h, after which MeOH (0.50 mL) was added and the solvent removed in vacuo. The residue was purified by flash column chromatography using gradient elution ($MeOH/CH_2Cl_2/Et_3N$, 0:99:1 to 95:4:1), to yield **6** (20 mg, 95 %) as a yellow solid. ^1H NMR (400 MHz, $CDCl_3$): δ = 8.18–8.09 (m, 3H), 7.64–7.56 (m, 2H), 7.49 (d, *J* = 7.8 Hz, 4H), 7.40 (d, *J* = 8.2 Hz, 4H), 7.31 (t, *J* = 7.6 Hz, 2H), 7.20 (t, *J* = 7.3 Hz, 1H), 6.86 (dd, *J* = 8.7, 3.8 Hz, 4H), 6.52–6.46 (m, 1H), 6.43 (s, 1H), 6.25 (s, 1H), 4.70–4.56 (m, 1H), 4.15 (dd, *J* = 8.8, 5.2 Hz, 1H), 3.75 (d, *J* = 6.6 Hz, 6H), 3.41 (ddd, *J* = 26.5, 10.7, 3.2 Hz, 2H), 2.71 (d, *J* = 12.8 Hz, 1H), 2.37–2.21 (m, 1H), 1.48 ppm (d, *J* = 12.2 Hz, 12H); ^{13}C NMR (101 MHz, $CDCl_3$): δ = 166.21, 159.56, 154.79, 154.60, 148.34, 144.57, 142.44, 139.75, 139.32, 136.66, 133.17, 130.10, 130.05, 129.60, 129.38, 128.60, 128.15, 128.14, 128.05, 127.97, 126.91, 126.30, 122.05, 113.27, 108.58, 106.64, 86.88, 86.33, 86.26, 71.33, 68.65, 68.54, 63.40, 60.42, 55.21, 41.79, 39.06, 29.37, 28.87, 25.44, 21.07, 14.22 ppm; HRMS (ESI): *m/z* calcd. for $C_{49}H_{48}N_4O_9 + Na^+$: 859.3319 $[M + Na]^+$, found 859.3313.

Ç-Bz phosphoramidite (3). A solution of compound **6** (21 mg, 0.02 mmol) in CH_2Cl_2 (1 mL) was treated with diisopropyl ammonium tetrazolide (5 mg, 0.03 mmol) and 2-cyanoethyl *N*,*N*,*N*′,*N*′-tetraisopropylphosphane (11 µL, 0.03 mmol). The resulting solution was stirred at 22 °C for 2 h. CH_2Cl_2 (50 mL) was added and the solution washed with satd. aq. $NaHCO_3$ (3 × 50 mL) and brine (50 mL), dried with Na_2SO_4 and concentrated in vacuo. The residue was dissolved in a minimum amount of CH_2Cl_2 (few drops), followed by slow addition of *n*-hexane (40–50 mL) at 22 °C. The solvent was decanted from the precipitate and discarded. This procedure was repeated four times to give **3** (20 mg, 80 %) as a yellowish solid. ^1H NMR (400 MHz, $CDCl_3$): δ = 8.06–8.04 (m, 2H), 7.53 (s, 1H), 7.46–7.34 (m, 6H), 7.32–7.24 (m, 6H), 7.16 (dd, *J* = 7.4, 4.0 Hz, 1H), 6.79 (dq, *J* = 6.3, 2.2 Hz, 4H), 6.30–6.19 (m, 1H), 6.17 (d, *J* = 8.2 Hz, 1H), 4.58 (d, *J* = 14.0 Hz, 1H), 4.08 (t, *J* = 3.8 Hz, 1H), 3.69 (dd, *J* = 5.3, 2.1 Hz, 6H), 3.61–3.25 (m, 6H), 2.52 (q, *J* = 10.7, 8.4 Hz, 2H), 2.38 (t, *J* = 6.4 Hz, 1H), 2.22 (d, *J* = 11.4 Hz, 1H), 1.41 (t, *J* = 11.0 Hz, 12H), 1.13–0.97 (m, 12H) ppm; ^{13}C NMR (101 MHz, $CDCl_3$): δ = 158.61, 144.36, 139.29, 133.10, 130.18, 130.13, 130.10, 129.62, 129.47, 128.56, 128.26, 127.96, 126.99, 113.28, 113.25, 108.46, 86.88, 85.76, 77.22, 68.66, 68.59, 62.60, 58.36, 58.16, 55.24, 55.21, 43.38, 43.26, 43.20, 40.45, 31.59, 25.49, 24.65, 24.58, 24.51, 22.66, 20.25, 20.18, 14.12 ppm; ^{31}P NMR (162 MHz, $CDCl_3$): δ = 149.25, 148.63 ppm.

TBDMS-Çm (2). To a solution of **Çm**[26] (290 mg, 0.63 mmol) in DMF (6 mL) and pyridine (1.5 mL) were added TBDMSCl (286 mg, 1.89 mmol) and imidazole (129 mg, 1.89 mmol). The resulting solution was stirred at 22 °C for 16 h. H_2O (50 mL) and EtOAc (20 mL) were added, the organic phase separated and washed with satd. aq. $NaHCO_3$ (5 × 50 mL). The organic phase was dried with Na_2SO_4, concentrated in vacuo and purified by flash column chromatography using gradient elution ($MeOH/CH_2Cl_2$; 0:100 to 10:90), yielding **2** (299 mg, 81 %) as a yellow solid. HRMS (ESI): *m/z* calcd. for $C_{34}H_{55}N_4O_7Si_2 + Na^+$: 710.3501 $[M + Na]^+$, found 710.3500.

TBDMS-Çm-Bz (7). To a solution of **2** (235 mg, 0.34 mmol) in 1,4-dioxane (30 mL) was added *L*-ascorbic acid (301 mg, 1.71 mmol) in H_2O (5 mL). The reaction mixture was stirred at 40 °C for 1 h, after which CH_2Cl_2 (30 mL) and H_2O (30 mL) were added and the solution was stirred vigorously for 2 min. The organic phase was separated and filtered through a short pad of Na_2SO_4, in a dropping funnel under an inert atmosphere of Ar, into a solution of BzCl (198 µL, 0.34 mmol), Et_3N (953 µL, 6.83 mmol) in CH_2Cl_2 (10 mL). The solution was stirred at 22 °C for 2 h, washed with satd. aq. $NaHCO_3$ (3 × 100 mL), the organic phase dried with Na_2SO_4, concentrated in vacuo and the residue purified by flash column chromatography using gradient elution ($MeOH/CH_2Cl_2$; 0:100 to 10:90), to yield **7** (269 mg, quant.) as a yellow solid. ^1H NMR (400 MHz, $CDCl_3$): δ = 8.14 (s, 2H), 7.81 (s, 1H), 7.59 (t, *J* = 7.5 Hz, 1H), 7.49 (s, 1H), 7.51–7.44 (m, 2H), 6.41 (s, 1H), 5.88 (s, 1H), 4.22 (dt, *J* = 8.7, 4.3 Hz, 1H), 4.14–4.02 (m, 2H), 3.81 (dd, *J* = 11.9, 1.8 Hz, 1H), 3.68 (d, *J* = 4.6 Hz, 1H), 3.64 (s, 3H), 1.49 (s, 12H), 1.02 (s, 9H), 0.90 (s, 9H), 0.22 (dd, *J* = 7.5, 2.4 Hz, 6H), 0.09 ppm (dd, *J* = 5.9, 2.4 Hz, 6H); ^{13}C NMR (101 MHz, $CDCl_3$): δ = 171.21, 166.14, 160.84, 155.20, 153.56, 142.62, 140.04, 139.53, 133.19, 133.15, 130.29, 130.16, 129.63, 129.44, 129.03, 128.58, 128.29, 127.69, 126.27, 122.06, 111.93, 108.14, 88.08, 87.47, 84.14, 83.11, 68.71, 68.63, 68.61, 68.52, 68.03, 62.97, 61.64, 60.51, 57.98, 28.93, 26.37, 26.34, 25.82, 25.76, 25.49, 18.78, 18.73, 18.15, 18.10, –4.45, –4.50, –4.83, –5.11, –5.20, –5.29, –5.34 ppm; HRMS (ESI): *m/z* calcd. for $C_{41}H_{60}N_4O_8Si_2 + Na^+$: 815.3842 $[M + Na]^+$, found 815.3853.

Çm-Bz. To a solution of **7** (271 mg, 0.34 mmol) in THF (18 mL) was added TBAF (1.2 mL, 1.20 mmol, 1.0 M in THF) and the reaction stirred at 22 °C for 18 h. The reaction was concentrated in vacuo and the residue purified by flash column chromatography using gradient elution ($MeOH/CH_2Cl_2$; 0:100–10:90), to yield **Çm-Bz** (139 mg, 72 %) as a yellow solid. ^1H NMR (400 MHz, $CDCl_3$): δ = 8.11 (td, *J* = 7.3, 6.6, 1.4 Hz, 2H), 7.59 (td, *J* = 7.4, 3.6 Hz, 1H), 7.57–7.51 (m, 1H), 7.45 (dt, *J* = 18.4, 7.7 Hz, 2H), 6.45 (d, *J* = 18.7 Hz, 1H), 5.72–5.67 (m, 1H), 4.95 (s, 1H), 4.38 (t, *J* = 4.8 Hz, 1H), 4.31 (dt, *J* = 9.1, 4.8 Hz, 1H), 4.00 (d, *J* = 6.5 Hz, 2H), 3.89 (q, *J* = 5.4 Hz, 1H), 3.62 (d, *J* = 3.9 Hz, 3H), 1.51–1.24 ppm (m, 12H); ^{13}C NMR (101 MHz, $CDCl_3$): δ = 170.91, 166.35, 160.98, 154.87, 153.61, 142.50, 142.19, 141.16, 140.16, 139.44, 133.30, 130.12, 129.62, 129.23, 128.62, 128.36, 128.03, 127.93, 125.91, 125.39, 123.08, 111.54, 108.77, 100.90, 89.88, 84.49, 82.98, 77.39, 77.28, 77.08, 76.76, 68.61, 68.56, 68.11, 67.31, 67.26, 66.55, 63.66, 62.97, 60.69, 58.53, 53.46, 29.26, 28.77, 25.41, 24.99 ppm; HRMS (ESI): *m/z* calcd. for $C_{29}H_{32}N_4O_8 + Na^+$: 587.2112 $[M + Na]^+$, found 587.2096.

Çm-Bz-DMT (8). Toluene (3 × 5 mL) was evaporated from **Çm-Bz** (139 mg, 0.25 mmol), followed by sequential addition of pyridine (4 mL), DMTCl (834 mg, 2.46 mmol) and DMAP (6 mg, 0.05 mmol). The solution was stirred for 14 h, MeOH (400 µL) was added and the solvent removed in vacuo. The residue was purified by flash column chromatography using gradient elution ($MeOH/CH_2Cl_2/Et_3N$; 0:99:1 to 1:98:1), to yield **8** (87 mg, 41 %) as a yellow solid. ^1H NMR (400 MHz, $CDCl_3$): δ = 8.13 (d, J = 7.2 Hz), 7.72 (s, 1H), 7.60 (t, J = 7.7 Hz, 1H), 7.51–7.50 (m, 2H), 7.49–7.48 (m, 2H), 7.43–7.40 (m, 4H), 7.33–7.31 (m, 2H), 7.22–7.18 (m, 1H), 6.88 (s, 1H), 6.88–6.85 (m, 4H), 6.11 (s, 1H), 5.87 (s, 1H), 4.55–4.52 (m, 1H), 4.02 (d, J = 8.6 Hz, 1H), 3.93 (bs, 1H), 3.75 (s, 6H), 3.73 (s, 3H), 3.60–3.49 (m, 2H), 1.51 ppm (d, J = 25.2 Hz, 12H); ^{13}C NMR (101 MHz, $CDCl_3$): δ = 166.15, 158.57, 155.18, 153.79, 142.30, 139.88, 139.26, 135.57, 133.13, 130.09, 129.62, 129.47, 128.57, 128.23, 128.01, 127.84, 126.92, 125.98, 121.80, 113.36, 113.31, 111.78, 108.71, 87.87, 86.82, 83.77, 82.91, 68.70, 68.61, 68.19, 60.84, 58.56, 55.21, 45.82, 29.72, 25.47 ppm; HRMS (ESI): m/z calcd. for $C_{50}H_{50}N_4O_{10}$ + Na^+: 889.3419 $[M + Na]^+$, found 889.3395.

Çm-Bz phosphoramidite (4). A solution of **8** (20 mg, 0.02 mmol) in CH_2Cl_2 (1 mL) was treated with diisopropyl ammonium tetrazolide (6 mg, 0.04 mmol) and 2-cyanoethyl *N*,*N*,*N*′,*N*′-tetraisopropylphosphane (22 µL, 0.07 mmol). The reaction was stirred at 22 °C for 18 h. CH_2Cl_2 (15 mL) was added and the solution washed with satd. aq. $NaHCO_3$ (3 × 30 mL), dried with Na_2SO_4 and concentrated in vacuo. The residue was dissolved in Et_2O (2 mL) followed by slow addition of *n*-hexane (10 mL). The solvent was decanted from the precipitate and discarded. This procedure was repeated six times to yield **4** (18 mg, 71 %) as a yellow solid. ^1H NMR (400 MHz, $CDCl_3$): δ = 8.12 (dd, J = 8.3, 1.4 Hz, 4H), 7.64–7.57 (m, 3H), 7.53–7.44 (m, 10H), 7.44–7.34 (m, 11H), 7.31 (td, J = 7.8, 2.1 Hz, 6H), 7.22 (tt, J = 7.4, 1.9 Hz, 3H), 6.86 (ddt, J = 8.7, 5.9, 3.4 Hz, 10H), 6.14 (d, J = 15.5 Hz, 1H), 6.06 (d, J = 7.6 Hz, 1H), 5.97 (s, 1H), 4.29 (tt, J = 5.0, 2.6 Hz, 1H), 4.25–4.20 (m, 2H), 3.98 (q, J = 7.0, 6.4 Hz, 2H), 3.77–3.73 (m, 13H), 3.65 (dd, J = 4.0, 1.2 Hz, 6H), 2.46–2.38 (m, 2H), 1.55–1.38 (m, 28H), 1.26 (ddt, J = 5.7, 3.6, 2.2 Hz, 15H), 1.22–1.18 (m, 11H), 1.18–1.03 (m, 15H), 0.92–0.84 ppm (m, 8H); ^{13}C NMR (101 MHz, $CDCl_3$): δ = 165.92, 158.38, 155.03, 153.66, 142.02, 132.86, 130.10, 129.37, 128.32, 127.69, 126.77, 125.79, 121.65, 117.33, 113.00, 111.78, 108.29, 88.35, 86.49, 77.16, 68.45, 54.98, 43.16, 24.51, 20.10 ppm; ^{31}P NMR (162 MHz, $CDCl_3$): δ = 150.52, 150.08 ppm; HRMS (ESI): m/z calcd. for $C_{50}H_{60}N_4O_{10}$ + Na^+: 1089.4498 $[M + Na]^+$, found 1089.4498.

DNA and RNA Syntheses, Purification and Characterization. All commercial phosphoramidites, CPG columns, and solutions for oligonucleotide syntheses were purchased from ChemGenes Corp., USA. DNA and RNA solid-phase oligonucleotide syntheses were performed on an automated ASM800 DNA/RNA synthesizer (BIOSSET Ltd., Russia) using phosphoramidite chemistry. Unmodified and spin-labeled oligonucleotides were synthesized using a trityl-off protocol and phosphoramidites with standard protecting groups on 1 µmol scale (1000 Å CPG columns). Oxidation was performed with *tert*-butylhydroperoxide in toluene (1.0 M). Capping and detritylation were performed under standard conditions for DNA and RNA oligonucleotide synthesis.

The **Ç**-modified DNAs were synthesized using phosphoramidite **3**. Unmodified phosphoramidites were dissolved in CH_3CN (100 mM) and **3** was dissolved in 1,2-dichloroethane (100 mM). 5-Ethylthiotetrazole (250 mM) was used as a coupling agent and the coupling time was set to 1.5 min for unmodified phosphoramidites and to 5 min for the **Ç**-modified phosphoramidites. The DNAs were deprotected in satd. aqueous NH_3 at 55 °C for 8 h and dried in vacuo.

For the RNA synthesis, 2′*O*-TBDMS protected ribonucleoside phosphoramidites were used and dissolved in CH_3CN (100 mM). The **Çm**-modified RNAs were synthesized using phosphoramidite **4**, dissolved in 1,2-dichloroethane (100 mM). 5-Ethylthiotetrazole (250 mM) was used as a coupling agent for phosphoramidite **4**, 5-benzylthiotetrazole (250 mM) was used as a coupling agent for unmodified phosphoramidites and the coupling time was set to 7 min. The RNAs were deprotected and cleaved from the resin by adding a 1:1 solution (2 mL) of CH_3NH_2 (8 M in EtOH) and NH_3 (satd. in H_2O) and heating at 65 °C for 1 h. The solvent was removed in vacuo and the 2′*O*-TBDMS groups were removed by incubation in $Et_3N{\cdot}3HF$ (300 µL) in DMF (100 µL) at 55 °C for 1.5 h, followed by addition of deionized and sterilized water (100 µL). This mixture was transferred to a 50 mL Falcon tube and *n*-butanol (20 mL) was added and stored at –20 °C for 14 h, centrifuged and the solvent decanted from the RNA pellet.

All oligonucleotides were subsequently purified by 20 % DPAGE and extracted from the gel slices using the "crush and soak method" with Tris buffer (250 mM NaCl, 10 mM Tris, 1 mM Na_2EDTA, pH 7.5). The solutions were filtered through GD/X syringe filters (0.45 µm, 25 mm diameter, Whatman, USA) and were subsequently desalted using Sep-Pak cartridges (Waters, USA), following the instructions provided by the manufacturer. Dried oligonucleotides were dissolved in deionized and sterilized water (200 µL for each oligonucleotide). Concentrations of the oligonucleotides were determined by measuring absorbance at 260 nm using a Perkin Elmer Inc. Lambda 25 UV/Vis spectrometer and calculated by Beer's law. Mass spectrometric analyses of **Ç**- and **Çm**-labeled oligonucleotides were performed on an HRMS (ESI) (Bruker, MicrOTOF-Q) in negative ion mode.

Enzymatic Digestion of DNA and RNA and HPLC Analysis. To the oligonucleotide (4 nmol) in sterile water (8 µL) was added calf intestinal alkaline phosphatase (1 µL, 2 U), snake venom phosphodiesterase I (4 µL, 0.2 U), nuclease P1 from penicillium citrinum (5 µL, 1.5 U) and Tris buffer (2 µL, 500 mM Tris and 100 mM $MgCl_2$). The samples were incubated at 37 °C for 50 h. Enzymatically digested oligonucleotides were run on a Beckman Coulter Gold HPLC system using Beckman Coulter Ultrasphere C18 4.6 × 250 mm analytical column with UV detection at 254 nm. Solvent gradients for analytical RP-HPLC were run at 1.0 mL/min using following gradient program: solvent A, TEAA buffer (50 mM, pH 7.0); solvent B, CH_3CN; 0–4 min isocratic 4 % B, 4–14 min linear gradient 4–20 % B, 14–24 min linear gradient 20–50 % B, 24–29 min linear gradient 50–80 % B, for 29–30 min isocratic 80 % B, 30–35 min linear gradient 80–4 % B and 35–45 min isocratic 4 % B.

Acknowledgments

The authors acknowledge financial support by the Icelandic Research Fund (141062-051). The authors thank Dr S. Jonsdottir for assistance with collecting analytical data for structural characterization of new compounds and members of the Sigurdsson research group for helpful discussions.

Keywords: EPR spectroscopy · Nitroxides · Oligonucleotides · Site-directed spin labeling

[1] K. Chen, Boxuan S. Zhao, C. He, *Cell Chem. Biol.* **2016**, *23*, 74–85.
[2] A. Ducruix, R. Giegé, *Crystallization of Nucleic Acids and Proteins: A Practical Approach*, Oxford University Press, **1999**.
[3] D. R. Cooper, P. J. Porebski, M. Chruszcz, W. Minor, *Expert Opin. Drug Discovery* **2011**, *6*, 771–782.

[4] a) A. M. Spring-Connell, M. Evich, M. W. Germann, *Curr. Protoc. Nucleic Acid Chem.* **2018**, *72*, 7.28.21–27.28.39; b) L. G. Scott, M. Hennig, in *Bioinformatics: Data, Sequence Analysis and Evolution* (Ed.: J. M. Keith), Humana Press, Totowa, NJ, **2008**, pp. 29–61; c) M. Getz, X. Sun, A. Casiano-Negroni, Q. Zhang, H. M. Al-Hashimi, *Biopolymers* **2007**, *86*, 384–402.

[5] J. H. Lee, Y. Okuno, S. Cavagnero, *J. Magn. Reson.* **2014**, *241*, 18–31.

[6] S. Preus, L. M. Wilhelmsson, *ChemBioChem* **2012**, *13*, 1990–2001.

[7] M. F. Juette, D. S. Terry, M. R. Wasserman, Z. Zhou, R. B. Altman, Q. Zheng, S. C. Blanchard, *Curr. Opin. Chem. Biol.* **2014**, *20*, 103–111.

[8] a) N. K. Kim, A. Murali, V. J. DeRose, *Chem. Biol.* **2004**, *11*, 939–948; b) J. C. Macosko, M. S. Pio, I. Tinoco, Y. K. Shin, *RNA* **1999**, *5*, 1158–1166.

[9] a) G. W. Reginsson, O. Schiemann, *Biochem. Soc. Trans.* **2011**, *39*, 128; b) T. Schmidt, M. A. Wälti, J. L. Baber, E. J. Hustedt, G. M. Clore, *Angew. Chem. Int. Ed.* **2016**, *55*, 15905–15909; *Angew. Chem.* **2016**, *128*, 16137; c) P. Z. Qin, K. Warncke, *Electron Paramagnetic Resonance Investigations of Biological Systems by Using Spin Labels, Spin Probes, and Intrinsic Metal Ions*, Elsevier Science **2015**.

[10] M. Wanunu, Y. Tor, *Methods for Studying Nucleic Acid/Drug Interactions*, CRC Press, **2016**.

[11] a) B. Endeward, A. Marko, V. P. Denysenkov, S. T. Sigurdsson, T. F. Prisner, in *Methods in Enzymology, Vol. 564* (Eds.: P. Z. Qin, K. Warncke), Academic Press, **2015**, pp. 403–425; b) T. F. Prisner, A. Marko, S. T. Sigurdsson, *J. Magn. Reson.* **2015**, *252*, 187–198.

[12] a) A. Potapov, H. Yagi, T. Huber, S. Jergic, N. E. Dixon, G. Otting, D. Goldfarb, *J. Am. Chem. Soc.* **2010**, *132*, 9040–9048; b) Y. Yang, F. Yang, Y.-J. Gong, J.-L. Chen, D. Goldfarb, X.-C. Su, *Angew. Chem. Int. Ed.* **2017**, *56*, 2914–2918; *Angew. Chem.* **2017**, *129*, 2960.

[13] a) N. Kocherginsky, H. M. Swartz, *Nitroxide Spin Labels: Reactions in Biology and Chemistry*, Taylor & Francis, **1995**; b) M. Martinho, E. Fournier, N. Le Breton, E. Mileo, V. Belle, in *Electron Paramagnetic Resonance: Volume 26, Vol. 26*, The Royal Society of Chemistry, **2019**, pp. 66–88.

[14] a) G. Z. Sowa, P. Z. Qin, in *Progress in Nucleic Acid Research and Molecular Biology, Vol. 82* (Ed.: P. M. Conn), Academic Press, **2008**, pp. 147–197; b) M. M. Haugland, J. E. Lovett, E. A. Anderson, *Chem. Soc. Rev.* **2018**, *47*, 668–680; c) N. R. Kamble, S. T. Sigurdsson, *Chem. Eur. J.* **2018**, *24*, 4157–4164; d) S. A. Shelke, S. T. Sigurdsson, *Eur. J. Org. Chem.* **2012**, *2012*, 2291; e) S. Saha, T. Hetzke, T. F. Prisner, S. T. Sigurdsson, *Chem. Commun.* **2018**, *54*, 11749–11752.

[15] a) K. Nakatani, Y. Tor, *Modified Nucleic Acids*, Springer International Publishing, **2016**; b) I. Tkach, S. Pornsuwan, C. Höbartner, F. Wachowius, S. T. Sigurdsson, T. Y. Baranova, U. Diederichsen, G. Sicoli, M. Bennati, *Phys. Chem. Chem. Phys.* **2013**, *15*, 3433–3437; c) P. E. Spindler, P. Schöps, W. Kallies, S. J. Glaser, T. F. Prisner, *J. Magn. Reson.* **2017**, *280*, 30–45.

[16] N. Barhate, P. Cekan, A. P. Massey, S. T. Sigurdsson, *Angew. Chem. Int. Ed.* **2007**, *46*, 2655–2658; *Angew. Chem.* **2007**, *119*, 2709.

[17] a) N. Piton, Y. Mu, G. Stock, T. F. Prisner, O. Schiemann, J. W. Engels, *Nucleic Acids Res.* **2007**, *35*, 3128–3143; b) P. Cekan, A. L. Smith, N. Barhate, B. H. Robinson, S. T. Sigurdsson, *Nucleic Acids Res.* **2008**, *36*, 5946–5954.

[18] A. Hatano, N. Terado, Y. Kanno, T. Nakamura, G. Kawai, *Synth. Commun.* **2019**, *49*, 136–145.

[19] B. A. Chalmers, J. C. Morris, K. E. Fairfull-Smith, R. S. Grainger, S. E. Bottle, *Chem. Commun.* **2013**, *49*, 10382–10384.

[20] E. L. Dane, B. Corzilius, E. Rizzato, P. Stocker, T. Maly, A. A. Smith, R. G. Griffin, O. Ouari, P. Tordo, T. M. Swager, *J. Org. Chem.* **2012**, *77*, 1789–1797.

[21] a) I. Seven, T. Weinrich, M. Gränz, C. Grünewald, S. Brüß, I. Krstić, T. F. Prisner, A. Heckel, M. W. Göbel, *Eur. J. Org. Chem.* **2014**, *2014*, 4037–4043; b) T. Weinrich, E. A. Jaumann, U. Scheffer, T. F. Prisner, M. W. Göbel, *Chem. Eur. J.* **2018**, *24*, 6202–6207.

[22] a) C. Brieke, F. Rohrbach, A. Gottschalk, G. Mayer, A. Heckel, *Angew. Chem. Int. Ed.* **2012**, *51*, 8446–8476; *Angew. Chem.* **2012**, *124*, 8572; b) S. Keyhani, T. Goldau, A. Blümler, A. Heckel, H. Schwalbe, *Angew. Chem. Int. Ed.* **2018**, *57*, 12017–12021; *Angew. Chem.* **2018**, *130*, 12193.

[23] Y. Sato, H. Hayashi, M. Okazaki, M. Aso, S. Karasawa, S. Ueki, H. Suemune, N. Koga, *Magn. Reson. Chem.* **2008**, *46*, 1055–1058.

[24] M. Kurita, Y. Higuchi, J. W. Mirc, S. Matsumoto, K. Usui, H. Suemune, M. Aso, *ChemBioChem* **2016**, *17*, 2346–2352.

[25] a) J. F. W. Keana, G. S. Heo, G. T. Gaughan, *J. Org. Chem.* **1985**, *50*, 2346–2351; b) D. R. Alessi, J. E. T. Corrie, J. Feeney, I. P. Trayer, D. R. Trentham, *J. Chem. Soc., Perkin Trans. 1* **1991**, 2243–2247; c) É. G. Rozantsev, V. A. Golubev, *Zzv. Akad. Nauk SSSR, Ser. Khim.* **1966**, 000–000; d) V. D. Sholle, V. A. Golubev, É. G. Rozantsev, *Bull. Acad. Sci. USSR Div. Chem. Sci. (Engl. Transl.)* **1972**, *21*, 1163–1165; e) K. E. Fairfull-Smith, F. Brackmann, S. E. Bottle, *Eur. J. Org. Chem.* **2009**, *2009*, 1902–1915; f) K. Hideg, J. Csekö, H. O. Hankovszky, P. Sohár, *Can. J. Chem.* **1986**, *64*, 1482–1490.

[26] C. Höbartner, G. Sicoli, F. Wachowius, D. B. Gophane, S. T. Sigurdsson, *J. Org. Chem.* **2012**, *77*, 7749–7754.

[27] H. Gustmann, A.-L. J. Segler, D. B. Gophane, A. J. Reuss, C. Grünewald, M. Braun, J. E. Weigand, S. T. Sigurdsson, J. Wachtveitl, *Nucleic Acids Res.* **2019**, *47*, 15–28.

Received: April 10, 2019

Supporting Information

Benzoyl-Protected Hydroxylamines for Improved Chemical Synthesis of Oligonucleotides Containing Nitroxide Spin Labels

Haraldur Y. Juliusson, Anna-Lena J. Segler, and Snorri Th. Sigurdsson*

ejoc201900553-sup-0001-SupMat.pdf

Table of contents

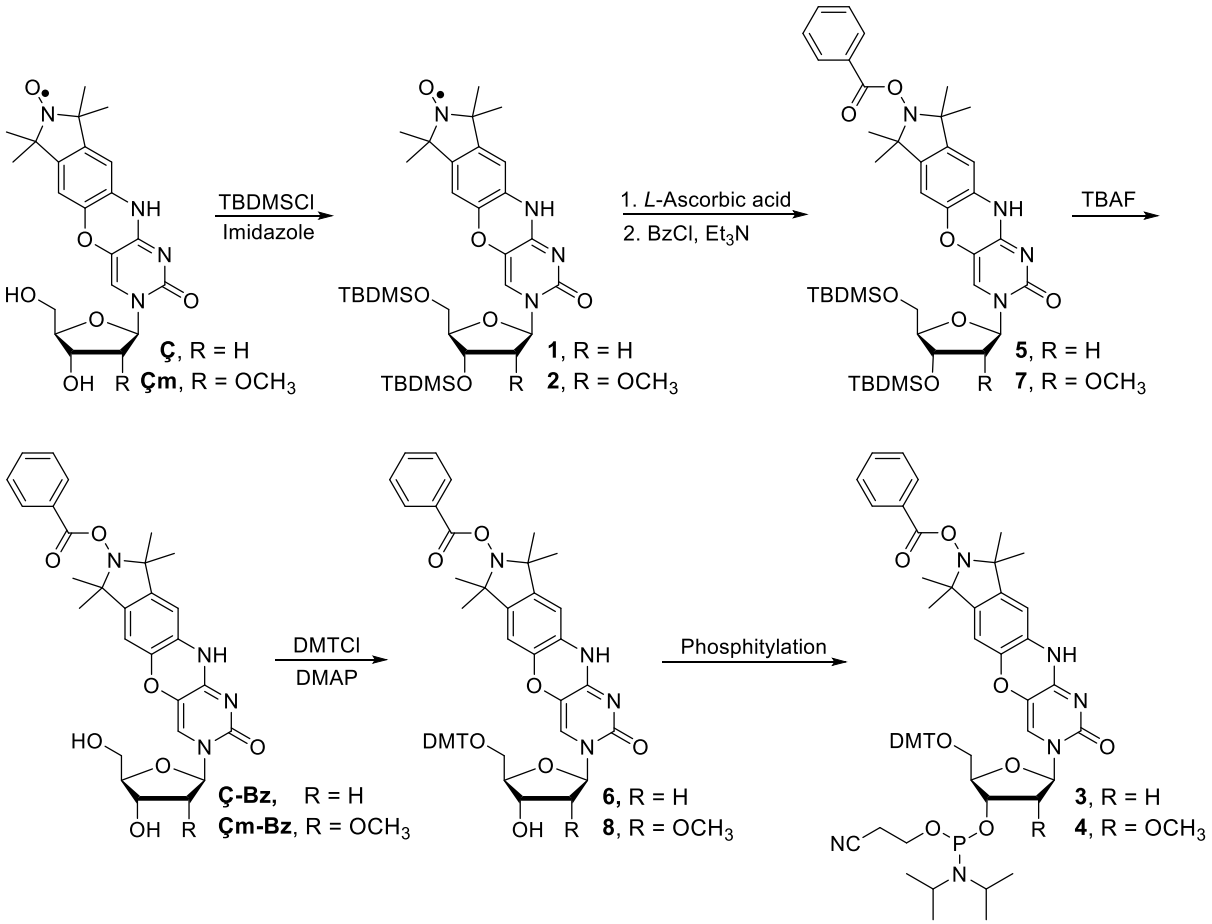

Scheme S1. Synthesis of phosphoramidites **3** and **4.**

MS analyses of oligonucleotides. The incorporation of **Ç** and **Çm** into oligonucleotides was confirmed by HRMS (ESI) analysis. The calculated and observed monoisotopic masses of spin-labeled oligonucleotides are listed in **Table S1**.

Table S1. Monoisotopic masses of spin-labeled oligonucleotides. Oligonucleotides II* and VI* were synthesized with the phosphoramidite of unprotected nitroxide spin-labels **Çm** and **Ç**, respectively. PHO is a phosphate.

Name	Sequence	(calculated)	(found)
I	5‘-UGCAU**Çm**UU-3‘	2662.4	2662.3
II*	5‘-UGCAU**Çm**UU-3‘	2662.4	2662.7
III	5‘-AGA-UGC-GCG-**Çm**GC-GCG-ACU-GAC-3‘	6953.0	6952.5
IV*	5‘-d(PHO-TGAGGTAGTAGGTTGTATA**Ç**T)-3	6809.2	6807.7
V	5‘-d(PHO-TGAGGTAGTAGGTTGTATA**Ç**T)-3	6809.2	6808.0
VI	5‘-d(TGTAA**Ç**GCACTACCAGCGGCTGGAAATCT**Ç**TCTCGT)-3‘	11400.4	11400.1

^{1}H and ^{13}C NMR spectra

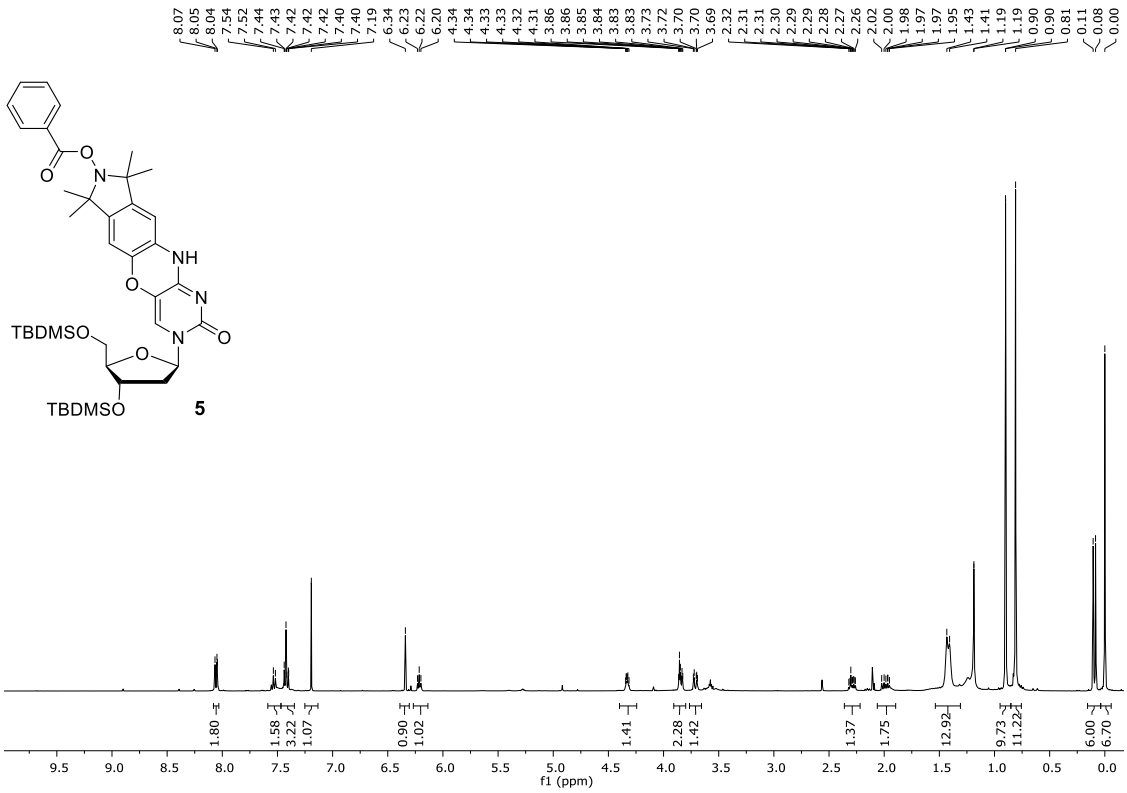

Figure S1. ^{1}H NMR of **5**.

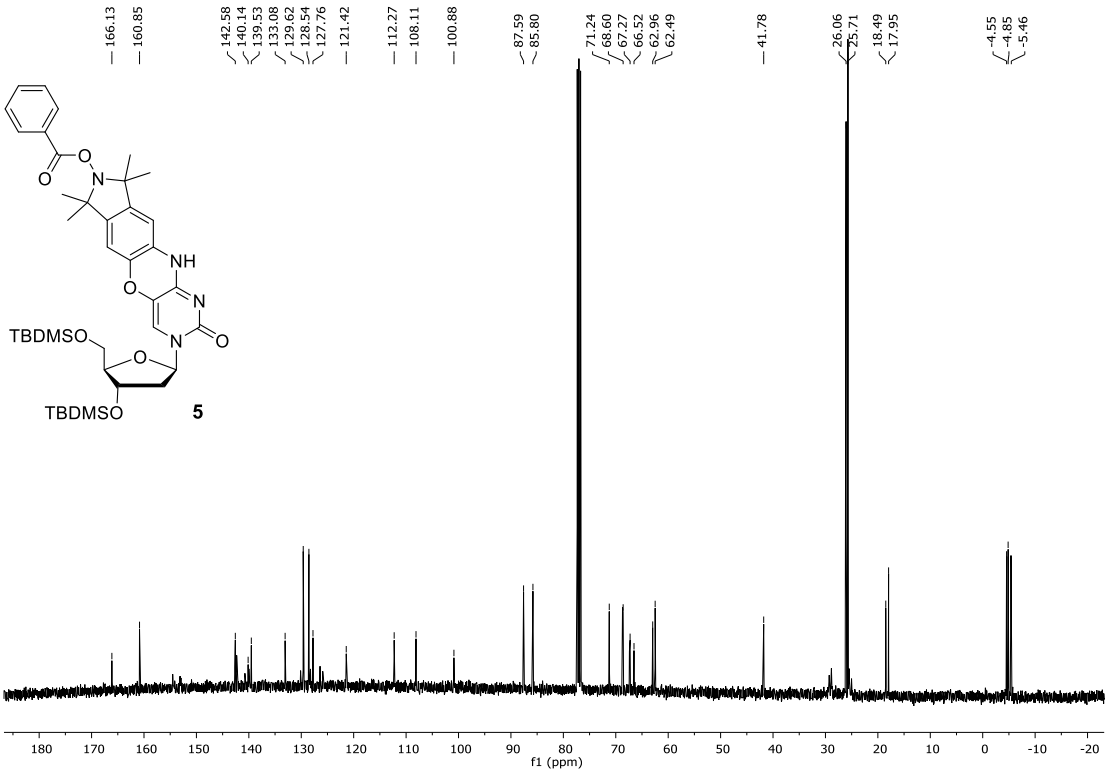

Figure S2. ^{13}C NMR of **5**.

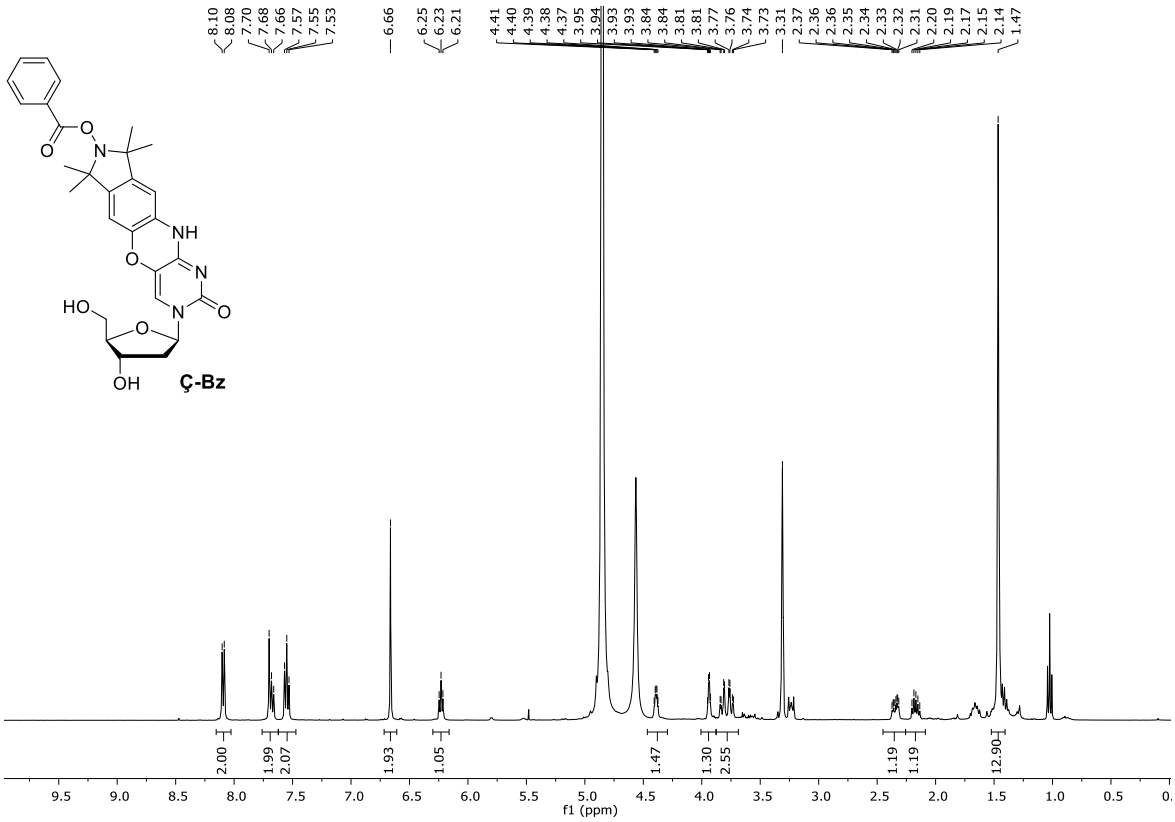

Figure S3. ^{1}H NMR of **Ç-Bz**.

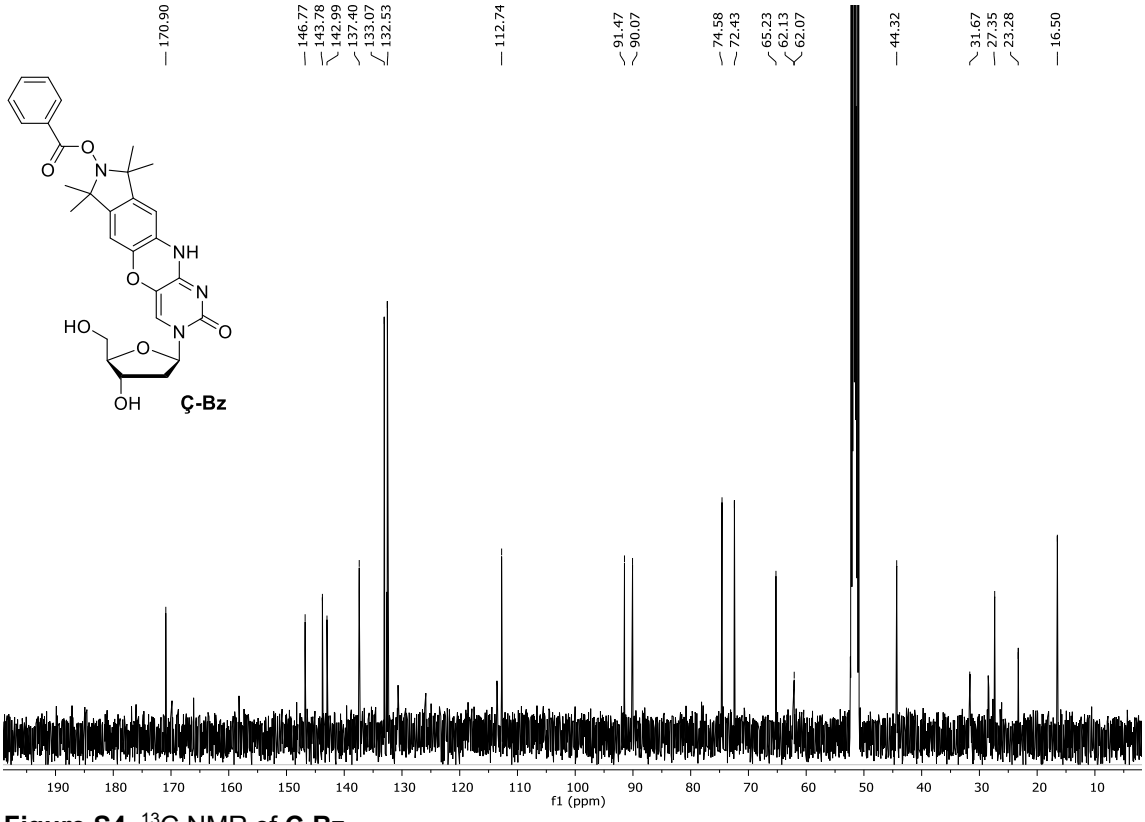

Figure S4. ^{13}C NMR of **Ç-Bz**.

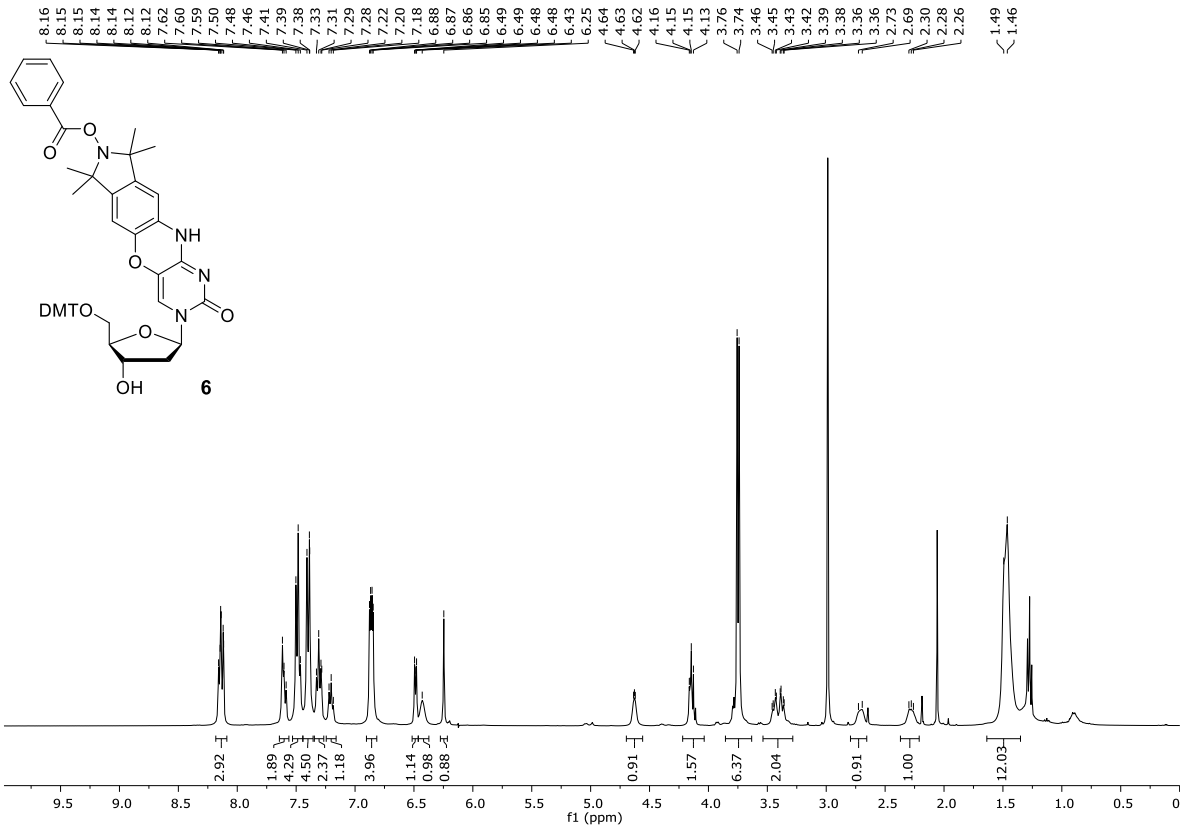

Figure S5. ^{1}H NMR of tritylated nucleoside **6**.

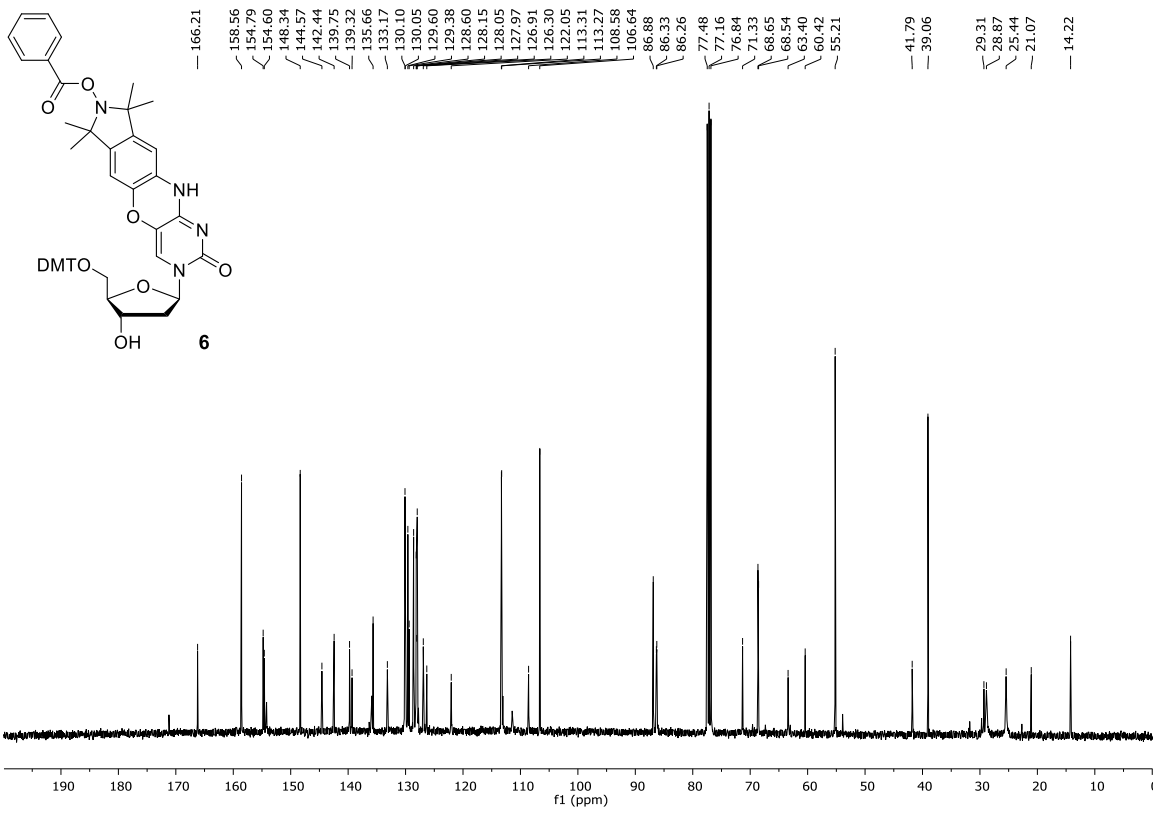

Figure S6. ^{13}C NMR of tritylated nucleoside **6**.

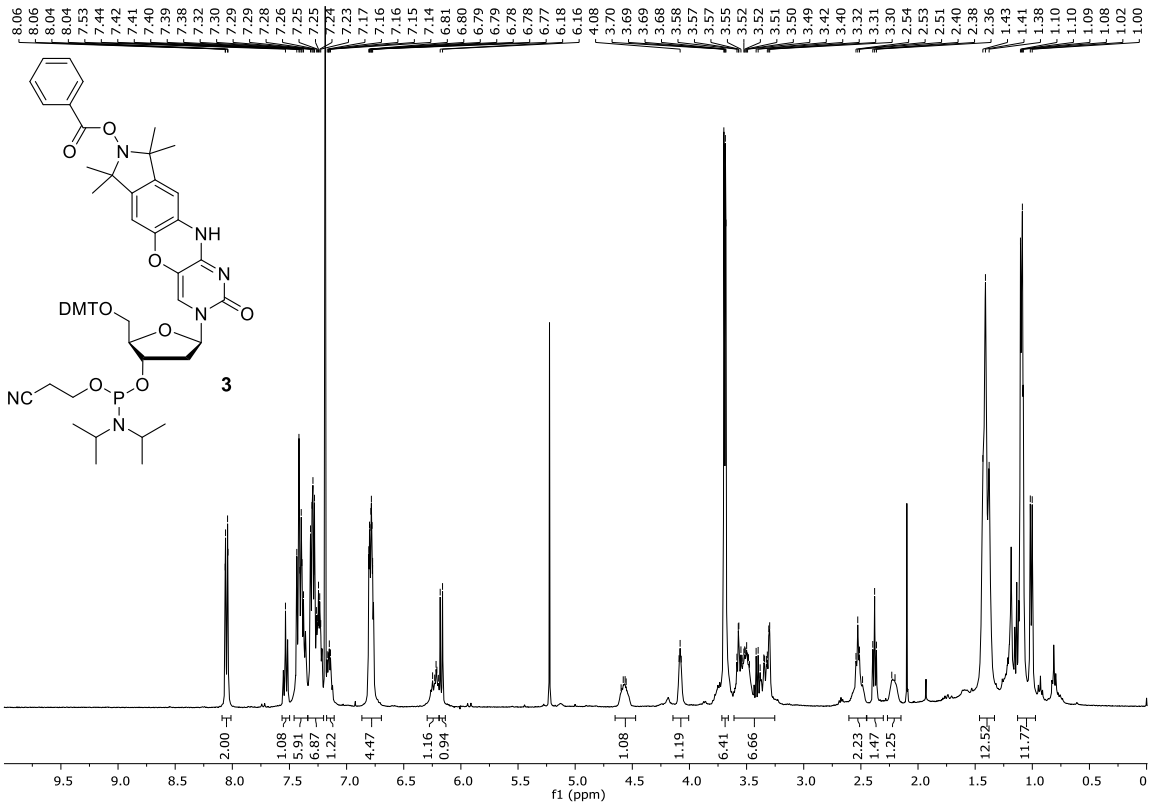

Figure S7. ^{1}H NMR of phosphoramidite **3**.

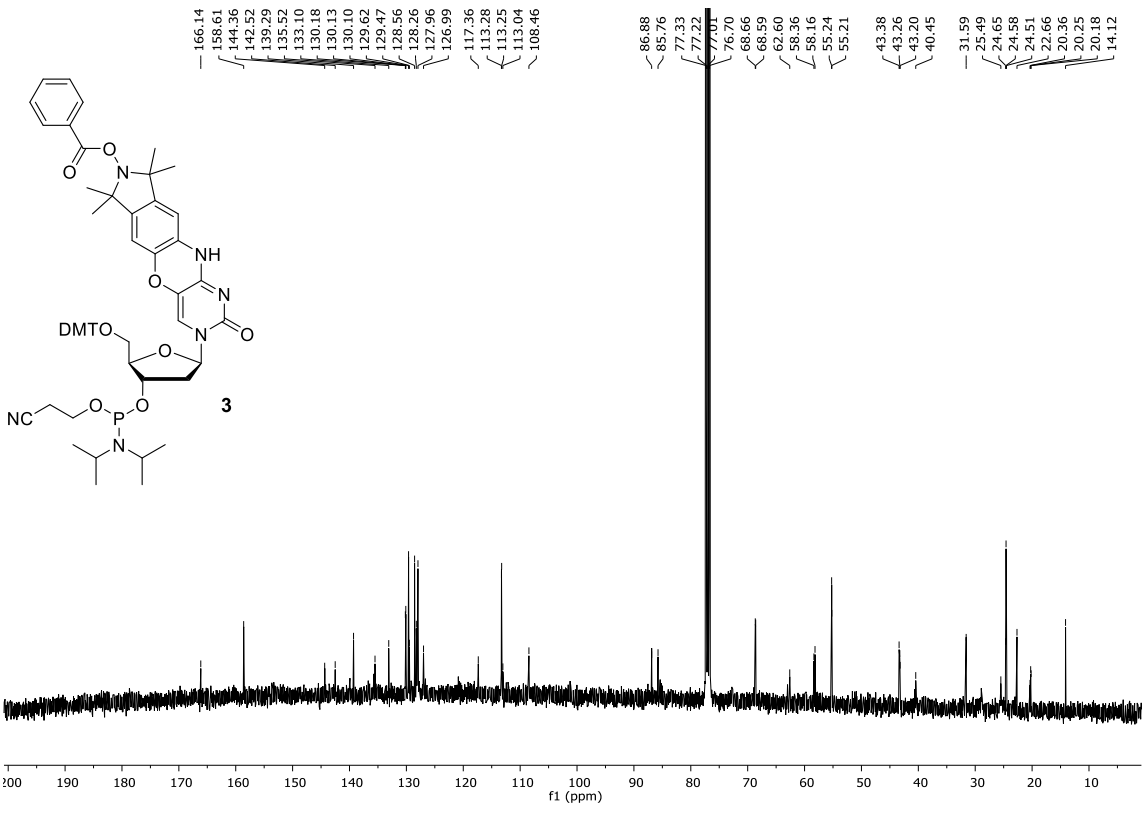

Figure S8. ^{13}C NMR of phosphoramidite **3**.

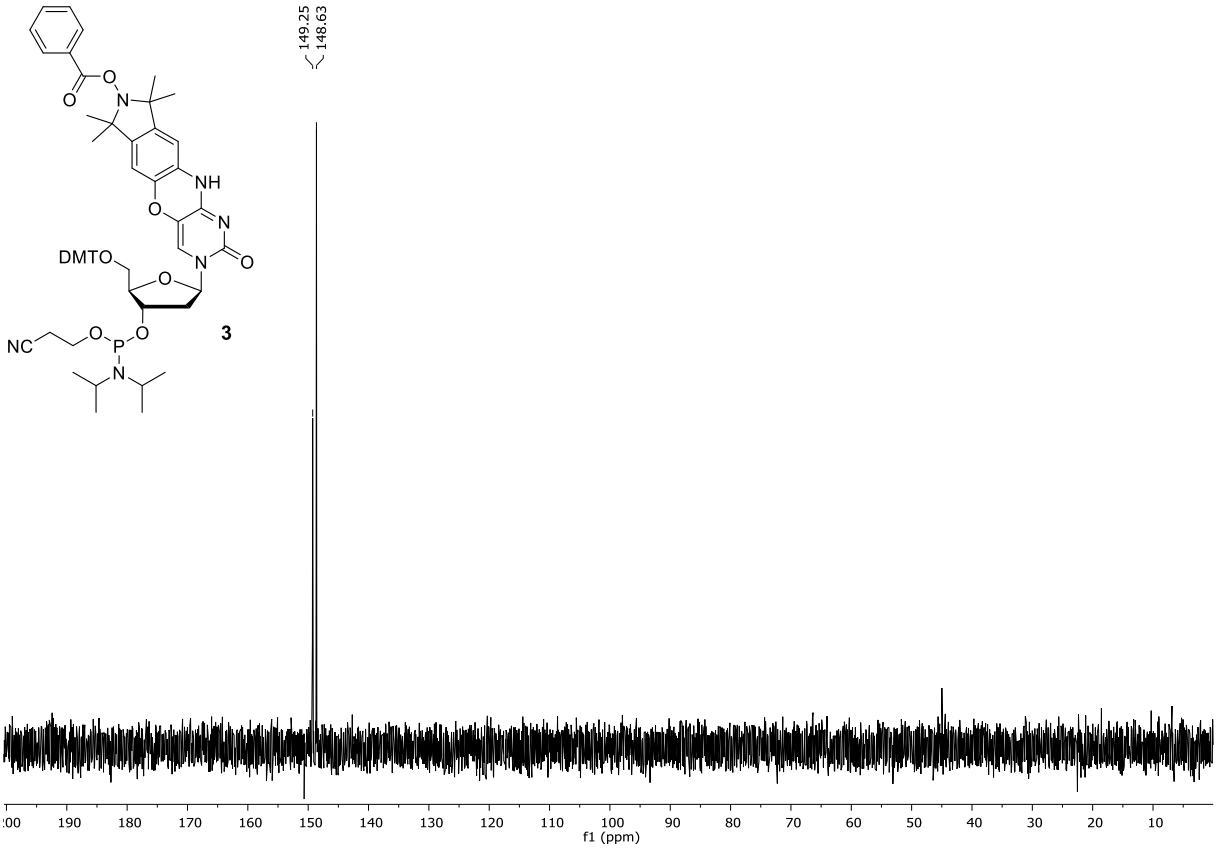

Figure S9. ^{31}P NMR of phosphoramidite **3**.

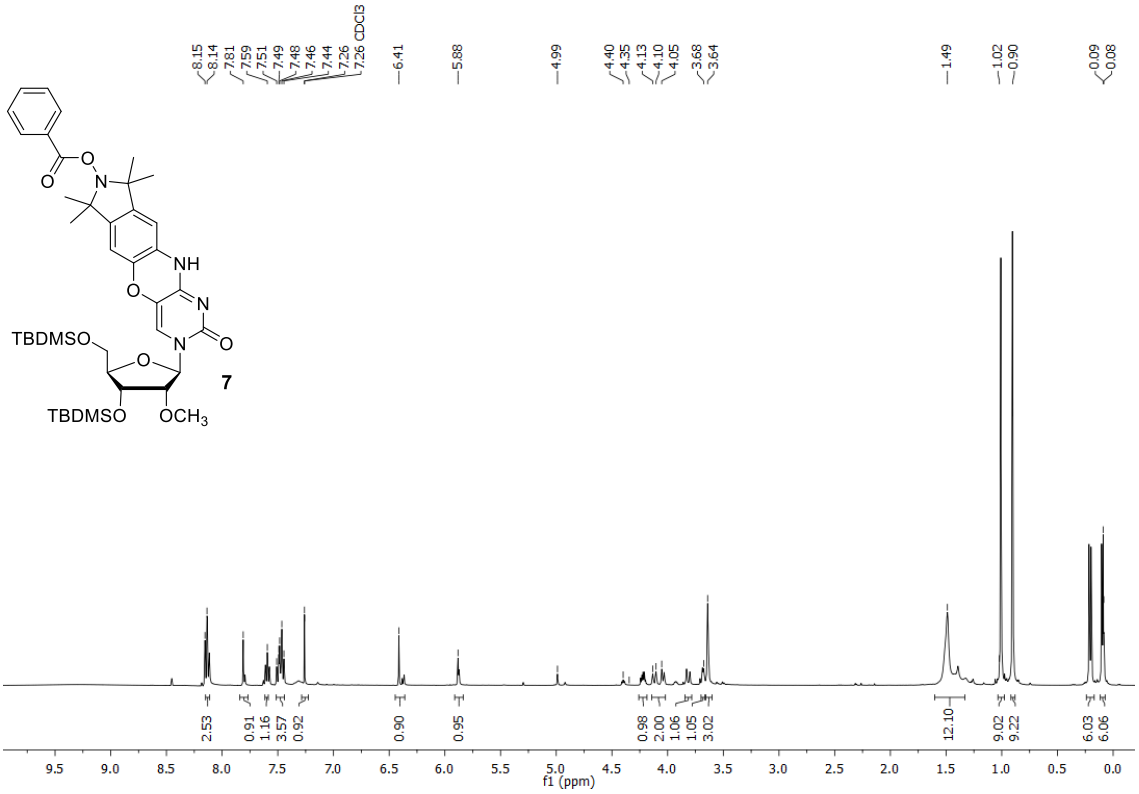

Figure S10. ^{1}H NMR of **7**.

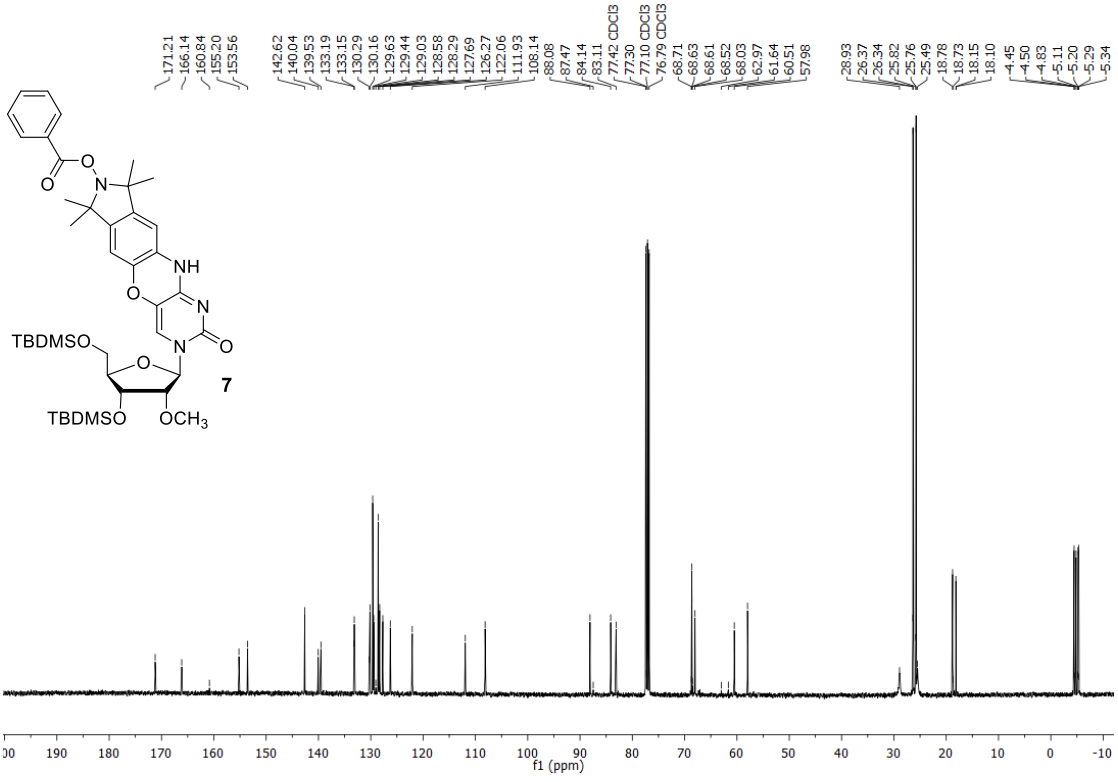

Figure S11. ^{13}C NMR of **7**.

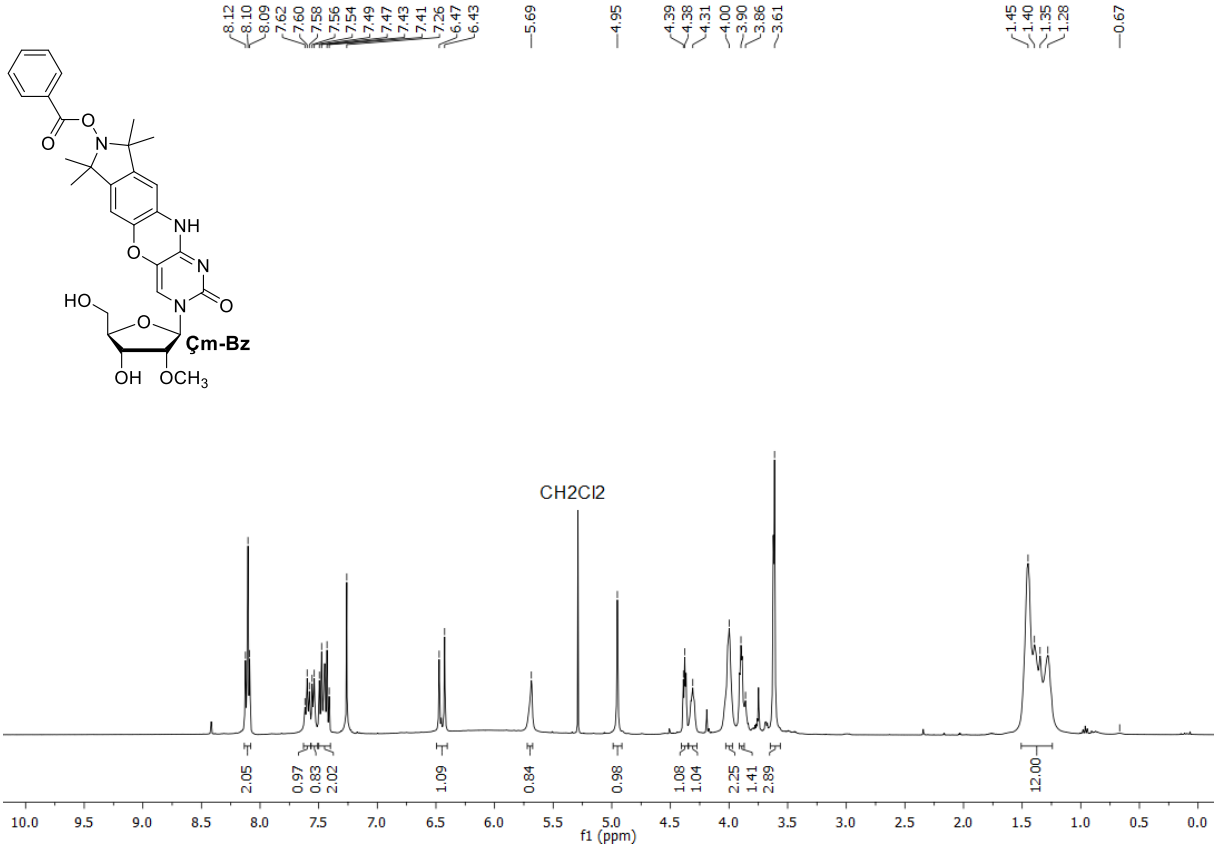

Figure S12. ^{1}H NMR of **Çm-Bz.**

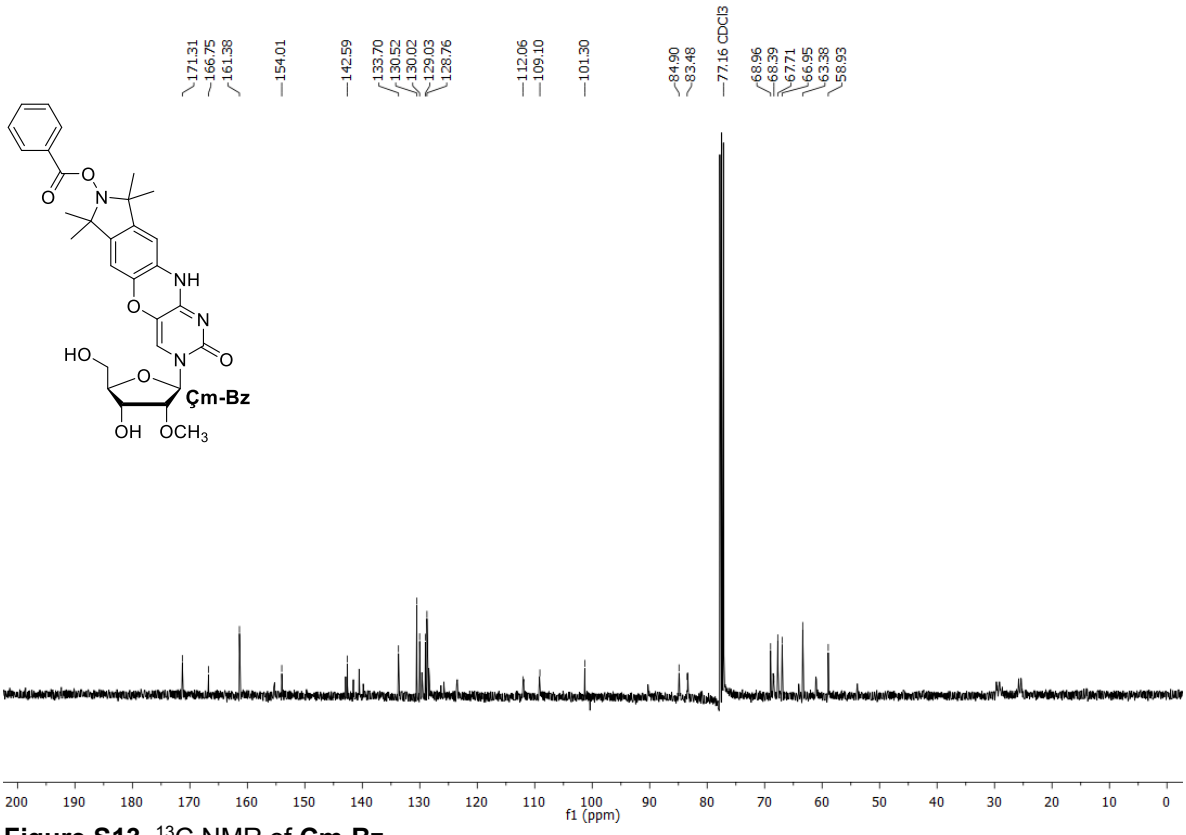

Figure S13. ^{13}C NMR of **Çm-Bz**.

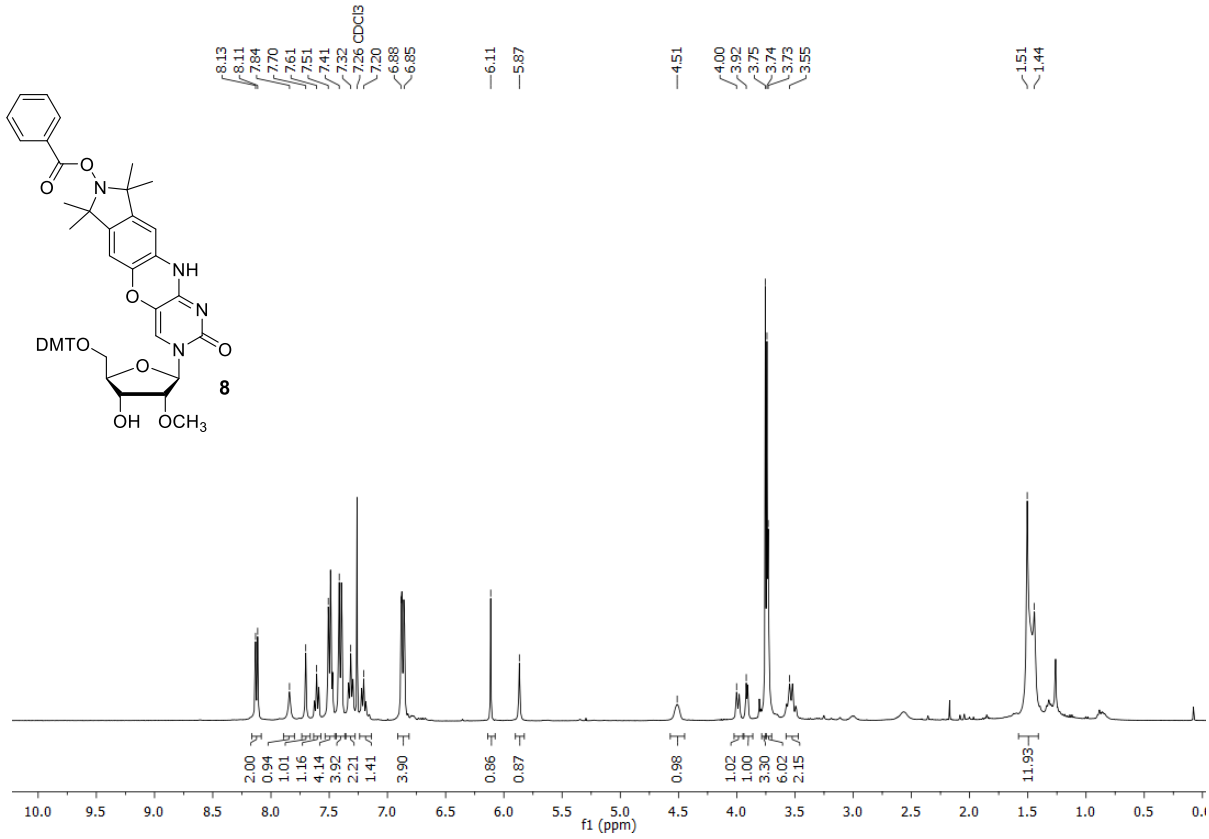

Figure S14. ^{1}H NMR of tritylated nucleoside **8**.

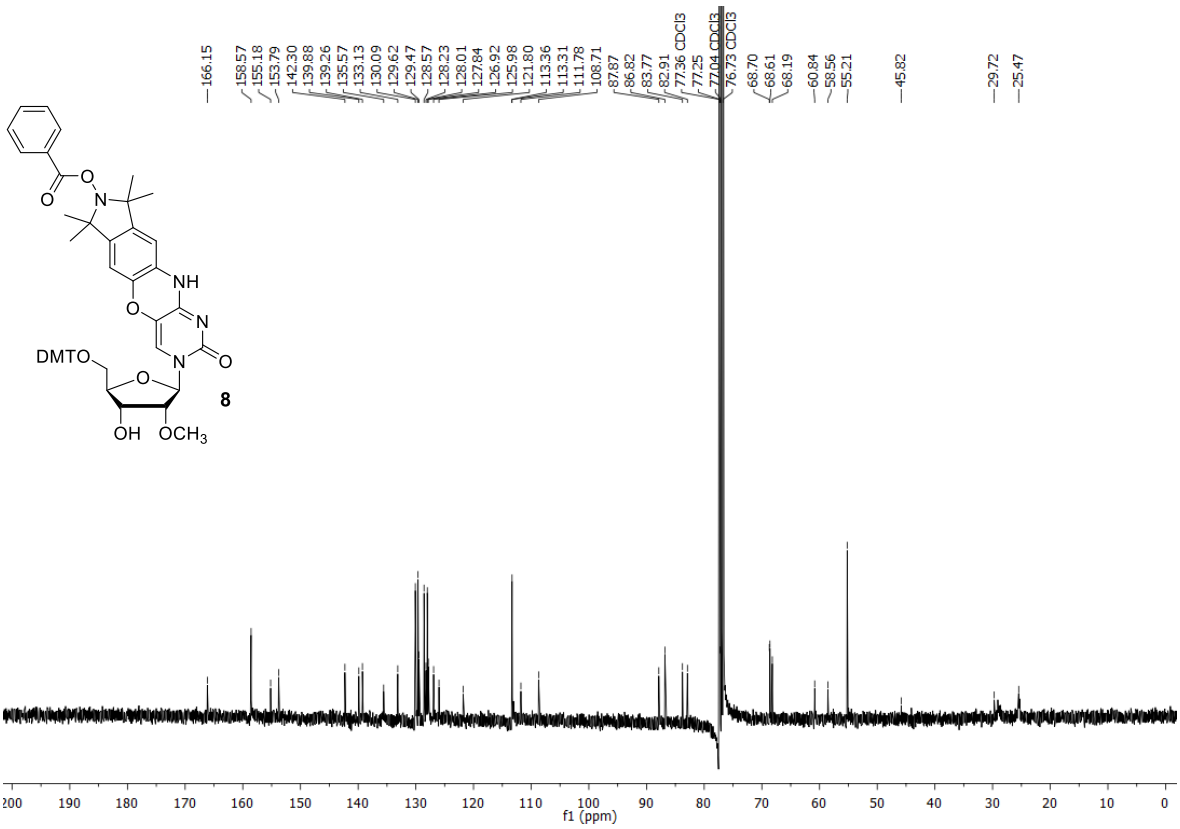

Figure S15. ^{13}C NMR of tritylated nucleoside **8**.

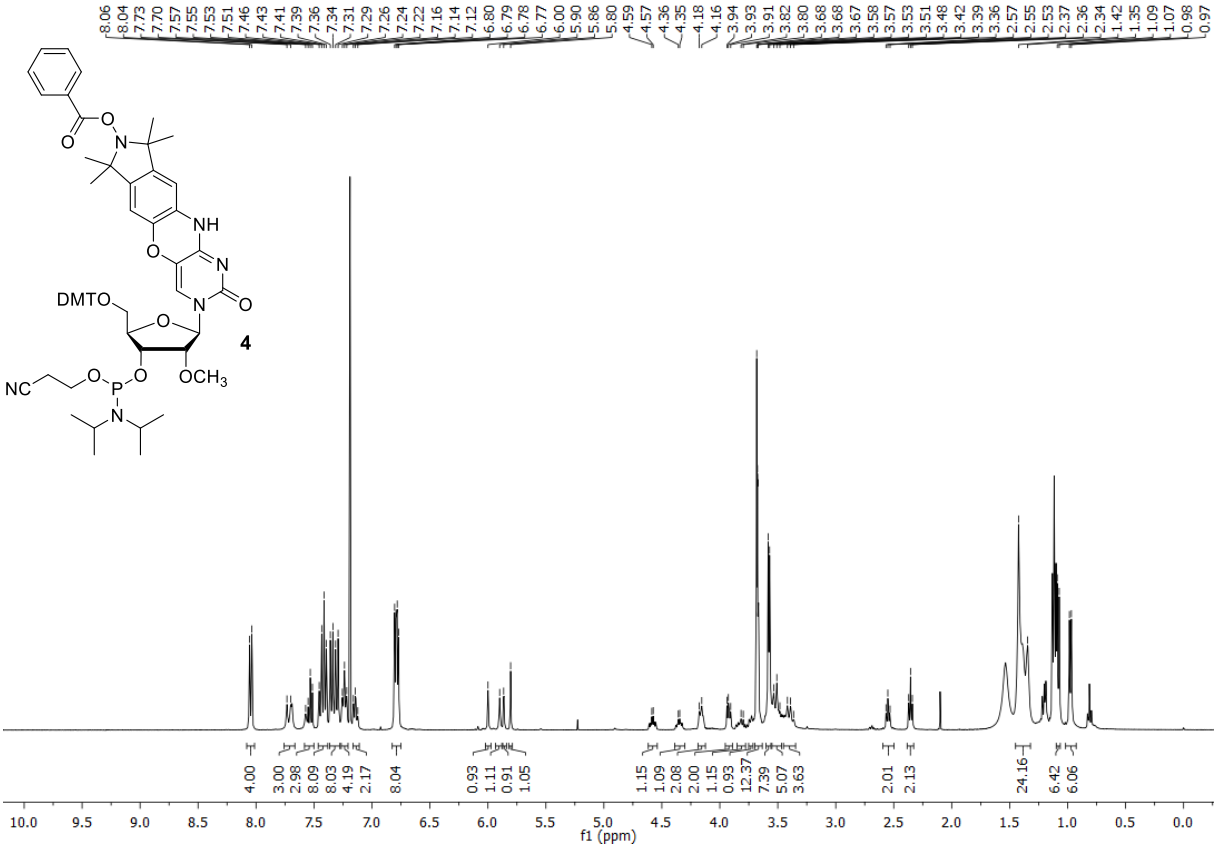

Figure S16. ^{1}H NMR of phosphoramidite **4**.

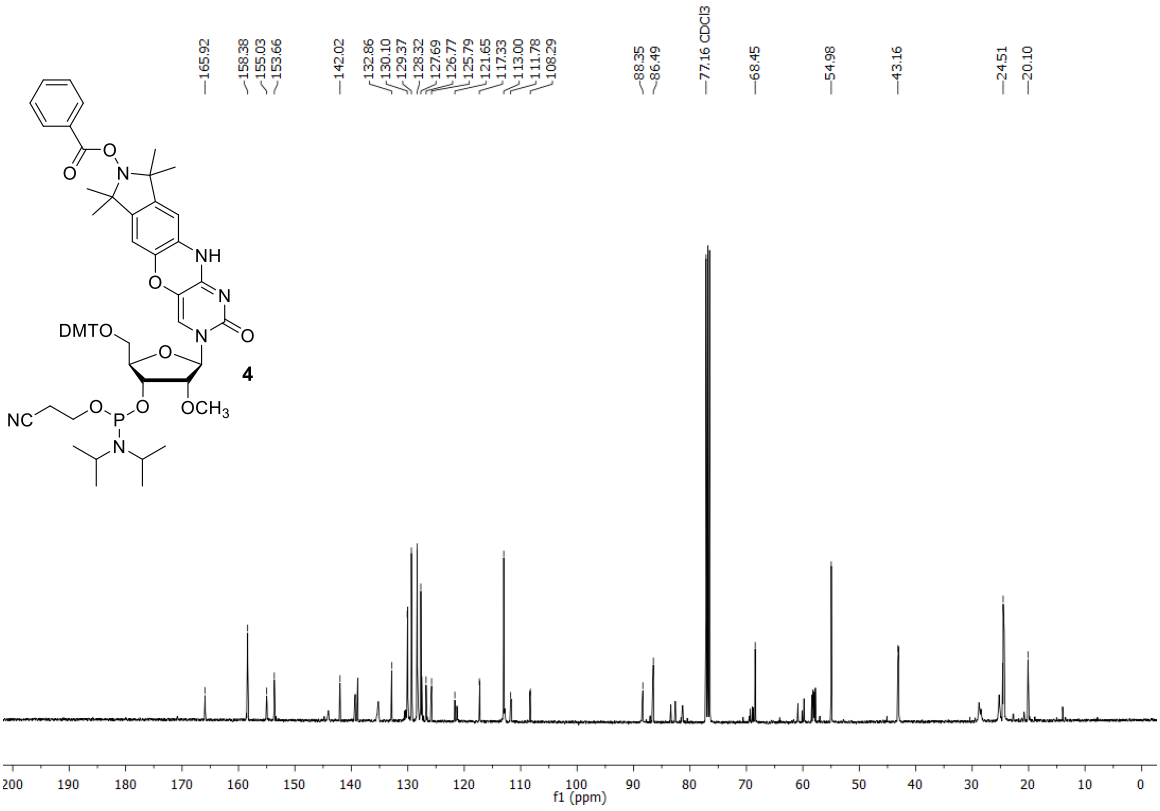

Figure S17. ^{13}C NMR of phosphoramidite **4**.

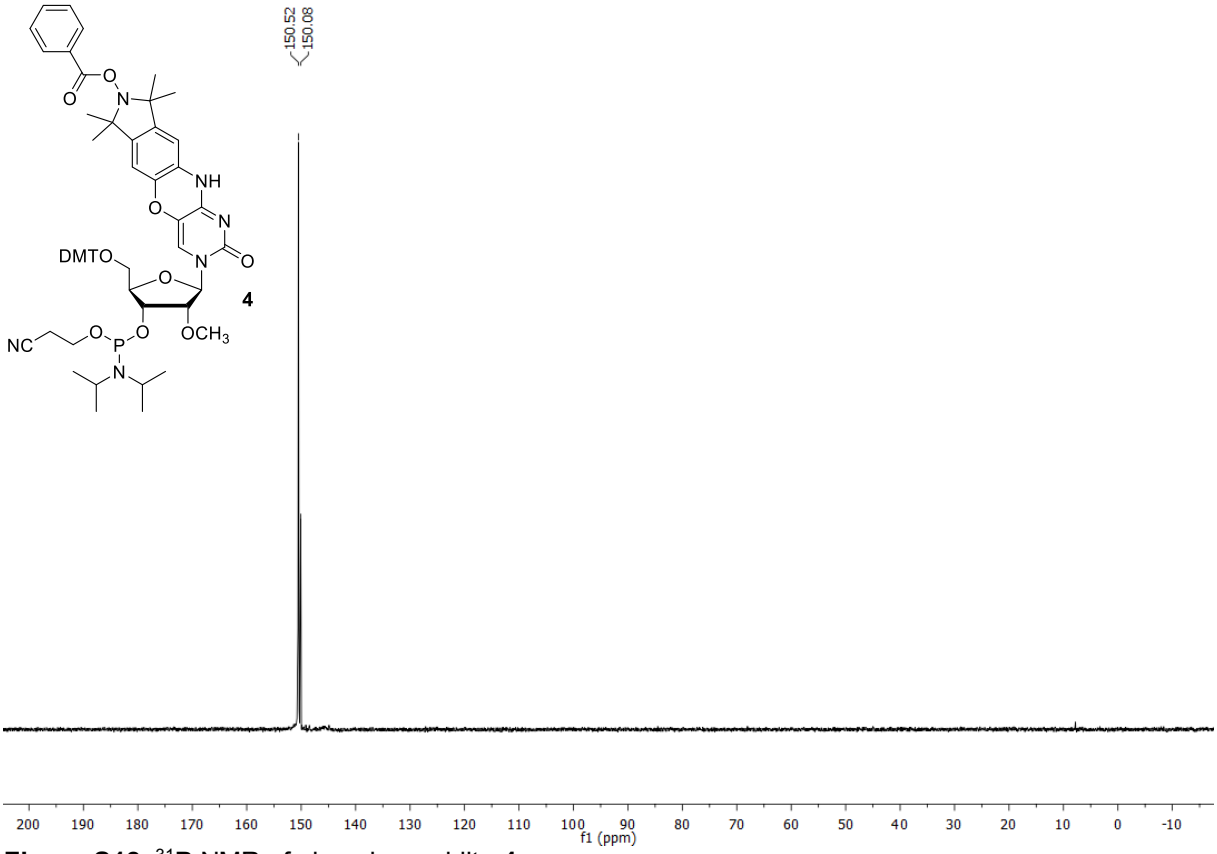

Figure S18. ^{31}P NMR of phosphoramidite **4**.

Mass spectra measured by HRMS (ESI)

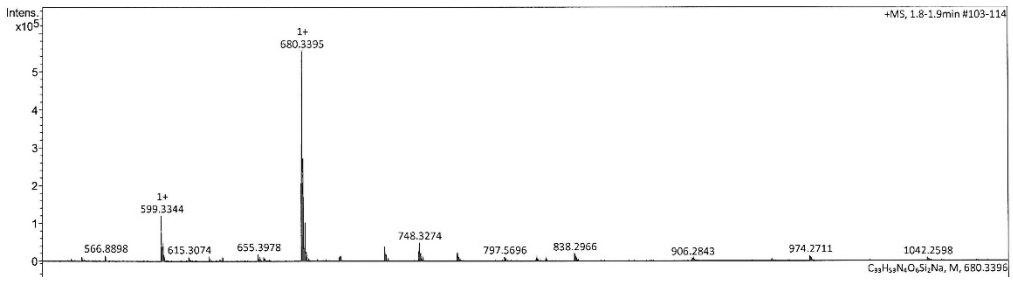

Figure S19. Mass spectrum of **1**.

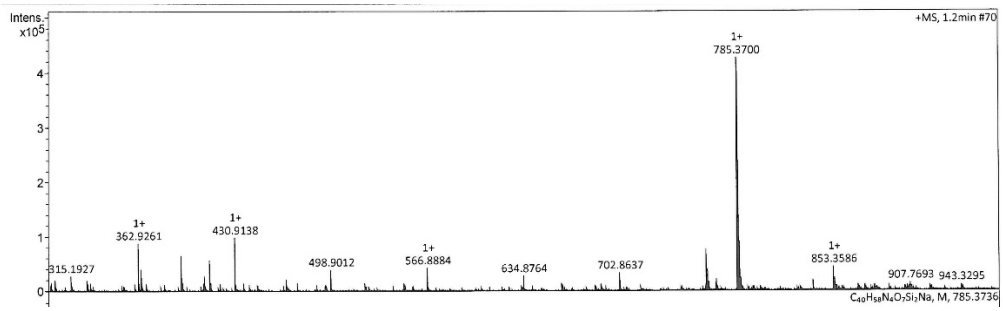

Figure S20. Mass spectrum of **5**.

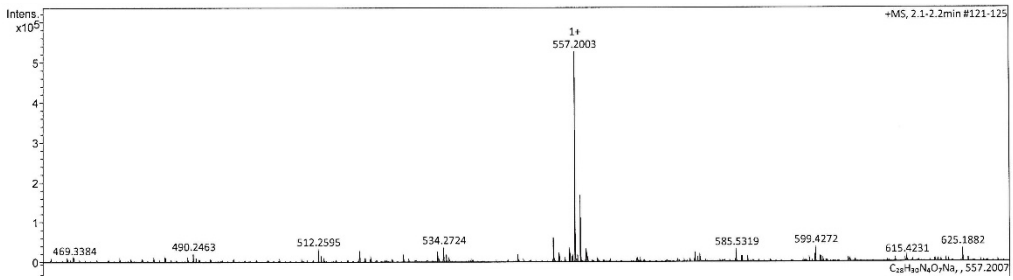

Figure S21. Mass spectrum of **Ç-Bz**.

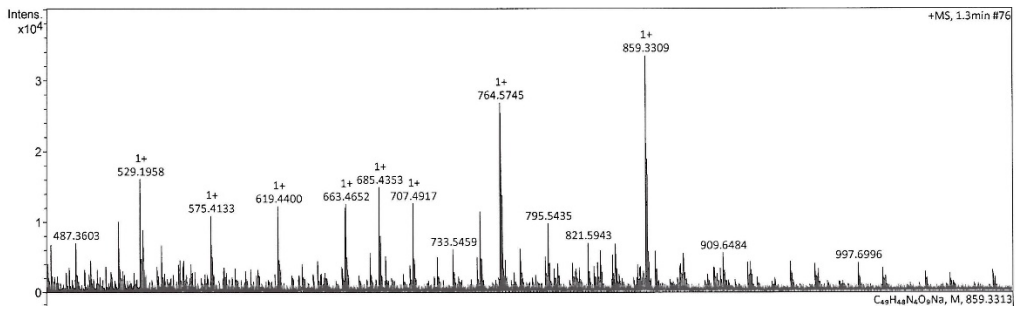

Figure S22. Mass spectrum of **6**.

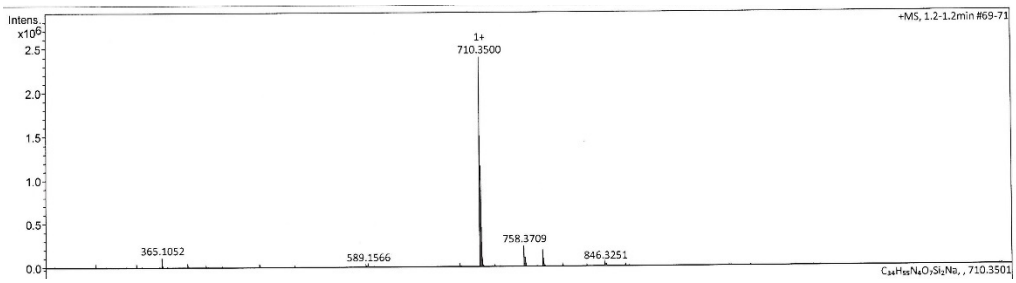

Figure S23. Mass spectrum of **2**.

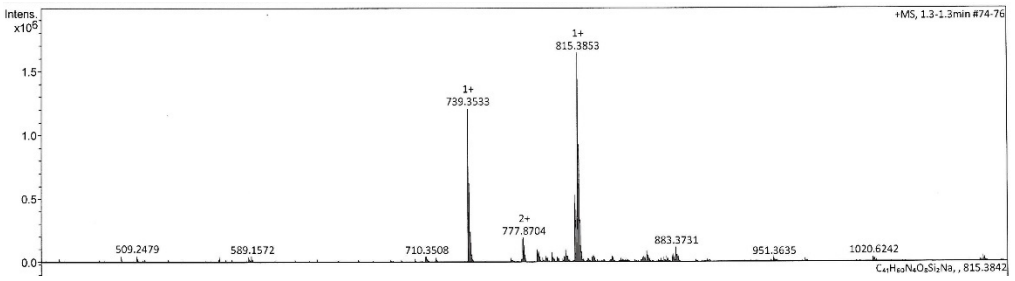

Figure S24. Mass spectrum of **7**.

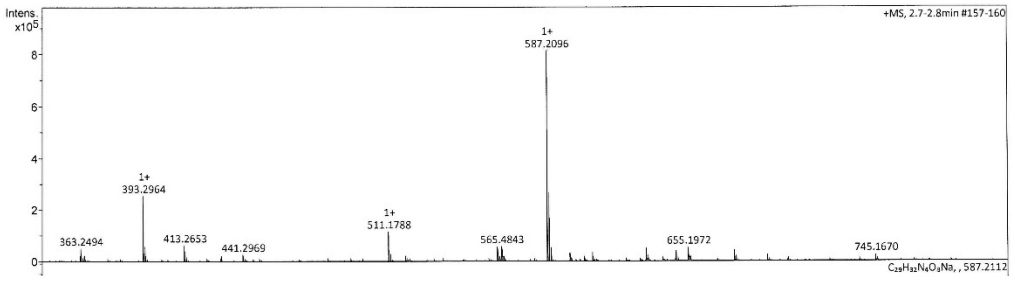

Figure S25. Mass spectrum of **Çm-Bz**.

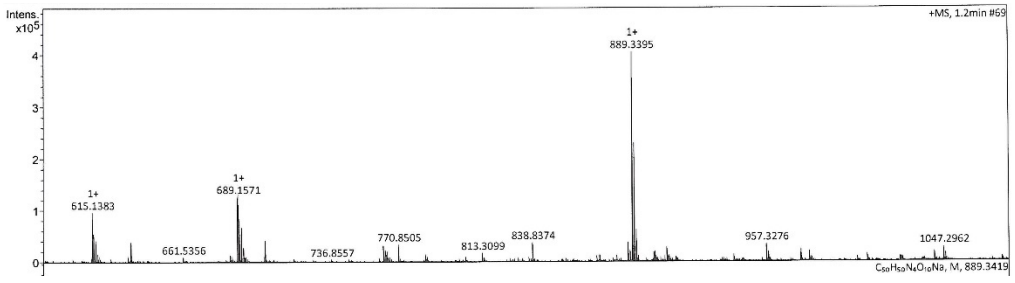

Figure S26. Mass spectrum of **8**.

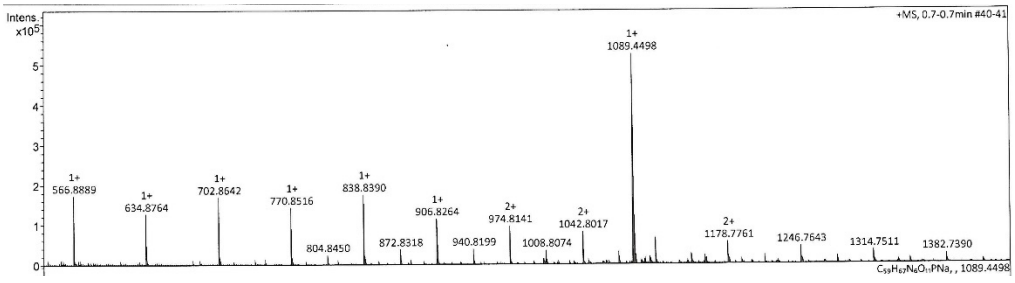

Figure S27. Mass spectrum of **4**.

CW-EPR measurements and spin counting. CW-EPR spectra were recorded on a MiniScope MS200 spectrometer using 100 kHz modulation frequency, 1.0 G modulation amplitude, and 2.0 mW microwave power. The samples were placed in a quartz capillary (BLAUBRANDintraMARK) prior to EPR measurements. Samples of spin-labeled oligonucleotides for EPR measurements were prepared by dissolving spin-labeled, single-stranded DNA or RNA (2.0 nmol) in phosphate buffer (10 mM phosphate, 100 mM NaCl, 0.1 mM Na_2EDTA, pH 7.0; 10 µL, oligonucleotide final conc. 200 µM). The EPR spectra of spin-labeled oligonucleotides I-VI are shown in **Figure S28**.

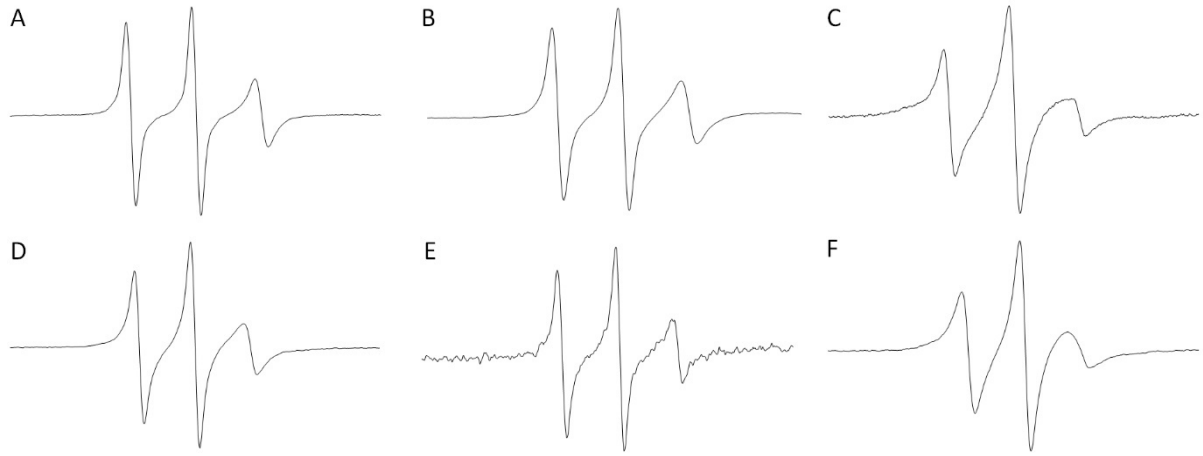

Figure S28. EPR spectra of oligonucleotides. **A**. Crude RNA **I** (5'-UGCAU**Çm**UU-3') synthesized using **4**. **B**. Crude RNA **II** (5'-UGCAU**Çm**UU-3') synthesized using the phosphoramidite of unprotected **Çm**. **C**. RNA **III** (5'-AGAUGCGCG**Çm**GCGCGACUGAC-3') synthesized using **4**. **D**. Crude DNA **IV** (5'-d(PHO-TGAGGTAGTAGGTTGTATA**Ç**T)-3') synthesized using **3**. **E**. Crude DNA **V** (5'-d(PHO-TGAGGTAGTAGGTTGTATA**Ç**T)-3') synthesized using the phosphoramidite of unprotected **Ç**. **F**. DNAzyme **VI** (5'-d(TGTAA**Ç**GCACTACCAGCGGCTGGAAATCTÇTCTCGT)-3') synthesized using **3**. PHO is a phosphate.

The amount of spin labels in each oligonucleotide was determined by spin counting. A stock solution of 4-hydroxy-TEMPO (1.0 M) was prepared in phosphate buffer (10 mM phosphate, 100 mM NaCl, 0.1 mM Na_2EDTA, pH 7.0). The stock solution was diluted into samples of different concentrations (0-0.5 mM) and each sample was measured by EPR spectroscopy. The area under the peaks of each sample, obtained by double integration, was plotted against its concentration to yield a standard curve, used to determine the spin-labeling efficiency with an error margin of 5-10% (**Table S2**).

Table S2. Spin labeling efficiency of oligonucleotides. Oligonucleotides II* and V* were synthesized with the phosphoramidite of unprotected nitroxide spin-labels **Çm** and **Ç**, respectively. PHO is a phosphate.

Name	Sequence	Efficiency (%)
I	5‘-UGCAU**Çm**UU-3‘	96
II*	5‘-UGCAU**Çm**UU-3‘	49
III	5‘-AGA-UGC-GCG-**Çm**GC-GCG-ACU-GAC-3‘	93
IV	5‘-d(PHO-TGAGGTAGTAGGTTGTATA**Ç**T)-3	96
V*	5‘-d(PHO-TGAGGTAGTAGGTTGTATA**Ç**T)-3	5
VI	5‘-d(TGTAA**Ç**GCACTACCAGCGGCTGGAAATCT**Ç**TCTCGT)-3‘	99

Article III

JOC The Journal of Organic Chemistry

pubs.acs.org/joc Article

A Carbazole-Derived Nitroxide That Is an Analogue of Cytidine: A Rigid Spin Label for DNA and RNA

Anna-Lena Johanna Segler and Snorri Th. Sigurdsson*

Cite This: https://doi.org/10.1021/acs.joc.1c01176 Read Online

ACCESS | Metrics & More | Article Recommendations | Supporting Information

ABSTRACT: A variety of semirigid and rigid spin labels comprise a valuable arsenal for measurements of biomolecular structures and dynamics by electron paramagnetic resonance (EPR) spectroscopy. Here, we report the synthesis and characterization of rigid spin labels **Ċ** and **Ċm** for DNA and RNA, respectively, that are carbazole-derived nitroxides and analogues of cytidine. **Ċ** and **Ċm** were converted to their phosphoramidites and used for their incorporation into oligonucleotides by solid-phase synthesis. Analysis of **Ċ** and **Ċm** by single-crystal X-ray crystallography verified their identity and showed little deviation from planarity of the nucleobase. Analysis of the continuous-wave (CW) EPR spectra of the spin-labeled DNA and RNA duplexes confirmed their incorporation into the nucleic acids and the line-shape was characteristic of rigid spin labels. Circular dichroism (CD) and thermal denaturation studies of the **Ċ**-labeled DNAs and **Cm**-labeled RNAs indicated that the labels are nonperturbing of duplex structure.

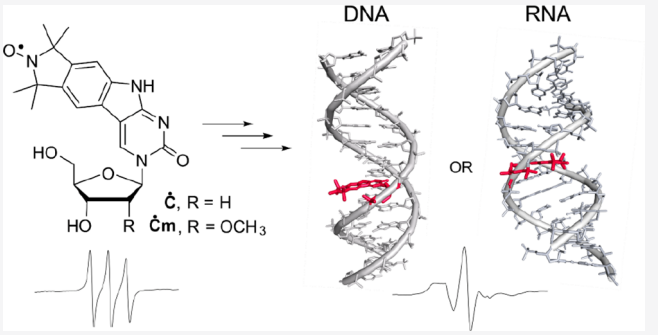

INTRODUCTION

Nucleic acids are the basis of life. Deoxyribonucleic acid (DNA) contains the genetic code and ribonucleic acid (RNA) plays major roles in sustainability of the cell, for example, by transmitting genetic information, regulating gene expression, and catalyzing chemical reactions.[1−4] To gain a deeper understanding into the properties and processes of nucleic acids, it is essential to study their structure and dynamics. Several techniques have been used for this purpose. X-ray crystallography[5,6] and nuclear magnetic resonance (NMR) spectroscopy[7,8] give information about the structure and dynamics of nucleic acids at atomic resolution. In recent years, cryo electron microscopy (EM) has also emerged as a useful technique to gain atomistic structures of biomolecules and their complexes at high resolution.[9−12] Furthermore, Förster resonance energy transfer (FRET) has been used to study tertiary structure and dynamics of nucleic acids[13−16] and can even be used to investigate single molecules.[17,18]

Electron paramagnetic resonance (EPR) spectroscopy is also a very useful method to study structure and dynamics of nucleic acids.[19−22] Using continuous-wave (CW) EPR spectroscopy, the dynamics can be studied by line-shape analysis of the EPR spectra,[23] and distances between two paramagnetic-centers can be measured within a range of 5−25 Å.[24] Pulsed dipolar spectroscopies, such as pulsed electron−electron double resonance (PELDOR), relaxation induced dipolar modulation enhancement (RIDME), single-frequency technique for refocusing dipolar couplings (SIFTER), and double quantum coherence (DQC), have been used to measure distances between 15 and 160 Å.[25−27] With pulsed EPR methods, information can also be obtained about relative orientations between two rigid spin centers.[28]

Most biomolecules, including nucleic acids, are diamagnetic; thus, spin labels need to be incorporated for EPR studies.[29,30] The most commonly used spin labels are aminoxyl radicals, usually called nitroxides. Nitroxides are highly persistent radicals, due to the delocalization of the radical between the nitrogen and the oxygen and because of the shielding effect of the alkyl groups flanking the radical center.[31,32] Spin labels can be incorporated at specific sites in nucleic acids, either covalently or noncovalently by a method called site-directed spin labeling (SDSL).[29,30,33,34] For covalent labeling, the spin labels can be incorporated into the nucleic acids postsynthetically or by using spin-labeled phosphoramidites as building blocks in the chemical synthesis of nucleic acids. The phosphoramidite method enables incorporation of involute labels at specific sites of nucleic acids.[30,35]

Spin labels that are covalently attached through single-bond tethers can move independently of the labeled biomolecule. Such flexibility leads to a large distance distribution.[36]

Received: May 20, 2021

Conformationally unambiguous spin labels[37] are semirigid spin labels that give more accurate distance measurements. They contain single-bond tethers, but the bonds lie on the axis of the nitroxide. Thus, the rotation around the single bonds does not cause a displacement of the nitroxide relative to the biomolecule. CW-EPR spectra of conformationally unambiguous benzimidazole-derived spin labels, incorporated into duplex DNA, show restricted mobility[38] and PELDOR distance measurements have shown a strong angular dependence.[39,40] Furthermore, *in-cell* PELDOR experiments of duplex RNA, doubly labeled with such semirigid spin labels, identified small distance changes that indicated compaction of RNA duplexes inside the cell.[41]

Rigid spin labels are even less mobile. In fact, rigid labels can be immobilized in helical regions of nucleic acids where they have no motion independent of the nucleic acid. As a result, they give more accurate distance measurements. Furthermore, the relative orientation of two rigid spin labels can be determined by dipolar EPR spectroscopy.[28,42] With rigid spin labels, room-temperature PELDOR measurements have even become possible,[43] but PELDOR studies are usually carried out at cryogenic temperatures. Rigid spin labels also give more precise information about the dynamics of biomolecules.[44] The nucleoside nitroxide analogues **Ç**[35] and **Çm**[45] (Figure 1) are rigid spin labels for DNA and RNA, respectively, that have been used to gain valuable information on structure and dynamics of nucleic acids. They have been used to obtain information on internal motions of DNA[46] and conformational changes and dynamics of both DNA and RNA.[47−49]

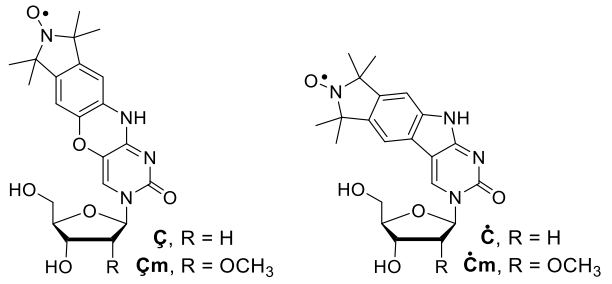

Figure 1. Structures of the rigid nitroxides **Ç**, **Çm**, **Ċ**, and **Ċm**.

Although **Ç** and **Çm** have shown to be very valuable spin labels due to their rigidity, they seem to have some flexibility in the middle of the conjugated ring system, where the cytidine and the benzene are connected by an oxygen and a nitrogen atom, as indicated by the X-ray structure of **ç**, the nucleobase of **Ç**. Although the crystal structure of **Ç**-labeled DNA showed that **Ç** has a planar geometry inside DNA,[50] the crystal structure of **ç** has a 20° bend over the oxazine linkage. The observed nonplanar geometry of **ç** could be an indication that there is some degree of flexibility at the oxazine linkage that could affect the use of **Ç** and **Çm** as rigid spin labels. Such flexibility would not be surprising since these labels are formally antiaromatic according to the Hückel rule, as they contain 16 π-electrons.

Here we describe the synthesis and characterization of the rigid nitroxide **Ċ** for DNA and **Ċm** for RNA (Figure 1). **Ċ** and **Ċm** are derivatives of **Ç** and **Çm** where the oxygen at the oxazine linkage has been removed, yielding in a carbazole derived nitroxide that is aromatic, which should be more rigid. Spin labels **Ċ** and **Ċm** were incorporated into oligonucleotides by solid-phase synthesis with high spin-labeling efficiency. When paired with guanine, **Ċ** was well-tolerated in B-form DNA duplexes and **Ċm** in A-form RNA duplexes, as judged by thermal denaturation studies and circular dichroism (CD).

RESULTS AND DISCUSSION

Synthesis of Ċ and Ċm. The synthesis of **Ċ** and **Ċm** began by TBDPS protection of the 3′- and 5′-hydroxyl groups of nucleosides **1** and **2**, respectively, followed by chlorination of the fourth position of the nucleobase (Scheme 1). Nucleosides **5** and **6** were subsequentially coupled with tetramethyl isoindoline derivative **7**[51] to yield **8** and **9**, respectively. The secondary amines of **8** and **9** were protected by *tert*-butoxycarbonyl (boc) to avoid poisoning of the palladium catalyst,[52,53] which was used in the next step. An intramolecular Pd-catalyzed C−C cross-coupling reaction[54] fol-

Scheme 1. Synthesis of Nitroxides Ċ and Ċm[a]

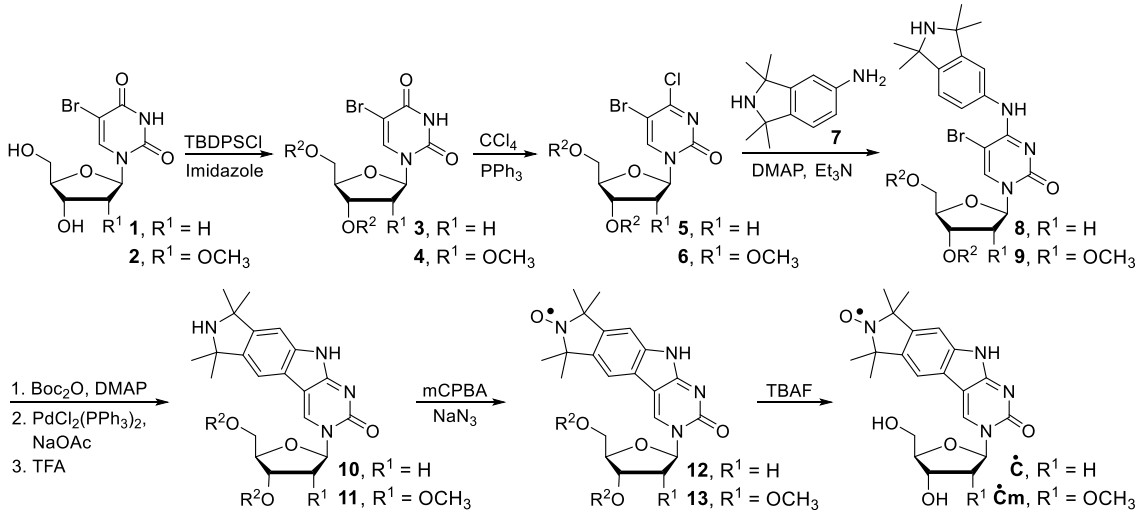

[a]Yields were as follows: **3** (95%), **4** (80%), **5** (88%), **6** (77%), **8** (66%), **9** (63%), **10** (47%, 3 steps), **11** (59%, 3 steps), **12** (65%), **13** (76%), **Ċ** (84%), and **Ċm** (67%). R^2 stands for TBDPS.

https://doi.org/10.1021/acs.joc.1c01176
J. Org. Chem. XXXX, XXX, XXX−XXX

lowed by boc-deprotection, yielded carbazole derivatives **10** and **11**. Oxidation with *m*-CPBA only proceeded in good yield when NaN_3 was included in the reaction, which presumably provides transitory protection from side-reactions by a reversible addition to the nucleobase.[38] We have not seen any evidence of oxidation of the sec-amine in the five-membered carbazole ring.[55] Subsequent removal of the TBDPS groups gave rigid nitroxides **Ċ** and **Ċm**.

Crystal Structures of Ċ and Ċm. To investigate the three-dimensional structures of **Ċ** and **Ċm**, particularly with regards to the planarity of the aromatic system, single crystals were grown, and their crystal structures were determined. As expected, the crystal structure of **Ċ** adopts a planar geometry (Figure 2A). **Ċm**, in contrast, is slightly twisted from the plane

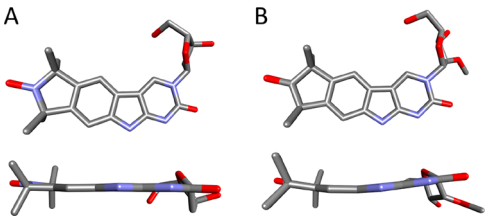

Figure 2. Side and top views of the crystal structures of **Ċ** (A) and **Ċm** (B).

with a 9° overall bend (Figure 2B). The nonplanar geometry is most likely due to the crystal packing. Nonplanar crystal structures of aromatic polycycles, resulting from intermolecular interactions are quite common as the energy required for bending is small.[56,57] The nature of the bend of **Ċm** is different from what was found in the aforementioned **ç**, where the bend is confined to the oxazine linkage, as if it was a hinge. The crystal structure of **Ċm**, however, slightly winds up on itself which induces a bend that is spread over the whole nucleobase. Taking these facts together, namely, that the crystal structure of **Ċ** is planar, that the bend of **Ċm** is smaller than for **ç**, and that **ç** has a bend at one location, indicates that **Ċ** and **Ċm** are more rigid than **Ç** and **Çm**.

Phosphoramidites of Ċ and Ċm. Intricate labels such as **Ċ** and **Ċm** can only be incorporated into nucleic acids through the phosphoramidite approach by solid-phase oligonucleotide synthesis. However, during the synthesis of spin-labeled oligonucleotides, nitroxides are partially reduced to their corresponding EPR-silent amines.[58,59] To circumvent such reduction, we used a recently developed strategy for protecting the nitroxides as benzoyl ethers of the corresponding hydroxylamine.[60] First, nitroxides **12** and **13** were reduced with ascorbic acid to their hydroxyl amines, followed by benzoylation (Scheme 2). The TBDPS groups were subsequently removed to yield nucleosides **16** and **17**, and the 5′-hydroxyl groups were protected as 4,4′-dimethoxytrityl ethers to yield **18** and **19**. Phosphitylation of the 3′-hydroxyl groups yielded phosphoramidites **20** and **21**, used for incorporation of **Ċ** and **Ċm** into DNA and RNA oligonucleotides, respectively, by solid-phase synthesis.

Synthesis and Characterization of Spin-Labeled DNA Oligonucleotides. **Ċ** was incorporated into six DNA oligonucleotides through automated solid-phase synthesis using phosphoramidite **20**. The **Ċ**-labeled oligonucleotides varied in length and position of the spin label (Table S1). The spin-labeled phosphoramidite coupled well during the solid-phase synthesis, as indicated by a strong orange color of the

Scheme 2. Synthesis of Benzoyl-Protected Ċ and Ċm and Their Corresponding Phosphoramidites[a]

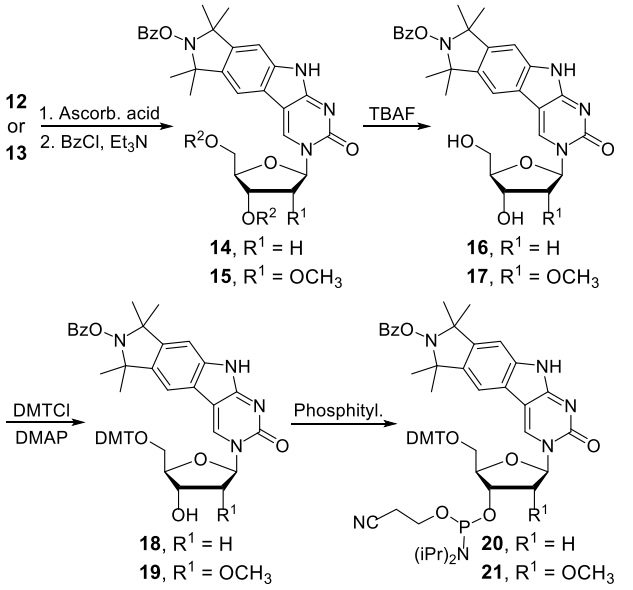

[a]Yields were as follows: **14** (51%, 2 steps), **15** (43%, 2 steps), **16** (77%), **17** (74%), **18** (81%), **19** (75%), **20** (91%) and **21** (65%). R^2 stands for TBDPS.

trityl cation that appeared during removal of the DMT group. Moreover, analysis by denaturing polyacrylamide gel electrophoresis (DPAGE) showed no failure bands for the synthesized oligonucleotides (data not shown). After purification of the oligonucleotides by DPAGE, the spin-labeling efficiency was determined (Figure S50) by spin-counting using CW-EPR spectroscopy. As can be seen in Table S1, all oligonucleotides (**I**–**VI**) were quantitatively spin labeled. To further analyze the spin labeling efficiency, oligonucleotides **I**–**VI** were enzymatically digested, and the digests were analyzed by high-performance liquid chromatography (HPLC) (Figure S51). All chromatograms had five peaks, one for each natural nucleoside and one for **Ċ**, the identity of which was confirmed by coinjection of free nucleoside **Ċ**. Quantification of the nucleosides in the digest showed that **Ċ** had the expected ratio compared to the other four nucleosides in all the samples, further confirming quantitative spin labeling of all DNA oligonucleotides.

DNA duplexes **B**–**D**, **F**, and **H** were formed by annealing spin-labeled oligonucleotides **I**–**VI** (Table S1) to their complementary strands (Table 1). The CW-EPR spectra of **Ċ**, the **Ċ**-labeled DNA single-strand **I**, and corresponding DNA duplex **B** are shown in Figure 3. **Ċ** shows three fairly sharp lines (Figure 3A) due to the fast tumbling of the nucleoside in solution. The lines broadened after incorporation of **Ċ** into the oligonucleotide (Figure 3B), consistent with incorporation into an oligonucleotide that has a longer rotational correlative time. Upon annealing to its complementary strand, the CW-EPR spectrum broadened further, showing a splitting of the high- and low-field components (Figure 3C), which is characteristic for duplexes containing rigid spin labels.[35,45]

A molecular model of **Ċ** within a B-form DNA duplex showed a good fit of the spin label in the major groove of the duplex (Figure S49). To analyze experimentally if **Ċ** causes structural perturbation of the DNA duplex, thermal denaturation studies of duplexes **A**–**H** were carried out and their

https://doi.org/10.1021/acs.joc.1c01176
J. Org. Chem. XXXX, XXX, XXX−XXX

Table 1. Sequences of Spin-Labeled DNA and RNA Duplexes and Their Thermal Denaturation Analysis[a]

	sequence	T_M (°C)	ΔT_M
A	5′-d(GACCTCGCATCGTG)-3′ 3′-d(CTGGAGCGTAGCAC)-5′	63.0	
B	5′-d(GACCTCG**Ċ**ATCGTG)-3′ 3′-d(CTGGAGCGTAGCAC)-5′	60.0	-3.0
C	5′-d(GA**Ċ**CTCGCATCGTG)-3′ 3′-d(CTGGAGCGTAGCAC)-5′	60.9	-2.1
D	5′-d(GACCTCGCATCGTG)-3′ 3′-d(CTGGAGCGTAGCA**Ċ**)-5′	62.5	-0.5
E	5′-d(GACCTCGCATCGTGGACCTCGCATCGTGGACCTCGCATCGTG)-3′ 3′-d(CTGGAGCGTAGCACCTGGAGCGTAGCACCTGGAGCGTAGCAC)-5′	83.7	
F	5′-d(GACCTCG**Ċ**ATCGTGGACCTCGCATCGTGGACCTCGCATCGTG)-3′ 3′-d(CTGGAGCGTAGCACCTGGAGCGTAGCACCTGGAGCGTAGCAC)-5′	83.1	-0.6
G	5′-d(GTCAGTGCGCGCGCGCGATC)-3′ 3′-d(CAGTCACGCGCGCGCGCTAG)-5′	79.2	
H	5′-d(GT**Ċ**AGTGCGCGCGCGCGATC)-3′ 3′-d(CAGTCACGCG**Ċ**GCGCGCTAG)-5′	77.0	-2.2
I	5′-GACCUCGCAUCGUG-3′ 3′-CUGGAGCGUAGCAC-5′	73.5	-3.2
J	5′-GACCUCG**Ċm**AUCGUG-3′ 3′-CUGGAGCG UAGCAC-5′	70.3	-3.2
K	5′-UGUCAGUCGCGCGCGCGCAUC -3′ 3′- CAGUCAGCGCGCGCGCGUAGU-5′	85.9	
L	5′-UGU**Ċm**AGUCGCGCGCG CGCAUC -3′ 3′- CAG UCAGCGCGCG**Ċm**GCGUAGU-5′	83.4	-2.5
M	5′-d(GACCTCG**Y**ATCGTG)-3′ 3′-d(CTGGAGCGTAGCAC)-5′	61.8	-1.2

[a]**Y** stands for nucleoside **25**.

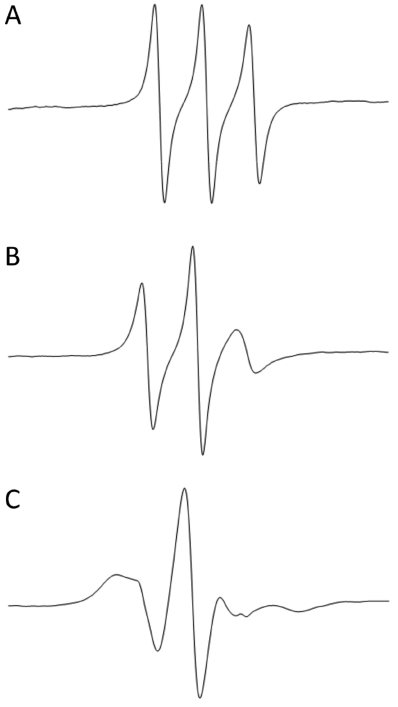

Figure 3. CW-EPR spectra of free nitroxide **Ċ** (A), spin-labeled DNA oligonucleotide **I** (B), and spin-labeled DNA duplex **B** (C).

circular dichroism (CD) spectra were recorded. The thermal denaturation curves showed a cooperative melting-transition (Figure S53) and confirmed duplex formation of the **Ċ**-labeled oligonucleotides. The melting temperatures (T_M's) of the **Ċ**-labeled duplexes were slightly lower than those of the unmodified duplexes (0.5−3.0 °C, Table 1). Comparison of the T_M's of duplex **B** and the same duplex labeled with **Ç** at the same position showed that the T_M of duplex **B** is 1.9 °C lower than that for the **Ç**-labeled duplex.[58] However, in general the decrease of the T_M's compared to the unmodified duplexes is minor and shows that **Ċ** is well-accommodated within DNA duplexes.

The CD spectra of the **Ċ**-labeled and unmodified DNA duplexes (**A**−**H**, Figure S54) all possessed negative and positive molar ellipticities at ca. 250 and 280 nm, respectively, characteristic of right-handed B-DNA (Figure S54). However, the CD spectra were different for the **Ċ**-labeled and unmodified duplexes, namely, there is a decrease in the CD signal between 270 and 280 nm for the modified duplex. A similar result has previously been described by Wypijewska del Nogal et al. for 2CNqA, an analogue of adenosine, in DNA duplexes.[61] The authors ascribe this discrepancy to "differences in molar absorptivity of the adenine that is exchanged with a 2CNqA in the modified duplex",[61] but 2CNqA absorbs strongly between 275 and 290 nm.[62] Nucleoside **Ċ** has an absorption maxima at 279 nm, where the CD spectra differs between the **Ċ**-modified and unmodified duplexes (Figure 4A); thus, the difference in the CD spectra could originate in the strong absorption of **Ċ** at 279 nm.

To investigate this issue further, we synthesized carbazole-analogue **25** (Scheme 3), where the five-membered ring of **Ċ**, containing the nitroxide and the four methyl groups, has been removed. Nucleoside **25** should, therefore, be less perturbing of the DNA duplex structure than **Ċ**. Nucleoside **25** was converted to phosphoramidite **27** (Scheme 3) and incorporated into DNA oligonucleotide **X** (Table S1) through solid-phase synthesis. Thermal denaturation experiments of duplex **M** (Table 1), containing **25**, showed a 1.2 °C decrease of the T_M compared to the unmodified duplex (**A**, Table 1), indicating that nucleoside **25** is nonperturbing of duplex structure. The CD spectrum of DNA duplex **M** (Figure 4B) had a strong resemblance to the CD spectra of the **Ċ**-labeled duplexes, but the decrease in the intensity of the 279 nm peak

https://doi.org/10.1021/acs.joc.1c01176
J. Org. Chem. XXXX, XXX, XXX−XXX

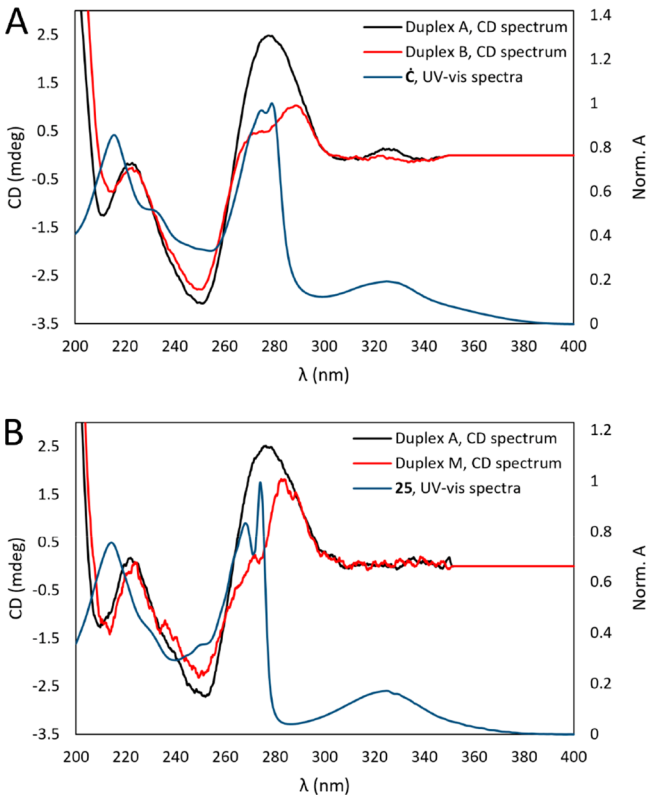

Figure 4. Comparison of CD spectra of DNA duplexes and of absorption spectra of nucleosides. CD spectra of duplex A (black) and B (red) and absorption spectra of nucleoside Ċ (blue) (A). CD spectra of duplex A (black) and M (red) and absorption spectra of nucleoside **25** (blue) (B).

Scheme 3. Synthesis of Nucleoside 25 and Its Corresponding Phosphoramidite[a]

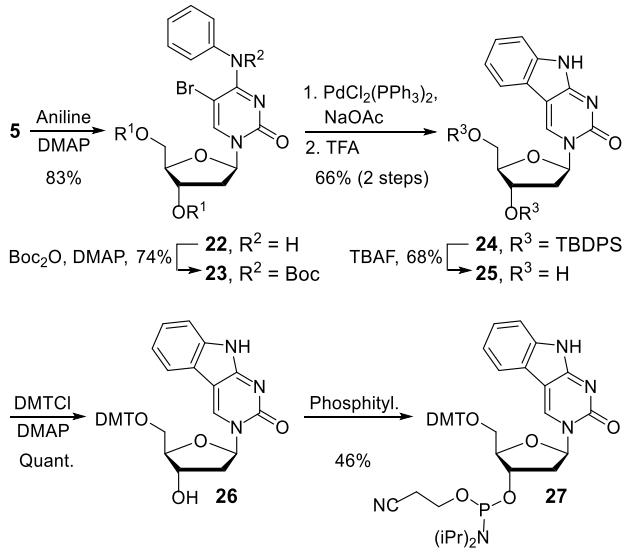

[a]R^1 stands for TBDPS.

was blue-shifted to 274 nm which is the absorption maximum of **25**. It is noteworthy that there are two maxima around 274 nm in the UV spectrum of **25** and that the small dip between the two peaks is mirrored in the CD spectrum. This data is a further indication that the difference in the CD spectra of the Ċ-modified and unmodified DNA duplexes is not due to conformational rearrangement of the duplex itself.

Synthesis and Characterization of Spin-Labeled RNA Oligonucleotides. Phosphoramidite **21** was used to incorporate **Ċm** into one 14- and two 21-nucleotide long RNAs through automated solid-phase synthesis (Table 1). As for the DNA synthesis, the phosphoramidite coupled well during the RNA solid-phase synthesis and spin-counting by CW-EPR spectroscopy confirmed high spin-labeling efficiency (Table S1). Oligonucleotides **VII**–**IX** were enzymatically digested, and the digests were analyzed by HPLC (Figure S52), showing the natural nucleosides and **Ċm**. Quantification of the five peaks gave the expected ratios.

CW-EPR spectra of RNA duplexes **J** and **L** showed the expected line-shape for a rigid spin label in a duplex RNA (Figure S50). A model of an RNA A-form helix, labeled with **Ċm**, showed that the spin label fits well into the major groove of the duplex (Figure S49). Thermal denaturation experiments resulted in sigmoidal melting curves that also confirmed duplex formation of the **Ċm**-labeled oligonucleotides (Figure S53). The melting temperatures of the **Ċm**-labeled duplexes were only ca. 3.2 °C lower (Table 1) than for the corresponding unmodified duplexes, indicating only minor destabilization. The CD spectra for the unmodified and **Ċm**-labeled RNA duplexes showed negative and positive molar ellipticities at ca. 210 and 263 nm, respectively, typical for A-form RNA (Figure S54). Thus, both the thermal denaturation studies and the CD spectra indicate that **Ċm** fits well in A-form RNA duplexes.

CONCLUSION

Rigid spin labels **Ċ** and **Ċm** were synthesized and characterized. Comparison of their single-crystal X-ray structures with the known structure of **ç**,[50] the nucleobase of **Ç** and **Çm**, indicates that **Ċ** and **Ċm** are more rigid than known rigid spin labels **Ç** and **Çm**. However, it remains to be seen if this will result in better performance of **Ċ** and **Ċm** as spin labels compared to **Ç** and **Çm**. Another advantage of **Ċ** and **Ċm**, compared to **Ç** and **Çm**, is that their synthesis is two steps shorter. **Ċ** and **Ċm** were incorporated into DNA and RNA, respectively, with high spin-labeling efficiency. Thermal denaturation experiments and CD spectra indicate that the spin labels are nonperturbing of duplex structures. These new rigid spin labels are promising candidates for future studies of DNA and RNA structures and dynamics by pulsed EPR methods.

EXPERIMENTAL SECTION

General Materials and Methods. All commercially available reagents were purchased from Sigma-Aldrich, Inc. GmbH or Acros Organics and used without further purification, except for diisopropylammonium tetrazolide and 2-cyanoethyl *N*,*N*,*N*′,*N*′-tetraisopropylphosphorodiamidite, which were purchased from ChemGenes Corp. All commercial phosphoramidites, controlled pore glass (CPG) solid support, and solutions for oligonucleotide syntheses were also purchased from ChemGenes Corp. Columns for the CPG solid-support were purchased from BioAutomation. 2′-Deoxyuridine and 2′-*O*-methyluridine were purchased from Rasayan Inc. USA. CH_2Cl_2, pyridine, and CH_3CN were dried over CaH and freshly distilled before use. Et_3N, 1,4-dioxane, and DMA where dried over molecular sieves (3 Å). All moisture- and air-sensitive reactions were carried out in oven-dried glassware under an inert atmosphere of argon. Thin-layer chromatography (TLC) was carried out using glass plates precoated with silica gel (0.25 mm, F-25, Silicycle) and compounds were visualized under UV light and by *p*-anisaldehyde

https://doi.org/10.1021/acs.joc.1c01176
J. Org. Chem. XXXX, XXX, XXX−XXX

staining. Column chromatography was carried out using 230−400 mesh silica gel (Silicycle). ^{1}H, ^{13}C, and ^{31}P NMR spectra were recorded with a Bruker Avance 400 MHz spectrometer. Commercial-grade $CDCl_3$ was passed over basic alumina shortly before dissolving tritylated nucleosides for NMR analysis. Chemical shifts are reported in parts per million (ppm) relative to the partially deuterated NMR solvents $CDCl_3$ (7.26 ppm for ^{1}H NMR and 77.16 ppm for ^{13}C) and DMSO-d_6 (2.50 ppm for ^{1}H NMR and 39.52 ppm for ^{13}C). ^{31}P NMR chemical shifts are reported relative to 85% H_3PO_4 (at 0.0 ppm) as an external standard. All coupling constants were reported in Hertz (Hz). Nitroxide radicals show broadening and loss of NMR signals due to their paramagnetic nature and, therefore, those NMR spectra are not shown. Mass spectrometric analyses of all organic compounds were carried out on a high-resolution electrospray ionization mass spectrometer (ESI-HRMS) (Bruker, MicrOTOF-Q) in positive ion mode. UV−vis absorption spectra were recorded on a PerkinElmer Lambda 25 UV/Vis Spectrometer.

DNA and RNA solid-phase oligonucleotide syntheses were carried out on an automated ASM800 DNA/RNA synthesizer (BIOSSET Ltd., Russia) using phosphoramidite chemistry. Unmodified and spin-labeled oligonucleotides were synthesized using a trityl-off protocol and phosphoramidites with standard protecting groups on a 1.5 μmol scale (1000 Å CPG columns). Oxidation was carried out with *tert*-butylhydroperoxide (1.0 M) in toluene. Capping and detritylation were carried out using standard conditions for DNA and RNA syntheses. Molecular weights of the oligonucleotides were determined by MALDI-TOF analysis on a Voyager-DE STR Biospectrometry Workstation. HPLC analyses of enzymatic digests were carried out on an analytical Agilent 1200 HPLC system using a GL Science Inc. C18 4.6 × 150 mm^2 analytical column with UV detection at 260 nm. Solvent gradients for analytical RP-HPLC were run at 1.0 mL/min using the following gradient: solvent A, triethylammonium acetate (TEAA) buffer (50 mM, pH 7.0), solvent B, CH_3CN; 0−4 min isocratic 4% B, 4−30 min linear gradient 4−100% B, 30−34 min isocratic 100% B, 34−36 min linear gradient 100−4% B, and 36−40 min isocratic 4% B. Sample preparation for CD, thermal denaturation, and EPR measurements was as follows: An appropriate quantity of each DNA or RNA stock solution was dried in an Eppendorf Concentrator Plus and dissolved in phosphate buffer (10 mM phosphate, 100 mM NaCl, 0.1 mM Na_2EDTA, pH 7.0). DNA and RNA duplexes were formed by annealing in an MJ Research PTC 200 thermal cycler using the following protocol: 90 °C for 2 min, 60 °C for 5 min, 50 °C for 5 min, 40 °C for 5 min, and 22 °C for 15 min. CW-EPR spectra were recorded on a MiniScope MS200 spectrometer using 100 kHz modulation frequency, 1.0 G modulation amplitude, and 2.0 mW microwave power. The samples were placed in a quartz capillary (BLAUBRAND intraMARK) prior to EPR measurements. CD spectra of the duplexes were recorded on a Jasco J-810 spectropolarimeter and were recorded from 350 to 200 nm at 25 °C.

*5-Bromo-1-((2R,4S,5R)-4-((tert-butyldiphenylsilyl)oxy)-5-(((tert-butyldiphenylsilyl)oxy)methyl)tetrahydrofuran-2-yl)pyrimidine-2,4-(1H,3H)-dione (**3**).* To a solution of compound **1** (10.0 g, 3.3 mmol) in DMF (31 mL) and pyridine (12 mL) were added TBDPSCl (3.3 mL, 13.1 mmol) and imidazole (0.7 g, 9.8 mmol). After stirring at 22 °C for 48 h, aqueous HCl (50 mL, 1 M) was added, the solution extracted with EtOAc (3 × 50 mL) and the combined organic phases washed with aqueous HCl (2 × 50 mL, 1 M) and brine (2 × 50 mL). The organic phase was dried over Na_2SO_4 and concentrated *in vacuo*. The residue was purified by flash column chromatography using a gradient elution (EtOAc/petroleum ether, 10:90 to 20:80) to yield compound **3** (2.4 g, 95% yield) as a white fluffy powder. ^{1}H NMR (400 MHz, $CDCl_3$): δ 8.64 (s, 1H), 8.00 (s, 1H), 7.60 (dd, J = 8.0, 1.4 Hz, 2H), 7.54 (td, J = 8.0, 1.3 Hz, 4H), 7.47−7.32 (m, 10H), 7.29−7.24 (m, 4H), 6.43 (dd, J = 9.0, 5.1 Hz, 1H), 4.49 (d, J = 5.3 Hz, 1H), 3.98 (s, 1H), 3.71 (dd, J = 11.7, 2.1 Hz, 1H), 3.28 (dd, J = 11.7, 2.6 Hz, 1H), 2.42 (dd, J = 12.9, 5.7 Hz, 1H), 2.00−1.91 (m, 1H), 1.07 (s, 9H), 0.95 (s, 9H) ppm. $^{13}C\{^{1}H\}$ NMR (101 MHz, $CDCl_3$) δ 158.8, 149.3, 149.3, 139.2, 135.7, 135.6, 135.5, 135.4, 133.1, 133.0, 132.4, 132.1, 130.1, 130.03, 130.0, 127.9, 127.89, 97.0, 88.3, 86.0, 77.2, 74.1, 63.9, 41.9, 27.0, 26.9, 22.7, 19.2, 19.0, 14.1 ppm. HRMS (ESI) m/z: $(M + Na)^+$ Calcd for $[C_{41}H_{47}BrN_2O_5Si_2Na]^+$ 807.2088. Found 807.2078.

*5-Bromo-1-((2R,3R,4R,5R)-4-((tert-butyldiphenylsilyl)oxy)-5-(((tert-butyldiphenylsilyl)oxy)methyl)-3-methoxytetrahydrofuran-2-yl)pyrimidine-2,4(1H,3H)-dione (**4**).* To a solution of compound **2** (3.0 g, 8.9 mmol) in DMF (84 mL) and pyridine (33 mL) were added TBDPSCl (9.2 mL, 35.6 mmol) and imidazole (1.8 g, 26.7 mmol). After stirring at 22 °C for 48 h, aqueous HCl (200 mL, 1 M) was added, and the solution was extracted with EtOAc (3 × 100 mL). The combined organic phases were washed with aqueous HCl (2 × 200 mL, 1 M) and brine (2 × 200 mL). The organic phase was dried over Na_2SO_4 and concentrated *in vacuo*. The residue was purified by flash column chromatography using a gradient elution (EtOAc/petroleum ether, 10:90 to 20:80) to yield compound **4** (5.8 g, 80% yield) as a white fluffy powder. ^{1}H NMR (400 MHz, $CDCl_3$): δ 8.63 (s, 1H), 7.83 (s, 1H), 7.69 (d, J = 6.7 Hz, 2H), 7.57 (d, J = 6.7 Hz, 4H), 7.52 (d, J = 8.0 Hz, 2H), 7.45−7.27 (m, 12H), 6.22 (d, J = 6.2 Hz, 1H), 4.33 (dd, J = 4.6, 3.0 Hz, 1H), 4.03 (d, J = 2.2 Hz, 1H), 3.79 (dd, J = 11.9, 1.8 Hz, 1H), 3.60 (dd, J = 6.1, 4.9 Hz, 1H), 3.33 (dd, J = 11.9, 2.6 Hz, 1H), 3.23 (s, 3H), 1.08 (s, 9H), 1.03 (s, 9H) ppm. $^{13}C\{^{1}H\}$ NMR (101 MHz, $CDCl_3$): δ 251.9, 158.6, 149.4, 138.8, 135.9, 135.7, 135.6, 135.4, 133.2, 132.9, 132.5, 132.1, 130.1, 130.05, 130.0, 127.9, 127.85, 127.7, 97.5, 86.3, 85.8, 83.6, 71.03, 63.6, 58.4, 31.9, 27.1, 26.9, 26.5, 22.7, 19.3, 19.3, 14.1 ppm. HRMS (ESI) m/z: $(M + Na)^+$ Calcd for $[C_{42}H_{49}BrN_2O_6Si_2Na]^+$ 837.2194. Found 837.2163.

*5-Bromo-1-((2R,4S,5R)-4-((tert-butyldiphenylsilyl)oxy)-5-(((tert-butyldiphenylsilyl)oxy)methyl)tetrahydrofuran-2-yl)-4-chloropyrimidin-2(1H)-one (**5**).* To a solution of compound **3** (1.94 g, 2.47 mmol) in CH_2Cl_2 (15 mL) and CCl_4 (15 mL) was added PPh_3 (1.62 g, 6.17 mmol). The reaction mixture was refluxed at 65 °C for 2 h, cooled to 22 °C, and concentrated *in vacuo*, and the residue was purified by flash column chromatography using a gradient elution (EtOAc/petroleum ether, 10:90 to 20:80) to yield compound **5** (1.75 g, 88% yield) as a pale-yellow fluffy powder. ^{1}H NMR (400 MHz, $CDCl_3$): δ 8.42 (s, 1H), 7.62−7.24 (m, 23H), 6.34 (dd, J = 8.1, 5.4 Hz, 1H), 4.47−4.40 (m, 1H), 4.06 (q, J = 2.3 Hz, 1H), 3.71 (dd, J = 11.8, 2.3 Hz, 1H), 3.23 (dd, J = 11.8, 2.9 Hz, 1H), 2.88 (ddd, J = 13.4, 5.5, 1.3 Hz, 1H), 2.00 (ddd, J = 13.5, 8.2, 5.5 Hz, 1H), 1.09 (s, 9H), 0.95 (s, 9H) ppm. $^{13}C\{^{1}H\}$ NMR (101 MHz, $CDCl_3$): δ 262.3, 250.6, 165.4, 151.8, 144.4, 135.7, 135.6, 135.5, 135.5, 135.4, 133.2, 132.8, 132.4, 132.1, 130.1, 130.05, 130.0, 127.9, 127.89, 127.87, 127.6, 97.1, 89.5, 89.1, 74.5, 63.9, 43.0, 27.0, 26.9, 26.86, 26.7, 19.2, 19.0, 14.1 ppm. HRMS (ESI) m/z: $(M + Na)^+$ Calcd for $[C_{41}H_{46}BrClN_2O_4Si_2Na]^+$ 825.1745. Found 825.1738.

*5-Bromo-1-((2R,3R,4R,5R)-4-((tert-butyldiphenylsilyl)oxy)-5-(((tert-butyldiphenylsilyl)oxy)methyl)-3-methoxytetrahydrofuran-2-yl)-4-chloropyrimidin-2(1H)-one (**6**).* To a solution of compound **4** (1.9 g, 2.3 mmol) in CH_2Cl_2 (14 mL) and CCl_4 (14 mL) was added PPh_3 (1.5 g, 5.7 mmol). The reaction mixture was refluxed at 65 °C for 2 h, cooled to 22 °C, and concentrated *in vacuo*, and the residue was purified by flash column chromatography using a gradient elution (EtOAc/petroleum ether, 10:90 to 25:75) to yield compound **6** (1.5 g, 77% yield) as a pale-yellow fluffy powder. ^{1}H NMR (400 MHz, $CDCl_3$): δ 8.10 (s, 1H), 7.68 (s, 2H), 7.58 (d, J = 11.4 Hz, 6H), 7.40 (d, J = 31.9 Hz, 11H), 7.29−7.24 (m, 3H), 6.02 (s, 1H), 4.20 (s, 1H), 4.15 (s, 1H), 4.03 (d, J = 13.8 Hz, 1H), 3.61 (d, J = 15.1 Hz, 1H), 3.36 (s, 1H), 3.29 (s, 3H), 1.06 (s, 18H) ppm. $^{13}C\{^{1}H\}$ NMR (101 MHz, $CDCl_3$): δ 165.7, 151.5, 143.8, 135.9, 135.8, 135.7, 135.6, 135.56, 135.5, 135.4, 133.0, 132.9, 132.8, 132.5, 132.1, 130.1, 130.03, 130.0, 128.0, 127.9, 127.85, 127.8, 127.7, 100.0, 97.4, 88.7, 86.2, 85.9, 84.7, 83.9, 83.6, 70.3, 62.9, 58.1, 35.4, 31.9, 31.9, 29.7, 29.4, 29.0, 27.3, 27.1, 26.9, 26.86, 26.5, 22.7, 19.5, 19.3, 19.29, 14.1. HRMS (ESI) m/z: $(M + Na)^+$ Calcd for $[C_{42}H_{48}BrClN_2O_5Si_2Na]^+$ 855.1819. Found 855.1851.

*5-Bromo-1-((2R,4S,5R)-4-((tert-butyldiphenylsilyl)oxy)-5-(((tert-butyldiphenylsilyl)oxy)methyl)tetrahydrofuran-2-yl)-4-((1,1,3,3-tetramethylisoindolin-5-yl)amino)pyrimidin-2(1H)-one (**8**).* To a solution of nucleoside **5** (4.5 g, 5.6 mmol) in CH_2Cl_2 (147 mL) were added compound **7**[S1] (1.2 g, 6.2 mmol), DMAP (0.07 g, 0.7 mmol), and Et_3N (1 mL, 7.2 mmol), and the resulting solution was stirred at 22 °C for 14 h. H_2O (100 mL) was added, and the organic phase was

https://doi.org/10.1021/acs.joc.1c01176
J. Org. Chem. XXXX, XXX, XXX−XXX

extracted with CH_2Cl_2 (2 × 100 mL). The combined organic phases were washed with saturated aqueous $NaHCO_3$ (50 mL) and brine (100 mL), dried over Na_2SO_4, and concentrated *in vacuo*. The residue was purified by flash column chromatography using a gradient elution ($MeOH/CH_2Cl_2$, 0:100 to 10:90) to yield compound **8** (3.6 g, 66% yield) as a light yellow foam. ^1H NMR (400 MHz, $CDCl_3$): δ 8.09 (s, 1H), 7.68−7.63 (m, 1H), 7.63−7.58 (m, 2H), 7.54 (s, 4H), 7.34 (d, J = 7.5 Hz, 11H), 7.25−7.21 (m, 1H), 7.11 (d, J = 8.2 Hz, 1H), 6.49−6.43 (m, 1H), 4.46 (s, 1H), 4.03 (s, 1H), 3.71 (d, J = 13.8 Hz, 1H), 3.28 (d, J = 14.5 Hz, 1H), 2.68 (d, J = 19.6 Hz, 1H), 1.97−1.85 (m, 1H), 1.57 (s, 12H), 1.07 (s, 9H), 0.94 (s, 9H) ppm. $^{13}C\{^1H\}$ NMR (101 MHz, $CDCl_3$): δ 242.9, 157.5, 154.2, 141.0, 136.9, 135.9, 135.8, 135.7, 135.6, 133.5, 133.2, 132.9, 132.4, 130.1, 130.0, 128.0, 127.95, 122.2, 122.1, 115.0, 88.6, 88.3, 87.6, 74.4, 64.1, 42.9, 31.3, 31.26, 27.2, 27.15, 27.1, 27.0, 19.4, 19.1 ppm. HRMS (ESI) m/z: $(M + H)^+$ Calcd for $[C_{53}H_{64}BrN_4O_4Si_2]^+$ 957.3637. Found 957.3615.

*4-5-Bromo-1-((2R,3R,4R,5R)-4-((tert-butyldiphenylsilyl)oxy)-5-(((tert-butyldiphenylsilyl)oxy)methyl)-3-methoxytetrahydrofuran-2-yl)-4-((1,1,3,3-tetramethylisoindolin-5-yl)amino)pyrimidin-2(1H)-one (**9**).* To a solution of compound **6** (4.4 g, 5.2 mmol) in CH_2Cl_2 (137 mL) were added compound 7[S1] (1.2 g, 6.2 mmol), DMAP (0.04 g, 0.5 mmol), and Et_3N (0.9 mL, 6.5 mmol), and the resulting solution was stirred at 22 °C for 12 h. H_2O (100 mL) was added, and the mixture was extracted with CH_2Cl_2 (2 × 200 mL). The combined organic phases were washed with saturated aqueous $NaHCO_3$ (50 mL) and brine (100 mL), dried over Na_2SO_4, and concentrated *in vacuo*. The residue was purified by flash column chromatography using a gradient elution ($MeOH/CH_2Cl_2$, 0:100 to 2:90) to yield compound **9** (3.3 g, 63% yield) as a light yellow foam. ^1H NMR (400 MHz, $CDCl_3$): δ 7.83 (s, 1H), 7.73−7.54 (m, 9H), 7.48−7.29 (m, 11H), 7.31−7.20 (m, 2H), 7.09 (d, J = 8.2 Hz, 1H), 6.11 (d, J = 3.1 Hz, 1H), 4.23 (dd, J = 6.5, 4.7 Hz, 1H), 4.17 (ddd, J = 6.5, 3.1, 1.9 Hz, 1H), 4.02 (dd, J = 11.8, 1.9 Hz, 1H), 3.62 (dd, J = 11.8, 3.2 Hz, 1H), 3.37 (dd, J = 4.8, 3.1 Hz, 1H), 3.29 (s, 3H), 1.58 (d, J = 6.6 Hz, 12H), 1.06 (d, J = 1.2 Hz, 18H) ppm. $^{13}C\{^1H\}$ NMR (101 MHz, $CDCl_3$): δ 262.4, 251.5, 157.4, 153.9, 147.9, 140.6, 137.0, 136.0, 135.8, 135.7, 135.6, 133.4, 133.3, 133.2, 132.8, 130.1, 130.05, 130.0, 129.98, 128.03, 128.0, 127.9, 127.7, 122.1, 122.0, 114.9, 88.6, 88.2, 84.1, 83.8, 70.6, 64.6, 63.2, 58.0, 53.5, 31.1, 31.05, 27.4, 27.0, 19.6, 19.5 ppm. HRMS (ESI) m/z: $(M + H)^+$ Calcd for $[C_{54}H_{66}BrN_4O_5Si_2]^+$ 987.3743. Found 987.3721.

*3-((2R,4S,5R)-4-((tert-Butyldiphenylsilyl)oxy)-5-(((tert-butyldiphenylsilyl)oxy)methyl)tetrahydrofuran-2-yl)-6,6,8,8-tetramethyl-6,7,8,10-tetrahydropyrimido[4,5-b]pyrrolo[3,4-f]indol-2(3H)-one (**10**).* To a solution of compound **8** (1150 mg, 1.20 mmol) in 1,4-dioxane (10 mL) were added Boc_2O (2.62 g, 12.02 mmol) and DMAP (15 mg, 0.12 mmol), and the resulting solution was stirred at 60 °C for 12 h. Saturated aqueous $NaHCO_3$ (50 mL) was added, and the mixture was extracted with EtOAc (3 × 20 mL). The combined organic phases were washed with brine (50 mL), dried over Na_2SO_4, and concentrated *in vacuo*. The residue was purified by flash column chromatography using a gradient elution (EtOAc/petroleum ether, 10:90 to 25:75), which yielded a mixture of two compounds that were carried to the next step without further purification by dissolving them (130 mg, 0.11 mmol) in DMA (4.5 mL) and adding anhydrous NaOAc (37 mg, 0.45 mmol) and $PdCl_2(PPh_3)_2$ (16 mg, 0.02 mmol). The resulting solution was stirred at 150 °C for 12 h, cooled to 22 °C, filtered through Celite, and concentrated *in vacuo*. H_2O (20 mL) was added and the mixture extracted with EtOAc (5 × 20 mL). The combined organic phases were washed with brine (3 × 50 mL), dried over Na_2SO_4, and concentrated *in vacuo*. The residue was dissolved in CH_2Cl_2 (20 mL), and TFA (10 mL) was added at 0 °C. The reaction was stirred at 22 °C for 3 h. Saturated aqueous $NaHCO_3$ was added to the solution until the effervescence, by release of CO_2 gas, had stopped. The two phases were separated and the aqueous phase was extracted with EtOAc (4 × 20 mL). The combined organic phases were washed with brine (50 mL), dried over Na_2SO_4, and concentrated *in vacuo*. The residue was purified by flash column chromatography using a gradient elution ($MeOH/CH_2Cl_2$, 0:100 to 10:90) to yield compound **10** (46 mg, 47%) as a brownish foam. ^1H NMR (400 MHz, $CDCl_3$): δ 8.77 (s, 1H), 7.53 (s, 4H), 7.45 (d, J = 7.3 Hz, 2H), 7.40 (d, J = 7.2 Hz, 2H), 7.25 (s, 9H), 7.16 (q, J = 7.6 Hz, 5H), 6.78 (s, 1H), 6.60 (s, 1H), 4.47 (s, 1H), 4.00 (s, 1H), 3.80 (s, 1H), 3.36 (s, 1H), 3.17 (s, 1H), 2.70 (s, 1H), 1.84 (s, 6H), 1.56 (d, J = 76.4 Hz, 6H), 0.96 (s, 9H), 0.84 (s, 9H) ppm. $^{13}C\{^1H\}$ NMR (101 MHz, $CDCl_3$): δ 163.0, 161.7, 154.6, 143.1, 141.4, 137.3, 135.7, 135.7, 135.5, 135.4, 135.3, 135.1, 133.3, 133.1, 132.99, 132.3, 132.2, 130.3, 130.2, 130.0, 129.9, 128.2, 128.1, 127.9, 127.8, 121.2, 112.6, 105.7, 105.2, 88.7, 88.1, 87.9, 72.9, 70.6, 69.5, 67.7, 67.2, 66.7, 66.7, 66.4, 64.1, 63.7, 53.5, 50.5, 43.5, 42.3, 42.0, 30.0, 29.8, 29.6, 29.5, 27.1, 27.0, 26.9, 25.0, 21.4, 19.3, 19.3, 19.1, 19.0, 18.8, 16.7, 15.2, 15.1 ppm. HRMS (ESI) m/z: $(M + H)^+$ Calcd for $[C_{53}H_{63}N_4O_4Si_2]^+$ 875.4382. Found 875.4381.

*3-((2R,3R,4R,5R)-4-((tert-Butyldiphenylsilyl)oxy)-5-(((tert-butyldiphenylsilyl)oxy)methyl)-3-methoxytetrahydrofuran-2-yl)-6,6,8,8-tetramethyl-6,7,8,10-tetrahydropyrimido[4,5-b]pyrrolo[3,4-f]indol-2(3H)-one (**11**).* To a solution of compound **9** (5.02 g, 5.01 mmol) in 1,4-dioxane (42 mL) were added Boc_2O (4.38 g, 40.1 mmol) and DMAP (0.062 g, 0.50 mmol), and the resulting solution was stirred at 60 °C for 12 h. Saturated aqueous $NaHCO_3$ (50 mL) was added, and the mixture was extracted with EtOAc (3 × 30 mL). The combined organic phases were washed with brine (50 mL), dried over Na_2SO_4, and concentrated *in vacuo*. The residue was purified by flash column chromatography using a gradient elution (EtOAc/petroleum ether, 10:90 to 25:75), which yielded a mixture of two compounds that were carried to the next step without further purification by dissolving them (133 mg, 0.11 mmol) in DMA (4.5 mL) and adding anhydrous NaOAc (37 mg, 0.45 mmol) and $PdCl_2(PPh_3)_2$ (16 mg, 0.023 mmol). The resulting solution was stirred at 150 °C for 12 h, cooled to 22 °C, filtered through Celite, and concentrated *in vacuo*. H_2O (25 mL) was added, and the mixture extracted with EtOAc (3 × 20 mL). The combined organic phases were washed with brine (3 × 50 mL), dried over Na_2SO_4, and concentrated *in vacuo*. The residue was dissolved in CH_2Cl_2 (18 mL), and TFA (9 mL) was added at 0 °C. The reaction was stirred at 22 °C for 3 h. Saturated aqueous $NaHCO_3$ was added to the solution until the effervescence, by release of CO_2 gas, had stopped. The two phases were separated, and the aqueous phase was extracted with EtOAc (4 × 40 mL). The combined organic phases were washed with brine (100 mL), dried over Na_2SO_4, and concentrated *in vacuo*. The residue was purified by flash column chromatography using a gradient elution ($MeOH/CH_2Cl_2$, 2:98 to 10:90) to yield compound **11** (60 mg, 59%) as a brownish foam. ^1H NMR (400 MHz, $CDCl_3$): δ 8.58 (s, 1H), 7.69 (ddd, J = 8.0, 2.7, 1.4 Hz, 4H), 7.63−7.54 (m, 4H), 7.48−7.26 (m, 12H), 7.22 (t, J = 7.3 Hz, 2H), 4.38 (t, J = 4.4 Hz, 1H), 4.19 (d, J = 4.7 Hz, 1H), 4.00 (d, J = 10.6 Hz, 1H), 3.66−3.60 (m, 1H), 3.46 (s, 1H), 3.27 (s, 3H), 1.65 (d, J = 23.4 Hz, 12H), 1.04 (d, J = 9.2 Hz, 18H) ppm. $^{13}C\{^1H\}$ NMR (101 MHz, $CDCl_3$): δ 258.3, 161.9, 154.6, 141.6, 136.1, 135.8, 135.5, 135.2, 133.4, 133.2, 133.1, 132.4, 130.5, 130.1, 130.0, 128.4, 128.3, 127.9, 127.7, 121.2, 112.9, 105.7, 100.1, 88.3, 85.4, 84.9, 71.3, 70.7, 66.0, 63.9, 58.4, 29.9, 29.7, 29.4, 27.3, 27.2, 27.1, 19.6, 19.5, 15.4 ppm. HRMS (ESI) m/z: $(M + H)^+$ Calcd for $[C_{54}H_{65}N_4O_5Si_2]^+$ 905.4488. Found 905.4445.

*TBDPDS-Protected Nitroxide **12**.* To a solution of **10** (683 mg, 0.78 mmol) in CH_2Cl_2 (38 mL) was added NaN_3 (203 mg, 3.12 mmol), and the reaction was stirred at 22 °C for 1 h. The solution was cooled to 0 °C, and *m*CPBA (359 mg, 2.08 mmol) was added. The reaction stirred at 22 °C for 4 h. Saturated aqueous $NaHCO_3$ (150 mL) was added, and the mixture extracted with CH_2Cl_2 (3 × 50 mL). The combined organic phases were washed with brine (150 mL), dried over Na_2SO_4, and concentrated *in vacuo*. The residue was purified by flash column chromatography using a gradient elution ($MeOH/CH_2Cl_2$; 0:100 to 10:90) to yield **12** (449 mg, 65%) as a light yellow solid. HRMS (ESI) m/z: $(M + Na)^+$ Calcd for $[C_{53}H_{61}N_4O_5Si_2Na]^+$ 912.4073. Found 912.4058.

*TBDPS-Protected Nitroxide **13**.* To a solution of **11** (500 mg, 0.74 mmol) in CH_2Cl_2 (36 mL) was added NaN_3 (193 mg, 2.97 mmol), and the reaction was stirred at 22 °C for 1 h. The solution was cooled to 0 °C, and *m*CPBA (367 mg, 2.12 mmol) was added. The reaction stirred at 22 °C for 3 h. Saturated aqueous $NaHCO_3$ (50 mL) was

https://doi.org/10.1021/acs.joc.1c01176
J. Org. Chem. XXXX, XXX, XXX−XXX

added, and the mixture extracted with CH_2Cl_2 (3 × 30 mL). The combined organic phases were washed with brine (100 mL), dried over Na_2SO_4, and concentrated *in vacuo*. The residue was purified by flash column chromatography using a gradient elution (MeOH/CH_2Cl_2; 0:100 to 5:95), to yield **13** (390 mg, 76%) as a light yellow solid. HRMS (ESI) *m/z*: $(M + Na)^+$ Calcd for $[C_{54}H_{63}N_4O_6Si_2Na]^+$ 942.4178. Found 942.4174.

Nitroxide **Ċ**. To a solution of **12** (200 mg, 0.225 mmol) in THF (12 mL) was added TBAF (674 μL, 0.67 mmol, 1.0 M in THF), and the reaction was stirred at 22 °C for 18 h. Dowex-50 (445 mg) and $CaCO_3$ (148 mg, 1.48 mmol) were added, and the mixture was stirred for 1 h, filtered through a plug of Dowex-50, and concentrated *in vacuo*. The residue was purified by flash column chromatography using a gradient elution (MeOH/CH_2Cl_2; 2:98−20:80) to yield **C** (78 mg, 84%) as a light yellow solid. HRMS (ESI) *m/z*: $(M + Na)^+$ Calcd for $[C_{21}H_{25}N_4O_5Na]^+$ 436.1717. Found 436.1719.

Nitroxide **Cm**. To a solution of **13** (178 mg, 0.19 mmol) in THF (10 mL) was added TBAF (674 μL, 0.67 mmol, 1.0 M in THF), and the reaction stirred at 22 °C for 18 h. Dowex-50 (500 mg) and $CaCO_3$ (150 mg, 1.50 mmol) were added, and the mixture was stirred for 1 h, filtered through a plug of Dowex-50, and concentrated *in vacuo*. The residue was purified by flash column chromatography using a gradient elution (MeOH/CH_2Cl_2; 0:100−10:90) to yield **Cm** (58 mg, 67%) as a light yellow solid. HRMS (ESI) *m/z*: $(M + Na)^+$ Calcd for $[C_{22}H_{27}N_4O_6Na]^+$ 466.1823. Found 466.1815.

*3-((2R,4S,5R)-4-((tert-Butyldiphenylsilyl)oxy)-5-(((tert-butyldiphenylsilyl)oxy)methyl)tetrahydrofuran-2-yl)-6,6,8,8-tetramethyl-2-oxo-2,6,8,10-tetrahydropyrimido[4,5-b]pyrrolo[3,4-f]indol-7(3H)-yl Benzoate (**14**)*. To a solution of **12** (450 mg, 0.506 mmol) in 1,4-dioxane (15 mL) was added L-ascorbic acid (445 mg, 2.53 mmol) in H_2O (6 mL). The reaction mixture was stirred at 40 °C for 4 h, after which CH_2Cl_2 (20 mL) and H_2O (20 mL) were added, and the solution was stirred vigorously for 2 min. The organic phase was separated and used directly in the next step by passing it through a plug of Na_2SO_4, under an inert atmosphere of Ar, into a solution of BzCl (588 μL, 5.06 mmol) and Et_3N (1.4 mL, 10.1 mmol) in CH_2Cl_2 (20 mL). The solution was stirred at 22 °C for 3 h. Saturated aqueous $NaHCO_3$ (100 mL) was added, and the phases were separated. The aqueous phase was extracted with CH_2Cl_2 (3 × 50 mL), and the combined organic phases were washed with brine (100 mL), dried over Na_2SO_4, and concentrated *in vacuo*. The residue was purified by flash column chromatography using a gradient elution (MeOH/CH_2Cl_2; 0:100 to 10:90) to yield **14** (259 mg, 51%) as a light yellow solid. ^1H NMR (400 MHz, $CDCl_3$): δ 8.76 (d, *J* = 24.1 Hz, 1H), 8.10−8.00 (m, 2H), 7.62−7.12 (m, 25H), 6.90 (s, 1H), 6.73 (s, 1H), 4.48 (d, *J* = 5.4 Hz, 1H), 4.07 (s, 1H), 3.83 (d, *J* = 12.9 Hz, 1H), 3.26 (d, *J* = 9.5 Hz, 1H), 2.77 (dd, *J* = 13.0, 5.3 Hz, 1H), 1.97 (dt, *J* = 13.5, 7.3 Hz, 1H), 1.58−1.07 (m, 12H), 1.01 (s, 9H), 0.83 (s, 9H) ppm. $^{13}C\{^1H\}$ NMR (101 MHz, $CDCl_3$): δ 259.0, 171.1, 166.6, 162.5, 162.3, 161.2, 155.1, 155.05, 145.0, 144.2, 141.0, 140.8, 139.0, 138.3, 136.1, 136.0, 135.8, 135.5, 135.3, 135.1, 133.7, 133.5, 133.45, 133.3, 133.2, 132.6, 131.3, 130.5, 130.45, 130.4, 130.34, 130.3, 130.0, 129.8, 128.9, 128.6, 128.4, 128.3, 128.2, 128.2, 120.4, 120.1, 113.5, 106.4, 106.2, 106.1, 101.8, 89.0, 88.9, 88.5, 88.4, 74.9, 69.2, 68.7, 68.0, 67.4, 66.9, 64.5, 63.4, 43.8, 29.5, 29.2, 27.3, 27.2, 26.2, 19.63, 19.6, 19.4 ppm. HRMS (ESI) *m/z*: $(M + Na)^+$ Calcd for $[C_{60}H_{66}N_4O_6Si_2Na]^+$ 1017.4413. Found 1017.4420.

*3-((2R,3R,4R,5R)-4-((tert-Butyldiphenylsilyl)oxy)-5-(((tert-butyldiphenylsilyl)oxy)methyl)-3-methoxytetrahydrofuran-2-yl)-6,6,8,8-tetramethyl-2-oxo-2,6,8,10-tetrahydropyrimido[4,5-b]pyrrolo[3,4-f]indol-7(3H)-yl Benzoate (**15**)*. To a solution of **13** (500 mg, 0.54 mmol) in 1,4-dioxane (16 mL) was added L-ascorbic acid (478 mg, 2.72 mmol) in H_2O (6 mL). The reaction mixture was stirred at 40 °C for 4 h, after which CH_2Cl_2 (20 mL) and H_2O (20 mL) were added, and the solution was stirred vigorously for 2 min. The organic phase was separated and used directly in the next step by passing it through a plug of Na_2SO_4, under an inert atmosphere of Ar, into a solution of BzCl (631 μL, 5.43 mmol) and Et_3N (1.5 mL, 10.9 mmol) in CH_2Cl_2 (20 mL). The solution was stirred at 22 °C for 3 h. Saturated aqueous $NaHCO_3$ (100 mL) was added, and the phases were separated. The aqueous phase was extracted with CH_2Cl_2 (3 × 50 mL), and the combined organic phases were washed with brine (100 mL), dried over Na_2SO_4, and concentrated *in vacuo*. The residue was purified by flash column chromatography using a gradient elution (MeOH/CH_2Cl_2; 1:99 to 4:96), to yield **15** (239 mg, 43%) as a light yellow solid. ^1H NMR (400 MHz, $CDCl_3$): δ 8.55 (d, *J* = 18.4 Hz, 1H), 8.20−8.15 (m, 2H), 7.81−7.29 (m, 23H), 7.25 (t, *J* = 7.1 Hz, 1H), 6.82 (s, 1H), 4.41−4.27 (m, 2H), 3.73−3.66 (m, 1H), 3.62−3.52 (m, 1H), 3.40 (d, *J* = 5.0 Hz, 3H), 1.63 (s, 6H), 1.46−1.26 (m, 6H), 1.10 (d, *J* = 13.9 Hz, 18H) ppm. $^{13}C\{^1H\}$ NMR (101 MHz, $CDCl_3$): δ 170.9, 166.3, 162.1, 161.9, 160.9, 154.6, 154.5, 145.0, 144.1, 140.7, 138.8, 138.0, 135.9, 135.7, 135.5, 135.2, 134.7, 133.3, 133.2, 133.1, 133.0, 132.4, 130.8, 130.2, 130.1, 130.0, 129.9, 129.7, 129.5, 128.6, 128.3, 128.2, 128.1, 127.8, 127.78, 127.6, 119.8, 119.5, 113.3, 106.2, 106.1, 101.0, 88.5, 84.8, 84.5, 71.0, 68.9, 68.4, 67.7, 67.1, 66.6, 63.8, 63.0, 58.3, 29.2, 28.9, 27.1, 27.0, 26.9, 25.8, 19.5, 19.45, 19.4 ppm. HRMS (ESI) *m/z*: $(M + Na)^+$ Calcd for $[C_{61}H_{68}N_4O_7Si_2Na]^+$ 1047.4519. Found 1047.4509.

*3-((2R,4S,5R)-4-Hydroxy-5-(hydroxymethyl)tetrahydrofuran-2-yl)-6,6,8,8-tetramethyl-2-oxo-2,6,8,10-tetrahydropyrimido[4,5-b]pyrrolo[3,4-f]indol-7(3H)-yl Benzoate (**16**)*. To a solution of **14** (332 mg, 0.33 mmol) in THF (18 mL) was added TBAF (1 mL, 1.00 mmol, 1.0 M in THF), and the reaction was stirred at 22 °C for 14 h. Saturated aqueous $NaHCO_3$ (50 mL) was added, and the mixture was extracted with EtOAc (3 × 50 mL). The combined organic phases were washed with brine (50 mL), dried over Na_2SO_4, and concentrated *in vacuo*. The residue was purified by flash column chromatography using a gradient elution (MeOH/CH_2Cl_2; 2:98−10:90), to yield **16** (134 mg, 77%) as a light yellow solid. ^1H NMR (400 MHz, $CDCl_3$): δ 9.05 (d, *J* = 26.1 Hz, 1H), 8.00 (d, *J* = 7.2 Hz, 2H), 7.51 (s, 1H), 7.45 (s, 1H), 7.38 (s, 2H), 6.99 (d, *J* = 24.0 Hz, 1H), 6.26 (s, 1H), 4.35 (d, *J* = 5.3 Hz, 1H), 3.96−3.86 (m, 2H), 3.76 (d, *J* = 11.9 Hz, 1H), 2.50 (d, *J* = 13.4 Hz, 1H), 2.15 (s, 1H), 1.45 (s, 12H) ppm. $^{13}C\{^1H\}$ NMR (101 MHz, $CDCl_3$): δ 166.9, 161.1, 155.6, 143.5, 139.9, 138.1, 136.0, 133.4, 129.4, 128.8, 128.6, 120.4, 113.4, 105.6, 105.0, 87.7, 87.5, 69.9, 69.3, 68.8, 68.5, 60.8, 49.6, 49.3, 49.1, 48.9, 48.7, 48.5, 48.3, 48.1, 41.7, 28.6, 25.8, 25.6 ppm. HRMS (ESI) *m/z*: $(M + Na)^+$ Calcd for $[C_{28}H_{30}N_4O_6Na]^+$ 541.5058. Found 541.2055.

*3-((2R,3R,4R,5R)-4-Hydroxy-5-(hydroxymethyl)-3-methoxytetrahydrofuran-2-yl)-6,6,8,8-tetramethyl-2-oxo-2,6,8,10-tetrahydropyrimido[4,5-b]pyrrolo[3,4-f]indol-7(3H)-yl Benzoate (**17**)*. To a solution of **15** (464 mg, 0.45 mmol) in THF (24 mL) was added TBAF (1.4 mL, 1.40 mmol, 1.0 M in THF), and the reaction was stirred at 22 °C for 13 h. Saturated aqueous $NaHCO_3$ (100 mL) was added, and the mixture was extracted with EtOAc (3 × 70 mL). The combined organic phases were washed with brine (70 mL), dried over Na_2SO_4, and concentrated *in vacuo*. The residue was purified by flash column chromatography using a gradient elution (MeOH/CH_2Cl_2; 2:98−10:90), to yield **17** (184 mg, 74%) as a light yellow solid. ^1H NMR (400 MHz, $CDCl_3$): δ 9.26 (d, *J* = 42.3 Hz, 1H), 8.04−7.97 (m, 2H), 7.55−7.48 (m, 1H), 7.44−7.36 (m, 3H), 6.96 (d, *J* = 31.9 Hz, 1H), 6.00 (s, 1H), 4.19 (dd, *J* = 8.6, 4.9 Hz, 1H), 4.02 (dd, *J* = 20.5, 10.7 Hz, 2H), 3.84−3.71 (m, 2H), 3.60 (s, 3H), 1.44 (d, *J* = 10.7 Hz, 12H) ppm. $^{13}C\{^1H\}$ NMR (101 MHz, $CDCl_3$): δ ^{13}C NMR (101 MHz, $CDCl_3$) δ 166.9, 161.0, 155.2, 143.7, 139.9, 138.2, 136.6, 136.3, 133.4, 129.5, 128.8, 128.6, 120.5, 113.3, 105.5, 105.0, 89.4, 84.1, 68.8, 68.5, 66.9, 59.2, 58.5, 49.6, 49.4, 49.2, 49.0, 48.8, 48.6, 48.3, 48.1, 28.6, 25.8, 14.8 ppm. HRMS (ESI) *m/z*: $(M + Na)^+$ Calcd for $[C_{29}H_{32}N_4O_7Na]^+$ 571.2163. Found 571.2136.

*3-((2R,4S,5R)-5-((Bis(4-methoxyphenyl)(phenyl)methoxy)methyl)-4-hydroxytetrahydrofuran-2-yl)-6,6,8,8-tetramethyl-2-oxo-2,6,8,10-tetrahydropyrimido[4,5-b]pyrrolo[3,4-f]indol-7(3H)-yl Benzoate (**18**)*. Toluene (3 × 5 mL) was evaporated from **16** (95 mg, 0.18 mmol), followed by sequential addition of pyridine (4 mL), DMTCl (93 mg, 0.27 mmol) and DMAP (3 mg, 0.02 mmol). The solution was stirred for 12 h, MeOH (400 μL) was added and the solvent removed *in vacuo*. The residue was purified by flash column chromatography using a gradient elution (MeOH/CH_2Cl_2/Et_3N; 0:99:1 to 5:94:1), to yield **18** (122 mg, 81%) as a light yellow solid. ^1H NMR (400 MHz, $CDCl_3$): δ 9.22 (s, 1H), 8.16−8.02 (m, 2H),

https://doi.org/10.1021/acs.joc.1c01176
J. Org. Chem. XXXX, XXX, XXX−XXX

7.49 (ddt, J = 47.4, 32.1, 8.7 Hz, 10H), 7.23−7.05 (m, 3H), 6.75 (dd, J = 8.6, 3.2 Hz, 5H), 6.60 (d, J = 17.9 Hz, 1H), 4.61 (d, J = 24.3 Hz, 1H), 4.32 (s, 1H), 3.67 (s, 7H), 3.24 (s, 1H), 3.01 (d, J = 12.0 Hz, 1H), 2.47 (s, 1H), 1.99 (s, 1H), 1.44 (s, 6H), 1.26−0.94 (m, 6H) ppm. $^{13}C\{^1H\}$ NMR (101 MHz, $CDCl_3$): δ 250.2, 166.3, 162.3, 158.7, 155.6, 143.9, 140.5, 138.1, 136.0, 135.8, 135.5, 133.2, 130.0, 129.7, 129.5, 128.7, 128.2, 128.0, 127.3, 120.1, 113.54, 113.5, 113.46, 106.1, 105.8, 100.1, 88.2, 87.1, 87.0, 72.2, 70.7, 68.9, 68.3, 55.3, 43.1, 29.1, 28.9, 25.7 ppm. HRMS (ESI) m/z: $(M + Na)^+$ Calcd for $[C_{49}H_{48}N_4O_8Na]^+$ 843.3364. Found 843.3346.

*3-((2R,3R,4R,5R)-5-((Bis(4-methoxyphenyl)(phenyl)methoxy)-methyl)-4-hydroxy-3-methoxytetrahydrofuran-2-yl)-6,6,8,8-tetramethyl-2-oxo-2,6,8,10-tetrahydropyrimido[4,5-b]pyrrolo[3,4-f]-indol-7(3H)-yl Benzoate (**19**).* Toluene (3 × 5 mL) was evaporated from **17** (128 mg, 0.23 mmol), followed by sequential addition of pyridine (5 mL), DMTCl (239 mg, 0.64 mmol), and DMAP (3 mg, 0.02 mmol). The solution was stirred for 10 h. MeOH (0.5 mL) was added, and the solvent was removed *in vacuo*. The residue was purified by flash column chromatography using a gradient elution ($MeOH/CH_2Cl_2/Et_3N$; 0:99:1 to 5:94:1), to yield **19** (148 mg, 75%) as a light yellow solid. ^1H NMR (400 MHz, $CDCl_3$): δ 9.34 (s, 1H), 8.09 (d, J = 7.6 Hz, 2H), 7.64−7.39 (m, 10H), 7.33−7.12 (m, 3H), 6.87−6.71 (m, 4H), 6.40 (d, J = 8.9 Hz, 1H), 6.28 (s, 1H), 4.65 (d, J = 12.5 Hz, 1H), 4.25−4.09 (m, 2H), 3.87 (s, 3H), 3.88−3.83 (m, 1H), 3.70 (s, 6H), 3.33 (dd, J = 11.3, 2.5 Hz, 1H), 2.76 (s, 1H), 2.05 (s, 1H), 1.64−1.44 (m, 6H), 1.23−0.73 (m, 6H) ppm. ^{13}C NMR (101 MHz, $CDCl_3$): δ $^{13}C\{^1H\}$ NMR (101 MHz, $CDCl_3$) δ 249.0, 166.2, 162.4, 158.7, 155.1, 143.9, 140.5, 137.9, 136.1, 135.4, 133.1, 129.8, 129.6, 129.5, 128.6, 128.2, 127.9, 127.3, 119.9, 114.0, 113.5, 113.4, 105.9, 105.7, 89.7, 86.8, 84.0, 83.7, 68.6, 68.2, 68.0, 65.9, 62.5, 59.1, 55.2, 46.0, 31.6, 29.1, 28.7, 25.8, 22.7, 15.3, 14.2 ppm. HRMS (ESI) m/z: $(M + Na)^+$ Calcd for $[C_{50}H_{50}N_4O_9Na]^+$ 873.3470. Found 873.3442.

*3-((2R,4S,5R)-5-((Bis(4-methoxyphenyl)(phenyl)methoxy)-methyl)-4-(((2-cyanoethoxy)(diisopropylamino)phosphaneyl)oxy)-tetrahydrofuran-2-yl)-6,6,8,8-tetramethyl-2-oxo-2,6,8,10-tetrahydropyrimido[4,5-b]pyrrolo[3,4-f]indol-7(3H)-yl Benzoate (**20**).* A solution of **18** (596 mg, 0.77 mmol) in CH_2Cl_2 (25 mL) was treated with diisopropyl ammonium tetrazolide (370 mg, 2.18 mmol) and 2-cyanoethyl *N,N,N′,N′*-tetraisopropylphosphane (692 μL, 2.18 mmol). The reaction was stirred at 22 °C for 6 h. CH_2Cl_2 (30 mL) was added, and the solution was washed with saturated aqueous $NaHCO_3$ (3 × 30 mL), dried over Na_2SO_4, and concentrated *in vacuo*. The residue was dissolved in Et_2O (15 mL) and a few drops of CH_2Cl_2, followed by slow addition of *n*-hexane (80 mL), and the mixture was centrifuged for 10 min. The solvent was decanted from the precipitate and discarded. This procedure was repeated five times to yield **20** (673 mg, 91%) as a light yellow solid. ^1H NMR (400 MHz, $CDCl_3$): δ 9.22 (d, J = 22.6 Hz, 2H), 8.10 (dt, J = 8.5, 1.5 Hz, 4H), 7.64−7.56 (m, 2H), 7.56−7.32 (m, 18H), 7.25−7.14 (m, 6H), 6.84−6.72 (m, 8H), 6.65 (d, J = 6.8 Hz, 1H), 6.62 (t, J = 6.0 Hz, 1H), 6.51 (d, J = 17.8 Hz, 2H), 4.67 (s, 2H), 4.30 (d, J = 9.4 Hz, 2H), 3.82−3.75 (m, 2H), 3.70 (d, J = 2.0 Hz, 12H), 3.62−3.49 (m, 6H), 3.24 (d, J = 10.1 Hz, 2H), 2.59 (t, J = 6.3 Hz, 2H), 2.50 (s, 2H), 2.41−2.33 (m, 2H), 1.55 (d, J = 19.1 Hz, 12H), 1.18−1.10 (m, 18H), 1.03 (d, J = 6.8 Hz, 6H) ppm. $^{13}C\{^1H\}$ NMR (101 MHz, $CDCl_3$): δ 166.0, 162.1, 158.5, 154.9, 143.6, 140.2, 137.8, 135.5, 135.1, 132.9, 129.7, 129.4, 129.3, 128.4, 127.9, 127.1, 119.9, 117.3, 117.2, 113.2, 113.15, 105.6, 105.4, 86.7, 86.0, 85.8, 68.6, 68.0, 58.3, 58.2, 58.1, 58.0, 55.03, 55.0, 43.2, 43.1, 43.0, 42.98, 41.4, 28.6, 25.7, 25.6, 24.5, 24.4, 24.36, 24.3, 20.2, 20.16, 20.0, 19.9 ppm. ^{31}P NMR (162 MHz,$CDCl_3$): δ 149.0, 148.5 ppm. HRMS (ESI) m/z: $(M + Na)^+$ Calcd for $[C_{58}H_{65}N_6O_9PNa]^+$ 1043.4443. Found 1043.4412.

*3-((2R,3R,4R,5R)-5-((Bis(4-methoxyphenyl)(phenyl)methoxy)-methyl)-4-(((2-cyanoethoxy)(diisopropylamino)phosphaneyl)oxy)-3-methoxytetrahydrofuran-2-yl)-6,6,8,8-tetramethyl-2-oxo-2,6,8,10-tetrahydropyrimido[4,5-b]pyrrolo[3,4-f]indol-7(3H)-yl Benzoate (**21**).* A solution of **19** (322 mg, 0.38 mmol) in CH_2Cl_2 (13 mL) was treated with diisopropyl ammonium tetrazolide (193 mg, 1.14 mmol) and 2-cyanoethyl *N,N,N′,N′*-tetraisopropylphosphane (361 μL, 1.14 mmol). The reaction was stirred at 22 °C for 12 h. CH_2Cl_2 (25 mL) was added, and the solution was washed with saturated aqueous $NaHCO_3$ (3 × 25 mL), dried over Na_2SO_4, and concentrated *in vacuo*. The residue was dissolved in Et_2O (10 mL) and a few drops of CH_2Cl_2, followed by slow addition of *n*-hexane (60 mL), and the mixture was centrifuged for 10 min. The solvent was decanted from the precipitate and discarded. This procedure was repeated six times to yield **21** (258 mg, 65%) as a light yellow solid. ^1H NMR (400 MHz, $CDCl_3$): δ 9.44 (s, 1H), 9.35 (s, 1H), 8.09 (dd, J = 7.4, 2.0 Hz, 4H), 7.62−7.34 (m, 20H), 7.24−7.11 (m, 6H), 6.77 (t, J = 9.6 Hz, 8H), 6.38−6.19 (m, 4H), 4.64 (d, J = 37.0 Hz, 2H), 4.38 (dd, J = 13.9, 8.2 Hz, 2H), 4.24 (s, 2H), 3.91 (dd, J = 22.3, 10.9 Hz, 2H), 3.81 (s, 3H), 3.79 (s, 3H), 3.74−3.66 (m, 12H), 3.56 (ddp, J = 10.6, 7.2, 3.3 Hz, 4H), 3.24 (d, J = 11.2 Hz, 2H), 2.54 (s, 2H), 2.32−2.10 (m, 4H), 1.61−1.45 (m, 12H), 1.16−1.08 (m, 18H), 1.00 (d, J = 6.8 Hz, 6H) ppm. $^{13}C\{^1H\}$ NMR (101 MHz, $CDCl_3$): δ 262.5, 249.6, 166.2, 162.5, 162.48, 158.7, 155.2, 155.1, 143.7, 140.6, 137.7, 136.1, 135.4, 135.3, 133.1, 130.4, 129.8, 129.6, 129.5, 128.5, 128.14, 128.1, 127.3, 120.0, 119.97, 117.6, 117.5, 114.1, 113.8, 113.4, 113.36, 113.3, 106.0, 105.8, 105.7, 90.8, 86.8, 86.7, 84.2, 82.9, 82.5, 82.3, 82.27, 69.5, 69.4, 68.8, 68.2, 59.1, 58.8, 58.6, 58.4, 58.3, 58.1, 55.2, 55.2, 43.3, 43.30, 43.2, 43.18, 29.1, 28.7, 25.8, 25.5, 24.7, 24.67, 24.6, 24.5, 20.4, 20.3, 20.0 ppm. ^{31}P NMR (162 MHz,$CDCl_3$): δ 150.3, 149.7 ppm. HRMS (ESI) m/z: $(M + Na)^+$ Calcd for $[C_{59}H_{67}N_6O_{10}PNa]^+$ 1073.4548. Found 1073.4549.

*5-Bromo-1-((2R,4S,5R)-4-((tert-butyldiphenylsilyl)oxy)-5-(((tert-butyldiphenylsilyl)oxy)methyl)tetrahydrofuran-2-yl)-4-(phenylamino)pyrimidin-2(1H)-one (**22**).* To a solution of nucleoside **5** (8.4 g, 10.5 mmol) in CH_2Cl_2 (250 mL) were added aniline (1.2 g, 16.2 mmol), DMAP (0.13 g, 1.1 mmol), and Et_3N (1.7 mL, 23.2 mmol), and the resulting solution was stirred at 22 °C for 12 h. Saturated aqueous $NaHCO_3$ (200 mL) was added, and the organic phase extracted with CH_2Cl_2 (2 × 100 mL). The combined organic phases were washed with saturated aqueous $NaHCO_3$ (50 mL) and brine (100 mL), dried over Na_2SO_4, and concentrated *in vacuo*. The residue was purified by flash column chromatography using a gradient elution (EtOAc/petroleum ether, 10:90 to 20:80) to yield compound **22** (7.5 g, 83% yield) as a white foam. ^1H NMR (400 MHz, $CDCl_3$): δ 8.08 (s, 1H), 7.71 (d, J = 7.8 Hz, 2H), 7.61 (d, J = 8.0 Hz, 2H), 7.55 (d, J = 6.2 Hz, 4H), 7.49−7.25 (m, 18H), 7.15 (t, J = 7.4 Hz, 1H), 6.47 (dd, J = 8.3, 5.4 Hz, 1H), 4.48 (d, J = 5.6 Hz, 1H), 4.05−4.01 (m, 1H), 3.72 (dd, J = 11.6, 2.3 Hz, 1H), 3.28 (dd, J = 11.6, 2.9 Hz, 1H), 2.68 (ddd, J = 13.4, 5.4, 1.6 Hz, 1H), 1.97−1.89 (m, 1H), 1.08 (s, 9H), 0.95 (s, 9H) ppm. $^{13}C\{^1H\}$ NMR (101 MHz, $CDCl_3$) δ 157.1, 140.8, 137.3, 135.7, 135.7, 135.6, 135.6, 135.4, 133.3, 133.1, 132.8, 132.3, 130.0, 129.9, 129.91, 129.1, 127.9, 127.88, 127.8, 125.0, 121.5, 88.4, 88.36, 87.4, 74.3, 64.0, 42.7, 35.5, 27.0, 26.92, 26.9, 23.9, 20.8, 19.2, 19.0, 18.98 ppm. HRMS (ESI) m/z: $(M + Na)^+$ Calcd for $[C_{47}H_{52}BrN_3O_4Si_2Na]^+$ 882.2563. Found 882.2564.

*tert-Butyl(5-bromo-1-((2R,4S,5R)-4-((tert-butyldiphenylsilyl)oxy)-5-(((tert-butyldiphenylsilyl)oxy)methyl)tetrahydrofuran-2-yl)-2-oxo-1,2-dihydropyrimidin-4-yl)(phenyl)carbamate (**23**).* To a solution of compound **22** (7.0 g, 8.2 mmol) in 1,4-dioxane (67 mL) were added Boc_2O (5.3 g, 24.5 mmol) and DMAP (99 mg, 0.8 mmol), and the resulting solution was stirred at 60 °C for 12 h. Saturated aqueous $NaHCO_3$ (100 mL) was added, and the mixture was extracted with EtOAc (3 × 50 mL). The combined organic phases were washed with brine (100 mL), dried over Na_2SO_4, and concentrated *in vacuo*. The residue was purified by flash column chromatography using a gradient elution (EtOAc/petroleum ether, 10:90 to 25:75) to yield compound **23** (5.8 g, 74% yield) as a white foam. ^1H NMR (400 MHz, $CDCl_3$): δ 8.44 (s, 1H), 7.62−7.51 (m, 6H), 7.48−7.32 (m, 14H), 7.29−7.25 (m, 5H), 6.39 (dd, J = 8.2, 5.4 Hz, 1H), 4.44 (dd, J = 5.5, 1.5 Hz, 1H), 4.08−4.05 (m, 1H), 3.71 (dd, J = 11.8, 2.4 Hz, 1H), 3.26 (dd, J = 11.7, 3.2 Hz, 1H), 2.83 (ddd, J = 13.3, 5.4, 1.4 Hz, 1H), 2.03−1.93 (m, 1H), 1.49, (s, 9H), 1.08 (s, 9H), 0.95 (s, 9H) ppm. $^{13}C\{^1H\}$ NMR (101 MHz, $CDCl_3$) δ 165.4, 154.2, 151.7, 144.8, 139.4, 135.7, 135.6, 135.5, 135.49, 133.2, 132.9, 132.5, 132.2, 130.1, 130.0, 128.9, 128.1, 127.9, 127.86, 127.4, 127.2, 97.1, 89.1, 88.7, 83.0, 74.4, 63.8, 42.9, 35.4, 28.1, 26.9, 26.88, 26.5,

https://doi.org/10.1021/acs.joc.1c01176
J. Org. Chem. XXXX, XXX, XXX−XXX

26.3, 22.7, 19.2, 19.0, 14.1 ppm. HRMS (ESI) m/z: $(M + Na)^+$ Calcd for $[C_{52}H_{60}BrN_3O_6Si_2Na]^+$ 982.3089. Found 982.3090.

*3-((2R,4S,5R)-4-((tert-Butyldiphenylsilyl)oxy)-5-(((tert-butyldiphenylsilyl)oxy)methyl)tetrahydrofuran-2-yl)-3,9-dihydro-2H-pyrimido[4,5-b]indol-2-one (**24**).* To a solution of compound **23** (110 mg, 0.11 mmol) in DMA (4.6 mL) were added anhydrous NaOAc (38 mg, 0.46 mmol) and $PdCl_2(PPh_3)_2$ (16 mg, 0.023 mmol). The resulting solution was stirred at 150 °C for 12 h, cooled to 22 °C, filtered through Celite, and concentrated *in vacuo*. H_2O (20 mL) was added, and the mixture was extracted with EtOAc (5 × 20 mL). The combined organic phases were washed with brine (3 × 50 mL), dried over Na_2SO_4, and concentrated *in vacuo*. The residue was dissolved in CH_2Cl_2 (20 mL), TFA (10 mL) was added at 0 °C, and the reaction was stirred at 22 °C for 3 h. Saturated aqueous $NaHCO_3$ was added to the solution until the effervescence, by release of CO_2 gas, had stopped. The two phases were separated and the aqueous phase was extracted with EtOAc (4 × 20 mL). The combined organic phases were washed with brine (50 mL), dried over Na_2SO_4, and concentrated *in vacuo*. The residue was purified by flash column chromatography using a gradient elution ($MeOH/CH_2Cl_2$, 0:100 to 10:90) to yield compound **24** (59 mg, 66%) as a light brown foam. ^1H NMR (400 MHz, $CDCl_3$) δ 8.76 (s, 1H), 7.73−7.69 (m, 1H), 7.67−7.58 (m, 6H), 7.49−7.45 (m, 2H), 7.45−7.42 (m, 1H), 7.41−7.28 (m, 10H), 7.28−7.21 (m, 3H), 6.98−6.92 (m, 2H), 6.75 (dd, J = 8.3, 5.4 Hz, 1H), 4.56 (d, J = 4.1 Hz, 1H), 4.15 (s, 1H), 3.87 (dd, J = 11.6, 2.3 Hz, 1H), 3.35 (dd, J = 11.6, 2.9 Hz, 1H), 2.89 (dd, J = 12.8, 6.0 Hz, 1H), 2.13−2.04 (m, 1H), 1.11 (s, 9H), 0.94 (s, 9H) ppm. $^{13}C\{^1H\}$ NMR (101 MHz, $CDCl_3$) δ 162.0, 154.9, 140.7, 135.8, 135.7, 135.5, 135.3, 135.2, 133.4, 133.1, 133.0, 132.4, 130.1, 130.0, 129.99, 129.97, 128.0, 127.9, 127.86, 127.2, 121.6, 120.1, 119.8, 112.7, 105.8, 88.6, 88.2, 74.4, 64.2, 53.4, 43.4, 27.0, 26.9, 19.1 ppm. HRMS (ESI) m/z: $(M + Na)^+$ Calcd for $[C_{47}H_{51}N_3O_4Si_2Na]^+$ 800.3310. Found 800.3336.

*3-((2R,4S,5R)-4-Hydroxy-5-(hydroxymethyl)tetrahydrofuran-2-yl)-3,9-dihydro-2H-pyrimido[4,5-b]indol-2-one (**25**).* To a solution of **24** (1220 mg, 1.57 mmol) in THF (85 mL) was added TBAF (4.7 mL, 4.7 mmol, 1.0 M in THF), and the reaction was stirred at 22 °C for 4 h. Dowex-50 (2830 mg) and $CaCO_3$ (942 mg, 9.41 mmol) were added, and the mixture was stirred for 1 h, filtered through a plug of Dowex-50, and concentrated *in vacuo*. The residue was purified by flash column chromatography using a gradient elution ($MeOH/CH_2Cl_2$; 0:100−10:90), to yield **25** (320 mg, 68%) as a white solid. ^1H NMR (400 MHz, DMSO-d_6) δ 11.64 (s, 1H), 9.14 (s, 1H), 7.79 (d, J = 7.6 Hz, 1H), 7.36−7.24 (m, 2H), 7.17 (t, J = 7.4, 1H), 6.27 (t, J = 6.2 Hz, 1H), 5.34−5.21 (m, 2H), 4.34−4.26 (m, 1H), 3.94−3.89 (m, 1H), 3.81−3.73 (m, 1H), 3.72−3.64 (m, 1H), 2.41−2.31 (m, 1H), 2.16−2.06 (m, 1H) ppm. $^{13}C\{^1H\}$ NMR (101 MHz, DMSO-d_6) δ 162.0, 154.9, 140.5, 137.2, 127.0, 121.7, 121.1, 120.4, 111.8, 104.1, 88.2, 87.2, 70.0, 61.2, 41.8, 40.6, 40.4, 40.2, 40.0, 39.8, 39.6, 39.3 ppm. HRMS (ESI) m/z: $(M + Na)^+$ Calcd for $[C_{15}H_{15}N_3O_4Na]^+$ 324.0955. Found 324.0952.

*3-((2R,4S,5R)-5-((Bis(4-methoxyphenyl)(phenyl)methoxy)-methyl)-4-hydroxytetrahydrofuran-2-yl)-3,9-dihydro-2H-pyrimido-[4,5-b]indol-2-one (**26**).* Toluene (3 × 5 mL) was evaporated from **25** (100 mg, 0.33 mmol), followed by sequential addition of pyridine (7.4 mL), DMTCl (169 mg, 0.50 mmol), and DMAP (4 mg, 0.03 mmol). The solution was stirred for 12 h. MeOH (0.8 mL) was added, and the solvent was removed *in vacuo*. The residue was purified by flash column chromatography using a gradient elution ($MeOH/CH_2Cl_2/Et_3N$; 0:99:1 to 2:97:1) to yield **26** (205 mg, quant.) as a white solid. ^1H NMR (400 MHz, $CDCl_3$) δ 12.83 (s, 1H), 9.05 (s, 1H), 7.65 (d, J = 8.0 Hz, 1H), 7.53 (d, J = 7.7 Hz, 2H), 7.41 (d, J = 8.5 Hz, 4H), 7.30 (t, J = 5.0 Hz, 2H), 7.26−7.19 (m, 2H), 6.89 (t, J = 7.6 Hz, 1H), 6.82 (d, J = 7.5, 4H), 6.72 (t, J = 6.2 Hz, 1H), 6.64 (d, J = 7.8 Hz, 1H), 4.71−4.65 (m, 1H), 4.41−4.36 (m, 1H), 3.72 (s, 3H), 3.71 (s, 3H), 3.63 (dd, J = 10.7, 3.1 Hz, 1H), 3.42 (dd, J = 10.7, 3.9 Hz, 1H), 3.11−3.01 (m, 1H), 2.53−2.41 (m, 1H) ppm. $^{13}C\{^1H\}$ NMR (101 MHz, $CDCl_3$) δ 162.0, 158.7, 155.5, 144.4, 140.5, 135.7, 135.4, 130.0, 129.97, 128.2, 128.1, 127.2, 127.1, 121.7, 120.1, 120.0, 113.4, 112.4, 106.0, 88.0, 87.0, 86.7, 71.7, 68.0, 63.4, 55.2, 53.5, 45.9, 42.8 ppm. HRMS (ESI) m/z: $(M + Na)^+$ Calcd for $[C_{36}H_{33}N_3O_6Na]^+$ 626.2262. Found 626.2265.

*(2R,3S,5R)-2-((Bis(4-methoxyphenyl)(phenyl)methoxy)methyl)-5-(2-oxo-2,9-dihydro-3H-pyrimido[4,5-b]indol-3-yl)tetrahydrofuran-3-yl(2-cyanoethyl) Diisopropylphosphoramidite (**27**).* A solution of **26** (175 mg, 0.29 mmol) in CH_2Cl_2 (10 mL) was treated with diisopropyl ammonium tetrazolide (74 mg, 0.43 mmol) and 2-cyanoethyl *N*,*N*,*N*′,*N*′-tetraisopropylphosphane (138 μL, 0.43 mmol). The reaction was stirred at 22 °C for 5 h. CH_2Cl_2 (25 mL) was added, and the solution was washed with saturated aqueous $NaHCO_3$ (3 × 25 mL), dried over Na_2SO_4, and concentrated *in vacuo*. The residue was dissolved in Et_2O (8 mL) and a few drops of CH_2Cl_2, followed by slow addition of *n*-hexane (40 mL), and the mixture was centrifuged for 10 min. The solvent was decanted from the precipitate and discarded. This procedure was repeated five times to yield **27** (107 mg, 46%) as a white solid. ^1H NMR (400 MHz, $CDCl_3$) δ 13.51 (s, 2H), 9.03 (s, 1H), 8.98 (s, 1H), 7.67 (dd, J = 8.0, 2.7 Hz, 2H), 7.51 (t, J = 7.2 Hz, 4H), 7.39 (t, J = 7.4, 8H), 7.31−7.21 (m, 8H), 6.87−6.78 (m, 10H), 6.62−6.51 (m, 3H), 6.45 (d, J = 7.8 Hz, 1H), 4.77−4.63 (m, 2H), 4.35−4.28 (m, 2H), 3.89−3.68 (m, 10H), 3.70 (s, 6H), 3.65−3.55 (m, 6H), 3.43−3.34 (m, 2H), 2.95−2.80 (m, 2H), 2.63 (t, J = 6.4 Hz, 2H), 2.54−2.44 (m, 2H), 2.42 (t, J = 6.4 Hz, 2H), 1.17 (d, J = 6.8 Hz, 18H), 1.06 (d, J = 6.8 Hz, 6H) ppm. $^{13}C\{^1H\}$ NMR (101 MHz, $CDCl_3$) δ 162.1, 158.8, 155.0, 144.3, 144.2, 140.7, 140.66, 135.6, 135.57, 135.3, 130.1, 130.07, 128.4, 128.3, 128.1, 127.3, 127.2, 127.1, 127.08, 121.6, 120.1, 120.0, 119.9, 117.5, 117.4, 113.4, 112.5, 112.4, 105.9, 105.89, 87.6, 87.5, 87.0, 86.9, 85.8, 85.7, 85.6, 73.0, 72.9, 71.9, 71.7, 62.9, 62.2, 58.5, 58.4, 58.3, 58.2, 55.23, 55.2, 43.4, 43.3, 43.25, 43.2, 41.8, 41.79, 41.44, 41.4, 31.6, 25.6, 24.7, 24.62, 24.6, 24.55, 24.5, 22.7, 20.4, 20.35, 20.2, 20.17, 14.2 ppm. ^{31}P NMR (162 MHz, $CDCl_3$) δ 149.4, 148.7 ppm. HRMS (ESI) m/z: $(M + Na)^+$ Calcd for $[C_{45}H_{50}N_5O_7PNa]^+$ 826.3340. Found 826.3343.

X-ray Crystallography. X-ray quality single crystals of $\dot{\mathbf{C}}$ and $\dot{\mathbf{C}}$**m** were obtained by dissolving the compounds in 10% $MeOH/CHCl_3$ and layering the solution with Et_2O. The crystals were isolated from the solvent, immersed in cryogenic oil, and mounted on a Bruker D8 VENTURE (Photon100 CMOS detector) diffractometer equipped with a Cryostream open-flow nitrogen cryostat. The data were collected using Mo Kα (λ = 0.71073 Å) radiation. The unit cell determination, data collection, data reduction, structure solution/refinement, and empirical absorption correction (SADABS) were carried out using Apex-III (Bruker AXS: Madison, WI, 2015). The structures were solved by a direct method and refined by full-matrix least-squares on F^2 for all data using SHELXTL version 2017/1[63] and Olex2 software.[64] All nondisordered non-hydrogen atoms were refined anisotropically except the disordered oxygen atom of the methoxy group in $\dot{\mathbf{C}}$**m**, which was refined using free variable (FVAR) instruction. The hydrogen atoms were placed in the calculated positions and refined using a riding model.

DNA Synthesis. Unmodified 2′-deoxy phosphoramidites were dissolved in CH_3CN (0.1 M) and phosphoramidite **20** was dissolved in 1,2-dichloroethane (0.1 M). 5-Ethylthiotetrazole (0.25 M in CH_3CN) was used as a coupling agent for the unmodified phosphoramidites and **20**. The coupling time was 1.5 min for unmodified DNA phosphoramidites, whereas **20** was coupled manually for 10 min. After completion of the DNA synthesis, the DNAs were cleaved from the resin and deprotected in a saturated aqueous NH_3 solution at 55 °C for 8 h, after which the solvent was removed *in vacuo*.

RNA Synthesis. Unmodified 2′O-TBDMS phosphoramidites were dissolved in CH_3CN (0.1 M), and phosphoramidite **21** was dissolved in 1,2-dichloroethane (0.1 M). 5-Benzylthiotetrazole (0.25 M in CH_3CN) was used as a coupling agent for the unmodified RNA phosphoramidites, and 5-ethylthiotetrazole (0.25 M in CH_3CN) was used for **21**. The coupling time was 7 min for the unmodified RNA phosphoramidites, and **21** was coupled manually for 10 min.

The RNAs were deprotected and cleaved from the resin in a 1:1 solution (2 mL) of CH_3NH_2 (8 M in EtOH) and saturated aqueous NH_3 at 65 °C for 1 h. The solvent was removed *in vacuo*, and the 2′O-TBDMS groups were removed by incubation in a solution of $Et_3N\cdot$

https://doi.org/10.1021/acs.joc.1c01176
J. Org. Chem. XXXX, XXX, XXX−XXX

3HF (300 μL) in DMF (100 μL) at 55 °C for 1.5 h, followed by addition of deionized and sterilized water (100 μL). This solution was transferred to a 50 mL Falcon tube, and *n*-butanol (20 mL) was added. The mixture was stored at −20 °C for 14 h and centrifuged (4000 rpm) at 4 °C for 1 h. The solvent was decanted from the RNA pellet, and the pellet was dried *in vacuo*.

DNA and RNA Purification. All oligonucleotides were purified by 20% DPAGE and extracted from the gel slices using the "crush and soak method" with Tris buffer (250 mM NaCl, 10 mM Tris, 1 mM Na_2EDTA, pH 7.5; 2×(3 mL gel/9 mL buffer)). The solutions were filtered through GD/X syringe filters (0.45 μm, 25 mm diameter, Whatman) and were subsequently desalted using Sep-Pak cartridges (Waters), following the instructions provided by the manufacturer. The dried oligonucleotides were dissolved in deionized and sterilized water (200 μL for each oligonucleotide). Concentrations of the oligonucleotides were determined by measuring UV absorbance at 260 nm and calculation using Beer's law.

CW-EPR Measurements and Spin Counting. Samples of spin-labeled oligonucleotides for EPR measurements were prepared by dissolving single-stranded DNA or RNA (2.0 nmol) in phosphate buffer (10 μL, 10 mM phosphate, 100 mM NaCl, 0.1 mM Na_2EDTA, pH 7.0, oligonucleotide final concentration 200 μM). DNA and RNA duplexes were prepared by dissolving complementary single-stranded oligonucleotides (2.0 nmol of each) in a phosphate buffer (10 μL; 10 mM phosphate, 100 mM NaCl, 0.1 mM Na_2EDTA, pH 7.0, duplex final concentration 200 μM) and annealing (Figures 3 and S50). The amount of spin labels in each oligonucleotide was determined by spin counting. A stock solution of 4-hydroxy-TEMPO (1.0 M) was prepared in phosphate buffer (10 mM phosphate, 100 mM NaCl, 0.1 mM Na_2EDTA, pH 7.0). The stock solution was diluted into samples of different concentrations (0−0.5 mM), and each sample was measured by EPR spectroscopy. The area under the peaks of each spectrum, obtained by double integration, was plotted against its concentration to yield a standard curve, which was used to determine the spin-labeling efficiency with an error margin of 5−10% (Table S1).

Enzymatic Digestion of Oligonucleotides and HPLC Analysis. To an oligonucleotide (4 nmol) in sterile water (8 μL) was added calf intestinal alkaline phosphatase (1 μL, 2 U), snake venom phosphodiesterase I (4 μL, 0.2 U), nuclease P1 from *Penicillium citrinum* (5 μL, 1.5 U), and Tris buffer (2 μL, 500 mM Tris and 100 mM $MgCl_2$). The samples were incubated at 37 °C for 24 h, after which they were analyzed by HPLC chromatography (Figures S51 and S52).

Thermal Denaturing Experiments. To determine if **Ċ** and **Ċm** affected the stability of the DNA and RNA duplexes, respectively, the thermal denaturation curves of unmodified and spin-labeled oligomers were recorded. Both DNA and RNA duplexes were prepared by dissolving complementary single-stranded oligonucleotides (4.0 nmol) in a phosphate buffer (100 μL; 10 mM phosphate, 100 mM NaCl, 0.1 mM Na_2EDTA, pH 7.0), followed by annealing. The samples were diluted to 1.0 mL with the phosphate buffer (pH 7.0), degassed with Ar and heated from 24 to 90 °C (1.0 °C/min). The absorbance at 260 nm was subsequently recorded at 0.2 °C intervals (Table 1 and Figure S53).

CD Measurements. To determine if **Ċ** and **Ċm** labels had any effect on the conformation of the DNA and RNA duplexes, CD spectra of all unmodified duplexes and their spin-labeled counterparts were recorded. DNA and RNA duplexes were prepared by dissolving complementary single-stranded oligonucleotides (2.5 nmol of each) in a phosphate buffer (100 μL; 10 mM phosphate, 100 mM NaCl, 0.1 mM Na_2EDTA, pH 7.0) and annealing. The annealed samples were diluted to 200 μL with the same buffer before CD measurements (Figure S54).

■ ASSOCIATED CONTENT

Supporting Information

The Supporting Information is available free of charge at https://pubs.acs.org/doi/10.1021/acs.joc.1c01176.

Crystallographic data for **Ċ** and **Ċm**, extinction coefficients and UV−vis absorption spectra. Models of spin-labeled duplexes, spin-labeled oligonucleotides, and their analysis by MS and EPR spectroscopy, ^{1}H, ^{13}C, and ^{31}P NMR spectra, HPLC analyses of enzymatic digests, thermal denaturing experiments of spin-labeled duplexes, CD spectra of oligonucleotide duplexes and CW-EPR spectra of spin-labeled oligonucleotides (PDF)

Accession Codes

CCDC 2084624 and 2084625 contain the supplementary crystallographic data for this paper. These data can be obtained free of charge via www.ccdc.cam.ac.uk/data_request/cif, or by emailing data_request@ccdc.cam.ac.uk, or by contacting The Cambridge Crystallographic Data Centre, 12 Union Road, Cambridge CB2 1EZ, UK; fax: +44 1223 336033.

■ AUTHOR INFORMATION

Corresponding Author

Snorri Th. Sigurdsson − *University of Iceland, Department of Chemistry, Science Institute, 107 Reykjavik, Iceland;* orcid.org/0000-0003-2492-1456; Phone: +354 525 4801; Email: snorrisi@hi.is

Author

Anna-Lena Johanna Segler − *University of Iceland, Department of Chemistry, Science Institute, 107 Reykjavik, Iceland*

Complete contact information is available at: https://pubs.acs.org/10.1021/acs.joc.1c01176

Notes

The authors declare no competing financial interest.

■ ACKNOWLEDGMENTS

We acknowledge financial support from the Icelandic Research Fund (206708). We thank Dr. S. Jonsdottir and Dr. T. Halbritter for assistance with collecting analytical data for structural characterization of new compounds, Prof. K. K. Damodaran for solving the crystal structures of **Ċ** and **Ċm**, and members of the Sigurdsson research group for helpful discussions.

■ REFERENCES

(1) Breaker, R. R.; Joyce, G. F. The expanding view of RNA and DNA function. *Chem. Biol.* **2014**, *21* (9), 1059−1065.
(2) Minchin, S.; Lodge, J. Understanding biochemistry: Structure and function of nucleic acids. *Essays Biochem.* **2019**, *63* (4), 433−456.
(3) Sharp, P. A. The centrality of RNA. *Cell* **2009**, *136* (4), 577−580.
(4) Blanco, A.; Blanco, G. Chapter 6 - Nucleic Acids. In *Medical Biochemistry*; Academic Press, 2017; pp 121−140.
(5) Egli, M. Nucleic acid crystallography: current progress. *Curr. Opin. Chem. Biol.* **2004**, *8* (6), 580−591.
(6) Egli, M.; Pallan, P. S. Crystallographic studies of chemically modified nucleic acids: A backward glance. *Chem. Biodiversity* **2010**, *7* (1), 60−89.
(7) Cheung, T.; Ramesh, V. Biomolecular NMR spectroscopy and structure determination of DNA. *Biomolecular and bioanalytical techniques* **2019**, 421−469.
(8) Bothe, J. R.; Nikolova, E. N.; Eichhorn, C. D.; Chugh, J.; Hansen, A. L.; Al-Hashimi, H. M. Characterizing RNA dynamics at atomic resolution using solution-state NMR spectroscopy. *Nat. Methods* **2011**, *8* (11), 919−931.

(9) Yip, K. M.; Fischer, N.; Paknia, E.; Chari, A.; Stark, H. Atomic-resolution protein structure determination by cryo-EM. *Nature* **2020**, *587* (7832), 157−161.
(10) Nakane, T.; Kotecha, A.; Sente, A.; McMullan, G.; Masiulis, S.; Brown, P. M. G. E.; Grigoras, I. T.; Malinauskaite, L.; Malinauskas, T.; Miehling, J.; Uchański, T.; Yu, L.; Karia, D.; Pechnikova, E. V.; de Jong, E.; Keizer, J.; Bischoff, M.; McCormack, J.; Tiemeijer, P.; Hardwick, S. W.; Chirgadze, D. Y.; Murshudov, G.; Aricescu, A. R.; Scheres, S. H. W. Single-particle cryo-EM at atomic resolution. *Nature* **2020**, *587* (7832), 152−156.
(11) Murata, K.; Wolf, M. Cryo-electron microscopy for structural analysis of dynamic biological macromolecules. *Biochim. Biophys. Acta, Gen. Subj.* **2018**, *1862* (2), 324−334.
(12) Ognjenović, J.; Grisshammer, R.; Subramaniam, S. Frontiers in cryo electron microscopy of complex macromolecular assemblies. *Annu. Rev. Biomed. Eng.* **2019**, *21* (1), 395−415.
(13) Preus, S.; Wilhelmsson, L. M. Advances in quantitative FRET-based methods for studying nucleic acids. *ChemBioChem* **2012**, *13* (14), 1990−2001.
(14) Robinson, P. J.; Woolhead, C. A. Implementation of FRET technologies for studying the folding and conformational changes in biological structures. In *FRET − Förster Resonance Energy Transfer*; Wiley, 2013; pp 357−396.
(15) Lilley, D. M. J.; Wilson, T. J. Fluorescence resonance energy transfer as a structural tool for nucleic acids. *Curr. Opin. Chem. Biol.* **2000**, *4* (5), 507−517.
(16) Kaur, A.; Kaur, P.; Ahuja, S. Förster resonance energy transfer (FRET) and applications thereof. *Anal. Methods* **2020**, *12* (46), 5532−5550.
(17) Helm, M.; Kobitski, A. Y.; Nienhaus, G. U. Single-molecule Förster resonance energy transfer studies of RNA structure, dynamics and function. *Biophys. Rev.* **2009**, *1* (4), 161.
(18) Bacic, L.; Sabantsev, A.; Deindl, S. Recent advances in single-molecule fluorescence microscopy render structural biology dynamic. *Curr. Opin. Struct. Biol.* **2020**, *65*, 61−68.
(19) Endeward, B.; Marko, A.; Denysenkov, V. P.; Sigurdsson, S. T.; Prisner, T. F. Advanced EPR methods for studying conformational dynamics of nucleic acids. *Methods Enzymol.* **2015**, *564*, 403−425.
(20) Nguyen, P.; Qin, P. Z. RNA dynamics: perspectives from spin labels. *Wiley Interdiscip. Rev.: RNA* **2012**, *3* (1), 62−72.
(21) Bennati, M.; Prisner, T. F. New developments in high field electron paramagnetic resonance with applications in structural biology. *Rep. Prog. Phys.* **2005**, *68* (2), 411−448.
(22) Krstić, I.; Endeward, B.; Margraf, D.; Marko, A.; Prisner, T. F. Structure and dynamics of nucleic acids. *Top. Curr. Chem.* **2011**, *321*, 159−198.
(23) Zhang, X.; Cekan, P.; Sigurdsson, S. T.; Qin, P. Z. Studying RNA using site- directed spin-labeling and continuous-wave electron paramagnetic resonance spectroscopy. *Methods Enzymol.* **2009**, *469*, 303−328.
(24) Kim, N. K.; Murali, A.; DeRose, V. J. A distance ruler for RNA using EPR and site-directed spin labeling. *Chem. Biol.* **2004**, *11* (7), 939−48.
(25) Jeschke, G. The contribution of modern EPR to structural biology. *Emerging Top. Life Sci.* **2018**, *2* (1), 9−18.
(26) Reginsson, G. W.; Schiemann, O. Studying biomolecular complexes with pulsed electron−electron double resonance spectroscopy. *Biochem. Soc. Trans.* **2011**, *39* (1), 128−139.
(27) Schiemann, O.; Prisner, T. F. Long-range distance determinations in biomacromolecules by EPR spectroscopy. *Q. Rev. Biophys.* **2007**, *40* (1), 1−53.
(28) Denysenkov, V. P.; Prisner, T. F.; Stubbe, J.; Bennati, M. High-field pulsed electron− electron double resonance spectroscopy to determine the orientation of the tyrosyl radicals in ribonucleotide reductase. *Proc. Natl. Acad. Sci. U. S. A.* **2006**, *103* (36), 13386−13390.
(29) Shelke, S. A.; Sigurdsson, S. T. Site-directed spin labelling of nucleic acids. *Eur. J. Org. Chem.* **2012**, *2012* (12), 2291.
(30) Haugland, M. M.; Lovett, J. E.; Anderson, E. A. Advances in the synthesis of nitroxide radicals for use in biomolecule spin labelling. *Chem. Soc. Rev.* **2018**, *47* (3), 668−680.
(31) Volodarsky, L. B.; Reznikov, V. A.; Ovcharenko, V. I. *Synthetic Chemistry of Stable Nitroxides*; Taylor & Francis, 1993.
(32) Karoui, H.; Moigne, F. L.; Ouari, O.; Tordo, P. Nitroxide radicals: Properties, synthesis and applications. *Stable radicals* **2010**, 173−229.
(33) Bartosik, K.; Debiec, K.; Czarnecka, A.; Sochacka, E.; Leszczynska, G. Synthesis of nucleobase-modified RNA oligonucleotides by post-synthetic approach. *Molecules* **2020**, *25* (15), 3344.
(34) Sowa, G. Z.; Qin, P. Z. Site-directed spin labeling studies on nucleic acid structure and dynamics. *Prog. Nucleic Acid Res. Mol. Biol.* **2008**, *82*, 147−197.
(35) Barhate, N.; Cekan, P.; Massey, A. P.; Sigurdsson, S. T. A nucleoside that contains a rigid nitroxide spin label: A fluorophore in disguise. *Angew. Chem., Int. Ed.* **2007**, *46* (15), 2655−2658.
(36) Jeschke, G.; Chechik, V.; Ionita, P.; Godt, A.; Zimmermann, H.; Banham, J.; Timmel, C. R.; Hilger, D.; Jung, H. DeerAnalysis2006—a comprehensive software package for analyzing pulsed ELDOR data. *Appl. Magn. Reson.* **2006**, *30* (3), 473−498.
(37) Sajid, M.; Jeschke, G.; Wiebcke, M.; Godt, A. Conformationally unambiguous spin labeling for distance measurements. *Chem. - Eur. J.* **2009**, *15* (47), 12960−12962.
(38) Gophane, D. B.; Sigurdsson, S. T. Hydrogen-bonding controlled rigidity of an isoindoline-derived nitroxide spin label for nucleic acids. *Chem. Commun.* **2013**, *49* (10), 999−1001.
(39) Gophane, D. B.; Endeward, B.; Prisner, T. F.; Sigurdsson, S. T. Conformationally restricted isoindoline-derived spin labels in duplex DNA: Distances and rotational flexibility by pulsed electron−electron double resonance spectroscopy. *Chem. - Eur. J.* **2014**, *20* (48), 15913−15919.
(40) Erlenbach, N.; Endeward, B.; Schöps, P.; Gophane, D. B.; Sigurdsson, S. T.; Prisner, T. F. Flexibilities of isoindoline-derived spin labels for nucleic acids by orientation selective PELDOR. *Phys. Chem. Chem. Phys.* **2016**, *18* (24), 16196−16201.
(41) Collauto, A.; von Bülow, S.; Gophane, D. B.; Saha, S.; Stelzl, L. S.; Hummer, G.; Sigurdsson, S. T.; Prisner, T. F. Compaction of RNA duplexes in the cell. *Angew. Chem., Int. Ed.* **2020**, *59* (51), 23025−23029.
(42) Schiemann, O.; Cekan, P.; Margraf, D.; Prisner, T. F.; Sigurdsson, S. T. Relative orientation of rigid nitroxides by PELDOR: Beyond distance measurements in nucleic acids. *Angew. Chem., Int. Ed.* **2009**, *48* (18), 3292−3295.
(43) Gränz, M.; Erlenbach, N.; Spindler, P.; Gophane, D. B.; Stelzl, L. S.; Sigurdsson, S. T.; Prisner, T. F. Dynamics of nucleic acids at room temperature revealed by pulsed EPR spectroscopy. *Angew. Chem., Int. Ed.* **2018**, *57* (33), 10540−10543.
(44) Prisner, T. F.; Marko, A.; Sigurdsson, S. T. Conformational dynamics of nucleic acid molecules studied by PELDOR spectroscopy with rigid spin labels. *J. Magn. Reson.* **2015**, *252*, 187−198.
(45) Höbartner, C.; Sicoli, G.; Wachowius, F.; Gophane, D. B.; Sigurdsson, S. T. Synthesis and characterization of RNA containing a rigid and nonperturbing cytidine-derived spin label. *J. Org. Chem.* **2012**, *77* (17), 7749−7754.
(46) Marko, A.; Denysenkov, V.; Margraf, D.; Cekan, P.; Schiemann, O.; Sigurdsson, S. T.; Prisner, T. F. Conformational flexibility of DNA. *J. Am. Chem. Soc.* **2011**, *133* (34), 13375−13379.
(47) Grytz, C. M.; Marko, A.; Cekan, P.; Sigurdsson, S. T.; Prisner, T. F. Flexibility and conformation of the cocaine aptamer studied by PELDOR. *Phys. Chem. Chem. Phys.* **2016**, *18* (4), 2993−3002.
(48) Grytz, C. M.; Kazemi, S.; Marko, A.; Cekan, P.; Guntert, P.; Sigurdsson, S. T.; Prisner, T. F. Determination of helix orientations in a flexible DNA by multi-frequency EPR spectroscopy. *Phys. Chem. Chem. Phys.* **2017**, *19* (44), 29801−29811.
(49) Hetzke, T.; Vogel, M.; Gophane, D. B.; Weigand, J. E.; Suess, B.; Sigurdsson, S. T.; Prisner, T. F. Influence of Mg2+ on the conformational flexibility of a tetracycline aptamer. *RNA* **2019**, *25* (1), 158−167.

https://doi.org/10.1021/acs.joc.1c01176
J. Org. Chem. XXXX, XXX, XXX−XXX

(50) Edwards, T. E.; Cekan, P.; Reginsson, G. W.; Shelke, S. A.; Ferré-D'Amaré, A. R.; Schiemann, O.; Sigurdsson, S. T. Crystal structure of a DNA containing the planar, phenoxazine-derived bifunctional spectroscopic probe Ç. *Nucleic Acids Res.* **2011**, *39* (10), 4419−4426.
(51) Miller, T. R.; Hopkins, P. B. Toward the synthesis of a second-generation nitroxide spin probe for DNA dynamics studies. *Bioorg. Med. Chem. Lett.* **1994**, *4* (8), 981−986.
(52) Albers, P.; Pietsch, J.; Parker, S. F. Poisoning and deactivation of palladium catalysts. *J. Mol. Catal. A: Chem.* **2001**, *173* (1), 275−286.
(53) Keddie, D. J.; Johnson, T. E.; Arnold, D. P.; Bottle, S. E. Synthesis of profluorescent isoindoline nitroxides via palladium-catalysed Heck alkenylation. *Org. Biomol. Chem.* **2005**, *3* (14), 2593−2598.
(54) Bogányi, B.; Kámán, J. A concise synthesis of indoloquinoline skeletons applying two consecutive Pd-catalyzed reactions. *Tetrahedron* **2013**, *69* (45), 9512−9519.
(55) Beyer, M.; Fritscher, J.; Feresin, E.; Schiemann, O. Synthesis of novel aromatic nitroxides as potential DNA intercalators. An EPR spectroscopical and DFT computational study. *J. Org. Chem.* **2003**, *68* (6), 2209−2215.
(56) Marczyk, J.; Waluk, J.; Fetzer, J. C. Determination of structure of nonplanar polycyclic aromatic hydrocarbons by polarized spectroscopy. *Polycyclic Aromat. Compd.* **1996**, *9* (1−4), 283−290.
(57) Pascal, R. A. Twisted acenes. *Chem. Rev.* **2006**, *106* (12), 4809−4819.
(58) Cekan, P.; Smith, A. L.; Barhate, N.; Robinson, B. H.; Sigurdsson, S. T. Rigid spin-labeled nucleoside Ç: a nonperturbing EPR probe of nucleic acid conformation. *Nucleic Acids Res.* **2008**, *36* (18), 5946−5954.
(59) Piton, N.; Mu, Y.; Stock, G.; Prisner, T. F.; Schiemann, O.; Engels, J. W. Base-specific spin-labeling of RNA for structure determination. *Nucleic Acids Res.* **2007**, *35* (9), 3128−3143.
(60) Juliusson, H. Y.; Segler, A.-L. J.; Sigurdsson, S. T. Benzoyl-protected hydroxylamines for improved chemical synthesis of oligonucleotides containing nitroxide spin labels. *Eur. J. Org. Chem.* **2019**, *2019* (23), 3799−3805.
(61) Wypijewska del Nogal, A.; Füchtbauer, A. F.; Bood, M.; Nilsson, J. R.; Wranne, M. S.; Sarangamath, S.; Pfeiffer, P.; Rajan, V. S.; El-Sagheer, A. H.; Dahlén, A.; Brown, T.; Grøtli, M.; Wilhelmsson, L. M. Getting DNA and RNA out of the dark with 2CNqA: a bright adenine analogue and interbase FRET donor. *Nucleic Acids Res.* **2020**, *48* (14), 7640−7652.
(62) Foller Larsen, A.; Dumat, B.; Wranne, M. S.; Lawson, C. P.; Preus, S.; Bood, M.; Gradén, H.; Marcus Wilhelmsson, L.; Grøtli, M. Development of bright fluorescent quadracyclic adenine analogues: TDDFT-calculation supported rational design. *Sci. Rep.* **2015**, *5* (1), 12653.
(63) Sheldrick, G. Crystal structure refinement with SHELXL. *Acta Crystallogr., Sect. C: Struct. Chem.* **2015**, *71* (1), 3−8.
(64) Dolomanov, O. V.; Bourhis, L. J.; Gildea, R. J.; Howard, J. A. K.; Puschmann, H. OLEX2: a complete structure solution, refinement and analysis program. *J. Appl. Crystallogr.* **2009**, *42* (2), 339−341.

https://doi.org/10.1021/acs.joc.1c01176
J. Org. Chem. XXXX, XXX, XXX−XXX

A carbazole-derived nitroxide that is an analogue of cytidine – a rigid spin label for DNA and RNA

Anna-Lena Johanna Segler[1] and Snorri Th. Sigurdsson[1*]

[1]*University of Iceland, Department of Chemistry, Science Institute, Dunhaga 3, 107 Reykjavik, Iceland.*

*Email: snorrisi@hi.is

Table of Contents

Analysis of spin-labeled oligonucleotides by MS and EPR spectroscopy. The incorporation of **Ċ** and **Ċm** into oligonucleotides (**Table S1**) was confirmed by MALDI-TOF analysis; their calculated and observed monoisotopic masses are listed in **Table S1**. The amount of radical in each oligonucleotide was determined by spin counting using EPR spectroscopy[1] (**Table S1**).

Table S1. Monoisotopic masses of modified oligonucleotides and spin-labeling efficiency of spin-labeled oligonucleotides. Y stands for nucleoside **25**.

	Sequence	(calcd.)	(found)	Radical (%)
I	5'-d(GACCTCG**Ċ**ATCGTG)-3'	4424.83	4425.84	100
II	5'-d(GA**Ċ**CTCGCATCGTG)-3'	4424.83	4426.63	97
III	5'-d(**Ċ**ACGATGCGAGGTC)-3'	4473.85	4474.58	95
IV	5'-d(GACCTCG**Ċ**ATCGTG(GACCTCGCATCGTG)$_2$)-3'	13024.22	13024.10	96
V	5'-d(GT**Ċ**AGTGCGCGCGCGATC)-3'	6319.14	6321.08	100
VI	5'-d(GATCGCGCG**Ċ**GCGCACTGAC)-3'	6288.14	6292.53	96
VII	5'-GACCUCG**Ċm**AUCGUG-3'	4620.73	4622.90	99
VIII	5'-UGU**Ċm**AGUCGCGCGCGCAUC-3'	6877.02	6881.32	95
IX	5'-UGAUGCG**Ċm**GCGCGCGACUGAC-3'	6940.06	6944.60	90
X	5'-d(GACCTCG**Y**ATCGTG)-3'	4311.75	4314.30	

Crystallographic data

Table S2. Crystal data.

Crystal data	**Ċm**	**Ċ**
Empirical formula	$C_{23}H_{31}N_4O_7$	$C_{21}H_{25}N_4O_5$
Color	Yellow	Yellow
Formula weight	475.52	413.45
Crystal size (mm)	0.38 x 0.21 x 0.18	0.50 x 0.23 x 0.12
Crystal system	Orthorhombic	Triclinic
Space group	$P2_12_12_1$	P1
a (Å)	5.6483(4)	8.0192(5)
b (Å)	15.7903(12)	11.0816(7)
c (Å)	26.219(2)	12.3628(8)
α (°)	90	98.313(2)
β (°)	90	97.337(2)
γ (°)	90	106.490(2)
Volume (Å^3)	2338.4(3)	1025.75(11)
Z	2	2
$D_{calc.}$ (g/cm^3)	1.351	1.339
F(000)	1012	438
μMoK$_\alpha$ (mm^{-1})	0.101	0.097
Temperature (K)	150(2)	150(2)
Reflections collected/ unique/observed [I>2σ(I)]	80870/ 9770/8495	40344/12515/11879
Data/restraints/parameters	9770/0/329	12515/3/557
Goodness of fit on F^2	1.056	1.031
Final R indices [I>2σ(I)]	R_1 = 0.0466 wR_2 = 0.1199	R_1 = 0.0329 wR_2 = 0.0904
R indices (all data)	R_1 = 0.0570 wR_2 = 0.1259	R_1 = 0.0356 wR_2 = 0.0924

UV-vis analysis of Ċ and Ċm and their extinction coefficients. The extinction coefficients (ε) of **Ċ** and **Ċm** (**Table S3**) were determined in H_2O at three wavelengths (λ), 325 nm, 279 nm and 260 nm, using Beer's law. A series of solutions of **Ċ/Ċm** was made with specific concentration (5 μM – 100 μM) and the UV-vis spectra (**Figure S2**) of each sample were recorded. The absorption at a given λ was plotted against the concentration of the samples resulting in a linear curve and the ε was obtained from the slope of the line.

Table S3. The molar extinction coefficients (ε) of nitroxides **Ċ** and **Ċm** at various wavelengths in H_2O.

	$\varepsilon_{260\ nm}$ (L/mol·cm)	$\varepsilon_{279\ nm}$ (L/mol·cm)	$\varepsilon_{325\ nm}$ (L/mol·cm)
Ċ	18400 ± 700	42800 ± 1200	8400 ± 300
Ċm	18900 ± 500	40400 ± 1000	8600 ± 200

UV-vis absorption spectrum of Ċ

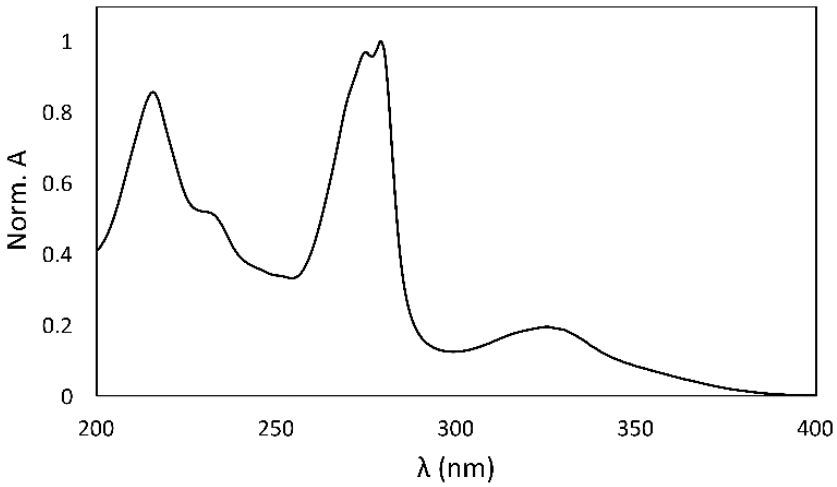

Figure S1. UV-vis absorption spectrum of **Ċ**. **Ċ** and **Ċm** have identical spectra and therefore, only one of their spectra is shown.

^{1}H-, ^{13}C- and ^{31}P-NMR spectra

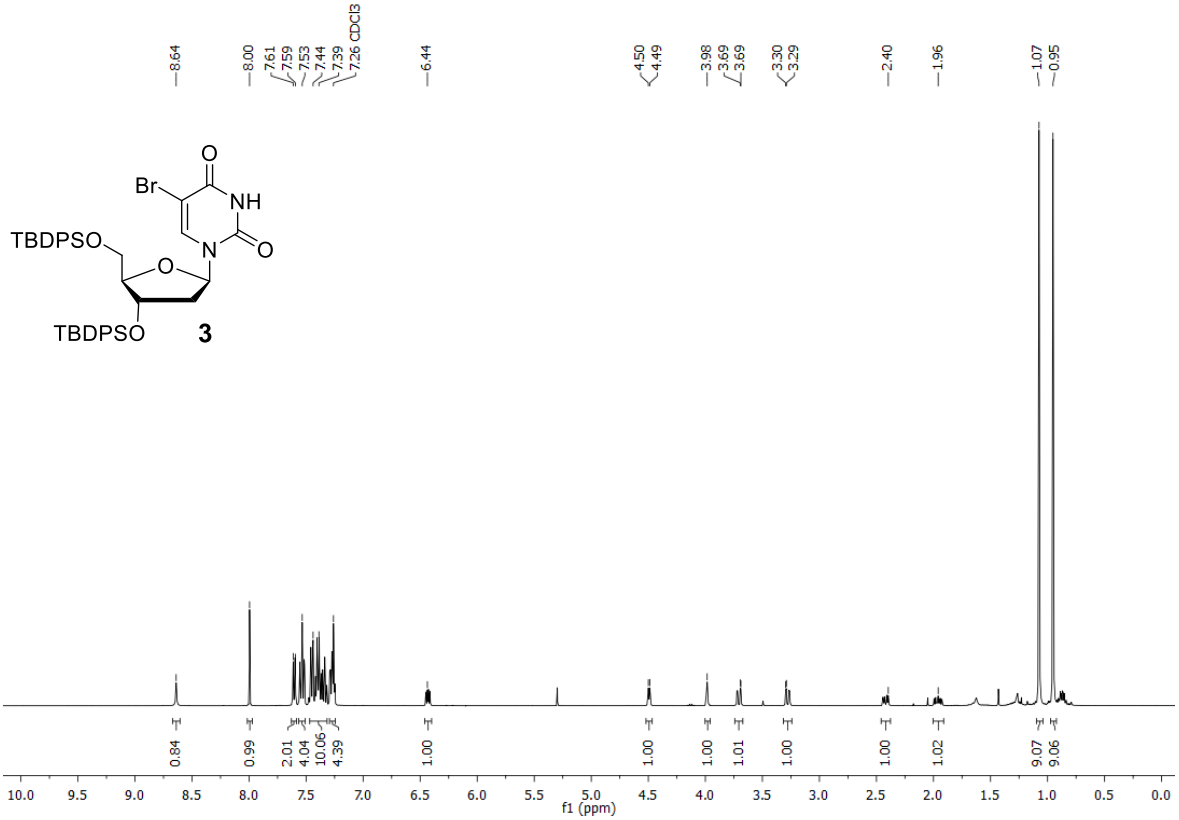

Figure S2. ^{1}H-NMR spectrum of **3** in $CDCl_3$ at 400 MHz.

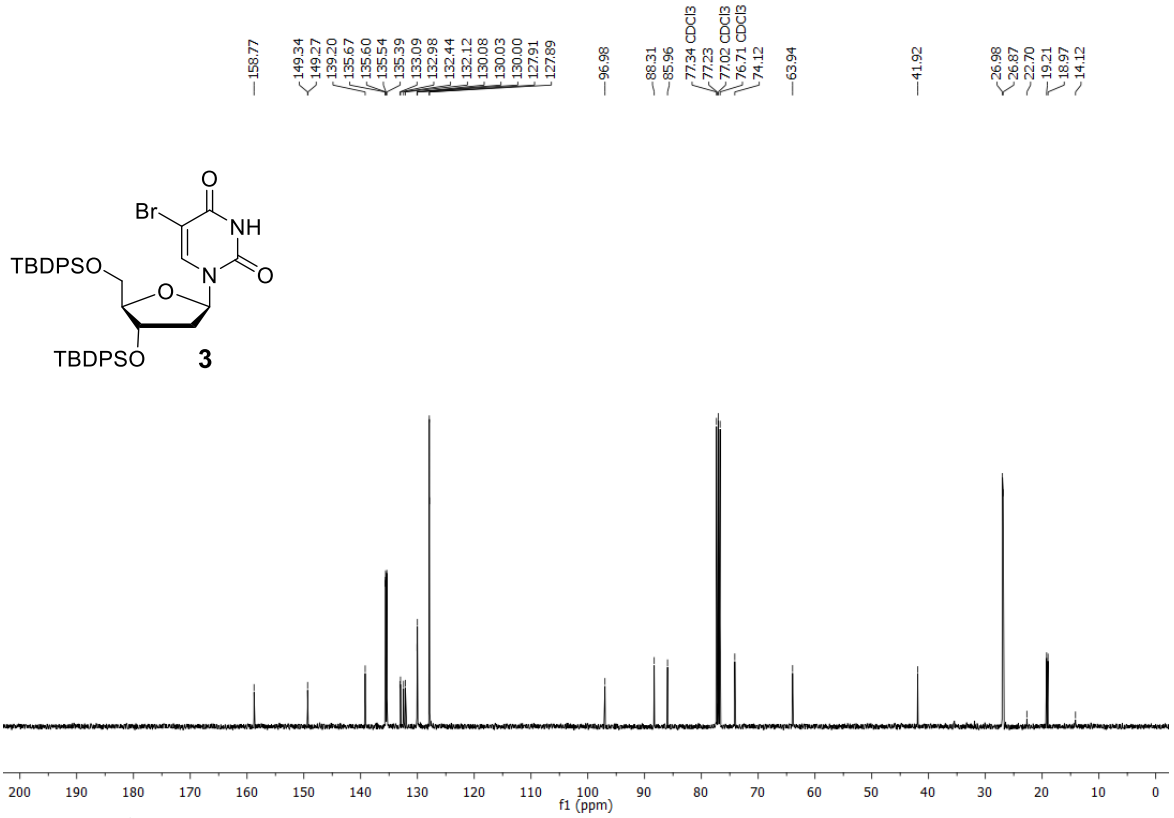

Figure S3. ^{13}C{^{1}H}-NMR spectrum of **3** in $CDCl_3$ at 101 MHz.

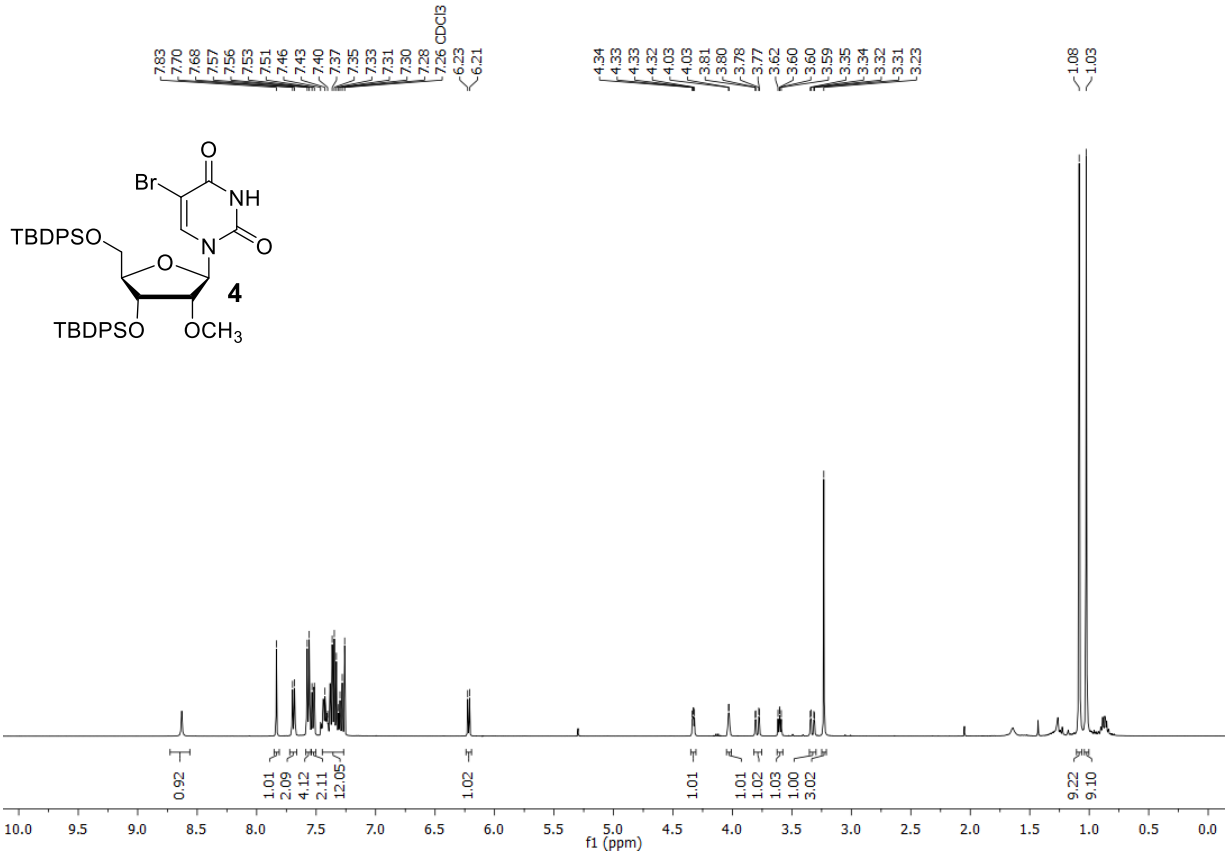

Figure S4. ^{1}H-NMR spectrum of **4** in $CDCl_3$ at 400 MHz.

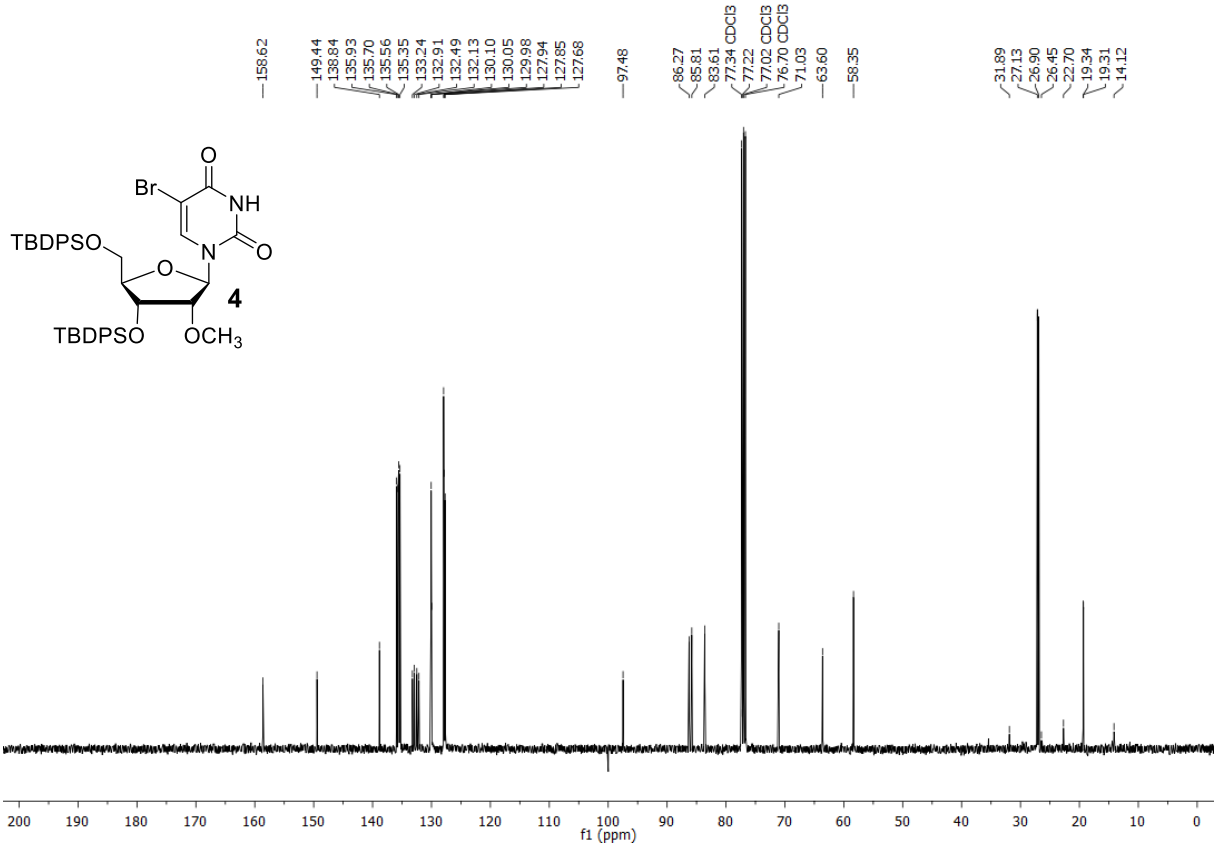

Figure S5. ^{13}C{^{1}H}-NMR spectrum of **4** in $CDCl_3$ at 101 MHz.

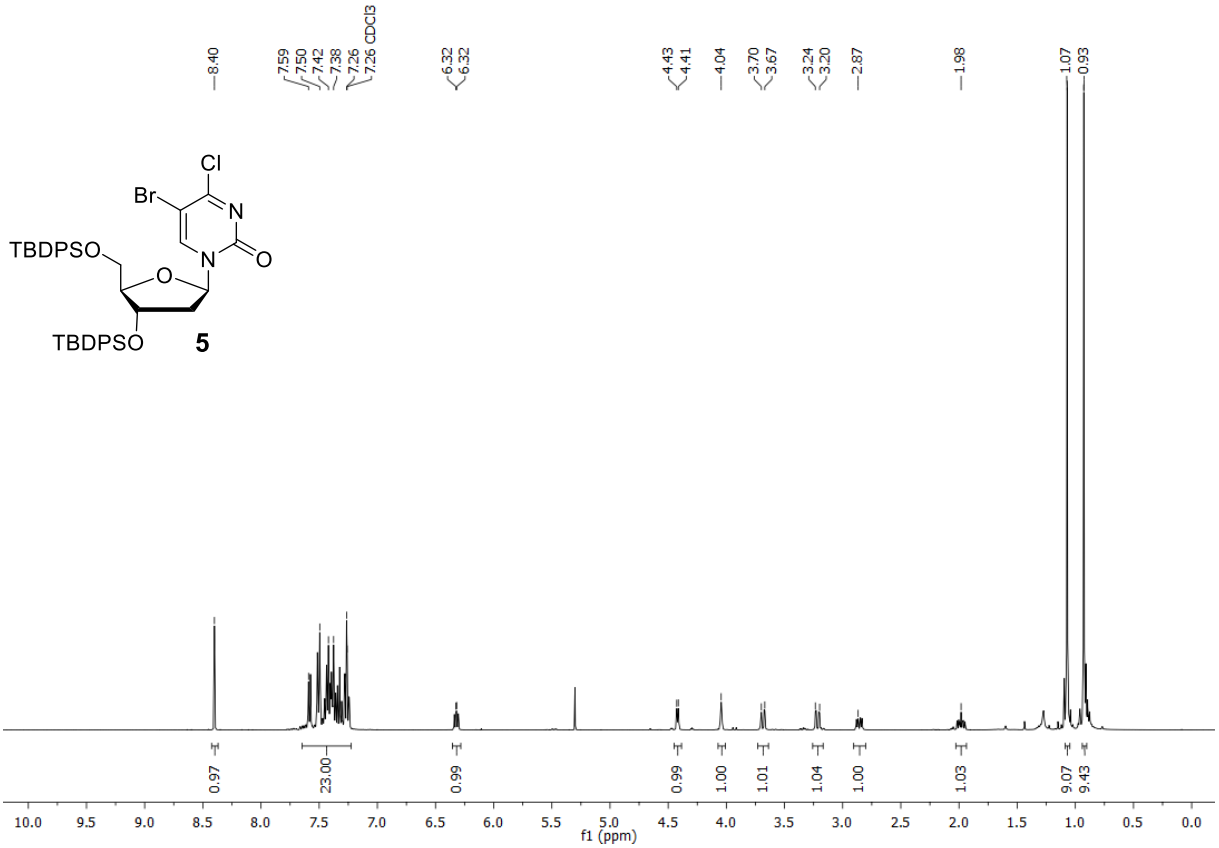

Figure S6. ^{1}H-NMR spectrum of **5** in $CDCl_3$ at 400 MHz.

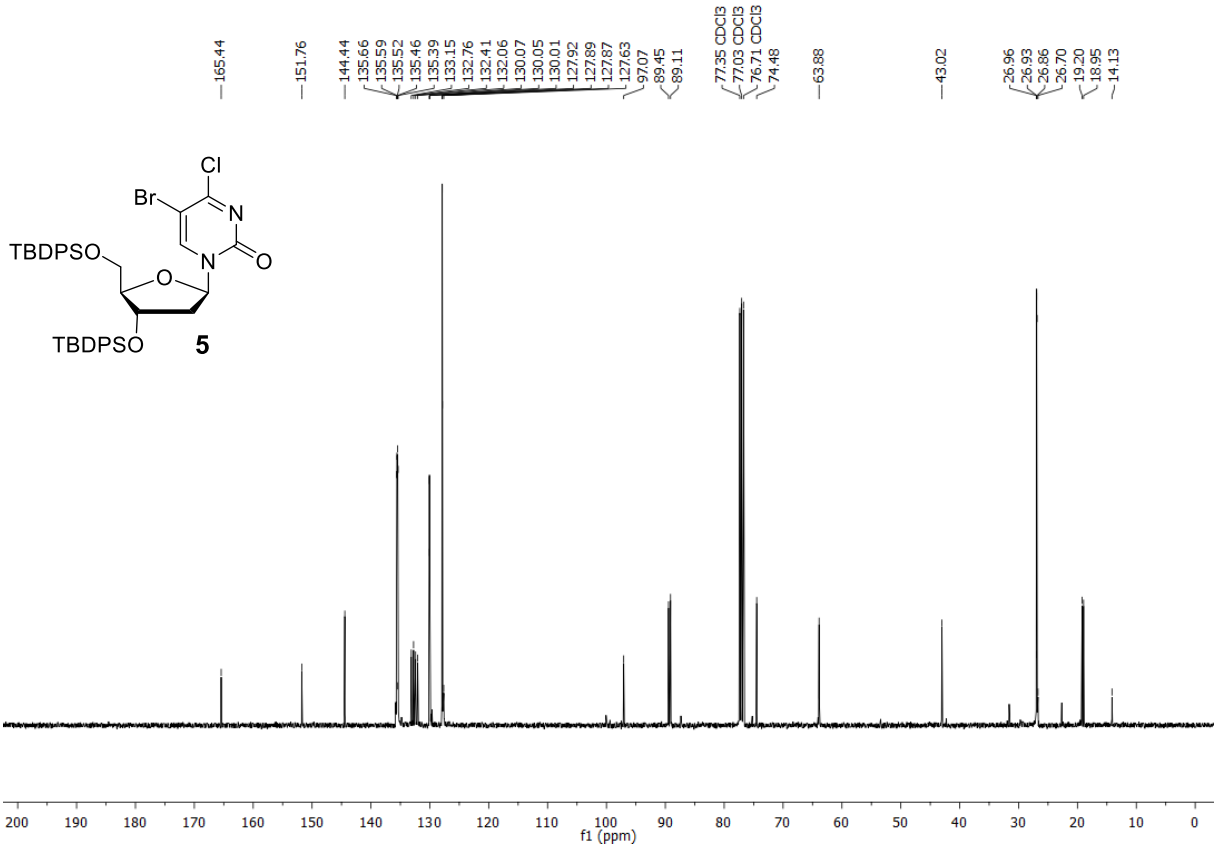

Figure S7. $^{13}C\{^{1}H\}$-NMR spectrum of **5** in $CDCl_3$ at 101 MHz.

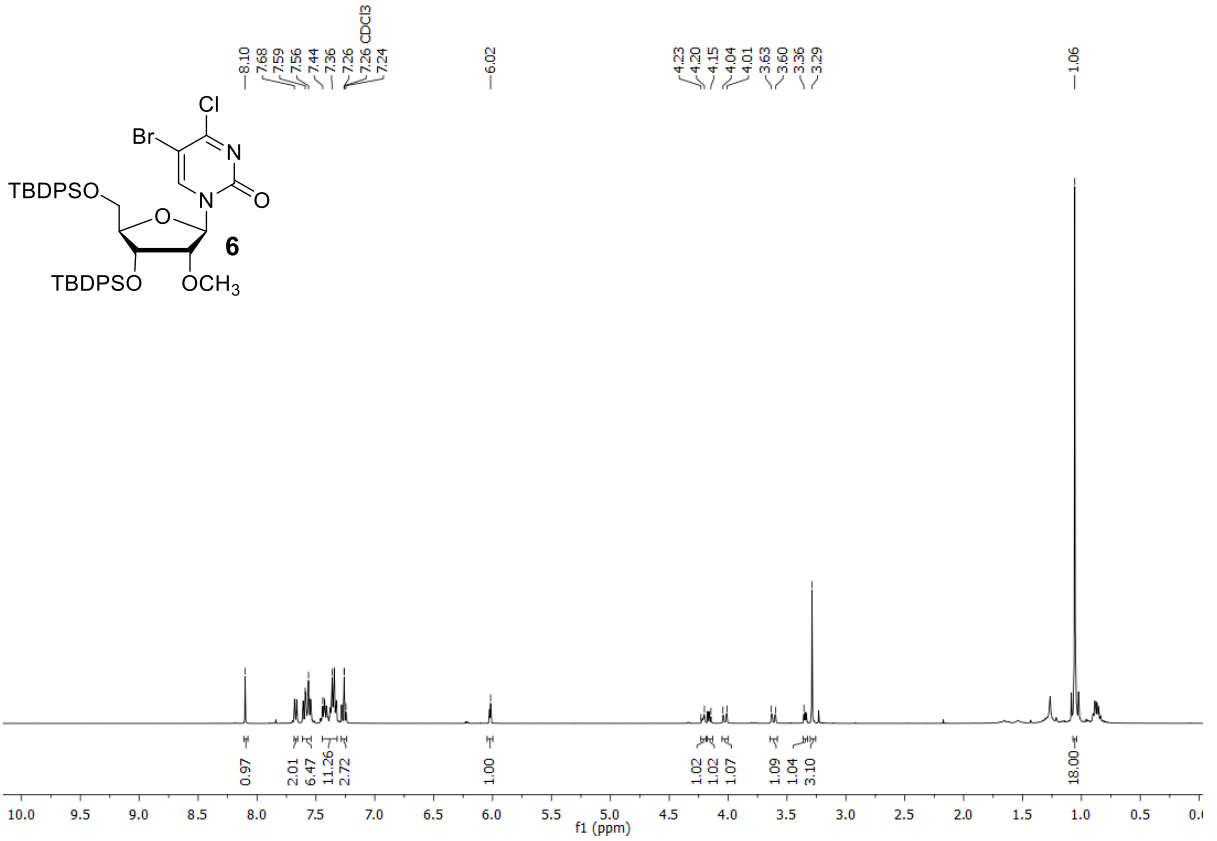

Figure S8. ^{1}H-NMR spectrum of **6** in $CDCl_3$ at 400 MHz.

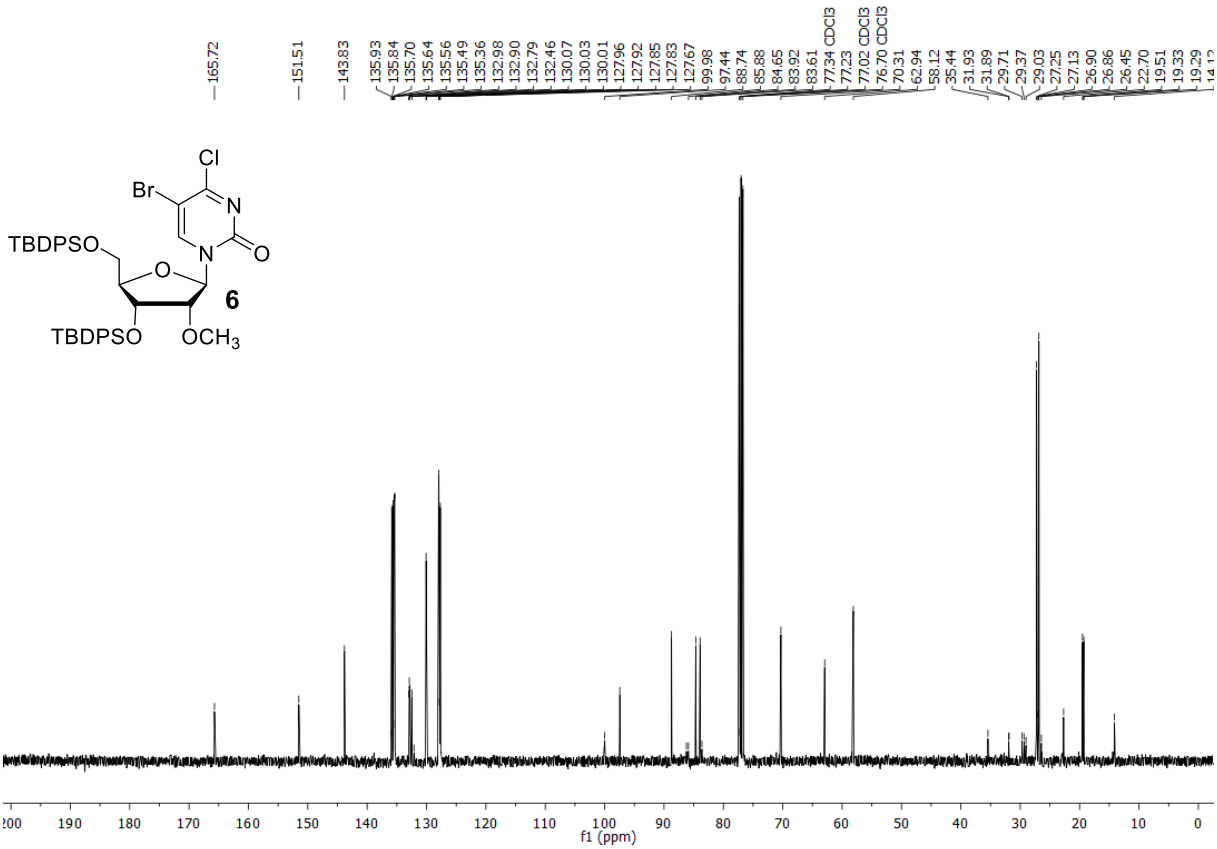

Figure S9. $^{13}C\{^{1}H\}$-NMR spectrum of **6** in $CDCl_3$ at 101 MHz.

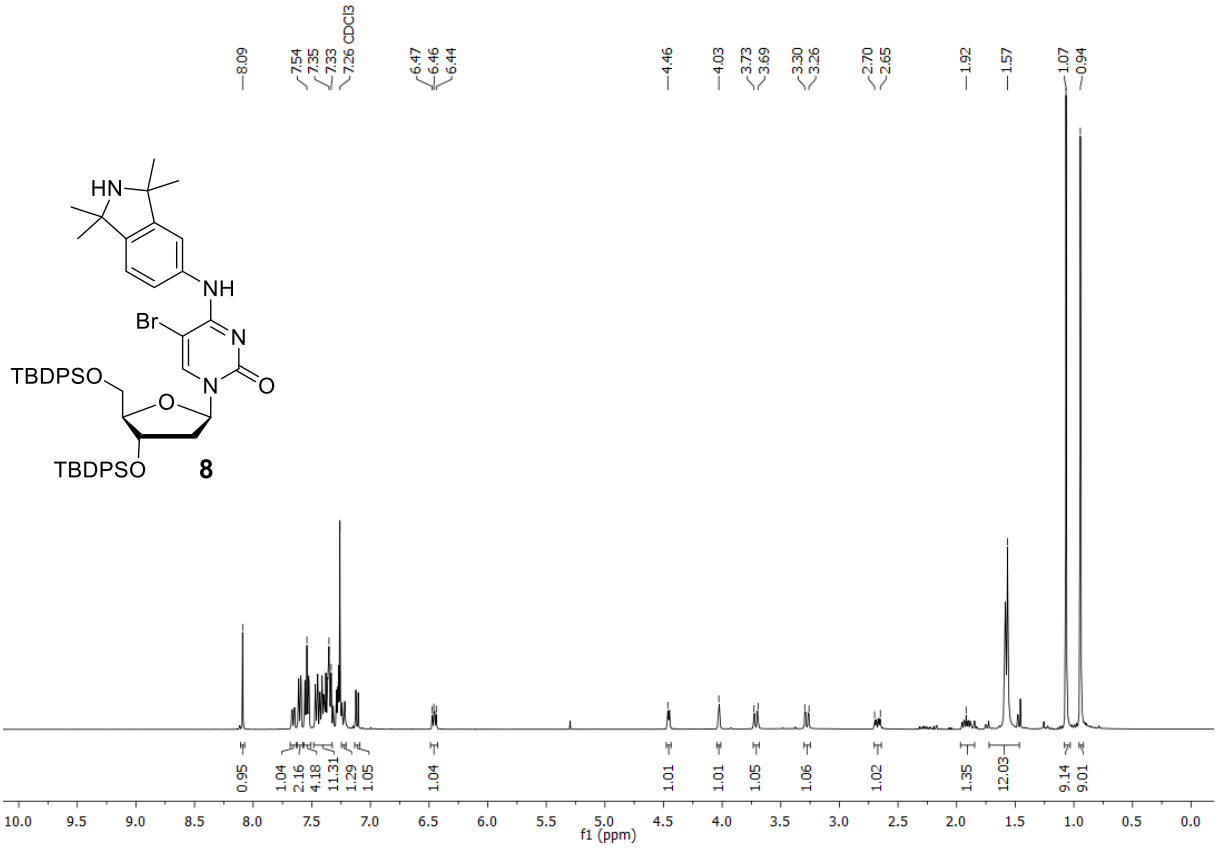

Figure S10. ^{1}H-NMR spectrum of **8** in $CDCl_3$ at 400 MHz.

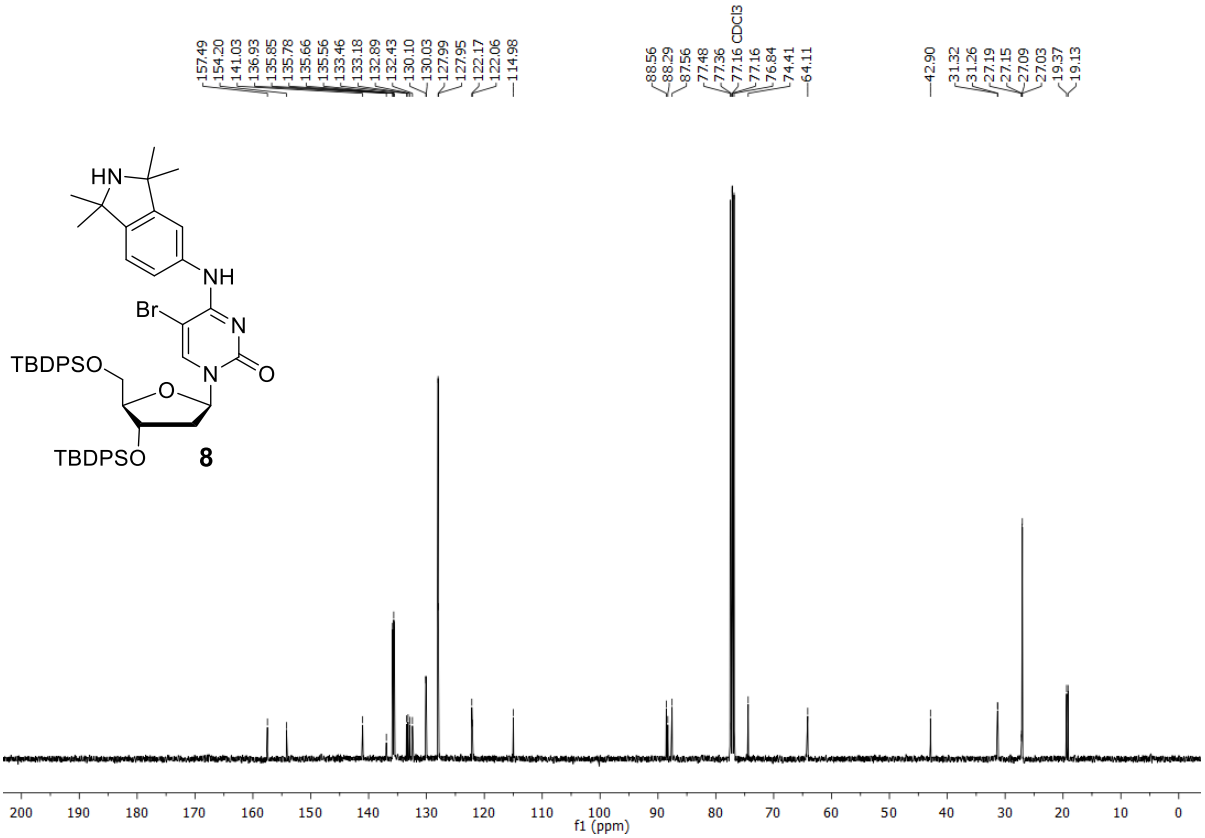

Figure S11. ^{13}C{^{1}H}-NMR spectrum of **8** in $CDCl_3$ at 101 MHz.

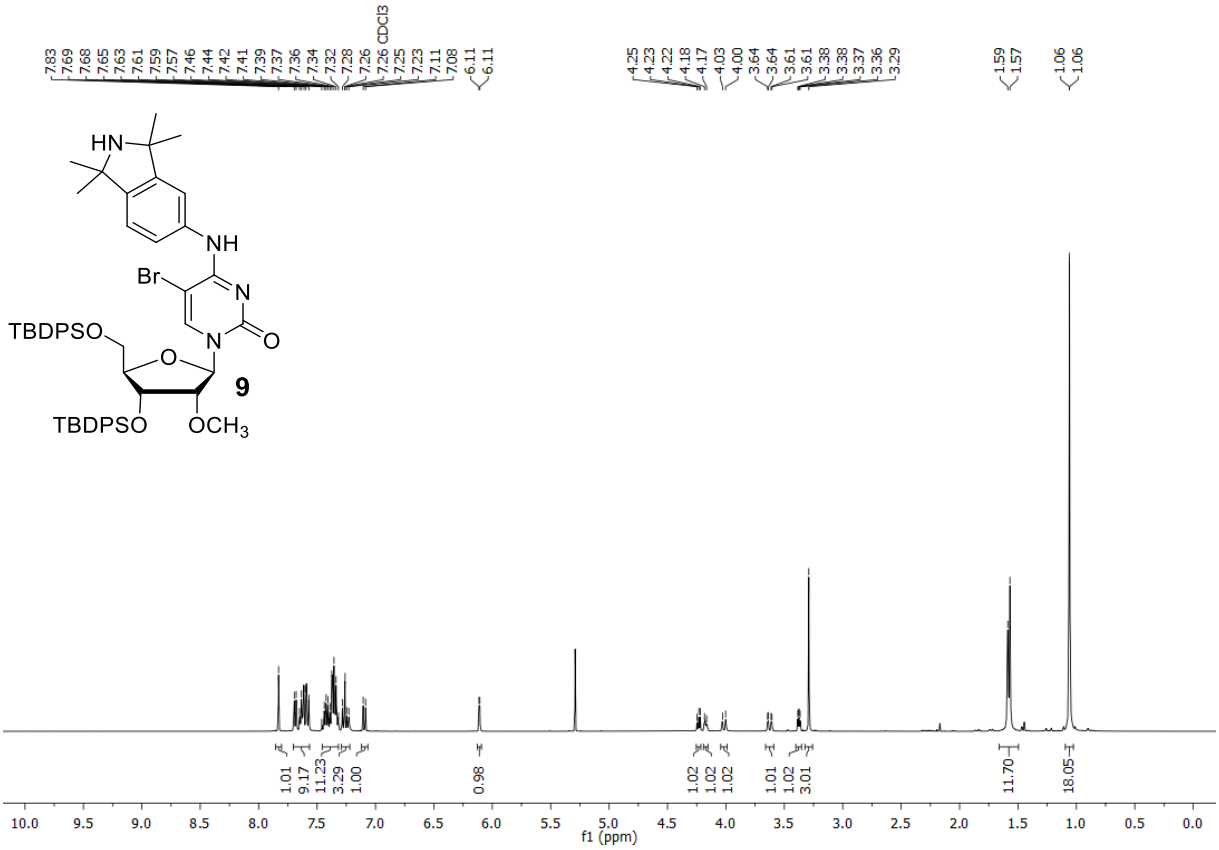

Figure S12. ^{1}H-NMR spectrum of **9** in $CDCl_3$ at 400 MHz.

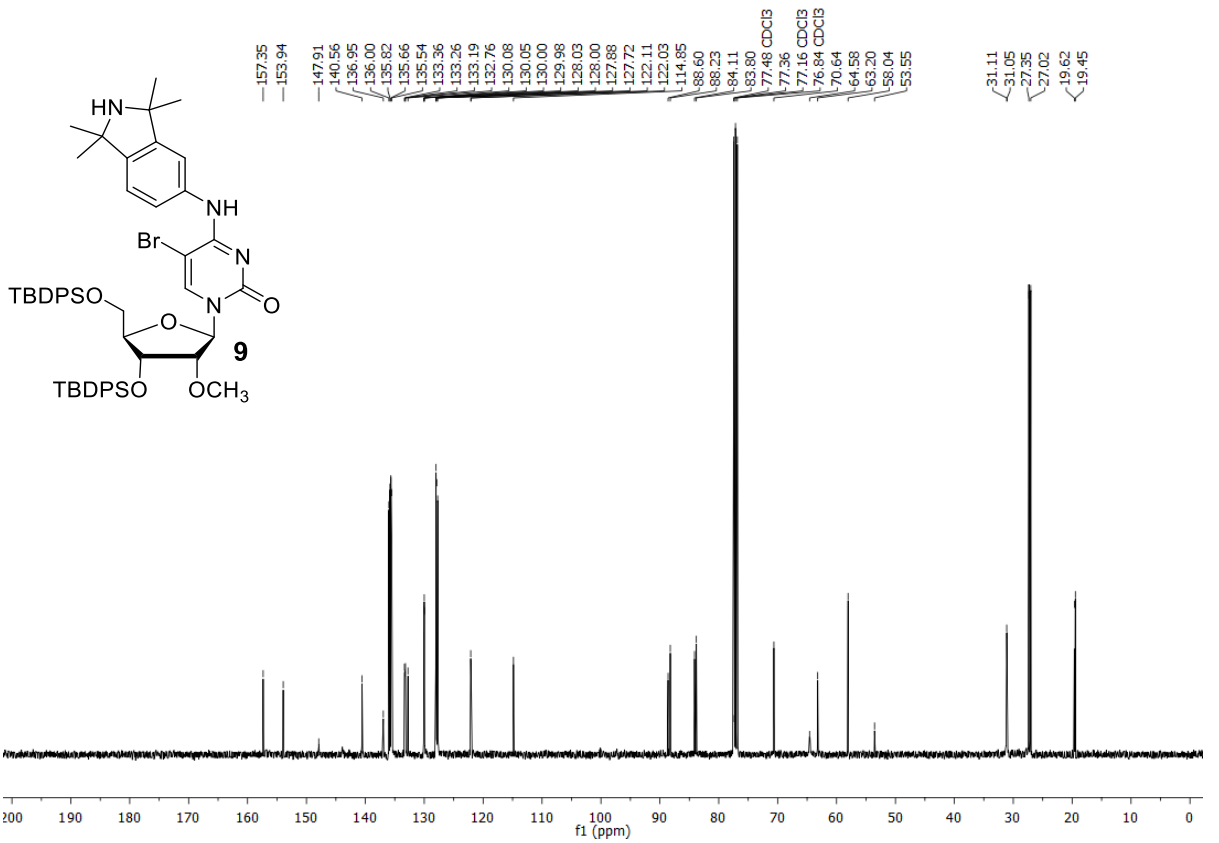

Figure S13. ^{13}C{^{1}H}-NMR spectrum of **9** in $CDCl_3$ at 101 MHz.

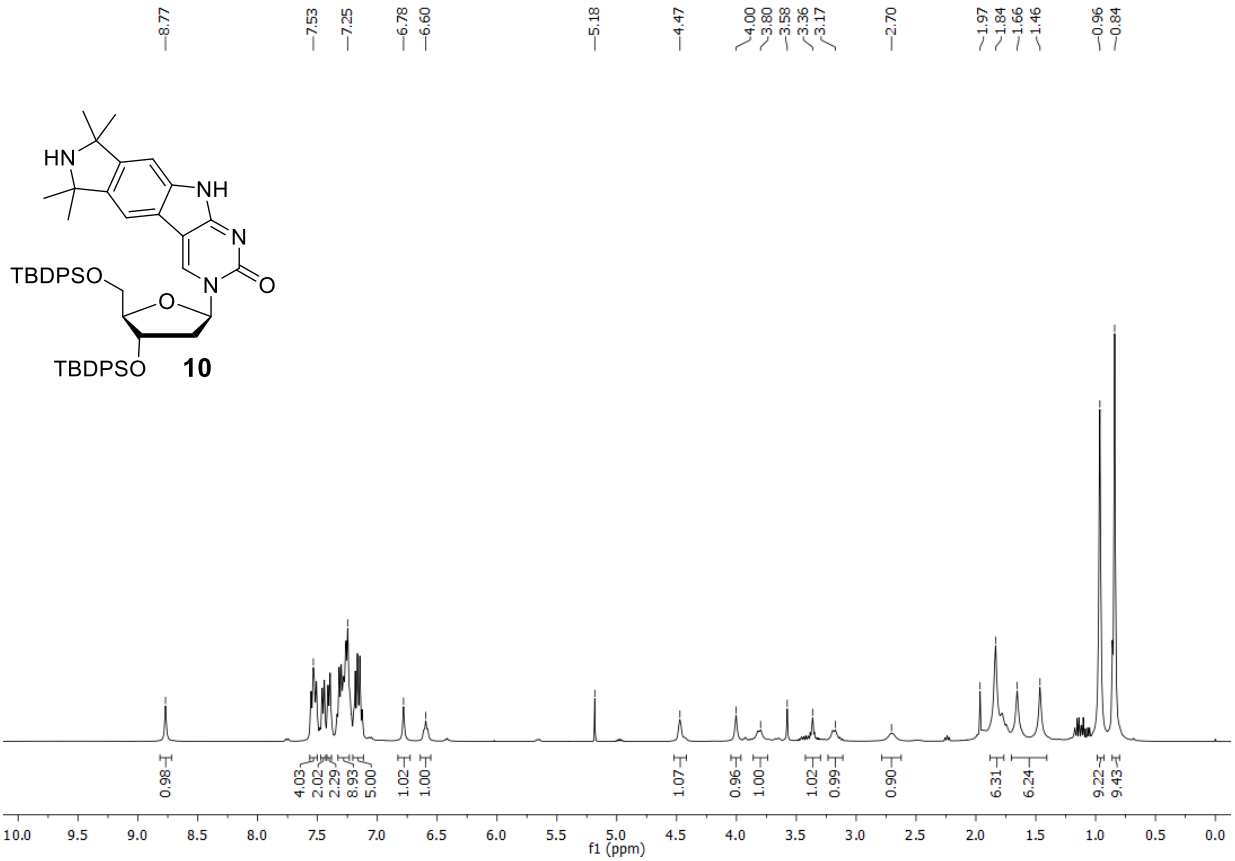

Figure S14. ^{1}H-NMR spectrum of **10** in $CDCl_3$ at 400 MHz.

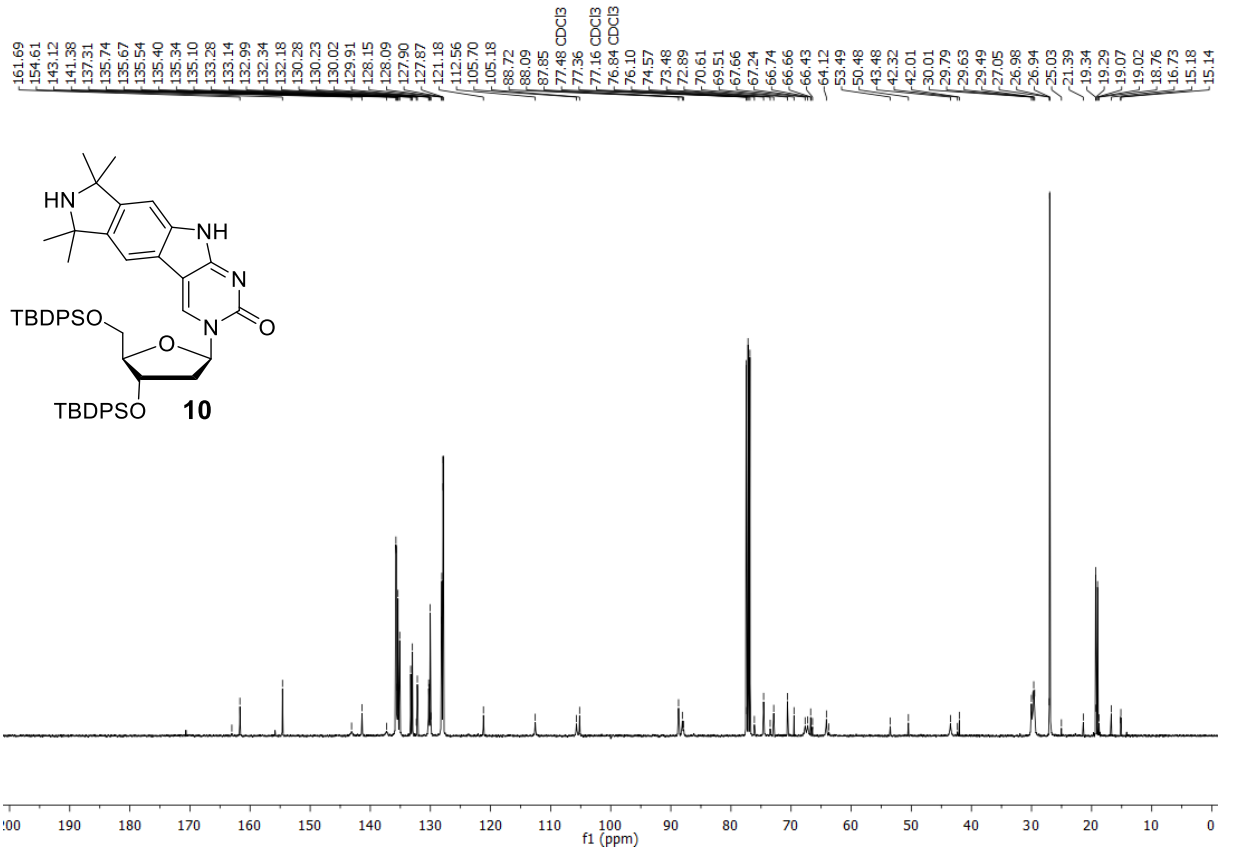

Figure S15. ^{13}C{^{1}H}-NMR spectrum of **10** in $CDCl_3$ at 101 MHz.

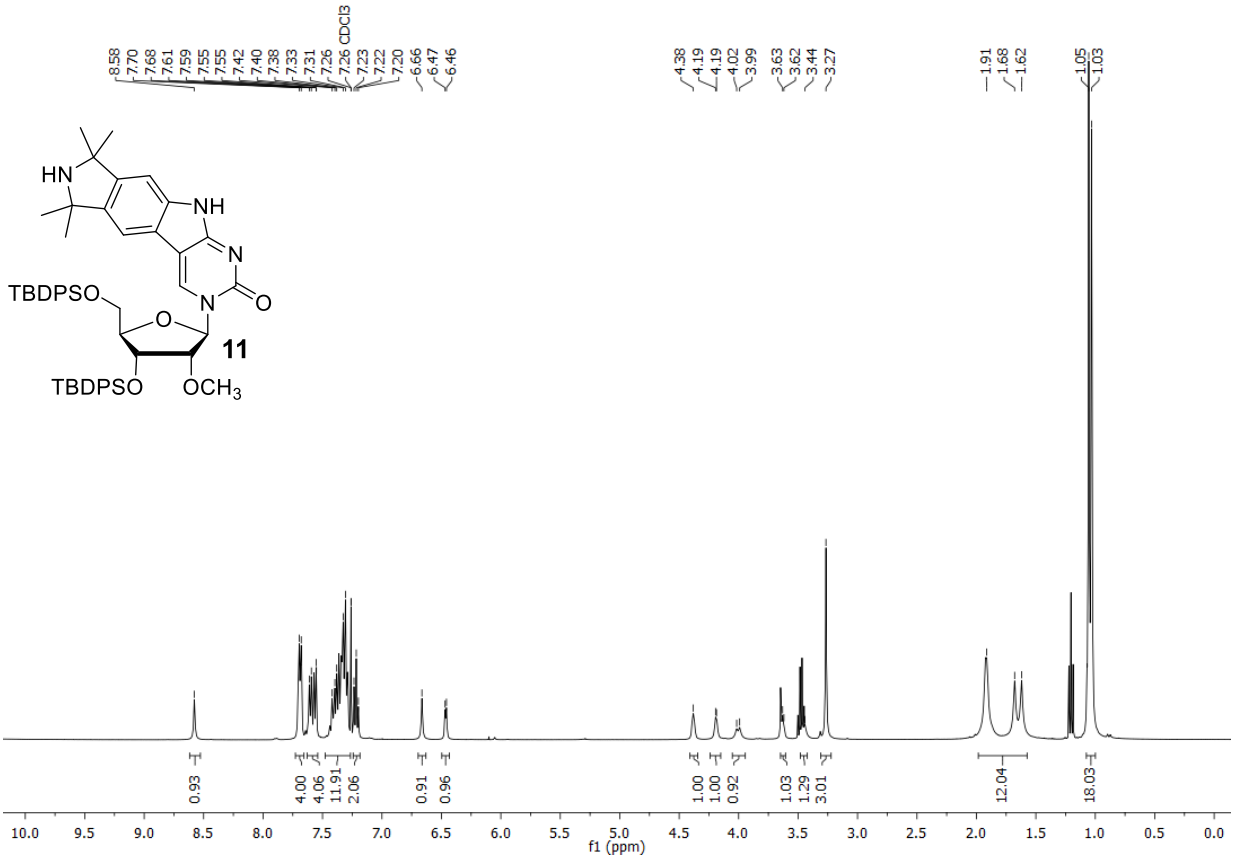

Figure S16. ^{1}H-NMR spectrum of **11** in $CDCl_3$ at 400 MHz.

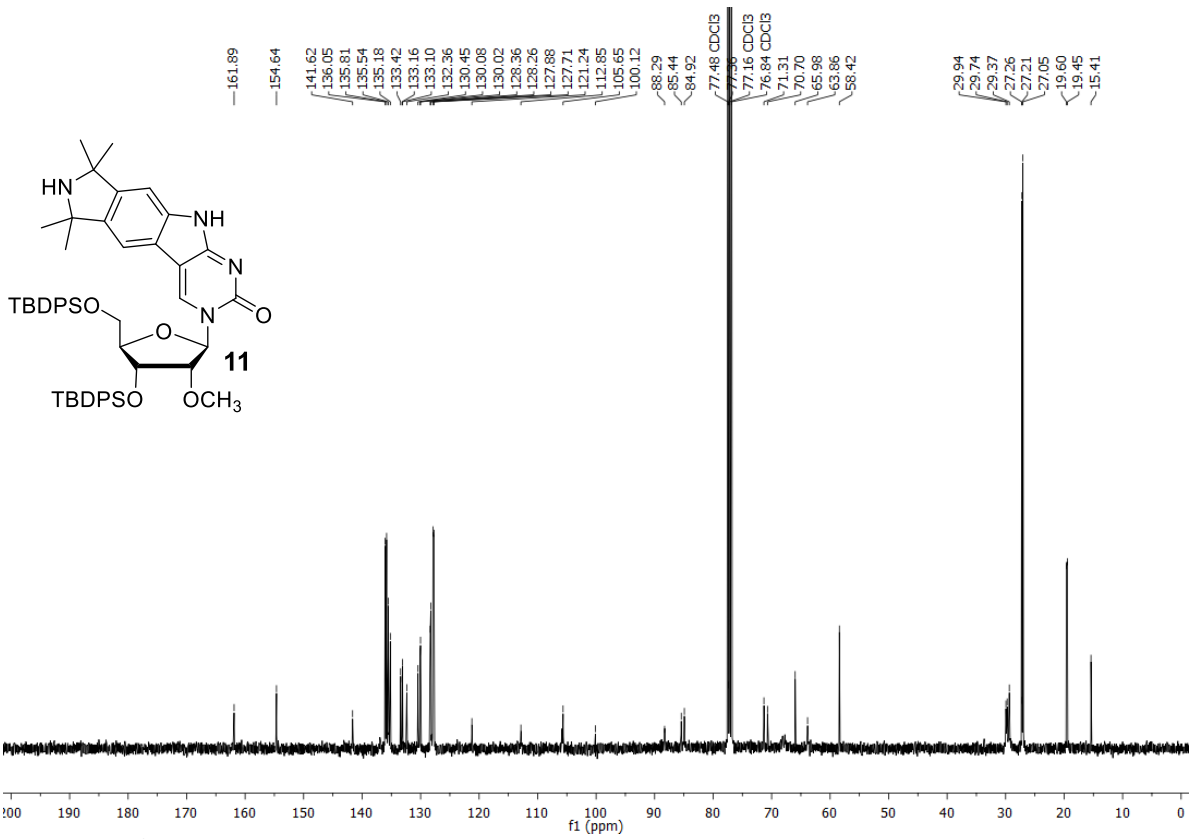

Figure S17. $^{13}C\{^{1}H\}$-NMR spectrum of **11** in $CDCl_3$ at 101 MHz.

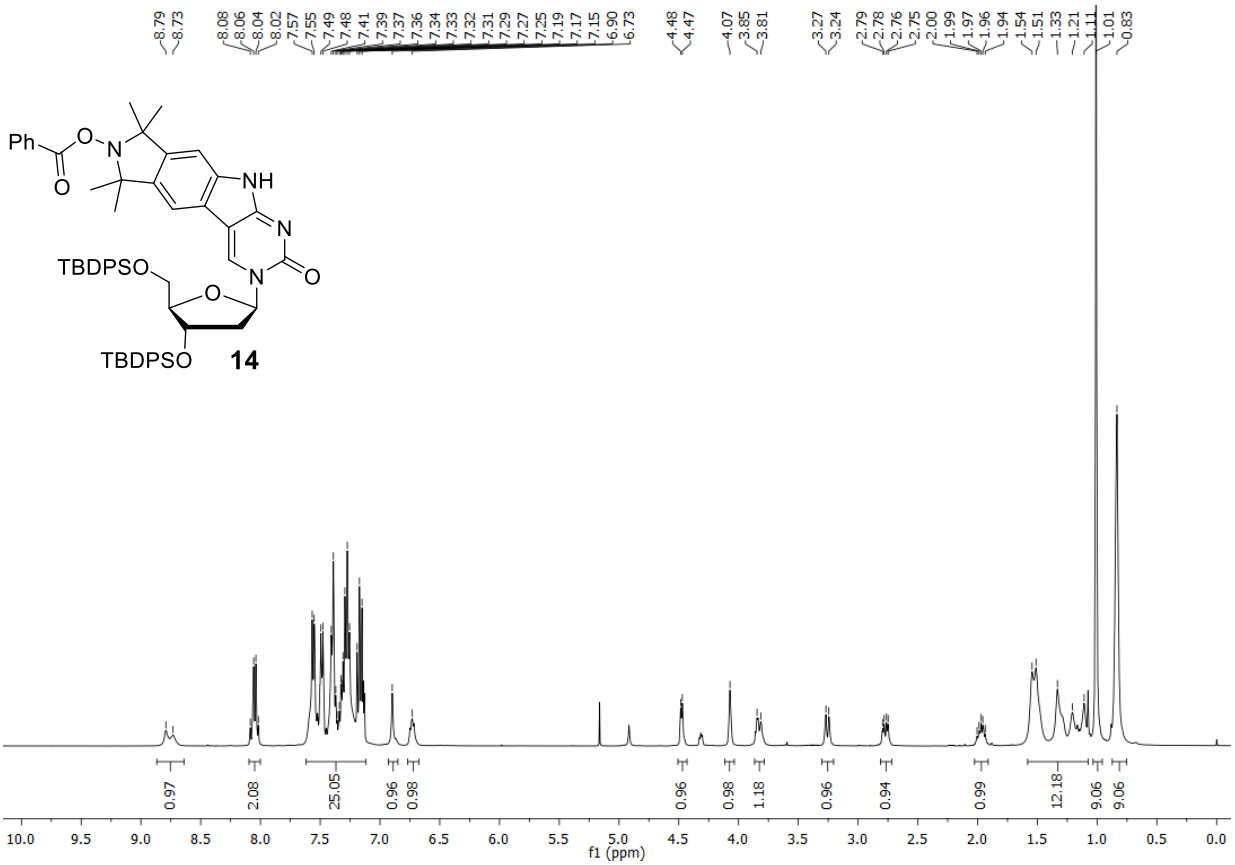

Figure S18. ^{1}H-NMR spectrum of **14** in $CDCl_3$ at 400 MHz.

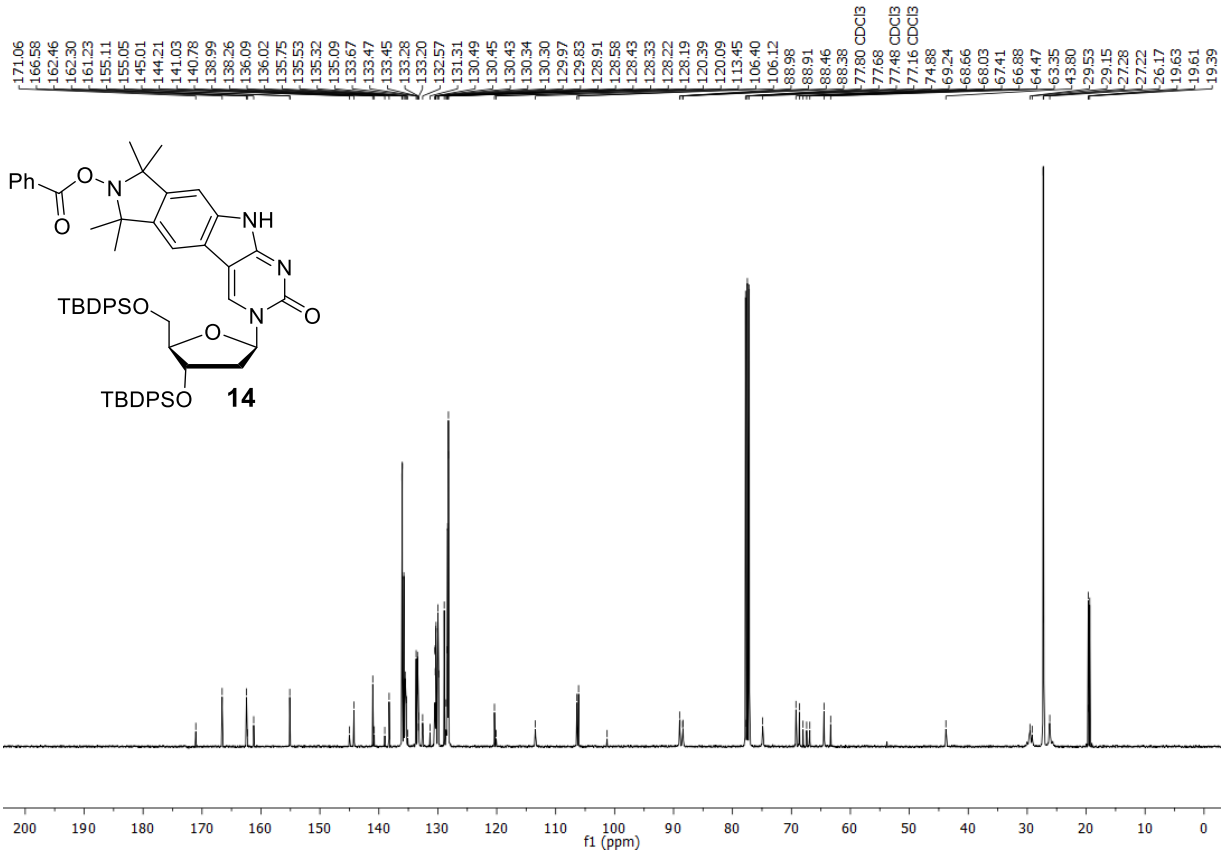

Figure S19. $^{13}C\{^{1}H\}$-NMR spectrum of **14** in $CDCl_3$ at 101 MHz.

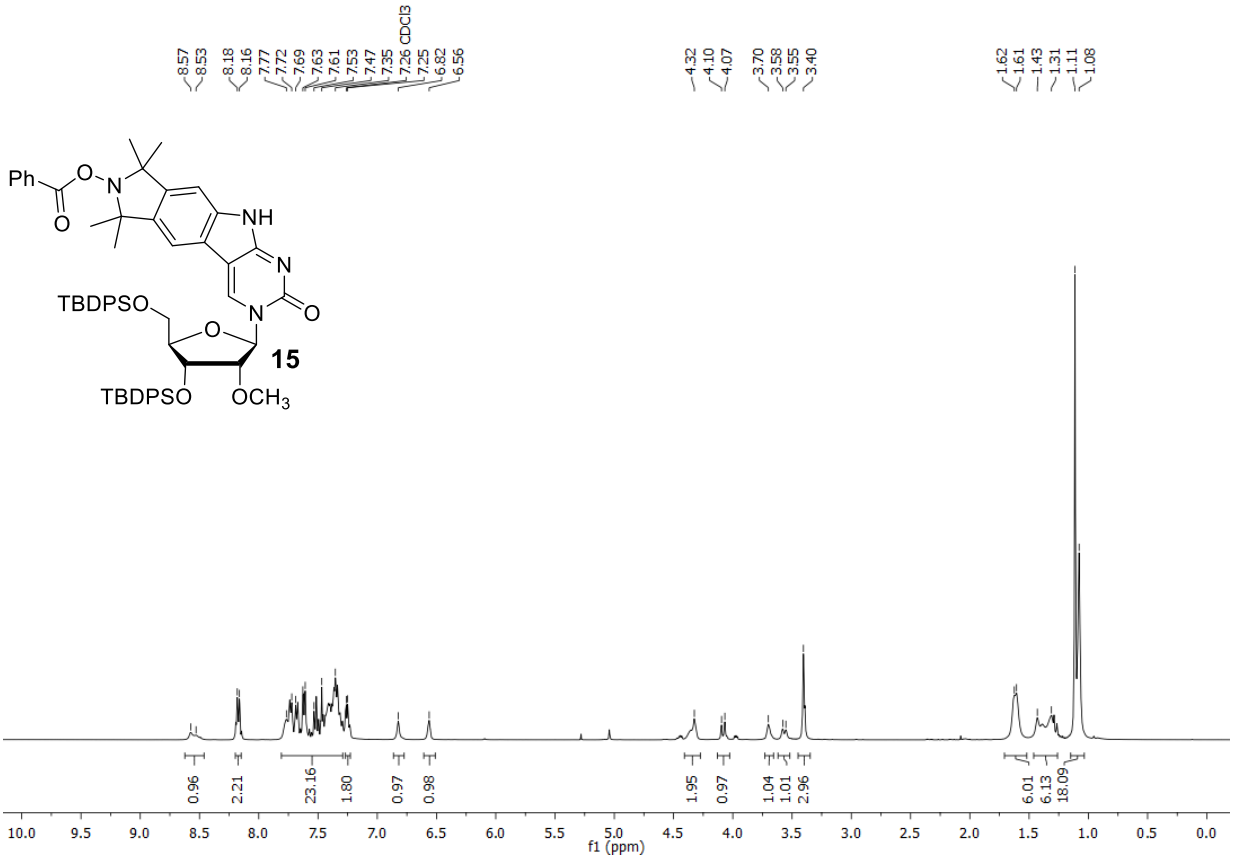

Figure S20. ^{1}H-NMR spectrum of **15** in $CDCl_3$ at 400 MHz.

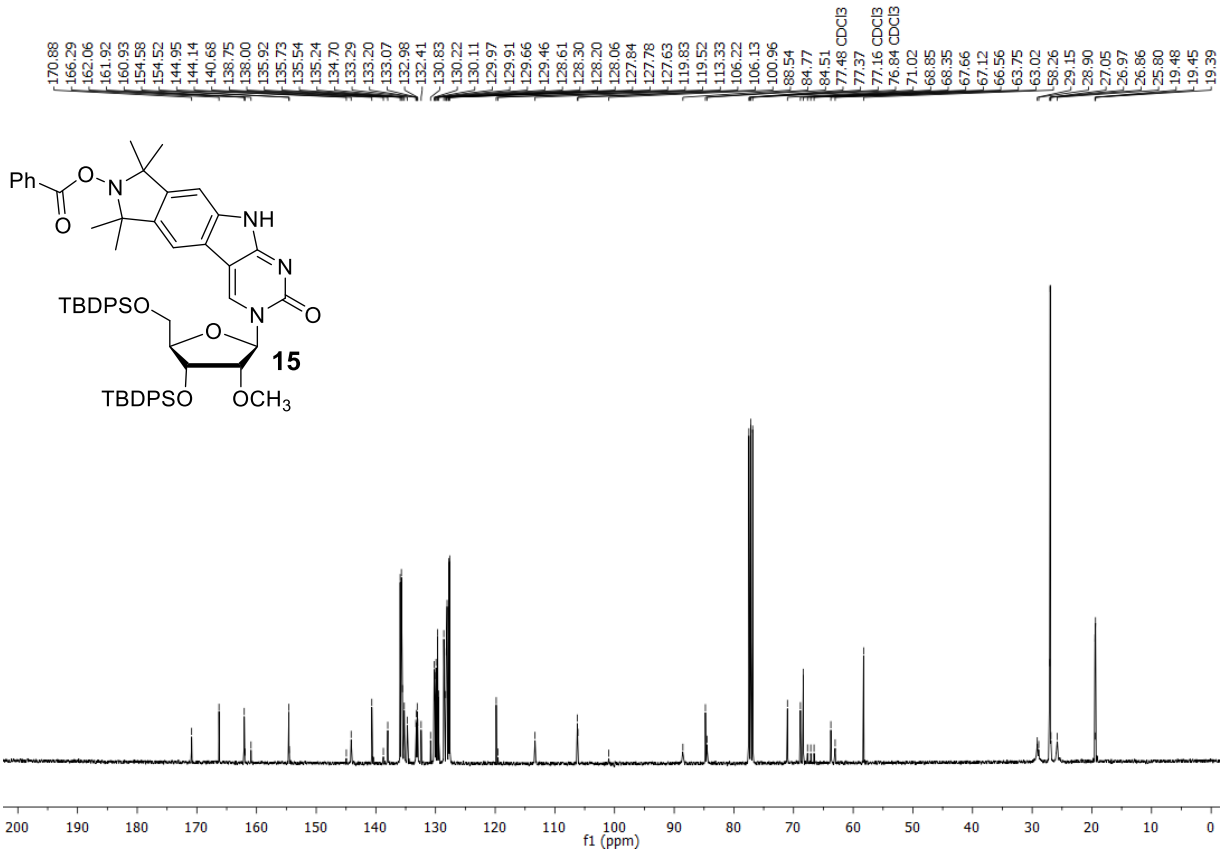

Figure S21. $^{13}C\{^{1}H\}$-NMR spectrum of **15** in $CDCl_3$ at 101 MHz.

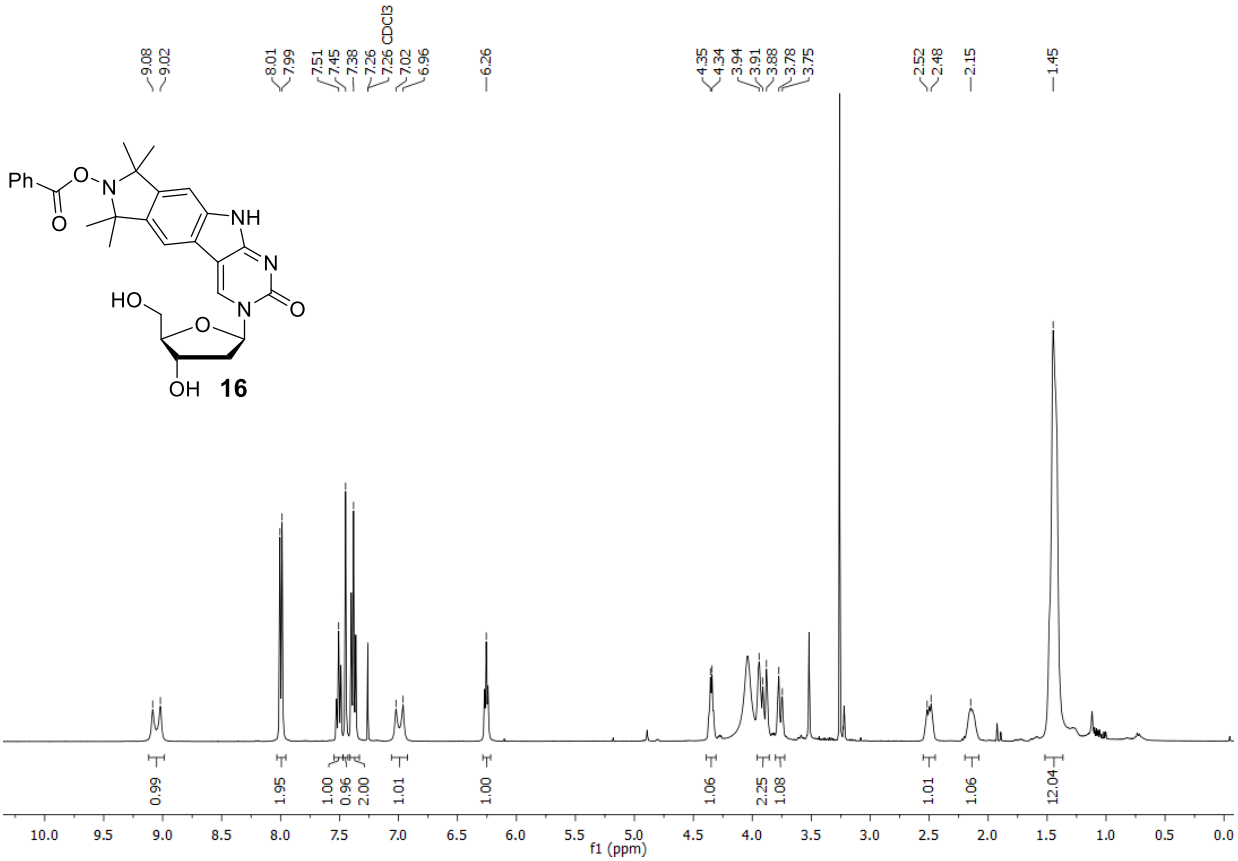

Figure S22. ^{1}H-NMR spectrum of **16** in $CDCl_3$ at 400 MHz.

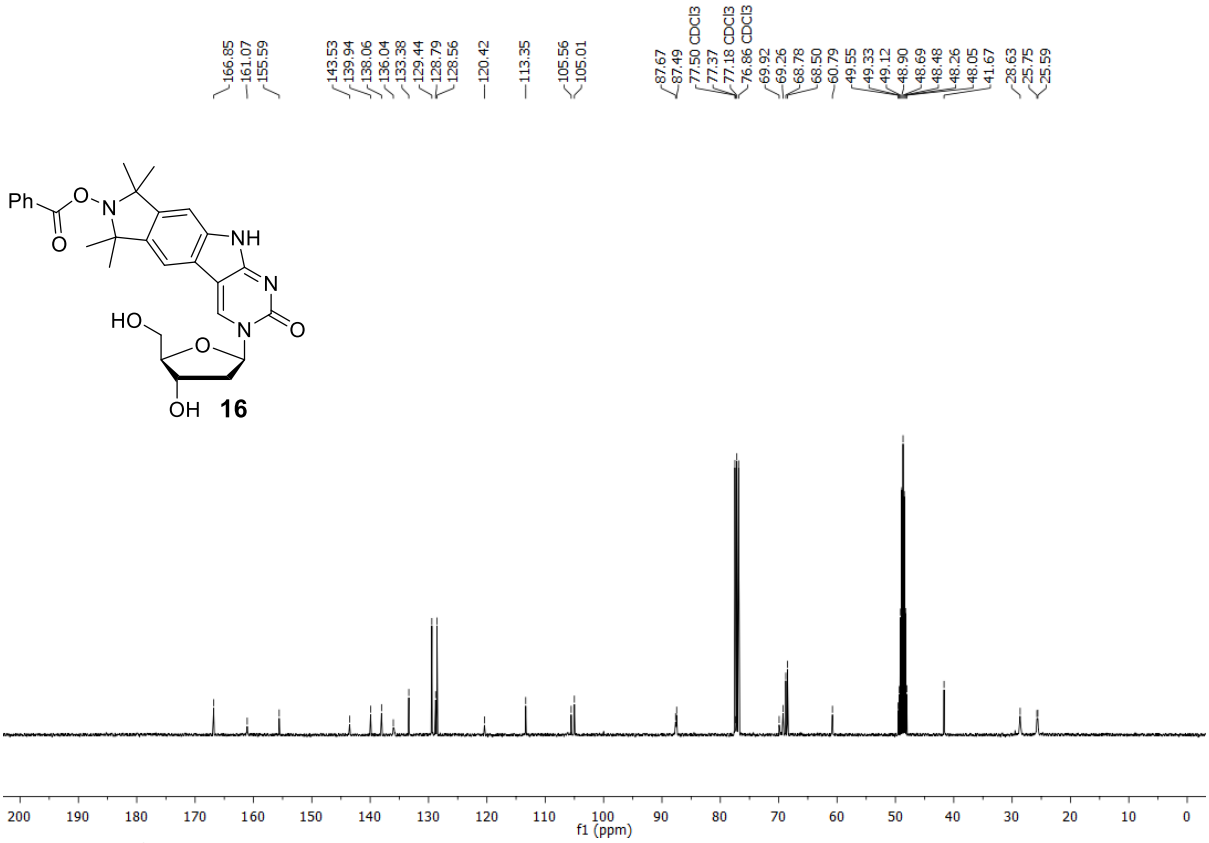

Figure S23. $^{13}C\{^{1}H\}$-NMR spectrum of **16** in $CDCl_3$ at 101 MHz.

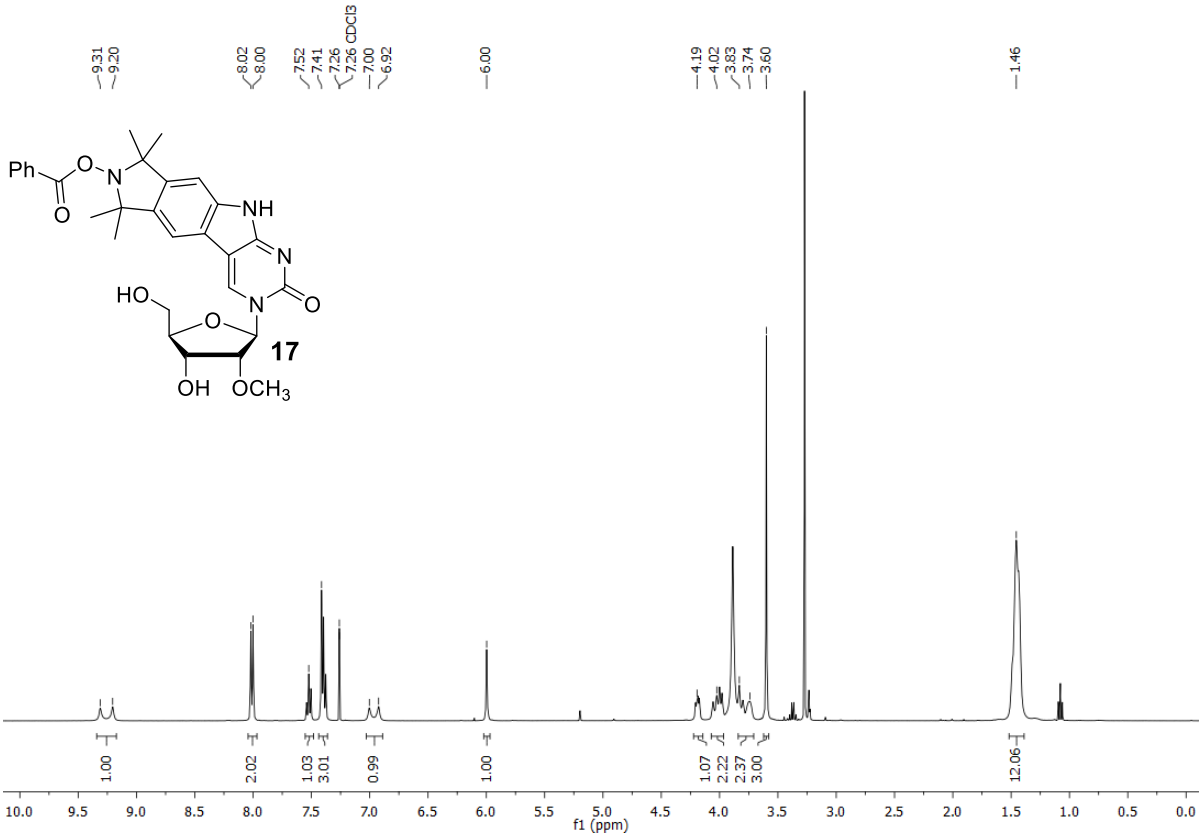

Figure S24. ^{1}H-NMR spectrum of **17** in $CDCl_3$ at 400 MHz.

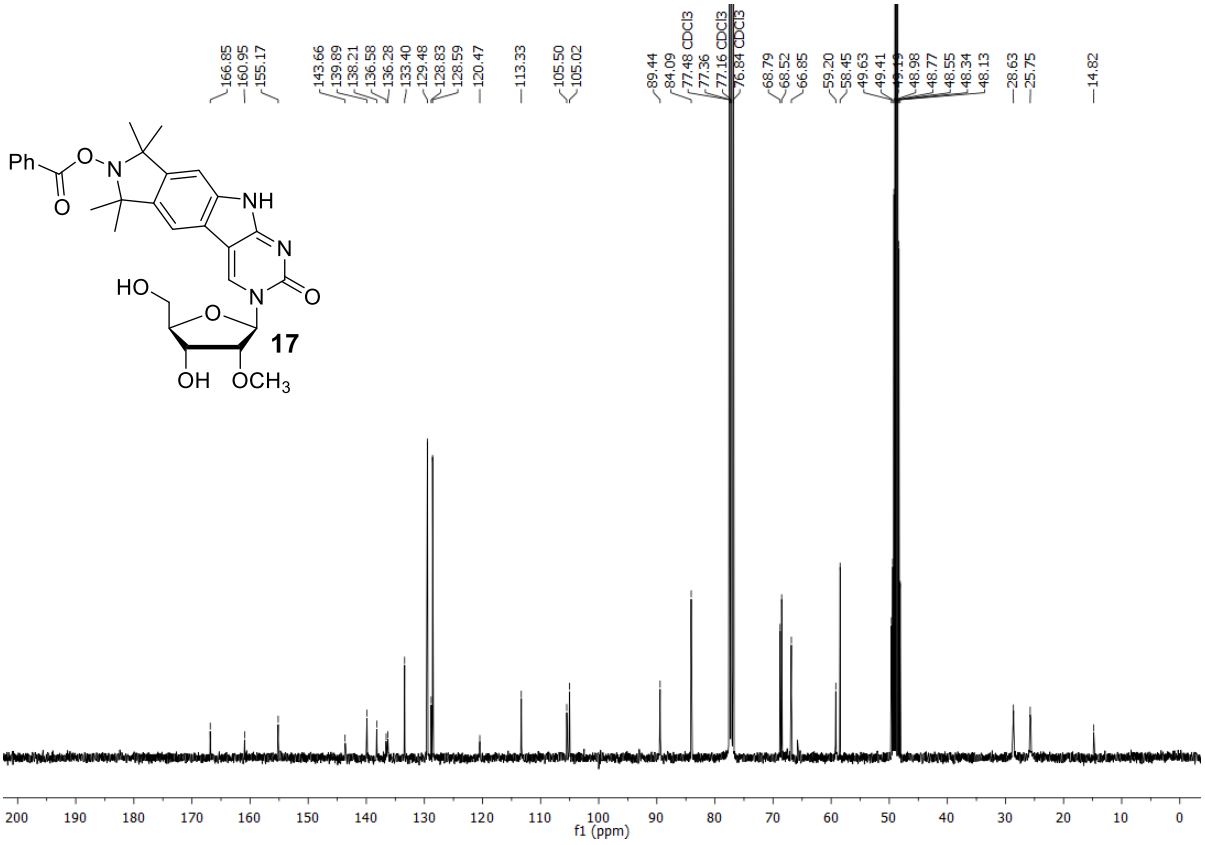

Figure S25. $^{13}C\{^{1}H\}$-NMR spectrum of **17** in $CDCl_3$ at 101 MHz.

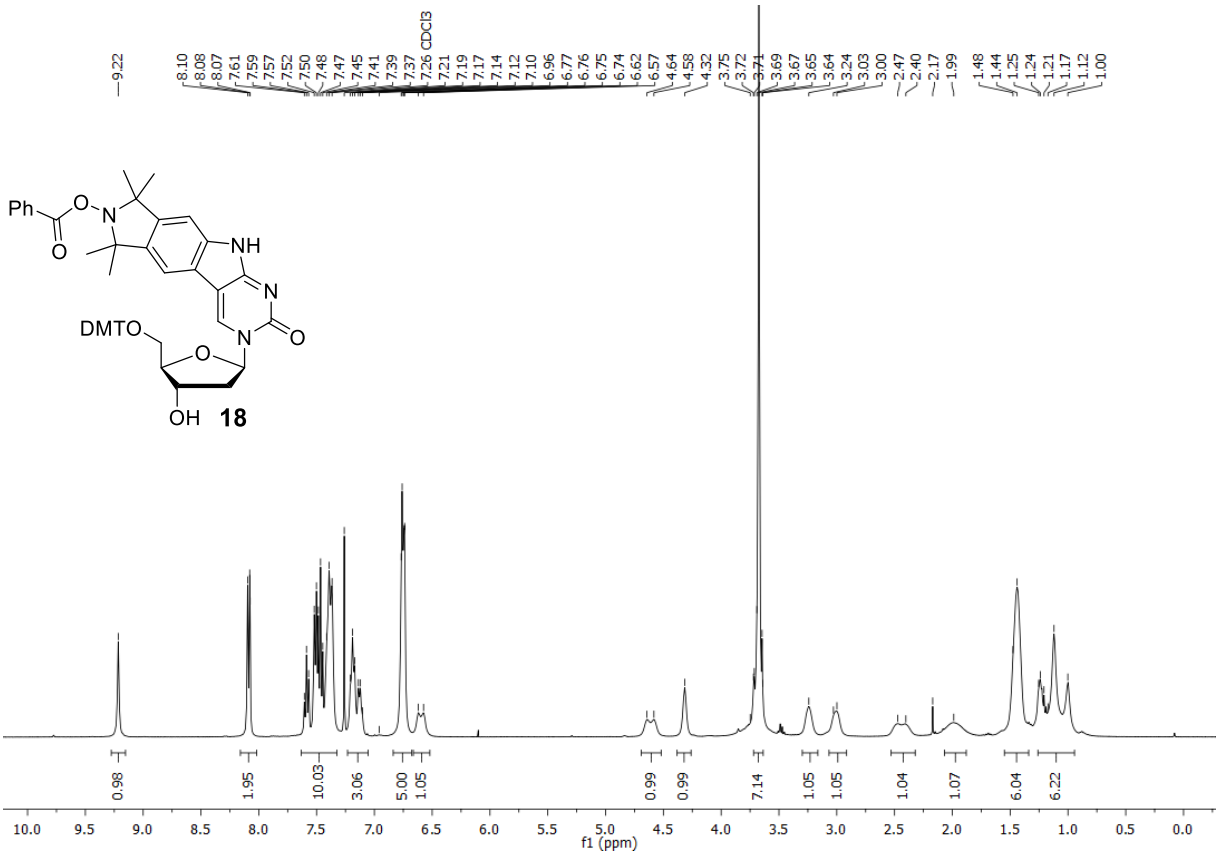

Figure S26. ^{1}H-NMR spectrum of **18** in $CDCl_3$ at 400 MHz.

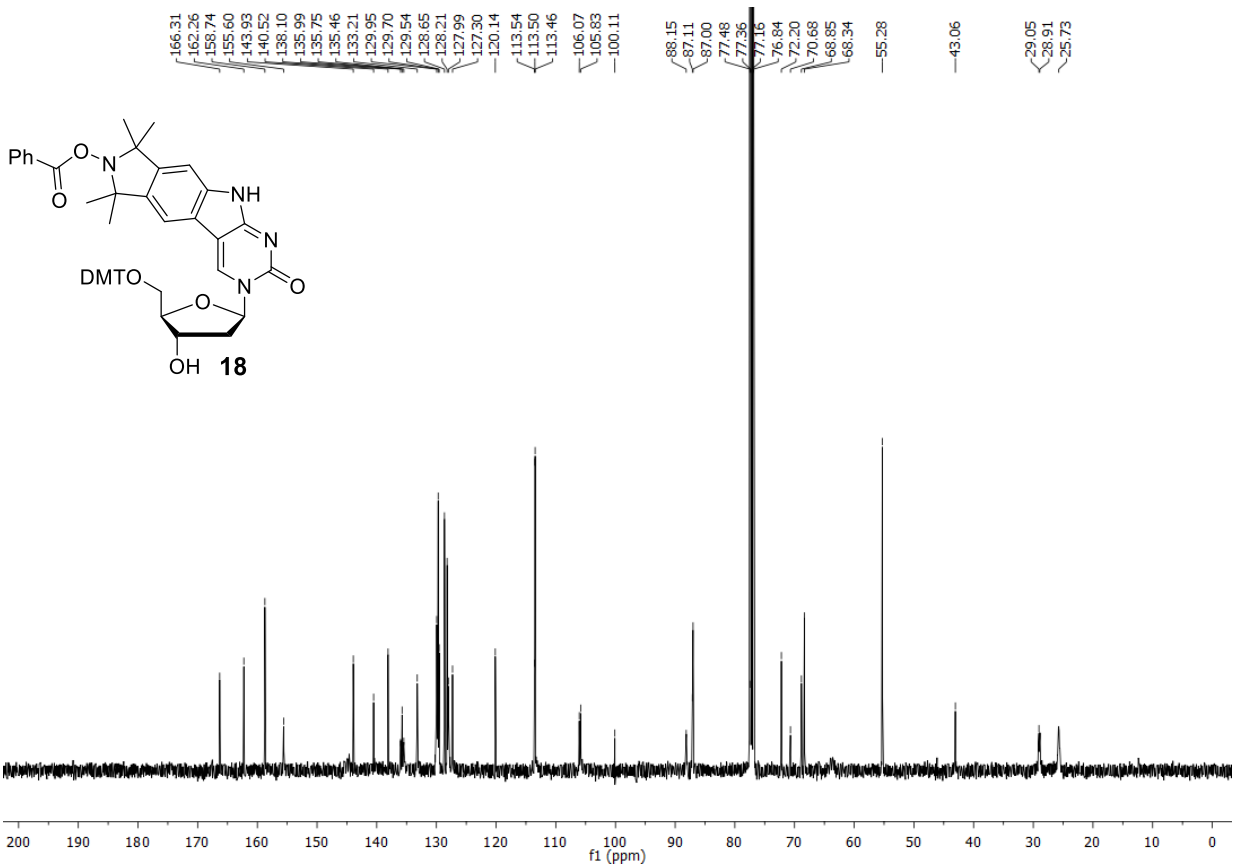

Figure S27. $^{13}C\{^{1}H\}$-NMR spectrum of **18** in $CDCl_3$ at 101 MHz.

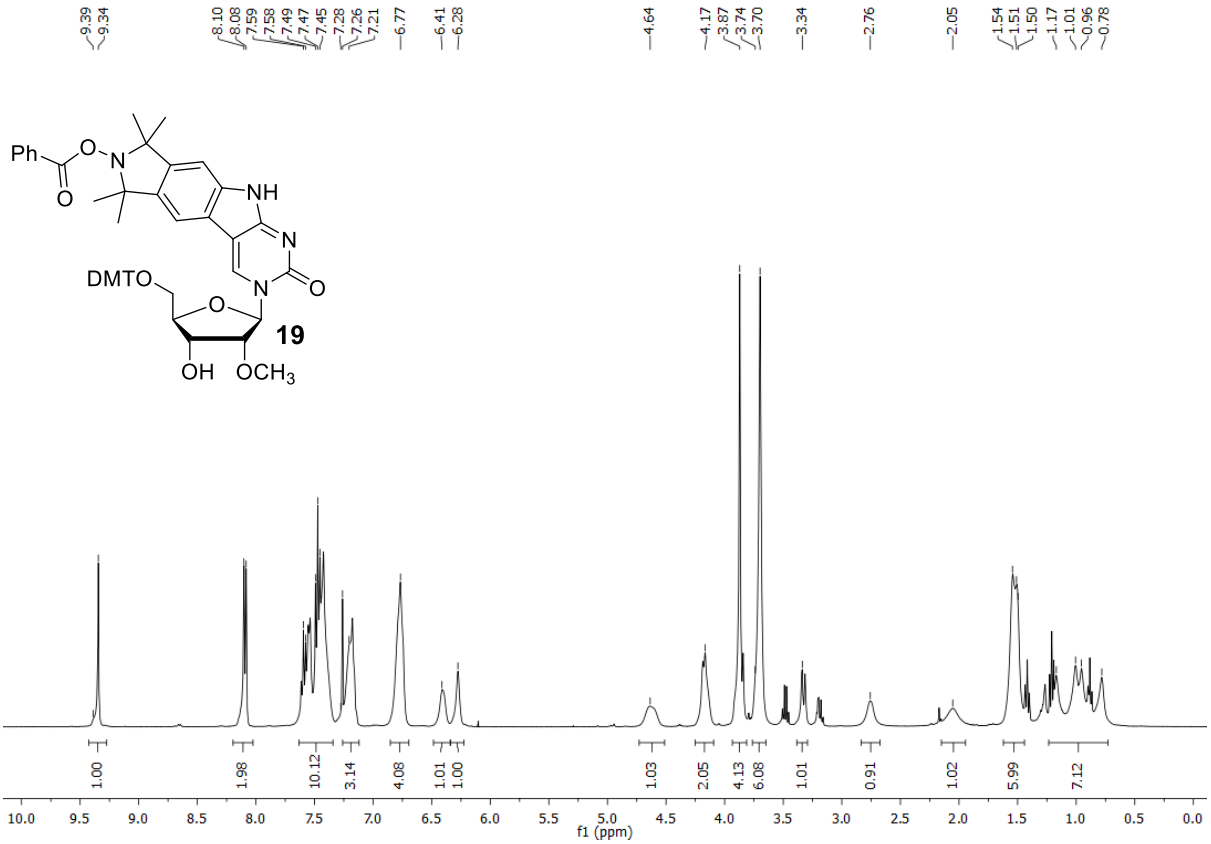

Figure S28. ^{1}H-NMR spectrum of **19** in $CDCl_3$ at 400 MHz.

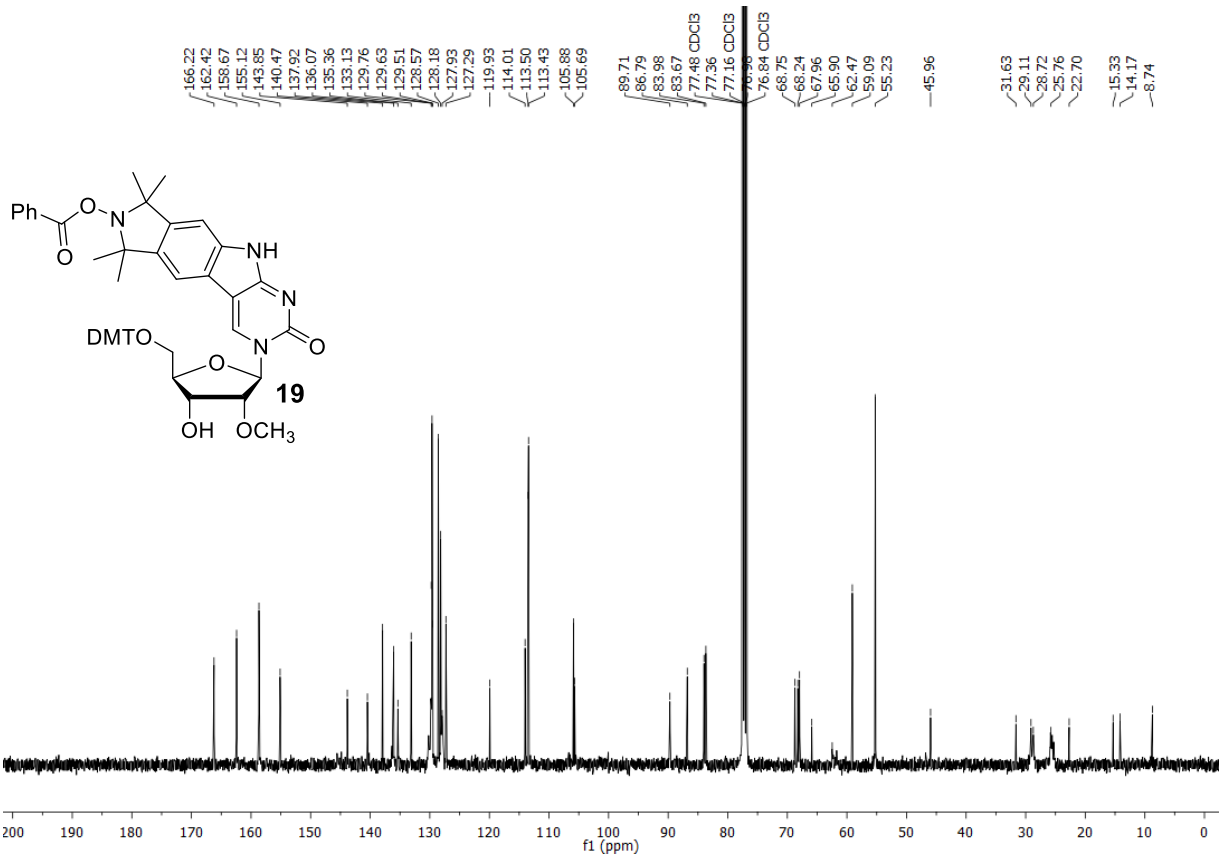

Figure S29. ^{13}C{^{1}H}-NMR spectrum of **19** in $CDCl_3$ at 101 MHz.

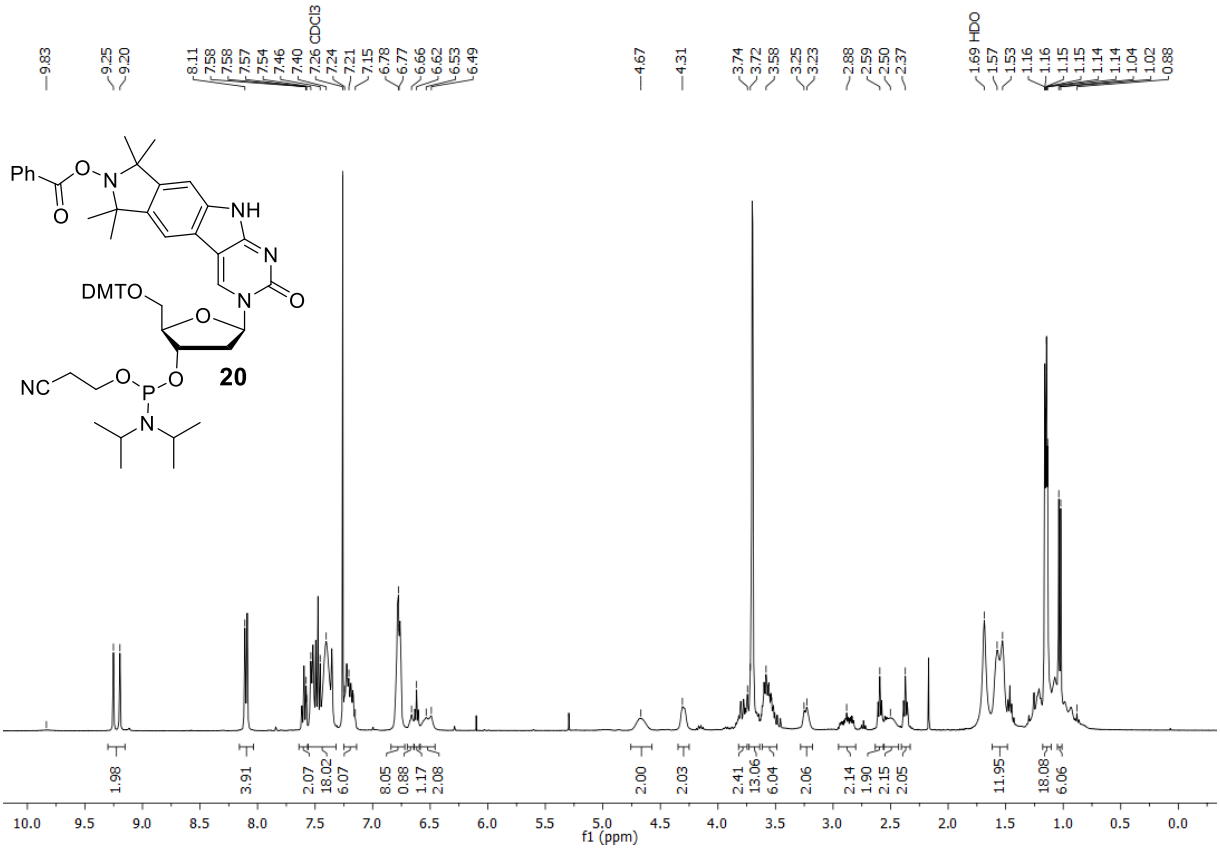

Figure S30. 1H-NMR spectrum of **20** in CDCl3 at 400 MHz.

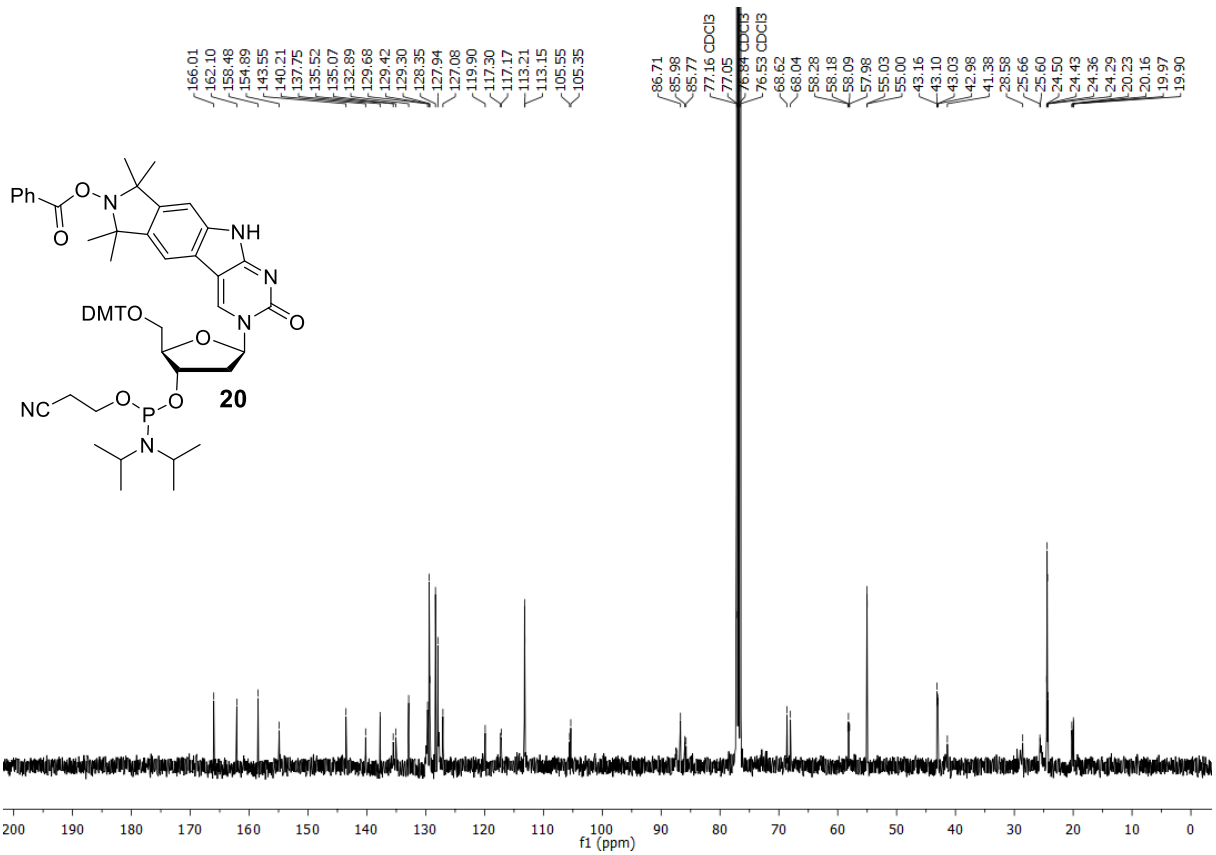

Figure S31. 13C{1H}-NMR spectrum of **20** in CDCl3 at 101 MHz.

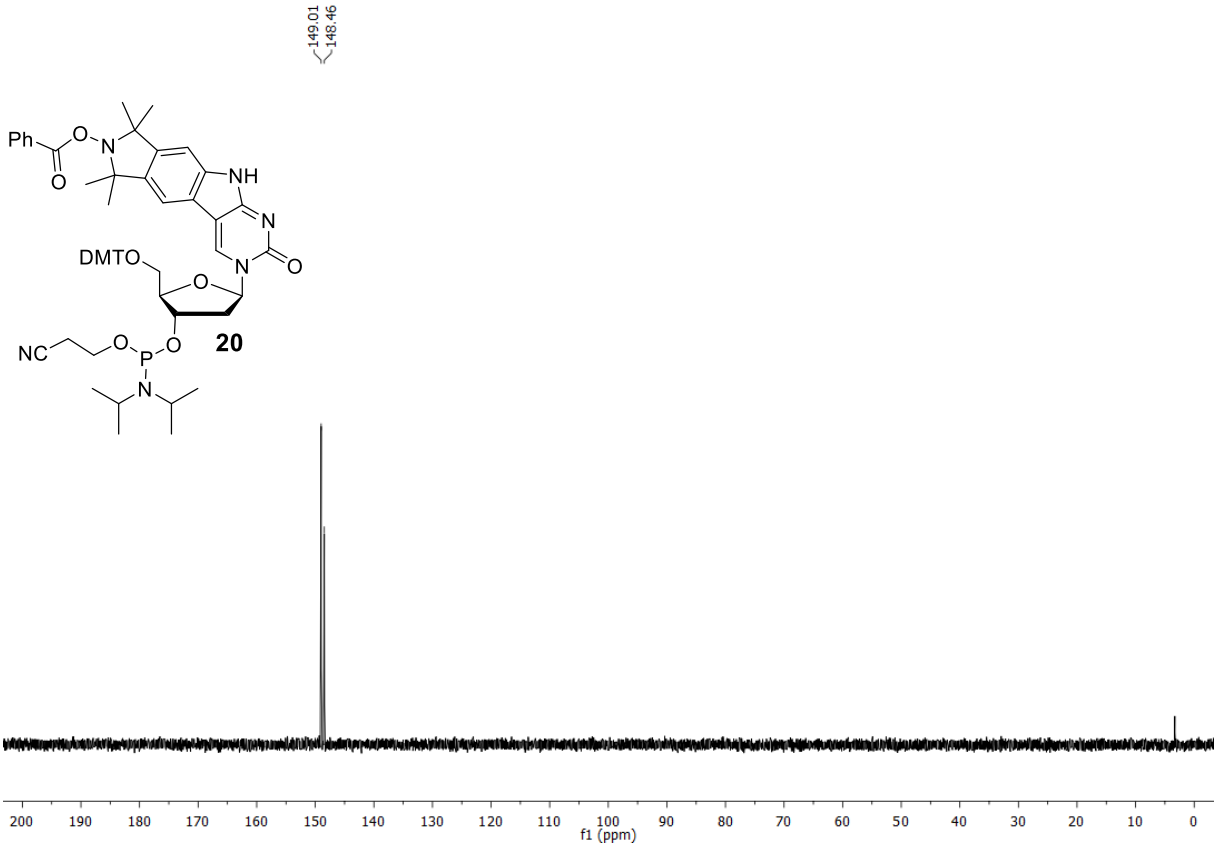

Figure S32. ^{31}P-NMR spectrum of **20** in $CDCl_3$ at 162 MHz.

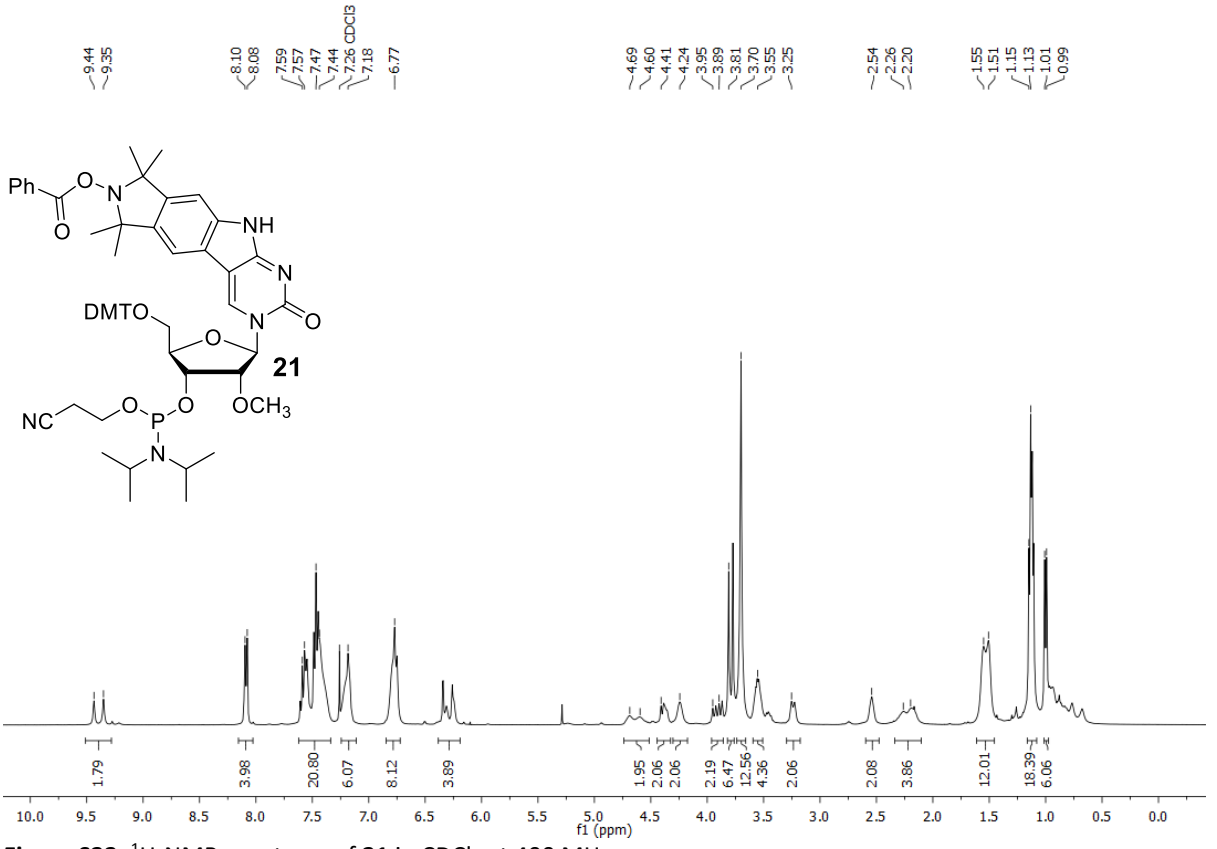

Figure S33. ^{1}H-NMR spectrum of **21** in $CDCl_3$ at 400 MHz.

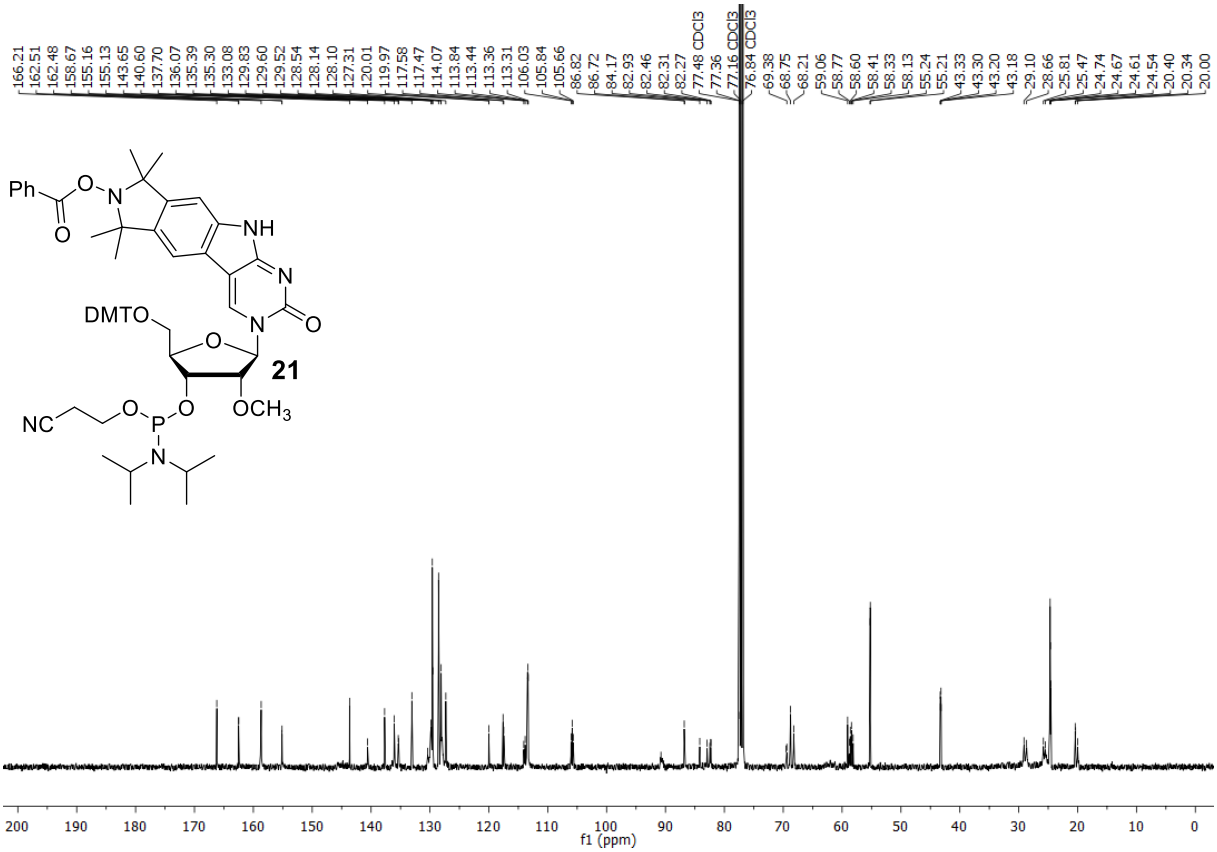

Figure S34. $^{13}C\{^{1}H\}$-NMR spectrum of **21** in $CDCl_3$ at 101 MHz.

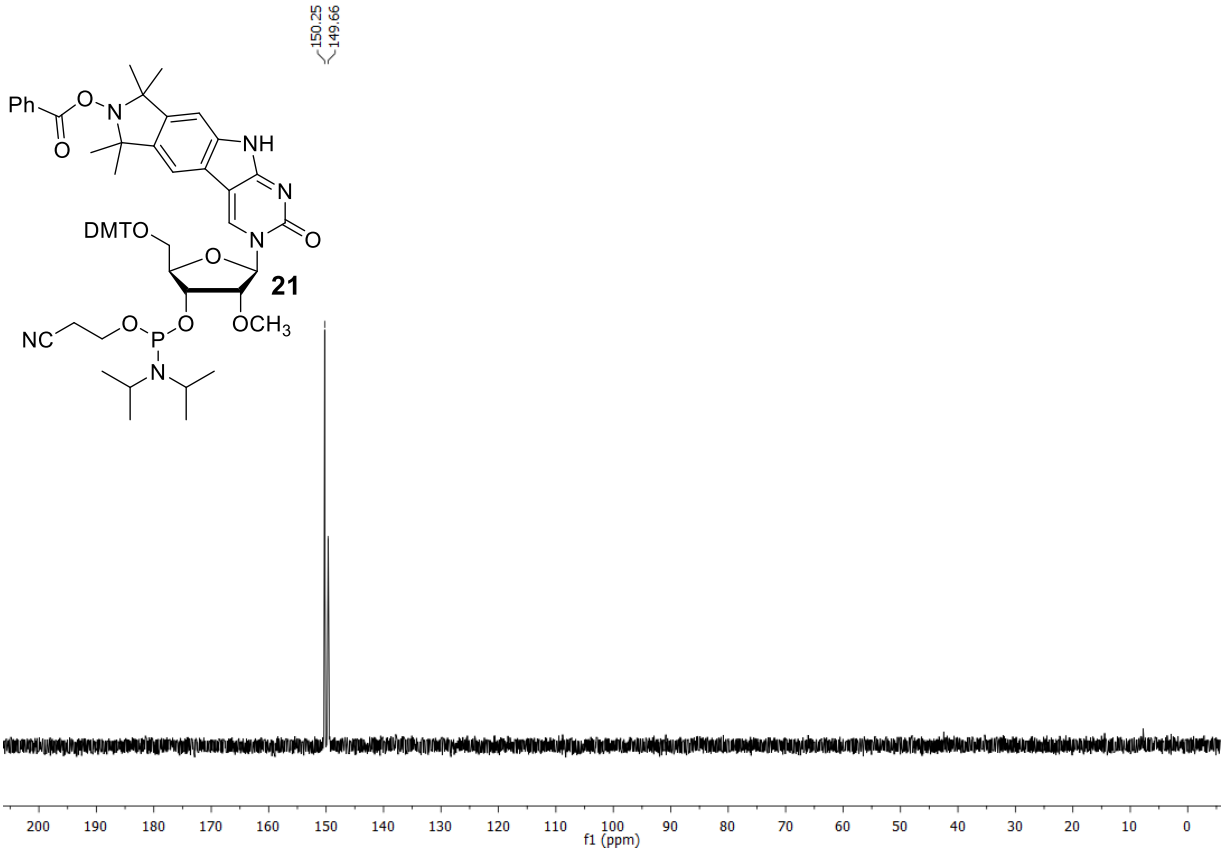

Figure S35. ^{31}P-NMR spectrum of **21** in $CDCl_3$ at 162 MHz.

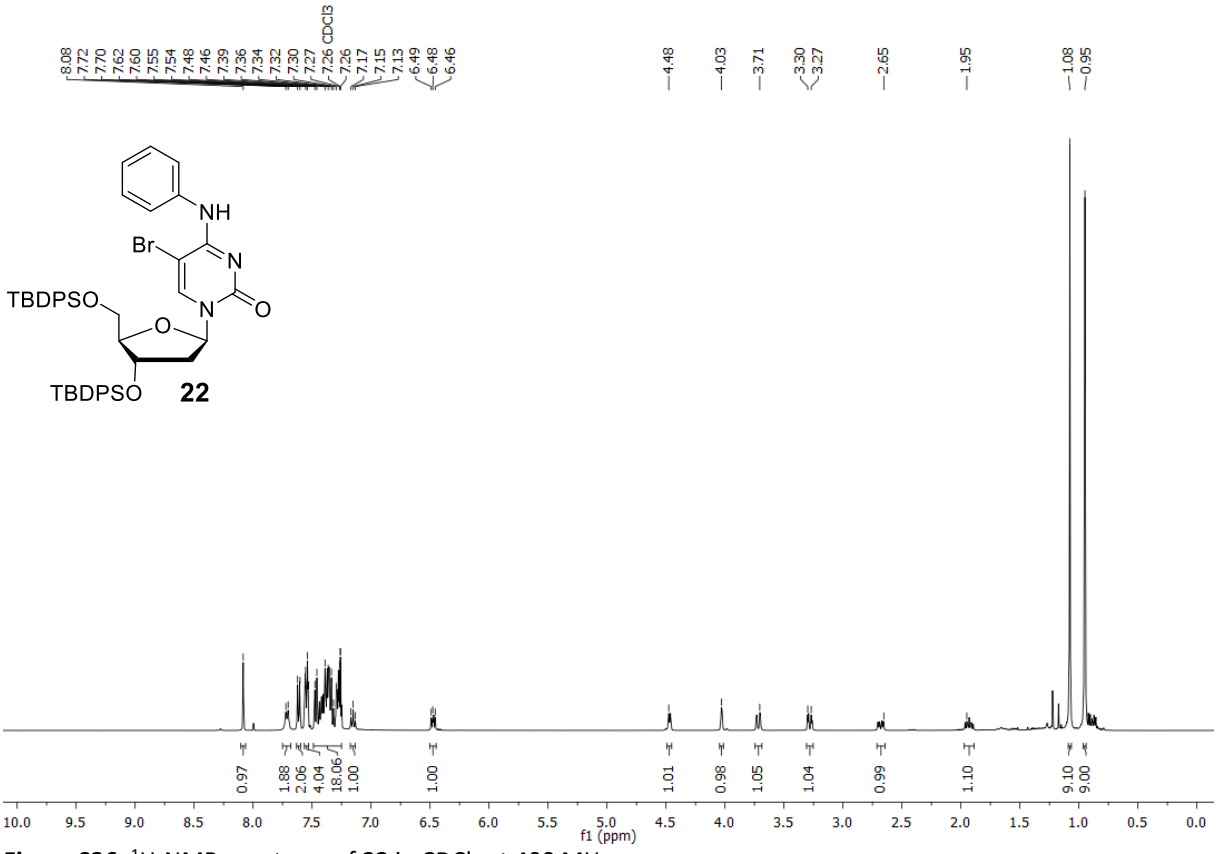

Figure S36. ^{1}H-NMR spectrum of **22** in $CDCl_3$ at 400 MHz.

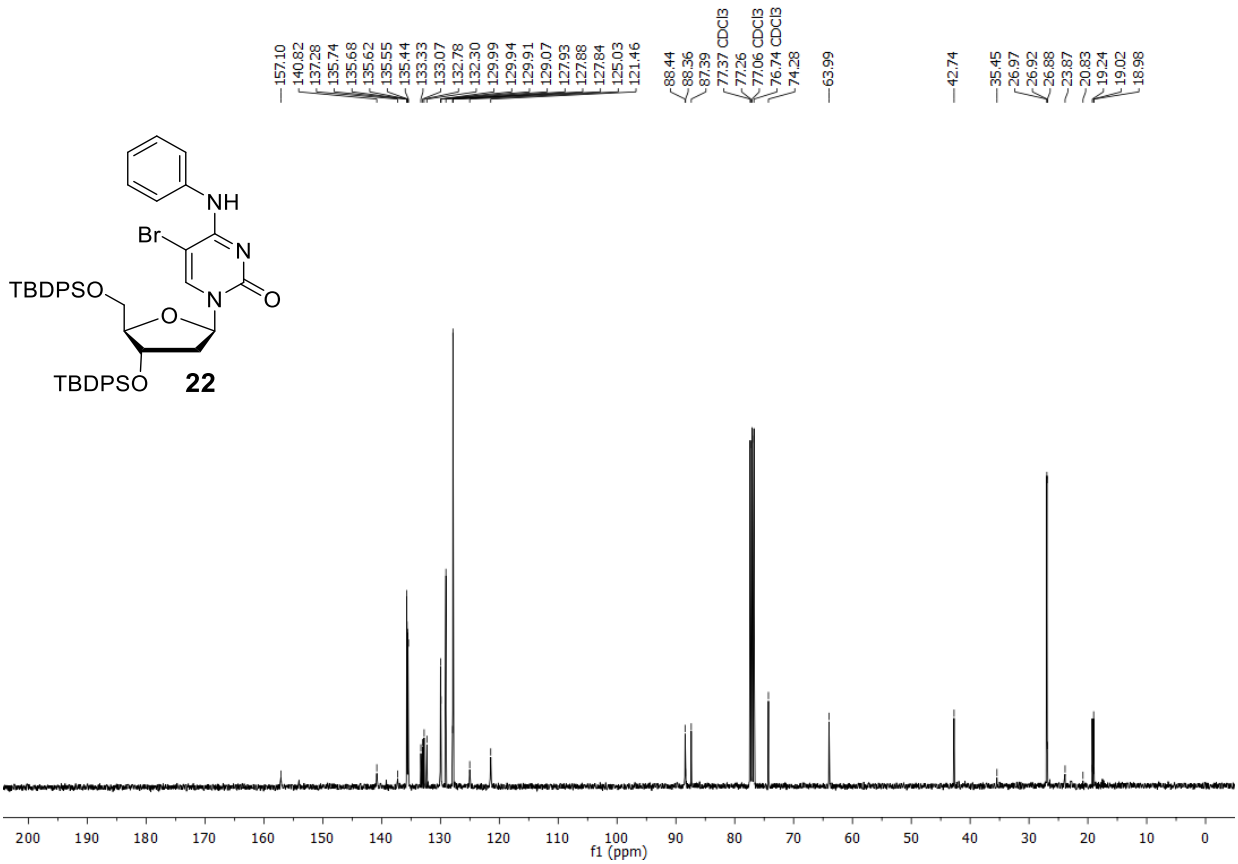

Figure S37. ^{13}C{^{1}H}-NMR spectrum of **22** in $CDCl_3$ at 101 MHz.

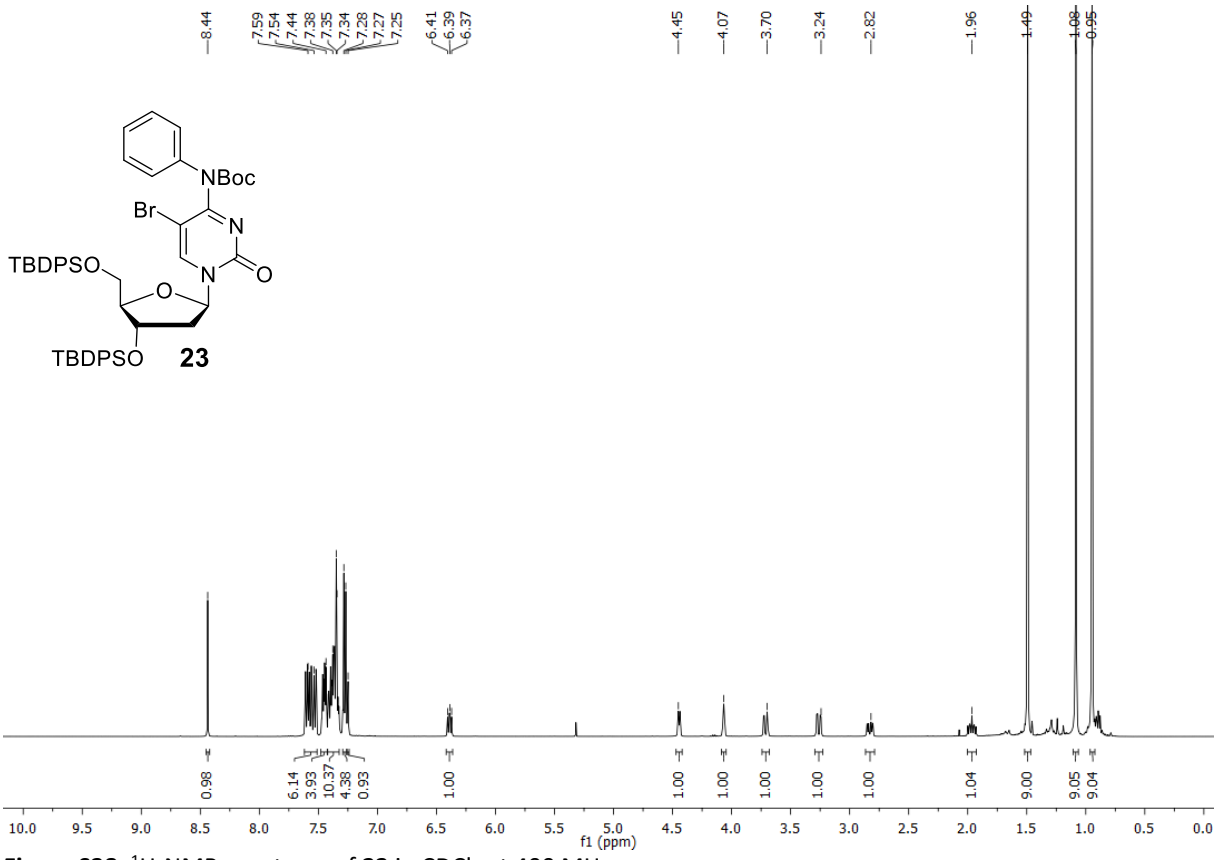

Figure S38. ^{1}H-NMR spectrum of **23** in $CDCl_3$ at 400 MHz.

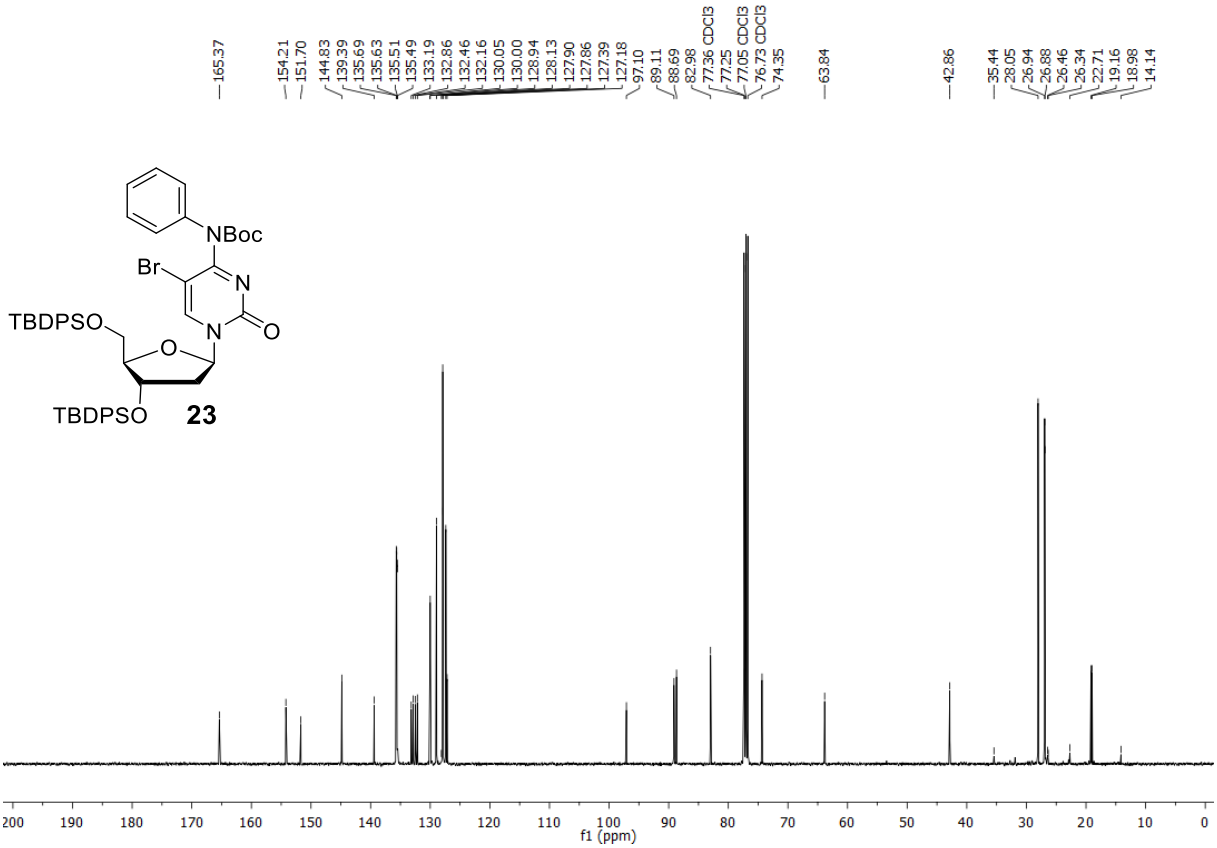

Figure S39. $^{13}C\{^{1}H\}$-NMR spectrum of **23** in $CDCl_3$ at 101 MHz.

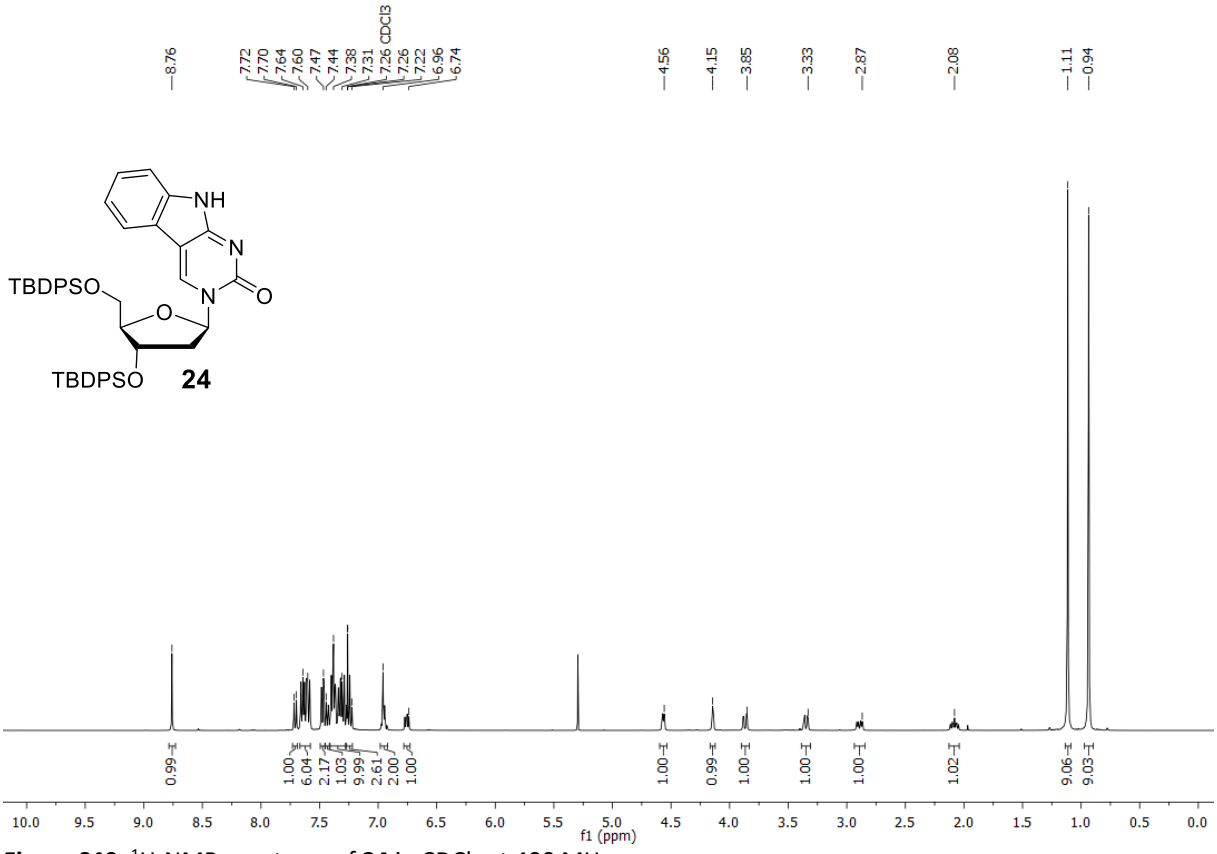

Figure S40. ^{1}H-NMR spectrum of **24** in $CDCl_3$ at 400 MHz.

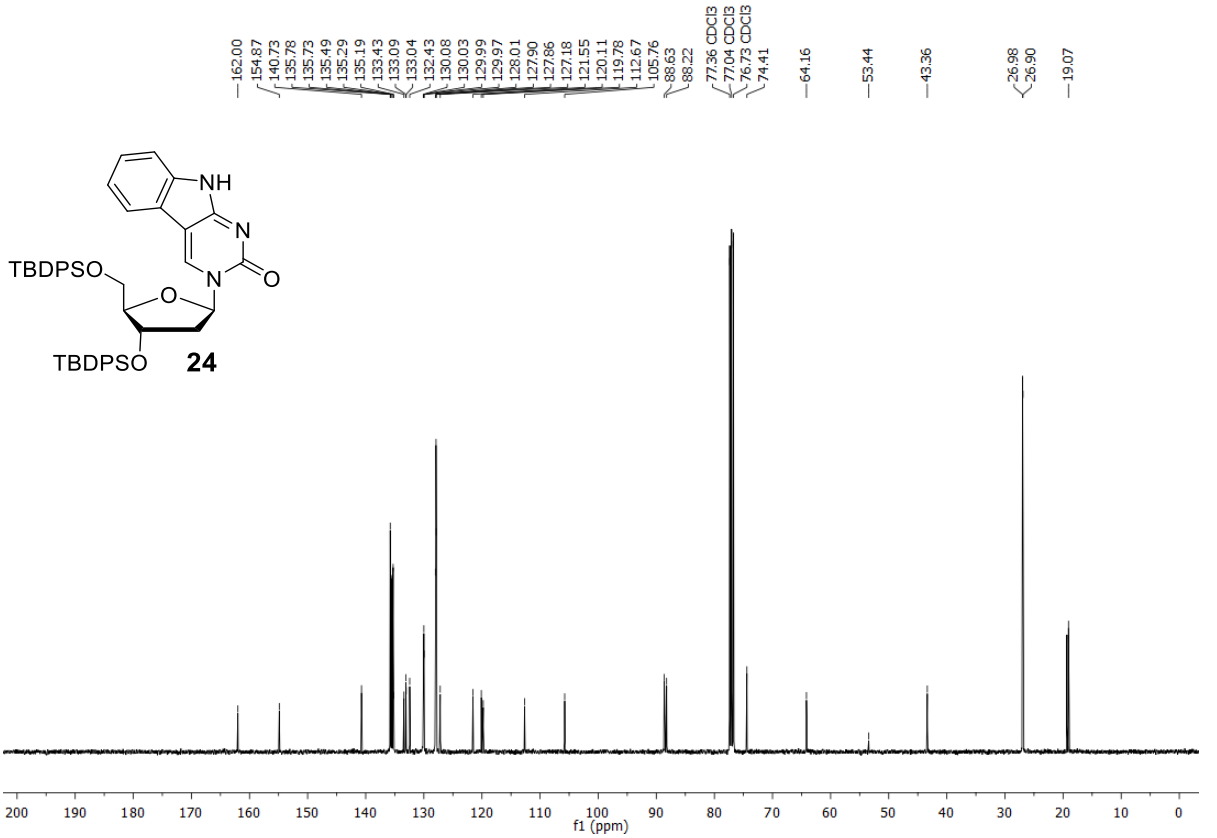

Figure S41. ^{13}C{^{1}H}-NMR spectrum of **24** in $CDCl_3$ at 101 MHz.

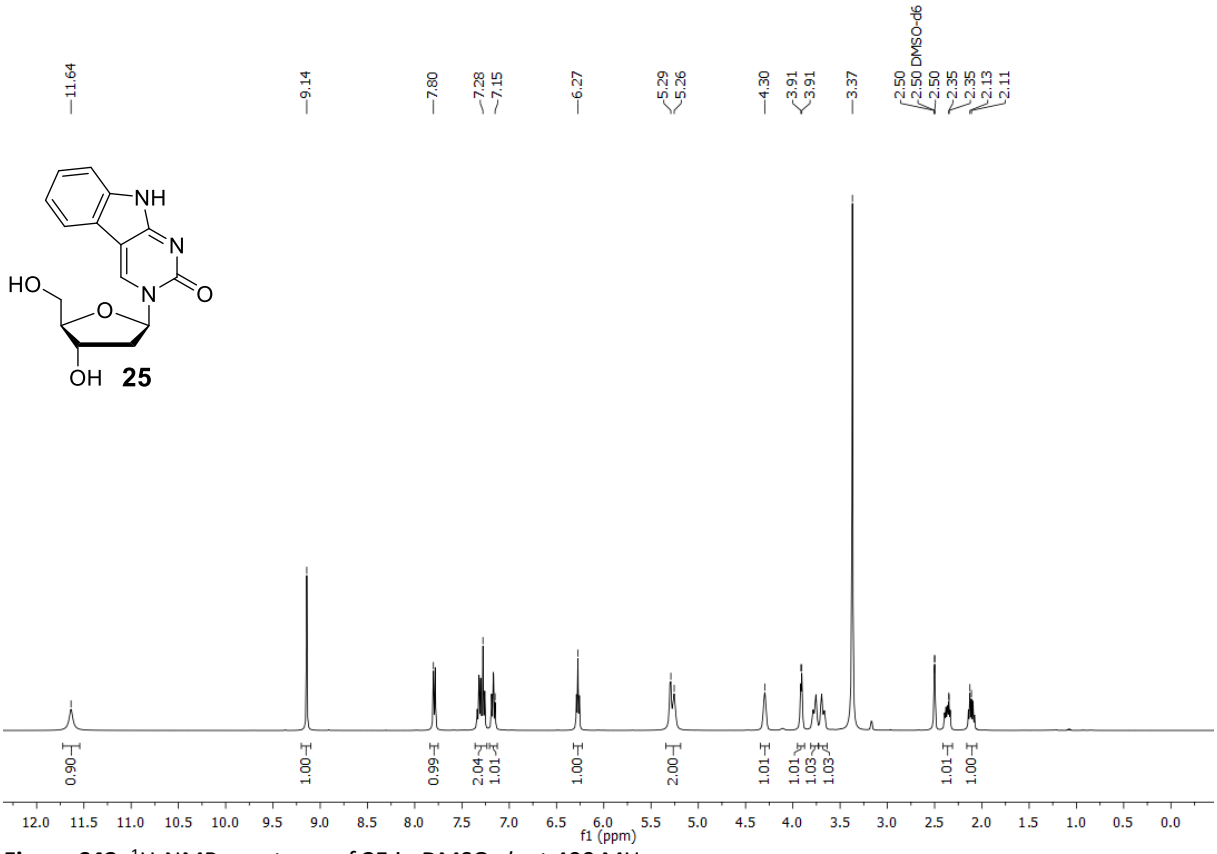

Figure S42. ^{1}H-NMR spectrum of **25** in DMSO-d_6 at 400 MHz.

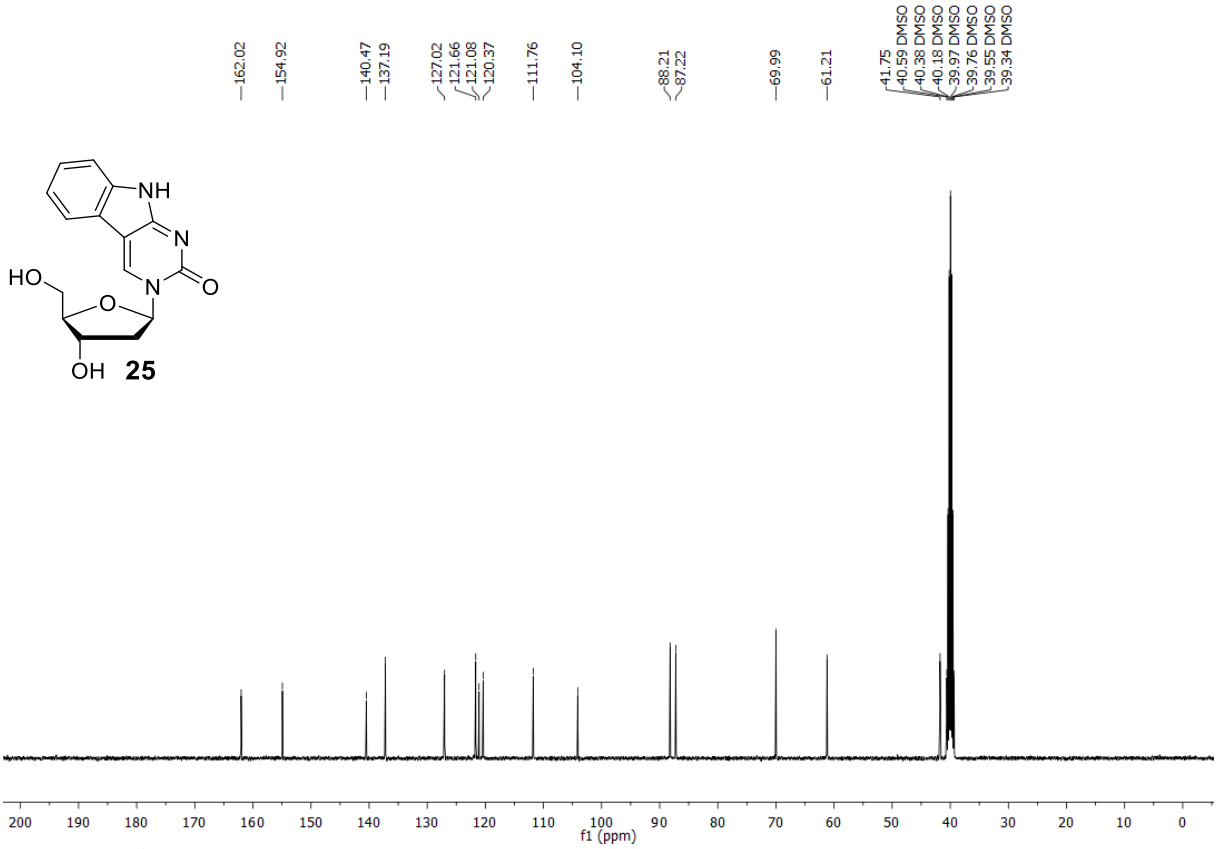

Figure S43. ^{13}C{^{1}H}-NMR spectrum of **25** in DMSO-d_6 at 101 MHz.

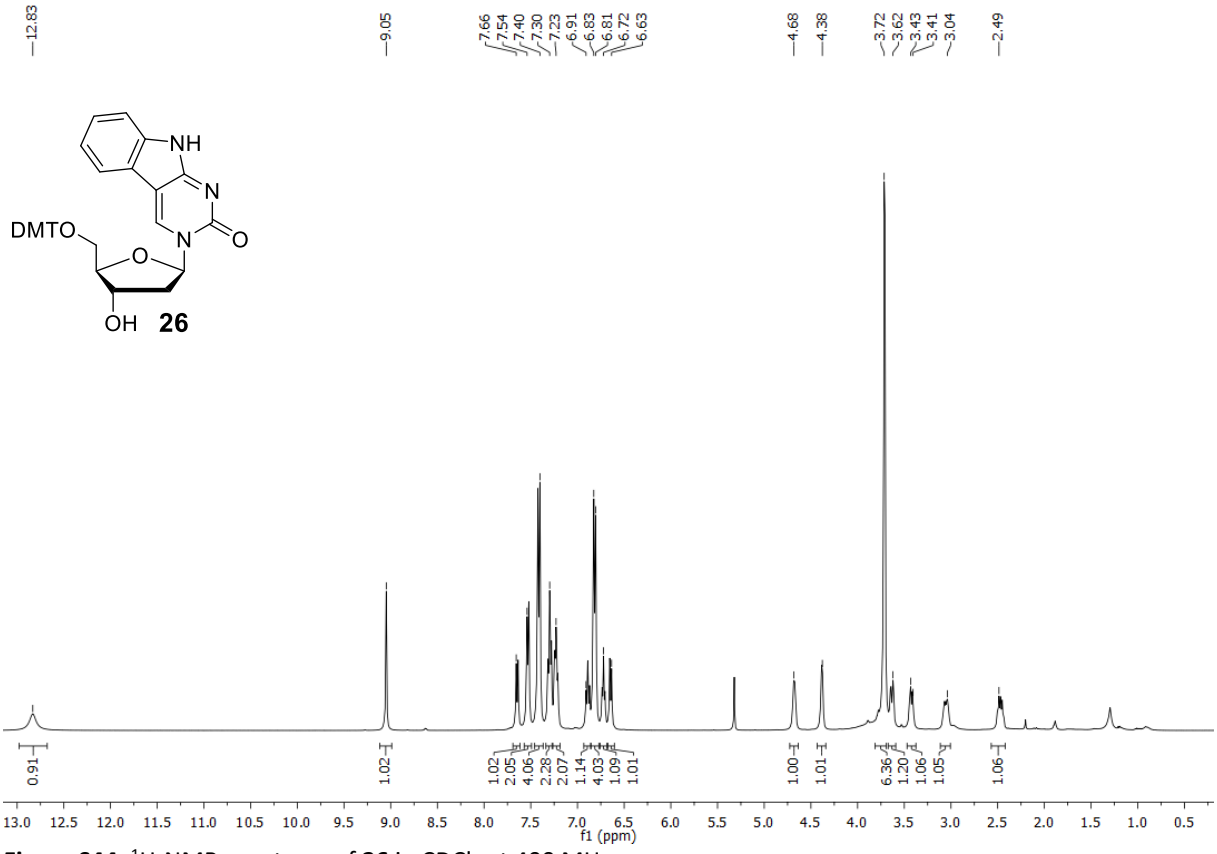

Figure S44. ^{1}H-NMR spectrum of **26** in $CDCl_3$ at 400 MHz.

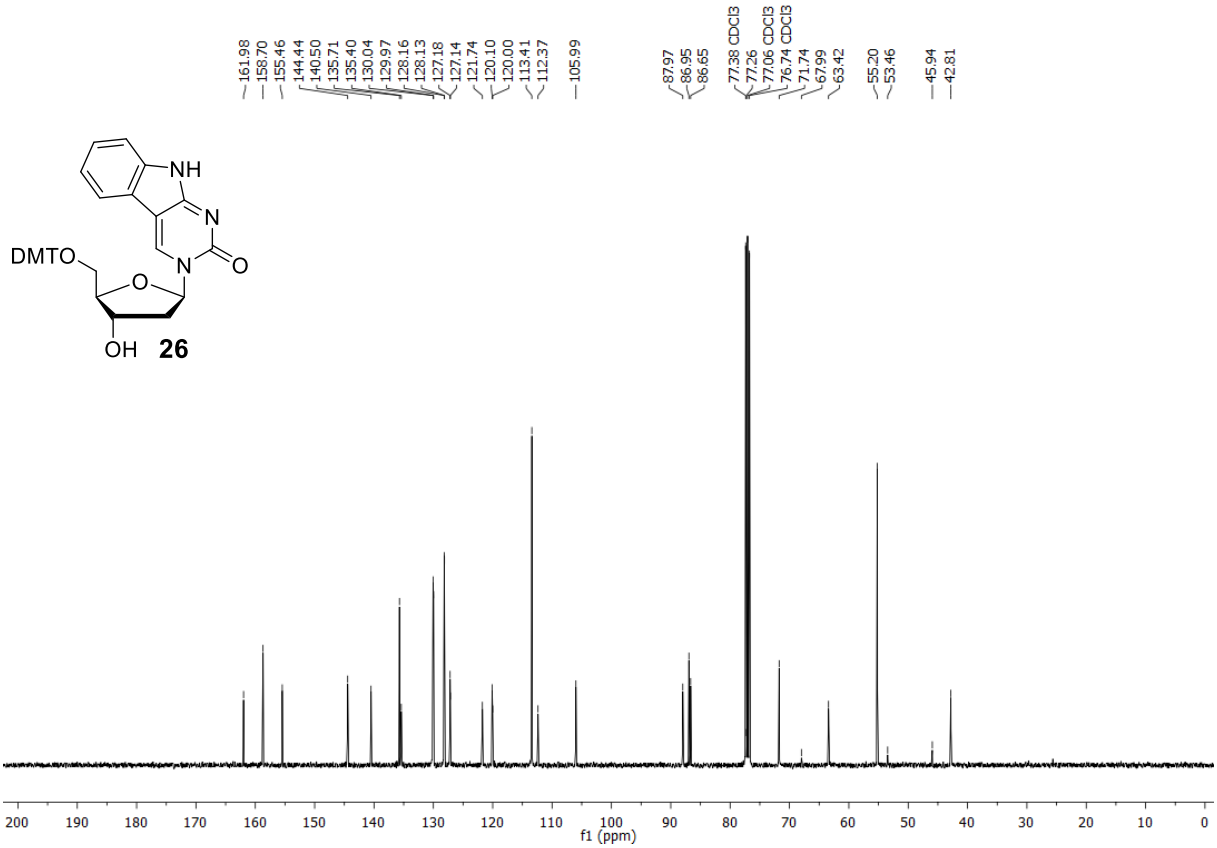

Figure S45. ^{13}C{^{1}H}-NMR spectrum of **26** in $CDCl_3$ at 101 MHz.

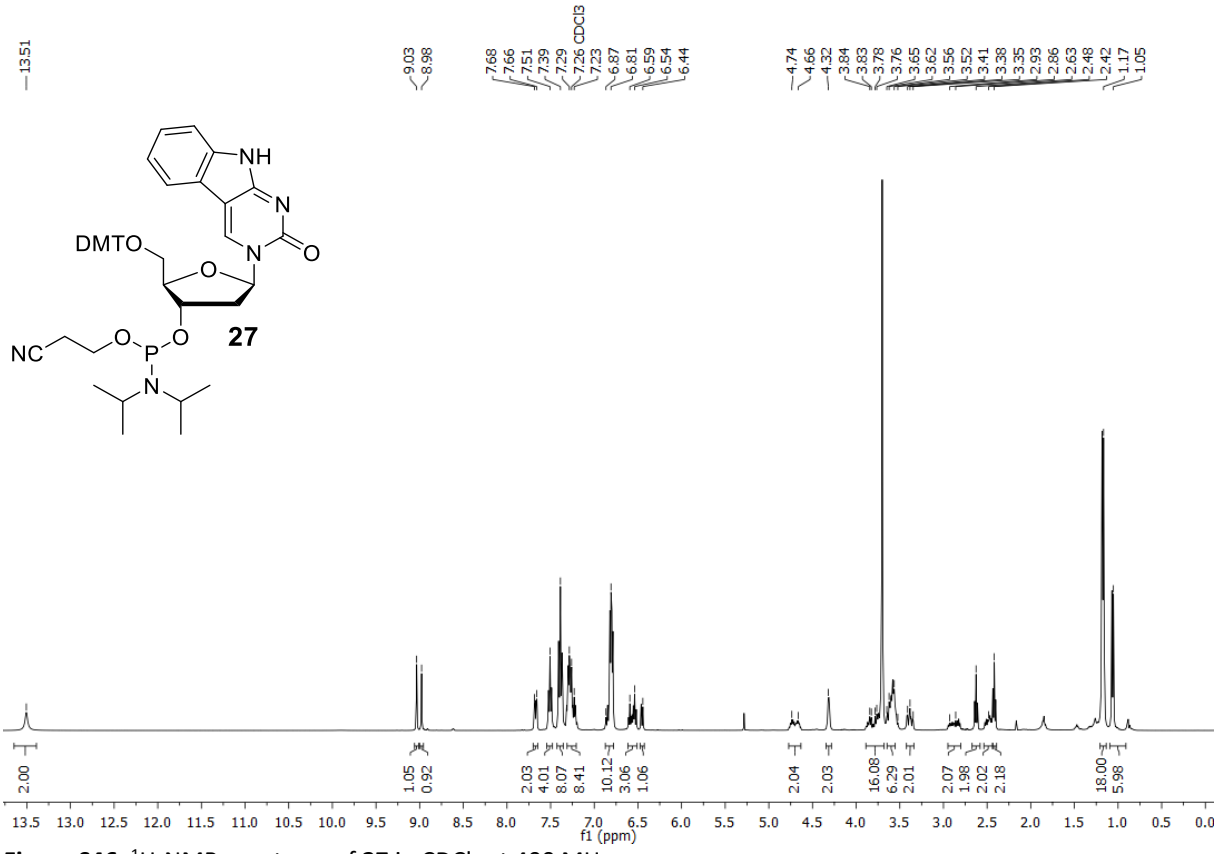

Figure S46. ^{1}H-NMR spectrum of **27** in $CDCl_3$ at 400 MHz.

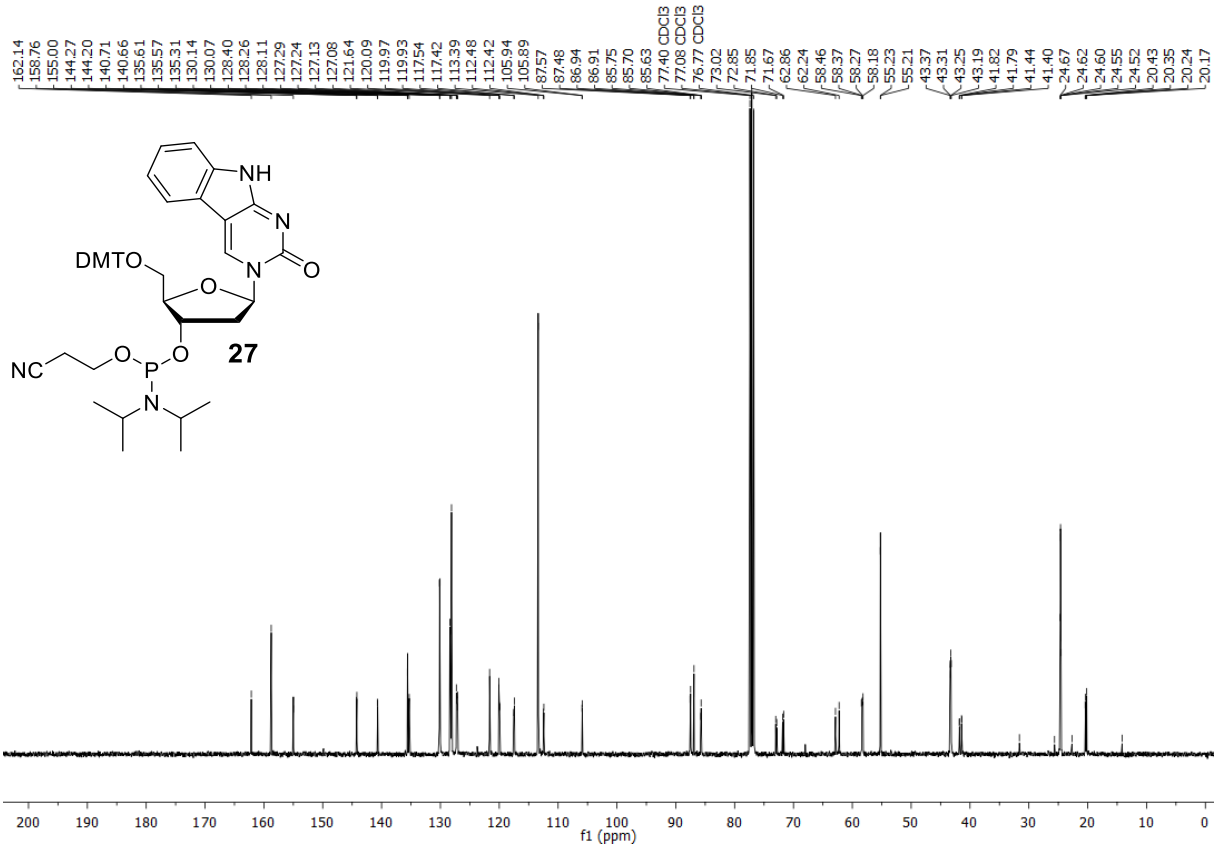

Figure S47. $^{13}C\{^{1}H\}$-NMR spectrum of **27** in $CDCl_3$ at 101 MHz.

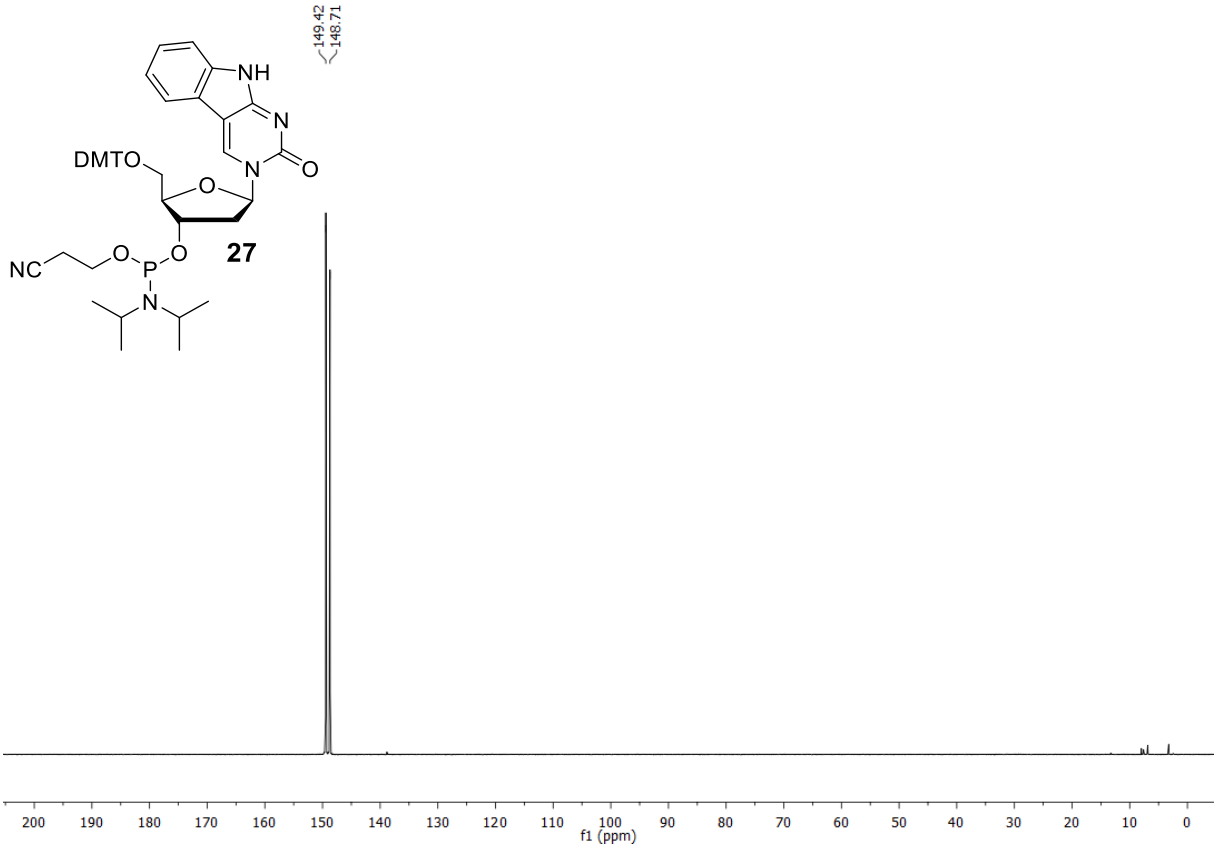

Figure S48. ^{31}P-NMR spectrum of **27** in $CDCl_3$ at 162 MHz.

Models of Ċ-labeled DNA and Ċm-labeled RNA

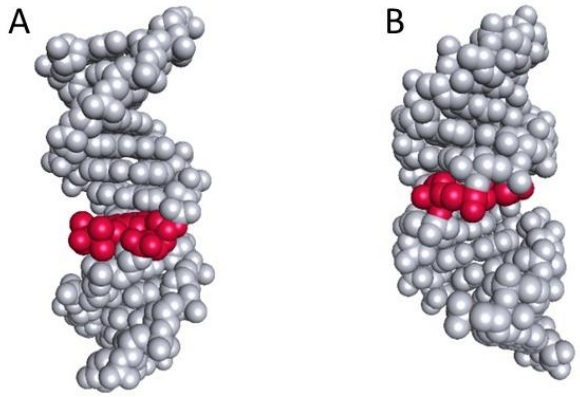

Figure S49. Space-filling models of **Ċ**- and **Ċm**-labeled oligonucleotide duplexes. A. B-form DNA duplex with **Ċ** projected into the major groove. B. A-form RNA duplex containing **Ċm**. The spin-labeled nucleotides are shown in pink. Modeling of the spin labels inside the duplexes was performed with the following software: BIOVIA, Dassault Systèmes, Discovery Studio Visualizer, v16.1.0.15350, San Diego: Dassault Systèmes, 2016.

CW-EPR spectra of spin-labeled oligonucleotides

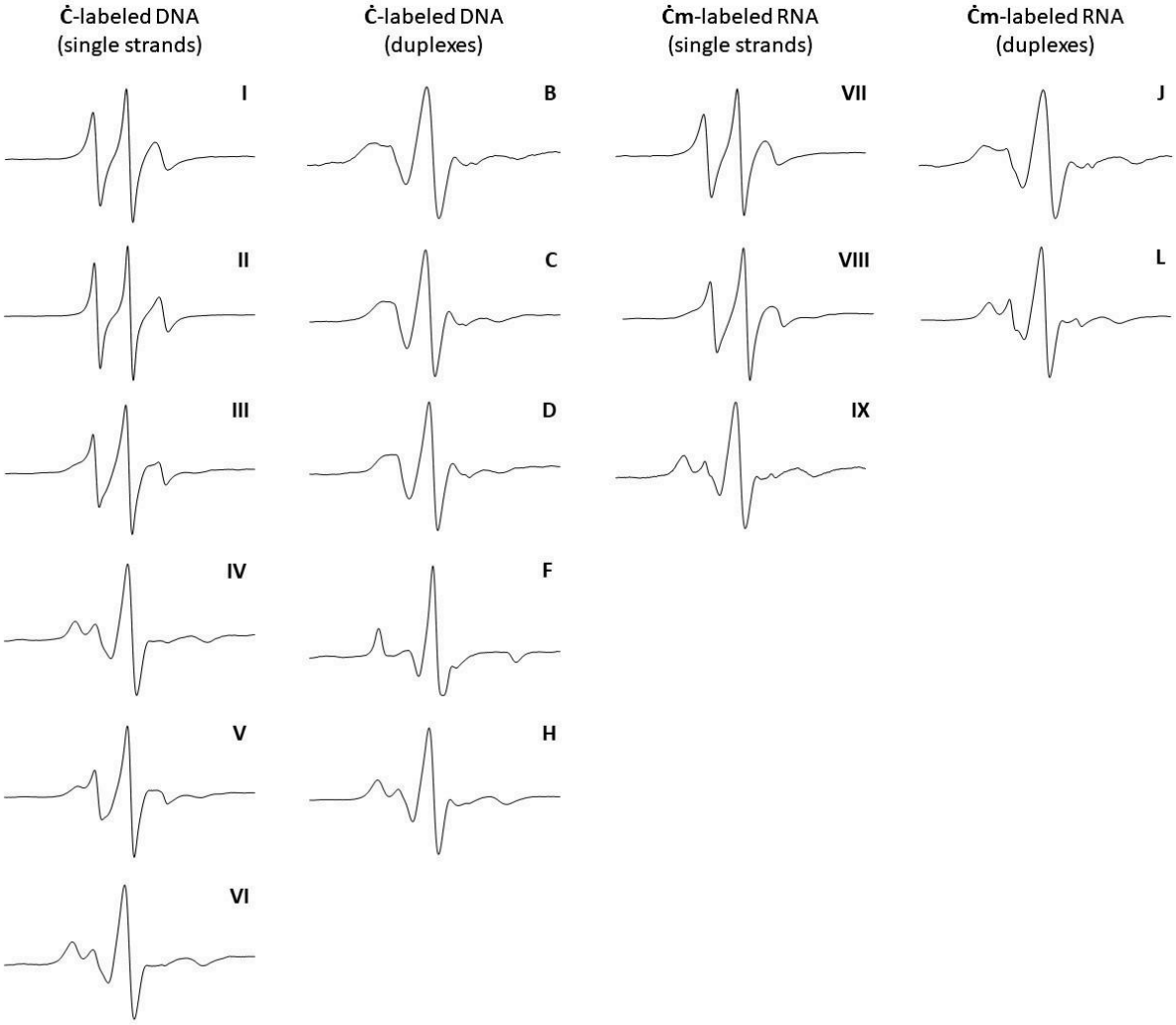

Figure S50. EPR spectra of spin-labeled oligonucleotides.

HPLC analyses of enzymatic digests

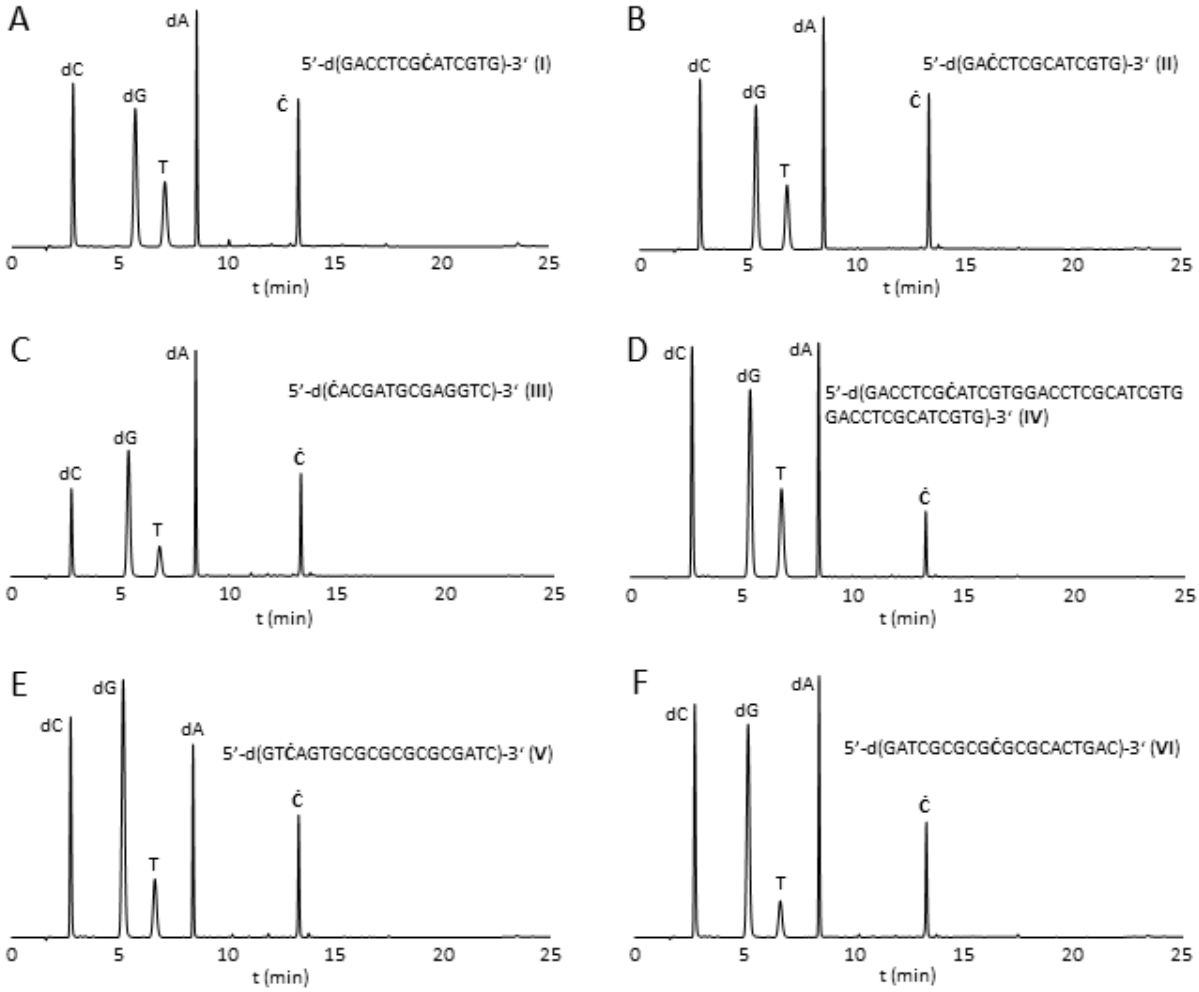

Figure S51. HPLC chromatograms of DNA oligonucleotides after enzymatic digestion with snake venom phosphodiesterase, nuclease P1, and alkaline phosphatase.[1-2]

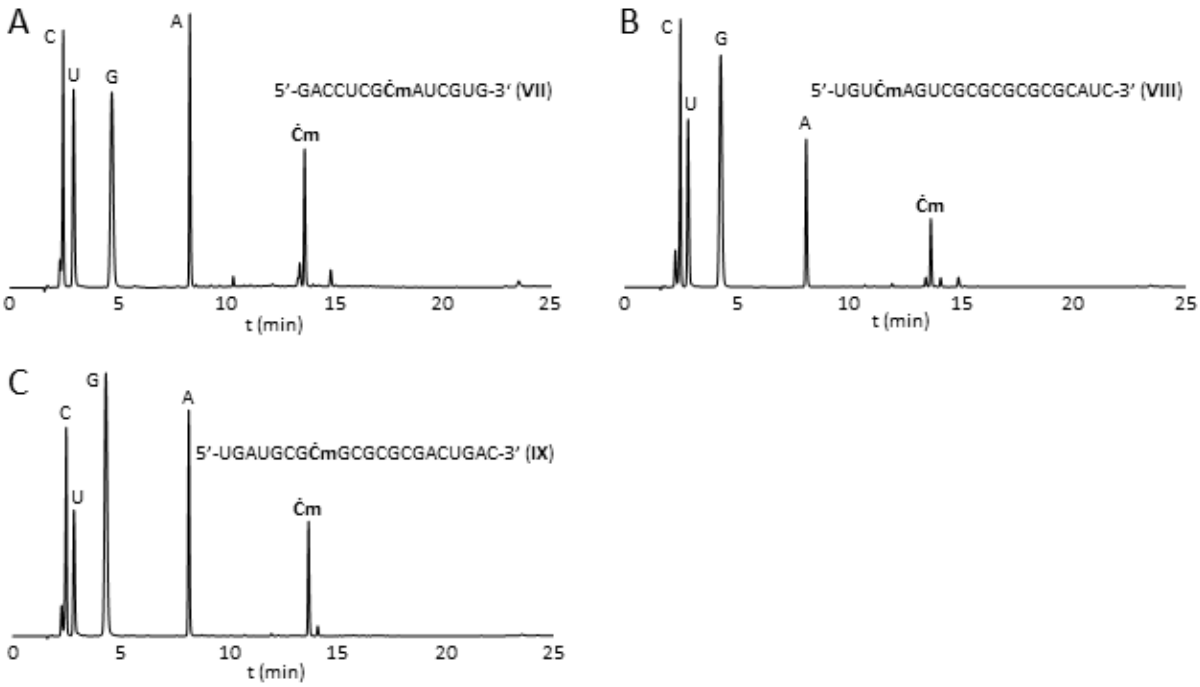

Figure S52. HPLC chromatograms of RNA oligonucleotides after enzymatic digestion with snake venom phosphodiesterase, nuclease P1, and alkaline phosphatase.[1-2]

Thermal denaturation curves of spin-labeled oligonucleotide duplexes

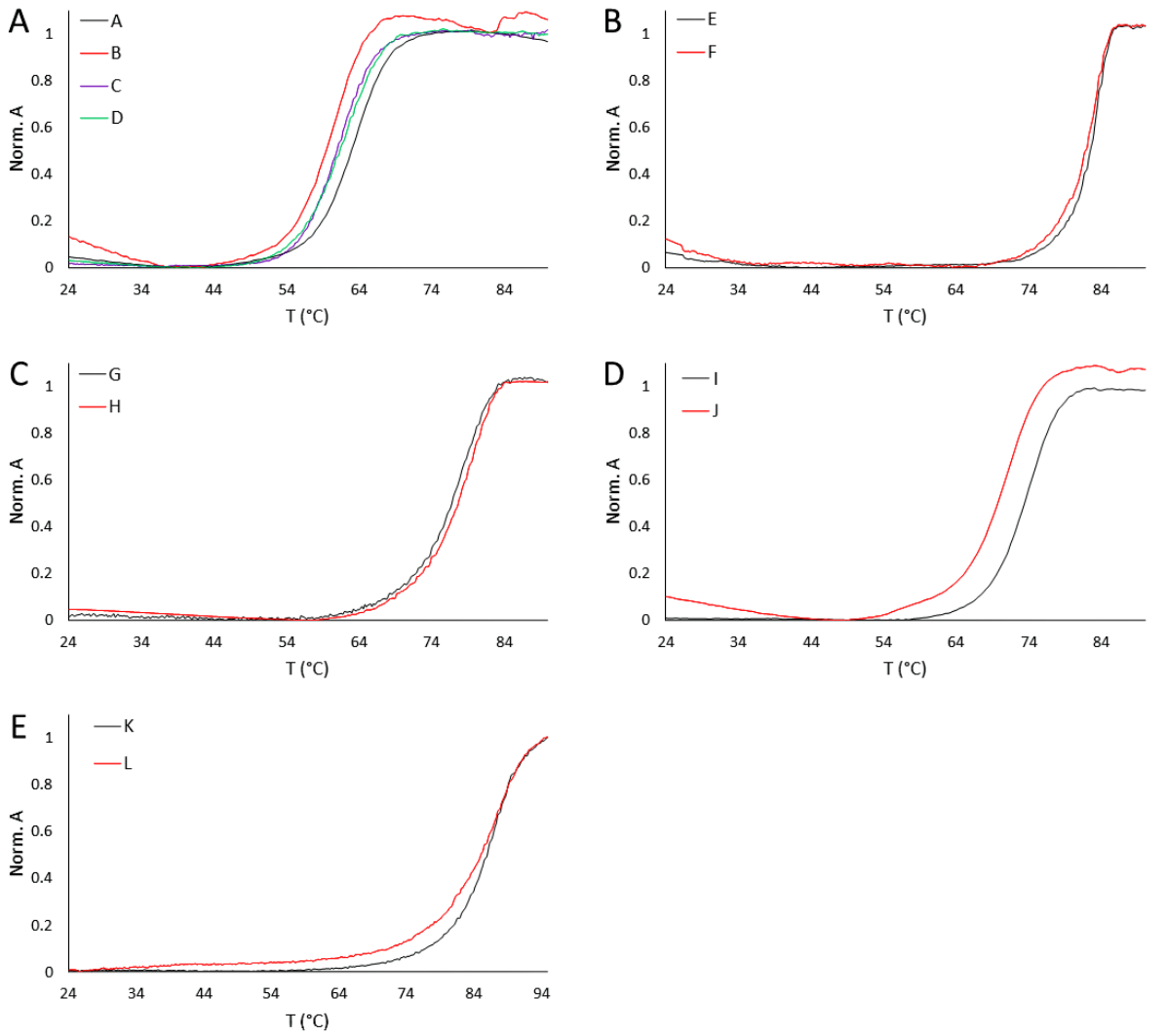

Figure S53. Thermal denaturing analysis of duplexes A, B, C, D (**A**); E, F (**B**); G, H (**C**); I, J (**D**); K, L (**E**).

CD spectra of oligonucleotide duplexes

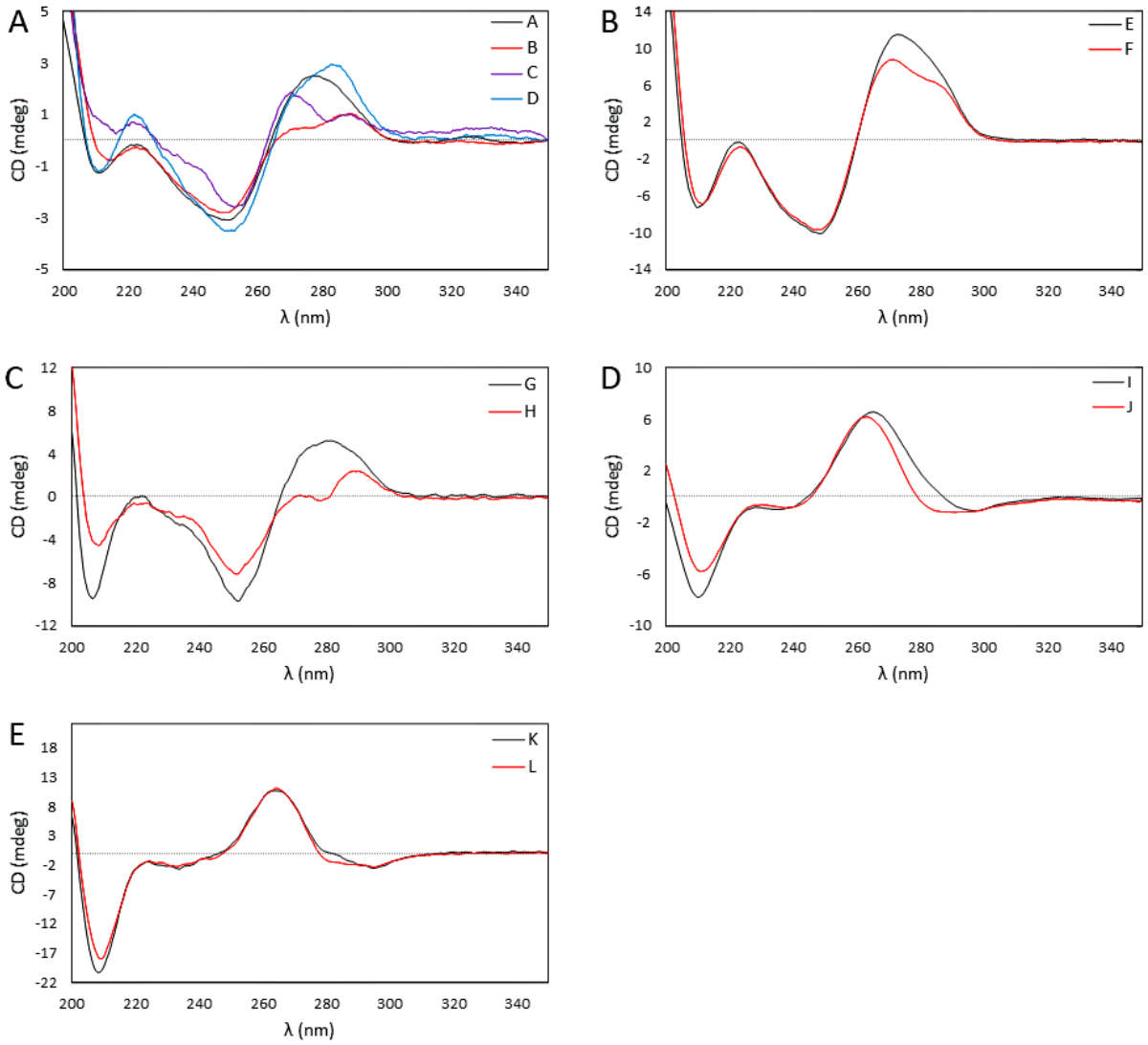

Figure S54. CD spectra of duplexes A, B, C, D (**A**); E, F (**B**); G, H (**C**); I, J (**D**); K, L (**E**).

References

1. Juliusson, H. Y.; Segler, A.-L. J.; Sigurdsson, S. T., Benzoyl-protected hydroxylamines for improved chemical synthesis of oligonucleotides containing nitroxide spin labels. *Eur. J. Org. Chem.* **2019,** *2019* (23), 3799-3805.
2. Cekan, P.; Smith, A. L.; Barhate, N.; Robinson, B. H.; Sigurdsson, S. T., Rigid spin-labeled nucleoside Ç: a nonperturbing EPR probe of nucleic acid conformation. *Nucleic Acids Res.* **2008,** *36* (18), 5946-5954.